Transactions of the ASME®

Journal of Turbomachinery

Published Quarterly by The American Society of Mechanical Engineers

VOLUME 115 • NUMBER 4 • OCTOBER 1993

TECHNICAL PAPERS

ANNOUNCEMENTS

Technical Editor, **T. H. OKIISHI**
Associate Technical Editors
Gas Turbine
E. M. GREITZER (1994)
Nuclear Engineering
H. H. CHUNG (1996)
Power
P. H. GILSON (1996)

BOARD ON COMMUNICATIONS
Chairman and Vice-President
R. D. ROCKE

Members-at-Large
T. BARLOW, T. DEAR, L. KEER,
J. KITTO, W. MORGAN, E. M. PATTON,
S. PATULSKI, R. E. REDER, R. SHAH,
A. VAN DER SLUYS, F. M. WHITE,
J. WHITEHEAD

OFFICERS OF THE ASME
President, **J. H. FERNANDES**
Executive Director
D. L. BELDEN
Treasurer
R. A. BENNETT

PUBLISHING STAFF
Mng. Dir., Publ.,
CHARLES W. BEARDSLEY
Managing Editor,
CORNELIA MONAHAN
Sr. Production Editor,
VALERIE WINTERS
Production Assistant,
MARISOL ANDINO

Transactions of the ASME, Journal of Turbomachinery (ISSN 0889-504X) is published quarterly (Jan., Apr., July, Oct.) for $130.00 per year by The American Society of Mechanical Engineers, 345 East 47th Street, New York, NY 10017. Second class postage paid at New York, NY and additional mailing offices. POSTMASTER: Send address change to Transactions of the ASME, Journal of Turbomachinery, c/o THE AMERICAN SOCIETY OF MECHANICAL ENGINEERS, 22 Law Drive, Box 2300, Fairfield, NJ 07007-2300.
CHANGES OF ADDRESS must be received at Society *headquarters seven weeks before they are to be* effective. Please send old label and new address.
PRICES: To members, $40.00, annually; to nonmembers, $130.00.
Add $24.00 for postage to countries outside the United States and Canada.
STATEMENT from By-Laws. The Society shall not be responsible for statements or opinions advanced in papers or . . . printed in its publications (B7.1, Par. 3).
COPYRIGHT © 1993 by The American Society of Mechanical Engineers. Authorization to photocopy material for internal or personal use under circumstances not falling within the fair use provisions of the Copyright Act is granted by ASME to libraries and other users registered with the Copyright Clearance Center (CCC) Transactional Reporting Service provided that the base fee of $3.00 per article is paid directly to CCC, 27 Congress St., Salem, MA 01970. Request for special permission or bulk copying should be addressed to Reprints/Permission Department.
INDEXED by Applied Mechanics Reviews and Engineering Information, Inc.
Canadian Goods & Services
Tax Registration #126148048

Downloaded 01 Jun 2010 to 171.66.16.52. Redistribution subject to ASME license or copyright; see http://www.asme.org/terms/Terms_Use.cfm

The 1993 IGTI Scholar Lecture

Loss Mechanisms in Turbomachines

J. D. Denton
Whittle Laboratory,
Cambridge University
Engineering Department,
Cambridge, United Kingdom

The origins and effects of loss in turbomachines are discussed with the emphasis on trying to understand the physical origins of loss rather than on reviewing the available prediction methods. Loss is defined in terms of entropy increase and the relationship of this to the more familiar loss coefficients is derived and discussed. The sources of entropy are, in general: viscous effects in boundary layers, viscous effects in mixing processes, shock waves, and heat transfer across temperature differences. These are first discussed in general and then the results are applied to turbomachinery flows. Understanding of the loss due to heat transfer requires some discussion of cycle thermodynamics. Sections are devoted to discussing blade boundary layer and trailing edge loss, tip leakage loss, endwall loss, effects of heat transfer, and miscellaneous losses. The loss arising from boundary layer separation is particularly difficult to quantify. Most of the discussion is based on axial flow machines, but a separate section is devoted to the special problems of radial flow machines. In some cases, e.g., attached blade boundary layers, the loss mechanisms are well understood, but even so the loss can seldom be predicted with great accuracy. In many other cases, e.g., endwall loss, the loss mechanisms are still not clearly understood and prediction methods remain very dependent on correlations. The paper emphasizes that the use of correlations should not be a substitute for trying to understand the origins of loss, and suggests that a good physical understanding of the latter may be more valuable than a quantitative prediction.

1 Introduction

Efficiency is probably the most important performance parameter for most turbomachines. This is especially true for gas turbine engines, whether used for aircraft propulsion or for land-based power plants, because their net power output is the difference between the turbine work and the compressor work. These are roughly in the ratio 2:1 so a small change in the efficiency of either component causes a much larger proportional change in the power output.

Over the years enormous effects have been expended in trying to improve the efficiency of all types of turbomachines, and for many large machines the total-to-total efficiency is now over 90 percent. This makes further improvements ever more difficult to obtain; however, advances are still possible, not only in the efficiency itself but also in the amount, and hence cost, of the development work needed to achieve the required performance. Present levels of efficiency have been achieved by an ever-improving understanding of the fluid mechanics and thermodynamics of the flow, which in turn has been obtained by a combination of improved experimental and theoretical methods applied both to whole machines and to individual components. In particular the advent of modern numerical methods of flow calculation has greatly improved our ability to model the flow through a machine.

The factors influencing efficiency are extremely complex. Before the advent of the aircraft gas turbine they were scarcely recognized and the development of turbomachines such as steam and hydraulic turbines, pumps, and fans proceeded largely on a trial and error basis. The explosion of research on aircraft engines in the 1940s and 50s led to a great improvement in our understanding and several performance prediction methods were developed, e.g., Howell (1945), and Ainley and Mathieson (1951), some of which are still in use today. These methods categorized the sources of loss in the machine, typically as profile loss, secondary (or endwall) loss, and tip leakage loss, and attempted to predict each independently of the others. The predictions were usually based on correlations of experimental data obtained either from cascade tests or from the performance of actual machines. In some cases analytical models of the loss production mechanisms were formulated, e.g., Carter (1948), but these were usually highly idealized.

These performance prediction methods were widely used in the 60s and 70s with comparatively little development. Although the predictions of the individual loss components were sometimes shown to be of very limited accuracy (Denton, 1973; Dunham, 1970), the overall methods were empirically tuned by each manufacturer to obtain agreement with his existing machines and were then extrapolated to predict the performance of new designs. In this way the efficiency could usually be predicted to an accuracy of about ±2 percent. This success sometimes led to a view that the predictions were based on a sound understanding of the flow physics. It is the author's

---

Contributed by the International Gas Turbine Institute and presented at the International Gas Turbine and Aeroengine Congress and Exposition, Cincinnati, Ohio May 24-27, 1993. Manuscript received at ASME Headquarters April 1993. Paper No. 93-GT-435. Associate Technical Editor: H. Lukas.

view that this is seldom the case and that the success of these methods has led to an excessive reliance upon them and a reluctance to query their basic principles and assumptions. There have been many instances where a designer was unwilling to try out a new idea because a 30-year-old loss correlation predicted that it would give no improvement.

In the late 1970s and 1980s the advent of new instrumentation, e.g., laser anemometer measurements and ensemble-averaged hot-wire data, led to a greatly improved understanding of the flow, both in cascades and in actual machines. Better numerical predictions of the flow also contributed to this understanding, especially as regards three-dimensional effects. These new measurements and calculations showed that the real flow in a turbomachine is extremely complicated due to both three-dimensional effects and unsteadiness. In particular boundary layer transition was found to be a much more complex phenomenon than previously imagined (Mayle, 1992). Although the simple models used for performance prediction were shown to be grossly oversimplified, it was not apparent how they could be extended to include the new physics. The latter was too complex to be described by a simple model while numerical solutions were (and are) not yet accurate enough to give *quantitative* predictions of unsteady turbulent flow.

The result of these developments is currently that, while the improved understanding of the flow has been assimilated by many research workers and designers, most practical performance prediction methods continue to be based on correlations. Such correlations can tell us nothing about new design features that were not available at the time the correlation was developed. For example, such features as three-dimensional blade stacking for turbines or end-bending for compressors are not included in any published performance prediction method. Although the effects of such geometric changes on the inviscid flow can now be predicted numerically, their effects upon the loss can still not be quantified. In these circumstances a designer can only use his judgment and understanding of the flow physics in deciding on desirable changes. It is the author's view that a good physical understanding of the flow, and particularly of the origins of loss, is more important to the designer than is the availability of a good but oversimplified loss correlation. The objectives of this paper are to try to help young engineers to develop this understanding and to make more experienced engineers see things in a new light.

Most publications are concerned with emphasizing how well their authors understand the problem they are addressing. In contrast this paper will emphasize our lack of understanding of many loss generating mechanisms in the hope that if we realize our limitations we will more easily be able to overcome them.

2 Loss Components and Loss Coefficients

The historical breakdown of loss into "profile loss," "endwall loss," and "leakage loss" continues to be widely used although it is now clearly recognized that the loss mechanisms are seldom really independent.

Profile loss is usually taken to be the loss generated in the blade boundary layers well away from the end walls. It is often assumed that the flow here is two dimensional so the loss may be based on two-dimensional cascade tests or boundary layer calculations. The extra loss arising at a trailing edge is usually included as profile loss.

Endwall loss is still sometimes referred to as "secondary" loss because it arises partly from the secondary flows generated when the annulus boundary layers pass through a blade row. However, it will become clear that the loss does not arise directly from the secondary flow but is due to a combination of many factors. It is often difficult to separate endwall loss from profile loss and leakage loss and the title "secondary loss" is sometimes taken to include all the losses that cannot otherwise be accounted for.

Tip leakage loss arises from the leakage of flow over the

Nomenclature

A = area
A_r = aspect ratio
C = chord
C_d = dissipation coefficient
C_p, C_v = specific heat capacities
C_{pb} = base pressure coefficient
C_s = blade surface length
C_f = skin friction factor
C_o = velocity based on stage isentropic enthalpy change
C_x = blade axial chord
D = drag force
f = frictional force per unit mass
F = total frictional force
g = tip clearance
H = boundary layer or wake shape factor
h = static enthalpy, blade height
h_o = stagnation enthalpy
I = momentum flux = $PA+mV$
M = Mach number
m = mass flow rate
m_{fc} = mass fraction of coolant
p = blade pitch
P = static pressure
P_o = stagnation pressure
Q, q = heat flow
R = gas constant
Re = Reynolds number based on blade chord
Re_θ = Reynolds number based on momentum thickness
r = radius
S = total entropy
s = specific entropy
s_δ = specific entropy at edge of boundary layer
$\dot{S}_a$ = entropy creation rate per unit surface area
$\dot{S}_v$ = entropy creation rate per unit volume
T = static temperature
T_o = stagnation temperature
T_q = blade row torque
t = trailing edge thickness
U = blade rotational speed
V = flow velocity
V_o, V_δ = blade surface velocity, at edge of boundary layer
w = throat width
x, y, z = Cartesian coordinates
Y = stagnation pressure loss coefficient
z = distance along streamline
α = flow angle measured from the axial direction
γ = specific heat ratio
δ = boundary layer overall thickness
δ^* = boundary layer displacement thickness
δ_e = boundary layer energy thickness
η, η_c = efficiency, cycle efficiency
ϕ = flow coefficient = V_x/U
ρ = fluid density
ψ = stage loading coefficient = $\Delta h_o/U^2$
τ = shear stress
θ = boundary layer momentum thickness
ζ_s, ζ = entropy and energy loss coefficient

Subscripts

1 = at inlet to blade row or stage
2 = at exit from blade row or stage
δ = at the edge of the boundary layer
c = coolant flow
is = isentropic
m = mainstream flow
o = stagnation conditions
te = just before the trailing edge

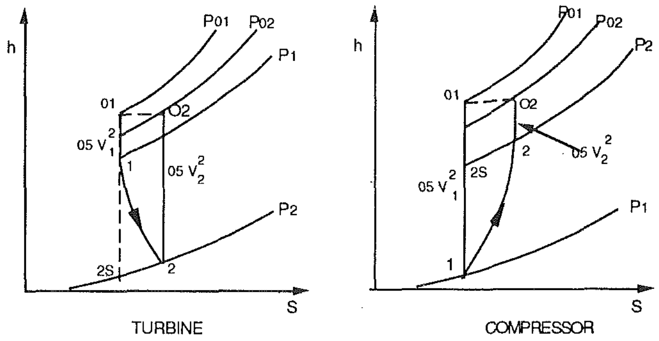

Fig. 1 Enthalpy-entropy diagram for cascade flow

tips of rotor blades and the hub clearance of stator blades. The detailed loss mechanisms clearly depend on whether the blades are shrouded or unshrouded. The interaction between the leakage loss and the endwall loss may be very strong, especially for unshrouded compressor blades, and some methods do not distinguish between endwall loss and leakage loss.

The relative magnitudes of the above three categories of loss are dependent on the type of machine and on such details as blade aspect ratio and tip clearance. However, in many machines the three are comparable in magnitude, each accounting for about 1/3 of the total loss.

So far we have used the word "loss" without defining what we really mean by it. In general any flow feature that reduces the efficiency of a turbomachine will be called loss, but this does not include factors that affect the cycle efficiency as opposed to the turbine or compressor efficiency.

2.1 Definitions of Loss Coefficient. There are many different definitions of loss coefficient in regular use for individual blade rows. Perhaps the most common is the stagnation pressure loss coefficient; referring to Fig. 1 this is defined by

$$Y=(P_{o1}-P_{o2})/(P_{o1}-P_1) \quad \text{for a compressor blade} \qquad (1a)$$

and

$$Y=(P_{o1}-P_{o2})/(P_{o2}-P_2) \quad \text{for a turbine blade} \qquad (1b)$$

The reason that this definition of loss coefficient is so common is that it is easy to calculate it from cascade test data and not because it is the most convenient to use in design.

A more useful loss coefficient for design purposes is the energy or enthalpy loss coefficient; again referring to Fig. 1 this is defined by

$$\zeta=\frac{h_2-h_{2s}}{h_{o2}-h_2} \quad \text{for a turbine blade} \qquad (2a)$$

and

$$\zeta=\frac{h_2-h_{2s}}{h_{o1}-h_1} \quad \text{for a compressor blade} \qquad (2b)$$

where the isentropic final enthalpy, h_{2s}, is the value obtained in an isentropic expansion or compression to the same final static pressure as the actual process. There are many other definitions of blade row loss coefficient in use; these are compared by Brown (1972) who shows that the energy loss coefficient is most likely to be independent of Mach number.

These blade row loss coefficients are perfectly satisfactory for cascade tests but are not directly applicable in machines where, in a rotating blade row, the relative stagnation pressure and the relative stagnation enthalpy can change as a result of changes in radius without there being any implied loss of efficiency. In a machine we define the isentropic efficiency as the ratio of the actual work to the isentropic work and so the only factors that change this efficiency are departures from isentropic flow. These may be due to either heat transfer or to thermodynamic irreversibility. For most machines the flow is closely adiabatic and so only entropy creation by irreversibilities contributes significantly to the loss of efficiency.

From the above we can conclude that the only rational measure of loss in an adiabatic machine is entropy creation. Any irreversible flow process creates entropy and so inevitably reduces the isentropic efficiency. It follows that individual blade row loss coefficients should really be defined in terms of entropy increase rather than stagnation pressure or kinetic energy loss. Entropy is a particularly convenient measure because, unlike stagnation pressure, stagnation enthalpy, or kinetic energy, its value does not depend on whether it is viewed from a rotating or a stationary blade row. Once the entropy increase in every blade row has been calculated the results may be summed to find the entropy increase for the whole machine. If we know one other thermodynamic property of the flow at exit from the machine, e.g., pressure or enthalpy, the state of the fluid leaving it is completely determined and hence the machine efficiency can be calculated.

Entropy is an unfamiliar quantity because it cannot be seen or measured directly, its value can only be inferred by measuring other properties. Basic thermodynamics tells us that for a single phase fluid entropy is a function of any two other thermodynamic properties such as temperature and pressure. For a perfect gas two of the relationships between specific entropy and more familiar quantities are

$$s-s_{\text{ref}}=C_p\ln(T/T_{\text{ref}})-R\ln(P/P_{\text{ref}}) \qquad (3a)$$

and

$$s-s_{\text{ref}}=C_v\ln(T/T_{\text{ref}})-R\ln(\rho/\rho_{\text{ref}}) \qquad (3b)$$

The temperatures, pressures, and densities used in these equations may be either all static values or all stagnation values because by definition the change from static to stagnation conditions is isentropic. Note that these equations only give *changes* of entropy, but this is also what determines turbomachine performance. The absolute value of entropy is always arbitrary.

For adiabatic flow through a stationary blade row stagnation temperature is constant and so entropy changes depend only on stagnation pressure changes via

$$\Delta s=-R\ln(P_{o2}/P_{o1}) \qquad (4a)$$

or, for small changes in stagnation pressure

$$\Delta s=-R\,\Delta P_o/P_o \qquad (4b)$$

Hence for stator blades and cascade flows loss of stagnation pressure can be taken to be synonymous with increase of entropy.

We must always be careful to distinguish between specific and total entropy. When we calculate entropy increases in the future we will usually obtain the total rate of entropy creation and must then divide it by the mass flow rate to obtain the change of specific entropy.

Because great use will be made of entropy throughout this paper it may be useful to introduce an analogy to help to understand it. Entropy may be considered to be like "smoke" that is created within the flow whenever something deleterious to machine efficiency is taking place. For example, "smoke" is continually being created in blade boundary layers and in shock waves. Once created the "smoke" cannot be destroyed and it is convected downstream through the machine and diffuses into the surrounding flow. The concentration of "smoke" at the exit from the machine includes a contribution from every source within the machine and the loss of machine efficiency is proportional to the average concentration of "smoke" at its exit.

We can define an entropy loss coefficient by

$$\zeta_s=\frac{T_2\Delta s}{h_{o2}-h_2} \quad \text{for turbine blades} \qquad (5a)$$

and

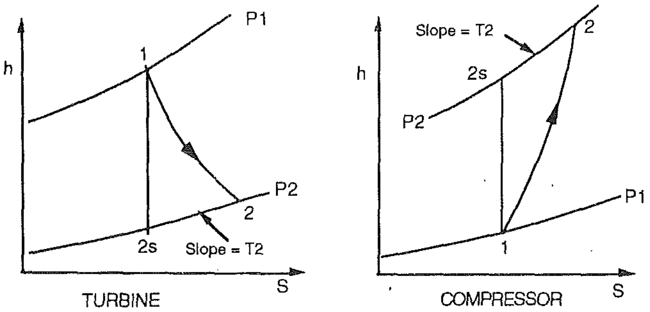

Fig. 2 Expansion and compression processes on the h-s chart

$$\zeta_s = \frac{T_2 \Delta s}{h_{o1} - h_1} \quad \text{for compressor blades} \tag{5b}$$

Using the fact that the slope of the constant pressure lines on the $h-s$ chart is equal to the local static temperature, it can be shown that the difference between the energy and entropy loss coefficients is

$$\zeta_s - \zeta \approx 0.25(\gamma - 1) M^2 \zeta \zeta_s \tag{5c}$$

which is of order 10^{-3} and so is always negligible. Throughout the remainder of this paper no distribution will be made between energy and entropy loss coefficients.

The entropy loss coefficients defined by Eq. (5) may be used directly as a measure of entropy production both in a cascade flow with constant stagnation temperature and also in the flow through the rotating blade rows of a machine where the relative stagnation temperature and pressure change due to change of radius.

At low speeds all definitions of loss coefficient approach the same value. The differences between them are only significant at relative Mach numbers greater than about 0.3. When deriving theoretical results for incompressible flow later in this paper no distinction will be made between the various definitions of loss coefficient.

2.2 Relation of Loss to Drag. In external aerodynamics the ultimate measure of lost performance is the drag on the aircraft or other object under consideration. It is not surprising, therefore, that the concept of drag has been carried over into turbomachinery flows. However, in order to define a drag we must first define a direction in which it acts. The choice of this direction is obvious for external flows but is not at all obvious in turbomachinery where a force acting in the direction of blade motion is essential for work transfer and a force acting in the meridional direction is essential for pressure changes. For example, the skin friction force acting on a highly staggered compressor blade has a large component in the opposite direction to rotation and so contributes to the work input. It is not immediately clear whether or not this work input contributes to the pressure rise.

In incompressible two-dimensional cascade flow it is possible to relate the component of blade force in the vector mean flow direction to the loss of stagnation pressure and hence to the entropy rise. This analysis is given in most textbooks, e.g., Horlock (1958). However, no such simple relationship exists for compressible flow or for flows that are not strictly two dimensional. Even when the relationship is valid it does not help us to understand the origins of loss. For example, does it imply that skin friction on parts of the blade surface that are highly inclined to the vector mean direction do little harm while that on parts of the surface aligned with the vector mean direction do most harm? Again the answer is not apparent.

It is the author's view that the concept of drag is of little use in turbomachinery and should be replaced by the concept of entropy generation. However, there are relationships between the two that can sometimes be useful. It is shown in Appendix 1 that in any flow with constant stagnation enthalpy the rate of entropy increase along a streamline is related to the viscous force per unit mass F_x acting on the fluid in the direction of the streamline by

$$T\frac{ds}{dx} = -F_x \tag{6}$$

For one-dimensional flow in a duct of cross-sectional area A Eq. (6) can be integrated over the duct to give the change in specific entropy Δs along a short length of the duct as

$$T\Delta s = -\frac{\Delta F}{\rho A} \tag{7}$$

where ΔF is the streamwise component of the viscous force exerted by the boundaries on the fluid and may arise either from skin friction or from pressure drag. However, application of the equation in this form is difficult and may be misleading because it is only valid for uniform flow, i.e., with no gradients in the cross-stream direction. Nonuniform flow, even if there are no frictional forces on the walls, can cause the entropy to increase. For example, the mixing of two parallel streams with different velocities is considered in Appendix 2 and is shown to be irreversible even when there is no force acting.

Turning Eq. (6) into one for the total rate of entropy creation in the duct we get

$$\dot{S} = m\dot{s} = -\int \frac{1}{T} \mathbf{V} \cdot \mathbf{F}_v dVol \tag{8}$$

where $\mathbf{V}$ is the local flow velocity vector, $\mathbf{F}_v$ is the vector representing the local viscous force per unit volume, and the integral is over the volume of the duct. This relationship between the viscous forces and entropy creation is always valid for adiabatic flow but it is not generally useful because we need to know the viscous force acting on every particle of fluid, not only the drag on the solid boundaries. It does, however, show that the entropy creation rate is likely to be high in regions where high velocities coincide with high viscous forces.

2.3 Relation of Entropy Change to Machine Efficiency. The relationship between entropy creation and machine isentropic efficiency can be clearly seen by considering the expansion or compression process on an enthalpy-entropy diagram, Fig. 2.

Neglecting any difference between static and stagnation conditions and assuming no external heat transfer, the efficiency is closely given by

$$\eta_t \approx \frac{h_1 - h_2}{h_1 - h_2 + T_2(s_2 - s_1)} \quad \text{for a turbine} \tag{9a}$$

and by

$$\eta_c \approx 1 - \frac{T_2(s_2 - s_1)}{(h_2 - h_1)} \quad \text{for a compressor} \tag{9b}$$

The approximation only arises because we have assumed that the static temperature is constant along the line $2-2s$ in Fig. 2. This is unlikely to produce a significant error in most practical cases.

We see (Eq. (9b)) that the loss of efficiency of a compressor is directly proportional to the increase in specific entropy through the machine and also to its exit temperature. The same is very closely true for a turbine (Eq. (9a)) provided that the efficiency is high.

When entropy is created by a fluid dynamic process, the magnitude of entropy creation is usually inversely proportional to the *local* temperature, e.g., $T\Delta s = \zeta \times 1/2\, V^2$ is a common result. The loss coefficient ζ is unlikely to depend on temperature and so a flow process with fixed values of loss coefficient and flow velocity creates less entropy at a high temperature than does the same process taking place at a lower temperature.

The enthalpy change through a stage is always proportional to V^2 so the changes in enthalpy and entropy as fluid passes through a machine are related by

$$\Delta s \propto \zeta \Delta h / T \tag{10}$$

i.e., for constant values of loss coefficient, the magnitude of the slope dh/ds of the expansion or compression line on the $h-s$ chart is proportional to temperature. This is reflected in the slopes of the compression and expansion processes illustrated in Fig. 2.

Since the loss of *overall* isentropic efficiency is proportional to the *total* entropy creation for both compressors and turbines, an irreversible flow process taking place at high temperatures produces a lower loss of *overall* efficiency than does the same process at low temperatures. This is the origin of the well-known "reheat effect," which causes the polytropic efficiency of a machine to be different from the isentropic efficiency. The result is that irreversibilities in the flow through the high-pressure stages of turbines and compressors tend to be less deleterious to the overall isentropic efficiency than those in the low-pressure stages. An estimate of the contribution of individual stage efficiencies to the overall isentropic efficiency may be obtained by summing the stage entropy increases, giving

$$\frac{1-\eta_{\text{overall}}}{\eta_{\text{overall}}}=\frac{T_{\text{exit}}}{\Delta h_{\text{overall}}}\sum_{\text{all stages}}\frac{(1-\eta_{\text{stage}})\Delta h_{\text{stage}}}{\eta_{\text{stage}}T_{2\,\text{stage}}} \tag{11}$$

The importance of this "reheat effect" increases with the overall temperature ratio of the machine. It is of approximately equal magnitude in high-pressure-ratio steam turbines and in aircraft engine compressors and turbines and is negligible for low-speed machines.

2.4 Mechanisms for Entropy Creation. Basic thermodynamics tells us that entropy creation occurs due to the following fluid dynamic processes:

1 Viscous friction in either boundary layers or free shear layers. The latter include the mixing processes in, for example, a leakage jet.
2 Heat transfer across finite temperature differences, e.g., from the mainstream flow to a flow of coolant gas.
3 Nonequilibrium processes such as occur in very rapid expansions or in shock waves.

The remainder of this paper will examine the entropy creation by each of these mechanisms in detail and will show how it can be quantified or approximated in practical situations.

3 Entropy Generation in Boundary Layers

Appendix 1 derives an expression for the rate of change of entropy flux in a two-dimensional boundary layer as

$$\dot{S}_a=\frac{d}{dx}\int_0^\delta(\rho V_x(s-s_\delta))dy=\int_0^\delta\frac{1}{T}\tau_{yx}dV_x \tag{12}$$

$\dot{S}_a$ may be thought of the rate of entropy production per unit surface area. Note that this is the *total* rate of entropy creation not the change in specific entropy.

Locally, within the boundary layer, the rate of entropy creation *per unit volume* is

$$\dot{S}_v=\frac{1}{T}\tau\frac{dV}{dy} \tag{13}$$

This may be interpreted as the viscous shear work, $\tau dV/dy$, being converted to heat at temperature T.

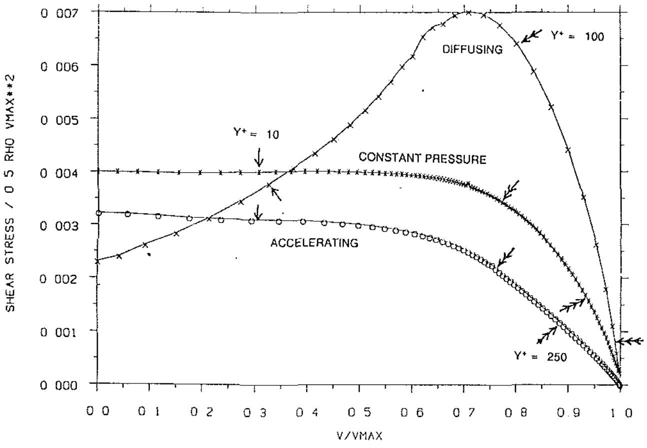

Fig. 3 Variation of shear stress with velocity through boundary layers with $\text{Re}_\theta = 1000$

Typical variations of shear stress with velocity through turbulent boundary layers with $\text{Re}_\theta \approx 1000$ are given in Fig. 3. These were obtained from calculations using the Cebeci and Carr (1978) boundary layer code. Equation (12) shows that the area under the $\tau - V$ curve is proportional to the rate of entropy creation per unit surface area. It is noteworthy that for most boundary layers the velocity changes most rapidly near the surface and so most of the entropy generation is concentrated in the inner part of the layer. This is especially the case for turbulent boundary layers where much of the entropy creation occurs within the laminar sublayer and the logarithmic region. The well-known "universal velocity profile" of the boundary layer shows that only the outer part of the layer ($Y^+ > 500$) is greatly affected by the streamwise pressure gradient. Since this part generates little of the entropy, this result suggests that the entropy generation may be relatively insensitive to the detailed state of the boundary layer. Dawes (1990) gives a more detailed breakdown of the entropy generation in a boundary layer showing that about 90 percent of the entropy generation occurs within the inner part of the layer.

For practical use it is convenient to turn the entropy production rate into a dimensionless dissipation coefficient, which is defined by

$$C_d = T\dot{S}_a/\rho V_\delta^3 \tag{14}$$

where V_δ is the velocity at the edge of the boundary layer.

The exact magnitude of the dissipation coefficient cannot be calculated without knowing full details of the state of the boundary layer. However, correlation of much experimental work has led to some general results. These are described by Schlichting (1966). The most striking feature is that for turbulent boundary layers the dissipation coefficient is much less dependent on the state of the boundary layer, i.e., on the shape factor, than is the more familiar skin friction coefficient. Schlichting gives the following equation for turbulent boundary layers with $1.2 < H < 2.0$ and with $10^3 < \text{Re}_\theta < 10^5$:

$$C_d = 0.0056\,\text{Re}_\theta^{-1/6} \tag{15}$$

This equation is compared with results from the Cebeci calculation for three different boundary layers in Fig. 4. The boundary layer code gives similar results to Eq. (15) for a constant pressure boundary layer but the accelerated boundary layer has a significantly lower rate of entropy generation. The diffusing boundary layer represents a compressor blade suction surface at a Reynolds number of 5×10^5 where the boundary layer is near separation and the dissipation coefficient is predicted to be about 45 percent greater than that suggested by Eq. (15).

This comparison suggests that for $\text{Re}_\theta > 500$ the dissipation coefficient is relatively insensitive to the boundary layer thickness (i.e., proportional to $\theta^{-1/6}$). In the range $500 < \text{Re}_\theta < 1000$ it is also relatively insensitive to the shape factor of the boundary layer. Denton and Cumpsty (1987) suggest that for many turbomachine blades where the average Re_θ is of order 1000, a reasonable approximation is simply to take

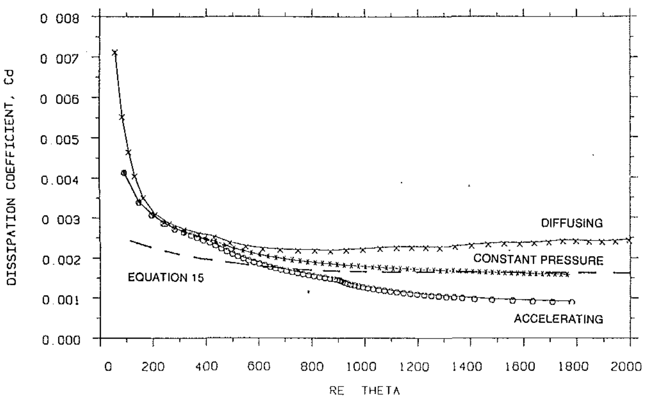

Fig. 4 Calculated dissipation coefficients for turbulent boundary layers

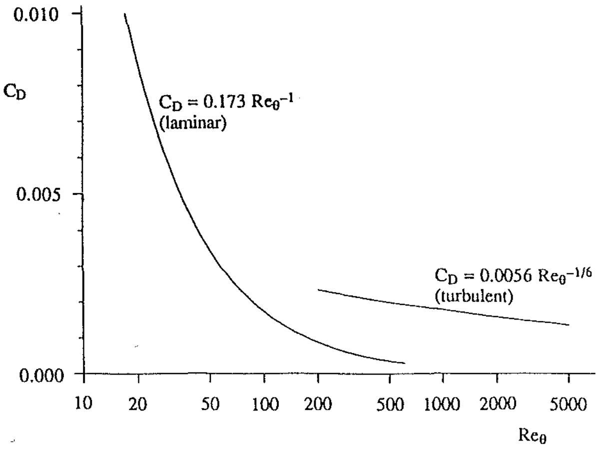

Fig. 5 Dissipation coefficient for laminar and turbulent boundary layers

$$C_d = 0.002 = \text{const} \tag{16}$$

for turbulent boundary layers. Moore and Moore (1983) found a similar value of $C_d = 0.0024$ for one particular boundary layer. However, Eq. (15) and the results from Fig. 4 suggest that a value of $C_d = 0.0018$ may be more appropriate.

For laminar boundary layers, the dissipation coefficient is more dependent on boundary layer thickness. Truckenbrodt (1952) quotes results showing

$$C_d = \beta\,\text{Re}_\theta^{-1} \tag{17}$$

where the value of β varies only slightly with shape factor, being about 0.17 for typical laminar boundary layers. The same author also quotes an analytical result giving $\beta = 0.173$ for a laminar boundary layer with no pressure gradient.

An analytical result can be derived for laminar boundary layers by integrating the well-known Pohlhausen family of velocity profiles (Schlichting, 1978, p. 206) to give

$$C_d = \text{Re}_\theta^{-1}\,(0.1746 + 0.0029\lambda + 0.000076\lambda^2) \tag{18}$$

where terms with higher powers of λ have been neglected. λ is the Pohlausen pressure gradient parameter whose value ranges from $+12$ for a highly accelerated boundary layer to -12 at separation. The corresponding range of β is 0.220 to 0.151. Hence Eq. (18) confirms that the dissipation coefficient is relatively insensitive to the state of the boundary layer, the dissipation being slightly increased in an accelerating boundary layer and reduced in one near separation. Since laminar boundary layers are much more likely to exist on turbomachinery blades with favorable pressure gradients, i.e., with λ positive, a typical value of $\beta = 0.2$ as suggested by Denton and Cumpsty is realistic.

The variation of C_d with Re_θ obtained from Eqs. (15) and (17) is shown in Fig. 5. It is noteworthy that in the Re_θ range where either a laminar or a turbulent boundary layer could exist, i.e., $300 < \text{Re}_\theta < 1000$, the dissipation in the laminar boundary layer is much less (by a factor of between 2 and 5) than that in the turbulent one. This large difference highlights the importance of predicting boundary layer transition on turbomachine blades.

There are no known results for the effects of Mach number on the dissipation coefficient. However, over the Mach number range prevalent in turbomachines, $0 < M < 2$, the effects of Mach number on skin friction are generally considered to be small. The effects on entropy generation, as shown by Eq. (12), should be similar. However, the increase in temperature near the surface, where most of the entropy generation is taking place, implies that the surface temperature rather than the free-stream static temperature should be used in Eq. (12). For adiabatic surfaces this will not be significantly different from the stagnation temperature of the flow.

The entropy increase of fluid in the boundary layer may be used to define an entropy thickness of the boundary layer by

$$\delta_s = \frac{T_\delta}{\rho_\delta V_\delta^3}\int_0^\delta \rho V(s - s_\delta)\,dy \tag{19}$$

When defined in this way the entropy thickness becomes identical to the more familiar energy thickness δ_e of the boundary layer at low speeds.

Since all the entropy produced upstream of a point on the surface is contained in the boundary layer at that point, we can write an equation relating the total entropy generation to the local entropy thickness as

$$\dot{S} = \frac{\rho V_\delta^3 \delta_s}{T_\delta} = \int_0^x \frac{\rho V_\delta^3 C_d}{T_\delta}\,dx \tag{20}$$

The terms in this equation represent all of the entropy produced up in the boundary layer up to the point in question; in particular, at the trailing edge they represent all the entropy produced on the blade surface.

4 Entropy Generation in Mixing Processes

Entropy creation due to viscous shear occurs whenever a fluid is subject to a rate of shear strain. The rate of shear strain is not the same as the vorticity and so viscous dissipation is not confined to boundary layers. Even in the mainstream of an irrotational flow the fluid is being sheared and so entropy is being created (e.g., a free vortex flow will gradually change to a forced vortex, which has no shearing) but the rate of creation is usually negligible compared to that in shear layers.

Relatively high rates of shearing occur in wakes, at the edges of separated regions, in vortices, and in leakage jets. Since these are usually associated with turbulent flow the effective viscosity may be large, typically over 100 times the laminar viscosity, and the local entropy creation rates are considerable. The flow processes involved are extremely complex and often unsteady so it is seldom possible to quantify the *local* entropy creation rates. However, in many such processes the *overall* entropy creation can be calculated from a control volume analysis, which applies the equations for the conservation of mass, energy, and momentum between an upstream boundary, at which the flow is assumed known, and a far downstream boundary where the mixing processes are assumed to have restored the flow to a completely uniform condition. They key feature that makes such an approach possible is that we know that mixing will continue until the flow has become uniform, even although we do not know how long this will take. For example, the velocity deficit in a wake decays continually with distance downstream; we do not need to know the exact rate of decay to predict the overall result. As long as the mixing is effectively complete by the time the flow leaves the region of

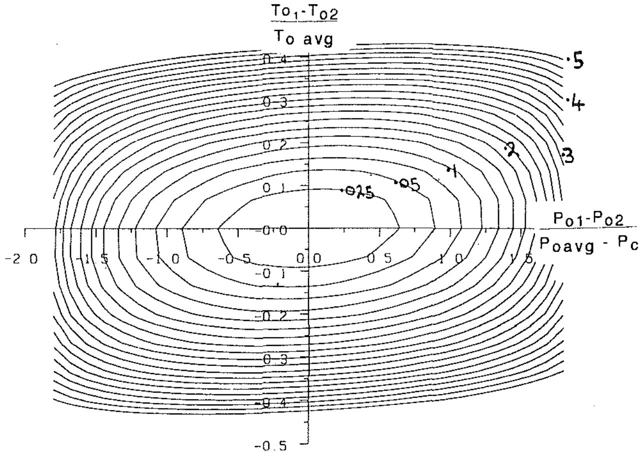

Fig. 6 Entropy loss coefficient for the mixing of two streams at different stagnation pressures and temperatures. See Fig. A2.1 for notation.

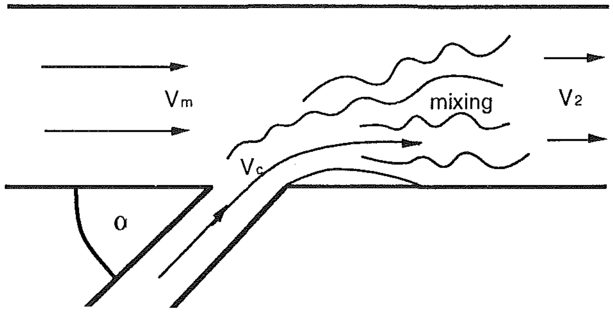

Fig. 7 Mixing of injected flow with a mainstream flow at a different velocity and temperature

interest we can calculate the total entropy created without knowing the details of how or where the mixing takes place.

As an example of such a mixing process Appendix 2 gives the theory for the mixing of two streams of fluid, which initially have different stagnation temperatures and pressures, in a constant area duct. Results for the entropy loss coefficient are presented in Fig. 6 for the case when the two streams initially occupy equal areas, and it can be seen that the total entropy creation depends on the difference in both the stagnation temperature and the stagnation pressure of the flows.

A great simplification of the theory is possible for the case when the flow rate of one of the steams is small. The theory for this case is presented by Shapiro (1953). For the case illustrated in Fig. 7 when a *small* flow of fluid, mass flow rate, m_c, is injected at an angle α and with velocity V_c and stagnation temperature T_{oc} into a mainstream flow, which has mass flow rate m_m, velocity V_m, Mach number M_m, and stagnation temperature T_{om}, the result is

$$\Delta s = C_p \frac{m_c}{m_m}\left\{\left(1+\frac{\gamma-1}{2}M_m^2\right)\frac{T_{oc}-T_{om}}{T_{om}} + (\gamma-1)M_m^2\left(1-\frac{V_c\cos\alpha}{V_m}\right)\right\} \quad (21)$$

If the two streams have the same stagnation temperature, this gives the rate of entropy creation as

$$T m_m \Delta s = T\dot{S} = m_c(V_m^2 - V_m V_c \cos\alpha) \quad (22)$$

This result is for the entropy change of the main flow and does not include the entropy change of the injected flow. It will be extensively used later in this paper. Equations (21) and (22) are valid for both constant pressure and constant area mixing provided that the pressure and area changes are small.

In practice we cannot usually say exactly where mixing takes place and so we may not be able to assume that the pressure and area changes during mixing are small. It is therefore of interest to see how the total entropy production depends on the area in which the mixing takes place. Consider the situation sketched in Fig. 7 where, for simplicity the angle α is chosen to be 90 deg, the flow is assumed incompressible, and the stagnation temperature and pressure of the injected fluid are the same as that of the mainstream. A continuity and momentum balance gives the following result for the *total* entropy creation:

$$T\dot{S} = -(m_m + m_c)\frac{\Delta P_o}{\rho} = 0.5\, V_m^2 m_c\left(2 + 3\frac{m_c}{m_m} + \left(\frac{m_c}{m_m}\right)^2\right) \quad (23)$$

We imagine that the flow rate of the injected fluid m_c is held constant while the height of the duct is changed with V_m constant. Then m_m changes in proportion to the area of the duct and Eq. (23) shows that, provided m_c/m_m is small, the *total* entropy creation does not depend greatly on m_m, i.e., on the area in which the mixing takes place. A similar result is obtained if the mixing is assumed to be at constant pressure rather than at constant area. This helps to justify a common assumption that the mixing (of say a coolant or a tip leakage jet) takes place with the whole mainstream flow rather than just with the adjacent fluid. Eq. (23) shows that most of the entropy creation will have taken place by the time the jet has mixed with about 5 times its own flow rate of the mainstream (i.e., $m_c/m_m = 0.2$) and this will occur within a few diameters of the jet. The remaining entropy generation as the diluted jet mixes with the whole mainstream is much less significant.

Some workers calculate the loss due to mixing of a primary flow with a much smaller secondary flow by simply assuming that all the *relative* kinetic energy of the secondary flow is lost. For the case predicted by Eq. (22) this gives

$$T\dot{S} = 0.5\, m_c(V_m - V_c\cos\alpha)^2 + (V_c\sin\alpha)^2 \quad (24)$$

Comparing Eqs. (22) and (24) show that they give exactly the same result when $V_m = V_c$, but the first equation gives a lower loss when $V_c > V_m$. This is because the lost kinetic energy argument does not account for the static pressure recovery that arises from the momentum of the jet. In most applications the two approaches will give very similar results but the mixing calculation, Eq. (22), is felt to be more correct.

A further important example of a mixing process is the mixing out of a wake behind a trailing edge. Appendix 3 gives the theory for entropy creation due to the mixing out of a wake behind a blunt trailing edge in a constant area passage with (for simplicity only) incompressible flow. The analysis includes the boundary layers on the blade surface immediately upstream of the trailing edge and also the base pressure acting on the trailing edge. The latter is usually below the free-stream pressure by an amount that may be defined in terms of a base pressure coefficient, C_{pb}, by

$$C_{pb} = (P_b - P_{\mathrm{ref}})/(0.5\,\rho\, V_{\mathrm{ref}}^2) \quad (25)$$

where P_{ref} and V_{ref} may be either the far downstream pressure and velocity or the values on the blade surfaces immediately before the trailing edge. The latter definition is used in the following analysis. Typical values of C_{pb} defined on this basis are in the range -0.1 to -0.2, although the value varies greatly with the state of the boundary layer, the shape of the trailing edge, and the ratio of trailing edge thickness to boundary layer thickness.

The resulting expression for the stagnation pressure loss coefficient (which in incompressible flow is identical to the entropy loss coefficient) is derived in Appendix 3 as

$$\zeta = \frac{\Delta P_o}{0.5\,\rho V_{te}^2} = -\frac{C_{pb}t}{w} + \frac{2\theta}{w} + \left(\frac{\delta^* + t}{w}\right)^2 \quad (26)$$

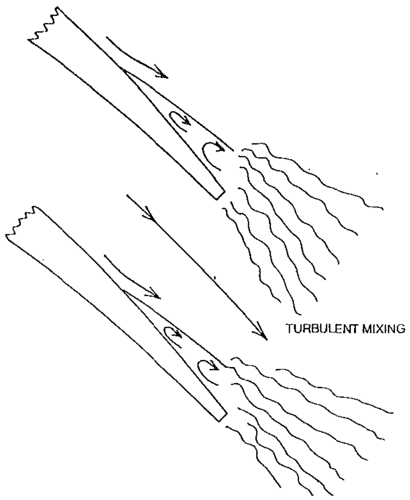

Fig. 8 Trailing edge with a separated boundary layer

Note how this result is independent of the details of the mixing process, which is likely to be unsteady with the formation of a Karman vortex street and with much of the entropy creation due to the viscous decay of the vortices. The details of this process cannot yet be predicted accurately by even the most sophisticated viscous flow calculations, but as we see the overall result is predictable using simple theory.

The theory of Appendix 3 requires an assumption for the average pressure acting on the suction surface downstream of the throat (see Fig. A3.1). Equation (26) assumes that this is the same as the far downstream pressure, P_2. A more common assumption, e.g., Stewart (1955), is that the pressure is the same as the throat pressure P_1. The actual suction surface pressure is likely to lie somewhere between these two assumptions. The author prefers to use the first assumption because it implies that the loss is not affected by the blade stagger, i.e., by the presence of adjacent blades. Since most of the dissipation takes place within a few trailing edge thicknesses this is felt to be realistic. The value assumed for the suction surface pressure has a large effect on the last term of Eq. (26) but not much effect on the other two terms. Fortunately the last term is usually comparatively small.

The major difficulty in applying this and similar theories to real blade rows is knowing the value of the base pressure coefficient. Much early work on this subject, e.g., Stewart et al. (1960), neglected the base pressure completely and so greatly underestimated the importance of trailing edge loss. Typically the value of C_{pb} is about -0.15 and a typical turbine blade trailing edge blockage is 0.05 so the base pressure term contributes about 0.0075 to the loss coefficient while the last term of Eq. (26) contributes about 0.0025. For modern turbine blades the profile loss coefficient is of the order 0.03 and so the trailing edge contributes about 1/3 of the total profile loss. For compressor blades the trailing edge blockage is usually small but the boundary layers are thicker so the last term of Eq. (26) may be more important than the base pressure term.

Physically it is difficult to decide if the low base pressure produces the dissipation in the wake or if the dissipation causes the low base pressure. In fact the two are directly connected via Eq. (26) and anything that changes one must change the other. For example it is well known that for isolated blunt trailing edges the vortex shedding can be suppressed by attaching a splitter plate to the trailing edge; this therefore reduces the dissipation and so increases the base pressure. Similarly, the use of an elliptical rather than a square or semicircular trailing edge delays the separation of the boundary layers and this increases the average base pressure and reduces the dissipation and loss.

When considering base pressure, it would be more meaningful to measure it relative to the average pressure around the trailing edge in an inviscid flow. Since the latter has no loss and no boundary layers, Eq. (26) shows that for incompressible flow this pressure, P_{bo}, is given by

$$\frac{(P_{bo}-P_{te})}{(0.5\,\rho V_{te}^2)} = C_{pbo} = t/w \tag{27}$$

This is a positive base pressure, relative to the pressure P_{te} just upstream of the trailing edge, and any value of base pressure below this value must be associated with a loss.

The fact that the mixed out loss depends on the momentum thickness of the boundary layers at the trailing edge, i.e., the middle term of Eq. (26), is an interesting result. The entropy that has been created in the boundary layers upstream of the trailing edge is measured by their entropy thickness, which, in incompressible flow, is identical to their energy thickness, so the entropy present just before the trailing edge would be

$$T\Delta S_{te} = 0.5\,\rho V_{te}^3\delta_e \tag{28}$$

Hence, for a blade with zero trailing edge thickness, an amount of entropy given by

$$T\Delta S_w = 0.5\,\rho V_{te}^3(2\theta-\delta_e) \tag{29}$$

is being created behind the trailing edge as a direct result of the mixing out of the boundary layers on the blade. This is entropy created by the viscous dissipation in the wake but is an inevitable consequence of the boundary layers on the blade surfaces. For the case of negligible trailing edge thickness the amount of dissipation in the wake depends on the difference between 2θ and δ_e of the boundary layers just upstream of the trailing edge.

The ratio δ_e/θ is a type of shape factor whose value depends on the state of the boundary layer. For a typical turbulent boundary layer its value is about 1.7 (Schlichting, 1978, p. 675) and so, *for thin trailing edges*, the ratio of the entropy present just before the trailing edge to that present far downstream is typically 0.85, i.e., about 15 percent of the total entropy is created behind the trailing edge. For boundary layers near separation this proportion rises to about 22 percent. For separated boundary layers and thick trailing edges an even greater proportion of the entropy is generated downstream and in the limit for a bluff body with very thin boundary layers all the entropy is generated in the wake.

The theory of Appendix 3 also applies to the case where the boundary layers are separated at the trailing edge, as illustrated in Fig. 8, provided that the static pressure just upstream of the trailing edge can still be assumed to be uniform. In this case the value of δ^* is likely to be greater than the trailing edge thickness and Eq. (26) suggests that there will be an extra loss due to the separation given by

$$\zeta_{\text{sep}} = \left(\frac{\delta^{*2}+2t\delta^*}{w^2}\right). \tag{30}$$

This implies that only large separations will cause significant loss, e.g., for a thin trailing edge a separation causing 10 percent blockage produces only 1 percent loss. However, this result makes the dubious assumption that a uniform pressure continues to act over the whole of the trailing edge plane. It is probable that in reality a low pressure extends over much of the separated region giving an increased contribution to the base pressure term in Eq. (26). Physically the separated region will give rise to larger vortices and so greater dissipation in the wake than would the trailing edge alone. On this basis it can be argued that the total dissipation will be roughly proportional to the combined thickness of the trailing edge and separation rather than to the square of the blockage as suggested by Eq. (26). A crude approximation that is compatible with this suggestion is to apply a low base pressure over the combined thickness of the trailing edge plus separation, i.e., to use $(t+\delta^*)$

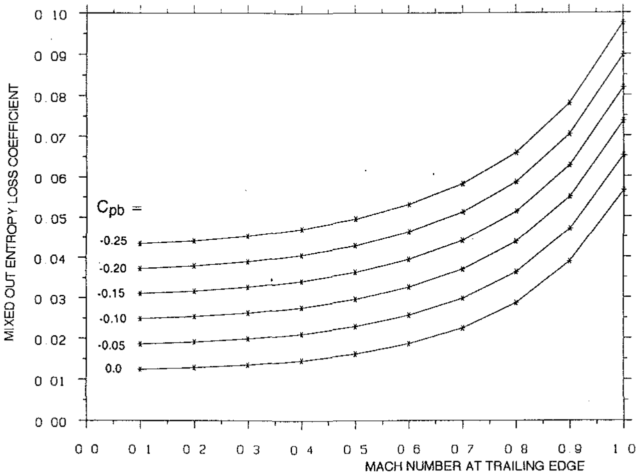

Fig. 9 Variation of trailing edge loss with base pressure coefficient and Mach number for 10 percent throat blockage

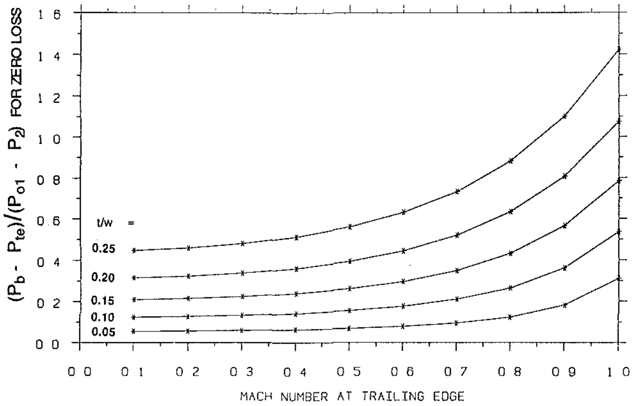

Fig. 10 Base pressure coefficient for zero loss as a function of Mach number and trailing edge blockage

instead of t in the base pressure term of Eq. (26). However, with this assumption the value of the base pressure that should be used remains very uncertain.

From the preceding discussion it can be seen that the influence of a separated boundary layer at the trailing edge remains a major unknown when calculating loss. It is clear from test data (and from Lieblein's correlation of loss versus diffusion factor) that separated boundary layers do give rise to high loss and this can only be reconciled with Eq. (26) by applying a low base pressure over the whole separated region. The author is not aware of any method of predicting this pressure. As discussed in section 7.2 this is likely to be especially important for compressor blades.

A very similar type of calculation can be applied to the mixing of coolant flow injected through the blade surfaces, (e.g., Hartsel, 1972) and also to the mixing of a tip leakage jet emerging into the mainstream from the tip gap (Denton and Cumpsty, 1987). In these cases the uncertainty about the magnitude of the base pressure does not arise, and so the results are more directly usable to quantify loss.

All the above theory assumes incompressible flow with mixing taking place at a constant area. For compressible flow the same equations may be solved numerically. Figure 9 shows the variation of trailing edge loss coefficient with downstream Mach number for a trailing edge with 10 percent blockage at various values of base pressure coefficient. For other values of blockage the loss may be taken as being proportional to blockage. Although the base pressure itself can only be found by experiment, the base pressure for zero loss can be found exactly from the conservation equations and it is interesting to see how it varies with Mach number. Figure 10 shows the result from numerical solutions of the equations for varying trailing edge blockage and varying downstream Mach number with the assumption that $P_s = P_2$ (Appendix 3). It is significant that as the Mach number is increased the base pressure for zero loss becomes significantly greater than the pressure on the blade surface immediately before the trailing edge. Since experiments (e.g., Sieverding et al., 1983) usually show that the base pressure is lower than the latter pressure, this helps to explain why trailing edge loss increases rapidly as the downstream Mach number approaches unity.

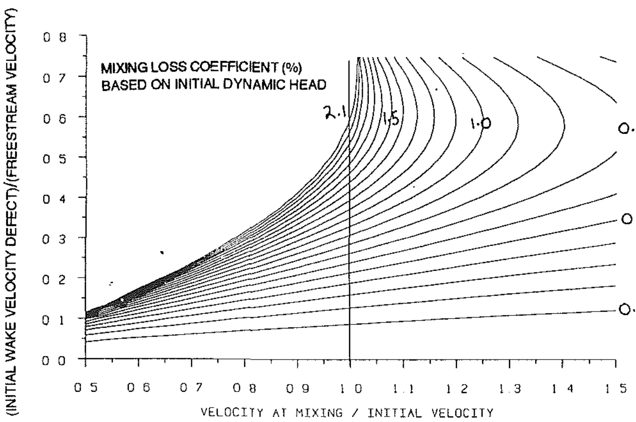

Fig. 11 Effect of wake acceleration or deceleration on the mixing loss. Calculations for $t/w = 0.1$, $M_1 = 0.5$.

The assumption of constant area mixing, which was made in the preceding theory, will not always be valid. Wakes in turbomachines mix out in a complex environment, which will be unsteady if the mixing is not complete before the next blade row. Neglecting unsteadiness for the moment, we can illustrate the effects of a change of area by means of simple physical arguments and numerical calculations.

Physically, when a shear layer is subjected to a favorable streamwise pressure gradient the transverse velocity gradient, dV/dy, is reduced because the slower moving fluid speeds up by more than the faster moving fluid. Hence the rate of shear strain is decreased and the rate of entropy generation, which is proportional to $\mu_{\text{eff}}\,(dV/dy)^2$, will be reduced. From this argument we would expect acceleration of a wake to reduce the dissipation and hence the mixing loss. Conversely deceleration should amplify the velocity gradient and increase the loss. A simple illustration of this is possible for two-dimensional incompressible flow. Using the momentum integral equation and the continuity equation for a wake it can be shown that

$$\frac{d\Delta P_o}{dx} = \Delta P_o(1-H)\,\frac{1}{V}\,\frac{dV}{dx} \tag{31}$$

where ΔP_o is the stagnation pressure loss that would be obtained from a mixing calculation at the local flow area; x is the distance along the wake and H is its local shape factor. Since H is always greater than unity Eq. (31) shows that acceleration will decrease the mixed out loss and deceleration increase it. Large values of H, such as occur close to the trailing edge, increase the magnitude of the effect. Only when the wake is nearly mixed out so that $H \rightarrow 1$ does a change in velocity cease to have any effect on the mixed out loss.

As a numerical example of the same phenomenon, Fig. 11 shows the mixing loss coefficient for a "square" wake that is (hypothetically) accelerated or decelerated isentropically to the mixing velocity and then allowed to mix out at constant area. This is a very idealized model since in reality mixing continues while the wake is being accelerated or decelerated, but its does serve to illustrate the magnitude of the effect. Deceleration is seen to cause a very significant increase in loss while acceleration causes a slight reduction.

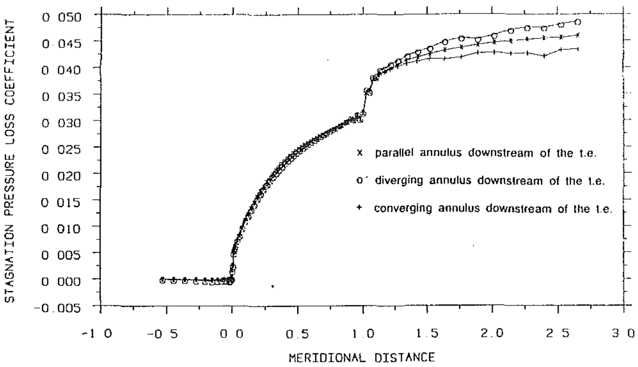

Fig. 12 Computed growth of stagnation pressure loss within and downstream of a compressor cascade

The importance of this effect in a turbomachine is difficult to establish since mixing is a continuous process and cannot be said to take place at one location or one velocity. In a wake mixing is initially very rapid and the velocity on the wake centerline may reach 90 percent of free-stream velocity within a few trailing edge thicknesses. However, as shown by Prato and Lakshimarayana (1993) mixing continues for up to one chord downstream of the blade row, by which time the free-stream velocity may have changed considerably.

An important consequence of the control volume approach to mixing is that numerical calculations do not have to predict the details of the mixing processes exactly in order to compute the correct loss. As long as conditions at the trailing edge are predicted correctly then the mixed out loss should also be correct. As an illustration of the ideas presented in this section, Fig. 12 shows results from a viscous calculation on a compressor cascade. The flow is just subsonic and the suction surface boundary layer is very nearly separated at the trailing edge. The change of mass-averaged stagnation pressure through and downstream of the cascade is plotted and shows that in this case about 1/3 of the total loss is generated behind the trailing edge. The calculation was repeated with the change of stream surface thickness downstream of the trailing edge varied by ±25 percent, while keeping the flow on the blade surface constant. Figure 12 shows that this has only a small effect on the overall loss, changing it by about ±5 percent. This is a consequence of most of the mixing occurring close to the trailing edge before the area has changed significantly.

5 Entropy Production in Shock Waves

It is well known that shock waves are irreversible and hence are sources of entropy. The entropy creation occurs due to heat conduction and high viscous normal stresses within the shock wave, which is only a few molecular free paths in thickness. Text books, e.g., Shapiro (1953), often derive the equation for the entropy increase across a *plane normal* shock wave. Expanding this in powers of (M^2-1), where M is the upstream Mach number, leads to the following approximate result for weak shocks:

$$\Delta s \approx C_v \frac{2\gamma(\gamma-1)}{3(\gamma+1)^2}(M^2-1)^3 + O(M^2-1)^4 \qquad (32)$$

This shows that the entropy creation varies roughly as the cube of (M^2-1).

The above result is for normal shock waves. Oblique shocks will always produce less entropy than a normal one with the same upstream Mach number. In fact Eq. (32) is equally applicable to oblique shock waves provided M is interpreted as the component of Mach number perpendicular to the shock front.

The pressure rise across a weak shock wave is also proportional to (M^2-1) and Eq. (32) can be rewritten as

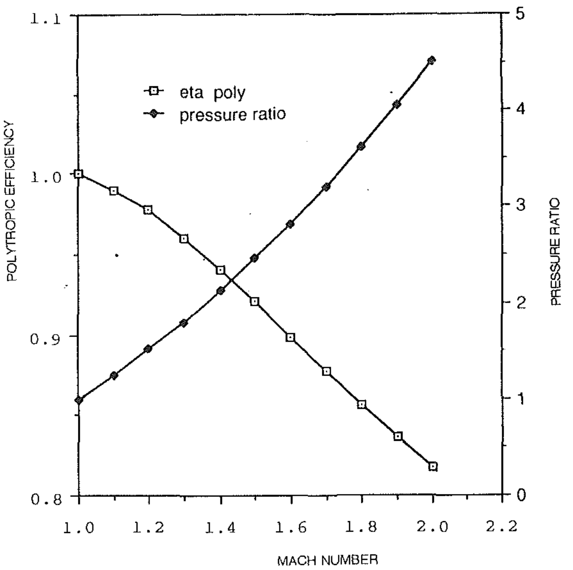

Fig. 13 Compression in a normal shock wave expressed as a polytropic efficiency

$$\Delta s \approx R\frac{\gamma+1}{12\gamma^2}\left(\frac{\Delta P}{P_1}\right)^3 + O\left(\frac{\Delta P}{P_1}\right)^4 \qquad (33)$$

which applies to both normal and oblique shocks.

The efficiency of a compression process in a weak shock may be defined by

$$\eta = 1 - \frac{T\Delta s}{\Delta h} \approx 1 - \frac{\Delta s}{R\,\Delta P/P} \approx 1 - \frac{\gamma+1}{12\gamma^2}\left(\frac{\Delta P}{P}\right)^2 \qquad (34)$$

For $\Delta P/P = 0.5$, $\gamma = 1.4$ (which corresponds to a normal shock with an upstream Mach number of about 1.2) this gives $\eta \approx 0.97$, which suggests that weak shock waves are a relatively efficient compression process. This is further illustrated in Fig. 13, which shows the polytropic efficiency of the compression process through a shock where the efficiency has been defined as

$$\eta_p = \frac{(\gamma-1)}{\gamma}\frac{\ln(P_2/P_1)}{\ln(T_2/T_1)} \qquad (35)$$

and has been calculated using exact theory for a gas with $\gamma = 1.4$.

It is clear that a shock is actually a comparatively efficient compression mechanism if the component of upstream Mach number perpendicular to the shock front is less than 1.5. This helps to explain the development of efficient transonic compressors with inlet Mach numbers typically in the range 1.5–1.7.

5.1 Shock Waves in Compressors. For a single shock wave, the entropy generation is a unique function of the static pressure rise. However, Eq. (34) shows that this function is highly nonlinear so that if the same pressure rise can be accomplished by two shock waves instead of by a single one then the shock loss will be greatly reduced (by a factor of 4 if both shocks have the same pressure rise). On this argument it is hard to explain why the fans of most civil aero-engines seem to operate most efficiently with a single normal shock wave near the leading edge (e.g., Pierzga and Wood, 1985). It is also hard to explain the claimed reduction of shock loss by sweep for transonic compressor blading (Wennerstrom and Puterbaugh, 1984). Shock sweep will reduce the shock strength for a given upstream Mach number but not for a given pressure ratio. Possibe explanations are that a second shock is formed as a result of the sweep or that, since the sweep is usually produced by a change in radius, some of the pressure rise takes place by centrifugal effects, thereby reducing the pressure rise required from the shock and increasing its efficiency.

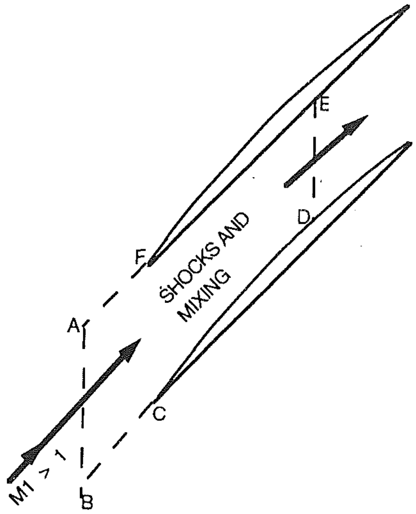

Fig. 14 Control volume used for the shock loss of transonic compressor blades

A recent paper by Freeman and Cumpsty (1989) shows that the performance of transonic compressors can be remarkably well predicted by applying conservation of mass, energy, and momentum between the upstream flow and the flow downstream of the shock system. The equation are applied to the control volume shown in Fig. 14. The flow is assumed to be uniform both upstream of the blade row, i.e., across *AB*, and at plane *DE* downstream of the leading edge shock system. As in the case of mixing loss the control volume formulation predicts the overall changes without needing to consider the details of the flow within the control volume. In this case the loss occurs through the complex shock system within the control volume and so the method only applies to the loss generated by the leading edge shock system and not to any passage or trailing edge shocks.

Only the continuity equation and the streamwise momentum equation are solved and the streamwise force exerted on the flow by the blade is approximated by assuming that the average pressure on the blade surfaces *CD* and *FE*, including the leading edge itself, is the same as the downstream pressure on *DE*. This assumption is very approximate and only gives realistic answers because transonic compressor blades are so thin. The assumption that the flow leaving the control volume through *DE* is uniform is also dubious. Despite these approximations the method gives remarkably good predictions of the behavior of transonic compressors between peak efficiency and stall when the shock is near the leading edge. The fact that much of the performance can be predicted by a control volume analysis also explains why the performance of such compressors can be well predicted by modern three-dimensional flow calculations (e.g., Adamczyk et al., 1993), which do satisfy conservation of mass, energy, and momentum even when the details of the shock system are not captured accurately.

5.2 Shock Waves in Turbines. Compression is seldom a desirable feature of turbines, however, transonic turbines are commonly used to obtain high-stage pressure ratios and so shock waves do occur. Although local Mach numbers may be high, the shocks within the blade passage are usually oblique so that $\Delta P/P$ is small and they generate little direct loss (Eq. (33)). The most serious consequence of transonic flow in turbines is the shock system at the trailing edge, as illustrated in Fig. 15. The low base pressure formed immediately behind the trailing edge can generate a very large trailing edge loss. The flow expands around the trailing edge to this low pressure and is then recompressed by a strong shock wave at the point where the suction and pressure side flows meet. The entropy generation comes from the intense viscous dissipation at the edges of the separated region immediately behind the trailing edge and from the strong shock formed at the close of this region. For cooled turbine blades with thick trailing edges this may be the largest single source of loss in the machine.

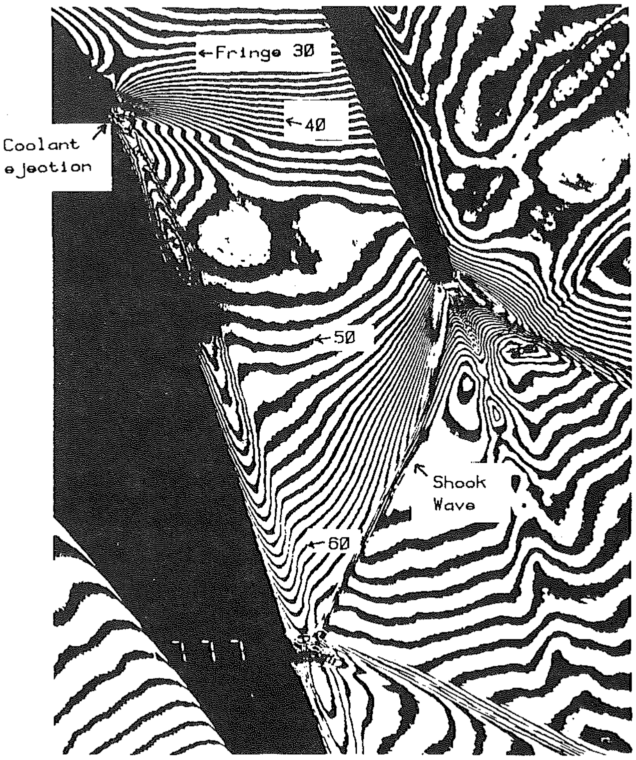

Fig. 15 Trailing edge shock system for a turbine blade, with suction surface coolant ejection

Denton and Xu (1990) apply a control volume argument very similar to that of Freeman and Cumpsty, to the trailing edge of choked turbine blades. Their model uses both of the momentum equations and uses the assumption that the flow is choked at the throat of the blade to determine the mass flow rate; it does not assume that the blade is thin. The method is therefore rigorous and based on reasonable assumptions. It shows that even in this case the loss can be calculated from conservation of mass, momentum, and energy provided the average pressure acting on the blade suction surface downstream of the throat can be predicted. Low values of this pressure are shown to reduce the loss. In practice the suction surface pressure must be obtained from a separate calculation of the flow field. However, the predicted loss is extremely sensitive to the value of this pressure and it is unlikely that it will be known accurately enough for the method to give a useful prediction.

5.3 Shock Wave–Boundary Layer Interaction. There are indirect sources of loss associated with shock waves in both compressors and turbines because of the interaction of the shock wave with the boundary layer. A boundary layer separation bubble will usually be formed at the foot of a weak shock and extra dissipation is likely to occur within and downstream of the bubble. If the boundary layer was laminar the bubble will almost certainly cause transition. Strong shock waves, which are especially likely to arise in transonic compressors, may cause complete boundary layer separation. For a normal shock wave this is likely if the upstream Mach number is greater than about 1.4 (Atkin and Squire, 1992). Hence, increases in the boundary layer loss are likely to occur from shock wave–boundary layer interaction in both turbines and compressors. In view of the high pressure rise obtainable via

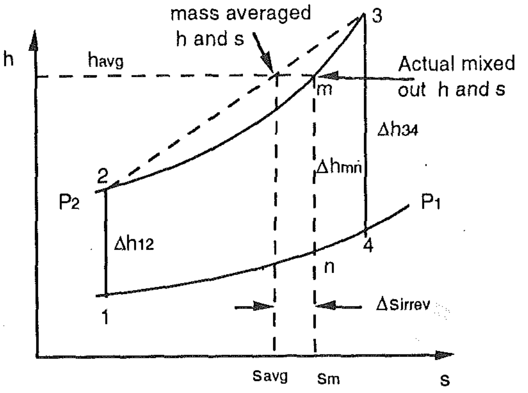

Fig. 16 Mixing of two flows at constant pressure

the shock wave, these may be perfectly acceptable in transonic compressors even when the shock separates the boundary layer.

6 Entropy Creation by Heat Transfer

Heat transfer from a turbomachine to its surroundings is usually small and the flow is almost invariably regarded as being adiabatic. Small machines with a large surface area to volume ratio (e.g., small turbochargers) are most likely to violate this assumption. For a compressor the work input to achieve a required pressure ratio is reduced by heat loss from the fluid to its surroundings and it is well known that isothermal compressors, with interstage cooling, are preferable to adiabatic ones for many applications. This does not apply to the compressors of gas turbines where any heat loss from the compressor has to be made up by burning extra fuel in the combustion chamber and results in a loss of cycle efficiency. For a turbine, heat loss to the environment will always decrease the work output and so should be avoided, e.g., by lagging the turbine if necessary.

The main effect of heat transfer is felt in cooled turbines where a separate stream of cool fluid is used to maintain the blades and disks at an acceptable temperature. The coolant flow is subsequently mixed with the main flow and expanded with it through the remaining stages of the turbine. Heat transfer from the main flow to the coolant flow takes place in three stages: first from the hot gas of the main flow to the cooled metal, second from the metal to the coolant flow within the internal passages of the blade, and finally from the mainstream flow to the coolant flow as the two flows are mixed. As a result of this heat transfer the main flow will do less work than if it were expanded adiabatically from its supply pressure and temperature to the exhaust pressure whilst the coolant flow will do more work than if it were expanded from its supply conditions to the same exhaust pressure. We will examine the effect of the heat transfer and mixing on the turbine performance.

6.1 Thermodynamics of a Gas Turbine Cycle With Blade Cooling. It is difficult to consider the entropy changes due to coolant flows without considering the whole thermodynamic cycle. The problem is highlighted by Fig. 16, which shows that when two flows of perfect gas at the same pressure but different temperatures are mixed at constant pressure there is an increase of entropy but no loss of potential work, i.e.,

$$(1-m_{fc})\Delta h_{34}+m_{fc}\Delta h_{12}=\Delta h_{mn} \tag{36}$$

where m_{fc} is the mass fraction of cooling flow bled off at point 2.

Appendix 4 gives an analysis of a simple cycle. The cycle pressure ratio is assumed fixed and its efficiency is influenced by the turbine entry temperature T_3, by m_{fc}, and by the efficiency of the cooled part of the turbine η_t. The analysis shows that the change in overall cycle efficiency due to cooling can be written as

$$\Delta\eta_o=\left\{\frac{\partial\eta_c}{\partial T_3}\frac{dT_3}{dm_{fc}}+\left[\frac{\partial\eta_c}{\partial m_{fc}}+\frac{\partial\eta_c}{\partial\eta_t}\frac{d\eta_t}{dm_{fc}}\right]\right\}\Delta m_{fc} \tag{37}$$

The first term on the right-hand side of this equation represents the change of cycle efficiency due to a change in turbine entry temperature, which can be increased by increasing m_{fc}. This will be a positive term and represents the main objective of using cooling flows to increase cycle efficiency.

The second term represents the rate of change of cycle efficiency with cooling flow for constant values of turbine entry temperature and turbine efficiency. This will be a negative term because the net cycle efficiency can be thought of as a weighted average of the efficiency of the main cycle and of the lower efficiency cycle undergone by the cooling flow. This term includes the loss of work due to the heat transfer from the mainstream flow.

The third term will also be negative because it represents the change of cycle efficiency due to a change in the efficiency of the cooled part of the turbine. As described in Appendix 4, this efficiency is defined to include only viscous effects within the turbine which in turn are assumed to depend on the amount of coolant added. It is only this term that we will consider in detail in this paper.

Figure A 4.1 shows an idealized cycle in which coolant is assumed to be added at a uniform rate along the cooled part of the turbine expansion. Analyzing this cycle numerically for an overall pressure ratio 25:1, cooled turbine pressure ratio 4:1 and turbine entry temperature 1500 K, gives for the terms in Eq. (37):

$$\Delta\eta_o=\left\{1.03\times10^{-4}\frac{dT_3}{dm_{fc}}-0.18+0.38\frac{d\eta_t}{dm_{fc}}\right\}\Delta m_{fc} \tag{38}$$

The value of dT_3/dm_{fc} is likely to be about 10^4 (100°C per 1 percent cooling flow) and the value of $d\eta_t/dm_{fc}$ is likely to be about -1 (1 percent loss of efficiency per 1 percent cooling flow) and so Eq. (38) shows that the rate of loss of turbine efficiency with cooling flow has a large effect on the overall efficiency. The second term is also significant and emphasizes the importance of making the best possible use of the cooling flow, i.e., by making it do useful work and avoiding pressure drops due to throttling in the cooling passages.

6.2 Thermodynamics of a Cooled Turbine. The thermodynamics of a cooled turbine are also considered in Appendix 4, where it is shown that the loss of output from the mainstream flow is due mainly to the entropy creation by viscous effects rather than that caused by heat transfer. Using Shapiro's (1953) influence coefficients, it is shown that, for the situation shown in Figs. 7 and 15, when a mass flow m_c of coolant is injected at velocity V_c and angle α to a main flow with Mach number M and velocity V_m the change of effective turbine efficiency is

$$\Delta\eta_t=-\frac{T_4}{\Delta T_{\text{ois}}}(\gamma-1)\mathrm{M}^2\left(1-\frac{V_c\cos\alpha}{V_m}\right)\frac{m_c}{m_m} \tag{39}$$

From this it is clear that coolant addition to a mainstream flow at high Mach number is much more harmful than at low Mach numbers and also that coolant should be injected as nearly parallel to the main flow as is possible. If the coolant has a higher stagnation pressure than the main flow, so that $V_c > V_m$, and is injected almost parallel to it, then the stagnation pressure of the main flow and the efficiency of the turbine (which is defined in terms of the mainstream flow properties) may even be increased by the mixing. Interestingly, if the coolant is injected perpendicular to the main stream ($\alpha = 90$ deg) then its temperature and pressure, which determine V_c, have no effect on the turbine efficiency, which depends only on the mass fraction of coolant injected.

The entropy creation by irreversible mixing of cooling flows can also be calculated by applying conservation of mass, mo-

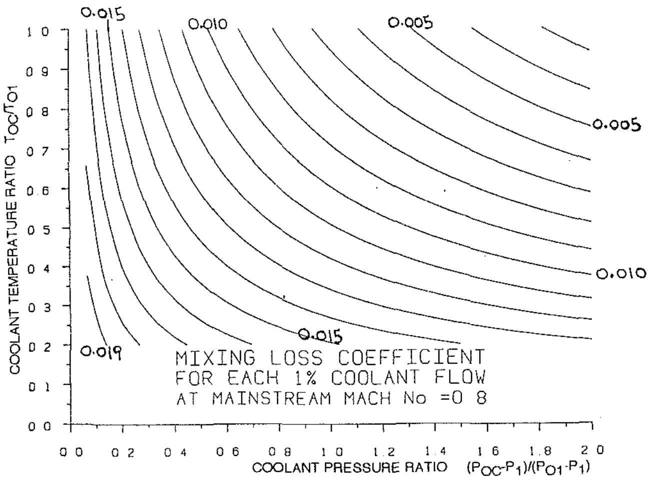

Fig. 17 Entropy loss coefficient as a function of temperature ratio and pressure ratio for 1 percent of coolant flow injected at 45 deg to a main flow with Mach number = 0.8

mentum, and energy in a very similar way to the method of Appendix 2. Such a method is described by Hartsel (1972). The analysis is complicated by the need to assume compressible flow, even at low Mach numbers, because of the large changes in temperature. Appendix 4 shows that only the entropy creation due to viscous effects, not that due to heat transfer, should be considered as a loss of turbine efficiency.

Results from a numerical calculation applied to cooling flow ejected through a slot with a velocity inclined at 45 deg to the mainstream direction ($\alpha = 45$ deg) are illustrated in Fig. 17 where the loss is presented as the loss coefficient of the mainstream flow per percent of coolant addition. Appendix 4 shows that only the entropy change due to viscous dissipation, and not that due to heat transfer, influences the turbine efficiency. Hence the loss coefficient plotted in Fig. 17 is defined using

$$\zeta_s = To_{\rm mix}\frac{\Delta s_{\rm tot} - dq/T_{\rm avg}}{0.5\,V_{\rm mix}^2} \qquad (40)$$

where the heat dq removed from the mainstream flow is assumed to have been transferred at a temperature $T_{\rm avg} = 0.5\,(T_1 + T_{\rm mix})$. This definition is consistent with Eq. (A4.9) of Appendix 4.

Figure 17 shows that the aerodynamic loss on mixing is almost equally influenced by the stagnation pressure and the stagnation temperature of the coolant. Low coolant temperatures and pressures cause a high loss because they produce a low value of V_c in Eq. (39). Numerical calculations show that the loss coefficient as defined by Eq. (40) is not greatly affected by the value of free-stream Mach number.

The addition of coolant flow may cause other losses by disturbing the boundary layers on the blade or endwall surfaces, as shown in Fig. 15. These are not considered in the above analysis.

7 Two-Dimensional Losses in Turbomachinery

7.1 Blade Boundary Layer Loss. Application of the ideas presented above to real turbomachinery is complicated by the complexity of the geometry and flow. In particular the real flow is usually three-dimensional so that simplified one-dimensional and two-dimensional results should be used as guidelines and as an aid to understanding the physics of the flow rather than to obtain quantitative results.

Using Eq. (20), the total entropy generation in the blade boundary layers can be evaluated from

$$\dot S = \sum C_s \int_0^1 \frac{C_d \rho V_o^3}{T}\, d(x/C_s) \qquad (41)$$

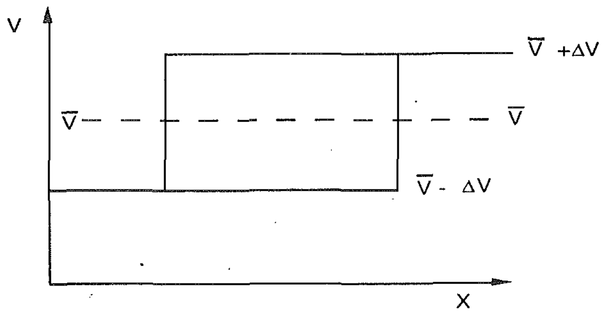

Fig. 18 Idealized blade surface velocity distribution

where the summation is for both blade surfaces, x is the surface distance, and C_s is the total length of the surface. To turn this into an entropy loss coefficient for the blade we must divide the total entropy produced by the mass flow rate and by a reference dynamic head, which would usually be based on V_1 for a compressor blade and on V_2 for a turbine blade, e.g.,

$$\zeta_s = \frac{T\dot S}{m\,0.5\,V_{\rm ref}^2} \qquad (42)$$

Combining these two equations gives, for low-speed flow,

$$\zeta_s = 2\sum \frac{C_s}{p\cos\alpha_{\rm ref}} \int_0^1 C_d \left(\frac{V_o}{V_{\rm ref}}\right)^3 d(x/C_s) \qquad (43)$$

If the blade surface velocity distribution and the variation of C_d are known this equation can be used to estimate the loss coefficient. The occurrence of the blade surface velocity in the form $(V/V_{\rm ref})^3$ is very important. It shows that the suction surface is dominant in producing loss and that regions of high surface velocity contribute proportionally much higher amounts of loss.

The value of loss coefficient obtained from Eq. (43) is dominated by the location of the transition point where C_d undergoes a rapid change, as shown in Fig. 5. In order to minimize the loss the boundary layers should be kept laminar for as long as possible. The extent of the laminar boundary layer will depend mainly on the Reynolds number, turbulence level, and on the detailed surface velocity distribution. At the high turbulence levels prevalent in turbomachines transition is likely to occur in the Re_θ range 200–500 while Re_θ at the trailing edge is usually in the range 500–2000 (although it will be greater than this for large high-pressure steam turbines and large hydraulic turbines). Figure 4 shows that over much of this range the dissipation coefficient is of the order of 0.002, as suggested by Denton and Cumpsty. Although one cannot expect this crude approximation to give accurate results for any one blade it can be used to predict *systematic* trends for the variation of loss with blade and stage design.

These equations also show clearly why for any specified combination of inlet and outlet flow angles there is an optimum pitch to chord ratio (p/c). We assume a rectangular velocity distribution as illustrated in Fig. 18, and that C_d is constant. Equation (41) gives

$$\dot S = C_d \rho C (2\bar V^3 + 6\bar V \Delta V^2) \qquad (44)$$

Using the definition of blade circulation to obtain V_x we get

$$m = \rho V_x p = \frac{2C\Delta V\rho}{(\tan\alpha_2 - \tan\alpha_1)} \qquad (45)$$

and so the loss coefficient, based on mean velocity, becomes

$$\zeta_s = \frac{\dot S}{0.5 m \bar V^2} = C_d\left(2\frac{\bar V}{\Delta V} + 6\frac{\Delta V}{\bar V}\right)(\tan\alpha_2 - \tan\alpha_1) \qquad (46)$$

which has a minimum value, corresponding to an optimum pitch-chord ratio, when $\Delta V/\bar V = 1/\sqrt{3}$. If C_d is taken as 0.002 this simple method gives quite realistic loss coefficients.

If C_d is assumed constant the value of loss obtained from

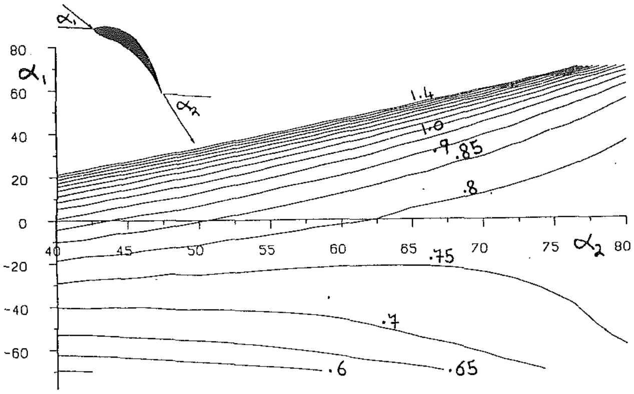

Fig. 19 Predicted optimum pitch-chord ratio of turbine blades

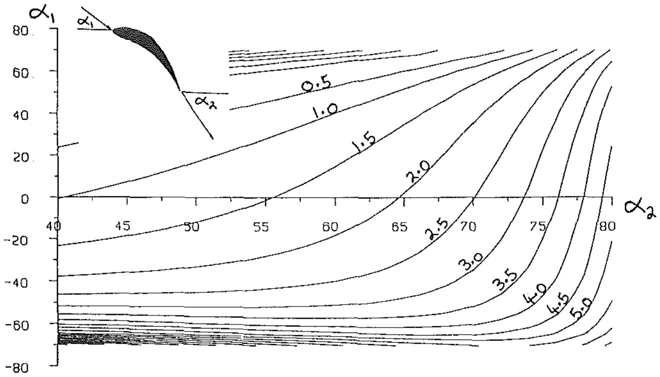

Fig. 20 Predicted profile loss coefficient (percent) of turbine blades at their optimum pitch-chord ratio

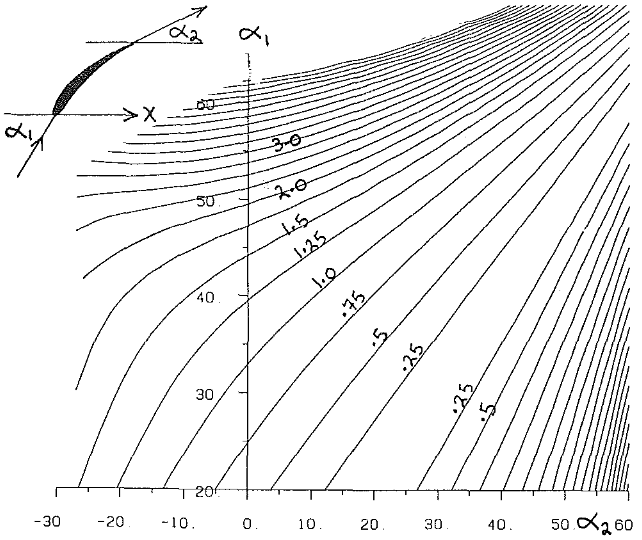

Fig. 21 Profile loss coefficient of compressor blades (percent) predicted by Eq. (43)

Eq. (43) is not greatly dependent on the surface velocity distribution and this permits a simple method of estimating the loss coefficients. If the inlet and outlet flow angles are specified and a plausible surface velocity distribution, more realistic than that of Fig. 18, is guessed then the pitch to chord ratio can be calculated from the tangential momentum change and an estimate of loss can be obtained from Eq. (43). By systematically varying the guessed velocity distribution one can then estimate the optimum p/c ratio and minimum loss. Figure 19 shows the resulting optimum p/c ratio and Fig. 20 the minimum loss calculated in this way for turbine blades. The results agree well with the predictions of Zweifel's rule for optimum p/c ratio and with cascade measurements of loss coefficient.

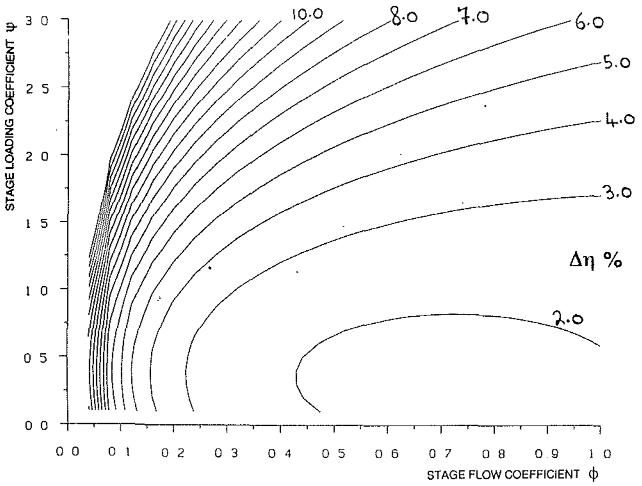

Fig. 22 Loss of efficiency (percent) due to profile loss alone for turbines with zero interstage swirl angle

For compressor blades the predictions, using exactly the same method, are not realistic. The calculated value of optimum pitch-chord ratio is too high, giving a diffusion factor well over 0.6. Consequently the predicted minimum loss is too low. The reason is that the method takes no account of boundary layer separation and one must conclude that this is a dominant feature in the design of compressor blades. The minimum loss will occur when the boundary layer is on the verge of separation; this can be simulated in the method by causing the predicted loss to rise very rapidly with diffusion factor when this is greater than about 0.55. The optimum pitch-chord ratio then occurs just above that which gives a diffusion factor of 0.55. The results from such a prediction are shown in Fig. 21.

When considering the design of a complete stage the entropy creation should be considered relative to the stage enthalpy change. If we define an isentropic velocity C_o, based on the stage isentropic enthalpy change, by

$$\Delta h_{is} = 0.5 C_o^2 \tag{47}$$

then the overall increase in specific entropy due to the blade surface boundary layers on both rows may be estimated from

$$\Delta s \approx \Delta h_{is} 2 \frac{C_o}{V_x} \sum \frac{C_s}{p} \int_0^1 \frac{C_d}{T} \left(\frac{V_o}{C_o}\right)^3 d(x/C_s) \tag{48}$$

where the summation is over all the blade surfaces. This result is easily converted into the stage efficiency via Eq. (9) and shows that it is the blade surface velocity relative to the isentropic velocity C_o that is most important as regards stage efficiency. For high reaction stages V/C_o will be greater in the rotor, which is then likely to contribute most to the loss of efficiency and conversely for low reaction stages. Again, by guessing likely surface velocity distributions, assuming that C_d is constant, and calculating the optimum p/c ratio for each blade row the integrals and summations of Eq. (48) can be performed and the stage efficiency estimated for any specified stage velocity triangles. Figure 22 shows the result for axial turbine stages with zero interstage swirl angle. It must be emphasized that this gives the loss of efficiency due to blade boundary layer losses alone. Given that a typical turbine stage efficiency is about 90 percent we can conclude that these are only responsible for about 1/3 of the total loss in most turbines.

The blade surface boundary layer loss varies significantly with Reynolds number and surface roughness. The variation with Re is as suggested by Fig. 5 with the loss increasing rapidly at very low Re ($\text{Re} < 10^5$) due to the high dissipation in laminar boundary layers and possibly to laminar separation of the boundary layer. Within the transition region, $2 \times 10^5 < \text{Re} < 6 \times 10^5$; the variation is complex and depends on the

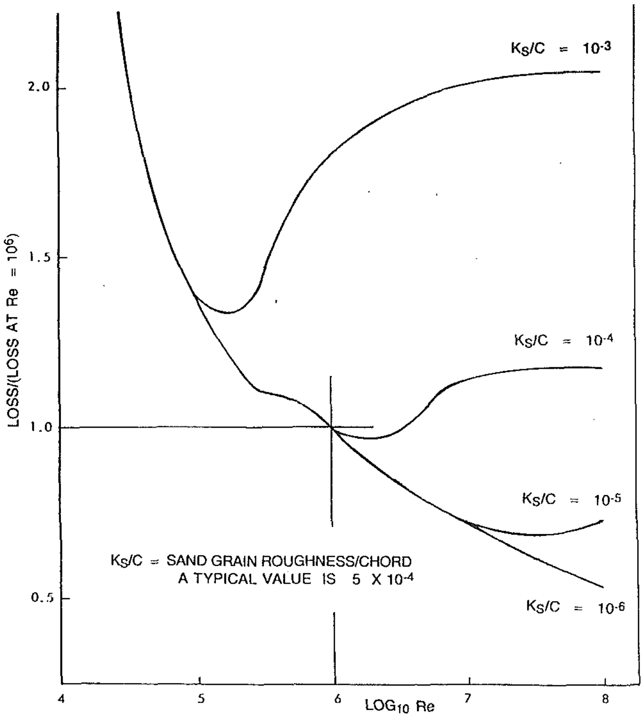

Fig. 23 Variation of profile loss with Reynolds number and surface roughness

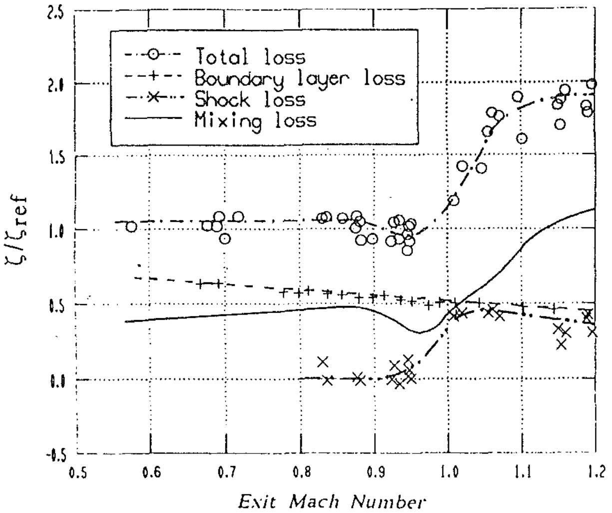

Fig. 24 Variation of the two-dimensional components with Mach number for a turbine cascade (from Mee et al., 1992)

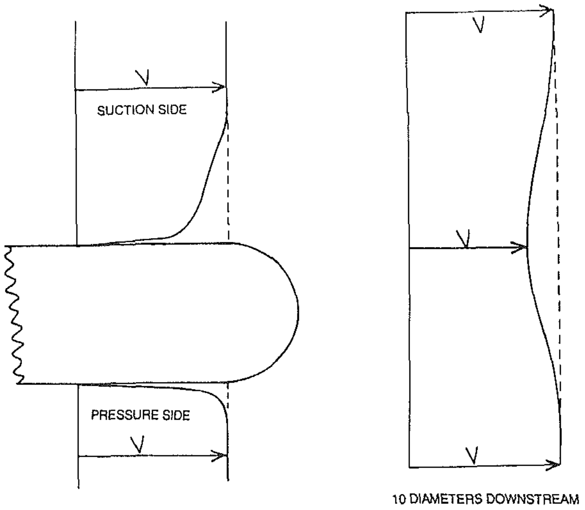

Fig. 25 Velocity profiles at and downstream of a simulated turbine blade trailing edge

details of the surface velocity distribution. The net result is a combination of the general decrease in loss with increasing Re and an increase in loss as the transition point moves upstream. At $\mathrm{Re} > 6 \times 10^5$ the loss varies approximately as $\mathrm{Re}^{-1/6}$ for very smooth blades. However, in this regime the turbulent boundary layer is significantly influenced by the surface roughness so that for machines that operate at very high Re the surface finish of the blades is very important. Curves for the variation of profile loss with Re and with roughness have been given by Koch and Smith (1976) for compressors and by Denton and Hoadley (1972) for turbines. Both sets of curves show similar trends although the latter, reproduced in Fig. 23, predicts an increase of loss with Re in the transition region at high values of roughness.

All the preceding analysis assumes two-dimensional flow in the blade surface boundary layers. The same approach can be applied to three-dimensional boundary layers where the convergence or divergence of the surface streamlines may thicken or thin the layer. Although this can have a considerable effect on the boundary layer thickness, it should not have a great effect on the entropy creation per unit surface area, unless convergence of the surface streamlines causes the boundary layer to separate. Hence it is suggested that Eq. (41) can be modified to estimate the entropy production over the whole blade surface, even in three-dimensional flow.

7.2 Trailing Edge Loss. The other major contribution to two-dimensional blade loss comes from the trailing edge. The magnitude of trailing edge loss has been seriously underestimated in the past, especially for turbine blades, due to the neglect of the base pressure term in Eq. (26). Figure 24 from Mee et al. (1992) shows that for a blade with a trailing edge blockage of 6.3 percent about 1/3 of the total two-dimensional loss is mixing loss behind the trailing edge in subsonic flow. The same figure shows that in supersonic flow this proportion rises to about 50 percent. Figure 25 (Roberts, 1992) shows the measured velocity profiles before and after the trailing edge of a simulated low-speed turbine blade with representative boundary layer to trailing edge thickness ratios, again about 1/3 of the total loss was found to be generated behind the trailing edge. Figure 25 serves to illustrate how thin the boundary layers are relative to the trailing edge and it is not surprising that the trailing edge itself can cause such a large proportion of the loss.

As explained previously the entropy can be expected to increase by about 18 percent behind a *thin* trailing edge due to the mixing out of the surface boundary layers. In the two cases just quoted it increases by about 50 percent so the loss attributable to trailing edge thickness is about 32 percent of the boundary layer loss or 21 percent of the total loss. The value of base pressure coefficient necessary to explain this increase is about -0.075, which is typical of the values found by Sutton (1990) for a wide range of trailing edge shapes.

An alternative means of estimating the base pressure coefficient is to compare measured losses with losses calculated from boundary layer loss alone and to attribute the difference to trailing edge loss. This has been done by Hart et al. (1991) for a total of 180 turbine cascade measurements. Hart used an inviscid calculation to find the base pressure for no loss and a boundary layer calculation to obtain the boundary layer parameters at the trailing edge. He then correlated his results to find the average value of C_{pb} necessary to make the calculations agree with the measured loss. He found the average value of C_{pb} to be -0.13 and that it did not correlate with either trailing edge thickness or boundary layer thickness. It

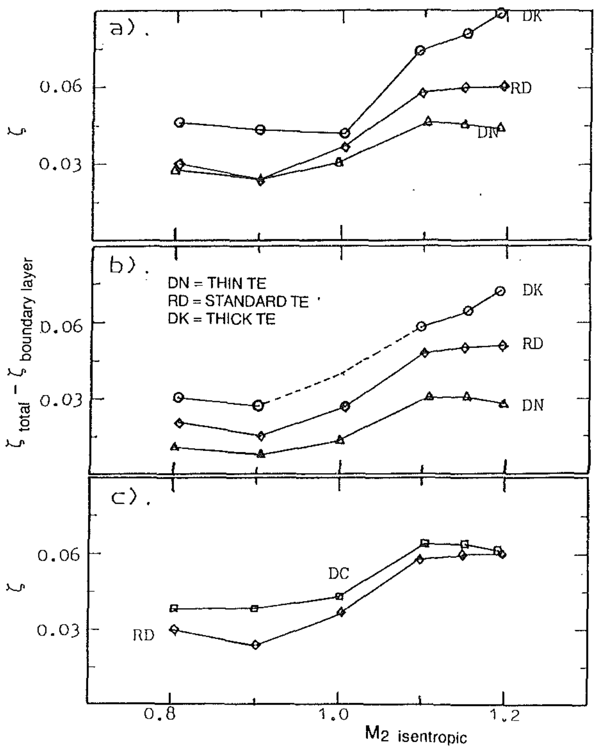

Fig. 26 The variation of loss with Mach number for turbine blades with varying trailing edge thickness, from Xu and Denton (1988)

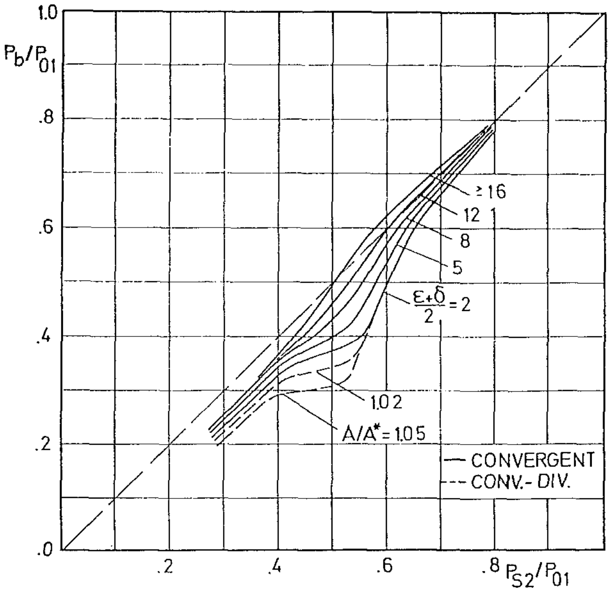

Fig. 27 Sieverding's base pressure correlation for transonic turbine blades

is suggested that this value should be used in Eq. (26) to calculate the mixed out loss of subsonic two-dimensional cascades.

7.3 Effect of Mach Number on the Two-Dimensional Loss. The loss of both turbine and compressor blades increases rapidly as sonic conditions are approached. Figure 26 from Xu and Denton (1988), shows typical results for a family of turbine cascades with different trailing edge thicknesses. This figure shows the difference between the overall two-dimensional loss and the measured boundary layer loss, illustrating how much of the loss is arising from the trailing edge. Figure 24 showed a similar result.

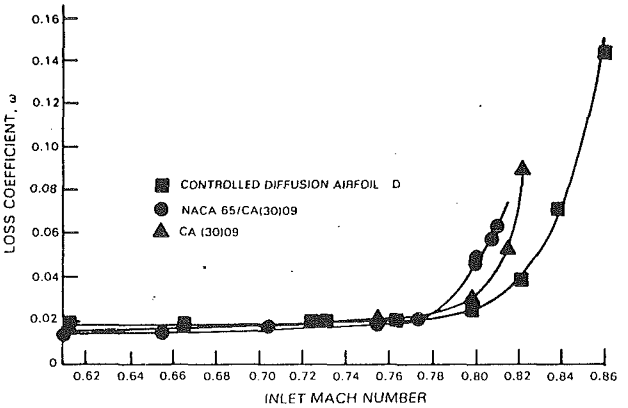

Fig. 28 Profile loss versus inlet Mach number for compressor blades (from Hobbs and Weingold, 1983)

For turbine cascades most of the increase can be attributed to the trailing edge loss. Figure 10 shows that the base pressure required for zero loss increases rapidly as the exit Mach number approaches unity. The actual base pressure is even more difficult to predict accurately at high exit Mach numbers than it is in subsonic flow but the most widely used method is the correlation by Sieverding et al. (1983), which is shown in Fig. 27. The correlation predicts the base pressure as a function of the far downstream pressure, P_{s2}, the change in suction surface slope downstream of the throat δ and the trailing edge wedge angle ϵ. Surprisingly it does not include any measure of trailing edge blockage. The correlation shows that the base pressure falls below the downstream pressure as the Mach number is increased. The loss will be proportional to the difference between the actual base pressure and the base pressure for zero loss illustrated in Fig. 10.

Chen (1987) presents a correlation for the variation of turbine profile loss with Mach number. This shows the loss rising rapidly as M_2 approaches unity but decreasing between $M_2 = 1.0$ and 1.2 before increasing again at higher Mach numbers ($M_2 > 1.2$). Surprisingly the correlation does not include any measure of trailing edge thickness and so it must be assumed to be for blades with thin trailing edges. There is little published experimental evidence for the decrease of loss at high Mach numbers although Denton and Xu (1990) predict the result theoretically and explain it as being due to the expansion from sonic conditions at the throat to the supersonic far downstream flow being matched to the increase in flow area at the trailing edge. A similar result is obtained for blades with converging-diverging passages, which only work well at high supersonic exit Mach numbers.

Figure 28, from Hobbs and Weingold (1984) shows the variation of loss with inlet Mach number for a compressor cascade. The increase of loss in this case is due to a completely different mechanism to that for turbine blades. For conventional compressor blades the peak suction surface velocity is well above the inlet velocity and will reach sonic conditions when M_1 is about 0.7. Further increase of M_1 causes the peak Mach number and hence the ratio V_{max}/V_1 to rise extremely rapidly. In general the sonic region is terminated by a normal shock. Thus the increase in M_1 causes shock loss, high suction surface entropy generation (Eq. (41)), and possibly boundary layer separation, all of which contribute to the rapid rise in loss.

Compressor blades specially designed for supersonic inflow delay this loss increase by being very thin and having low or reverse suction surface camber so that the peak suction surface Mach number is not much greater than the inlet Mach number. The lift is obtained from a low velocity on the pressure surface rather than a high one on the suction surface so the boundary layer loss is comparatively low. This, coupled with the high blade loading, means that the shock loss, illustrated in Fig. 13, can be tolerated at least up to the point at which the shock separates the suction surface boundary layer. This is likely when M_1 is greater than about 1.4 (Atkin and Squire, 1992).

There has been much discussion about the relative importance of shock loss and boundary layer loss in supersonic compressor blading and it is sometimes claimed that the shock loss is small relative to the loss in the shock-induced boundary layer thickening and possibly separation. The author's view, based mainly on numerical predictions, is that the magnitudes of the two components are comparable at inlet Mach numbers around 1.4, but that the shock loss becomes dominant at higher Mach numbers. The success of Freeman and Cumpsty's method also supports the idea that the shock loss is dominant. Although, in principle, the shock loss could be greatly reduced by splitting the pressure rise between two shocks (section 5), this does not seem to occur in practical compressor blades.

8 Tip Leakage Losses

8.1 Effect on Blade Lift and Work. The loss of performance due to leakage of flow over blade tips has been intensively studied for many years. Early methods tended to work in terms of the induced drag on the blades, analogous to the induced drag on an aircraft wing. However, this drag is an inviscid effect. In the case of the wing it produces extra kinetic energy of the surrounding atmosphere but it does not create entropy. Hence, from the point of view of a turbomachine it does not cause loss. More recent studies have concentrated on measuring the tip leakage flow in great detail, e.g., Bindon (1989) for turbines and Storer (1991) for compressors. As a result the flow and loss mechanisms are now well understood for unshrouded blades. Much less work has been done on leakage flow over shrouded blades.

The most obvious effect of flow leakage over the tips of both shrouded and unshrouded blades is a change in the mass flow through the blade passage. At first sight this would seem to lead to a reduction in work for both turbines and compressors. However, considering shrouded blades first because they are simpler, flow will leak upstream over the shroud of a compressor blade. Hence, for a fixed overall flow rate, the mass flow through the blade itself will be increased by the leakage, which will tend to increase the work input but reduce the pressure rise. There will be other factors affecting this, such as a change in deviation caused by the disturbance to the inlet flow when the leakage flow mixes with the mainstream, but the main effect is likely to be an increase in blade work proportional to the leakage flow. For shrouded turbine blades the leakage will be from upstream to downstream of the blade row and so, for a fixed total throughflow, both the blade work and the pressure drop will be reduced. These changes of blade work and pressure difference are independent of any entropy generation or change of efficiency. They would occur in a complete inviscid flow where they would manifest themselves as changes in the mass flow-pressure ratio characteristic of the machine rather than as changes in efficiency.

The situation for unshrouded blades is qualitatively the same, although the interaction between the leakage flow and the mainstream flow is much stronger. In a compressor blade the meridional velocity of the flow leaking over the tips is certain to be less than that of the mainstream flow and may even be directed upstream. Hence, the mass flow through the remainder of the blade must be increased. In a turbine the leakage flow has an increased meridional velocity and forms a strong leakage jet, so the flow through the remainder of the blade must be decreased.

The change in blade work must be reflected in a change of lift, which occurs partly in the immediate vicinity of the tip gap and partly over the whole span of the blade. For unshrouded blades there is always a loss of lift at the blade tip, which occurs both because the blade length is reduced and because the blade loading drops off toward the tip. Both experiments and calculations show that the latter is confined to a very small region not much greater than the tip gap. In fact simple theory, treating the leakage flow as flow through a two-dimensional orifice, shows that the *total* loss of lift at the tip, relative to a blade with no clearance, is given by

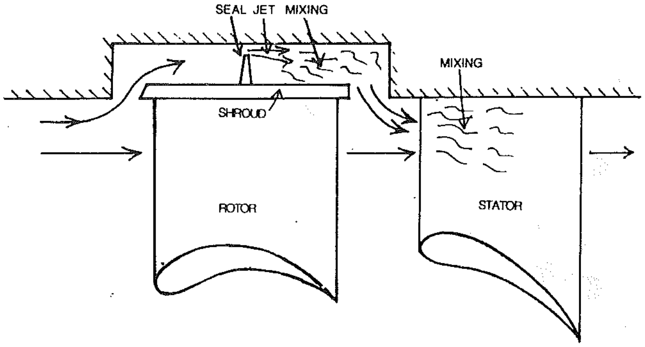

Fig. 29 Flow over a shrouded tip seal

$$\Delta L = L_{2d} g\left(\frac{2C_c^2}{1-2C_c+2C_c^2}\right) \qquad (49)$$

where C_c is the tip jet contraction coefficient, g is the tip gap, and L_{2d} is the two-dimensional lift per unit span.

The change of lift due to the changed mass flow is, however, not confined to the tip region and numerical calculations show that it affects most of the span. For a turbine blade both these effects contribute to a loss of lift while for a compressor blade the increase in lift over the span is likely to outweigh the loss of lift near the tip. Again it should be emphasized that these changes in lift and work are primarily inviscid and are not necessarily associated with a loss of efficiency.

8.2 Leakage Loss of Shrouded Blades. Entropy creation due to tip leakage flows is primarily associated with the mixing processes that take place between the leakage flow and the mainstream. Considering first shrouded blades, the flow over the shrouded turbine blade with a single tip seal is illustrated in Fig. 29. The leaking flow contracts to a jet as it passes through the seal with the area of the jet being lower than the seal clearance by a contraction coefficient whose value is typically about 0.6. If there is no significant restriction upstream of the seal the flow up to the throat of the jet can be considered to be isentropic and so the amount of leakage flow is determined by the seal clearance, the contraction coefficient, the upstream stagnation pressure based on meridional velocity and by the static pressure in the jet. The latter will be influenced to some extent by the method of injecting the leakage flow back into the main flow; however, if there is no further restriction downstream of the seal, this pressure is not likely to be greatly different from the static pressure downstream of the blade row.

The jet mixes out in the clearance space and this mixing process is irreversible, creating entropy. In most practical cases the height of the clearance space is much larger than the leakage jet and so virtually all the kinetic energy associated with the *meridional velocity* of the jet is dissipated. However, measurements by Denton and Johnson (1976) show that the swirl velocity of the leakage flow is not greatly changed during this process and remains roughly the same as that of the flow approaching the blade row.

The leakage flow must now be re-injected into the main flow where the differences in both the meridional velocity and the swirl velocity of the two flows will generate further mixing loss. It can be verified by performing mixing calculations for a flow injected into a vortex that the theory of Appendix 4 for the mixing of a coolant jet can be applied independently to the meridional and swirl components of velocity. Equation (22) shows that the result depends on the angle at which the

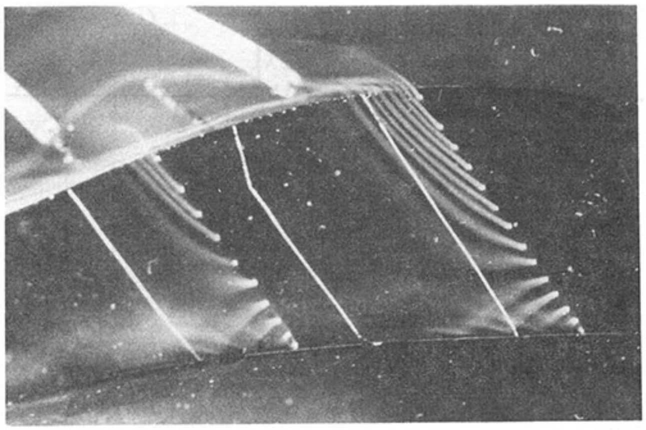

A) Smoke introduced through the blade tip showing reversed flow in the separation bubble

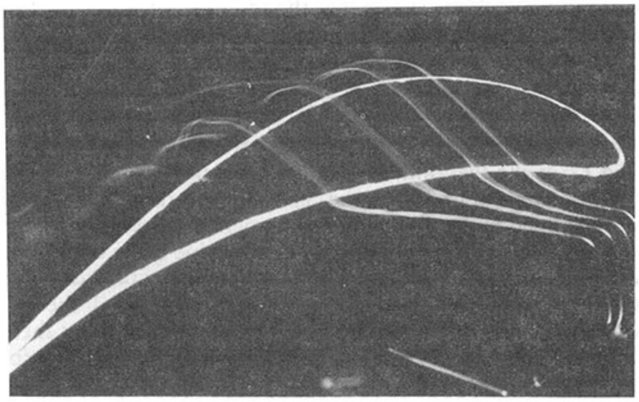

B) Smoke introduced on the pressure surface and passing over the blade tip to form the tip leakage vortex

Fig. 30 Smoke visualization of the flow in the tip gap of a turbine cascade

leakage flow is injected into the mainstream and that the difference in meridional velocity of the mainstream and the injected flow should be as small as possible. However, in most cases the difference in swirl velocity of the two flows is likely to be dominant and this does not depend on the angle of injection. If the leakage flow suffers no change in swirl velocity in the clearance space the difference in swirl velocity will be the same as the change in swirl velocity across the blade row.

A theory for the leakage flow and loss of a shrouded turbine blade, based on the above model, is presented in Appendix 5. The analysis is for incompressible flow but is easily extended to compressible flow by numerical calculations. This theory is based on simplification of an extremely complex flow; however, its predictions have been reasonably well verified by measurements of the flow over a model of a turbine shroud by Denton and Johnson (1976). The predicted rate of change of stage efficiency with tip clearance is also realistic with $d\eta/d(g/h)$ in the range 1.5–2.5, increasing with stage loading and with reaction. It is interesting to note that the theory predicts that any loss of swirl velocity of the leaking flow before it mixes with the mainstream flow, e.g., by friction on the casing, acts to reduce the overall loss. It is also interesting that the overall entropy rise per percent of leakage flow is determined almost entirely by the mixing process downstream of the blade row while the flow processes over the shroud mainly affect the leakage flow rate.

There are few other methods available for estimating the loss of shrouded turbine blades. Came (1969) suggests using the same formula as he recommends for unshrouded blades (a modified form of Ainley and Mathieson's method) but multiplying the result by about 0.9. For shrouded blades with multiple seals the blade pressure drop should be roughly equally divided between the seals (provided that they have the same clearance) and so, for incompressible flow, the resultant leakage and loss should vary inversely as the square root of the number of seals. Came quotes unpublished data suggesting that the loss varies as the number of seals to the power -0.42.

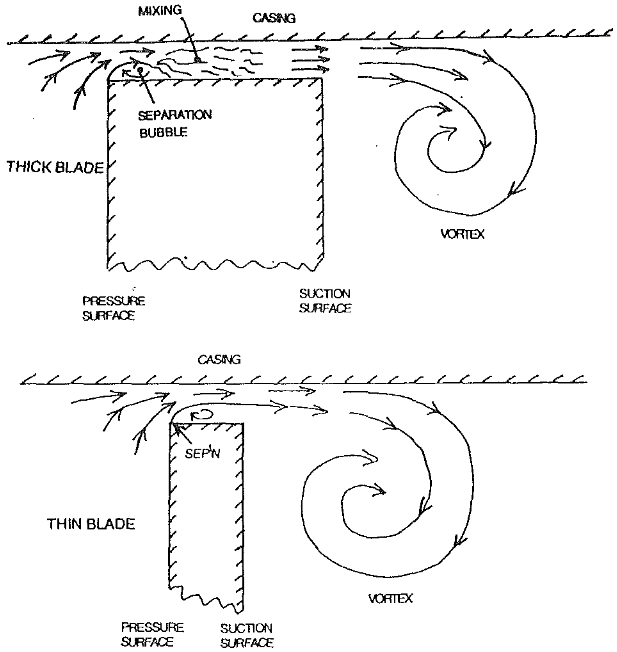

Fig. 31 Flow over the tip gap for an unshrouded blade

There is no known work on the detailed flow processes over shrouded compressor blades. The flow through the seal and clearance space can be assumed to be similar to that described above but the disturbance caused when the leakage flow reenters the main flow upstream of the blade row through which it is leaking is likely to be much more important. This flow will have substantial negative incidence relative to the blade inlet angle and this could cause increased losses in the flow through the blade tip region. However, the disturbance to the flow entering the next downstream blade row should be reduced by the bleeding off endwall fluid to leak upstream over the shroud.

8.3 Tip Leakage Loss of Unshrouded Blades. The leakage flow over unshrouded blades has been much more intensively studied than that over shrouded blades. For turbine blades detailed measurements are reported by Bindon (1989), Moore and Tilton (1988), Heyes and Hodson (1993), and Yaras and Sjolander (1992). Bindon's smoke visualization of the flow over the tip using smoke is shown in Fig. 30 and the flow in the tip gap is sketched in more detail in Fig. 31. The flow entering the tip gap from the pressure side of the blade separates from the blade tip and contracts to a jet, with a contraction coefficient of about 0.6. The exact value of the contraction coefficient depends on the radius of the pressure surface corner. The flow up to the throat of the jet is almost isentropic and is not greatly influenced by the component of velocity along the chord of the blade, i.e., out of the paper in Fig. 31. This chordwise velocity may be significant within the separation bubble and convects low-energy fluid to the point of minimum pressure above the tip. However, because the area of the bubble is so small, the mass flow involved is unlikely to be significant.

If the blade thickness is more than about four times the tip gap (Fig. 31*a*), as is usually the case for turbines, the jet mixes out above the blade tip with a consequent increase in static pressure and in entropy. The chordwise component of velocity is substantially conserved during this mixing. The static pressure after the mixing is usually assumed to be the same as that

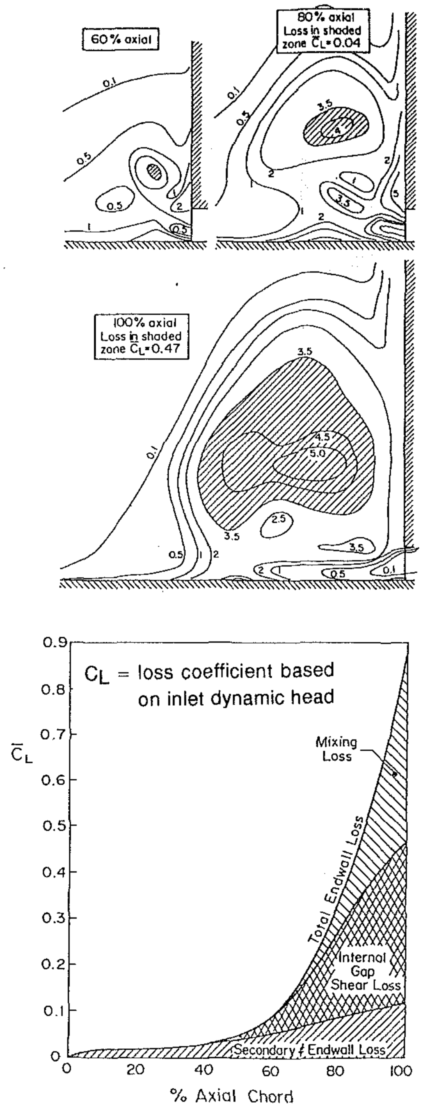

Fig. 32 The growth of tip leakage loss through a turbine blade passage, from Bindon (1988)

on the suction surface of the blade. However, some measurements (e.g., Bindon, 1989; Yaras and Sjolander, 1992) show this is significantly lower than the two-dimensional pressure because of the blockage effect of the tip leakage vortex. If the pressure after mixing is known the leakage flow rate and the entropy generation in the tip gap can be obtained by treating the flow as a two-dimensional orifice with a known contraction coefficient (Moore and Tilton, 1988).

The mixing of the leakage flow and the mainstream flow on the suction surface side of the tip gap is another example of the type of mixing process described in section 4 of this paper in which the overall loss can be obtained by applying the global conservation equations. Since the two flows have different velocities, in both magnitude and direction, there is a vortex sheet at their interface, Fig. 30, and this rolls up into a concentrated vortex as the leakage flow moves downstream along the suction surface–endwall corner. However, the overall entropy production in the mixing process is not dependent on the details of this vortex. Equation (22), for the mixing of a jet with a mainstream, can be applied directly and shows that the entropy generation is proportional to the difference in the streamwise velocity of the two flows. If the jet mixes out close to the suction surface, this is effectively the same as the difference between the surface velocities on the suction side and pressure sides of the blade. Figure 32, from Bindon (1989), shows stagnation pressure contours and loss growth through a turbine cascade with tip clearance and illustrates that most of the mixing takes place near the suction surface but that it is not complete at the trailing edge. In a machine mixing will continue through the next blade row and this makes it difficult to make accurate predictions of the overall loss.

The leakage flow over unshrouded compressor blades is not different in principle from that described above for turbines. The main difference arises because the thickness of the blades relative to the tip gap is likely to be much less than for turbines. As a result the leakage jet is unlikely to reattach to the blade tip within the gap, as shown in Fig. 31(*b*). Storer (1991) finds that the jet does not reattach within the gap if the latter is more than about 40 percent of the blade thickness. This means that there is no pressure recovery in the clearance gap and so the discharge coefficient relating the leakage flow rate to the tip gap and pressure difference will be less than for a turbine. Storer finds a typical value of 0.8 for this discharge coefficient.

Equation (22) shows that the *total* entropy production in the mixing process depends on the leakage flow rate and on the difference in the streamwise velocity of the mainstream (suction side) flow and the leakage flow. This velocity difference will be closely the same as the difference in blade surface velocities and so it can be argued that it is not affected by whether the mixing takes place above the blade tip or with the mainstream near the suction surface. Much of the mixing takes place near the suction surface of the blade and for compressor blades this will be a region of decelerating flow, hence the entropy production will be greater than that calculated for mixing at constant area. However, Storer finds that most of the entropy generation takes place near the point of leakage and so this effect may not be dominant.

A simple theory for the tip leakage loss of unshrouded blades based upon the above model is reproduced in Appendix 6. The model is equally applicable to compressors and turbines. It is developed for incompressible flow but is easily extended to compressible flow. The method assumes that the surface pressure distribution is known but for cases where it is not simple approximations to estimate the pressure distribution in terms of the inlet and outlet flow angles and blade solidity are suggested. These approximations take no account of the lowering of the suction surface pressure near the tip by the blockage effect of the leakage vortex.

The only empiricism contained in the theory is a value (usually 0.6) for the contraction coefficient of the leakage jet. Despite this it gives realistic predictions of the rate of change of efficiency with tip clearance. For both turbines and compressors the value of $d\eta/d(g/h)$ is predicted to lie in the range 2.0–3.0, increasing with increased stage loading and with reduced flow coefficient. This is typical of the values quoted by Roelke (1973) for turbines and by Moyle (1988) for compressors.

8.4 Effect of Relative Motion Between the Blade Tip and Casing.

All known theories for leakage loss neglect the relative motion between the blade tip and the endwall. In a compressor this relative motion is such as to increase the leakage flow and in a turbine it acts to reduce it. The motion may also affect the pressure difference across the blade tip by forming a scraping vortex on the leading surface of the blade. The importance of the relative motion has been investigated by Morphis and Bindon (1988) and by Yaras and Sjolander (1992) all of whom worked on turbine blades. Both found that the general flow pattern over the tip was not greatly affected by the relative motion and that the relative motion increases the pressure on the suction side of the clearance gap. The latter effect acts to reduce the leakage and loss. Yaras and Sjolander found that the discharge coefficient was approximately halved by this effect at full tip speed. This reduction in leakage flow appeared to be caused by the change in the tip pressure dif-

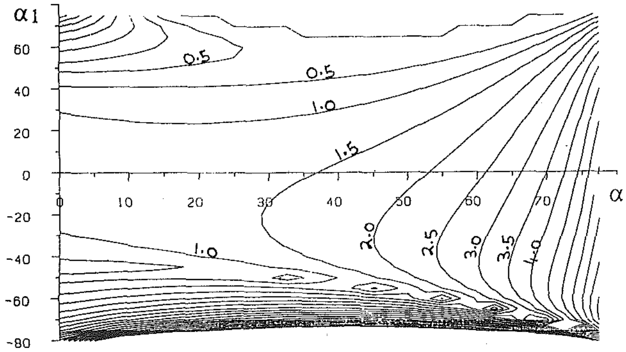

Fig. 33 The tip leakage loss coefficient of shrouded blades: contours in percent exit dynamic head per 1 percent clearance/height

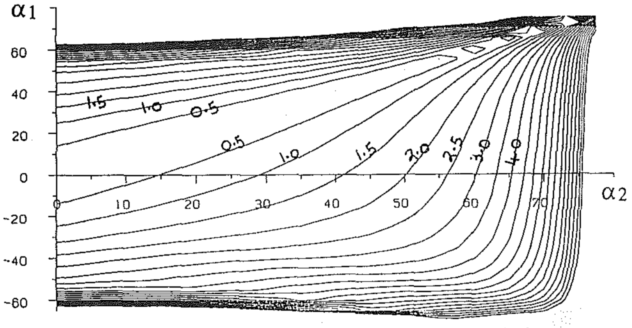

Fig. 34 The tip leakage loss coefficient of unshrouded blades: contours in percent exist dynamic head per 1 percent clearance/height

ference rather than a change in the velocity profile within the tip gap. In particular the boundary layer on the endwall within the gap appeared to be *extremely* thin. This implies that theories such as that of Appendix 6 can still be used either with a modified surface pressure distribution or with an empirical modification to the discharge coefficient.

The main weakness of all these methods is the assumption that the mixing between the main flow and the leakage flow takes place immediately after they meet. Equation (23) suggests that most of the mixing takes place very quickly and this is supported by Storer's findings for compressor blades. However, Bindon's results for turbine blades, Fig. 32, show that some of the mixing continues well downstream of the point of leakage. Hence, in practice diffusion during mixing may increase the mixing loss, for both compressors and turbines.

8.5 Comparison of Shrouded and Unshrouded Blades. It is of interest to compare the tip leakage loss of shrouded and unshrouded blades. Results from the theories of Appendices 5 and 6 are presented in Figs. 33 and 34. The loss coefficients plotted are those obtained at a tip clearance of 1 percent of blade height and are defined in terms of the blade exit dynamic head, even when the blade represents a compressor. Figure 34 for unshrouded blades is applicable to both turbines and compressors, but Fig. 33 is only really applicable to shrouded turbines. For unshrouded blades the pressure difference driving the leakage flow is that between the pressure and suction surfaces of the blades, while for shrouded blades it is the overall pressure change over the blade tip. For most blade rows these two pressure differences are similar and so, for the same tip clearance, the leakage flow rates will be similar for shrouded and unshrouded blades. However, for low-reaction rotor blades, the pressure drop over the blade row becomes much less than that between the blade surfaces and so shrouded blades will have a lower leakage flow rate.

The leakage flow coefficient depends both on the proportional leakage flow and on the magnitude of the velocity difference between the leaking flow and the mainstream flow with which it mixes. This is the suction side to pressure surface velocity difference for unshrouded blades and the change in swirl velocity across the whole row for shrouded blades. Again these two velocity differences will be comparable for most blade rows but for low-reaction shrouded blades, which have high turning, the overall change in swirl velocity will be larger than the suction to pressure side surface velocity difference.

Hence we may conclude that for most blade rows there is little to choose between unshrouded blades and shrouded blades *with a single tip seal*. For low-reaction blades the situation is less clear since shrouded blades will have a lower leakage flow rate but a greater loss per unit leakage. Only for impulse blades, where the leakage flow drops to zero, do shrouded blades have a decided advantage. This is confirmed by Figs. 33 and 34, which predict that shrouded blades have a slightly lower loss coefficient for most combinations of flow angle but a significantly lower one for near impulse conditions. For most blade rows the real advantage of using shrouded blades comes from the ability to use more than one tip seal.

9 Endwall Loss

The term "endwall loss" will be used in preference to "secondary loss" to describe all the loss arising on the annulus walls both within and outside of the blade passage. This is the most difficult loss component to understand and to predict and virtually all prediction methods are still based on correlations of empirical data, often with very little underlying physics. The flow patterns near the endwalls are determined by the secondary flow whose strength depends mainly on the thickness of the upstream boundary layer and on the amount of turning in the blade row. They can be predicted approximately by classical secondary flow theory, or nowadays, more accurately, by numerical calculations. It is important to realize that the secondary flow is an inviscid phenomenon that does not by itself give rise to any entropy generation. Conversely, secondary flow is caused by streamwise vorticity, which is itself a direct result of viscous shear on the endwalls.

For turbines, endwall loss is a major source of lost efficiency, contributing typically 1/3 of the total loss. It is generally accepted that in order to explain observed turbine efficiencies the entropy generation per unit surface area of the endwall must be considerably greater than that on the blade surfaces.

For compressors it is more difficult to separate endwall loss from tip leakage loss and from losses due to flow separation, and some prediction methods make no distinction between the two. The reduced turning of compressor blades tends to reduce the strength of the secondary flows but the thicker endwall boundary layers increase the amount of fluid involved. The fact that the flow is being decelerated makes fluid near the endwalls of compressors prone to separate with consequent major effects on the blockage factor and the stalling point of the blade rows. Overall, the effects of endwall flow and losses in compressors are probably even more important than in turbines. Because of the major differences between them the endwall loss of turbines and compressors will be considered separately.

9.1 Endwall Loss in Turbines. Dunham (1970) reviewed the available correlations for turbines and compared them with cascade data. He found very large discrepancies both between the correlations themselves and between the correlations and the data. Based on this survey Dunham and Came (1970) suggested an improved correlation for use in turbines where, in order to predict the correct overall efficiency, they found that it was necessary to use an endwall loss several times greater than measured in cascades. This correlation is still widely used; however, it contains little physics and in fact predicts that the loss is independent of blade solidity while simple physical arguments would suggest that this is one of the most important factors influencing endwall loss. More recent correlations have

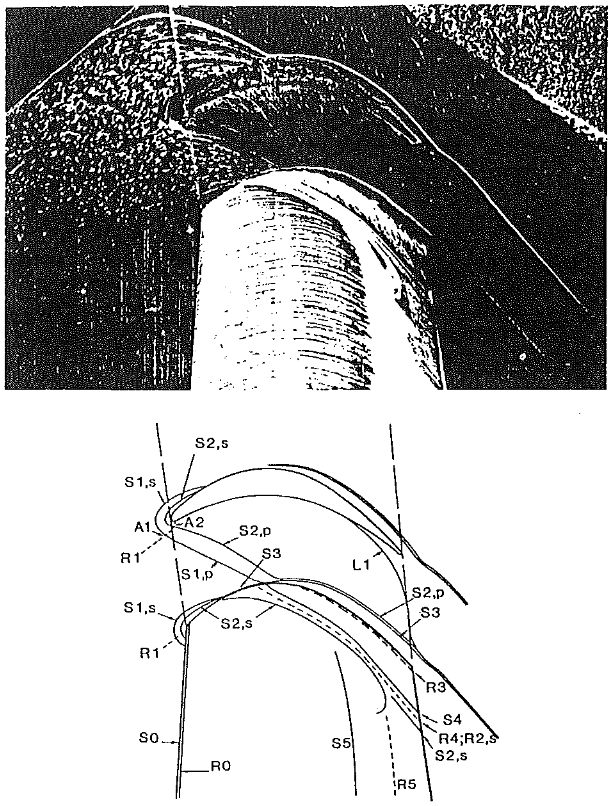

Fig. 35 Flow visualization on the endwall and suction surface of a turbine cascade from Hodson and Dominy (1985)

been produced by Sharma and Butler (1987) and by Gregory-Smith (1982). Both of these include some simple physical modeling of the flow processes and both base their loss predictions partly on simplified endwall boundary layer calculations. Sharma and Butler suggest that the skin friction on the endwall needs to be increased considerably above two-dimensional values (in fact by a factor of about 5) to explain the observed loss, while Gregory-Smith uses a conventional two-dimensional turbulent boundary layer calculation, with no increase in skin friction, and includes an estimate of the secondary kinetic energy as a loss.

The flow processes near the endwall of turbine cascades have been intensively studied and there is an enormous literature on the subject. The first detailed measurements of the secondary flow processes in a turbine cascade were given by Langston et al. (1977) and more recently Sieverding (1985) presented a comprehensive review of the flow processes in cascades. Very detailed measurements of the endwall flow within turbine cascade passages have recently been published by Walsh and Gregory-Smith (1990) and by Harrison (1989). As a result of this and much other work the flow processes near the endwalls of turbine cascades are well understood. Figure 35, from Hodson and Dominy (1987) illustrates some aspects of this complex flow and a brief description of it is necessary if we are to consider the loss-producing mechanisms.

The endwall boundary layer undergoes a three-dimensional separation as it approaches the leading edge stagnation point, giving rise to the well-known horseshoe vortex. The boundary layer fluid is funneled between the two lift-off lines of this separation (e.g., lines $S1,s$ and $S1,p$ in Fig. 35) and is driven toward the suction surface of the blade by the cross-passage pressure gradient. The greater the blade turning and loading the sooner the endwall boundary layer fluid moves onto the suction surface. Once on the suction surface this fluid is driven up it (between lines $S2,s$ and $S4$) by the secondary flow and convected along it by the mainstream flow so that at the trailing edge it appears as a region of high-entropy fluid above the suction surface–endwall corner.

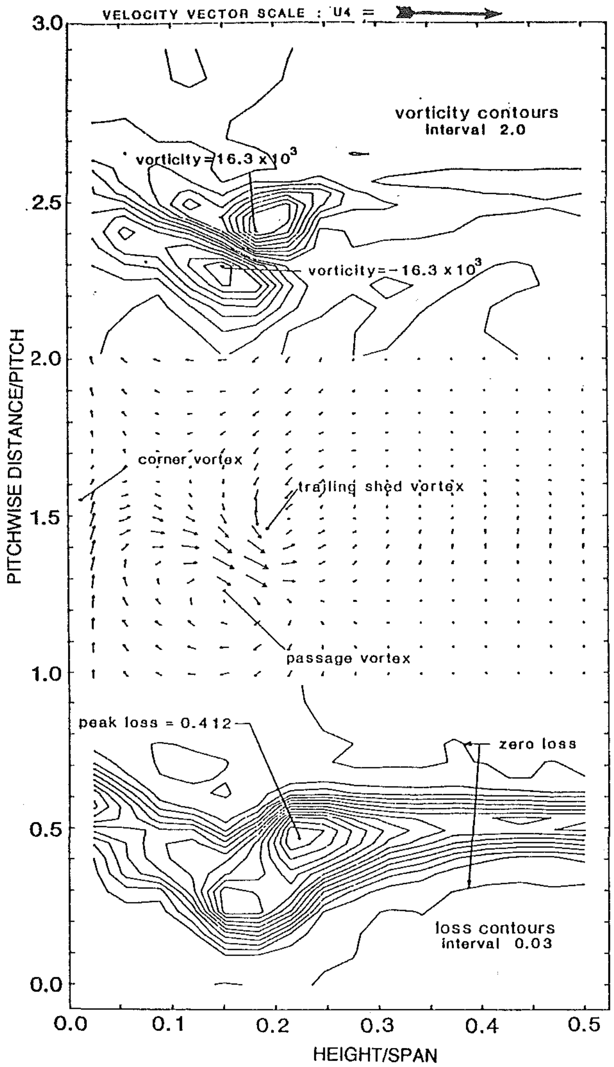

Fig. 36 Loss coefficient and vorticity contours and secondary velocity vectors downstream of the cascade of Fig. 35

A new endwall boundary layer must grow downstream of the separation lines. Initially this is extremely thin and probably laminar. It is subject to a strong cross-stream pressure gradient and to the "scouring effect" of the secondary flow, both of which make the boundary layer highly three dimensional and try to sweep it toward the suction surface. As a result fluid is continually being removed from this boundary layer and swept onto the suction surface so that the new endwall boundary layer itself stays thin. Harrison (1989) gives detailed measurements of the development of this boundary layer and finds that it remains laminar over much of the endwall. The strong crossflow in the new boundary layer induces a small corner vortex, rotating in the opposite sense to the main passage vortex, in the endwall–suction surface corner. Figure 36 shows results from traverses behind the cascade of Fig. 35 illustrating the loss concentration and the secondary flow vortex.

Downstream of the trailing edge the high-entropy fluid from the upstream boundary layer and the blade wake are both distorted and convected by the passage vortex and gradually mix out with the mainstream flow. In a turbine this mixing is unlikely to be complete before the next blade row. The endwall boundary layer is still very thin at the trailing edge. In a cascade, it continues to grow relatively undisturbed downstream of the blade row and becomes more two dimensional as the passage vortex and the cross stream pressure gradient decay. In a turbine the boundary layer will have to cross the gap separating the stationary and rotating parts of the endwall and will then find itself adjacent to a surface moving with a different velocity before it enters the next blade row. As a result of this change of frame of reference the endwall boundary layers entering all except the first blade row in a turbine will be skewed relative to the mainstream flow. Hence cascade tests, which usually have a comparatively thick collateral endwall boundary layer, may not be representative of conditions in a turbine.

The direction of the boundary layer skew in a turbine is such as to induce negative incidence onto the blade row and so the direction of the relative inlet flow in the boundary layer reinforces the secondary flow. This can also be thought of as being due to the increased streamwise vorticity resulting from the skew. Unless the inlet boundary layer is very thick, the effects of the skew on blade loading are not large and so the local negative incidence does not significantly reduce the cross-passage pressure gradient driving the secondary flow.

The effects of skewing of the inlet boundary layer on the flow and loss have been examined by Bindon (1979), Boletis et al. (1983), and by Walsh and Gregory-Smith (1990). All of them used cascades with moving endwalls and found that the skewing had a large effect on the secondary flow and loss. The latter in particular found that skewing in the direction found in a turbine greatly increased the magnitude of the secondary flow and increased the loss by about 50 percent while skewing in the opposite sense reduced both. The effects of skew clearly need to be included in a realistic turbine prediction method but this is seldom done.

We can now consider the effects of this complex flow on the entropy generation in turbines. The first question that comes to mind is whether the entropy generation per unit surface area of the endwalls can be estimated in the same way as that on the blade surfaces by using a simple approximation to the dissipation factor, C_d. As far as is known there are no published results for the dissipation in a boundary layer with strong crossflow. Equation (A1.6) includes the dissipation due to crossflow but it cannot be integrated until the variation of the transverse shear stress through the boundary layer is known. Harrison (1989) makes an estimate of the effects of skew on the dissipation. By using his measured velocity profiles, which have up to 50 deg of skew, and assuming that the distribution of turbulent viscosity is unchanged, he concludes that the skew changes the dissipation by at most 10 percent. This is only a tentative conclusion, but it suggests that the dissipation rate on the endwalls is unlikely to be greatly different from that in a collateral boundary layer with the same Re_θ. However, the state of the endwall boundary layer is a major unknown and will have a very large effect on the dissipation coefficient. The boundary layer entering the blade row is almost certain to be turbulent but that after the separation line is likely to be laminar with a very low value of Re_θ. Harrison found that it remained laminar over most of the region near the pressure surface but became turbulent in the higher velocity region near to the suction surface.

If we make the gross assumption that the dissipation coefficient is constant over the whole endwall and obtain the relative velocity from blade to blade calculations, we can integrate Eq. (39) to calculate the entropy production rate. Harrison obtained an average dissipation coefficient of 0.0014 on the endwall of his cascade in this way, i.e., rather less than the value of 0.002 suggested in section 3 for use on the blade surfaces. This is to be expected given that the boundary layer was partly laminar.

A rough idea of the magnitude of the dissipation on the endwalls can be obtained by assuming that the relative velocity varies linearly across the pitch from the suction surface to the pressure surface. If the endwall is not moving relative to the blades the entropy production rate can then be integrated across the pitch to give

$$\dot{S} = 0.25 \int_0^{C_x} \frac{C_d}{T} \frac{(V_s^4 - V_p^4)}{(V_s - V_p)} \rho \, w \, dx \qquad (50)$$

where x is the axial distance and w is the local suction to pressure surface gap.

Denton (1990) gives estimates of this integral obtained in a similar manner to the estimates of blade surface loss presented in Fig. 20. However, comparison of Eqs. (50) and (41) shows that for the same value of C_d the average loss per unit surface area on the endwall is predicted to be only about one quarter of that on the blade surfaces. This is because the dissipation varies as the cube of the velocity and only a small area of the endwalls, adjacent to the suction surface, is subject to high velocity levels similar to those on the suction surface. The ratio of the surface area of *both* endwalls to that of the blade suction surface is approximately

$$\frac{A_{\text{wall}}}{A_{\text{suct}}} = \frac{2}{A_r} \frac{C_x}{C} \frac{p}{C} \qquad (51)$$

where A_r is the blade aspect ratio based on the true chord. both C_x/C and p/C are likely to be about 0.75 and so the ratio of areas is of the same order as the reciprocal of the aspect ratio. Hence Eqs. (41) and (50) predict that at an aspect ratio of unity the entropy generation on the endwalls within the blade row would be only about 1/4 of that on the blade surfaces. In fact at this aspect ratio the total endwall loss is usually considered to be comparable to the blade surface loss. Hence, even allowing for a slightly increased value of C_d due to the skewing and low Re_θ it seems unlikely that entropy generation in the boundary layer within the blade row can explain the observed magnitude of turbine endwall loss.

The endwalls downstream of a turbine blade are subject to the full blade exit velocity and so their entropy generation rate per unit area will be comparable to the maximum value on the suction surface. In a turbine these downstream endwalls typically extend about 1/4 of an axial chord behind the blades before the relative velocity between the flow and the wall is reduced by the change from stationary to rotating walls, or vice versa. Thus the entropy generation in this region is comparable to that on the endwall within the blade row. This is a significant loss component, which can only be reduced by minimizing the area of endwall exposed to the full blade exit flow velocity.

The endwalls upstream of a turbine blade are subject to the relative inlet velocity, which is usually significant less than the exit velocity. The axial extent of these walls is unlikely to be more than about 1/4 of an axial chord and so the entropy generated in the inlet boundary layers is usually much less than that on the downstream endwalls. Hence it seems that the total entropy generation in the endwall boundary layers, upstream of, within, and downstream of the blade row can only explain about 2/3 of the observed endwall loss.

There is a good deal of evidence, summarized by Sharma and Butler (1987), that the endwall loss generated within the blade row, i.e., the total loss minus the loss present in the inlet boundary layer, remains almost constant as the thickness of the inlet boundary layer is changed. This implies that the loss generated by the mixing out of the inlet boundary layer within the blade row is small. On a one-dimensional basis this mixing takes place in an accelerating flow so the mixing loss should be reduced. However, secondary flow and inlet skew produce streamwise vorticity and streamwise acceleration amplifies this and increases the kinetic energy associated with it. This is often called secondary kinetic energy (s.k.e.).

Kinetic energy is a relative quantity and so care is needed in defining exactly what is meant by s.k.e. It is usually taken to be the kinetic energy associated with the velocity component perpendicular to some primary flow direction, but exactly how this direction is defined is arbitrary. The production of s.k.e. by secondary flow is an inviscid process and so is not initially a loss. Classical secondary flow theory (Hawthorne, 1955) predicts that there is a value of the ratio of inlet boundary layer thickness to blade pitch that maximizes the s.k.e., but it is not known how well this applies to real flows with large disturbances. The s.k.e. also increases with blade turning and with inlet boundary layer skew. Some of the s.k.e. arises from the inviscid secondary flow induced by the inlet boundary layer and some of it comes from the secondary flow induced by the new endwall boundary layer. Comparison of results from viscous and inviscid calculations suggests that most of the secondary flow is generated by the inlet boundary layer and in fact viscous effects within the blade row appear to reduce its strength slightly.

When the mean flow is accelerated, the s.k.e. of a streamwise vortex increases and it can be shown that in inviscid flow the s.k.e. is proportional to the square of the length of the vortex. It is known that dissipation within a vortex core is very high and so the subsequent decay of this s.k.e. leads to an increase in entropy. Hence vortex stretching provides a mechanism for the generation of high endwall losses in highly accelerating blade rows. Some of the dissipation within the vortex core occurs within the blade row and will be measured as a loss at the trailing edge. However, the dissipation continues downstream of the blade row and it is often assumed that all the s.k.e. of the vortex at the trailing edge is lost. Gregory-Smith's method of estimating the loss assumes this. The magnitude of the s.k.e. in cascades has been measured by many workers. Its value is typically in the range 0.2–0.50 of the endwall loss present at the trailing edge.

The flow downstream of a trailing edge has been studied in detail by Moore and Adhye (1985) who found that the decay of s.k.e. as the flow progressed downstream from the trailing edge closely matched the increase in entropy. The mixing loss downstream of a trailing edge can of course be calculated by applying the conservation equations between the trailing edge flow and a completely uniform mixed out downstream flow. This is often done in presenting cascade results. However, a completely uniform mixed out flow is not representative of what happens in a machine where spanwise variations in the circumferentially averaged flow decay slowly and will certainly remain at entry to the next blade row. They will be seen by this row as a spanwise variation in average inlet angle, which will be reflected in the blade work. Hence they are not a loss, and cascade measurements based on a completely uniform mixed out downstream flow will overestimate the endwall loss. The pitchwise variations in flow decay more rapidly than the spanwise variations (as found by Moore and Adhye) and it is not obvious whether they can be used by a following blade row.

The interaction between a secondary flow vortex (or a tip leakage vortex) and a downstream blade row is an extremely difficult problem that has not been widely researched. Some results are available from Sharma et al. (1992) and from Binder (1985). These illustrate the complexity of the unsteady flow but they tell us little about loss. The possibility of the highly dissipative process known as vortex breakdown occurring in turbomachines deserves investigation.

To summarize the loss-producing mechanisms associated with a turbine endwall we may say that the total loss is a combination of many factors. About 2/3 of it comes from entropy generation in the annulus wall boundary layers within, upstream of, and downstream of the blade row. When turned into a loss coefficient, this will vary inversely with aspect ratio as illustrated by Eq. (51). A further part comes from mixing loss of the inlet boundary layer, which is amplified by the secondary flow and will give a loss coefficient proportional to the ratio of inlet boundary layer thickness to span but which is an unknown function of blade load and turning. A third component is the loss associated with the s.k.e., which is of the order of 1/4 of the total endwall loss. This proportion will depend on inlet boundary layer thickness and skew and on blade turning and blade loading but there are no simple theories relating the loss to any of these factors. The proportion of the s.k.e. that is lost is also not yet predictable. Other contributions to endwall loss may come from local flow separations and from thickening and premature transition of the blade surface boundary layers as a result of the secondary flow. In all the situation is too complex and too dependent on details of the flow and geometry for simple quantitative predictions to be made. The main hope in the near future is that the loss can be quantified by three-dimensional Navier–Stokes solutions, which already give good qualitative predictions of the flow.

9.2 Endwall Loss in Compressors. The endwall flow in a compressor cascade has been less intensively studied than that in a turbine, possibly because the flow in a cascade is less relevant to that in a real machine than is the case for a turbine. The major differences between the endwall flows in compressors and turbines are that the blade turning is much less, the endwall boundary layers are much thicker relative to the blade chord, and the boundary layers are being decelerated. The first two of these factors tend to make the secondary flow less intense but the last tends to amplify it. The endwall losses are, if anything, more important in compressors than in turbines and Howell's (1945) well-known graph of the breakdown of losses in a typical axial compressor shows about 2/3 of the loss due to "annulus loss" and "secondary loss" at design conditions.

Cumpsty (1989) points out clearly that the endwall boundary layers cannot be considered as conventional boundary layers during their interaction with a blade row. The overall thickness of the endwall boundary layer in a multistage compressor is typically half the blade chord, hence the pressure changes take place in a few boundary layer thicknesses, which is very much more rapid than those considered by conventional boundary layer theory. This means that viscous forces play relatively little part in the flow behavior, which is likely to be more like that of an inviscid shear layer than a boundary layer. If we assume that a compressor blade has a collateral endwall boundary layer with a free-stream inlet velocity V_1 and an exit velocity V_2, then on a one-dimensional, incompressible and inviscid basis, all the fluid in the inlet boundary layer with a velocity less than

$$V_{\text{sep}} = V_1\sqrt{1-(V_2/V_1)^2} \qquad (52)$$

must separate within the blade row. At a typical value of $V_2 = 0.7\,V_1$ this implies that all fluid with velocity less than about 30 percent of the inlet free-stream velocity would separate. In practice this fluid does not separate in the conventional two-dimensional sense. As it decelerates, it becomes more susceptible to the cross-passage pressure gradient, which is driving the secondary flow, so that before its meridional velocity becomes zero it has acquired a component of velocity toward the suction surface. On reaching the suction surface–endwall corner this high entropy fluid accumulates and is further decelerated by the overall pressure rise to form the large corner separation that is almost invariably seen in compressor cascades. This separation is responsible for much of the blockage observed in compressor blade rows. Its effects may not be localized and it can interact with the suction surface boundary layers to cause separation over much of the blade span. Figure 37 (zero tip clearance case) shows an example of such a separation in a compressor cascade.

The above behavior applies directly to cascade flows with collateral inlet boundary layers; however, in an actual compressor the picture is altered by the effects of skewing and tip leakage. In a compressor the lower meridional velocity in the annulus boundary layer causes positive incidence onto the blades and so directs the relative velocity of the boundary layer fluid toward the pressure surface. In unshrouded blade rows

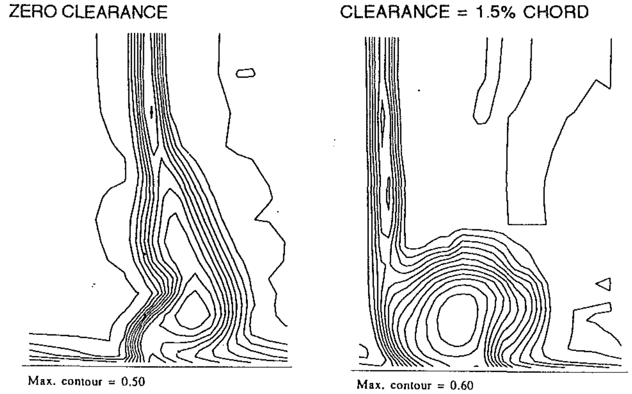

Fig. 37 Loss contours near the endwall of a compressor cascade with and without tip clearance

the relative motion of the endwall within the blade passage enhances this effect. The increase in *relative* tangential velocity within the skewed boundary layer may be greater than the deficit in meridional velocity so that the endwall fluid can have higher *relative* stagnation pressure than the mainstream flow. Both these factors act to oppose the conventional secondary flow. For rotor tip sections, where the blade turning is low, the effect of skewing is likely to dominate and drive the endwall fluid toward the blade pressure surface. Here it will enter a region of favorable pressure gradient and so may cause less harm than if there were no skew. For rotor hub and stator tip sections the blade turning is greater and so the effects of secondary flow usually dominate those of skew and the endwall boundary layer fluid ends up on the suction surface–endwall corner where it is likely to cause separation.

The interaction between tip clearance and the endwall flow can have a dominant influence in compressors with unshrouded blade tips. The tip leakage flow directs a jet of high-velocity fluid from the pressure surface into the suction surface–endwall corner where the high-entropy inlet boundary layer fluid tends to concentrate. This may succeed in re-energizing the boundary layer fluid sufficiently to prevent the corner separation with a consequent reduction of loss. This interaction accounts for the observation that in some compressors there is an optimum tip clearance that gives higher efficiency than either zero clearance or larger clearances. This corresponds to the leakage flow being just sufficient to prevent the corner separation but not sufficient to generate a large tip leakage loss. This phenomenon has been studied in detail in cascade by Storer (1991), some of whose results are shown in Fig. 37.

If compressor endwall boundary layers remain attached the entropy generation per unit surface area of the endwalls can be estimated from Eq. (50). In fact, because the Re_θ of the endwall boundary layer is so large it is possible that the dissipation per unit surface area may be somewhat less than on the blades. Storer measured an endwall loss of about the same magnitude as the profile loss on his compressor cascade with no tip clearance and infers a similar level when tip clearance is present. However, if this were always the case compressors would be much more efficient than they are in practice.

The effects of endwall flow on the loss of compressor blades are believed to be dominated by mixing and by the promotion or suppression of separations. The mixing loss in the endwall boundary layer will be increased because of the diffusing flow and the very large increases of mixing loss, shown by Fig. 11 at typical levels of compressor blade diffusion, would correspond to the endwall boundary layer separating. As described above this separation will be highly three-dimensional and so cannot be predicted by the usual diffusion factor arguments. Once a separation occurs it will mix out partly within the blade passage and partly downstream. Storer's results, Fig. 37, show that the mixing is far from complete half a blade chord behind his cascade.

The interblade row gap is so small in most axial compressors that it is likely that much of the mixing takes place in the unsteady environment of the downstream blade row. Even for mixing within and immediately downstream of the blade row there is no satisfactory theory to calculate the entropy generated by the mixing out of a separation. When mixing occurs in the downstream blade row the situation is even less predictable.

There are comparatively few published methods for predicting endwall losses in axial compressors. Howell (1945) distinguished between annulus loss and secondary loss and predicted each of them in terms of a drag coefficient. However, the expression for annulus loss does not include the surface area of the annulus and the secondary loss is based on the induced drag of a wing tip vortex, which, as previously noted, is an inviscid phenomenon. Hence, although Howell's method has been widely used for many years, it cannot be said to be related to the physics of the flow. Koch and Smith (1976) use a method that is described in more detail by Smith (1970). Their method is based on the concept of a repeating stage for which one can use the definition of efficiency in the form

$$\frac{\Delta\eta}{\eta}=\frac{\Delta m}{m}-\frac{\Delta T_q}{T_q} \qquad (53)$$

where T_q is the blade row torque, to relate changes of efficiency relative to a stage with no endwall loss to changes of mass flow and to changes of blade tangential force. The change of flow is found from the endwall boundary layer displacement thickness, which is correlated against the ratio of tip clearance to staggered gap, and the pressure rise as a fraction of maximum pressure rise. The change of torque is found from the tangential force defect in the tip region, which is correlated as a function of the displacement thickness and pressure rise. Equation (53) is thereby effectively a vehicle for correlating the annulus boundary layer displacement thickness and tangential force deficit thickness. The method is useful in including the effects of tip clearance, endwall loss, and blockage in a single method and it includes some of the physics of the endwall flow. However, it cannot pretend to allow for the complexities of the real flow and so can only be used reliably when experimental data on similar designs are available.

Several methods that calculate the annulus boundary layer displacement thickness via a two-dimensional boundary layer calculation along the whole endwall of a compressor have been published (e.g., de Ruyck and Hirsch, 1983). These use conventional boundary layer theory and in view of what has been said about endwall boundary layer behavior in compressors this must be regarded as dubious. However, they also include considerable empiricism, including correlations for the tangential force defect, and so are able to give reasonable predictions.

Despite these criticisms of current compressor endwall loss prediction methods the author cannot offer any alternatives that will be generally valid. The flows are so complex and depend so much on the details of the geometry and of the incoming boundary layers that it is hard to believe that anything other than three-dimensional Navier–Stokes calculations can give general results. It is hoped that an understanding of the loss mechanisms will bring about improvements in design but at present these can only be quantified by experiment.

10 Application to Radial Flow Machines

Most of discussion so far has been in the context of axial flow turbomachines. Many of the ideas presented are directly applicable to radial flow turbines and compressors but there are significant differences in the relative importance of the various loss mechanisms. These will be discussed in this section.

Both radial inflow turbines and centrifugal compressors typically have a stage loading coefficient, $\Delta h_o/U_{\mathrm{tip}}^2$ around unity, where U_{tip} is the maximum blade speed. This means that for both types of machine the change in V_θ is comparable to U_{tip}. The major difference from axial flow machines arises because the blade speed U varies considerably through the rotor. This causes the change of *relative* velocity through the rotor to be less than that in an axial flow machine with the same U_{tip} and Δh_o. Hence, in a centrifugal compressor we can produce the same enthalpy rise with less diffusion of the relative flow in the rotor, and in a radial inflow turbine we can produce the same enthalpy drop with less acceleration, than in a comparable axial machine. However, in both cases the change in absolute velocity through the stators is comparable to that in an axial flow machine with the same enthalpy change.

The lower change in relative velocity through the rotor is particularly advantageous for compressors since it is the diffusion of the *relative* velocity that brings about boundary layer growth and separation. Hence centrifugal compressors can obtain much higher pressure ratios for the same rotor diffusion factor than can axial compressors. In effect most of the pressure rise is being balanced by the centrifugal force field rather than by deceleration of the relative velocity. In radial inflow turbines the reduced change in relative velocity means that higher pressure ratios can be obtained before choking, and without the losses associated with transonic flow, than is possible in axial turbines.

As regards entropy generation: In both types of machine, the average relative velocity through the rotor will be less than that in an axial flow machine with the same U_{tip} and Δh_o while that through the stator will be comparable to that in the axial flow machine. On this basis one would expect radial flow machines to be more efficient than comparable axial flow machines while in practice they are generally accepted to be slightly less efficient. The discrepancy is probably due to the more complex geometry inherent in the change of flow direction from axial to radial and vice versa. This involves a 90 deg bend, which causes stronger secondary flows than in most axial machines and also a decrease of blade span with radius, which means that radial flow machines are usually of relatively low effective aspect ratio. In comparing them with axial machines we should choose machines of comparable aspect ratio (or specific speed) and on this basis their efficiency is not obviously lower.

10.1 Radial Inflow Turbines. Radial inflow turbines usually have stator blades located in a flow where the meridional velocity is radially inward, although in small turbochargers a vaneless volute may be used to accelerate the flow. The flow through the stator blades is highly accelerating and, because of the decrease in radius the blade throat is close to, or even behind, the trailing edge. Hence blades can be designed with little or no suction surface diffusion. This means that the boundary layers on the stator may be largely, or even completely, laminar and so very low levels of loss can be achieved. In fact most of the two-dimensional loss may arise from the trailing edge, which should therefore be kept thin relative to the blade throat. The endwall loss per unit surface area should also be small but the aspect ratio is usually low and so the total endwall loss may be significant. Huntsman (1993) measured a profile loss coefficient of 1.2 percent and an overall loss coefficient of 3.3 percent for his stator blade. Both of these are very low relative to comparable values for an axial flow turbine.

The annulus boundaries in the gap between stator and rotor are subject to the highest relative velocity in the machine and so this gap should be kept as small as is possible, subject to mechanical constraints. The velocity *relative* to the rotor is low at entry, but if the rotor is unshrouded, that relative to the casing continues to be high until well into the rotor passage. This will generate large amounts of entropy on the casing, which will be transported toward the casing-suction surface corner by both the relative motion of the casing and by the secondary flow. Shrouded rotors should generate less loss in this region. Farther into the blade passage the curvature of the radial-axial bend generates low pressures on the casing that drive the blade surface boundary layers toward the casing. Hence most of the high-entropy fluid ends up in the suction surface-casing (or shroud) corner where, in unshrouded rotors, it mixes with the tip leakage flow.

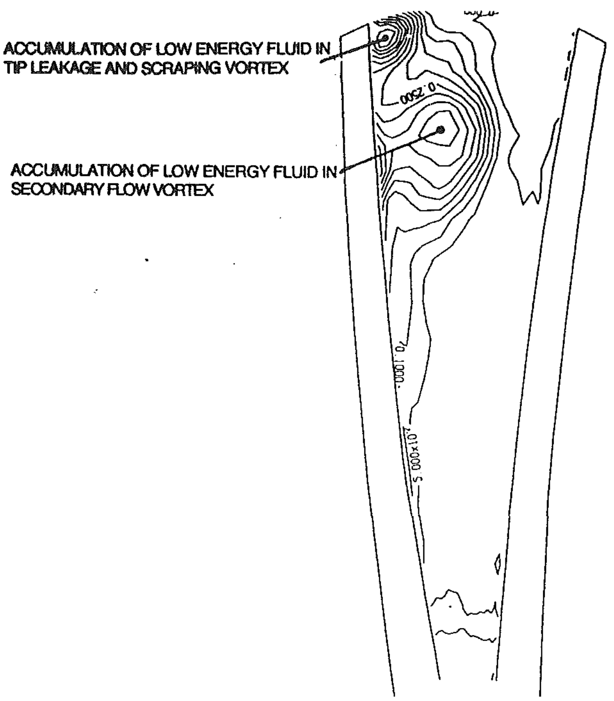

Fig. 38 Contours of relative stagnation pressure at exit from a radial inflow turbine (from Huntsman, 1993)

The entropy generation on the blade surfaces will increase rapidly as the relative velocity increases toward the blade exit. For a shrouded blade the loss on the shroud will increase similarly but for an unshrouded blade the casing loss will decrease as the velocity of the flow relative to the casing reduces. Hence, from the point of view of efficiency, it would be most beneficial to have a partly shrouded blade with a shroud only over the upstream part of the bladed passage.

For unshrouded blades tip leakage loss is likely to be more important than in an comparable axial flow machine because the low aspect ratio means that the ratio of leakage flow area to blade throat area is large. However, the relative motion of the thick casing boundary layer and blade tip will generate a scraping effect that will oppose the leakage. For shrouded blades the leakage should be very small because of the radial pressure gradient set up in the swirling leakage flow. In this case the windage loss of the shroud may be more significant than the loss due to tip leakage.

Trailing edge loss will be significant for many radial flow turbines, which, because of stressing problems, tend to have very thick trailing edges, especially near the hub where the blockage may approach 50 percent. Thus, although the rotor relative exit velocity is lower than in a comparable axial machine, the trailing edge loss may be greater. The spanwise pressure gradient resulting from the meridional curvature of the streamlines at the trailing edge is likely to produce considerable spanwise flow in the base region. The effect of this on the base pressure and trailing edge loss is not known.

Figure 38 shows contours of relative stagnation pressure measured downstream of the rotor of Huntsman's unshrouded radial inflow turbine. The accumulation of high-entropy (low-energy) fluid on the blade suction surface toward the tip can be seen, as can that in the tip leakage/scraping vortex. This turbine, which was designed using three-dimensional calculation methods, has an efficiency of about 93 percent, comparable to that of a good axial flow machine.

10.2 Centrifugal Compressors. Centrifugal compressors usually have axial inlet flow and radial outflow. The velocity of flow relative to the rotor is greatest near the tip at inlet, where it may be supersonic for high-pressure-ratio machines. Because the blade turning is much larger than in transonic axial compressors supersonic inflow can lead to very high Mach numbers and strong shocks within the inducer if it is not designed very carefully. The relative velocity decreases through the rotor and is usually comparatively modest at rotor exit. High-pressure-ratio compressors produce a large increase in density within the impeller so the meridional flow area must decrease, and the blade height decrease even more, to accommodate this. The effective aspect ratio, i.e., the mean blade height divided by the meridional chord, is of order 1/3 for many centrifugal impellers, this is much lower than in most axial flow compressors, and this should be borne in mind when comparing the two.

The flow within the impeller is now well understood, and is always highly three dimensional. The axial to radial bend induces strong secondary flows convecting the blade surface boundary layers toward the casing. Similarly the blade loading induces secondary flows convecting the hub and casing boundary layers toward the suction surface. In unshrouded impellers the latter is opposed by the relative motion of the casing. The net result is usually that a large concentration of high-entropy fluid collects in the vicinity of the casing–suction surface corner and it is this that forms the well-known jet-wake structure at the exit of the impeller. Figure 39 shows results from a numerical calculation predicting the growth of this wake through a shrouded impeller.

In unshrouded impellers the velocity of the flow relative to the casing is comparatively low at inlet and increases toward impeller exit where it becomes larger than the maximum blade surface relative velocity. Consequently the entropy generation on the casing of unshrouded blades is large while that on the rotating hub is much less. For shrouded blades the velocity relative to the shroud is always comparable to that relative to the blade surfaces and so decreases toward impeller exit. Hence, from the point of view of efficiency it would be preferable to have a shroud over the rear part of the impeller but to leave it unshrouded at inlet.

Despite these regions of high loss, the efficiency of the impeller alone is usually very high because the relative velocities are low compared to the enthalpy rise. Moore and Moore (1980) quote an impeller efficiency of 95.4 percent for Eckardt's low-pressure-ratio centrifugal impeller. The overall machine efficiency is much less than this because most of the entropy increase takes place downstream of the impeller.

Immediately downstream of the impeller there is usually a short vaneless space. The wake from the impeller starts to mix out in this space and the associated mixing loss can be calculated by applying the conservation equations, provided that the size and depth of the wake at the impeller exit are known. These may be obtained from either correlations or from numerical calculations. The methods available for this mixing calculation are reviewed by Cumpsty (1989) who concludes that the effect of the mixing loss on the overall efficiency is usually small. Since the swirl component of velocity leaving the impeller is much greater than the radial component most of the mixing loss arises from the difference in swirl velocity between the wake and the main flow. In practice it is unlikely that the mixing is complete before the flow enters the diffuser blades thus making the flow into them highly unsteady.

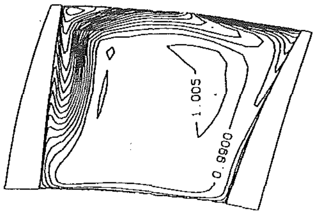

ABOUT MID PASSAGE

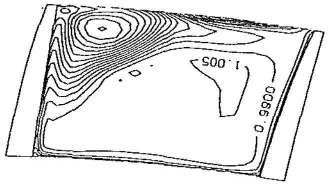

ABOUT 3/4 OF WAY THROUGH THE PASSAGE

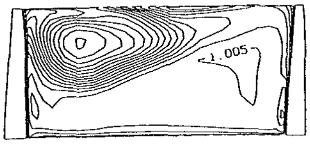

JUST BEFORE THE TRAILING EDGE

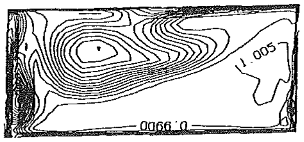

JUST AFTER THE TRAILING EDGE

Fig. 39 Growth of the wake through the impeller of a centrifugal compressor; contours of entropy

The flow leaving the impeller has a high velocity relative to both the hub and the casing; in fact this is the highest relative velocity anywhere in the machine and entropy generation on the walls of the vaneless space will be extremely high. Moore and Moore (1980) found that more than half the entropy rise in Eckardt's compressor occurred in the vaneless diffuser. Figure 40 shows numerical predictions of entropy growth on and downstream of a shrouded impeller illustrating the high loss on the shroud at rotor inlet and especially on the walls of the vaneless space. This result implies that for machines with vaned diffusers the length of the vaneless space should be kept as short as possible and there is a strong case for having rotating walls in this region if practicable.

There is a large radial pressure gradient in the vaneless space that arises mainly from the centripetal acceleration of the highly swirling flow. Because the meridional velocity is much less than the swirl velocity (the swirl angle is typically 70 deg), this pressure gradient has a disproportional effect on the radial velocity, tending to make it reverse near the endwalls. Numerical calculations predict this separation to be very prevalent (e.g., Krain and Hoffman, 1989) but although it has been measured (Inoue and Cumpsty, 1984) the effect does not seem to be as common as predicted. This must be because the mixing processes are more intense than are predicted by numerical solutions, which implies enhanced dissipation in the vaneless space. This effect is especially important for machines with vaneless diffusers.

The concept of entropy generation per unit surface area provides a particularly simple method for estimating the losses in the vaneless space. Simple analysis gives a loss coefficient, based on local velocity, of

$$\zeta=\frac{4\,C_d\,\Delta r}{h\cos\alpha} \tag{54}$$

where h is the passage height, Δr is the radius change, and α is the swirl angle. This is the same result as obtained from the conventional analysis using skin friction if $C_d=0.5\ C_f$. Equa-

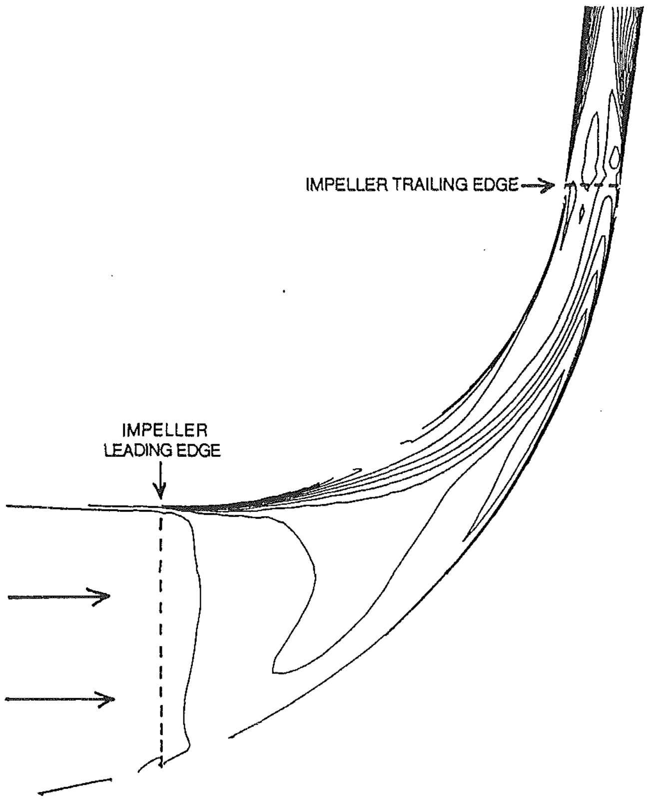

Fig. 40 Calculated loss generation in a centrifugal compressor; contours of pitchwise-averaged entropy

tion (54) explains why the loss increases with the swirl angle as observed in practice. They value of C_d must be found experimentally and is likely to be larger than is usual in two-dimensional boundary layers because of the highly three-dimensional nature of the flow.

The stator or diffuser blades have the most difficult task in a centrifugal compressor. The pressure rise in the impeller can be produced without excessive diffusion but the diffuser blades must produce a comparable pressure rise by diffusion alone. This is made more difficult by the fact that the flow entering them is nonuniform, unsteady, and possibly transonic. Some of the pressure rise occurs in the semivaneless space before the throat of the diffuser and the entropy generation here must be a continuation of the high level in the vaneless space itself.

The leading edge of the diffuser blades is invariably thin and this makes the effects of incidence very important. The velocity at the throat of the diffuser can be estimated from the mass flow rate and the stagnation conditions at its entry. At low flow rates this velocity will be much less than the flow velocity approaching the diffuser; the flow must then separate at the leading edge so that the resulting separation partly blocks the throat and increases the throat velocity. This is a separation in a relatively high-speed part of the flow and will create a large mixing loss. In transonic flow there will also be shock losses in this region. Morishita (1982) found that intense turbulent viscous dissipation occurred in the vicinity of his subsonic leading edge but that once inside the diffuser passage the flow was comparatively well ordered. He estimated that, even at design conditions, the entropy generation around the diffuser leading edge was the major cause of lost efficiency in the whole machine. Conversely, at high flow rates the flow must accelerate into the diffuser throat, possibly causing choking but certainly increasing the losses in the diffusion downstream of the throat.

The flow downstream of the diffuser throat is like that in a conventional two-dimensional diffuser with entropy generation in the boundary layers being greatest in the high-velocity region near the throat. However, the major source of entropy is likely to come from separation and the subsequent mixing of the boundary layers toward the exit of the diffuser. If the separation does not have time to mix out within the diffuser passage it will increase the kinetic energy of the flow leaving the diffuser. This kinetic energy may be either dissipated by discharging directly into a plenum or it may be partly recovered in a volute.

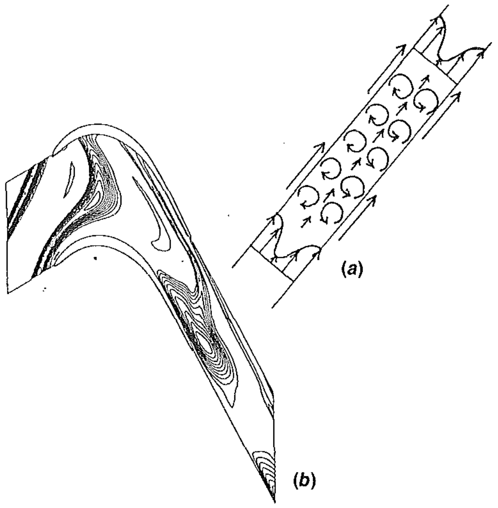

Fig. 41 (*a*) The wake as a vortex sheet; (*b*) the convection of a wake through a blade row; contours of entropy

11 Other Sources of Loss

There are numerous other sources of loss in turbomachines; most of them are small in most applications but can become significant in special cases. The most important of these will be discussed briefly in this section. More details of all but those due to unsteady effects can be found in Chap. 8 of Glassman (1973).

11.1 Loss Due to Unsteady Flow. The fact that wakes, vortices, and separations from one blade row often mix out in the downstream blade row has been mentioned several times in this paper. As they convect through the downstream row their pressure and velocity change continually so that they mix in an unsteady environment, quite different from that modeled in cascade tests. For a wake the effect of this on the dissipation can be thought of qualitatively in terms of the effect on the velocity difference between the center of the wake and the mainstream.

A two-dimensional wake can be thought of as being contained between two vortex sheets (Smith, 1966); this is illustrated in Fig. 41(*a*). The velocity difference between the center of the wake and the mainstream determines the strength of the sheets. Neglecting viscosity, as the wake convects the circulation in the vortex sheets bounding a fixed quantity of fluid must remain constant (by Kelvin's theorem) and so if the wake is stretched the velocity difference between its centerline and the mainstream is decreased. Conversely, the velocity difference is amplified if the wake is compressed. This is compatible with the results presented in section 4 for the effect of acceleration and deceleration on wake mixing loss. The convection of a wake through a blade row can now be calculated and typical results are shown in Fig. 41(*b*) (He, 1992). These show that the wake becomes highly distorted and stretched because the part adjacent to the suction surface convects more rapidly than that adjacent to the pressure surface. The velocity deficit of the center of the wake is reduced by this inviscid effect as it also is by viscous effects. The implication is that the dissipation in the wake will be reduced by mixing in a downstream blade row relative to that when mixing in a uniform flow. Since the mixing loss of a wake is comparatively small and most of the mixing takes place very close to the trailing edge this is probably not a very important effect. The same argument can be applied to a flow separation, which is in effect only a large wake; however, the mixing loss of a separation can be large and so any reduction may be significant.

A vortex from one blade row will be convected through a downstream blade row very much like a wake but the implications for loss are very different. Kelvin's theorem tells us that the circulation around a stream tube remains constant and so if the diameter of the tube is reduced by stretching the streamwise vorticity is amplified. When a vortex is stretched or compressed longitudinally it can be shown that its secondary kinetic energy will vary as the square of its length. Hence stretching a vortex will greatly amplify its secondary kinetic energy and when this is subsequently dissipated by viscous effects it will increase the loss. The magnitude of this effect is not known but if, as discussed in section 9.1, the kinetic energy of secondary flow vortices is significant, it could have important implications. Tip leakage vortices will be similarly affected.

Because the entropy increase in a shock wave is such a nonlinear function of the preshock Mach number, Eq. (31), any periodic motion of the shock will generate increased loss. Effectively the increase in entropy generation when the shock is moving forward will be greater than the reduction when it is moving backward. Ng and Epstein (1984) found evidence of high-frequency fluctuations in the loss of two transonic compressors and attributed it to oscillation of the shock position. They found that only a very small motion of the shock (0.3 mm) was needed to explain their results but the resulting loss of compressor efficiency was only 0.15 percent. It is not known how general this result is, but larger shock amplitudes with consequently larger increases in loss appear quite plausible. Similar mechanisms certainly occur in turbines when the trailing edge shock system from a stator interacts with the downstream rotor but no estimates of their magnitude are known.

Other means in which unsteady flow can affect entropy generation are through dissipation of the spanwise vorticity shed from a trailing edge as a result of changes in blade circulation, i.e., changing lift, and the presence of unsteady velocity profiles in the boundary layer due to wake passage. Both of these mechanisms have been examined by Fritsch and Giles (1992) who found that both have only a small effect on loss. The former was estimated to give at most 0.3 percent loss of efficiency for a turbine stage while the latter caused only a 0.09 percent loss.

The effects of unsteady boundary layer transition on the loss can be important, especially if the Reynolds number is in the transitional range. The large body of work on this topic is discussed by Mayle (1992).

11.2 Partial Admission Loss. Partial admission is used mainly in steam turbines as a means of varying the mass flow and hence the power output. Flow is only admitted to a segment of the first stator blades and leaves them as a jet occupying only part of the annulus. However, the full annulus area is available to the flow through the following rotor. Traditionally the first stage is of impulse design so that there is little circumferential pressure gradient after the stators and so little tendency for the jet leaving them to expand in the circumferential direction. The rotor blade passages well within this jet should behave as in a full annulus but the passages entering and leaving the jet are in an unsteady flow and will suffer additional losses. In both cases this may be regarded as a mixing loss between the jet and the surrounding stagnant fluid, similar to the mixing of a wake discussed in the previous section. However, in this case the "wake" is no longer small and will have a considerable effect on the blade loading and hence on the distortion of the interface between the jet and the nearly stagnant fluid. The flow pattern and losses can only really be predicted by an unsteady viscous calculation. What little is known about the magnitude of this effect is reviewed by Roelke (1973).

If the partial admission stage is followed by other full admission stages there must be a rapid circumferential redistribution of flow as its enters the second stator row. This is because there is a substantial pressure drop across stator passages that pass the full flow but little pressure drop across passages with low flow. Hence, if the static pressure is uniform at the second stator exit, there must be a strong circumferential pressure gradient at its entry. This can only be produced by a large curvature of the jet boundary in the blade to blade plane. The changes in flow direction near the jet boundary will lead to large circumferential variations of incidence onto the second stator and so will certainly induce additional losses. The author knows of no published information on this effect nor on how many such stages are needed for the flow to become circumferentially uniform.

In addition to the mixing loss at the boundaries of the jet there will be extra windage loss as the rotor blades move through the region with no throughflow. Here they will behave rather like the blades of a centrifugal compressor and will set up a complex recirculating flow, which will certainly generate significant amounts of entropy and will directly reduce the shaft torque. Results quoted by Roelke suggest that this pumping loss exceeds the mixing loss at small arcs of admission.

11.3 Windage Loss and Disk Cooling Flows. This is the loss due to viscous friction on all parts of the machine other than the blade and annulus boundaries, where it has already been accounted for. It is usually considered only in terms of the viscous torque on rotating disks and hence is often called disk friction loss. However, the idea of entropy creation shows that entropy is produced wherever fluid is moving relative to a solid boundary and this entropy must find its way into the flow and be present at machine exit. The views of the effect of windage in terms of lost torque and of entropy creation are entirely compatible since the lost power due to frictional torque is given by

$$\Delta W = \Omega \int \tau r \, dA \tag{55}$$

where the integral is over all rotating surfaces.

The total entropy creation is

$$\dot{S} = \int \frac{\tau \Delta V}{T} dA \tag{56}$$

where ΔV is the velocity difference across which the shear stress τ acts. In the case of the gap between stationary and rotating faces $\Delta V = \Omega r$ and so the two expressions predict the same loss of output. However, the entropy creation concept shows that loss does not only occur on rotating surfaces but on any surface exposed to the flow. It also shows that there is some reheat effect on the windage loss since the loss of machine output is given by

$$\Delta W = T_{\text{out}} \dot{S} = T_{\text{out}} \int \frac{\tau \Delta V}{T} dA \tag{57}$$

so that the lost work is reduced if the windage takes place at high temperatures. Physically this can be thought of as the frictional effects generating heat, which re-enters the flow and so increases the work output or input of any downstream stages. The view of windage loss in terms of lost torque does not account for this reheat effect.

Formulae for estimating the windage loss are given by Roelke (1973). These are effectively obtained by applying a skin friction factor to all rotating surfaces with the coefficient being a function of Reynolds number as shown in Fig. 42. The

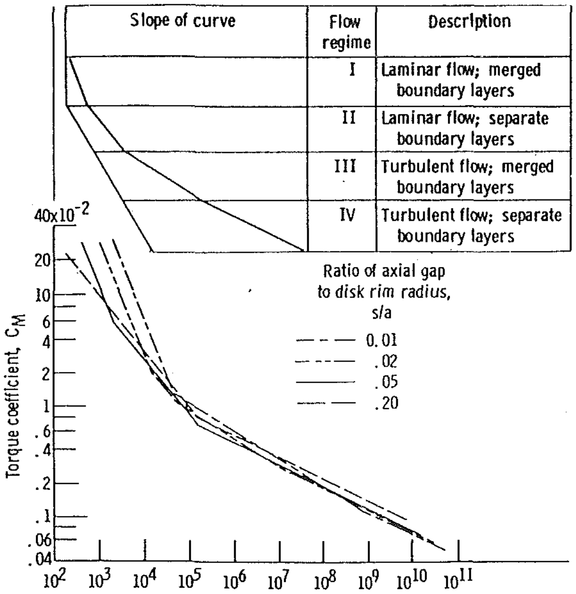

Fig. 42 Moment coefficient for frictional torque on rotating disks from Roelke (1973)

coefficient plotted in Fig. 42 is the moment coefficient C_m, which is related to the skin friction factor C_f by $C_f = 0.398\ C_m$. However, these friction factors were generally obtained from tests on smooth disks rotating in smooth chambers. They can be considerably increased by surface protuberances such as bolts or webs. The entropy generation concept shows that these are equally undesirable on stationary and rotating surfaces.

A simple estimate of the ratio of the power lost by windage to useful power, assuming an axial flow machine with a two-sided disk, is given by

$$\frac{\Delta W}{W} = 0.1\frac{C_f}{\phi\psi}\frac{D_d}{h_b}\frac{1}{1+4h_b/D_d} \tag{58}$$

where C_f is the skin friction factor, D_d is the hub diameter of the disk, h_b is the height of the blades, and ϕ and ψ are the stage flow and loading coefficients based on the mean blade speed. Figure 42 shows that the value of C_f ($=0.398\ C_m$) is of order 0.002. Hence Eq. (58) shows that the fraction of lost power is very small for most machines, being most significant for those with short blades and low flow and loading coefficients. It should be emphasized that this is a minimum estimate and the loss can be much greater if the disks are not smooth.

In some gas turbines cooling flows are introduced into the disk cavity to cool the disk. These flows subsequently enter the mainstream through the slot in the hub separating stator and rotor. Roelke states that such cooling flows enter the mainstream with a swirl velocity about 0.45 times the rotational speed of the hub and suggests that the extra torque needed to provide this angular momentum is simply added to the windage torque with no flow. This simple approach assumes that the cooling flow only affects the shear stress and entropy generation within the cavity sufficiently to provide its own change of angular momentum. This seems unlikely to be true; with no flow the shear stress must extend across the whole gap while a cooling flow is likely to make the shear layers behave more like boundary layers, which will be thinner and have higher rates of entropy generation. Chew and Vaughan (1988) present numerical predictions of the effect of cooling flows on the windage torque, which show agreement with Roelke's approach at low flow rates but show the torque becoming constant at about 1.7 times the zero flow value at high cooling flow rates.

The above discussion considers the effect of disk cooling flows on loss solely in terms of the entropy generation within the disk cavity. However, extra loss will occur when the cooling flow is injected into the main stream. Here the mixing process will be exactly like that of the leakage flow over a shroud, as discussed in section 8 and in Appendix 5. Most of the entropy generation will be due to the difference in swirl velocity between the flow leaving the cavity and the main flow. This velocity difference should be minimized by preswirling the cooling flow when possible.

11.4 Lacing Wires and Part-Span Shrouds. These are used in both turbines and compressors to control the vibration of long blades. In their simplest form they consist of a circular rod (a lacing wire) joining adjacent blades while more sophisticated versions replace the rod by an aerofoil section, which may be aligned to the local meridional flow direction. For convenience both types will be referred to as struts.

The flow over such a strut is complex. Because of the blade loading there will be a gradient of static pressure along its span and this will generate secondary flows on the strut very much like those on the endwalls. Traverses behind such struts show secondary vortices and loss concentrations near the intersection with the blade suction surface. If the strut has a blunt trailing edge, like a lacing wire, then the separated flow in its wake is also subject to this pressure gradient and the low-energy fluid in the wake will move onto the blade suction surface where it will merge with the loss in the secondary vortex. Hence, the drag and entropy generation will not be the same as for the same cross section of strut in a uniform flow. In fact the entropy generation is likely to be increased in the same way as that on endwalls was found to be greater than on blade surfaces.

The loss of such struts is usually obtained in terms of their drag, which, in a uniform flow, can be turned into an entropy rise by using Eq. (7) in the form

$$T\Delta s = \frac{D}{\rho A_f} \tag{59}$$

where D is the total drag force acting in the direction of the streamlines and A_f is the total flow area projected in that direction. However, the actual strut is not in a uniform flow, the local velocity varies considerably from suction surface to pressure surface and from its leading edge to trailing edge. There will also generally be a pitchwise component of velocity making the strut analogous to a swept wing. Hence neither estimation of the drag nor application of Eq. (59) is straightforward.

If C_d is the drag coefficient of the strut based on its frontal area A_s *projected in the relative flow direction* and on an average relative flow velocity V_{avg}, then the loss coefficient based on V_{avg} is

$$\zeta = \frac{T\Delta s}{0.5\ V_{\text{avg}}^2} = \frac{C_d A_s}{A_f} = \frac{C_d A_{ms}}{A_{mf}} \tag{60}$$

where A_{ms} and A_{mf} are the *meridional* projections of the areas. Given that C_d is of order unity for circular wires and of order 0.1 for aerofoils, the advantage of using streamlined struts is apparent.

Koch and Smith (1976) present a method for compressor blades based on this concept. The drag of the strut is estimated by treating it as a swept airfoil at the average relative Mach number and by also including a term for the interference drag generated at the junction of the strut and the blade surfaces. They find that the drag must be increased by a factor of 1.8 above the value calculated for an aerofoil to obtain agreement with the measured loss of struts on compressor blades.

The entropy generation concept provides an alternative method of estimating the loss due to the boundary layers on streamlined struts. The strut surface velocity distribution can only be obtained accurately from a three-dimensional calculation but it may be estimated from the blade surface velocity distribution and used in Eq. (41) to estimate the total entropy generation. This approach shows the importance of locating the strut in a region where its relative velocity is as low as possible, i.e., toward the trailing edge of compressor blades or toward the leading edge of turbine blades. If the strut is not streamlined and so has a large separated region behind the trailing edge, then the base pressure term in Eq. (26) is likely to be the dominant source of entropy. The base pressure coefficient will be particularly difficult to estimate because of the nonuniform flow.

12 Conclusions

It must be clear be now that there are many details of loss generation in turbomachines where our understanding is still very weak. The author believes that our understanding will be improved by thinking the loss in terms of entropy generation and one of the objectives of this paper has been to encourage this way of thinking.

There are a few sources of loss where we can say that we understand the mechanism clearly and can accurately quantify the rate of entropy generation. Flow is attached, two-dimensional, fully turbulent or fully laminar boundary layers, where numerical calculation methods should be very accurate, is an example of this. However, even for the straightforward problem of calculating the loss of a two-dimensional cascade the author maintains that an *a priori* prediction, using the best available methods, is unlikely to be accurate to better than about ±20 percent. Twenty years ago (Denton, 1973) he gave an estimate of ±10 percent! This is because he now realizes the difficulty of predicting boundary layer transition, separation bubbles, and base pressure coefficients.

For other sources of loss we understand the mechanism but cannot accurately quantify the entropy production without making considerable use of empirical data. Tip leakage loss, subsonic trailing edge loss, and loss due to blade surface separations all fall into this category. In such cases we may be able to identify good and bad features of the flow and modify our designs accordingly even though we cannot quantify the improvement before testing them. In this situation the ability to test modifications quickly and cheaply, and to relate the results to the physics of the flow, is very important.

There are still some major loss sources for which we do not yet fully understand the mechanisms. Endwall loss, transonic trailing edge loss, and loss due to mixing in a downstream blade row all fall into this category. In such cases predictions must use empirical correlations, which may not even be based on the correct physics. It is important that when using these correlations we recognize their limitations and do not develop a false sense of security if they happen to give the correct answer. This is especially dangerous when correlations are "verified" against the same data that were used to generate their empirical constants. For this type of loss we must strive to obtain a better understanding of the mechanism involved so that we can at least make qualitative improvements to our designs.

In computing flows through turbomachines the author has continually been struck by the ability of soundly based but grossly oversimplified models to give realistic predictions of the flow pattern and loss. The reason for this is that many flows are dominated by the conservation of mass, energy, and momentum and not by detailed viscous effects. The power of the conservation equations should never be underestimated and flow models that do not satisfy these equations are doomed to failure.

Finally, we should never be afraid to admit our lack of understanding of complex entropy generating mechanisms or to address fundamental questions. We are most likely to make progress when we know our limitations and continually strive to reduce them.

Acknowledgments

As will be obvious to many readers, this paper is largely based on work performed at the Whittle laboratory over the last 20 years. The authors is greatly indebted to all past and present staff and students of the laboratory for the stimulating environment that they provide. Thanks are also due to the colleagues who have read early drafts of this paper and commented constructively on them. Above all thanks are due to the IGTI Gas Turbine Scholar program for providing the opportunity for me to collect and present my thoughts on this fascinating topic.

References

Adamcyzk, J. J., Celestina, M. L., and Greitzer, E. M., 1993, "The Role of Tip Clearance in High Speed Fan Stall," ASME JOURNAL OF TURBOMACHINERY, Vol. 115, No. 1, pp. 28–39.

Ainley, D. G., and Mathieson, G. C. R., 1951, "An Examination of the Flow and Pressure Losses in Blade Rows of Axial Flow Turbines," ARC, R&M 2891.

Atkin, C. J., and Squire, L. C., 1992, "A Study of the Interaction of a Normal Shock Wave With a Turbulent Boundary Layer at Mach Numbers Between 1.3 and 1.55," *Eur. J. Mechanics B/Fluids*, Vol. 11, No. 1.

Binder, A., 1985, "Turbulence Production Due to Secondary Vortex Cutting in a Turbine Rotor," ASME *Journal of Engineering for Gas Turbine and Power*, Vol. 107, pp. 1039–1046.

Bindon, J. P., 1979, "The Effect of Hub Inlet Boundary Layer Skewing on the Endwall Shear Flow in an Annular Turbine Cascade," ASME Paper No. 79-GT-13.

Bindon, J. P., 1989, "The Measurement and Formation of Tip Clearance Loss," ASME JOURNAL OF TURBOMACHINERY, Vol. 111, pp. 257–263.

Boletis, E., Sieverding, C. H., and Van Hove, W., 1983, "Effects of a Skewed Inlet Boundary Layer on the 3D Flow Field in an Annular Turbine Cascade," *Viscous Effects in Turbomachines*, AGARD CP 351.

Brown, L. E., 1972, "Axial Flow Compressor and Turbine Loss Coefficients: A Comparison of Several Parameters," ASME Paper No. 72-GT-18.

Came, P. M., 1969, "Tip Clearance Losses in Turbines—A Review of Experimental Data and Prediction Methods," NGTE report NT.754.

Carter, A. D. S., 1948, "Three-Dimensional Flow Theories for Axial Compressors and Turbines," *Proc. IMechE*, Vol. 159.

Cebeci, T., and Carr, L. W., 1978, "A Computer Program for Calculating Laminar and Turbulent Boundary Layers for Two-Dimensional Time-Dependent Flows," NASA TM 78470.

Chen, S., 1987, "A Loss Model for the Transonic Flow Low Pressure Steam Turbine Blades," IMechE Paper No. C269/87.

Chew, J. W., and Vaughan, C. M., 1988, "Numerical Predictions of the Flow Induced by an Enclosed Rotating Disc," ASME Paper No. 88-GT-127.

Cumpsty, N. A., 1989, *Compressor Aerodynamics*, Longman.

Dawes, W. N., 1990, "A Comparison of Zero and One Equation Turbulence Models for Turbomachinery Calculations," ASME Paper No. 90-GT-303.

de Ruyck, J., and Hirsch, Ch., 1983, "Endwall Boundary Layer Calculations in Multistage Axial Compressors," *Viscous Effects in Turbomachines*, AGARD CP 351.

Denton, J. D., and Hoadley, D., 1972, "Calculation of the Effect of Surface Roughness on the Profile Loss of Turbine Blades," GEGB report R/M/N630.

Denton, J. D., 1973, "A Survey and Comparison of Methods of Predicting the Profile Loss of Turbine Blades," IMechE Paper No. C76/73.

Denton, J. D., and Johnson, C. G., 1976, "Tip Leakage Loss of Shrouded Turbine Blades," CEGB report R/M/N848.

Denton, J. D., and Cumpsty, N. A., 1987, "Loss Mechanisms in Turbomachines," IMechE Paper No. C260/87.

Denton, J. D., and Xu, L., 1990, "The Trailing Edge Loss of Transonic Turbine Blades," ASME JOURNAL OF TURBOMACHINERY, Vol. 112, pp. 277–285.

Denton, J. D., 1990, "Entropy Generation in Turbomachinery Flows," SAE SP-846.

Dunham, J., 1970, "A Review of Cascade Data on Secondary Losses in Turbines," *IMechE J. Mech. Eng. Sci.*, Vol. 12, No. 1.

Dunham, J., and Came, P. M., 1970, "Improvements to the Ainley–Mathieson Method of Turbine Performance Prediction," ASME *Journal of Engineering for Power*, Vol. 92.

Freeman, C., and Cumpsty, N. A., 1989, "A Method for the Prediction of Supersonic Compressor Blade Performance," ASME Paper No. 89-GT-326.

Fritsch, G., and Giles, M., 1992, "Second-Order Effects of Unsteadiness on the Performance of Turbomachines," ASME Paper No. 92-GT-389.

Glassman, A. J., "Turbine Design and Application," Vols. 1–3, NASA SP-290.

Gregory-Smith, D. G., 1982, "Secondary Flows and Losses in Axial Flow Turbines," ASME *Journal of Engineering for Power*, Vol. 104, pp. 819–822.

Gregory-Smith, D. G., Graves, C. P., and Walsh, J. A., 1988, "Growth of Secondary Losses and Vorticity in an Axial Turbine Cascade," ASME JOURNAL OF TURBOMACHINERY, Vol. 110, pp. 1–8.

Harrison, S., 1989, "The Influence of Blade Stacking on Turbine Losses," Ph.D. thesis, Cambridge University, United Kingdom.

Harrison, S., 1990, "Secondary Loss Generation in a Linear Cascade of High-

Turning Turbine Blades," ASME Journal of Turbomachinery, Vol. 112, pp. 618–624.

Hart, M., Hall, D. M., and Singh, G., 1991, "Computational Methods for the Aerodynamic Development of Large Steam Turbines," IMechE Paper No. C423/009.

Hartsel, J. E., 1972, "Prediction of Effects of Mass-Transfer Cooling on the Blade-Row Efficiency of Turbine Aerofoils," AIAA Paper No. 72-11.

Hawthorne, W. R., 1955, "Some Formulae for the Calculation of Secondary Flow in Cascades," Cambridge Univ. Engineering Dept. Report.

He, L., 1992, Whittle Lab., Cambridge, United Kingdom, personal communication.

Heyes, F. J. G., and Hodson, H. P., 1993, "Measurement and Prediction of Tip Clearance Flow in Linear Turbine Cascades," ASME Journal of Turbomachinery, Vol. 115, pp. 376–382.

Hobbs, D. E., and Weingold, H. D., 1984, "Development of Controlled Diffusion Aerofoils for Multistage Compressor Application," ASME *Journal of Engineering for Gas Turbines and Power*, Vol. 106, pp. 271–278.

Hodson, H. P., and Dominy, R. G., 1989, "Three-Dimensional Flow in a Low-Pressure Turbine Cascade at Its Design Condition," ASME Journal of Turbomachinery, Vol. 109, pp. 177–185.

Horlock, J. H., 1958, *Axial Flow Compressors*, Butterworths, United Kingdom.

Howell, A. R., 1945, "The Design of Axial Flow Compressors," *Proc. IMechE*, Vol. 153.

Huntsman, I., Hodson, H. P., and Hill, S. H., 1992, "The Design and Testing of a Radial Flow Turbine for Aerodynamic Research," ASME Journal of Turbomachinery, Vol. 114, pp. 411–418.

Huntsman, I., 1993, "An Investigation of Radial Inflow Turbine Aerodynamics," Ph.D. Thesis, Cambridge University, United Kingdom.

Inoue, M., and Cumpsty, N. A., 1984, "Experimental Study of Centrifugal Compressor Discharge Flow in Vaneless and Vaned Diffusers," ASME *Journal of Engineering for Gas Turbines and Power*, Vol. 106, pp. 455–467.

Koch, C. C., and Smith, L. H., 1976, "Loss Sources and Magnitudes in Axial Flow Compressors," ASME *Journal of Engineering for Power*, Vol. 98, No. 3.

Krain, H., and Hoffman, W., 1989, "Verification of an Impeller Design by Laser Measurements and 3D Viscous Flow Calculations," ASME Paper No. 89-GT-159.

Langston, L. S., Nice, M. L. and Hooper, R. M., 1977, "Three-Dimensional Flow in a Turbine Cascade Passage," ASME *Journal of Engineering for Power*, Vol. 99, No. 1.

Mayle, R. E., 1991, "The Role of Laminar-Turbulent Transition in Gas Turbine Engines," First IGTI Gas Turbine Scholar Lecture," ASME Journal of Turbomachinery, Vol. 113, pp. 509–537.

Mee, D. J., Baines, N. C., Oldfield, M. L. G., and Dickens, T. E., 1992, "An Examination of the Contributions to Loss on a Transonic Turbine Blade in Cascade," ASME Journal of Turbomachinery, Vol. 114, pp. 155–162.

Moore, J., and Moore, J. G., 1980, "Three Dimensional Viscous Calculations for Assessing the Thermodynamic Performance of Centrifugal Compressors—Study of the Eckardt Compressor," AGARD CP 282.

Moore, J., and Moore, J. G., 1983, "Entropy Production Rates From Viscous Flow Calculations. Part 1—A Turbulent Boundary Layer," ASME Paper No. 83-GT-70.

Moore, J., and Adhye, R. Y., 1985, "Secondary Flows and Losses Downstream of a Turbine Cascade," ASME *Journal of Engineering for Gas Turbines and Power*, Vol. 107, pp. 961–968.

Moore, J., Shaffer, D. M., and Moore, J. G., 1987, "Reynolds Stresses and Dissipation Mechanisms Downstream of a Turbine Cascade," ASME Journal of Turbomachinery, Vol. 109, pp. 258–267.

Moore, J., and Tilton, J. S., 1988, "Tip Leakage Flow in a Linear Turbine Cascade," ASME Journal of Turbomachinery, Vol. 110, pp. 18–26.

Morishita, E., 1982, "Centrifugal Compressor Diffusers," M Sc. Thesis, Cambridge University, United Kingdom.

Morphis, G., and Bindon, J. P., 1988, "The Effects of Relative Motion, Blade Edge Radius and Gap Size on the Blade Tip Pressure Distribution in an Annular Turbine Cascade With Clearance," ASME Paper No. 88-GT-256.

Moyle, I. N., 1988, "Analysis of Efficiency Sensitivity Associated with Tip Clearance in Axial Compressors," ASME Paper No. 88-GT-216; "A Note on Efficiency Sensitivity to Tip Clearance Changes in Axial Flow Compressors," Journal of Turbomachinery, Vol. 112, 1990, pp. 795–796.

Ng, W. F., and Epstein, A. H., 1984, "Unsteady Losses in Transonic Compressors," ASME Paper No. 84-GT-183.

Okan, M. B., and Gregory-Smith, D. G., 1992, "A Simple Method for Estimating Secondary Losses in Turbines at the Preliminary Design Stage," ASME Paper No. 92-GT-294.

Pierzga, M. J., and Wood, J. R., 1985, "Investigation of the Three Dimensional Flow Field Within a Transonic Fan Rotor," ASME *Journal of Engineering for Power*, Vol. 107, pp. 436–439.

Prato, J., and Lakshimarayana, B., 1993, "Investigation of Compressor Rotor Wake Structure at Peak Pressure Rise Coefficient and Effects of Loading," ASME Journal of Turbomachinery, Vol. 115, pp. 487–500.

Roberts, Q., 1992, "The Trailing Edge Loss of a Simulated Turbine Blade," Final Year Project, Cambridge University Eng. Dept., United Kingdom.

Roelke, R. J., 1973, *Turbine Design and Application*, NASA SP-290, A. J. Glassman, ed., Vol. 2, Chap. 8.

Schlichting, H., 1966, *Boundary Layer Theory*, 6th ed., McGraw-Hill, New York.

Schlichting, H., 1978, *Boundary Layer Theory*, 7th ed., McGraw-Hill, New York.

Shapiro, A. H., 1953, *The Dynamics and Thermodynamics of Compressible Fluid Flow*, Wiley, New York.

Sharma, O. P., and Butler, T. L., 1987, "Predictions of Endwall Losses and Secondary Flows in Axial Flow Turbine Cascades," ASME Journal of Turbomachinery, Vol. 109, pp. 229–236.

Sharma, O. P., Pickett, G. F., and Ni, R. H., 1992, "Assessment of Unsteady Flows in Turbines," ASME Journal of Turbomachinery, Vol. 114, pp. 79–90.

Sieverding, C. H., Stanislas, M., and Snoek, J., 1983, "The Base Pressure Problem in Transonic Cascades," ASME Paper No. 83-GT-50.

Sieverding, C. H., 1985, "Recent Progress in the Understanding of Basic Aspects of Secondary Flows in Turbine Blade Passages," ASME *Journal of Engineering for Gas Turbines and Power*, Vol. 107, pp. 248–257.

Smith, L. H., 1966, "Wake Dispersion in Turbomachines," ASME *Journal of Basic Engineering*, Vol. 88.

Smith, L. H., 1970, "Casing Boundary Layers in Multistage Axial Flow Compressors," in: *Flow Research on Blading*, L. S. Dzung, ed., Elsevier.

Stewart, W. L., 1955, "Analysis of Two Dimensional Compressible Flow Loss Characteristics Downstream of Turbomachine Blade Rows in Terms of Basic Boundary Layer Characteristics," NACA TN 3515.

Stewart, W. L., Whitney, W. J., and Wong, R. J., 1960, "A Study of Boundary Layer Characteristics of Turbomachine Blade Rows and Their Relation to Overall Blade Loss," ASME *Journal of Basic Engineering*, pp. 588–592.

Storer, J. A., 1991, "Tip Clearance Flow in Axial Compressors," Ph D thesis, Cambridge University, United Kingdom.

Sutton, A., 1990, "The Trailing Edge Loss of Subsonic Turbine Blades," M Sc Thesis, Cambridge University, United Kingdom.

Truckenbrodt, E., 1952, "A Method of Quadrature for the Calculation of Laminar and Turbulent Boundary Layers in Plane and Rotational Symmetric Flow," *Ingenieur-Archiv*, Vol. 20; translated as NACA TM 1379.

Walsh, J. A., and Gregory-Smith, D. G., 1990, "Inlet Skew and the Growth of Secondary Losses and Vorticity in a Turbine Cascade," ASME Journal of Turbomachinery, Vol. 112, pp. 633–642.

Wennerstrom, A. J., and Puterbaugh, S. L., 1984, "A Three-Dimensional Model for the Prediction of Shock Losses in Compressor Blade Rows," ASME *Journal of Engineering for Gas Turbines and Power*, Vol. 106, pp. 295–299.

Yaras, M. I., and Sjolander, S. A., 1992, "Effects of Simulated Rotation on Tip Leakage in a Planar Cascade of Turbine Blades. Parts 1 and 2," ASME Journal of Turbomachinery, Vol. 114, pp. 652–667.

Xu, L., and Denton, J. D., 1988, "The Base Pressure and Loss of a Family of Four Turbine Blades," ASME Journal of Turbomachinery, Vol. 110, pp. 9–17.

APPENDIX 1

Entropy Production in a Boundary Layer

Consider the flow along a stream tube in the boundary layer with the x direction aligned with the stream tube and the y direction being perpendicular to it. Hence V_y and V_z are both zero at the location considered.

For thin boundary layers the stream tube can be assumed to be very closely aligned with the surface so the x and y directions are effectively perpendicular and parallel to the surface respectively.

The second law applied along the stream tube gives

$$T\frac{ds}{dx}=\frac{dh}{dx}-\frac{1}{\rho}\frac{dP}{dx}=\frac{dh_o}{dx}-V_x\frac{dV_x}{dx}-\frac{1}{\rho}\frac{dP}{dx} \tag{A1.1}$$

Let F_x be the viscous force acting per unit mass of fluid in the x direction. The momentum equation in the x direction is then

$$F_x-\frac{1}{\rho}\frac{dP}{dx}=V_x\frac{dV_x}{dx} \tag{A1.2}$$

Combining (A1.1) and (A1.2) gives

$$T\frac{ds}{dx}=\frac{dh_o}{dx}-F_x \tag{A1.3}$$

This is a well-known result, which shows that if h_o is constant, as it often is in adiabatic flow, entropy is created by any frictional force acting along the streamline in the direction opposing the flow.

Now consider unit mass of fluid moving along the streamline from a Lagrangian point of view. The energy equation for the unit mass is:

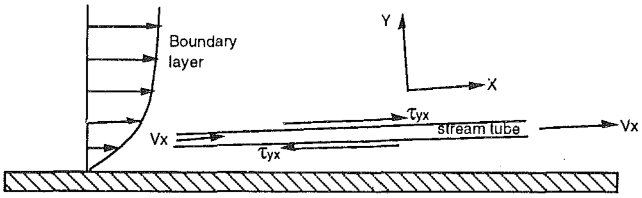

Fig. A1.1

$$\frac{D}{Dt}\left(e+\frac{1}{2}V^2\right)=-P\frac{D}{Dt}\left(\frac{1}{\rho}\right)+V_x\left(F_x-\frac{1}{\rho}\frac{\partial P}{\partial x}\right)$$
$$+\frac{1}{\rho}\left(\tau_{yx}\frac{\partial V_x}{\partial y}+\tau_{yz}\frac{\partial V_z}{\partial y}\right)-\frac{1}{\rho}\frac{\partial q}{\partial y} \qquad (A1.4)$$

where e is the specific internal energy ($e=C_vT$), q is the heat flow per unit area in the y direction and τ_{yx} and τ_{yz} are the viscous shear stresses. Viscous normal stresses and heat flow in the x and z direction are ignored.

For steady flow

$$\frac{D}{Dt}=V_x\frac{\partial}{\partial x}$$

and so Eq. (A1.4) becomes

$$V_x\frac{\partial h_o}{\partial x}=F_xV_x+\frac{1}{\rho}\left(\tau_{yx}\frac{\partial V_x}{\partial y}+\tau_{yx}\frac{\partial V_z}{\partial y}\right)-\frac{1}{\rho}\frac{\partial q}{\partial y} \qquad (A1.5)$$

Combining Eqs. (A1.3) and (A1.5) to eliminate h_o leads to

$$V_xT\frac{\partial s}{\partial x}=\frac{1}{\rho}\left(\tau_{yx}\frac{\partial V_x}{\partial y}+\tau_{yz}\frac{\partial V_z}{\partial y}\right)-\frac{1}{\rho}\frac{\partial q}{\partial y}$$

If ΔA is the cross-sectional area of the stream tube $\rho V_x\Delta A=\text{constant}$ along it, so

$$T\frac{\partial}{\partial x}(\rho V_xs\Delta A)=\Delta A\left(\tau_{yx}\frac{\partial V_x}{\partial y}+\tau_{yz}\frac{\partial V_z}{\partial y}-\frac{\partial q}{\partial y}\right)$$

If we consider unit depth in the z direction, $\Delta A=dy$ and so integrating through the boundary layer, thickness δ, gives

$$\int_0^\delta\frac{\partial}{\partial x}(\rho V_xs)dy=\int_0^\delta\frac{1}{T}(\tau_{yx}dV_x+\tau_{yz}dV_z-dq)$$

If we now assume an adiabatic surface $q=0$ both at the surface and at the edge of the boundary layer, where the entropy is s_δ, we end up with

$$\frac{d}{dx}\int_0^\delta(\rho V_x(s-s_\delta)dy)=\int_0^\delta\frac{1}{T}(\tau_{yx}dV_x+\tau_{yz}dV_z) \qquad (A1.6)$$

for the rate of change of entropy flux of the flow per unit depth in the z direction.

For a two-dimensional boundary layer τ_{yz} is zero (no skew) and so the result simplifies to

$$\frac{d}{dx}\int_0^\delta(\rho V_x(s-s_\delta))dy)=\int_0^\delta\frac{1}{T}\tau dV \qquad (A1.7)$$

The left-hand side of this equation is the rate of change of entropy flux per unit depth of the flow and so the right-hand side may be thought of as giving the rate of entropy creation per unit surface area by viscous effects within the boundary layer.

APPENDIX 2

Entropy Production Due to Mixing of Two Streams

Consider two streams of perfect gas mixing in a constant area duct as sketched in Fig. A2.1. The inlet stagnation pressure and stagnation temperature of both streams is supposed to be specified as are the areas A_1 and A_2 of the supply ducts. It is assumed that the two streams meet at plane C where they both have a common and uniform static pressure P_c. This assumption is almost universally made but is not exactly true because the mixing downstream of plane C can induce streamline curvatures and hence cross-stream pressure gradients at plane C. The pressure P_c may be varied at will by opening or closing a downstream throttle and so we can assume that it is specified and known. Downstream of plane C the two streams mix with turbulence and probably unsteadiness, but with no friction on the walls, until at a downstream plane m the flow has become completely uniform. The "no friction" assumption may be realized in practice by considering a periodic flow rather than one bounded by solid surfaces.

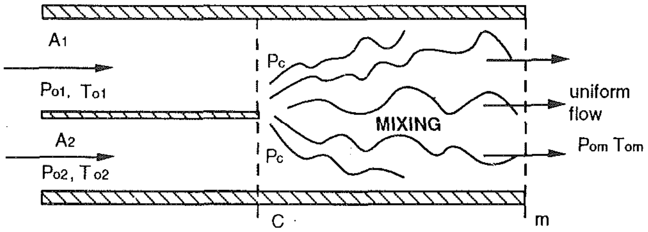

Fig. A2.1 Mixing of two streams in a constant area duct

Knowing P_{o1}, P_{o2}, and P_c, the Mach number of streams 1 and 2 at C may be calculated from standard compressible flow relationships:

$$\frac{P_c}{P_{o1}}=\left(1+\frac{\gamma-1}{2}\mathrm{M}_1^2\right)^{(\gamma/(1-\gamma))} \qquad (A2.1)$$

Hence the mass flow rates m_1 and m_2 can be calculated as can the velocities V_1 and V_2. We can now evaluate the total momentum flux of the two streams at C as

$$I_c=P_c(A_1+A_2)+m_1V_1+m_2V_1 \qquad (A2.2)$$

Since the mixing takes place at constant area and we neglect wall friction this must equal the total momentum flux I_m of the mixed out flow at m.

The energy equation applied between C and m, assuming adiabatic flow, gives

$$T_{om}=\frac{(m_1T_{o1}+m_2T_{o2})}{(m_1+m_2)} \qquad (A2.3)$$

Hence we can evaluate the impulse function

$$F_m=\frac{I_m}{(m_1+m_2)\sqrt{C_pT_{om}}} \qquad (A2.4)$$

at plane m. This is a function of Mach number and γ, given by

$$F_m=\frac{\sqrt{\gamma-1}}{\gamma\mathrm{M}_m}\frac{(1+\gamma\mathrm{M}_m^2)}{\sqrt{\left(1+\frac{\gamma-1}{2}\mathrm{M}_m^2\right)}} \qquad (A2.5)$$

and so knowing F_m we can find the Mach number M_m of the mixed out flow. From the Mach number, stagnation temperature and area all the other properties of the downstream flow can easily be evaluated using standard compressible flow functions. In particular the increase in mass-weighted specific entropy can be calculated and turned into an entropy loss coefficient for the process.

We have obtained this loss coefficient without knowing any details of the mixing process, even whether it is laminar or turbulent, steady or unsteady. This illustrates the power of the control volume analysis, i.e., the ability to use the global conservation equations to obtain overall results without having to solve the Navier–Stokes equations. It is the author's view that this ability accounts for much of the success of Computational Fluid Dynamics applied to turbomachinery flows. In many applications the overall result will be correct even when the turbulence model is grossly inadequate.

There are always two possible values of Mach number satisfying Eq. (A2.5), one subsonic and the other supersonic. If both the entering flows are subsonic then only the subsonic solution is possible since the supersonic solution would involve a decrease of mass averaged entropy. If one or both of the entering flows are supersonic then both subsonic and supersonic solutions may be physically possible.

Figure 6 shows the computed entropy loss coefficient for two flows, which initially occupy equal areas and mix at constant area as shown in Fig. A2.1. The static pressure at plane C is held constant at a value that would produce a Mach number of 0.5 when both flows have the same stagnation pressure $P_{o\mathrm{avg}}$ and stagnation temperature $T_{o\mathrm{avg}}$. The stagnation pressure of one flow is set at $P_{o\mathrm{avg}}+\Delta P$ and that of the other is $P_{o\mathrm{avg}}-\Delta P$, while the stagnation temperatures are similarly $T_{o\mathrm{avg}}+\Delta T$ and $T_{o\mathrm{avg}}-\Delta T$. ΔP and ΔT are systematically varied and a loss coefficient defined as $\zeta = T_{o\mathrm{avg}}\Delta s/0.5\, V_{\mathrm{avg}}^2$ is calculated for the mixing process.

It can be seen that the loss coefficient contours are almost symmetric about both axes and this shows that the increase of entropy due to differences in stagnation pressure is almost independent of the difference in stagnation temperature and vice versa. The relation of this entropy increase to turbine performance is discussed in section 6 and in Appendix 4.

Further examples of the application of the global conservation equations to mixing problems are given in Appendices 3 and 4.

APPENDIX 3

Entropy Production Due to the Mixing Out of a Wake Behind a Trailing Edge

Consider the idealized model sketched below, which represents a trailing edge of thickness t on a blade row with stagger angle α and pitch $(w/\cos\alpha)$. The flow is assumed uniform across the throat AB and also far downstream of the trailing edge on ED. The displacement and momentum thickness of the combined boundary layers on the blade surface at AB are δ^* and θ. The average pressure acting on the base of the trailing edge, AF, is P_b and that on the suction surface from B to C is P_s. For simplicity we assume incompressible flow but this restriction is easily removed in numerical solutions.

We will apply the equations for the conservation of mass and momentum to the dashed control volume $ABCDEF$. At inlet the mass flow rate is $m=\rho V_1(w-t-\delta^*)$ so the continuity equation is

$$m=\rho V_1(w-t-\delta^*)$$
$$=\rho V_2 w\cos(\alpha-\delta)/\cos\alpha \approx \rho V_2 w(1+\delta\tan\alpha) \quad \text{(A3.1)}$$

where the last term assumes that δ is small.

The deviation angle δ can be found from the momentum equation in the y direction, which is

$$(P_s-P_2)w\tan\alpha=\rho V_1(w-t-\delta^*)V^2\sin\delta \quad \text{(A3.2)}$$

Combining this with the continuity equation and assuming that δ is small gives

$$\delta\approx\frac{(P_s-P_2)w^2\tan\alpha}{\rho V_1^2(w-t-\delta^*)^2} \quad \text{(A3.3)}$$

The value of the deviation angle δ is therefore largely determined by the value of the pressure coefficient $(P_s - P_2)/\rho V_1^2$. This must be input to the calculation.

The momentum equation in the x direction gives

$$(w-t)P_1+tP_b+mV_1-\rho_1 V_1^2\theta = wP_2+mV_2\cos\delta \quad \text{(A3.4)}$$

Assuming that δ is small, this becomes

$$\rho V_1^2(w-t-\delta^*-\theta)-\rho V_2^2 w(1+\delta\tan\alpha)=(P_1-P_b)t+(P_2-P_1)w$$

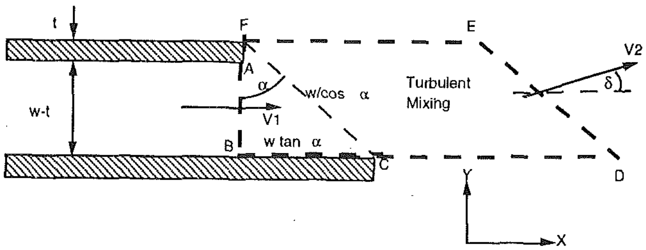

Fig. A3.1 Control volume model for a thick trailing edge

so

$$(P_1-P_2)=-\rho V_1^2\left(1-\frac{t}{w}-\frac{\delta^*}{w}-\frac{\theta}{w}\right)$$
$$+\rho V_2^2(1+\delta\tan\alpha)+(P_1-P_b)\frac{t}{w} \quad \text{(A3.5)}$$

Rearranging this gives

$$(P_{01}-P_{02})=0.5\,\rho V_2^2(2\delta\tan\alpha+1)$$
$$-0.5\,\rho V_1^2\left(1+2\left(\frac{t+\delta^*+\theta}{w}\right)\right)+(P_1-P_b)\frac{t}{w}$$

so

$$\frac{P_{01}-P_{02}}{0.5\,\rho\,V_1^2}=\frac{V_2^2}{V_1^2}(2\,\delta\tan\alpha+1)-1$$
$$+2\left(\frac{t+\delta^*+\theta}{w}\right)-C_{pb}\frac{t}{w} \quad \text{(A3.6)}$$

This may be solved by using the continuity equation to eliminate V_2/V_1 but the algebra becomes complex unless we make the assumption that the deviation angle δ is zero. This assumption is discussed in section 4 where it is justified on the grounds that it makes the total entropy creation behind a trailing edge almost independent of the blade stagger. The trailing edge loss coefficient then becomes

$$\zeta=-\frac{C_{pb}t}{w}+\frac{2\theta}{w}+\left(\frac{\delta^*+t}{w}\right)^2 \quad \text{(A3.7)}$$

An alternative common assumption (e.g., Stewart, 1955) is that $P_s=P_1$ in which case the deviation is negative and the algebra becomes much more complex. In practice the suction surface pressure is likely to lie somewhere between these two assumptions.

The first term on the right-hand side of Eq. (A3.7) is the loss due to the low base pressure acting on the trailing edge; in general this must be obtained from empirical data. The second term is the mixed out loss of the boundary layers on the blade surface just before the trailing edge and the third term arises from the combined blockage of the trailing edge and the boundary layers.

APPENDIX 4

Thermodynamics of a Cooled Turbine

(a) Cycle Analysis. Figure A4.1 shows an idealized cooled gas turbine cycle. Coolant flow m_c is assumed to be bled off at compressor delivery conditions and is gradually mixed with the turbine flow along the expansion from 3 to 4. Once added to the main flow the coolant flow subsequently expands with it and does useful work from its injection point to point 5. The efficiency of the cooled part of the turbine, 3–4, is assumed to be influenced by the mass flow rate of coolant while the efficiency of the uncooled part of the turbine from 4 to 5 is constant.

In a design situation we may imagine that the pressure ratio of the cycle and of the cooled turbine has been fixed and that the maximum temperature T_3 is being optimized by varying

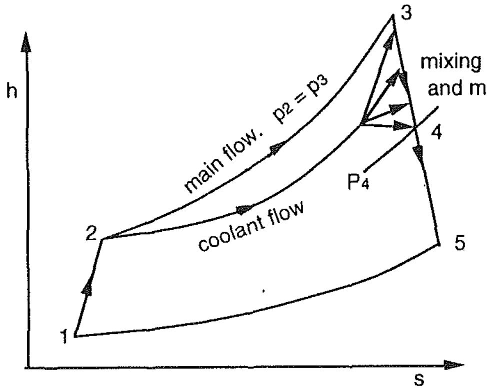

Fig. A4.1 Cycle for a cooled gas turbine

the proportion of cooling flow m_{fc}, where m_{fc} is the ratio of coolant flow rate to compressor flow rate. The compressor efficiency is also considered fixed as is the efficiency of the uncooled part of the turbine 4–5. The efficiency of the cooled part of the turbine is η_t, which is a function of m_{fc}. The cycle efficiency will then be a function of T_3, η_t, and m_{fc}, so we can write

$$\Delta\eta_c = \frac{\partial\eta_c}{\partial T_3}\Delta T_3 + \frac{\partial\eta_c}{\partial m_{fc}}\Delta m_{fc} + \frac{\partial\eta_c}{\partial\eta_t}\Delta\eta_t \tag{A4.1}$$

or, regarding m_{fc} as the independent variable,

$$\Delta\eta_c = \left\{\frac{\partial\eta_c}{\partial T_3}\frac{dT_3}{dm_{fc}} + \left[\frac{\partial\eta_c}{\partial m_{fc}} + \frac{\partial\eta_c}{\partial\eta_t}\frac{d\eta_t}{dm_{fc}}\right]\right\}\Delta m_{fc} \tag{A4.2}$$

It is only the last term that we will be concerned with in detail, i.e., the effect of coolant addition on the efficiency of the cooled part of the turbine. This efficiency is defined in terms of the change in properties of the main flow alone as will be described in section (b) of this appendix. The other terms in Eq. (A4.2) are equally important as regards cycle efficiency but cannot be considered as being the result of loss generation in the mainstream flow.

The values of the coefficients in Eq. (A4.2) can easily be calculated numerically for any specified cycle. For a typical civil aircraft engine cycle with overall pressure ratio 25, turbine entry temperature 1500 K and cooled turbine pressure ratio 4 we get

$$\frac{\partial\eta_c}{\partial T_3} = 1.035\,10^{-4}. \quad \frac{\partial\eta_c}{\partial m_{fc}} = -0.182. \quad \frac{\partial\eta_c}{\partial\eta_t} = 0.378.$$

(b) Turbine Analysis. Figure A4.2 illustrates the expansion through the cooled turbine where the expansion line 3–4 represents the state of main flow plus any cooling flow already added to it. We consider the main flow, flow rate m_m, which entered the turbine at 3 and the added coolant flow as two separate streams, which at any point in the turbine have identical properties. A total amount of heat Q is transferred from the mainstream to the coolant stream. We consider the work done by the main flow only. The total work output from this flow is

$$W = m_m(h_3 - h_4) - Q \tag{A4.3}$$

The isentropic work is

$$W_{is} = m_m(h_3 - h_4 + T_4\Delta s) = W + Q + m_m T_4 \Delta s \tag{A4.4}$$

and

$$m_m\Delta s = -\int dQ/T + m_m\Delta s_{\rm irrev} \tag{A4.5}$$

where T is the temperature at which the heat transfer dQ takes place and $\Delta s_{\rm irrev}$ is the increase in specific entropy due to irreversibility in the flow. This is the entropy created by viscous effects arising from the differences in velocity between the mainstream and the coolant.

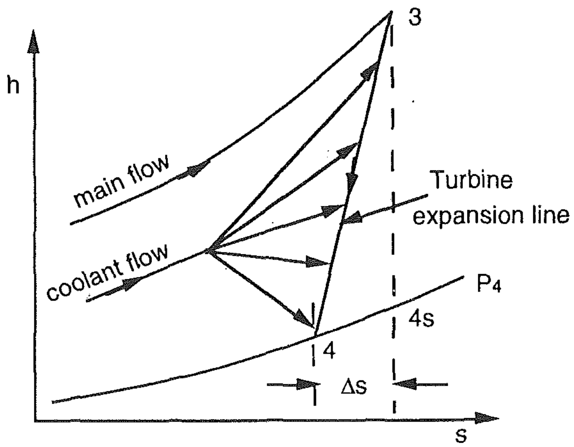

Fig. A4.2 The expansion through a cooled turbine

Hence,

$$W = W_{is} - \int (1 - T_4/T)\,dQ - m_m T_4 \Delta s_{\rm irrev} \tag{A4.6}$$

The middle term of this equation represents the reduction in isentropic work because the heat removal from the mainstream flow causes the expansion to move to the left on the $h-s$ diagram, as shown in Fig. A4.2. This is a thermodynamic effect, which is not related to any irreversibility in the flow, and so it does not contribute to the last term of Eq. (A4.2). Its magnitude depends on where the heat transfer takes place and it will be greatest if all the heat removal takes place at the start of the expansion and zero if all heat removal is at the end. Numerical evaluation of the term for the case where the coolant is added continuously gives a value equal to about 0.14 $m_{fc}W$ for a typical cycle. Let the magnitude of this term be $\Delta\eta_q W_{is}$, then the overall isentropic efficiency of the expansion is

$$\eta_t = \frac{W}{W_{is}} \approx \eta_o - \Delta\eta_q - \frac{T_4\Delta s_{\rm irrev}}{W_{is}} = \eta_o - \Delta\eta_q - \Delta\eta_{\rm irrev} \tag{A4.7}$$

where η_o is the efficiency of the uncooled turbine and $\Delta\eta_{\rm irrev}$ is the loss of efficiency due to irreversible mixing of the coolant flow and mainstream flow. It is only this term that we are concerned with in this paper.

The losses undergone by the coolant flow due to throttling within its supply ducts and passages affect the middle term of Eq. (A4.2). They depend mainly on the difference between the coolant supply pressure and the pressure at which it mixes with the mainstream flow. The value of $\partial\eta_c/\partial m_{fc}$ quoted above assumes that coolant is added continuously along the expansion with the amount added being proportional to the temperature change.

The last term $\Delta\eta_{\rm irrev}$ in Eq. (A4.7), is the only one that contributes to the last term in Eq. (A4.2). It is exactly the same as the expression for the efficiency of an uncooled turbine but in the case of a cooled turbine some of the entropy creation occurs as a result of the addition of the cooling flow. This may be evaluated as follows.

Shapiro (1953) shows that the effects of *small amounts* of heat transfer and mass addition on the specific entropy of a perfect gas can be calculated from

$$\Delta s = C_p\left(1 + \frac{\gamma - 1}{2}\mathrm{M}^2\right)\frac{\Delta T_o}{T_o} + C_p(\gamma - 1)\mathrm{M}_2\left(1 - \frac{V_c\cos\alpha}{V_m}\right)m_{fc} \tag{A4.8}$$

where ΔT_o is the change of stagnation temperature due to heat transfer and the coolant is injected with velocity V_c at an angle

α to the main flow, which has velocity V_m and Mach number M.

The first term can be written as $\Delta Q/T$ and so represents the entropy change due to heat transfer alone. The second term must therefore represent the entropy creation due to irreversibility. Using Eq. (3) to express Δs in terms of $\Delta T_o/T_o$ and $\Delta P_o/P_o$ gives

$$\Delta s_{\text{irrev}} = C_p(\gamma-1)\text{M}^2\left(1-\frac{V_c\cos\alpha}{V_m}\right)m_{fc}$$

$$= -R\frac{\Delta P_o}{P_o} - C_p\frac{\gamma-1}{2}\text{M}^2\frac{\Delta T_o}{T_o} \qquad \text{(A4.9)}$$

This equation shows that the irreversibility depends not only on the loss of stagnation pressure but also on the change of stagnation temperature. The last term is a result of the well-known effect of heat transfer on the stagnation pressure of a high-speed flow. Any heat removal from the mainstream flow will tend to increase its stagnation pressure while viscous dissipation due to the difference in velocity between the mainstream and the injected flow will always tend to decrease it. Hence, when heat is being removed from a flow, the net loss of stagnation pressure is always less than that due to viscous dissipation.

Substituting the above expression for Δs_{irrev} into Eq. (A4.7) gives for the change of cooled turbine efficiency

$$\Delta\eta_t = -\frac{T_4\Delta s_{\text{irrev}}}{C_p\Delta T_{ois}} = -\frac{T_4}{\Delta T_{ois}}(\gamma-1)\text{M}^2\left(1-\frac{V_c\cos\alpha}{V_m}\right)m_{fc} \qquad \text{(A4.10)}$$

where ΔT_{ois} is the isentropic temperature drop from 3 to 4.

It is significant that the loss of turbine efficiency does not explicitly involve the coolant temperature. This is because Δs_{irrev} is due solely to viscous effects, which depend on gradients of velocity and not on differences of temperature. It implies that experiments to determine the loss of efficiency due to cooling can be conducted without cooling the injected gas as long as the ratio of the velocity of injection to the main flow velocity is correct.

These results are for coolant addition through holes or slots in the blade or endwall surface and do not apply to coolant ejection through the trailing edge where the change of flow area and base pressure must also be included in the analysis. In fact coolant ejection through the trailing edge can increase the base pressure and so may be beneficial (see Denton and Xu, 1990).

APPENDIX 5

A Simple Theory for Tip Leakage Loss of Shrouded Blades

We consider the flow over a single tip seal as illustrated in Fig. (A5.1). We assume that the leakage flow suffers no loss before it reaches the throat of the leakage jet and that no tangential force acts on it so that it suffers no change of swirl velocity before it mixes with the main flow. It is also assumed that there is no significant restriction to the flow anywhere except at the seal and so the static pressure in the clearance space downstream of the seal is the same as the static pressure at exit from the blade row. The flow is viewed in a frame moving with the blade row and all quantities are measured relative to the row. If there is negligible change of radius the relative stagnation enthalpy of leakage flow and main flow is the same and remains constant.

For simplicity we will calculate the leakage flow rate assuming incompressible flow but this restriction can easily be relaxed at the expense of extra algebra.

At the throat of the leakage jet

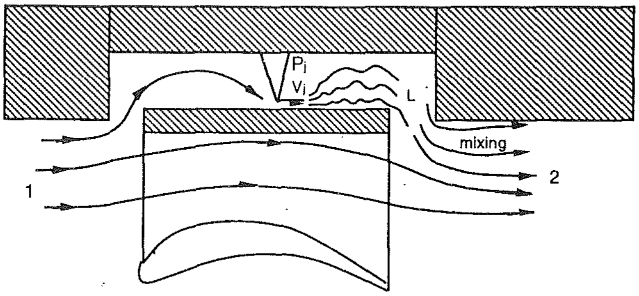

Fig. A5.1 Flow over a shrouded turbine tip seal

$$P_o = P_{o1} = P_j + 0.5\,\rho\,V_j^2 + 0.5\,\rho\,V_{\theta 1}^2 = P_2 + 0.5\,\rho\,V_2^2 \qquad \text{(A5.1)}$$

where V_j is the axial velocity of the leakage jet.

But we assume that $P_j = P_2$ so

$$V_j = \sqrt{V_2^2 - V_{\theta 1}^2} \qquad \text{(A5.2)}$$

The leakage mass flow is therefore

$$m_L = \rho g C_c \sqrt{V_2^2 - V_{\theta 1}^2} \qquad \text{(A5.3)}$$

where C_c is the jet contraction coefficient. The fractional leakage is therefore

$$\frac{m_L}{m_m} = \frac{gC_c\sqrt{V_2^2 - V_{\theta 1}^2}}{hV_2\cos\alpha_2} \qquad \text{(A5.4)}$$

where h is the blade span.

If V_x is constant through the blade row this can be written in terms of the flow angles as

$$\frac{m_L}{m_m} = \frac{gC_c}{h}\sqrt{\sec^2\alpha_2 - \tan^2\alpha_1} \qquad \text{(A5.5)}$$

Entropy increase of the mainstream flow only occurs when it mixes with the leakage flow. If the leakage flow re-enters the main flow with axial velocity V_{XL} and swirl velocity V_L it can be shown by applying the conservation equations to a swirling jet entering a vortex that Eq. (20) can be applied independently to the axial and tangential flow leading to

$$T\Delta s = \frac{m_L}{m_m}\left[V_{\theta 2}^2\left(1-\frac{V_{\theta L}}{V_{\theta 2}}\right) + V_{x2}^2\left(1-\frac{V_{xL}}{V_{x2}}\right)\right] \qquad \text{(A5.6)}$$

which is valid for compressible flow.

V_{xL} cannot be calculated without knowing the geometry of the re-entry slot but in most cases it is likely to be negligible both because the slot is comparatively wide and because the leakage flow is directed almost radially inward. Hence, neglecting V_{xL} we get

$$T\Delta s = \frac{m_L}{m_m}V_2^2\left(1-\frac{V_{\theta L}}{V_{\theta 2}}\sin^2\alpha_2\right) \qquad \text{(A5.7)}$$

By assuming constant axial velocity through the blade row this can be further simplified to

$$\frac{T\Delta s}{0.5\,V_2^2} = 2\frac{m_L}{m_m}\left(1-\frac{\tan\alpha_1}{\tan\alpha_2}\sin^2\alpha_2\right) \qquad \text{(A5.8)}$$

This result is valid for compressible flow if m_L/m_m has been calculated appropriately. Predictions from this theory are shown in Fig. 34.

APPENDIX 6

A Simple Theory for Tip Leakage Loss of Unshrouded Blades

We consider a model of tip leakage flow as illustrated in Figs. 31 and A6.1. The leakage flow passes over the blade tip with no change in its chordwise velocity component, which

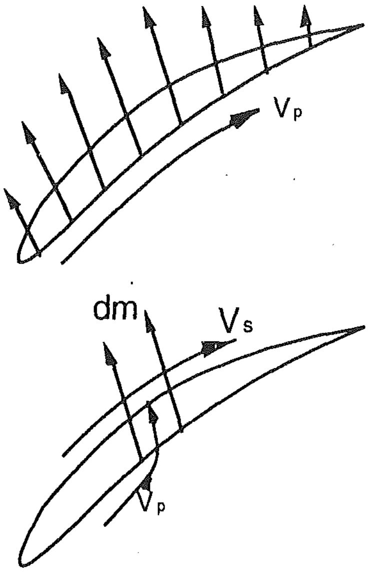

Fig. A6.1 Tip leakage viewed as a jet in a crossflow

remains equal to the surface velocity on the pressure side of the blade, V_p. The local rate of leakage flow is determined by the static pressure difference across the blade tip and by a discharge coefficient C_d, which may be either calculated theoretically assuming two-dimensional flow (Moore and Tilton, 1988) or determined empirically. The leakage flow therefore arrives at the suction side of the blade with a velocity component V_p in the streamwise direction. It is then assumed to mix immediately with the surrounding flow, which has velocity V_s. The mixing may be treated by exactly the same theory as was used for a coolant jet in Appendix 4 but without any stagnation temperature difference.

Applying Eq. (A4.9) to the leakage over a small part of the blade chord gives

$$\Delta s_{\text{irrev}} = C_p(\gamma-1)\mathrm{M}^2\left(1-\frac{V_p}{V_s}\right)\frac{dm}{m_m} \qquad (\text{A6.1})$$

where dm is the mass flow rate of the leakage flow and m_m is that of the mainstream. The Mach number at which the mixing takes place is taken as that of the mainstream flow on the suction surface and so we can rewrite this as

$$T\Delta s_{\text{irrev}} = V_s^2\left(1-\frac{V_p}{V_s}\right)\frac{dm}{m_m} \qquad (\text{A6.2})$$

To obtain the total entropy created we must integrate Eq. (A6.2) along the chord of the blade, giving

$$T\Delta s_{\text{tot}} = \frac{1}{m_m}\int V_s^2\left(1-\frac{V_p}{V_s}\right)dm \qquad (\text{A6.3})$$

which is valid for compressible flow provided that temperature changes are small.

The local leakage flow rate dm can be calculated by assuming two-dimensional flow and applying the momentum equation in the direction perpendicular to the blade chord. This is most easily done for incompressible flow but the theory can be extended to compressible flow in numerical calculations. For incompressible flow the leakage over a length dz along the chord of the blade is given by

$$dm = C_d g\sqrt{2\Delta P\rho}\,dz \qquad (\text{A6.4})$$

where g is the tip clearance, C_d is the discharge coefficient and ΔP is the pressure difference between the suction and pressure sides of the blade. A typical value of C_d would be about 0.7–0.8. Substituting this into Eq. (A6.3) gives

$$T\Delta s_{\text{tot}} = \frac{C_d g C}{m_m}\int_0^1 V_s^2\left(1-\frac{V_p}{V_s}\right)\sqrt{2\Delta P\rho}\,\frac{dz}{C} \qquad (\text{A6.5})$$

Since we have now assumed incompressible flow ΔP can also be related to the blade surface velocities

$$\Delta P = 0.5\,\rho\,(V_s^2 - V_p^2)$$

and the total mass flow through one blade passage can be written as

$$m_m = \rho V_2 h p\cos\alpha_2$$

where h is the blade span and p is the blade pitch.

Hence, Eq. (A6.5) becomes

$$T\Delta s_{\text{tot}} = \frac{C_d g C}{V_2 h p\cos\alpha_2}\int_0^1 V_s^2\left(1-\frac{V_p}{V_s}\right)\sqrt{(V_s^2 - V_p^2)}\,\frac{dz}{C} \qquad (\text{A6.6})$$

Turning the overall entropy increase into a loss coefficient based on $0.5\,V_2^2$ gives

$$\zeta = \frac{2C_d g C}{hp\cos\alpha_2}\int_0^1\left(\frac{V_s}{V_2}\right)^3\left(1-\frac{V_p}{V_s}\right)\sqrt{\left(1-\left(\frac{V_p}{V_s}\right)^2\right)}\,\frac{dz}{C} \qquad (\text{A6.7})$$

The terms in the integral can be evaluated when the blade surface velocity is known. Since for turbine blades the average value of V_s/V_2 is about unity and V_p/V_2 is about 0.3, the magnitude of the integral will be of the order 0.65. Hence, taking C_d to be about 0.8, the loss coefficient is of the same order as the ratio of leakage area, gC, to blade throat area, $hp\cos\alpha_2$. This ratio is sometimes used as a measure of tip leakage loss.

It is interesting to note the occurrence of the term $(V_s/V_2)^3$ in the expression for the loss coefficient. This means that, exactly as was the case for boundary layer loss, highly loaded blades with high suction surface velocities will have a large tip leakage loss.

The above theory applies equally to compressor blades and to turbine blades. Equation (A6.7) can be used for compressor blades if subscript 2 is replaced by subscript 1. We then obtain the loss coefficient based on inlet dynamic head. This will now be of order of the ratio of leakage area to inlet flow area and again it will increase rapidly for highly loaded blades.

In cases where the blade surface velocity distributions are not known we can *estimate* the average values of V_s and V_p *very approximately* by assuming the blade loading to be uniform. This gives from the blade circulation

$$V_s - V_p \approx \frac{p}{C}V_x(\tan\alpha_2 - \tan\alpha_1) \qquad (\text{A6.8})$$

and from continuity, assuming that the blade thickness is small

$$V_s + V_p \approx \frac{2V_x}{\cos\alpha}. \qquad (\text{A6.9})$$

The local value of $\cos\alpha$ may be reasonably estimated by assuming that $\tan\alpha$ varies linearly with x.

Equations (A6.8) to (A6.9) enable Eq. (A6.7) to be integrated numerically and so provide a general means of *estimating* the tip leakage loss coefficients of turbine and compressor blades. Results from this method are plotted in Fig. 33.

Hot Streaks and Phantom Cooling in a Turbine Rotor Passage: Part 1—Separate Effects

R. J. Roback

R. P. Dring

United Technologies Research Center,
East Hartford, CT 06108

This paper presents experimental documentation and analytical correlations demonstrating the effects of hot streak accumulation and phantom cooling on turbine rotor airfoil surface temperature. Results are shown that quantify the impact of (1) a nonuniform temperature profile at the entrance of a turbine due to combustor-generated hot and cold streaks, and (2) cooling air discharged from the trailing edge of the upstream stator. In Part 1 of this paper, experimental results are shown for a range of controlling variables to identify where streak accumulation and phantom cooling were most likely to be strongest. These variables include streak-to-free-stream density ratio, streak injection location, and coolant-to-free-stream density and velocity ratios. In Part 2 of this paper, experimental results are shown for the combined effects of hot streak and stator coolant. An analytical model is also presented to correlate the experimental results.

Introduction

Turbine heat transfer has historically been one of the barrier technologies in the development of the gas turbine. As the technology has advanced, the turbine cooling challenge that faces industry has become more formidable. The main impediment to meeting this challenge is the complexity of the highly three-dimensional and unsteady flow mechanisms in a turbine. The effects of these mechanisms on turbine heat transfer have been the focus of intense research over the years.

Two turbine heat transfer mechanisms, "hot streaks" and "phantom cooling," have received little attention because they are difficult to simulate experimentally. Hot streaks result because the temperature of the combustor-generated flow entering the turbine is highly nonuniform both radially and circumferentially. Phantom cooling occurs because the cooling air for each airfoil row can collect in a nonuniform manner on the downstream row. While the presence of these mechanisms has been acknowledged by the industry for many years, there is no definitive body of information available to quantify their impact on turbine heat transfer.

The intent of this work was to quantify the impact of both a nonuniform turbine inlet temperature distribution and cooling air discharging from the first stage stator, on the distribution of the adiabatic recovery temperature on the rotor airfoil. The experiment was carried out in a large-scale rotating rig, which comprised a one-and-one half stage turbine model. The experimental technique consisted of simulating streams of hot and cold streaks entering the turbine and coolant discharged from the trailing edge of the first stage stator. These streams were seeded with a trace gas (CO_2). The accumulation of the streaks or coolant on the rotor is directly related to the local concentration of the trace gas, which was measured on the rotor airfoil and endwall surfaces. Factors investigated included the effects of streak-to-free-stream density ratio, injection location of the streak, and coolant-to-free-stream density and velocity ratios.

The experimental program provides data in an area of heat transfer technology that has not been systematically studied to date. It provides the data required for the fundamental understanding necessary to guide the design of advanced turbines, for the assessment and validation of advanced analytical and computational fluid dynamic design tools, and for the calibration of the less computationally intensive approximate "design system" analyses and correlations in use throughout the industry.

Description of the Experiment

Large-Scale Rotating Rig (LSRR). The Large-Scale Rotating Rig (LSRR) was designed for conducting detailed experimental investigations of flow within turbine and compressor blading. Primary considerations were to provide a facility that would: (1) be large enough to permit a high degree of resolution of three-dimensional flows, (2) have a high degree of flexibility in regard to the configurations that could be tested, and (3) enable measurements to be made directly in the rotating frame of reference.

The LSRR facility is of the open circuit type with flow entering through a 12-ft. diameter inlet. A 6-in.-thick section of honeycomb is mounted at the inlet face to remove any crossflow effects. The inlet smoothly contracts the cross section to 5 ft. diameter. The flow is then passed through a series of

---

Contributed by the International Gas Turbine Institute and presented at the 37th International Gas Turbine and Aeroengine Congress and Exposition, Cologne, Germany, June 1-4, 1992. Manuscript received by the International Gas Turbine Institute February 4, 1992. Paper No. 92-GT-75. Associate Technical Editor: L. S. Langston.

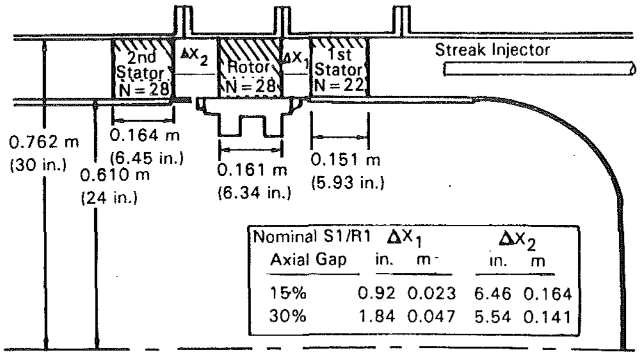

Nominal S1/R1 Axial Gap	ΔX_1 in.	ΔX_1 m	ΔX_2 in.	ΔX_2 m
15%	0.92	0.023	6.46	0.164
30%	1.84	0.047	5.54	0.141

Fig. 1 United Technologies Research Center Large-Scale Rotating Rig

fine mesh screens to reduce the turbulence level. Immediately downstream of the screens is a 7-ft-long section, which slides axially and permits access to the test section.

The test section consists of a series of constant-diameter casings enclosing the first-stage stator and rotor and the second stator of the the turbine model (Fig. 1). The rotor shaft is cantilevered from two downstream bearings, thus providing a clean flow path at the model inlet. Axial length of the test section is 36 in. The rotor is driven or braked by a hydraulic pump and motor system, which is capable of maintaining shaft speeds up to 890 rpm. Downstream of the test section flow passes through an annular diffuser into a centrifugal fan and exhausts from the rig. A vortex valve is mounted at the fan inlet face to control the flow rate.

The turbine model in this facility accurately replicated the flow in a high-speed aircraft gas turbine environment in every way that was essential to the program. The airfoils had contours typical of the first stage of a high-pressure turbine and were designed such that they were without boundary layer separation over a wide range of operation. All three airfoil rows have solidities and aspect ratios very near unity. The rotor tip clearance was 0.060 inches or 1 percent span, which is typical of aircraft engine design.

The axial spacing between the first stator and the rotor was 15 percent of the average of the first stage stator and rotor axial chords, *Bx*. This gap is relatively small compared to those gaps in aircraft turbines, but it will be shown that the accumulation process was insensitive to gap size. When operating at design conditions the turbine (at midspan) has a flow coefficient (Cx/U) of 0.78. The velocity triangles are typical of high-pressure turbines. The airfoil Reynolds numbers were approximately 600,000 (a value typical of altitude cruise).

Stator Trailing Edge Cooling. For the phantom cooling experiments conducted in this program, two first-stage stator airfoils were modified to provide simulated trailing edge coolant flows. Eleven 0.125 × 0.25 in. coolant discharge slots, spaced 0.50 in. on center, were machined into the trailing edge of each of the two airfoils. Each slot was fed by an individual internal feed line. Separate flow systems were employed to provide coolant flow to each stator. The total coolant flow to each stator was separately adjusted and metered upstream of a plenum, which fed each of the eleven feed lines leading to the stator. Metering valves were placed in each of the eleven feed lines, downstream of the plenum, to provide for adjustment of each flow so that uniform flow through each coolant channel in both airfoils was ensured. Each stator coolant flow system was periodically calibrated to be sure that a constant flow passed through each coolant channel.

Trace Gas Measurement. The LSRR has an independent system to measure trace gas (CO_2) concentrations. Concentrations are determined by drawing a gas sample through pressure taps on the rotor airfoil and endwall, and through rakes and traverse probes in the flow. The samples are passed through a Beckman Non-Dispersive Infrared (NDIR) CO_2 analyzer, which could determine the concentration of CO_2 in the gas sample to within approximately 5 ppm. Carbon dioxide (CO_2) was used as the trace gas because it is relatively inexpensive and can be handled safely. The trace gas simulation and measurement techniques have been successfully demonstrated previously in studies of (1) film cooling applications (Eckert and Goldstein, 1976; Pederson et al., 1977); (2) the redistribution of a simulated axisymmetrical inlet radial temperature profile (Joslyn and Dring, 1988, 1992a, 1992b); and (3) the redistribution of a simulated combustor generated hot streak (Butler et al., 1986).

The main assumptions in simulating heat transport with species transport are: (1) Turbulent transport dominates molecular transport, and (2) throughout the flow field the turbulent Prandtl number (which governs heat transfer) and the turbulent Schmidt number (which governs mass transfer) vary in such a manner that their ratio, the turbulent Lewis number, is close to unity. This assumption has been shown to be accurate for turbulent wakes and jets by Reynolds (1976). Although there are basic differences in the flow, it was expected that the analogy would be even better in the present turbine flow field due to the large-scale viscous and inviscid mechanisms involved.

The LSRR facility has provisions for heating the incoming streak. For the experiments conducted under this program, the total pressure of the streak was set equal to the total pressure of the free stream at the turbine inlet. Thus, the streak-to-freestream temperature ratio is the reciprocal of the streak-to-freestream density ratio. The density ratio was obtained by mixing air with CO_2 to achieve a particular molecular weight and then heating the mixture to arrive at the desired density ratio. The CO_2 concentration was nominally set to 18 percent for hot streaks (density ratios ≤ 1). This concentration provided trace gas concentrations entering the rotor airfoil enough above the ambient CO_2 concentration for accurate measurement.

Since there was no provision for cooling the streak for the cold streak measurements, density ratios greater than one had to be obtained by increasing the concentration of CO_2 in the streak. For the cold streak tests, undiluted CO_2 was required to achieve the maximum density ratio of 1.5 used in this program.

Instrumentation. The instrumentation used for setting operating parameters and sampling trace gas consisted of (1) a radial traverse probe at exit plane of streak injector to obtain radial distributions of total pressure, total temperature, and trace gas concentration, (2) a rake at the rotor leading edge plane to obtain trace gas concentration in the rotating frame of reference at seventeen locations from 3 to 98 percent span, (3) sampling sites at 22 locations around the rotor airfoil pe-

Nomenclature

Bx = airfoil axial chord
C = absolute flow speed
Cx/U = flow coefficient
P = pressure
S = airfoil surface arc length
S^* = scaled airfoil surface distance
U = wheel speed at midspan
V = fluid velocity
ρ = density

Subscripts

C or c = coolant, cold
F or f = freestream
r = radial distance
S or s = streak
rel = relative frame of reference
tot = total
x = axial distance

rimeter for each of 7 spanwise locations (2, 12.5, 25, 50, 75, 87.5, and 98 percent span), (4) rotor hub endwall sampling sites at 28 locations over one rotor pitch from 20 to 90 percent chord, and (5) a rotating, radial/circumferential traverse probe to obtain trace gas concentrations over two rotor pitches from 5 to 95 percent span at distances downstream of the rotor corresponding to 10 and 25 percent of rotor axial chord.

Test Conditions. Both the hot and cold streak experiments and the phantom cooling experiment were carried out in such a way as to demonstrate the impact of the individual sources on the simulated adiabatic recovery temperature of the rotor. Two-in. diameter streaks were generated by a single source located one chord length upstream of the first stator (Fig. 1). Since the total pressure, temperature, and density of the streak could be accurately controlled, a hot, neutral, or cold streak could be generated. By this means, the impact of an individual combustor fuel nozzle or an individual combustor dilution jet could be determined. Similarly, by accurately controlling the velocity ratio and the density ratio of the coolant being discharged from the stator trailing edge, the phantom cooling phenomenon could be studied over a wide range of coolant conditions.

The ranges of the controlling variables to be investigated were chosen to identify circumstances where hot and cold streak accumulation and phantom cooling were most likely to be strongest. Hot and cold streak density ratio (the inverse of the temperature ratio) was chosen to cover a wide range. Values of 0.5, 1.0, and 1.5 were chosen to satisfy this requirement. The phantom cooling experiment was conducted over a range of coolant-to-free-stream velocity ratios ($V_c/V_f = 0.57$, 0.91, and 1.25) and with coolant-to-free-stream density ratios of 1.1 and 1.5. All measurements reported here were made at the turbine model nominal design flow coefficient ($Cx/U = 0.78$).

Experimental Results

Data Presentation Format. It is desirable to present the trace gas distributions measured on the airfoil as contour maps of equal concentration. However, the shape of the rotor airfoil surface, unwrapped and flattened on a plane, is complex. In order to avoid this complexity, a coordinate system was developed to project the airfoil surface shape onto a rectangle with the same span/arc-length ratio. This coordinate system uniquely identifies a position on the rotor airfoil surface (1) radially in terms of percent span, and (2) chordwise in terms of percent distance along the respective (pressure or suction) surface. Surface distances along the airfoil, S, were measured between the tangent points on the tangent line connecting the leading edge circle and the trailing edge circle. The distance, S, is defined as increasing positive along the suction surface and increasing negative along the pressure surface.

The surface distance was first nondimensionalized by the total arc length for the respective (suction or pressure) surface. Although this scale has the advantage of 10 percent ending at the trailing edge, the inequality between the suction and pressure scales was considered to be cumbersome. To eliminate this problem, it was decided to nondimensionalize all arc lengths by the airfoil span, thus not only making grid increments equal for both the pressure and suction portions of the horizontal and vertical scales but also making the horizontal scale equal to the vertical scale. The airfoil surface, though having a constant span, was not rectangular when unwrapped because the total surface arc length (on both surfaces) was a function of span. Rectangular projections were achieved by plotting off-midspan data at surface distances proportionally scaled by the ratio of midspan/local arc length, i.e.,

$$S^* = [S/\text{SPAN}]\ [\text{STOT(MIDSPAN)}/\text{STOT}(R)]$$

The disadvantage of this, of course, is that the trailing edge lines coincide with values not equal to 100 percent. For the suction surface, the trailing edge line falls at 185 percent of S^* while it falls at 132 percent of S^* for the pressure surface.

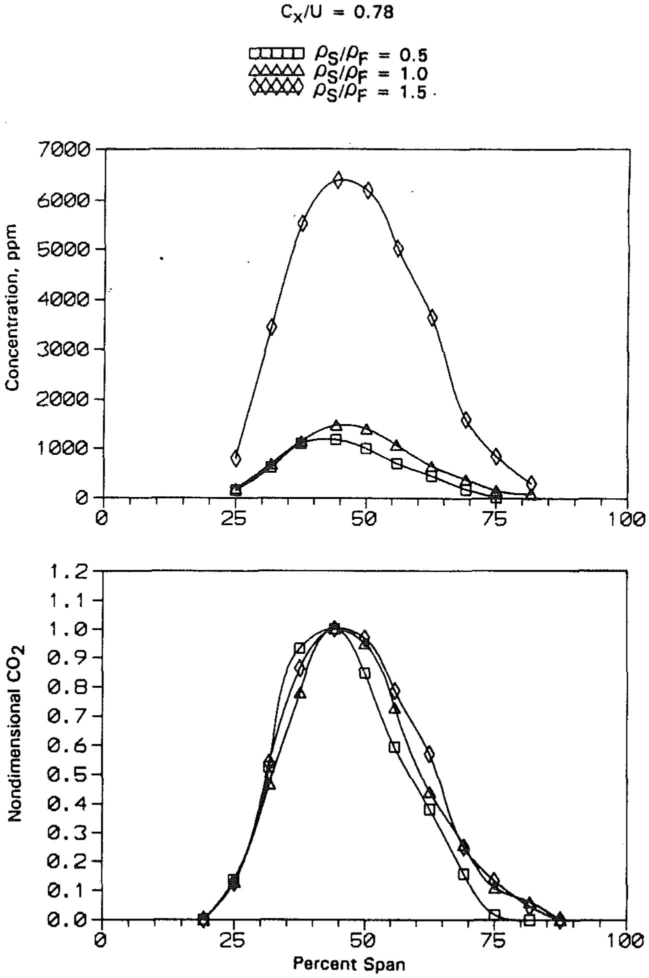

Fig. 2 Rotor leading edge plane concentration profile; effect of streak density ratio

Streak Measurements. Typical spanwise trace gas profiles measured with the rake at the rotor leading edge plane during the streak testing are shown in the top of Fig. 2. The streak was located at midspan and midway between two adjacent stators (midpitch). For the tests at streak density ratios of 0.5 and 1.0, the streak was heated to provide the appropriate density ratio. Therefore, for these tests, the concentration at the rotor leading edge was relatively low because air was mixed with CO_2 to "mark" the streak with enough CO_2 to provide accurately measurable concentrations above ambient on the rotor surface. Undiluted CO_2 was required to achieve the density ratio of 1.5, and so a much higher trace gas concentration is observed.

Throughout the test series, the rotor inlet trace gas profile was measured each time airfoil or endwall surface data were obtained. When all these were normalized (with the profile maximum), they had distributions very similar to the ones shown in the bottom of Fig. 2. For the presentation of streak results in this program, all trace gas concentrations (rake, airfoil, or hub endwall) acquired for a particular test condition were normalized to the rotor inlet rake profile maximum obtained for that test. In this way, the influence of long term drifts in the NDIR calibration, in the ambient concentration, and in the various operating pressures and flows is minimized.

The streak data acquired at midspan are shown in Fig. 3. The normalized concentration near the rotor leading edge

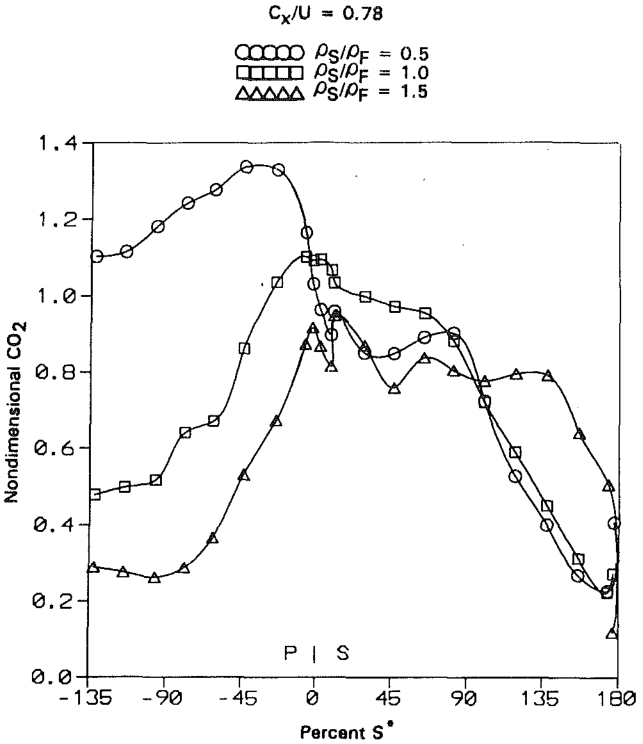

Fig. 3 Midspan trace gas concentration for streaks; effect of streak density ratio

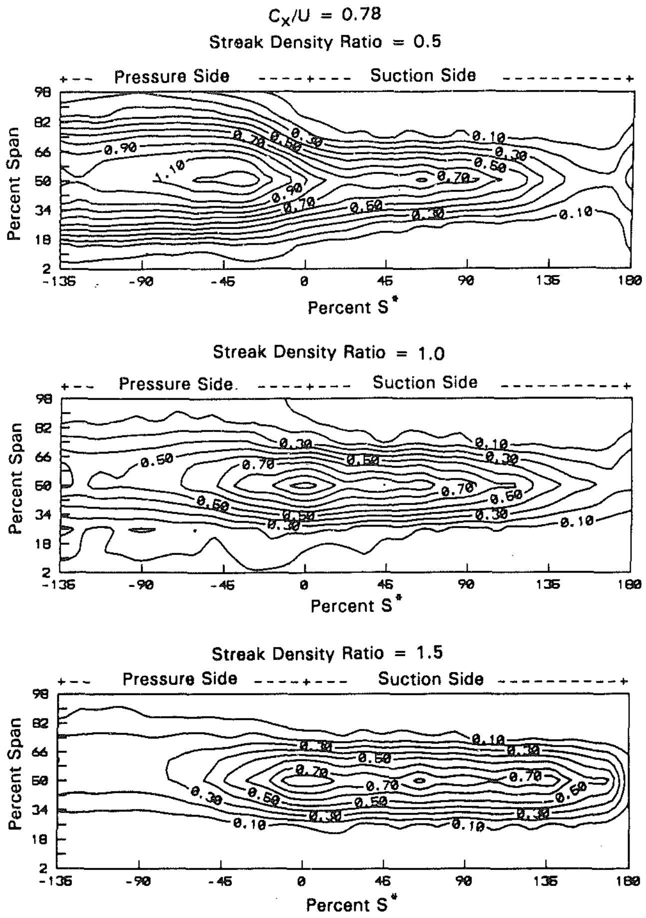

Fig. 4 Full-span trace gas concentration; effect of streak density ratio

($S^* = 0$) was always close to 1.0. This observation is due to the fact that the accumulation process was only just beginning at the leading edge. Hence, the concentration at this location should be nearly equal to that measured at midspan with the leading edge rake.

As shown in Fig. 3, the fluid from the low-density ratio streak (hot streak) accumulated on the pressure surface so strongly that the time-averaged concentration was as much as 35 percent higher than the maximum time-averaged inlet concentration measured with the leading edge plane rake. Accumulation on the suction surface was strongest near the leading edge with the high-density ratio streak (cold streak) but the time-averaged concentration generally did not exceed the maximum time-averaged inlet concentration. The rapid drop in suction surface accumulation near the trailing edge was due to the rotor hub and tip secondary flows bringing low-concentration endwall fluid into the midspan region.

The full-span data are illustrated in Fig. 4. The maximum concentrations observed in the full-span distributions are consistent with those observed in the midspan plot in Fig. 3. The maximum concentrations at the density ratios of 1.0 and 1.5 were near the leading edge and close to 1.0. The maximum concentration at the density ratio of 0.5 was far from the leading edge on the pressure surface and well above 1.0, i.e., 1.3. There were small differences between the maximum accumulation measured during the full-span tests (Fig. 4) and those obtained in the midspan tests (Fig. 3); i.e., 1.1 versus 1.0 for density ratio = 1.0 and 1.3 versus 1.2 for density ratio = 0.5. These differences are because the midspan data used in Fig. 4 were not the same as those used in Fig. 3. The two sets of data were taken many days apart and reflect the day-to-day variations in setting operating and flow conditions. The difference between them (0.1) is indicative of measurement repeatability.

At a density ratio of 1.5 (cold streak) accumulation was strongest on the suction surface and at 0.5 (hot streak), it was strongest on the pressure surface. The data for a neutral density ratio of 1.0 illustrate how a streak diffused as it was convected through the rotor passage in the absence of accumulation. Because of the relative eddy, there was a weak tendency for the streak to be convected toward the tip on the pressure surface for all density ratios. The streak fluid on the suction surface was confined to the midspan region because of the hub and tip secondary flows. As seen in Figs. 3 and 4, accumulation on the pressure surface can be much stronger than on the suction surface. Also, the pressure surface concentration distributions appear to be more sensitive to changes in the density ratio. The suction surface concentration distributions for all streak density ratios are similar to each other indicating a relative insensitivity to streak density ratio.

In addition to the above tests with the streak located at midspan and midway between two stators (mid pitch), tests with a hot streak (density ratio of 0.5) were carried out with the streak located at 25 and 75 percent span and at midpitch and also with it located at 50 percent span but aligned with a stator leading edge ("on stator"). Concentration profiles measured at the rotor leading edge plane for all four streak positions are shown in Fig. 5. The two profiles with the streak at midspan were shifted slightly toward the hub (≈5 percent span), but in general, directing the streak on-stator versus midpitch had relatively little effect on the concentration profile. The on-stator orientation of the streak had it aligned mechanically with the stator leading edge. The leading edge stagnation streamline, however, was displaced toward the pressure surface and hence, more than half of the on-stator streak fluid passed over the stator suction surface. Since the streak initial diameter was 2 in. (33 percent span), it was likely to have interacted with the stator hub and tip secondary flows on the suction surface.

The streak introduced at 25 percent span remained close to this spanwise location when it reached the rotor leading edge

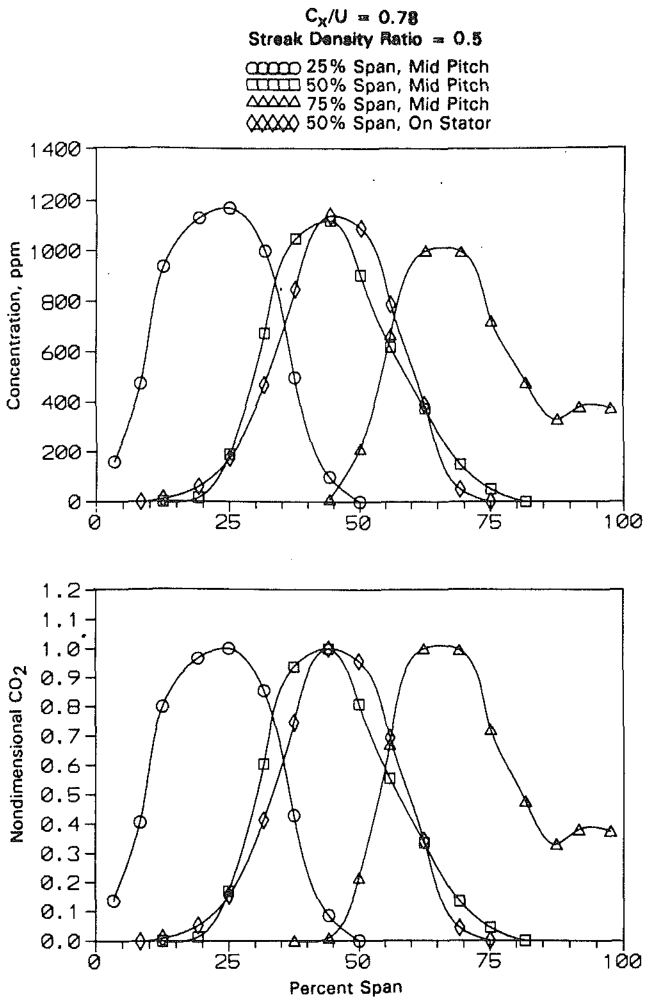

Fig. 5 Rotor leading edge plane concentration profile; effect of streak spanwise injection location

plane and it had a profile similar to that with the streak at midspan. The streak introduced at 75 percent span had moved toward the hub (≈5 to 10 percent span) by the time it reached the rotor leading edge plane and it had developed a high concentration region between 85 percent span and the tip. This region of high concentration was probably due to an interaction between the streak and the relatively large stator tip secondary flow field (see Joslyn and Dring, 1992a, 1992b).

Results from the tests with the hot streak located at 25, 50, and 75 percent span all at midpitch are shown in Fig. 6. For all of the streak injection locations, the hot streak accumulated primarily on the pressure surface. In addition, the concentration distributions on the rotor leading edge were similar to the distributions measured with the rake at the leading edge plane. However, the spanwise locations of the regions of maximum concentration changed with streak injection location. This observation is summarized in Table 1. For example, the streak that was injected at 25 percent span was located at 24 percent span on the rotor leading edge and the point of maximum pressure surface accumulation was located at 24 percent span. The radial shifts here were very small. A similar conclusion could be made for the streak injected at 50 percent span. The streak injected at 75 percent span had significant radial shifts. With injection at 75 percent span, the maximum leading edge concentration was at 66 percent span and the pressure surface maximum was at 87 percent span. This shift can be seen clearly in Fig. 6. The increasing radial displacement was consistent with the increasingly strong flow deflection toward the tip due to the relative eddy on the pressure surface.

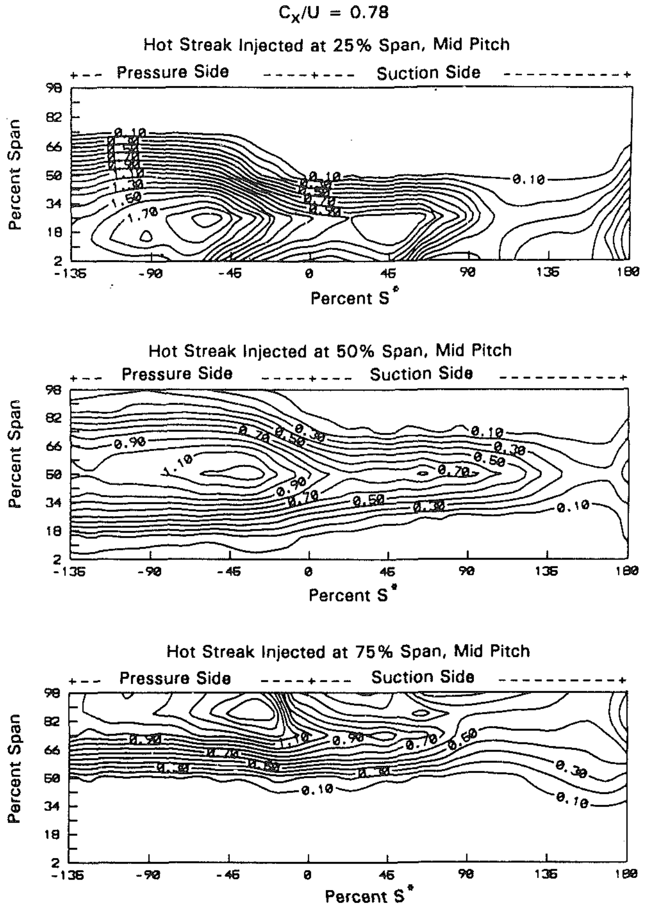

Fig. 6 Full-span trace gas concentration; effect of streak spanwise injection location

Table1 Location of peak trace gas concentration

Streak Injection Location	Rotor			
	Leading Edge	Pressure Surface		
		Radial Loc.	Circ. Loc.	Peak Conc.
% Span	% Span	% Span	% Span	
25	24	24	-60	2.0
50	43	51	-38	1.3
75	66	87	-30	1.6

In addition to the spanwise shift, there was also a chordwise shift of the location of maximum concentration (see Table 1). As the spanwise injection location increased from 25 to 50 to 75 percent span, the chordwise location of maximum accumulation on the pressure surface moved forward on the airfoil, from -60 to -38 to -30 percent surface distance, S^*. (Recall that both the spanwise and chordwise coordinates were normalized with the rotor span.) This shift can also be seen clearly in Fig. 6, and is consistent with the relative eddy in that the trajectories of the regions of highest accumulation were along the surface streamlines.

The data in Fig. 6 also indicated that the peak pressure surface concentration varied with the streak spanwise injection location. Strong accumulation occurred when the streak was near the endwalls, with the strongest occurring when the streak was near the tip. The reason for the higher accumulation near the endwalls was unclear, but it was probably related to interactions between the streaks and the stator and rotor secondary flows.

The accumulation pattern for the 75 percent span streak location indicates another important flow feature. Since there

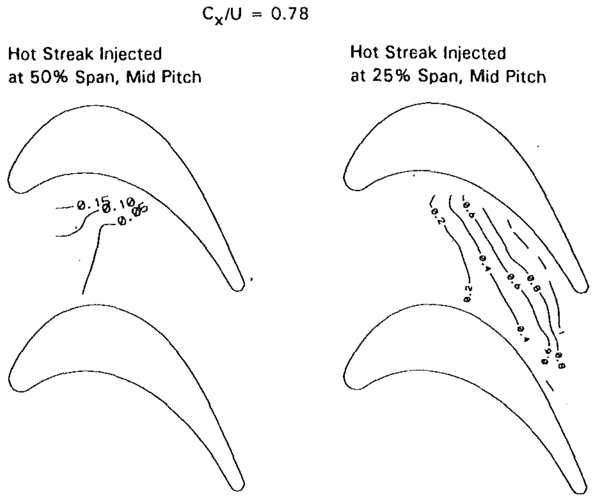

Fig. 7 Hub endwall trace gas concentration profile; hot streaks

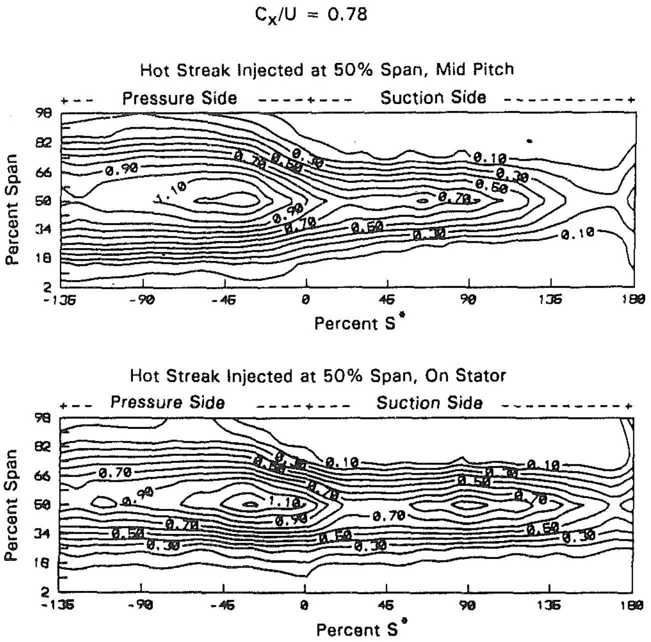

Fig. 8 Full-span trace gas concentration; effect of streak pitchwise injection location

was a high level of accumulation along the pressure surface near the tip, it was this high-concentration fluid that was convected over the rotor tip due to the tip leakage flow. The result of the leakage of the high-concentration flow could be seen as the region of relatively high concentration on the suction surface near the tip between 60 and 120 percent of S^*.

One conclusion from these tests with the streak injected at the various spanwise locations was that these streaks can reach both the hub and tip of the annulus. Thus, they can impact the heat transfer to the rotor hub platform, and to the rotor tip and outer air seal.

The accumulation pattern for the 25 percent span streak location indicated that streaks could cause significant accumulation on the rotor hub endwall. Results of measurements made on the hub endwall for hot streaks injected at 50 and 25 percent spans are presented in Fig. 7. The results for injection at 50 percent, shown on the left side of the figure, indicate that relatively small concentrations occur on the endwall. However, when the injection point of the streak is moved closer to the hub (25 percent span), significant accumulation of the streak occurs on the endwall. Concentrations near the pressure surface at the trailing edge are equal to the peak value measured at the rotor leading edge plane.

A comparison of the accumulation patterns with midspan hot streak injection both at midpitch and directly on-stator is illustrated in Fig. 8. Although the leading edge rake measurements showed little difference for the two injection locations (Fig. 5), the accumulation patterns on the airfoil were somewhat different. While the peak concentration and the distribution at midspan have not changed much, the radial extent of the accumulation pattern was reduced when the streak was directed on the stator. This was consistent with the remarks above that the streak injected on stator was primarily passing over the stator suction surface and that the secondary flow there would drive it toward midspan. This observation suggests that hot streaks are less likely to affect the hub and tip endwalls when they are directed on-stator, as opposed to between stators.

Measurements were made on the endwall for the condition where the hot streak was injected on stator at 50 percent span. Although the endwall concentrations were very low, the peak endwall concentration for streak injection on stator was about half that obtained when the streak was injected at midpitch, which supports at least qualitatively the conclusion that the flow is being driven toward midspan and less accumulation occurs on the endwall.

The impact on streak accumulation of opening the axial gap between the stator and the rotor from 15 to 30 percent *Bx* was also examined. The rotor surface results that are presented in Fig. 9 were obtained for streak density ratios of 0.5 (hot streak) and 1.5 (cold streak). The streaks were introduced at midspan and at midpitch. Note that since the nominal stator absolute exit flow angle was 22 deg from tangential, the streamwise distance that a streak traveled was 2.5 times the axial distance. Thus, going from an axial gap of 15 percent *Bx* to 30 percent *Bx* corresponded to a change in streamwise distance of 37 percent *Bx*. However, this change is small relative to the distance that the streak has traveled from where it was injected (one axial chord upstream of the stator).

At both density ratios, the distribution on the rotor surface was insensitive to axial gap. This result is expected because the small change in axial gap produces a relatively small change in the total length the streak travels from the injection site. However, there is a small increase in accumulation and a more radially outward movement of the accumulation toward the tip on the pressure side with the larger gap. This difference, however, is comparable to the measurement uncertainty (≈0.1).

In addition to trace gas concentration measurements on the rotor surface, full-span radial/circumferential traverse measurements of trace gas concentration were made at two locations downstream of the rotor at two stator–rotor axial gaps. The traverse results are summarized in Figs. 10 and 11. Results for the hot streak (density ratio = 0.5) are presented in Fig. 10 for the two axial gaps. For each axial gap concentration contour plots are presented at two locations downstream of the rotor trailing edge (10 and 25 percent *Bx* aft). The plot of the 10 percent aft data clearly shows that the hot streak had accumulated on the pressure surface side of the rotor wake near the midspan location where it was introduced into the flow. The radial flow toward the tip on the rotor pressure surface due to the relative eddy caused the contours near the pressure surface to be elongated in that direction. The relatively high maximum concentration in the flow aft of the rotor (≈0.7) was a result of the accumulation that had occurred along the rotor pressure surface. For both axial gaps the mixing between the traverse planes 10 and 25 percent aft of the rotor was rather weak. The maximum concentration decreased by only about 0.1 over this distance.

By comparing the hot streak data in Figs. 9 and 10 it can be seen that, for both stator–rotor axial gaps, the maximum concentration on the rotor pressure surface near the trailing

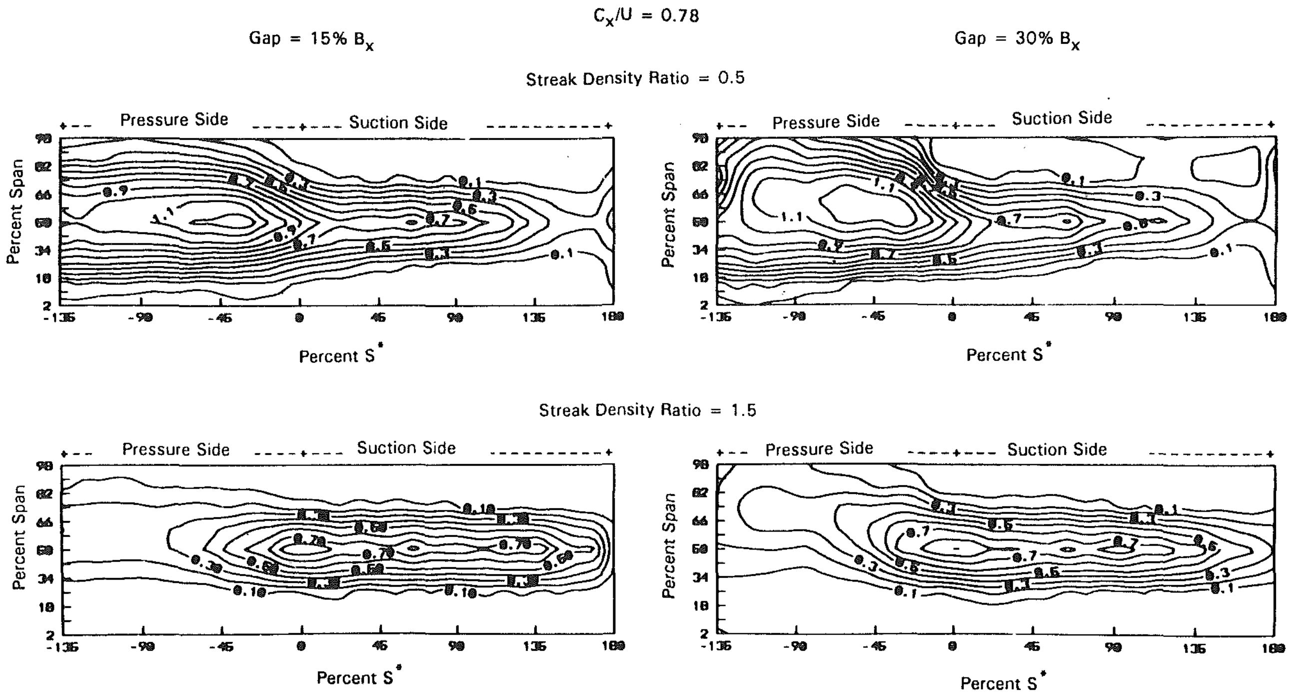
$C_x/U = 0.78$

Gap = 15% B_x

Gap = 30% B_x

Streak Density Ratio = 0.5

Streak Density Ratio = 1.5

Fig. 9 Full-span trace gas concentration for streaks; effect of stator-rotor axial gap

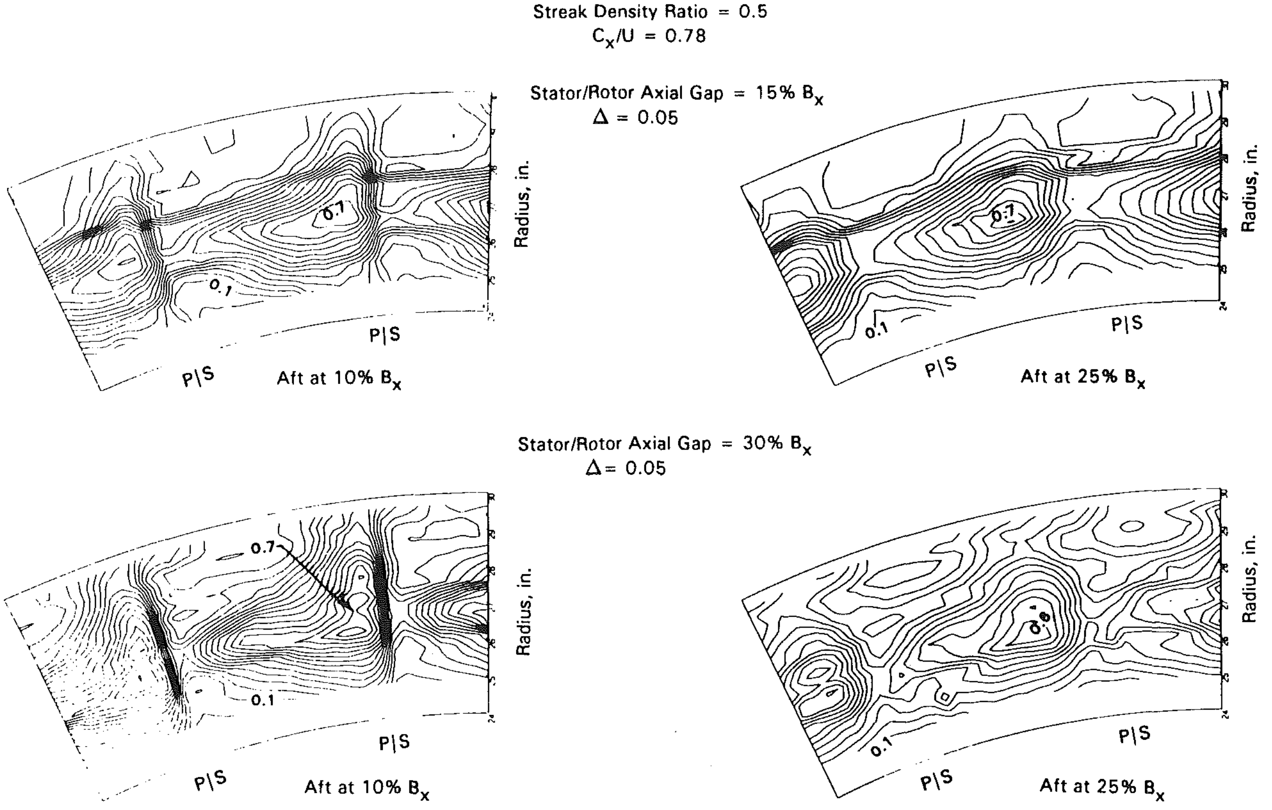
Streak Density Ratio = 0.5
$C_x/U = 0.78$

Stator/Rotor Axial Gap = 15% B_x
$\Delta = 0.05$

Stator/Rotor Axial Gap = 30% B_x
$\Delta = 0.05$

Fig. 10 Trace gas concentration aft of the rotor; effect of stator-rotor axial gap

edge (≈ 0.9) was greater than the maximum concentration in the flow aft of the rotor (≈ 0.7). This difference (≈ 0.2) was a result of mixing in the flow aft of the rotor.

Results for the 30 percent axial gap and for the hot and cold streaks are presented in Fig. 11. The data 10 percent aft clearly showed that the hot streak (density ratio = 0.5) had accumulated on the pressure surface side of the airfoil wake and that the cold streak (density ratio = 1.5) had accumulated on the suction surface side of the airfoil wake. This observation was also evident in the airfoil surface results presented in Fig. 9. The hot streak was elongated toward the tip by the relative eddy on the pressure surface but the cold streak was pinched toward midspan symmetrically by the hub and tip secondary flow vortices. The relatively high maximum concentration for the cold streak in the flow aft of the rotor (≈ 0.8) was a result of the accumulation that had occurred along the rotor suction surface. The cold streak also mixed out slowly with downstream distance in the same way as the hot streak.

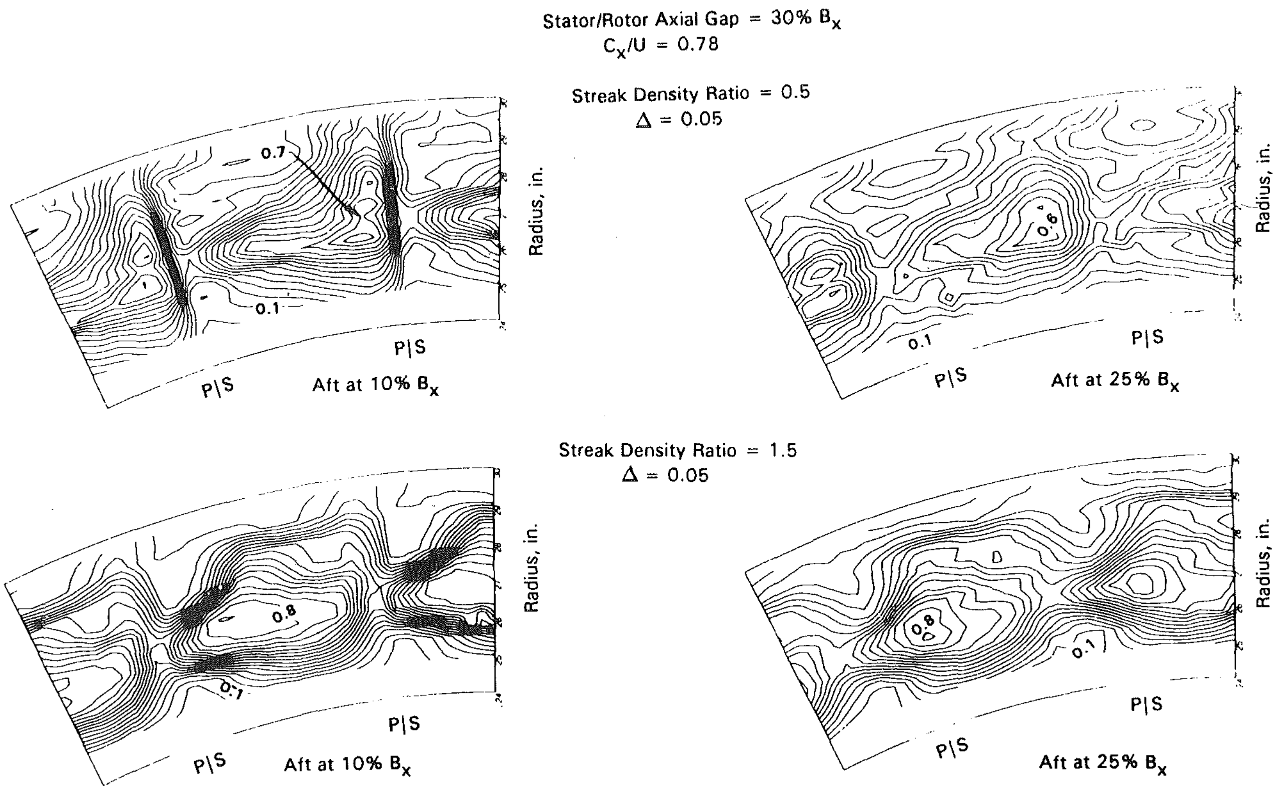

Fig. 11 Trace gas concentration aft of the rotor; effect of streak density ratio

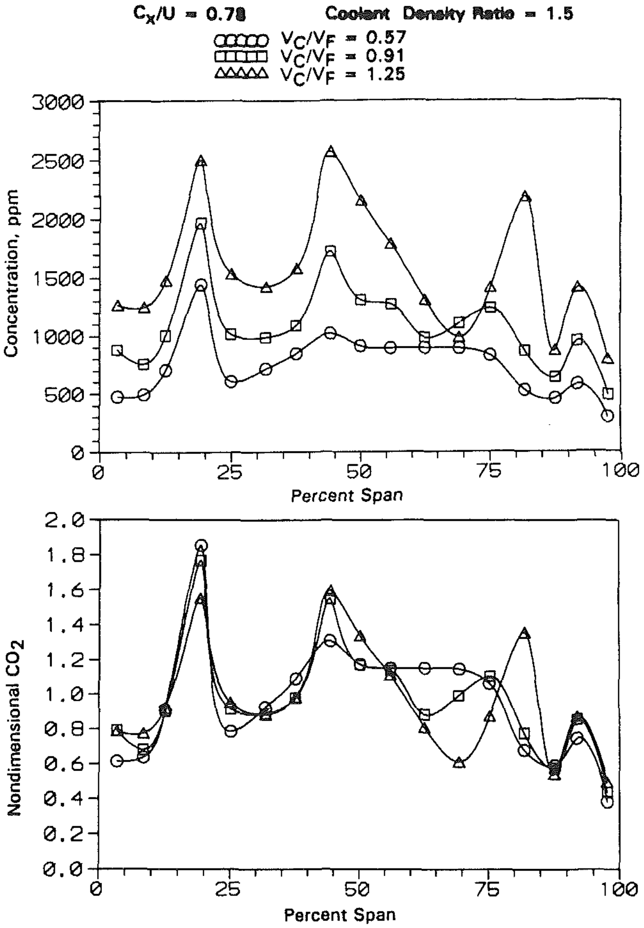

Fig. 12 Rotor leading edge plane concentration profile; effect of coolant velocity ratio

Comparing the cold streak data in Figs. 9 and 11, the maximum concentration on the rotor suction surface near the trailing edge (≈0.3) was much lower than the maximum concentration in the flow aft of the rotor (≈0.8). This large difference suggests that while the cold streak was accumulating on the rotor suction surface, it was being pinched toward midspan such that the highest concentration fluid was not on the surface, but rather somewhat off the surface. Thus, cool, high-density streaks only have a relatively weak tendency to accumulate on the suction surface for two reasons: (1) Suction surface accumulation is generally less than pressure surface accumulation (see Fig. 4), and (2) the hub and tip secondary flows toward midspan tend to retard the accumulation by driving the streak off the suction surface. It is likely that suction surface accumulation of cold streaks would be enhanced by increasing the rotor span (aspect ratio). No such secondary flow mechanism exists on the pressure surface to reduce the accumulation of hot streaks. Hence, the maximum hot streak concentration on the pressure surface (≈0.9) is only slightly greater than the maximum concentration in the flow aft of the rotor (≈0.7).

Stator Coolant Measurements. The discussion of the results of the streak testing gives insight as to the characteristics of the accumulation process for combustor-generated hot and cold streaks. A series of stator coolant tests was also conducted to show the nature of the accumulation process for the cooling air that was discharged from the trailing edge of the upstream stator.

Spanwise trace gas profiles for three stator coolant-to-free-stream velocity ratios and a density ratio of 1.5 are shown in Fig. 12. These profiles were measured with the rake at the rotor leading edge plane. What was immediately apparent was that the spanwise distributions were very nonuniform even though at each velocity ratio, there was the same flow through each of the eleven slots on both stators. There was also a degree of similarity between the distributions at the three velocity

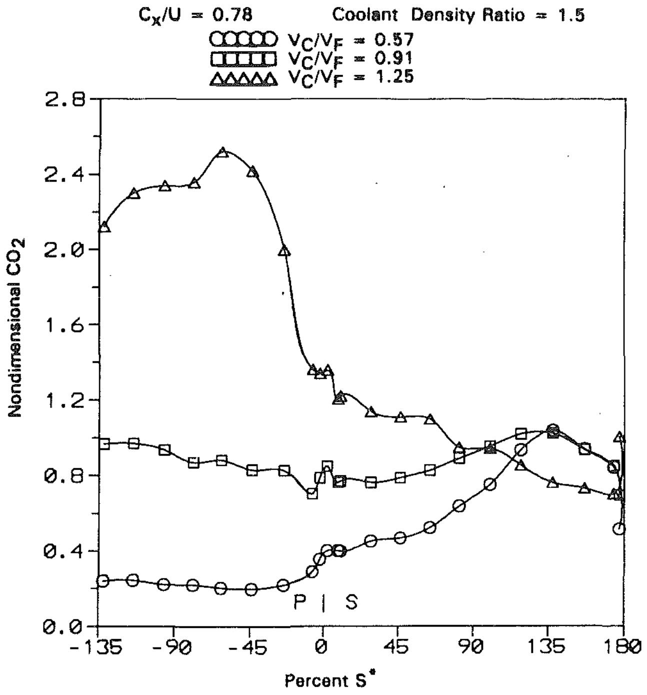

Fig. 13 Midspan trace gas concentration for stator coolant; effect of coolant velocity ratio

ratios. After conducting many diagnostic tests to isolate the cause of the nonuniformity, it was concluded that it was real and that the most probable explanation was that it was the result of an interaction between the coolant flow and the three-dimensional secondary flow produced by the stator. Because of this nonuniformity, the radially averaged concentration in the rotor leading edge rake profile (rather than the peak value) was used to normalize the measurements on the airfoil in the stator coolant tests. The normalized concentration profiles are shown in the bottom of Fig. 12.

The stator coolant data acquired at midspan are shown in Fig. 13. (Note that the ordinate scale has been doubled relative to that of the streak data in Fig. 3.) At the highest velocity ratio, the coolant was being driven toward the rotor pressure surface and the accumulation was strongest. Note that the nondimensionalized concentrations are as high as 2.5, which is partly the result of using the average and not the maximum concentration measured at the leading edge plane of the rotor. When the velocity ratio was decreased, the coolant was driven toward the rotor suction surface and the accumulation on the pressure surface decreased. As can also be seen in Fig. 13, the high coolant velocity ratio flow accumulates on the pressure surface so strongly that the concentration was well in excess of the average inlet concentration measured with the leading edge rake (≈2.5 times). However, accumulation on the suction surface was strongest with the lowest coolant velocity but it did not exceed the averaged inlet concentration.

The high coolant velocity ratios were used to establish a trend in accumulation with velocity ratio. If a turbine designer had no limit to the total pressure of the coolant being discharged from a stator trailing edge, he could use accumulation to cool the rotor pressure surface by operation at a high coolant velocity ratio. In an actual turbine, however, the stator coolant supply pressure exceeds the free-stream total pressure by the relatively small burner liner pressure drop. In addition, there is usually a large total pressure drop in the stator's internal cooling passages. For these reasons, and because of its higher density, the stator trailing edge coolant velocity in an actual turbine is usually well below the free-stream velocity ($V_c/V_f \approx 0.3$–0.6). As seen in Fig. 13, for this range of velocity ratio, stator trailing edge coolant won't reach the rotor pressure surface. Therefore, it will be hotter than it would have been if the stator wakes were completely mixed out and accumulation did not occur.

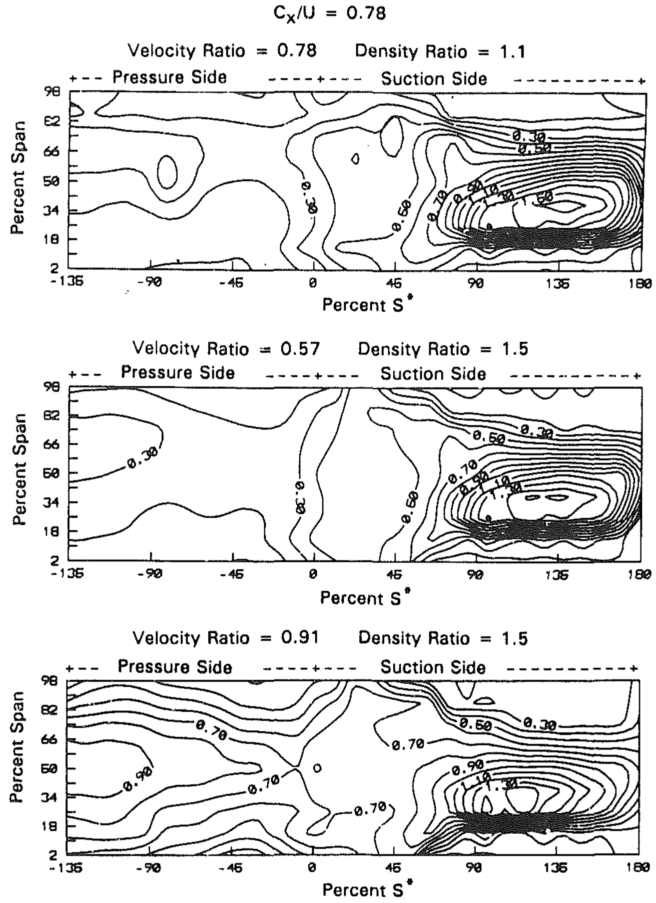

Fig. 14 Full-span trace gas concentration for stator coolant

Full-span data are illustrated in Fig. 14. Data are shown for one coolant-to-free-stream velocity ratio at a density ratio of 1.1, and for two coolant-to-free-stream velocity ratios at a density ratio of 1.5. The results for all three cases have the same general features. There was a region of strong accumulation (≈1.5) on the suction surface near 35 percent span and 135 percent of S^*. For the high velocity ratio and the 1.5 density ratio, the pressure surface concentrations were well above those of the other two cases.

For all three cases there was a very low concentration region on the suction surface near the tip and from about 90 percent of S^* to the trailing edge. Since the coolant flow was accumulating preferentially on the suction surface, the trace gas concentration in the the flow leaking from the pressure surface over the rotor tip was relatively low (≈0.2). The leakage of this low-concentration fluid over the rotor tip was the likely reason for the low concentration region on the suction surface near the tip.

There was no rapid drop in suction surface accumulation near the trailing edge as there was with the streaks (compare Figs. 4 and 14). The reason for this behavior can be attributed to the stator coolant fluid being injected from hub to tip and not just at midspan. Therefore, the rotor hub and tip secondary flows no longer have low-concentration endwall fluid to bring to the midspan region as they did for the streak tests.

Since coolant was being injected at equally spaced locations from the hub to the tip of the stator, significant accumulation of the coolant should occur on the rotor hub endwall. The results of rotor hub endwall measurements for coolant velocity

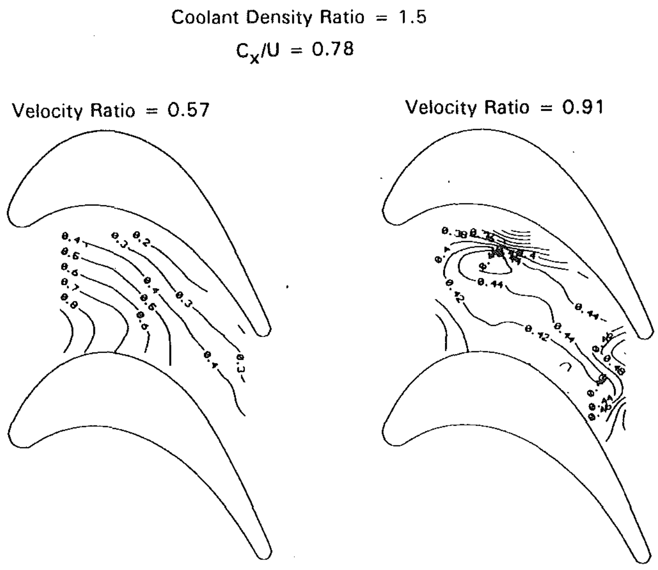

Fig. 15 Hub endwall trace gas concentration profile, stator coolant

ratios, $V_c/V_f = 0.57$ and 0.91, are shown in Fig. 15. The trends observed on the rotor endwall are similar to those shown on the rotor airfoil (Fig. 14). For $V_c/V_f = 0.57$, accumulation occurs closer to the suction surface. For $V_c/V_f = 0.91$, the concentration profile is more uniform throughout the entire endwall region.

Conclusions

This program has provided a fundamental understanding of the effects of hot and cold streak accumulation and phantom cooling on turbine airfoil adiabatic recovery temperature. A major conclusion that can be derived from the results of this program is that rectification of hot and cold streams of fluid that enter a turbine rotor passage can produce a large difference in the adiabatic recovery temperature between the pressure and suction surfaces of the rotor airfoil. Also, stator coolant flow accumulated on the rotor suction surface where hot streak accumulation was weakest. Under typical turbine operating conditions, coolant flow will not reach the pressure surface where hot streak accumulation is the strongest. Other conclusions that can be drawn include:

1 In general, the rectification process causes hot streaks to accumulate on the pressure surface. Cold streaks accumulate on the suction surface.

2 The fluid from the hot streak accumulated on the pressure surface so strongly that the time-averaged concentration was as much as 35 percent higher than the maximum time-averaged concentration measured at the leading edge plane of the rotor.

3 Accumulation on the suction surface was strongest with the cold streak but the concentration did not exceed the maximum concentration measured at the inlet to the rotor.

4 Accumulation of stator coolant flow is a strong function of coolant velocity. When the coolant velocity exceeded the free-stream velocity, accumulation occurred on the pressure surface. Accumulation occurred on the suction surface when the coolant velocity was less than the free-stream velocity.

5 Streaks can migrate to both the hub and tip regions of the rotor when they are introduced at different spanwise locations. Thus, they have the potential to impact the adiabatic temperature recovery on the rotor hub platform and on the rotor tip and outer air seal.

6 Hot streaks introduced at 25 percent span migrated to the hub endwall where the concentration approached the maximum concentration measured at the leading edge plane of the rotor.

7 Streaks with low density ratios are less likely to have an effect on the hub and tip endwalls when they are directed on stator, as opposed to between stators.

8 Hub and tip secondary flows on the rotor tend to reduce the accumulation of high density ratio (cold) streaks by preventing them from reaching the suction surface.

Acknowledgments

The authors owe a debt of gratitude to a number of our colleagues for their helpful and patient support in carrying out the work reported here. We are indebted to Mike Quinn for his skill in running the LSRR and acquiring the data; to Bill Tierney for the speed with which he often had to breathe life back into our data system; to Jerry Jaminet for his patience while making many modifications to the data system software; and to Sue Orr for her untiring effort in producing the graphics utilized throughout this paper.

The majority of the results reported here were obtained in an experimental program carried out with Air Force funding (Contract No. F33615-88-C-2829) under the direction of Mr. Michael J. Kinsella, Wright Laboratory (WL/POTC). The results that show the effect of axial gap and the traverse results obtained aft of the rotor were obtained in an experimental program funded by NASA Marshall Space Flight Center, (Contract No. NAS8-36801) under the direction of Ms. Lisa W. Griffin.

References

Butler, T. P., Sharma, O. P., Joslyn, H. D., and Dring, R. P., 1986, "Redistribution of an Inlet Temperature Distortion in an Axial Flow Turbine Stage," AIAA Paper No. AIAA-86-1468.

Dring, R. P., Blair, M. F., and Joslyn, H. D., 1980, "Experimental Investigation of Film Cooling on a Turbine Rotor Blade," ASME *Journal of Engineering for Power*, Vol. 102, pp. 81–87.

Eckert, E. R. G., and Goldstein, R. J., 1976, "Measurement Methods in Heat Transfer," 2nd ed., Hemisphere Publishing Corp., Washington, DC.

Joslyn, H. D., and Dring, R. P., 1988, "A Trace Gas Technique to Study Mixing in a Turbine Stage," ASME JOURNAL OF TURBOMACHINERY, Vol. 110, No. 1, pp. 38–43.

Joslyn, H. D., and Dring, R. P., 1989, "Three-Dimensional Flow and Temperature Profile Attenuation in an Axial Turbine." Final Report, AFSOR, Contract F49620-86-C-0020.

Joslyn, H. D., and Dring, R. P., 1992a, "Three-Dimensional Flow in an Axial Turbine: Part I—Aerodynamic Mechanisms," ASME JOURNAL OF TURBOMACHINERY, Vol. 114, pp. 61–70.

Joslyn, H. D., and Dring, R. P., 1992b, "Three-Dimensional Flow in an Axial Turbine: Part II—Profile Attenuation," ASME JOURNAL OF TURBOMACHINERY, Vol. 114, pp. 71–78.

Pederson, D. R., Eckert, E. R. G., and Goldstein, R. J., 1977, "Film Cooling With Large Density Differences Between the Mainstream and the Secondary Fluid Measured by the Heat-Mass Transfer Analogy," ASME *Journal of Heat Transfer*, Vol. 99, pp. 620–627.

Reynolds, A. J., 1976, "The Variation of Turbulent Prandtl and Schmidt Numbers in Wakes and Jets," *International Journal of Heat and Mass Transfer*, Vol. 19, pp. 757–764.

Hot Streaks and Phantom Cooling in a Turbine Rotor Passage: Part 2—Combined Effects and Analytical Modeling

R. J. Roback

R. P. Dring

United Technologies Research Center,
East Hartford, CT 06108

This paper presents experimental documentation and analytical correlations demonstrating the effects of hot streak accumulation and phantom cooling on turbine rotor airfoil surface temperature. In particular, results are shown that quantify the impact of (1) a nonuniform temperature profile at the entrance of a turbine due to combustor-generated hot and cold streaks, and (2) cooling air discharged from the trailing edge of the upstream stator. In Part 1 of this paper, experimental results were shown for a range of controlling variables to identify where streak accumulation and phantom cooling were most likely to be strongest. These variables include streak-to-free-stream density ratio, streak injection location, and coolant-to-free-stream density and velocity ratios. In Part 2 of this paper, experimental results will be shown for the combined effects of hot streak and stator coolant on the adiabatic recovery temperature on the rotor. An analytical model is also developed to correlate the experimental results documented in Parts 1 and 2 of the paper.

Introduction

An efficient turbine airfoil cooling scheme necessitates a delicate balance of aerodynamics and thermodynamics. External aerodynamics dictates the character of the inviscid velocity distribution on the airfoil surface. The surface boundary layer governs the heat load that the airfoil cooling scheme must absorb. The heat load is also influenced by at least two additional factors: (1) a nonuniform temperature profile at the entrance of a turbine due to combustor-generated hot and cold streaks, and (2) cooling air discharged from the trailing edge of an upstream airfoil.

Hot and cold streaks are rectified as they pass through the rotor of a turbine and accumulate at various locations on the rotor airfoil and endwall surfaces. As a result, airfoils rarely burn out "on average" but burn out locally. Therefore, the designer's goal is to devise an airfoil cooling scheme, which produces not only the desired average temperature but also an acceptably uniform temperature, i.e., controlling the temperature gradient.

Since the adiabatic recovery temperature of the flow is the driving potential for the heat load, it would be of value to the designer to be able to predict the impact of the migration and accumulation of hot and cold streaks and coolant flow from an upstream row on the adiabatic temperature recovery. In Part 1 of this paper (Roback and Dring, 1993), experimental results were documented for a variety of controlling parameters to identify where the separate effects of streak accumulation and coolant flow were strongest. In Part 2 of this paper, experimental results are presented for the combined effects of hot streak and stator coolant on the simulated adiabatic recovery temperature on the rotor.

The experimental data presented in this paper provide considerable insight into the various mechanisms that drove the accumulation process. These data are of value in the form presented for the assessment of viscous and inviscid computational simulations of the flow. However, to be of direct value to the turbine design community, they must be generalized into some analytical framework that can be used to estimate the impact of these mechanisms on the heat load of specific turbine rotor airfoils. A simple physical argument was developed into a correlating parameter, which gives good correlation for both the hot and cold streak accumulation as well as for the accumulation of stator coolant.

Description of the Experiment

The facility, equipment, and the trace gas technique that was used in the experimental portion of this study were described in detail in Part 1 of this paper. The description will not be repeated here.

Test Conditions

A series of tests were conducted to determine the combined effects of a hot streak passing through the rotor while coolant was being injected from the trailing edge of the upstream stator.

Contributed by the International Gas Turbine Institute and presented at the 37th International Gas Turbine and Aeroengine Congress and Exposition, Cologne, Germany, June 1-4, 1992. Manuscript received by the International Gas Turbine Institute February 4, 1992. Paper No. 92-GT-76. Associate Technical Editor: L. S. Langston.

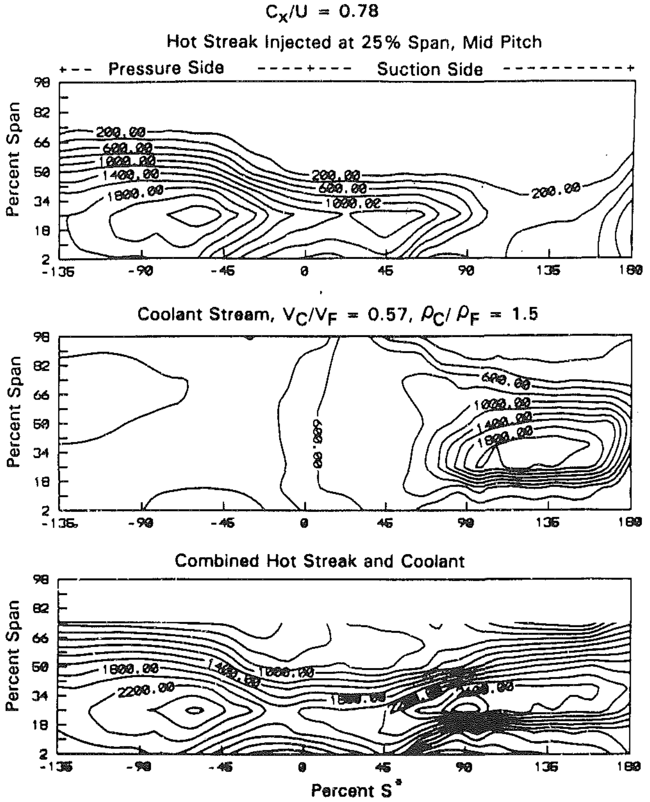

Fig. 1 Full-span trace gas concentration for hot streak injected at 25 percent span and midpitch

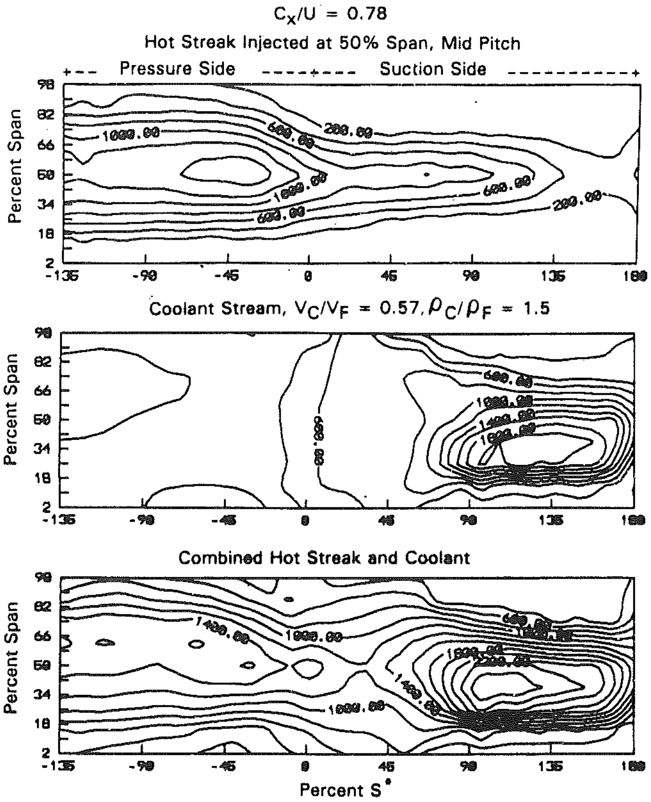

Fig. 2 Full-span trace gas concentration for hot streak injected at 50 percent span and midpitch

The question to be answered was whether the various accumulation effects observed independently for the hot streak and stator coolant in Part 1 of this paper were additive. For these tests, a coolant-to-free-stream density ratio of 1.5 and a coolant-to-free-stream velocity ratio of 0.57 were chosen. These ratios result in an average trace gas concentration entering the rotor, which is about the same as that of the hot streak. If there had been a large difference between the two, the larger one would have dominated the experiment and obscured the effects of the smaller one.

Experimental Results

Data Presentation Format. The trace gas distributions measured on the airfoil are presented as contour maps of equal concentration. However, the shape of the rotor airfoil surface, unwrapped and flattened on a plane, is complex. To alleviate the complexities involved with generating contours in this form, a special coordinate system was developed to project the complex airfoil surface shape onto rectangles with the same span/arc-length ratio. This coordinate system uniquely identifies a position, S^*, on the rotor airfoil surface (1) radially in terms of percent span, and (2) chordwise in terms of percent distance along the respective (pressure or suction) surface. It was decided to nondimensionalize all lengths by the span, thus not only making grid increments equal for both the pressure and suction portions of the horizontal and vertical scales but also making the horizontal scale equal to the vertical scale. The rationale for this data presentation format is discussed more completely in Part 1 of this paper.

Combined Full-Span Measurements. Four experiments where the hot streak was introduced at 25, 50, and 75 percent span at midpitch and at 50 percent span at the "on-stator" location were repeated with coolant flow discharging from the trailing edge of the first stator. Care was taken to achieve essentially the same flow conditions as were used in the separate hot streak and stator coolant tests. The results for these combined tests are shown in the bottom panel of Figs. 1–4. The results of each separate hot streak test are repeated in the top panel of the figures while the results of the separate coolant test are repeated in the center panel of each figure.

For ease of interpretation and because the data for the separate tests were normalized by two different reference concentrations, the combined data were presented in terms of measured surface concentration, ppm above ambient (as opposed to normalized concentration). In this way the separate results could be compared with the combined result by simply adding them. For all four cases it can be seen that both qual-

Nomenclature

AR = aspect ratio
Bx = airfoil axial chord
C = absolute flow speed
Cx/U = flow coefficient
P = pressure
Q = dynamic pressure
S^* = scaled airfoil surface distance

U = wheel speed at midspan
V = fluid velocity
α = absolute flow angle (from tangential)
β = relative flow angle (from tangential)
ϕ = flow coefficient = Cx/U
ρ = density

Subscripts

C or c = coolant, cold
F or f = free-stream
J or j = jet
rel = relative frame of reference
tot or t = total
x = axial distance

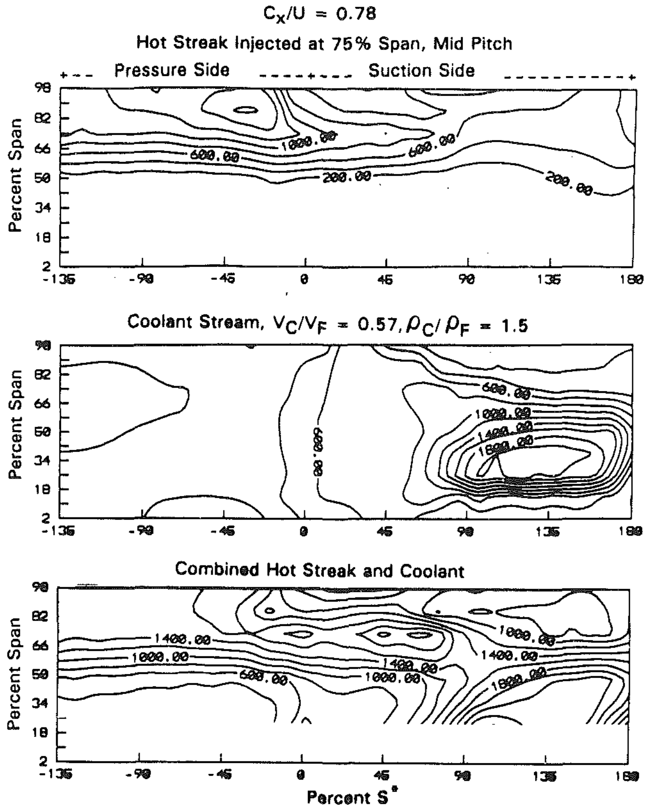

$C_x/U = 0.78$

Hot Streak Injected at 75% Span, Mid Pitch

Coolant Stream, $V_C/V_F = 0.57, \rho_C/\rho_F = 1.5$

Combined Hot Streak and Coolant

Fig. 3 Full-span trace gas concentration for hot streak injected at 75 percent span and midpitch

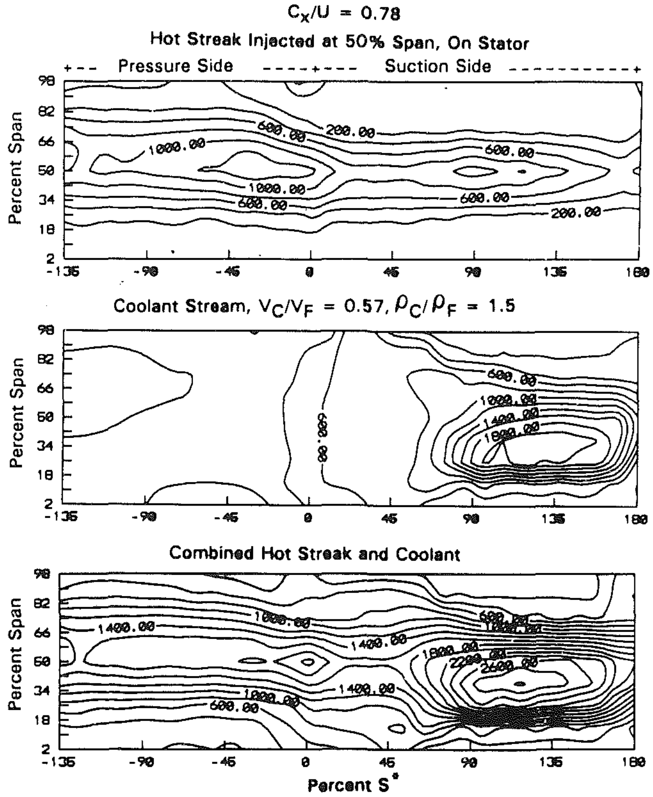

$C_x/U = 0.78$

Hot Streak Injected at 50% Span, On Stator

Coolant Stream, $V_C/V_F = 0.57, \rho_C/\rho_F = 1.5$

Combined Hot Streak and Coolant

Fig. 4 Full-span trace gas concentration for hot streak injected at 50 percent span and on-stator

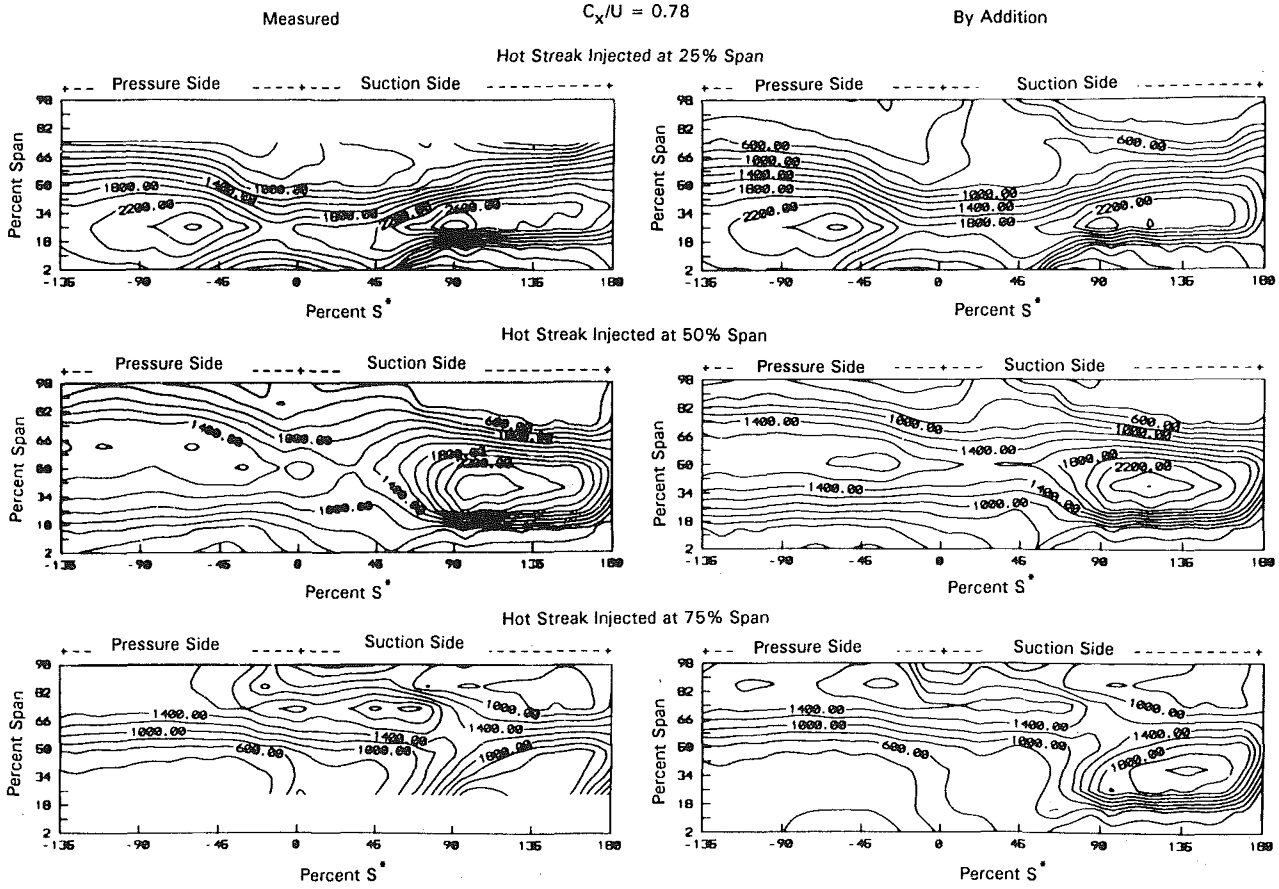

Measured

$C_x/U = 0.78$

By Addition

Hot Streak Injected at 25% Span

Hot Streak Injected at 50% Span

Hot Streak Injected at 75% Span

Fig. 5 Additive effect of hot streak and stator coolant

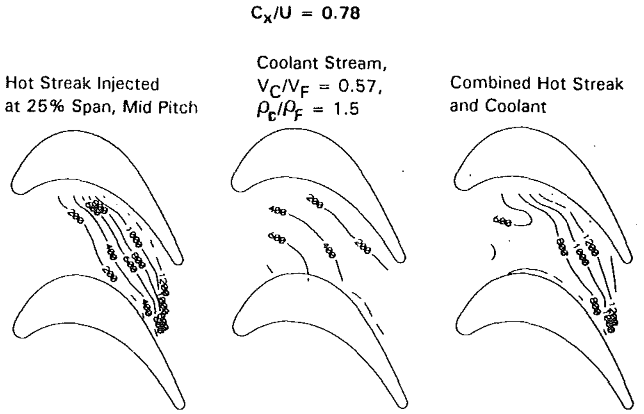

Fig. 6 Hub endwall trace gas concentration profile; combined hot streak/stator coolant

itatively and quantitatively, the combined result was very closely approximated by the sum of the two separate results.

To demonstrate further this additivity of results, a comparison was developed in Fig. 5 for the cases with the streak located at 25, 50, and 75 percent span and at midpitch. The distributions in the left-hand column are the measured combined results. Those in the right-hand column were determined by adding the separate measurements for the streaks and the stator coolant. Clearly there is a strong correspondence between the measured results with the combined flows and those obtained by adding the results of the two flows operating separately.

An important conclusion can be drawn by comparing the results shown in the upper and center panels of Figs. 1-4. Coolant flow from the stator trailing edge will not neutralize hot streak accumulation on the rotor surfaces. Coolant flow under typical turbine operating conditions will not reach the pressure surface where hot streak accumulation is strongest. Under the same conditions, hot streaks will not reach the suction surface where coolant accumulation is strongest. In addition, the combined results indicate that when there is both a hot streak and stator coolant, the difference between the adiabatic recovery temperatures on the suction and pressure surfaces will be the sum of those that occur when the two flows are operating separately.

This additivity effect for combined flows is also observed on the rotor hub endwall shown in Fig. 6. The measured results obtained on the endwall for the combined streak/coolant condition are compared with the added results for separate streak and coolant flows. As shown, the added result at the right side of the figure very closely approximates the result of the combined experiment shown to the left.

Analytical Modeling

The streak and stator coolant accumulation data that have been presented and discussed in both parts of this paper have provided considerable insight into the various mechanisms that drive the accumulation process. These data are of value in the form presented for the assessment of viscous and inviscid computational simulations of the flow. However, to be of direct value to the turbine design community, they must be generalized into some analytical framework that can be used to estimate the impact of these mechanisms on the heat load of specific turbine rotor airfoils. Such an analytical model is presented in the following paragraphs. As will be seen, a simple physical argument leads to a parameter that gives a surprisingly good correlation for both hot and cold streak accumulation as well as for the accumulation of stator coolant.

The nature of the flow incident on the rotor was modeled by assuming that it is composed of two streams of fluid with

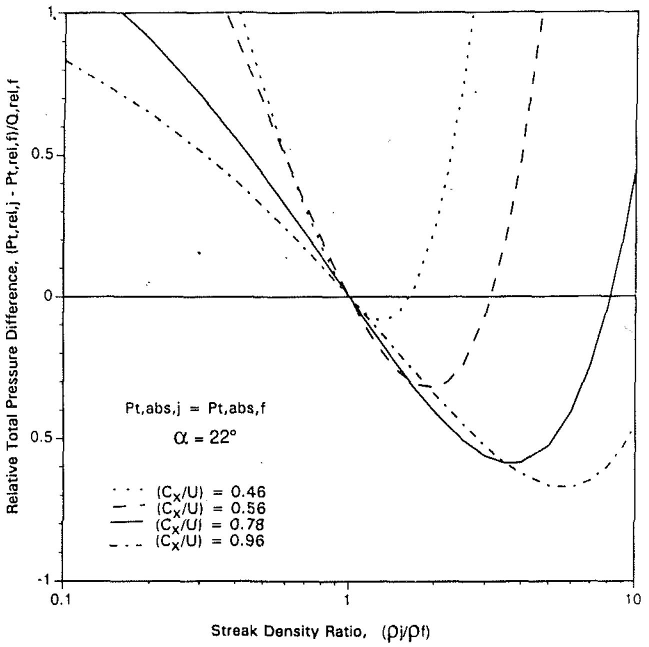

Fig. 7 Jet-to-free-stream relative total pressure difference; effect of streak density ratio

different properties: a "jet" of hot or cold fluid and the free-stream fluid around it. The jet can correspond to either a hot or cold streak, or to stator coolant. It was assumed that in the axial gap between the stator and the rotor, both the jet and the free-stream fluid were at the same static pressure and that they had the same flow direction in the absolute frame of reference (Munk and Prim, 1947).

Since the cause of most secondary flows is a gradient in total pressure, the difference between the jet and the free-stream relative total pressures might be indicative of the strength of the flow that produces jet accumulation. Therefore, the following expression was derived for the difference between the relative total pressures of the jet and the free stream, normalized by the relative dynamic pressure of the free stream:

$$\left(\frac{P_{t,\mathrm{rel},j}-P_{t,\mathrm{rel},f}}{Q_{,\mathrm{rel},f}}\right) = \left(\frac{\rho_j}{\rho_f}\right)\left(\frac{1-2\Phi_f\cot\alpha\left(\frac{C_j}{C_f}\right)+\Phi_f^2(1+\cot^2\alpha)\left(\frac{C_j^2}{C_f^2}\right)}{1-2\Phi_f\cot\alpha+\Phi_f^2(1+\cot^2\alpha)}\right)-1 \quad (1)$$

Since radial variations were not accounted for in the analysis, correlations with measurements were limited to the data taken at midspan.

This expression was applied to both hot and cold streak accumulation and to the accumulation of stator coolant on the rotor airfoil at midspan. For the case of hot and cold streaks it was assumed that the absolute total pressure of the streak was equal to that of the free stream. This assumption is reasonable because the source of the hot or cold streaks is the combustor where the Mach number is typically very low. Under this assumption, Eq. (1) was used to calculate the difference between the streak and free-stream relative total pressures as a function of jet-to-free-stream density ratio and flow coefficient. For the calculations, a stator exit flow angle, $\alpha = 22$ deg (from tangential) was used, which is the design angle for the turbine model used in the experiments. The results of the relative total pressure difference calculations for streaks are shown in Fig. 7. A wide range of density ratios (0.1 to 10.) was used to generate the results shown in Fig. 7. However,

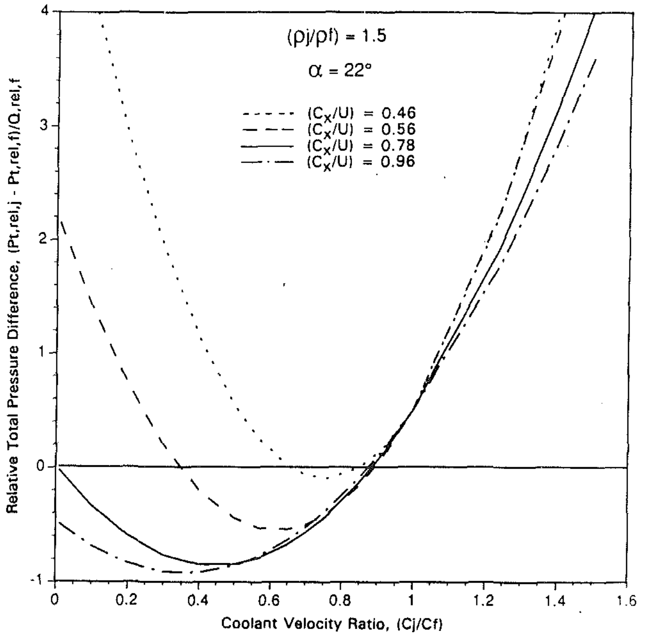

Fig. 8 Jet-to-free-stream relative total pressure difference; effect of coolant velocity ratio

values of density ratio used in the experiments ranged from only 0.5 to 1.5, which is felt to be typical of the density ratio range one might expect from combustor-generated hot streaks and from combustor dilution jets in a gas turbine.

Relative total pressure differences were also calculated for the stator coolant case. Results of these calculations are shown in Fig. 8 for the same four values of flow coefficient and a range of coolant-to-free-stream velocity ratios. For these calculations, the jet-to-free-stream density ratio was assumed to be 1.5. This value was used in the experiments; however, it is somewhat low compared to typical design values of 1.7 to 2.0. The jet-to-free-stream velocity ratios used in most of the experiments were 0.57, 0.91, and 1.25. Typical design values are in the range from 0.4 to 0.7. The highest value in the experiment was chosen to get sufficient range to clearly define the trends in the measured results.

Before discussing several general observations that can be made from the results shown in Figs. 7 and 8, it should be noted that a positive jet-to-free-stream relative total pressure difference will tend to cause the jet to accumulate on the rotor pressure surface while a negative difference will tend to cause it to accumulate on the suction surface.

The first observation that can be made from the results shown in Figs. 7 and 8 is that there is no limit to accumulation on the pressure surface, but accumulation is limited on the suction surface. For very large values of flow coefficient, the minimum pressure difference approaches a value of − 1. Thus, while there is no limit to the intensity with which a jet can impinge on the pressure surface, there is a limit to the intensity with which it can impinge on the suction surface.

A second observation from Fig. 7 is that for a given flow coefficient, hot streaks (density ratio < 1.0) will accumulate on the pressure surface. Cold streaks with density ratios not too far above 1.0. will accumulate on the suction surface. These trends were observed experimentally in Part 1 of this paper.

The results shown in Fig. 8 are consistent with the stator coolant results obtained experimentally as shown in Part 1 of this paper. At a velocity ratio of 0.57, the relative total pressure difference is negative and accumulation occurs on the suction surface. At the velocity ratio of 0.91, the relative total pressure difference is close to zero and accumulation should be weak on both the suction and pressure surfaces. For the highest velocity ratio considered in the experiment (1.25), strong accumulation occurs on the pressure surface and the relative total pressure difference is large.

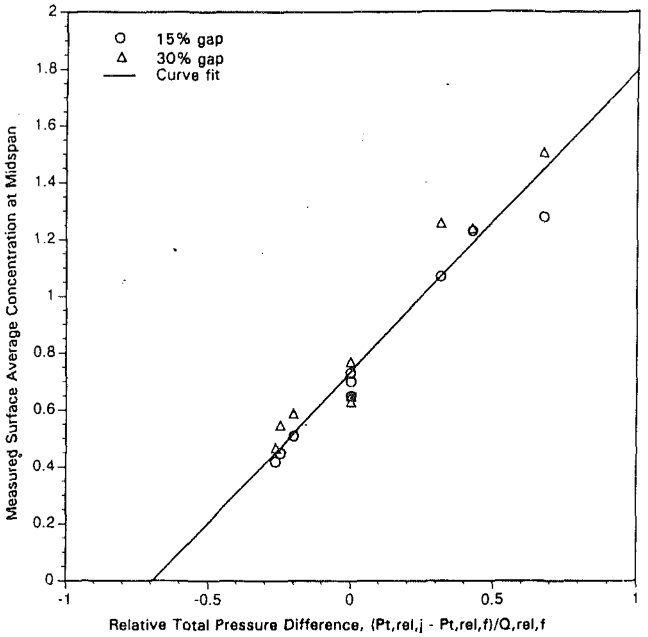

Fig. 9 Correlation for hot and cold streaks on the rotor pressure surface

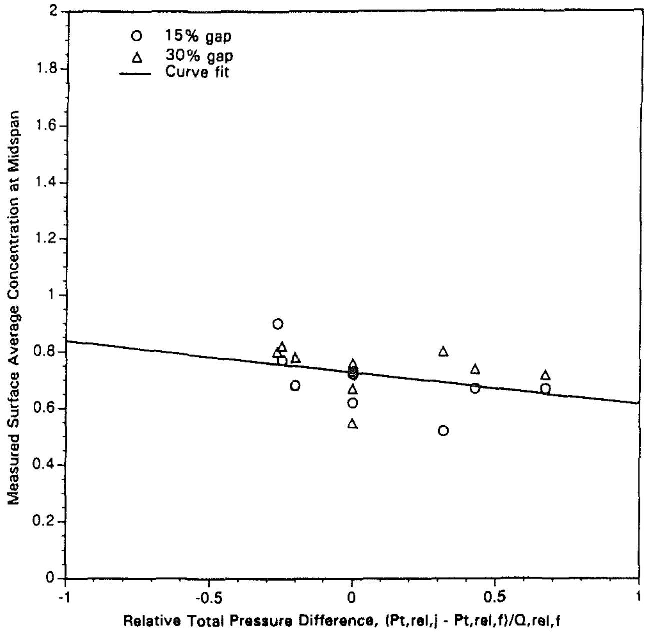

Fig. 10 Correlation for hot and cold streaks on the rotor suction surface

The consistency between the experimental results and the analytical model suggested that a correlation of accumulation with relative total pressure difference may be possible. The experimental results were compared to the analytical model by plotting the normalized midspan surface-averaged trace gas concentration against the dimensionless relative total pressure difference. These comparisons include data taken: (1) at axial gaps of 15 and 30 percent *Bx*, (2) for three streak-to-free-stream density ratios (0.5, 1.0, and 1.5), (3) for both of the jet-to-free-stream density ratios used in the stator coolant tests (1.1 and 1.5), and (4) for several rotor incidences. In each case a least-squares fit was included with the data.

The results for hot and cold streaks are shown in Figs. 9 and 10 for the pressure and suction surfaces. The results for

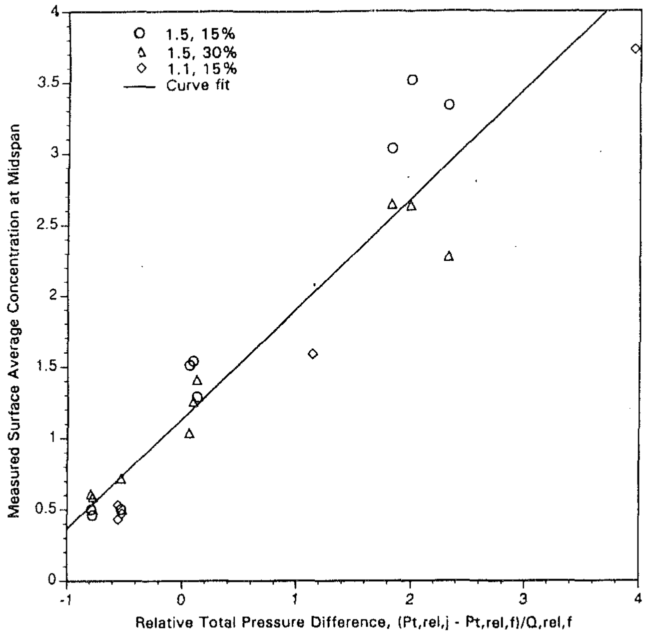

Fig. 11 Correlation for stator coolant on the rotor pressure surface

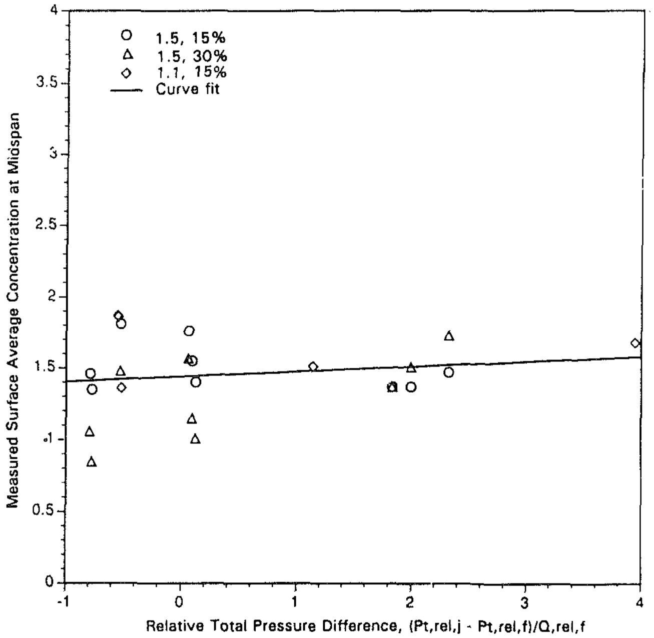

Fig. 12 Correlation for stator coolant on the rotor suction surface

the stator coolant tests are shown in Figs. 11 and 12. The hot and cold streak data had been normalized with the maximum concentration measured on the rake mounted on the rotor hub at the airfoil leading edge plane. The stator coolant data had been normalized with the span average of the rotor leading edge rake measurements.

The pressure surface data for the hot and cold streaks (Fig. 9) showed a very strong correlation with the results of Eq. (1), while the suction surface data (Fig. 10) showed little or no correlation and greater scatter. The relative degree of correlation is consistent with the relative strengths of the pressure and suction surface accumulation processes. Part of the variation in the suction surface data was probably due to the strong secondary flows on this relatively low aspect ratio airfoil ($AR \approx 0.95$). With a higher aspect ratio there might be less variation and stronger accumulation. However, it is unlikely that a higher rotor aspect ratio would change the weak dependence of the accumulation on the jet-to-free-stream relative total pressure difference.

A neutral condition exists when the difference between the streak and free stream relative total pressures is equal to zero. Therefore, no accumulation should occur and the surface average should be unity. However, as shown in Figs. 9 and 10, the correlated surface averages on both surfaces are 0.73. Molecular and turbulent mixing bring low concentration flow into the midspan region while radial transport is moving higher concentration material out. The net result is concentrations less than one.

Results similar to those obtained for streaks were obtained for the stator coolant data. The pressure surface data (Fig. 11) showed a very strong correlation, while the suction surface data (Fig. 12) showed little or no correlation. When the difference between the jet and free-stream relative total pressures is zero, the correlation gives a surface average on the pressure surface of 1.15 and a value of 1.45 on the suction surface. The high value on the suction surface is probably due to the hub and tip secondary flows, which tend to constrict the coolant flow to the midspan region.

Gas Turbine Applications. The analytical model can be applied to determine the effect of hot and cold streaks on the average heat load on gas turbine airfoils. For example, assume that the average exit temperature of a typical gas turbine combustor is 3000°F. If a defective fuel nozzle caused a stoichiometric streak at 4100°F, then its jet-to-free-stream density ratio would be 0.76. If there was also a 1100°F dilution jet in the combustor that was not mixing out, it would have a jet-to-free-stream density ratio of 2.2. Also assume that these jets were at midspan, the turbine flow coefficient was 0.78, and the stator exit flow angle was 22 deg; i.e., the value for the turbine model used in the experimental program.

From Fig. 7, the jet-to-free-stream relative total pressure differences for the hot and cold jets would be 0.17 and −0.45. The pressure surface correlation in Fig. 9 indicates that these correspond to surface average ratios of 0.91 and 0.25. The correlation also indicates that when the jet and free-stream relative total pressures are equal, the surface average ratio for the jet is 0.73. A measure of accumulation or temperature rise is the ratio of the surface average of the hot or cold jet to the surface average for a neutral jet; i.e., a streak density ratio of one. Therefore, the hot streak ratio is (0.91/0.73) or 1.25 and the cold streak ratio is (0.25/0.73) or 0.34. Thus, for every degree that the hot streak increases the average rotor inlet relative total temperature, it will increase the pressure surface average gas temperature by 1.25°F. Similarly, for every degree that the cold streak reduces the rotor inlet relative total temperature, it will reduce the pressure surface average gas temperature by 0.34°F.

If the hot streak made up 10 percent of the mass flow, it would represent an increase in the absolute total temperature above the 3000°F average of $(4100-3000)\times 0.10$, or 110°F. Similarly, if the cold streak made up 5.8 percent of the mass flow, it would represent a decrease in the absolute total temperature of $(3000-1100)\times 0.058$, or 110°F below the average. At these mass flows the streaks offset each other for an average inlet temperature of 3000°F.

Assume that the relative total temperature would be affected by the streaks in the same way as they affected the absolute total temperature. Using the results of the correlation above, the +110°F contribution to the total temperature due to the hot streak will increase the average rotor pressure surface gas temperature by (110×1.25) or 138°F. Similarly, the cold streak will decrease the average rotor pressure surface gas temperature by 37°F. The hot and cold streaks together will cause an increase of (138 − 37) or 101°F above the average pressure surface temperature that would have occurred with a uniform inlet temperature (no streaks).

The model can be used in a similar way to determine the impact of stator coolant on the average rotor surface temperature. Assume, for example, that a stator had trailing edge discharge cooling air with a density 1.5 times that of the hot free-stream fluid, and that the velocity of the coolant was half that of the free stream. Also, as above, assume that the turbine flow coefficient was 0.78, and that the stator exit flow angle was 22 deg. From Fig. 8, the jet-to-free-stream relative total pressure difference for the stator coolant jet would be -0.84. Using this value in the pressure surface correlation shown in Fig. 11 gives a surface average ratio of 0.50. When the difference between the jet and free-stream relative total pressures is zero, the correlation gives a surface average ratio of 1.15. Thus, for every degree that the stator trailing edge coolant reduces the average rotor inlet relative total temperature, it will reduce the pressure surface gas temperature by 0.50/1.15 or 0.43°.

For the heat load calculation, also assume that (1) the gas path flow entering the turbine was 80 percent of the gas generator flow and that its temperature was 3200°F, (2) 10 percent of the gas generator flow was used for first stator cooling with 2 percent being discharged from the stator trailing edge, and (3) the cooling air entered the stator at 1100°F. These assumptions lead to an average stator exit gas temperature of 2967°F, which corresponds to a dilution of 233°F with 47°F due to the stator trailing edge coolant. These dilutions in absolute total temperature correspond roughly to the dilution in relative total temperature. While the average dilution due to the stator trailing edge cooling is 47°F, this dilution will reduce the pressure surface gas temperature by only (0.43×47), or 20°F. Thus, the average pressure surface gas temperature would be 27°F higher than would be expected in the absence of accumulation. The remaining 8 percent of stator cooling air would cause this difference to be larger. If all 10 percent of the stator cooling air had been discharged from the stator trailing edge, the average pressure surface gas temperature would have been 135°F higher than would be expected in the absence of accumulation.

From the suction surface correlations presented in Figs. 10 and 12 it can be seen that the suction surface average ratios are not very sensitive to the relative total pressure differences. Therefore, for both the hot and cold streak and the stator coolant examples cited above, the impact on the average suction surface temperature would be small.

Liquid Rocket Turbopump-Drive Turbine Applications. The large density differences in the gases flowing through the drive turbine in a liquid rocket turbopump can cause significant hot and cold streak accumulation and heat loading on the turbine rotor surfaces. The impact of this accumulation on rotor heat transfer can also be estimated by applying the correlations. Assume that the turbopump is driven by the high-pressure combustion products of liquid hydrogen/liquid oxygen with the following mixture of flows entering the turbine: (1) 3 percent makes up a hot streak of stoichiometric combustion products (water) at ≈ 6000 R; (2) 7.2 percent of the flow is a cold streak (hydrogen) at the hydrogen inlet temperature of ≈ 200 R, and (3) the remainder of the flow is a hydrogen-rich mixture (molecular weight = 4.2) at an average temperature of 1900 R. Also, the turbine flow coefficient is assumed to be 0.61 and the stator exit flow angle is 22 deg.

For the conditions described above, the hot and cold streak density ratios are 1.36 and 4.52, respectively. From Fig. 7, the relative total pressure differences corresponding to these density ratios are -0.22 for the hot streak and 0.19 for the cold streak. Note that because of the large differences in molecular weights of the working gases between the gas turbine and rocket turbopump applications, the relative pressure differences for the two applications are very different and are in fact of different signs.

Applying the pressure surface streak correlation (Fig. 9), the hot streak would cause a 278 R increase in the average gas temperature on the pressure surface and the cold streak would cause a 524 R decrease. The net decrease in pressure surface average gas temperature below the 1900 R average gas temperature would be 246 R. This significant decrease in temperature was produced by hot and cold fluid making up only 10.2 percent of the total fluid entering the turbine.

All of the applications cited here were based on the correlations in Figs. 9–12, which give average surface results. However, airfoils seldom burn out on an average basis; they burn out locally. Thus, while these correlations provide a quantitative guide for average accumulation, they do not take into account the extreme variations of the local accumulation. For this effect, one must turn to the in-depth full-span data presented in Part 1 of this paper.

Conclusions

The results presented in this paper have provided insight as to the combined effects of hot streak and stator coolant accumulation on the simulated recovery temperature on the rotor. The main conclusion that can be derived from the discussion of results is that the hot streak and stator coolant do not interact significantly but behave as the sum of the two flows operating separately. The analytical study described in this paper demonstrated that the difference between the relative total pressures of the hot or cold streams and the surrounding free stream is a good correlative parameter for both the hot and cold streak accumulation as well as stator coolant accumulation. Other conclusions that can be drawn include:

1 Coolant flow accumulated on the rotor suction surface where hot streak accumulation was weakest. Under typical turbine operating conditions, coolant flow and hot streak flow accumulated at different places on the airfoil and hence, they can not be used to offset each other.

2 The analytical model of the accumulation process showed that there is no limit to the relative total pressure difference (of a jet and a free stream) on the pressure surface accumulation, but there is a limit on the suction surface.

3 The analytical model gave a strong correlation for the pressure surface accumulation.

4 The correlation for suction surface accumulation was much weaker as one might expect from the lower limit of the relative total pressure difference.

5 The analytical model was applied to estimate the average heat loading on a turbine rotor surface. For a gas turbine example, hot and cold streak accumulation and stator coolant accumulation could account for the rotor pressure surface being as much as 100°F hotter than one would have expected with a uniform inlet temperature. For a rocket turbopump application, hot and cold streak accumulation caused a net reduction in the average rotor pressure surface temperature of 240°F.

Acknowledgments

The authors owe a debt of gratitude to a number of our colleagues for their helpful and patient support in carrying out the work reported here. We are indebted to Mike Quinn for his skill in running the LSRR and acquiring the data; to Bill Tierney for the speed with which he often had to breathe life back into our data system; to Jerry Jaminet for his patience while making many modifications to the data system software; and to Sue Orr for her untiring effort in producing the graphics utilized throughout this paper.

The majority of the results reported here were obtained in an experimental program carried out with Air Force funding (Contract No. F33615-88-C-2829) under the direction of Mr.

Michael J. Kinsella, Wright Laboratory (WL/POTC). The results that show the effect of axial gap and the traverse results obtained aft of the rotor were obtained in an experimental program funded by NASA Marshall Space Flight Center, (Contract No. NAS8-36801) under the direction of Ms. Lisa W. Griffin.

References

Munk, M., and Prim, R. C., 1947, "On the Multiplicity of Steady Gas Flows Having the Same Streamline Pattern," *Proceedings of the National Academy of Sciences*, U. S., Vol. 33.

Roback, R. J., and Dring, R. P., 1993, "Hot Streaks and Phantom Cooling in a Turbine Rotor Passage: Part I—Separate Effects," ASME JOURNAL OF TURBOMACHINERY, Vol. 115, this issue, pp. 657-666.

Calculation of Wake-Induced Unsteady Flow in a Turbine Cascade

N.-H. Cho

X. Liu[1]

W. Rodi

B. Schönung[2]

Institute for Hydromechanics,
University of Karlsruhe,
Karlsruhe, Federal Republic of Germany

Numerical predictions are reported for two-dimensional unsteady flow in a linear turbine cascade, where the unsteadiness is caused by passing wakes generated by the preceding row of blades. In particular, an experiment is simulated in which the passing wakes were generated by cylinders moving on a rotating squirrel cage. Blade-to-blade calculations were carried out by solving the unsteady two dimensional flow equations with an accurate finite-volume procedure, thereby resolving the periodic unsteady motion. The effects of stochastic turbulent fluctuations are simulated with a two-layer turbulence model, in which the standard k-ϵ model is applied in the bulk of the flow and a one-equation model in the near-wall region. This involves also a transition model based on an empirical formula from Abu-Ghannam and Shaw (1980), which was adapted for the unsteady situation by applying it in a Lagrangian way, following fluid parcels in the boundary layer under disturbed and undisturbed free streams on their travel downstream. The calculations are compared with experiments for various wake-passing frequencies. On the whole, the complex unsteady flow behavior is simulated realistically, including the moving forward of transition when the wake-passing frequency increases, but not all details can be reproduced.

1 Introduction

Unsteady wakes passing through cascade channels of turbomachines have a great influence on the flow field and the heat transfer to the blades, especially because they strongly affect the boundary layer transition. In many situations, considerable portions of the blade surface are covered by laminar boundary layers, which are intermittently turbulent when wakes pass over the blade. The optimization of the blade design requires reliable models for the prediction of these unsteady effects. Most blade designs in practice today are based on steady flow analyses and cannot account properly for the important unsteady effects. In general, the disturbances introduced by the passing wakes cannot be considered as free-stream turbulence since the wake frequency is important and so is the different decay behavior of periodic and turbulent fluctuations. Rather, transition and overall boundary layer development depend on the disturbances by the discrete wakes and their interaction with the boundary layer. A realistic simulation of these processes requires an unsteady calculation.

A sizable body of literature exists on unsteady calculations of inviscid rotor–stator interaction phenomena, but numerical simulations of unsteady cascade flow including viscous effects are relatively rare. Scott and Hankey (1986) solved the unsteady Navier–Stokes equations in a compressor rotor channel, using the Baldwin–Lomax turbulence model in the near-wall shear layer, but otherwise the laminar equations. The unsteady flow was generated through the inflow boundary conditions. Abhari et al. (1992) calculated the two-dimensional unsteady flow and heat transfer in a turbine rotor cascade with preceding nozzle guide vanes with a coupled viscous/inviscid approach. The shear layers near the blade surface and in the immediate wakes were simulated with the Baldwin–Lomax model. The flow field resulting from the nozzle guide vanes was used as inlet condition for calculating the rotor cascade flow. Tran and Taulbee (1992) also adopted the viscous/inviscid approach to calculate the unsteady flow and heat transfer in a rotor cascade. The unsteadiness was brought in through the inlet profiles. The k-ϵ turbulence model was applied in the blade-to-blade flow to obtain the turbulence field in this region (with no feedback on the flow field) and to provide boundary conditions for the calculation of the boundary layers. These were simulated with the aid of a low-Reynolds-number k-ϵ model. A transition model was not used in any of these calculations, and there was no detailed study of the unsteady boundary layer behavior. Models for wake-induced transition have been proposed and used for determining the time-averaged boundary layer profile loss (Sharma et al., 1988; Addison and Hodson 1990a, b) or the time-averaged heat transfer distribution (Doorly and Oldfield, 1985; Mayle and Dullenkopf, 1990). These models were, however, not used in unsteady calculations.

---

[1] Present address: Pratt & Whitney Canada, Mississauga, Canada.

[2] Present address: ABB Turbosystems, Baden, Switzerland.

Contributed by the International Gas Turbine Institute and presented at the 37th International Gas Turbine and Aeroengine Congress and Exposition, Cologne, Germany, June 1–4, 1992. Manuscript received by the International Gas Turbine Institute February 21, 1992. Paper No. 92-GT-306. Associate Technical Editor: L. S. Langston.

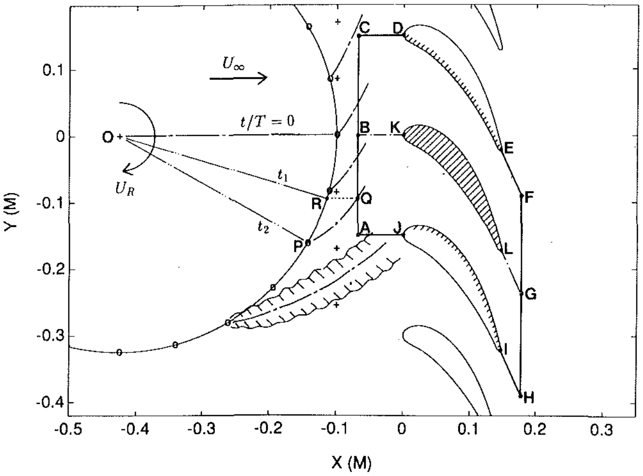

Fig. 1 Flow configuration and computational domain

Recently, Liu and Rodi (1991b, 1992) have carried out a detailed experimental study of the flow through a linear cascade exposed to unsteady wakes generated by a rotating squirrel cage (see Fig. 1). They provided time-resolved information on the velocity and turbulence behavior in the boundary layer, leading to a reasonable picture of the transition mechanism. Also, they carried out a systematic study of the influence of the wake-passing frequency. The purpose of the research reported here was to test a calculation procedure for unsteady cascade flow against these data. In contrast to the procedures discussed above, the ensemble-averaged Navier-Stokes equations are solved in the complete flow field by a finite-volume method (i.e., no viscous/inviscid coupling was applied) with a turbulence model, i.e., the influence of turbulence on the wake is simulated as it travels through the cascade channel. Further, the present study focuses on the development of the boundary layers and its dependence on the passing wakes. A two-layer turbulence model is employed (Rodi, 1991), involving a transition model based on Abu-Ghannam and Shaw's (1980) transition-length correlation, which was adapted to the unsteady situation by using it in a Lagrangian way. A preliminary version of this calculation model had been tested already by Rodi et al. (1989) for a similar unsteady flow over a flat plate.

2 Calculation Method

2.1 Mean-Flow Equation and Turbulence Model. In unsteady cascade flow, where the unsteadiness is caused by the passing of periodic wakes, an instantaneous flow quantity f can be conveniently split into three parts:

$$f=\bar{f}+\tilde{f}+f', \tag{1}$$

where $\bar{f}$ is the time-averaged value, $\tilde{f}$ is the periodic fluctuation, and f' the superimposed stochastic, turbulent fluctuation. The sum $\langle f\rangle=\bar{f}+\tilde{f}$ represents the ensemble- or phase-averaged value, which varies periodically with time. It is the distribution in time and space of ensemble-averaged values that is calculated in the present method by solving ensemble-averaged equations. The velocity and pressure field is governed by the continuity and momentum equations. Using a general nonorthogonal curvilinear coordinate system and Cartesian velocity components v_k, the equations may be written as follows (for convenience, the brackets of ensemble-averaged values are deleted hereafter):

$$\frac{\partial\rho\phi}{\partial t}+\frac{1}{J}\frac{\partial}{\partial x_i}\left(C_i\phi+D_i^\phi\right)=S_\phi, \tag{2}$$

where ϕ is the ensemble-averaged variable considered, J is the Jacobian of the coordinate transformation, C_i is convection, D_i^ϕ diffusion, and S_ϕ a source term. Table 1 shows the terms for each dependent variable. y_i denotes a reference Cartesian coordinate system while x_i is a general nonorthogonal coordinate system. The diffusion term contains the viscous stresses and also the turbulent (or Reynolds) stresses $-\rho\langle v_i' v_j'\rangle$. In

Nomenclature

A^+ = parameter in damping function (5)
C's = constants in turbulence model
C_i = convection term in ϕ equation (2)
C_p = pressure coefficient $=(p-p_{\text{ref}})/(\rho U_\infty^2/2)$
D_i^ϕ = diffusion term in ϕ equation (2)
f_μ = damping function defined in Eq. (5)
H = shape factor $=\delta^*/\theta$
J = Jacobian of the coordinate transformation
k = turbulent kinetic energy
L = length scale of turbulence
p = static pressure
p_{ref} = static pressure in oncoming flow
Re_θ = momentum thickness Reynolds number $=\rho U_{be}\theta/\mu_l$
Re_{tr} = critical transition Reynolds number
S = blade surface arc length coordinate
S_o = blade surface arc length from leading edge to trailing edge
S_ϕ = source term in ϕ, Eq. (2)
t = time
T = cycle period
Tu = turbulence level $=\sqrt{\overline{u'^2}}/\bar{U}$
U = velocity component in x direction (in boundary layer parallel to wall)
$\tilde{U}$ = periodic fluctuation of U velocity
u' = turbulent fluctuation of U velocity
U' = rms value of turbulent fluctuation $=\sqrt{\langle u'^2\rangle}$
V = velocity component in y direction
x = coordinate perpendicular to inlet plane AC (see Fig. 1)
y = coordinate parallel to inlet plane AC (see Fig. 1) (in boundary layer normal to wall)
y^+ = dimensionless wall distance $=\rho y\sqrt{\tau_w/\rho}/\mu_l$
δ = boundary layer thickness
δ^* = displacement thickness $=\int_0^\delta(1-U_b/U_{be})dy$
ϵ = dissipation rate of turbulent kinetic energy
θ = momentum thickness $=\int_0^\delta(1-U_b/U_{be})U_b/U_{be}dy$
κ = von Karman constant
μ_l = molecular viscosity
μ_t = turbulent (or eddy) viscosity
ρ = density
τ_w = wall friction
ϕ = general dependent variable

Subscripts

b = boundary layer
e = external (edge of boundary layer)
∞ = oncoming flow

Table 1 Contributing terms for the governing Eq. (2)

ϕ	C_i	D_i^ϕ	S_ϕ
1	$\beta_j^i \rho v_j$	0	0
v_k	$\beta_j^i \rho v_j$	$-\frac{\mu}{J}(B_j^i \frac{\partial v_k}{\partial x_j} + \beta_j^i \omega_k^j)$	$-\frac{1}{J}\frac{\partial}{\partial x_j}(p\beta_k^j)$
k	$\beta_j^i \rho v_j$	$-\frac{\mu}{\sigma_k J}(B_{j,}^i \frac{\partial k}{\partial x_j})$	$P_k - \rho\epsilon$
ϵ	$\beta_j^i \rho v_j$	$-\frac{\mu}{\sigma_\epsilon J}(B_j^i \frac{\partial \epsilon}{\partial x_j})$	$C_{\epsilon 1}\frac{\epsilon}{k}P_k - C_{\epsilon 2}\rho\frac{\epsilon^2}{k}$

β_j^i = cofactor of $J(= \partial y_i/\partial x_j), B_j^i = \beta_l^i \beta_l^j$

$\omega_k^j = \beta_k^l \frac{\partial v_j}{\partial x_l}, P_k = \frac{\mu_t}{J}(\beta_j^n \frac{\partial v_l}{\partial x_n} + \beta_l^m \frac{\partial v_j}{\partial x_m})(\beta_j^n \frac{\partial v_l}{\partial x_n})$

$\mu = \mu_l + \mu_t, \mu/\sigma_k \equiv (\mu_l + \mu_t/\sigma_k), \mu/\sigma_\epsilon \equiv (\mu_l + \mu_t/\sigma_\epsilon)$

the present work, these stresses are related to the ensemble-averaged velocity gradients with the aid of the eddy viscosity hypothesis introducing an eddy (or turbulent) viscosity μ_t. The diffusion terms in Table 1 are already written in eddy viscosity form.

The distribution of the eddy viscosity μ_t has to be determined with the aid of a turbulence model. Here, a two-layer model is used, in which the standard k-ϵ model is applied in the outer region of the flow and the one-equation model of Norris and Reynolds (1975) in the viscosity-affected near-wall region of the center blade of the calculation domain (see Fig. 1). In the k-ϵ model, the eddy viscosity is related to the turbulent kinetic energy k and the rate of its dissipation ϵ via the formula

$$\mu_t = \rho C_\mu \frac{k^2}{\epsilon}. \tag{3}$$

The distribution of the phase-averaged values of k and ϵ over the flow field is determined from unsteady semi-empirical transport equations, which can also be written in the form of Eq. (2), and for these variables the values of D_i^ϕ and S_ϕ are also given in Table 1.

The Norris–Reynolds model, with which the viscosity-affected region very near the center blade wall is resolved, calculates the eddy viscosity from the following relation:

$$\mu_t = \rho C_{N1} f_\mu \sqrt{k} \cdot L, \tag{4}$$

where f_μ is a wall damping function defined by

$$f_\mu = 1 - \exp(-C_{N2} \cdot \mathrm{Re}_y \cdot 25/A^+), \quad \mathrm{Re}_y = \frac{\rho\sqrt{k}y}{\mu_l}. \tag{5}$$

The turbulent kinetic energy in Eq. (4) is also determined from a transport equation, while the turbulent length scale L is prescribed by the following relation:

$$L_1 = C_{DN} \cdot \min(\kappa y,\ C_{LN} \cdot \delta),$$

$$L_2 = C_{DN} \cdot \min(\kappa y,\ \frac{k^{3/2}}{\epsilon \cdot C_{DN}} | e),$$

$$L = \max(L_1,\ L_2), \tag{6}$$

where μ_l is the molecular viscosity, y is the normal distance from the blade surface, and e denotes the matching position of the two turbulence models, which is described shortly. δ is the local boundary layer thickness, which is determined by the local peak position of U_b on the suction side and by the local peak position of the curvature of the U_b profile on the pressure side. The length scale relation, Eq. (6) is basically a ramp distribution, but when the boundary layer is turbulent, the one-equation model is applied only in the region where the linear distribution is effective. In the one-equation model, the dissipation rate ϵ appearing in the k equation (see Table 1) is not determined from a transport equation, but from the following algebraic relationship:

$$\epsilon = \left(1 + \frac{C_{\epsilon N}}{\mathrm{Re}_L}\right) \frac{k^{3/2}}{L}, \quad \mathrm{Re}_L = \frac{\rho\sqrt{k}L}{\mu_l}. \tag{7}$$

The damping function Eq. (5) in the eddy-viscosity relation Eq. (4) simulates the viscous and wall-proximity effects. In fully turbulent boundary layers with zero pressure gradient, the value of A^+ in the damping function is 25. To account for the influence of streamwise pressure gradient on the eddy viscosity in the one-equation model, the following relation devised by Crawford and Kays (1976) for the mixing-length hypothesis is adopted, but only in the case of favorable pressure gradient:

$$A_t^+ = \frac{25}{C \cdot p^+ + 1}, \qquad p^+ = \frac{dp}{dx} \frac{\mu_l}{\rho^2 (\tau_w/\rho)^{3/2}},$$

$$C = 30.175\ p^+ < 0, \quad C = 0.0\ p^+ \geq 0. \tag{8}$$

The A^+ parameter further plays an instrumental role in the transition model, as will be described in section 2.2.

The two turbulence models are matched at a wall distance where the damping effects are no longer important, i.e., when f_μ is close to 1 (a value of 0.95 was chosen). In zero pressure gradient boundary layers, this wall distance corresponds to $y^+ \approx 80$. If the location of $f_\mu = 0.95$ comes to lie outside the boundary layer, the matching position is set at the boundary layer edge.

The values of the empirical constants in the above model relations are as follows: $C_\mu = 0.09$, $C_{\epsilon 1} = 1.44$, $C_{\epsilon 2} = 1.92$, $\sigma_k = 1.0$, $\sigma_\epsilon = 1.3$, $C_{\epsilon N} = 12.45$, $C_{DN} = 6.09$, $C_{LN} = 0.085$, $C_{N1} = 0.09$, $C_{N2} = 0.0198$, $\kappa = 0.41$.

2.2 Transition Model. The parameter A^+ in the damping function Eq. (5) is given a large value (here 300) when the boundary layer is laminar so that μ_t resulting from Eq. (4) is small compared with the molecular viscosity μ_l. In fully turbulent boundary layers, A^+ is calculated from relation (8). In the transition region, A^+ is assumed to vary between the two limiting values according to the following formula (after Crawford and Kays, 1976):

$$A^+ = A_t^+ + (300 - A_t^+) \left[1 - \sin\left(\frac{\pi}{2} \frac{\mathrm{Re}_\theta - \mathrm{Re}_{tr}}{\mathrm{Re}_{tr}}\right)\right]^2, \tag{9}$$

which is effective when the momentum thickness Reynolds number Re_θ is larger than the critical transition Reynolds number Re_{tr} and smaller than twice Re_{tr}. The critical Reynolds number is obtained from the following correlation of Abu-Ghannam and Shaw (1980):

$$\mathrm{Re}_{tr} = 163 + \exp\left[F(\lambda) - \frac{F(\lambda) \cdot Tu}{6.91}\right], \tag{10}$$

where Tu denotes the free-stream turbulence level (here in percent) and $F(\lambda)$ is a function of the Pohlhausen parameter λ, introducing the influence of the pressure gradient on the transition location. Tu is taken at the edge of the boundary layer and $F(\lambda)$ is defined by

$$F(\lambda) = \begin{cases} 6.91 + 12.75\lambda + 63.64\lambda^2 & \text{if } \lambda \leq 0 \\ 6.91 + 2.48\lambda - 12.27\lambda^2 & \text{if } \lambda > 0 \end{cases} \quad \lambda = -\frac{\theta^2 \frac{dp}{dx}}{\mu_l U_{be}}, \tag{11}$$

where U_{be} is the velocity parallel to the blade surface at the edge of the boundary layer.

In a steady boundary layer calculation, Re_θ is compared with the critical Reynolds number Re_{tr} from Eq. (10) for each position as the calculation proceeds downstream. It is assumed that transition starts where Re_θ exceeds Re_{tr} for the first time. The value of Re_{tr} at this position is then frozen and is used in

Eq. (9) for calculating A^+ in the transition region. In unsteady flow with discrete wakes passing over the blade, the same model is used in a Lagrangian way. Fluid elements near the boundary layer edge traveling along the blade surface are followed, and the local growth in Re_θ is compared with Re_{tr} according to Eq. (10) at each time step during the travel. When Re_θ exceeds Re_{tr} for the first time, transition begins. As the fluid elements travel further downstream, Re_θ grows and transition is completed when Re_θ reaches twice the frozen value of Re_{tr} for this fluid element. Beyond this point, transition is complete and A^+ follows from relation (8).

2.3 Boundary Conditions. Since the conditions at the free boundaries are not periodic when the pitches of rotor and stator are different, the influence of using approximate conditions at these boundaries on the flow around the blade considered was minimized by moving the free boundaries away from the region of interest. This was achieved by taking as calculation domain two cascade channels, i.e., the domain *ACFHA* in Fig. 1. Boundary conditions need to be specified for the boundaries of this domain. The near-wall region of the center blade is resolved by the Norris–Reynolds one-equation model, and hence along the wall of this blade (*KL*) no-slip boundary conditions are imposed, i.e., the velocity components are set to zero at the wall. The turbulent kinetic energy is also set to zero. As the boundary layer development is of interest only along the walls of the center blade, only a crude near-wall treatment was adopted for the top and bottom blade surfaces, where the Norris–Reynolds model is not applied. Slip boundary conditions are imposed along these surfaces, *DE* and *JI*, respectively. The exact conditions at these blades do not have much influence on the calculations around the center blade.

If the pitches of stator blades and cylinders were the same, periodic boundary conditions could be applied to the *CD* and *AJ* planes and to the *EF* and *IH* planes. However, in the present study the pitches are different. Therefore, phase-lagged periodic conditions would have to be used as explained by Giles and Haimes (1993). Such boundary conditions are very complex, and they are also not suitable for the present situation because the movement of the cylinders generating the wakes is not linear but circular. Therefore the flow field in the upper channel *BCFGB* is not strictly repeated, in a phase-lagged manner, in the lower channel *ABGHA*. To overcome this difficulty, an approximate treatment was adopted for the boundaries *EF* and *IH* to which periodic conditions were applied. Once a solution is obtained in the inner field, the solution along *LG* is imposed on *EF* and *IH*, assuming that these are periodic. This explicit treatment appears to work rather well mainly because the influence of the trailing edge wake is strong enough to cover the weakness of this periodic boundary condition. The boundaries *CD* and *AJ* were treated as inflow boundaries as described shortly. At the outflow boundary *FH*, the streamwise gradient of all variables was set to zero.

Time-dependent ensemble-averaged profiles of all variables were prescribed on the inlet planes *AC*, *AJ*, and *CD*. In the present study, the *AC* plane is normal to the inlet flow direction and *AJ* and *CD* are parallel. The inlet profiles were based on the wake decay laws behind a stationary cylinder. Along the inlet plane *AC*, these laws were imposed on uniform inlet variables. The uniform variables are the axial velocity U_∞, the radial velocity V_∞ $(=0)$, the turbulent kinetic energy k by setting Tu $(=\sqrt{2/3k}/U_\infty)$, and the dissipation rate ϵ by setting the length scale L $(=k^{3/2}/\epsilon)$. A detailed description of the correlations is given by Schönung (1989). The inlet value of Tu was extrapolated from the measurements taken at $x=-30$ mm upstream of the leading edge of the blade. The levels of the turbulent length scale L were unknown from the experiments and could not be estimated from these. The inlet level of L and hence ϵ was chosen such that the correct level of Tu resulted at the measurement station $x=-30$ mm. The corresponding inlet values of μ_t/μ_l were in the range 3-30.

When Schönung (1989) derived his wake laws for the inlet profiles, he assumed that the wake-producing cylinders move along a straight line as shown by the crossed marks in Fig. 1. This then led to straight wake centerlines as the wakes are swept down-stream. In the experiment simulated in the present study, the wakes were produced by a rotating squirrel cage so that the wake-producing cylinders moved on a circle as shown in Fig. 1. This in turn caused the wake centerlines to curve, as sketched in Fig. 1. In order to allow the wake decay laws to be used, the curved traveling distance, e.g., *PQ* of the wake generated by the cylinder *P*, has to be calculated. This wake trace can be found by assuming that the wake center travels at the free-stream velocity U_∞. At time t_1, the cylinder *P* generates the wake at the position *R*. While this cylinder moves to *P* during the time t_2-t_1, the wake generated at *R* travels up to *Q* where the distance $RQ=U_\infty(t_2-t_1)$. With a much finer time step than sketched in Fig. 1, the positions of the curved wake trace can be deduced.

The time-dependent profiles on the *AJ* and *CD* planes were prescribed in a similar manner. However, the wake decay laws could here not be imposed on uniform profiles because the flow near the leading edge of the blade is not uniform at all. To simulate this effect, a steady flow solution without the effect of wakes was obtained first with periodic conditions at *CD* and *AJ*, and the wake decay laws were then imposed on this solution along *CD* and *AJ*.

2.4 Numerical Solution Procedure. The partial differential equations introduced above were solved numerically with an iterative finite-volume method on nonorthogonal, boundary-fitted grids. An *H*-grid was generated with the differential method of Naar and Schönung (1986), which is shown in Fig. 2 (91×83 grid lines in x_1, x_2 directions, every second grid line is shown). The grid lines are highly concentrated around the center blade where the one-equation model is applied.

The main features of the finite-volume method are described by Rodi et al. (1989) and a detailed description can be found from Schönung (1989). Hence, only a few central points need to be given here. The finite-volume method employs nonstag-

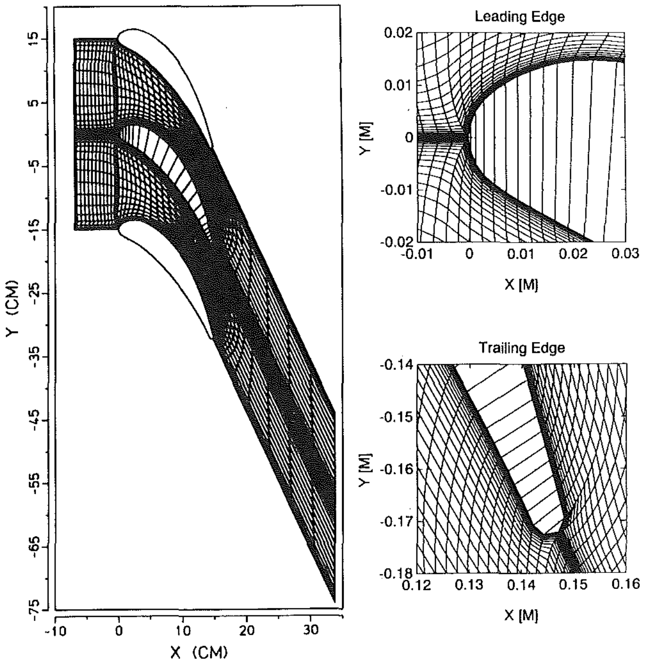

Fig. 2 Numerical H-grid used

Table 2 Test cases

Parameter / Cases ⇒	A	B	C	D	E
Cylinder (N)	-	24	24	48	48
Cage RPM (ω)	0	150	300	225	600
Tu (%) at $x = -$ 30mm	0.9	2.3	2.8	3.1	4.8
Rotor Pitch (mm)	-	85.08	85.08	42.54	42.54
Rotor Velocity (m/s)	-	5.105	10.210	7.658	10.210
One Cycle T (ms)	∞	16.67	8.33	5.56	4.17
Wake Passing Frequency (Hz)	-	60	120	180	240
U_∞=7.5 m/s, Stator Pitch≐150 (mm), Stator Chord=230, Cage Radius=325, Cylinder Radius=4, Spacing=100.					

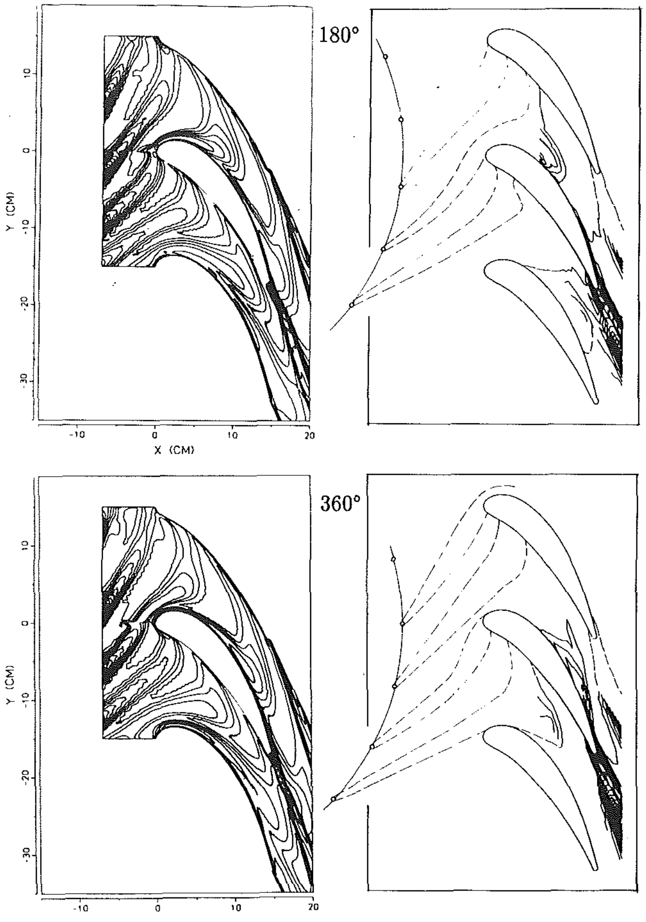

calculated measured

Fig. 3 Contours of turbulent kinetic energy at the phase angles 180 deg and 360 deg (0 deg) for case *C*

gered grids and Cartesian velocity components. For spatial discretization the HLPA (hybrid linear/parabolic approximation) scheme of Zhu (1991) is used, which combines a second-order upstream-weighted approximation with the first-order upwind differencing scheme under the control of a convection boundedness criterion. The scheme produces almost the same accuracy as the third-order unbounded QUICK scheme of Leonard (1979) but eliminates the unbounded behavior of the latter. The use of at least a second-order accurate method was found to be absolutely essential as the use of a first-order upwind scheme causes so much numerical diffusion that the passing wakes lose their identity very quickly. On the other hand, the third-order method QUICK was found to be numerically unstable, particularly so for solving the k and ϵ equations. For time discretization, the following fully implicit second-order method was used:

$$\frac{\partial \Phi}{\partial t}\bigg|_{n+1}=\frac{1}{2\Delta t}\,(3\Phi^{n+1}-4\Phi^{n}+\Phi^{n-1}), \tag{12}$$

where n denotes the time level and Δt the time step. Also for the time discretization, a second-order scheme was found necessary in order to avoid excessive numerical diffusion. Even with the second-order scheme, more than 30 time steps per cycle were necessary to prevent such diffusion. For numerical stability when employing the second-order schemes, a steady solution was obtained first by using the hybrid central/upwind scheme, and this solution was then used for starting the unsteady calculation. First-order time discretization was used for the first cycle of the unsteady calculation.

The SIMPLEC algorithm of Van Doormal and Raithby (1984) is used to handle the pressure-velocity coupling and a special momentum interpolation method of Rhie and Chow (1983) is used to avoid spurious oscillations of the pressure field, which may be encountered when a nonstaggered grid is employed. At each time step, the system of algebraic difference equations was solved iteratively with the strongly implicit method of Stone (1968) until a convergence criterion was satisfied. This criterion was set such that the total sum of the momentum residual normalized by the inlet flux was less than 0.01 percent. The first grid points from the center blade wall were located in the region $y^+ < 5$ as a one-equation model was used near the wall. Some calculations were also carried out with a finer mesh (163 × 83), but only small differences resulted for the solutions obtained on the 91 × 83 grid, which was hence found appropriate. The reference time was set to $t/T = 0$ when the cylinder on the cage was aligned with the line OK in Fig. 1. The cycle time T for a cylinder to rotate one pitch is given in Table 2. For most cases, 56 time steps per cycle were used. For the steady flow case (A) the time-stepping method was also applied as the transition model was used in a Lagrangian way. To calculate this case, simply the distance between the blade leading edge and the cylinder at zero angle position was set to such a large value that the effect of the wake decay laws on the inlet conditions became negligible. For case C, five cycles with 56 time steps each were solved and the CPU time on a Siemens S600/20 machine was 8.2 min/cycle (3.8672×10^{-5} s/node). It should be mentioned that the code is not vectorized.

3 Results and Discussion

Liu and Rodi (1991b, 1992) have studied experimentally the flow through a linear cascade consisting of five MTU blades. The unsteady wakes were generated by a rotating squirrel cage and five cases with different wake-passing frequencies ranging from zero to 240 were investigated. The details of the individual cases are given in Table 2; the Reynolds number based on the chord length was 1.1×10^5. For cases A (0 Hz) and C (120 Hz), blade-to-blade measurements were carried out, whereas for all cases detailed boundary layer measurements were performed. All five cases were simulated with the calculation procedure described above and the results are now presented.

Figure 3 compares calculated and measured contours of ensemble-averaged turbulent kinetic energy k for two phases of case C. Both sets of contours show clearly the traveling of the wakes through the cascade channels and the generation of new, steady wakes at the trailing edge. The qualitative agreement is good, and more cannot be expected from a comparison. It should be mentioned that with lower spatial and time discretization, the numerical diffusion generated by the calculation procedure was so severe that the wakes entering the inlet plane merged so quickly that they could not be identified anymore inside the cascade channel. The flow accelerates at the cascade channel inlet and reaches velocities around the trailing edge of the suction side, which are three times higher

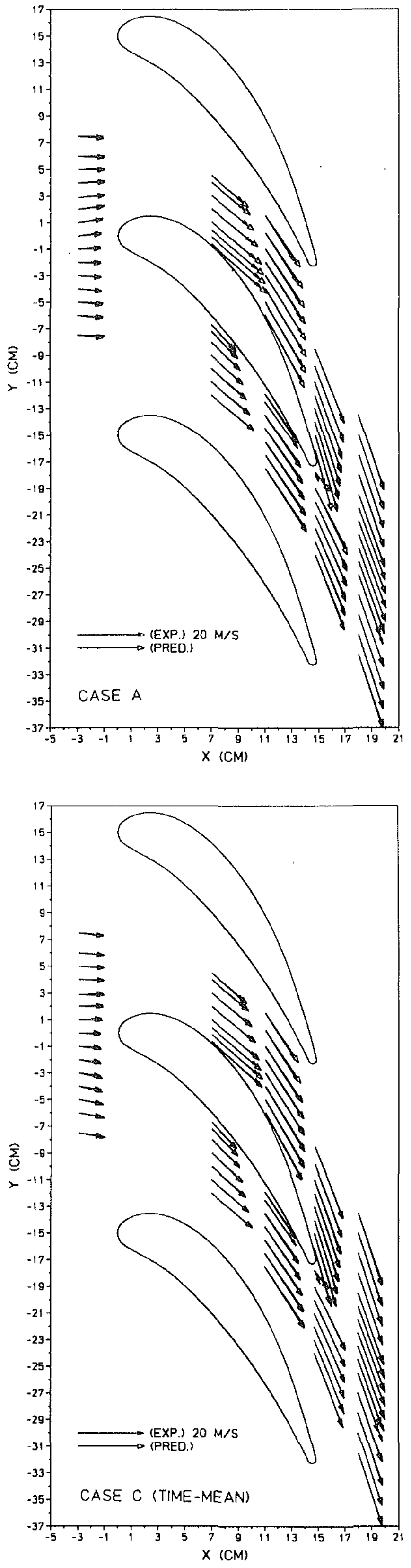

Fig. 4 Time-mean velocity vectors for cases *A* and *C*

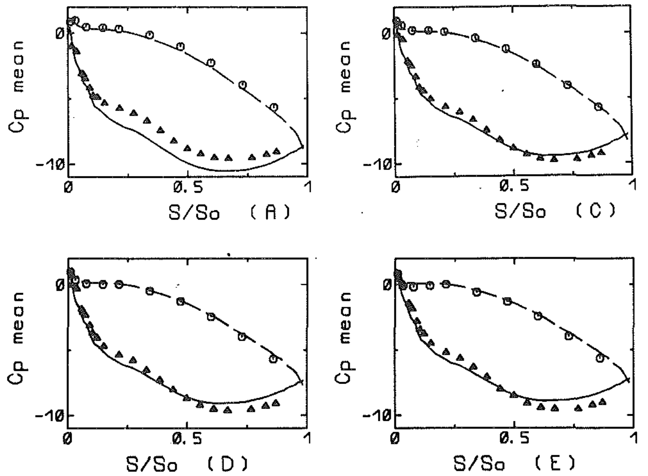

Fig. 5 Time-mean pressure coefficient $\overline{C_p}$ on the suction side (exp. = △, pred. = ——) and on the pressure side (exp. = ○, pred. = - - -) for cases *A, C, D, E*

than the inlet values. The wakes impinging on the blades are cut by the leading edges in two parts and are then swept downstream in the upper and lower cascade channel. They remain clearly distinguishable (high turbulence energy level) until they merge into the stationary trailing edge wakes. The calculations show that, at the inlet plane, the level of turbulence energy on the wake center decreases as the wakes move down toward the bottom blade. This is due to the increase in the wake traveling distance caused by the circular movement of the wake-generating cylinder and is brought about by the wake decay law incorporated. This effect is not very clear from the experimental results.

Figure 4 compares predicted (open arrows) and measured (full arrows) time-mean velocity vectors for cases *A* and *C*. The flow directions are predicted accurately, but there are some discrepancies in the magnitude. The exit flow vectors are reproduced faithfully except close to the trailing edge. For case *A*, the overprediction of the velocity in the upper channel manifests itself also in the time-mean pressure coefficient shown in Fig. 5. In case *C* with unsteady wakes, the oncoming velocity vectors near the core region of the lower channel are not entirely perpendicular to the inlet plane. This feature, which is due to the curved wakes generated by the squirrel cage, is reproduced well by the calculations.

Figure 5 displays the variation of the time-mean pressure coefficient $\overline{C_p}$ along the suction and the pressure sides of the blade. The flow on the suction side is accelerated first highly and then more gently until $S/S_o = 0.7$ beyond which point it is slightly decelerated. On the pressure side, the flow is mildly accelerated all the way to the trailing edge. The experiments have shown that the time-mean pressure coefficient is not influenced significantly by the passing wakes. Overall, the predictions are fairly satisfactory, even though the pressure is somewhat underpredicted on the suction side for case *A*, in which the boundary layer remained laminar. This is in line with the overprediction of the velocity discussed already. For the cases *C*, *D*, and *E* with unsteady wakes, the pressure recovery is predicted slightly faster than was observed in the measurements. Through the flow deceleration in the trailing edge region, the boundary layer becomes thicker, and this is somewhat overpredicted (see Fig. 6) causing the pressure recovery to be predicted somewhat too fast.

Figure 6 exhibits the variation along the suction side of the time-mean displacement thickness $\overline{\delta^*}$ and shape factor $\overline{H}$ for different cases. For case *A* without unsteady wakes, the shape factor is slightly above 2 virtually over the entire suction side, indicating that the boundary layer is laminar in this case. In cases *C–E* with passing wakes, the shape factor falls below 2 in the region near the trailing edge, indicating transition. Associated with this is an increase in the growth of the displacement thickness toward the trailing edge, which is, however, overpredicted. It is not very clear from Fig. 6 that, in accord

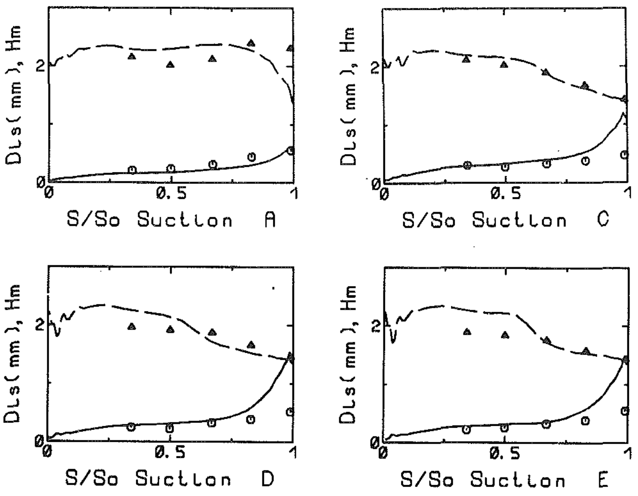

Fig. 6 Time-mean displacement thickness $\bar{\delta}^*$ (exp. = ○, pred. = —) and shape factor H (exp. = ▲, pred. = - - -) on the suction side for cases *A*, *C*, *D*, *E*

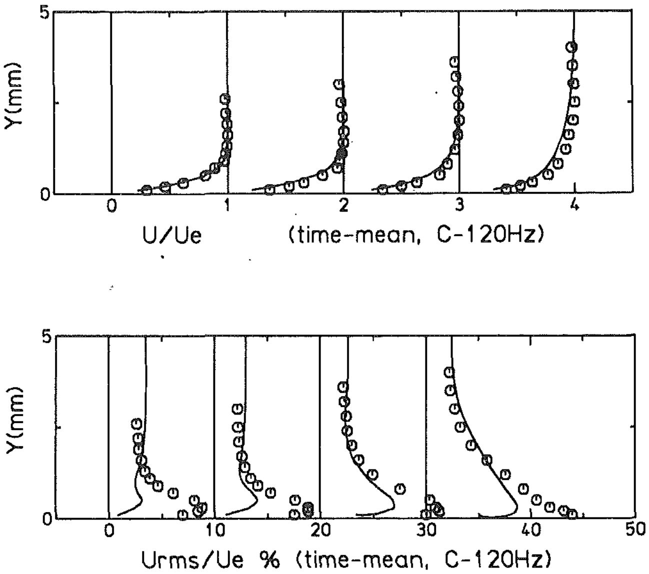

Fig. 7 Profiles of time-mean velocity U_b/U_{be} and turbulence intensity u'/U_{be} (percent) on the suction side for case *C*. Positions at $S/S_o = 0.341$, 0.498, 0.669, and 0.828. Pred. = —, exp. = ○

with the measurements, the beginning of transition moves forward as the wake-passing frequency increases. This can be seen more clearly from Figs. 12 and 13 to be presented later.

Figure 7 shows the profiles of the time-mean velocity and turbulence intensity for case C at four streamwise locations of the suction side. The values are nondimensionalized by the streamwise velocity at the edge of the boundary layer U_{be}, which is somewhat different in the experiments and the calculations. For the prediction, U' was obtained from k through the relation $U' = \sqrt{2/3k}$ assuming isotropic turbulence. Near the wall this assumption probably underestimates the value of U' as turbulence is nonisotropic and $U'/\sqrt{k}$ is closer to 1 than to $\sqrt{2/3}$ as implied by the isotropic relation. The time-mean velocity profiles are predicted quite well at the first three locations. At the last location, $S/S_o = 0.828$, the boundary layer thickness is overpredicted, and the discrepancy increases past this location, as can be seen from Fig. 6. Concerning the turbulence intensity, the experiments show that the level of U' increases downstream as the boundary layer undergoes transition. The relatively high level of U' near the leading edge is due to the impingement of the passing wakes on the blade surface. Apparently, this phenomenon cannot be simulated with the present simple turbulence and transition model, which predicts a laminar boundary layer at the first location at all times (see Fig. 12) and hence a strong damping of turbulence inside the boundary layer since A^+ has a large value. However, the right trend, i.e., increasing intensities near the wall in the downstream direction, is predicted.

Figure 8 displays the time variation of the periodic fluctuation velocity $\tilde{U}/U_\infty$ and the turbulent fluctuating component U'/U_∞ for case C at various measurement locations. These locations are identified in Fig. 8(*a*), which also shows the predicted time-mean streamlines. The time variations are shown only for locations inside the cascade channel and in the wake. Positions lying approximately along the same streamline are grouped and discussed together. Figure 8(*b*) shows the variation at points along the center of the upper channel. A passing wake corresponds to a valley in $\tilde{U}/U_\infty$ and a peak in U'/U_∞. An increase in index I means moving downstream along the channel center. There is fairly reasonable agreement between calculations and experiments in the movement of the valleys and peaks from location to location. The position of the velocity valley moves somewhat faster than the peak in the turbulence intensity. This is predicted qualitatively correctly by the calculation. The maxima of velocity deficit and turbulence intensity are also predicted fairly well, but there is a higher background turbulence level between passing wakes in the experiments. The value of this background turbulence depends to some extent on the value of ϵ at the inlet.

It should be mentioned that in the predictions the time axis was shifted 0.35 cycle periods forward in time so that calculated and experimental wake centers match at location $I=2$. With the original time axis ($t=0$ when a cylinder is on line OK in Fig. 1), the wake centers matched at the location $I=1$, 30 mm upstream of the leading edge. However, for reasons that are not clear at present (see also Liu and Rodi, 1992) the measured time for the wake to travel from $I=1$ to $I=2$ is $0.35T$ shorter than would follow from the experimental convection velocity. With the proposed time shift, calculated and measured time variations at $I=1$ upstream of the leading edge do not of course agree and hence are not shown here. Comparing the time variations at position $I=2$ in Figs. 8(*b*) and 8(*e*) it can be seen that there is another time shift between positions at the same x location in the upper and lower channels. This means that matching computational and experimental time variation at $I=2$ in the upper channel leads to some mismatch at $I=2$ in the lower channel. In the experiments the wakes moved somewhat faster from the upper to the lower channel than was to be expected from the given cylinder velocity. The wake-passing frequency would have to be increased by about 10 percent to correct for this. The cylinders mounted on a squirrel cage were flexible and hence the radius of the circle on which the cylinders moved may have been somewhat larger during rotation than the specified radius. This would increase the cylinder velocity and hence the wakes should arrive earlier in the lower channel, but it cannot fully explain the 10 percent discrepancy.

Figure 8(*c*) presents the temporal variation of periodic and turbulent fluctuations at positions along a streamline near the edge of the boundary layer on the suction side. The agreement between calculations and measurements is quite reasonable at all points. There is a fairly strong variation of the velocity as the wakes pass by. The amplitude of the periodic velocity fluctuations decreases in the downstream direction, but that of the turbulence intensity is more or less maintained. Figure 8(*d*) exhibits corresponding variations at positions on a streamline near the edge of the boundary layer on the pressure side. The level of turbulence intensity is lower than on the suction side, and it varies relatively little with time so that the wakes seem to have little influence on this quantity. The passing wakes can, however, be clearly seen from the variation of the periodic velocity fluctuation. Even though there is some time lag as discussed above, the calculation reproduces the observed variation correctly. The last axial position ($I=7$) is located near the trailing edge. The turbulence intensity is considerably higher than at the previous stations due to the generation of turbulence in the near-wake of the blade, but the high levels observed in the experiments are not reached in the calculation.

Finally in Fig. 8(*e*), the variations of periodic and turbulent fluctuations are presented along the mid-streamline of the lower channel. There are some differences to the corresponding variations in the upper channel, and these are due to the passing wake being curved; in particular the deficit velocity is larger in the lower channel. Further, it may be observed that the level of turbulence intensity is higher than near the pressure side wall and indicates the passing wakes more clearly. This is due to the fact that the wakes are convected more in the central and suction side parts through the cascade than near the pressure side, as can be seen from Fig. 3.

Figure 9 compares calculated and measured contours of turbulent intensity in a space–time diagram at near-wall points on the suction side for case *C*. A quantitative comparison should not be made as wall distance and cutoff level were somewhat different in experiments and calculations. However, both measurements and calculations show up to $S/S_0 = 0.6 \sim 0.7$ an intermittent character of the near-wall turbulence. When the wakes pass, the intensity is fairly high near the wall, while in between there are periods with relatively low intensity. These periods become shorter in the downstream direction and disappear at $S/S_0 = 0.6 \sim 0.7$ indicating that from there onward the boundary layer is turbulent or at least transitional at all times.

Figure 10 sheds more light on the temporal variation of the state of the boundary layer; it shows the variation with time of the ensemble-averaged displacement thickness δ^* and shape factor H at four downstream locations on the suction side for case *C*. Down to the third station ($S/S_0 = 0.669$) the shape factor remains more or less at a level of 2, indicating that the boundary layer state is laminar. At the last station, H has fallen below 2 and temporarily reaches values near 1.5, which are typical for turbulent boundary layers. On the whole, the

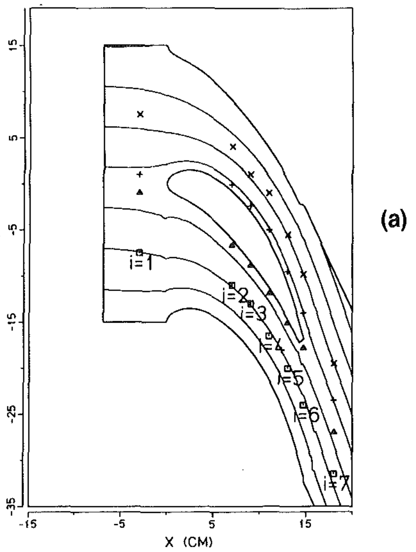

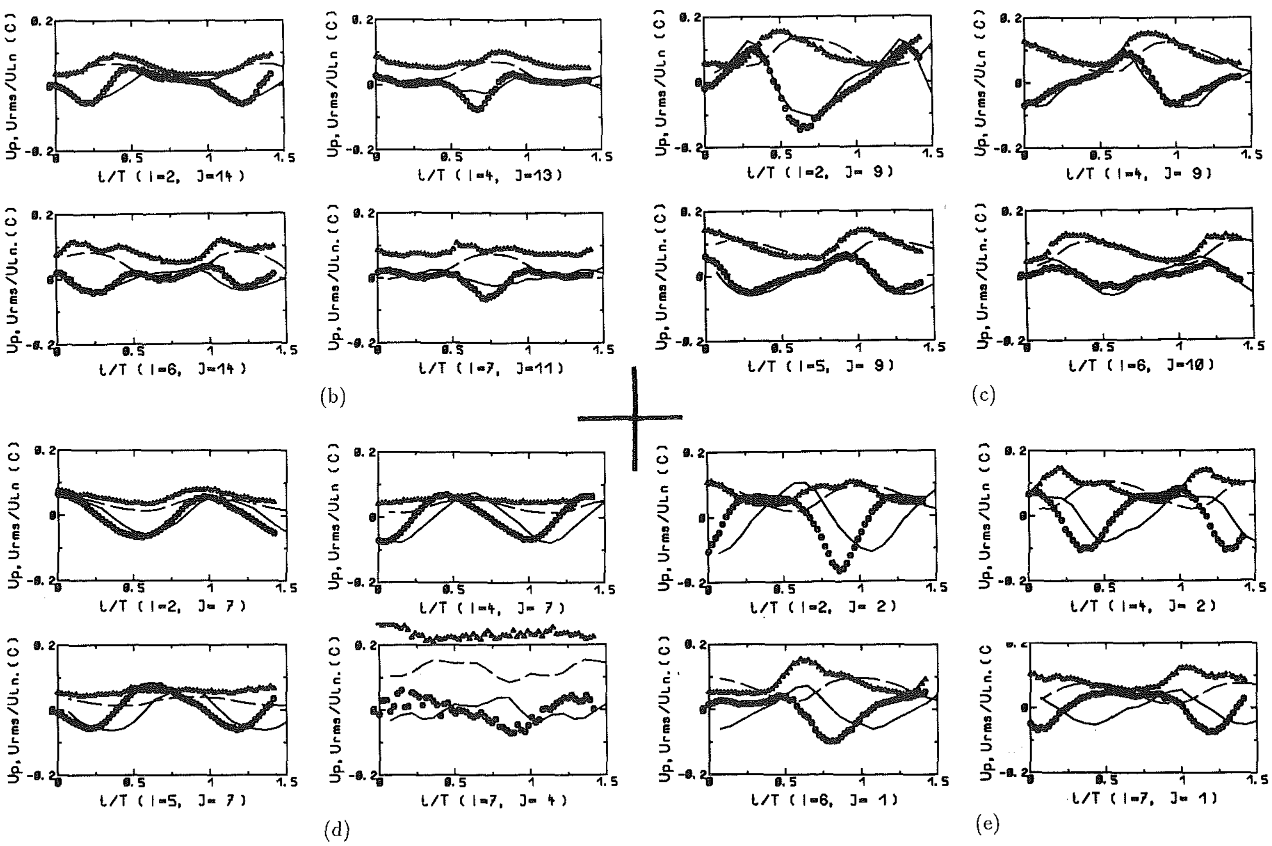

Fig. 8 (*a*) **Measurement locations and predicted time-mean streamlines for case** *C*. **Time-variation of periodic fluctuation velocity $\tilde{U}/U_\infty$ (exp. = ○, pred. = ——) and turbulence fluctuation u'/U_∞ (exp. = △, pred. = - - -); (*b*) along the upper midchannel (×)·(*c*) the suction side near-wall (+); (*d*) the pressure side near-wall (△); (*e*) the lower-midchannel streamlines (□).**

experiments show little variation of δ^* and H with time, i.e., no clearly intermittent boundary layer behavior could be observed as was found by Liu and Rodi (1991a) on a flat plate. The calculations show more variation, which can be explained with the behavior of the parameter A^+ characterizing the boundary layer state (see Fig. 12). At the third station, A^+ has a laminar value of 300 at small t/T values and drops to a turbulent value near $t/T\approx0.8$ yielding the variation of H in Fig. 10. At the last station ($S/S_o=0.828$) the calculations show a sharp increase in H around $t/T\approx0.4$. This is caused by a short laminar period of the boundary layer, which is otherwise turbulent over most of the cycle. On the whole, the behavior of H is quite well predicted by the model. The same is true for the displacement thickness at the first three stations; at the last station δ^* is too large during the times the boundary layer is turbulent, as was discussed already.

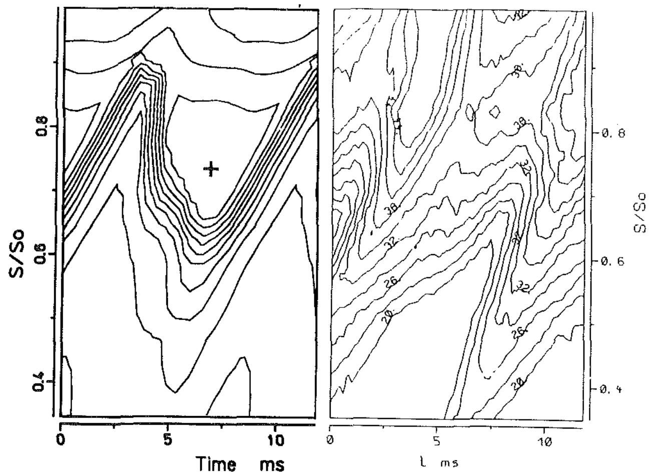

Fig. 9 Contours of turbulence intensity in t-s plane on the suction side for case C (at $y\approx0.2$ mm in predictions, at $y=0.1$ mm in experiments). The peak level is 33 percent and the contour step 3 percent in the predictions

Figure 11 shows the time variation of the periodic and turbulent fluctuations on the suction side for all unsteady cases B-E. For each case, the variations are given at three axial positions and at two wall distances, one inside and the other outside the boundary layer. It should be noted that the variables are nondimensionalized by the local free-stream velocity U_{be}.

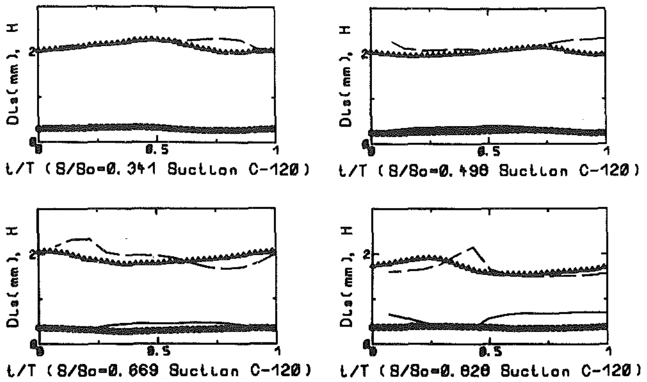

Fig. 10 Temporal development of displacement thickness δ^* (exp. = ○, pred. = ——) and shape factor H (exp. = △, pred. = - - -) on the suction side for case C

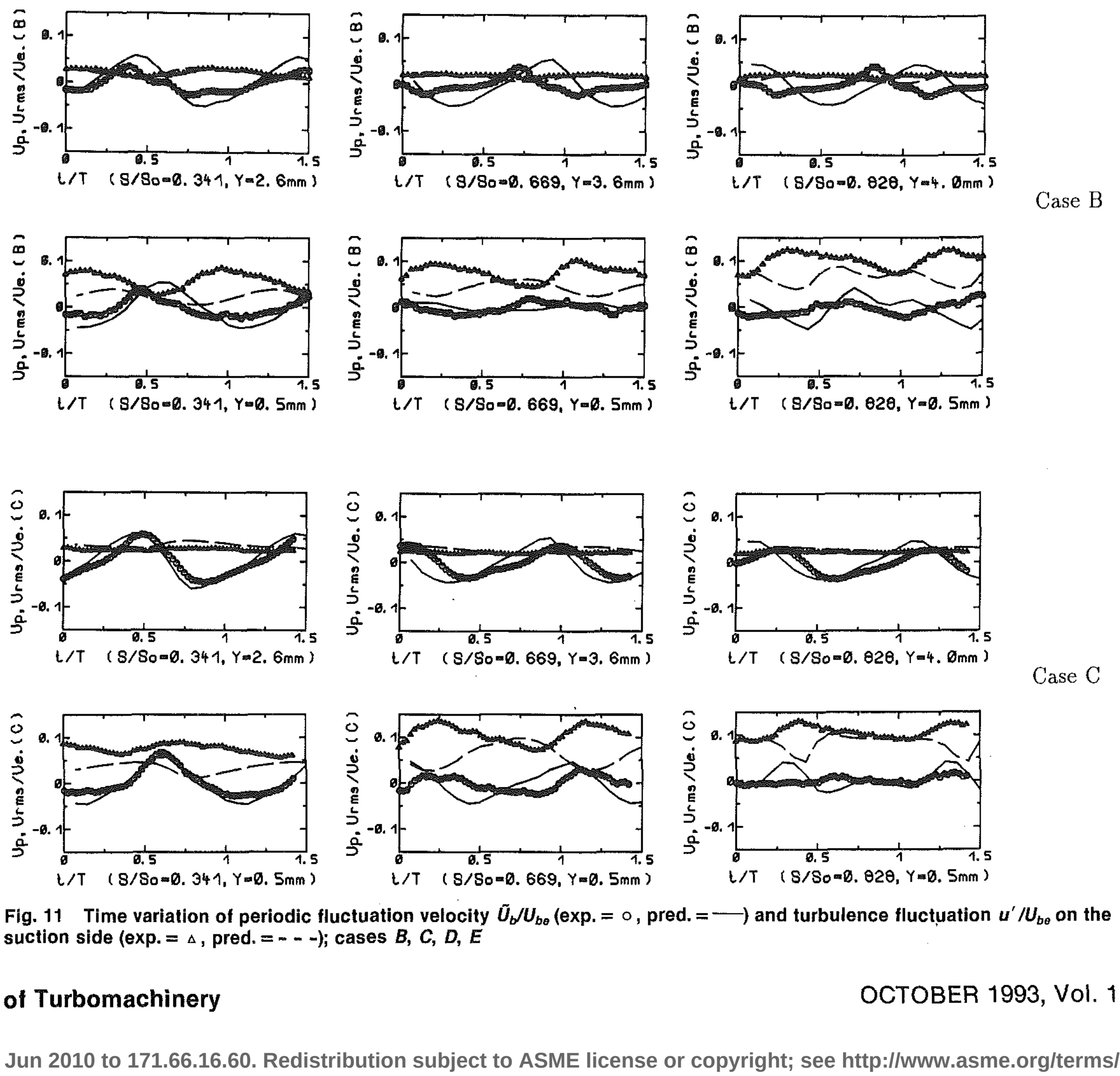

Fig. 11 Time variation of periodic fluctuation velocity $\tilde{U}_b/U_{be}$ (exp. = ○, pred. = ——) and turbulence fluctuation u'/U_{be} on the suction side (exp. = △, pred. = - - -); cases B, C, D, E

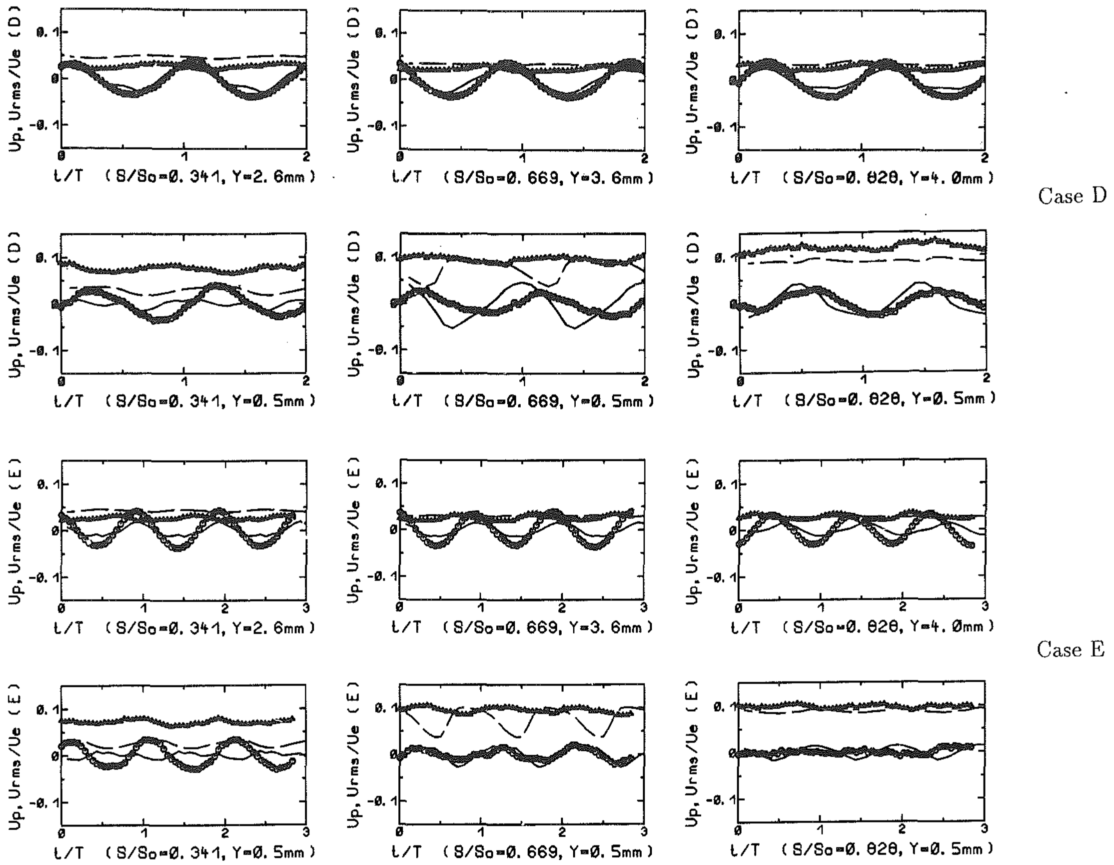

Fig. 11 Cont.

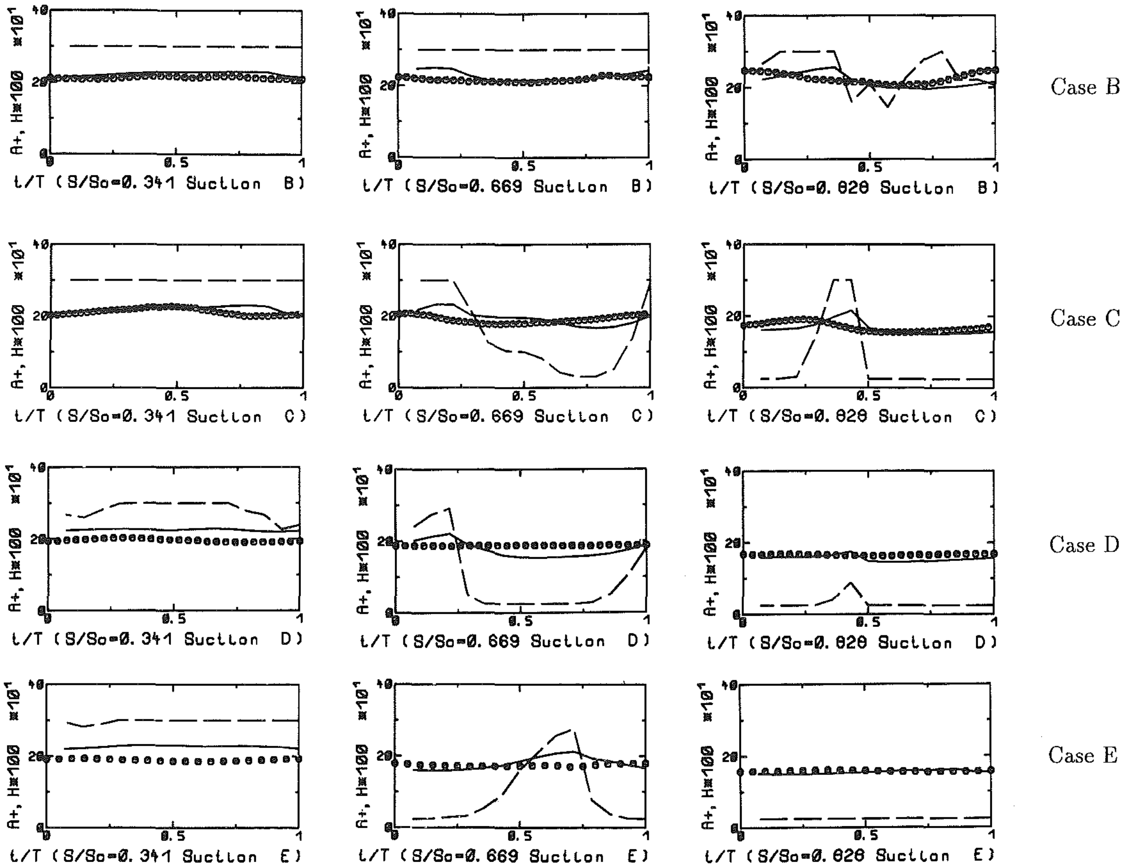

Fig. 12 Time-variation of parameter A^+ (pred. = - - -) and shape factor H (exp. = ○, pred. = ——) on the suction side; cases *B*, *C*, *D*, *E*

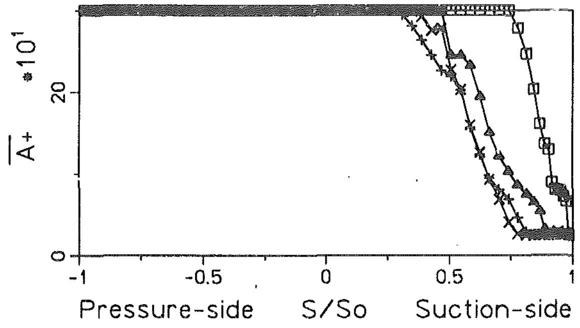

Fig. 13 Variation of the time-mean parameter A^+ along the blade; cases B= □, C= △, D= +, E= ×

For all cases, U_{be} = 19.5, 23.1, and 22.9 m/s at $S/S_o = 0.341$, 0.669, and 0.828 were used, respectively. All the time-dependent profiles are shifted $0.35T$ forward in time so as to match the correct wake location for case C as mentioned above. Some features common to all cases are noted first. The level of turbulence intensity outside the boundary layer is fairly low and responds much less to the passing wakes than the periodic velocity fluctuation. Inside the boundary layers, the turbulence level near the trailing edge, $S/S_o = 0.828$ does also not vary much in time except for cases B and C. This behavior is an indication of whether the flow at the position considered is under transition or mainly turbulent. The variation of the transition parameter A^+ in Fig. 12 shows this rather clearly. The near-wall turbulence intensity in the front part of the blade ($S/S_o = 0.341$) is underpredicted, as was discussed already in connection with Fig. 5. A more refined turbulence model is probably needed to simulate the behavior in this region. At $S/S_o = 0.669$ for cases D and E, the experiment shows a more or less constant, high level of turbulence intensity inside the boundary layer, while the calculations predict much more variation and show a laminar-turbulent intermittency effect in this case (see Fig. 12). However, the peak levels are well reproduced by the prediction. At the same location for cases B and C, both experiment and prediction show an intermittent effect, as was illustrated for case C already in Fig. 9.

Figure 12 shows the temporal variation of the transition parameter A^+ on the suction side for all unsteady cases. In the steady case A, the parameter A^+ was constant at the laminar value of 300 at all times. For case B, the boundary layer is still laminar at $S/S_o = 0.669$ and at $S/S_o = 0.828$ it is transitional about half of the time. As the wake-passing frequency increases, transition starts earlier. For case C at $S/S_o = 0.669$, the boundary layer is transitional over more than 70 percent of the cycle and at $S/S_o = 0.828$ it is fully turbulent over 70 percent of the cycle. At even higher frequencies, the flow becomes transitional already at the first station, is mainly turbulent already at the second station, and almost entirely so at the last one. On the pressure side, the parameter A^+ maintained a laminar value of 300 over the full blade length for all cases. This is in agreement with the experiments, which also indicate that the boundary layer remained laminar on the pressure side for all cases.

Finally, Fig. 13 presents the distribution of the calculated time-mean value of $\overline{A^+}$ on both sides of the blade. On the pressure side, the value is of course, 300, as mentioned already. On the suction side for case B with the lowest wake-passing frequency, $\overline{A^+}$ starts falling from the laminar value at $S/S_o \approx 0.75$ and approaches the turbulent value of 25 at the trailing edge. In case C, $\overline{A^+}$ starts to drop already at $S/S_o = 0.5$, indicating the start of transition. The $\overline{A^+}$ distribution indicates here that transition is complete near the trailing edge. In cases D and E, transition starts at $S/S_o \approx 0.3$ and is complete after $S/S_o \approx 0.8$ according to the $\overline{A^+}$ distribution. From the experiments, the starting points of transition were found to lie at $S/S_o = 0.7 \sim 0.8$ for case B, $0.5 \sim 0.6$ for case C, $0.3 \sim 0.6$ for case D, and $0.2 \sim 0.5$ for case E. Hence, the present calculations reproduce the transition locations reasonably well.

4 Conclusions

Two-dimensional unsteady flow in a linear turbine cascade with periodic wakes passing at various frequencies was calculated, simulating an experiment in which the wakes were generated by a rotating squirrel cage. Turbulence effects were simulated with a two-layer turbulence model, which involves a transition model based on Abu-Ghannam and Shaw's (1980) correlation applied in a Lagrangian way. The unsteady flow equations were solved with a finite-volume procedure using second-order accurate time and space discretization. The use of accurate discretization is absolutely essential for simulating the travel of the wakes through the cascade channel; lower-order discretization was found to introduce so much numerical diffusion that the wakes loose their identity shortly after the inlet plane.

With the computational model employed, the complex unsteady flow phenomena could be simulated fairly realistically. The predicted movement of the wakes through the cascade channel and their merging with the wakes generated at the trailing edge of the blades are in good qualitative agreement with the measurements. The temporal variation of periodic and ensemble-averaged turbulent fluctuations throughout the channel was reproduced reasonably well, even though there were some discrepancies concerning the time lag, which may be more due to experimental uncertainties. The main features of the boundary layer development and in particular the integral parameters are also well reproduced. For the case without passing wakes, the boundary layers remained laminar, and they did so also on the pressure side of the blade for all cases with passing wakes. In agreement with the experiments, transition was predicted on the suction side for the cases with passing wakes, the transition region moving forward as the wake frequency increases. There is generally good agreement about the beginning and the extent of transition. In the front part of the suction side, the turbulence intensity near the wall is intermittent, with high values when the wakes pass and low values in between, but the turbulence level during the wake-passing periods is underpredicted. On the other hand, judging from the integral parameters, the boundary layer state does not vary with time, i.e. it does not change from a laminar to a turbulent state during one cycle, which is due to the acceleration over most parts of the blade. The calculations produce a somewhat stronger temporal variation of the integral parameters than was measured. Also, the turbulence level between the wakes is underpredicted. On the whole, the pressure distribution is reproduced fairly well.

The underprediction of the turbulence intensity near the wall in the front part of the suction side does not impair the flow predictions because the boundary layer is very thin in this region. However, the heat transfer to the blade is strongly affected by this turbulence: The experiments of Liu and Rodi (1991b, 1992) have shown that in blade regions with laminar boundary layer the heat transfer increased significantly when background turbulence and wake-passing frequency were increased. With the present simple turbulence model this effect cannot be simulated. When the boundary layer is laminar, this model assumes a large value of the parameter A^+ leading to a very strong damping of the turbulence inside the laminar boundary layer. A more refined model has to be developed that allows the turbulence inflicted on a laminar boundary layer to penetrate into this layer.

Acknowledgments

The work reported here was sponsored by the Forschungsvereinigung Verbrennungskraftmaschinen e.V. and by the German Federal Ministry of Research and Technology through Program TURBOTECH under Contract No. 0326801G. The authors should like to thank Mrs. R. Zschernitz for her expert typing of the text.

References

Abhari, R. S., Guenette, G. R., Epstein, A. H., and Giles, M. B., 1992, "Comparison of Time-Resolved Turbine Rotor Blade Heat Transfer Measurements and Numerical Calculations," ASME Journal of Turbomachinery, Vol. 114, pp. 818–827.

Abu-Ghannam, B. J., and Shaw, R., 1980, "Natural Transition of Boundary Layers—The Effects of Turbulence, Pressure Gradient, and Flow History," *Journal of Mechanical Engineering Science*, Vol. 22, No. 5, pp. 213–228.

Addison, J. S., and Hodson, H. P., 1990a, "Unsteady Transition in an Axial Flow Turbine: Part 1—Measurements on the Turbine Rotor," ASME Journal of Turbomachinery, Vol. 112, pp. 206–214.

Addison, J. S., and Hodson, H. P., 1990b, "Unsteady Transition in an Axial Flow Turbine: Part 2—Cascade Measurements and Modeling," ASME Journal of Turbomachinery, Vol. 112, pp. 215–221.

Crawford, M. E., and Kays, W. M., 1976, "STAN5—A Program for Numerical Computation of Two-Dimensional Internal and External Boundary Layer Flow," NASA CR-2742.

Doorly, D. J., and Oldfield, M. L. G., 1985, "Simulation of the Effects of Shock Wave Passing on a Turbine Rotor Blade," ASME *Journal of Engineering for Gas Turbines and Power*, Vol. 107, pp. 998–1006.

Giles, M., and Haimes, R., 1993, "Validation of a Numerical Method for Unsteady Flow Calculation," ASME Journal of Turbomachinery, Vol. 115, pp. 110–117.

Leonard, B. P., 1979, "A Stable and Accurate Convective Modelling Procedure Based on Quadratic Upstream Interpolation," *Computational Methods in Applied Mechanics and Engineering*, Vol. 19, pp. 59–98.

Liu, X., and Rodi, W., 1991a, "Experiments on Transitional Boundary Layers With Wake-Induced Unsteadiness," *Journal of Fluid Mechanics*, Vol. 231, pp. 229–256.

Liu, X., and Rodi, W., 1991b, "Unsteady Flow and Heat Transfer in a Linear Turbine Cascade," Institute for Hydromechanics, University of Karlsruhe, Report No. 683.

Liu, X., and Rodi, W., 1992, "Measurement of Unsteady Flow and Heat Transfer in a Linear Turbine Cascade," ASME Paper No. 92-GT-323.

Mayle, R. E., and Dullenkopf, K., 1990, "A Theory for Wake-Induced Transition," ASME Journal of Turbomachinery, Vol. 112, pp. 188–195.

Naar, M., and Schönung, B., 1986, "Numerische Gittererzeugung bei Vorgabe von Randwinkeln und Randmaschenweiten," Institut für Hydromechanik, Universität Karlsruhe, Bericht No. 644.

Norris, H. L., and Reynolds, W. C., 1975, "Turbulent Channel Flow With a Moving Wavy Boundary," Stanford University, Dept. of Mechanical Eng., Report FM-10.

Rhie, C. M., and Chow, W. L., 1983, "A Numerical Study of the Turbulent Flow Past an Isolated Airfoil With Trailing Edge Separation," *AIAA Journal*, Vol. 21, pp. 1525–1532.

Rodi, W., Majumdar, S., and Schönung, B., 1989, "Finite Volume Methods for Two-Dimensional Incompressible Flows With Complex Boundaries," *Computer Methods in Applied Mechanics and Engineering*, Vol. 75, pp. 369–392.

Rodi, W., Liu, X., and Schönung, B., 1989, "Transitional Boundary Layers With Wake-Induced Unsteadiness," *Proc. 4th Symp. on Numerical and Physical Aspects of Aerodynamic Flows*, Long Beach, CA.

Rodi, W., 1991, "Experience With Two-Layer Models Combining the k-ϵ Model With a One-Equation Model Near the Wall," AIAA Paper No. 91-0216.

Schönung, B., 1989, "PIGAT—Periodisch instantationare Grenzschichten an Turbinenschaufeln," Programmbeschreibung, Institut für Hydromechanik, Universität Karlsruhe, Federal Republic of Germany.

Scott, J. N., and Hankey, W. L., Jr., 1986, "Navier-Stokes Solutions of Unsteady Flow in Compressor Rotor," ASME Journal of Turbomachinery, Vol. 108, pp. 206–215.

Sharma, O. P, Renaud, E., Butler, T. L., Milsaps, K., Jr., Dring, R. P., and Joslyn, H. D., 1988, "Rotor-Stator Interaction in Axial-Flow Turbines," AIAA Paper No. 88-3013.

Stone, H. L., 1968, "Iterative Solution of Implicit Approximation of Multidimensional Partial Differential Equation," *SIAM Journal of Numerical Analysis*, Vol. 5, No. 3, pp. 530–558.

Tran, L. T., and Taulbee, D. B., 1992, "Prediction of Unsteady Rotor-Surface Pressure and Heat Transfer From Wake Passings," ASME Journal of Turbomachinery, Vol. 114, pp. 807–817.

Van Doormal, J. P., and Raithby, G. D., 1994, "Enhancements of the SIMPLE Method for Predicting Incompressible Fluid Flow," *Numerical Heat Transfer*, Vol. 7, pp. 147–163.

Zhu, J., 1991, "A Low-Diffusive and Oscillation-Free Convection Scheme," *Communications in Applied Numerical Methods*, Vol. 7, pp. 225–232.

J. C. Collie

H. L. Moses

J. A. Schetz

Virginia Polytechnic Institute and State
University,
Blacksburg, VA 24061-0238

B. A. Gregory

Turbine Aero & Cooling Technology,
General Electric Aircraft Engines,
Cincinnati, OH 45249

Recent Advances in Simulating Unsteady Flow Phenomena Brought About by Passage of Shock Waves in a Linear Turbine Cascade

High-pressure-ratio turbines have flows dominated by shock structures that pass downstream into the next blade row in an unsteady fashion. Recent numerical results have indicated that these unsteady shocks may significantly affect the aerodynamic and mechanical performance of turbine blading. High cost and limited accessibility of turbine rotating equipment severely restrict the quantitative evaluation of the unsteady flowfield in that environment. Recently published results of the Virginia Tech transonic cascade facility indicate high integrity in simulation of the steady-state flow phenomena. The facility has recently been modified to study the unsteady effects of passing shock waves. Shock waves are generated by a shotgun blast upstream of the blade row. Shadowgraph photos and high-response pressure data are compared to previously published experimental and numerically predicted results. Plots are included that indicate large fluctuations in estimated blade lift and cascade loss.

Introduction

During the past decade, aircraft gas turbine engine designers have become increasingly interested in unsteady effects on turbine blade performance. Numerous studies have been published indicating that unsteady flow phenomena in the turbine stages have significant effects on blade performance. As a result, the general design assumptions of steady or quasi-steady flow have fallen under increasing scrutiny. In response to these relatively new findings, turbine blade designers are currently attempting to incorporate knowledge of unsteady flow behavior into new designs. Therefore, the demand for experimental data on unsteady phenomena in turbine stages has risen dramatically.

As described by Doorly and Oldfield (1985a), three major sources of flow unsteadiness exist in the interaction between turbine rotor and stator rows. Two of these, potential interaction and wake-passing effects, have received considerable attention in published literature. The third source of unsteadiness, shock-wave passing, has received somewhat less attention, especially in the areas of blade lift and profile loss. Therefore, it was the purpose of this research effort to develop an experimental method for advancement of the current understanding of unsteady shock wave effects on lift and loss of transonic turbine blading, and the cited literature is limited to these effects.

Shock waves produced at the trailing edges of transonic turbine rotor and stator blades impinge directly on the downstream blade row in an unsteady fashion. This periodic "chopping" of blades through the shock waves has been shown to have considerable effects on blade surface pressures and heat transfer (Doorly and Oldfield, 1985a; Ashworth et al., 1985; Johnson et al., 1989a, 1989b, 1990; Giles, 1990). It has been proposed by Giles (1990) that significant fluctuations in blade lift and a subsequent increase in stage loss may also result from this unsteady shock wave passage. In any case, very limited experimental information is currently available concerning unsteady shock effects on blade lift and loss.

There are a number of fully rotating rigs in operation, and these have an essential role in research. However, the use of these rigs for detailed studies of shock wave effects is severely limited by high cost and mechanical complexities, especially if a number of blade shapes is considered. Furthermore, as mentioned by Doorly and Oldfield (1985b), difficulties in flow visualization and instrumentation of rotating rigs are additional handicaps. Researchers at Oxford University have made use of a rotating bar shock generator in simulating the unsteady shock wave propagation of an actual transonic turbine engine (Doorly and Oldfield, 1985a, 1985b; Ashworth et al., 1985; Johnson et al., 1989a, 1989b, 1990). It was therefore an objective of this Virginia Tech research project to develop a

---

Contributed by the International Gas Turbine Institute and presented at the 37th International Gas Turbine and Aeroengine Congress and Exposition, Cologne, Germany, June 1-4, 1992. Manuscript received by the International Gas Turbine Institute January 13, 1992. Paper No. 92-GT-4. Associate Technical Editor: L. S. Langston.

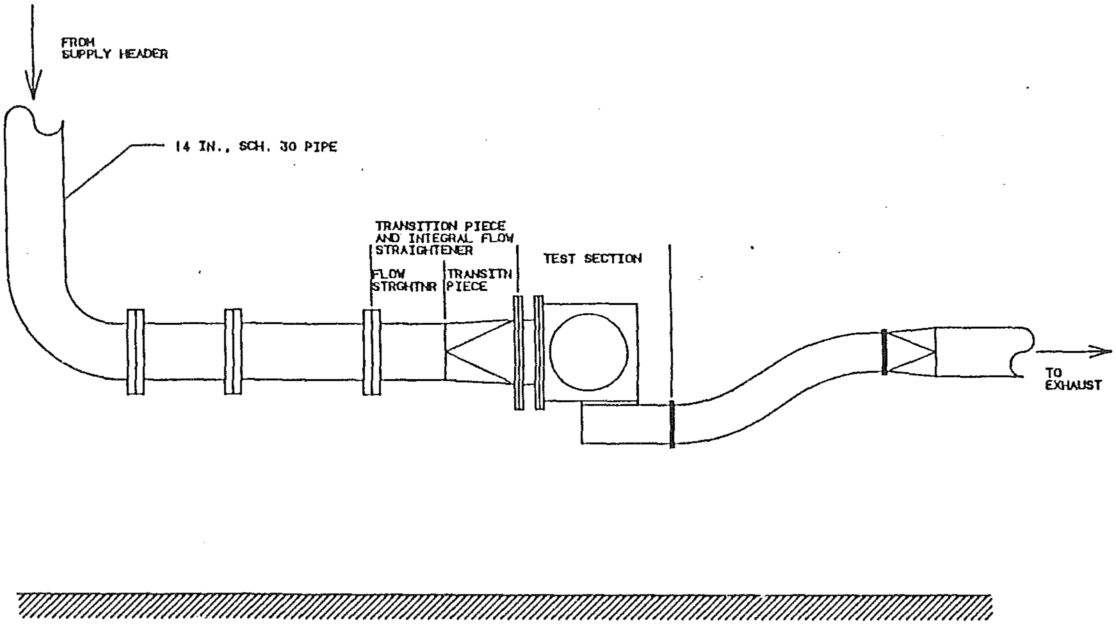

Fig. 1 Schematic: Virginia Tech transonic cascade wind tunnel

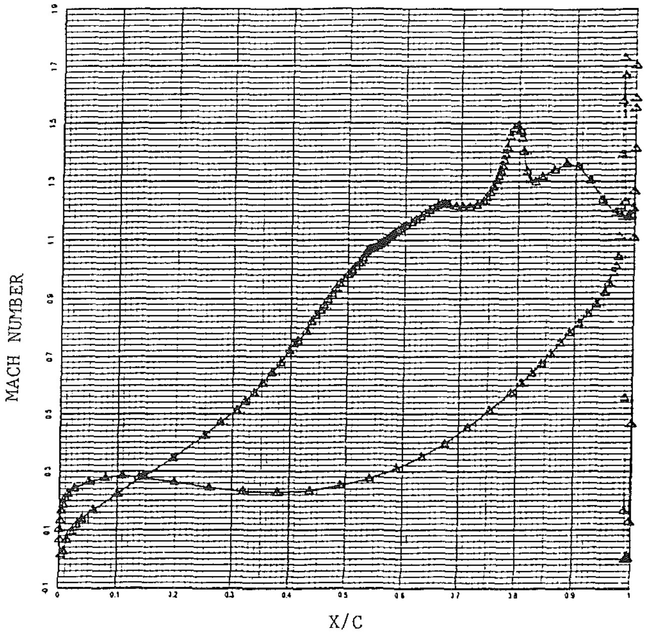

Fig. 2 Numerically predicted blade surface Mach number versus normalized axial distance

similar or alternate means of simulating the shock wave/blade interaction for implementation in the Virginia Tech Wind Tunnel Transonic Cascade Facility.

Test Facility

The Virginia Tech Wind Tunnel Transonic Cascade Facility is a blowdown-type tunnel fed by four large, reciprocating compressors via storage tanks. Flow conditions to the test section are controlled by a pneumatic, electronic feedback-controlled valve. The tunnel is typically capable of 18 second run times. Figure 1 is a schematic of the wind tunnel indicating the main features of the facility. More detailed explanations of the wind tunnel facility are provided by Bertsch (1990) and Doughty (1991).

The experiment was intended to be general insofar as the turbine blade profile selection. In an actual transonic turbine stage, both the rotor and stator rows experience the effects of unsteady shock waves from upstream blades. Therefore, selection of rotor versus stator blading was not considered to be critical. An existing cascade of turbine blades, which had previously undergone steady-state tunnel tests, was chosen for this experiment. These blades were approximately one third larger than the turbine rotor blades of a modern transonic turbine engine and were modified at the leading edge for zero degree inlet and incidence angles in the tunnel. Blade dimensions include an axial chord of 3.81 cm, true chord of 4.61 cm, and blade spacing of 3.72 cm. Figure 2 is a plot of the calculated blade surface Mach number distribution for the modified blade under steady flow conditions.

Figure 3 shows a schematic of the cascade test section. As indicated, the vertical cascade consists of eleven blades numbered 1 to 11 from bottom to top. Blade passages are lettered A to J, also from bottom to top. Also shown in Fig. 3 are two sets of static pressure taps located just downstream of the cascade in one of the plexiglass endwalls. The taps located 6.35 mm in the axial direction behind the cascade are used to measure the isentropic exit Mach number for each run; this number is computed based on the average of the 13 taps ratioed with the cascade upstream total pressure. The second set of taps shown in Fig. 3 was not utilized in this experiment. For information regarding the data acquisition system used to obtain the isentropic Mach number measurement, refer to Bertsch (1990). Discussion of the other components of Fig. 3 is included in a later section of this paper.

Figure 4 is a shadowgraph photo of the blades under steady-state flow conditions at a near-design Mach number of 1.16. Arrows are included to indicate trailing edge shock waves. The reader is warned not to confuse the shock waves with the static pressure tap tubing in the photograph. The nearly horizontal shock waves emanating from the blade trailing edges are the shocks, which produce the unsteady effect on the downstream blade row in an actual turbine engine. Corresponding shocks from transonic *stator* blading would be very similar in structure to the rotor blade shocks of Fig. 4.

Experimental Method

Capability for reliable, steady-state, transonic turbine cas-

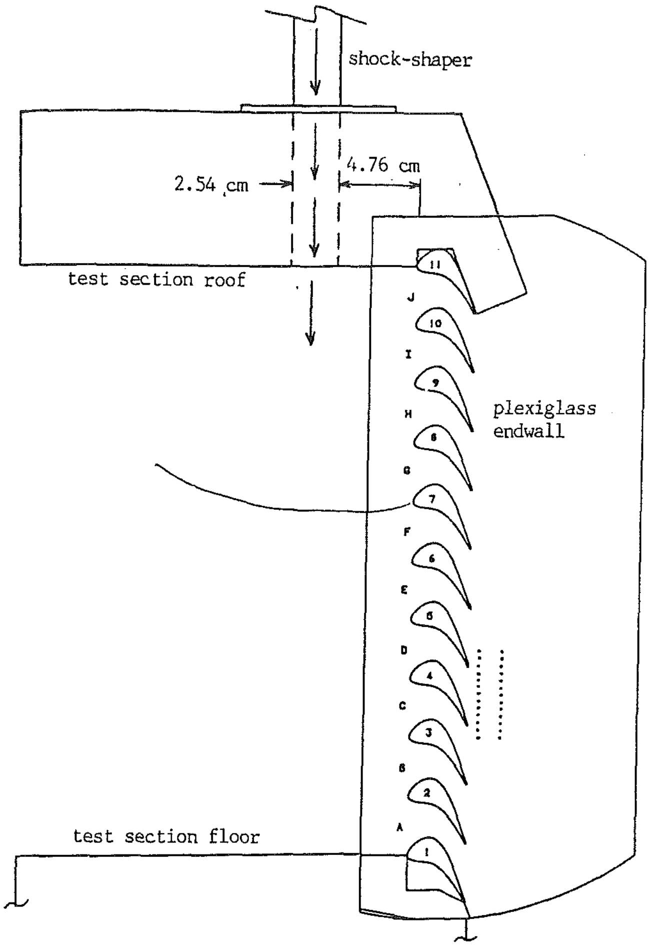

Fig. 3 Schematic: tunnel-mounted shock generation system as viewed normal to flow direction

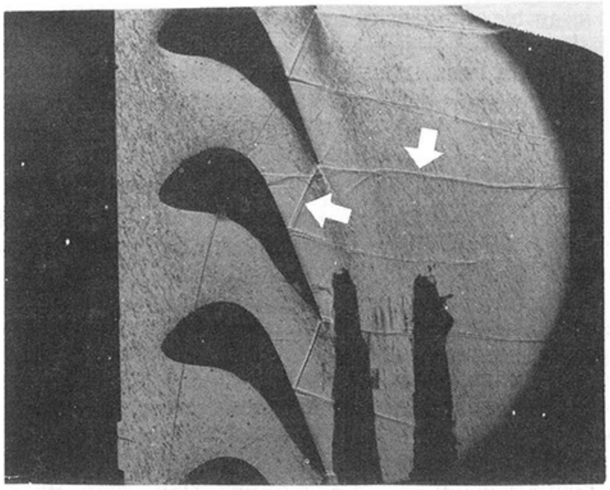

Fig. 4 Shadowgraph: cascade under steady-flow conditions at $M = 1.16$; arrows indicate trailing edge shocks

cade measurements has existed for the past several years at the VT Transonic Cascade Facility. Results from previous studies have been published by Collie et al. (1991) and Moses et al. (1991a). An overall review of the facility and its capabilities is presented by Moses et al. (1991b). Furthermore, Doughty et al. (1992) include results from a recent solidity study. However, no capability previously existed for study of unsteady shock wave passing effects on transonic cascades at the Virginia Tech facility. Therefore, development of experimental test apparatus was necessary before any data on shock effects could be obtained. A brief description of the shock-generation hardware and associated optical systems follows. For a more detailed discussion of the hardware development and assessment, please refer to the Master's thesis of Collie (1991).

Shadowgraph Optical System. In order to assess the characteristics of the extremely high-speed unsteady shock wave propagation, a shadowgraph optical system was developed. A major requirement of the shadowgraph system was the capability to synchronize its light source flash accurately with any specific position along the shock wave propagation. This feature would be particularly necessary in obtaining a detailed sequence of shadowgraphs to indicate the shock propagation patterns. Therefore, an electronic time-delay circuit was developed to control the timing of the light source flash. This circuit was designed to receive activation by a shock wave-induced voltage spike. The circuit could be user-adjusted to synchronize the light flash accurately with any desired shock location along its propagation. Effective operation of the shadowgraph system proved to be essential to both the development of the shock-generating equipment and analysis of the unsteady shock propagation across the blade row. A sequence of shadowgraph pictures taken with this arrangement is presented in the results section of this paper.

Shock Wave Generation. Several alternatives for producing unsteady effects in wind tunnels have appeared in previous literature. The most notable device for shock wave generation to date was designed by Doorly at Oxford University and is discussed by Doorly and Oldfield (1985a, 1985b) and Doorly (1983). This rotating bar shock generator consists of a circular array of stranded steel wires, all cantilevered from a central disk. The wires are spun through the wind tunnel test section at supersonic relative Mach numbers, producing unsteady, periodic shock waves. The rotating bar shock generator has evidently performed very well, and has led to significant advances in the understanding of unsteady wake and shock effects. Although the complexities of this system are not extreme, an even simpler means of unsteady shock production was sought for the present study. This project was intended to provide introductory insight into unsteady shock effects on blade lift and loss, so it was desired to keep developmental time relatively low. Other designs such as the "squirrel-cage" devices of Pfeil et al. (1983) and Priddy and Bayley (1985, 1988) were considered, but these also suffered from similar mechanical complexities as the rotating bar apparatus.

The final selection of a shock generation method was actually a variation on the shock tube system of Merritt and Aronson (1967). Utilizing a pressure-burst diaphragm shock tube, they were able to generate variable-strength single shock waves, which could be shaped and directed to travel as desired into a supersonic wind tunnel test section. This method of shock generation is somewhat limited to single-shot shock production, a disadvantage as compared to the rotating arrangements. However, production of *repeatable* single shocks could be a workable solution since data from separate shocks could be compared and coupled. Overall, design and construction of a shock tube system would be less costly and time-intensive than any of the previously discussed mechanisms.

The Virginia Tech apparatus consists of a 12-gage shotgun, which operates in a very similar manner to the shock tube of Merritt and Aronson (1967). The explosion from the shotgun shell creates a blast wave, which can be shaped and directed over the cascade test section in the wind tunnel. Just as in the shock tube system, the shotgun produces single shock waves rather than the periodically passing shocks of the rotating arrangements. Very minor modification was necessary to the shotgun itself, and total cost and mechanical complexity of the system is minimal.

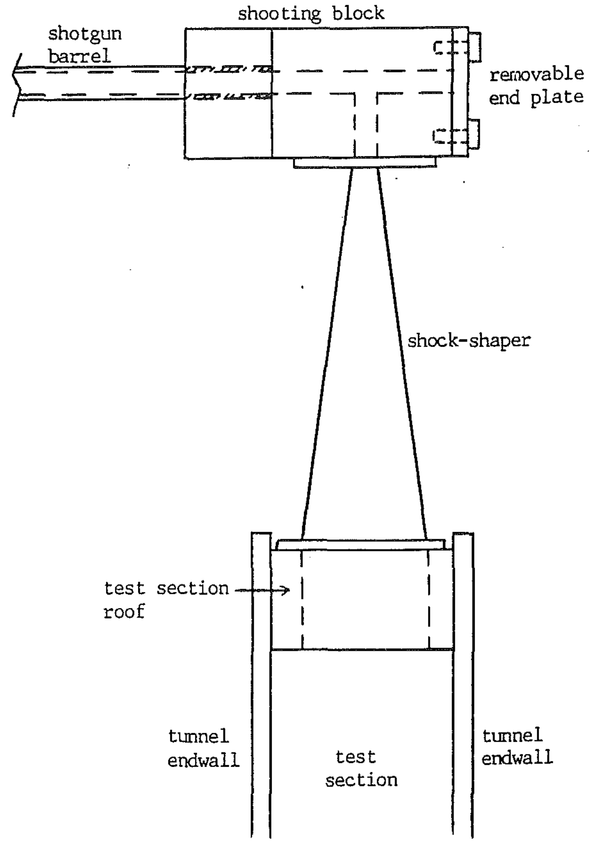

Fig. 5 Schematic: tunnel-mounted shock generation system as viewed along flow direction

A standard 12-gage shotgun was modified by replacing the stock of the gun with an AC solenoid actuator. A hand-operated electronic switch is connected to the solenoid through a small power supply and solid-state relay. Throwing of the switch activates the solenoid, which in turn pulls the shotgun trigger via a single-bar linkage. Winchester X12-FBL "Popper-Load" blank shotgun shells were used in all of the wind tunnel tests due to their excellent repeatability and relatively non-destructive barrel emission.

In an actual turbine, the relative motion between the stator blade trailing edge shock waves and the rotor blades is such that the waves move from the suction side of the rotor blades toward the pressure side. Proper simulation of this movement in the wind tunnel requires passage of the shock wave from top to bottom of the cascade. Therefore, the shotgun system was mounted on the roof of the test section as shown in the schematics of Figs. 3 and 5. Figure 5 indicates the components of the shock-generation system and the path of the shock wave. The shock wave is generated originally by the explosion of the shell. The shock travels down the gun barrel and into the aluminum shooting block. The circular channel within the shooting block is branched to allow for isolation of the shock wave from the shell-packing residue: The shock proceeds downward into the lower pressure test section while the residue, which cannot negotiate the sharp bend, accumulates at the plugged end of the passage. The shock wave then travels through the diverging "shock-shaper," which made the wave nearly two dimensional for better simulation of actual trailing edge shock waves. The shock finally passes through a slot in the test section roof and down across the blade row. Figure 3 gives some indication of the shock wave orientation in the test section.

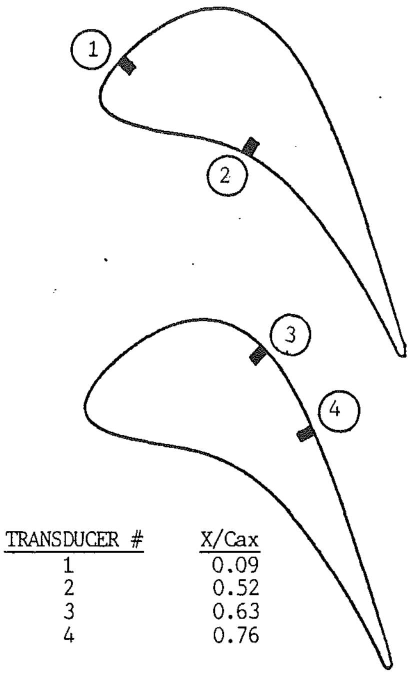

TRANSDUCER #	X/Cax
1	0.09
2	0.52
3	0.63
4	0.76

Fig. 6 Schematic: pressure transducer locations

Extensive preliminary testing in a separate experiment (Collie, 1991) was conducted to ensure that the shock wave generation was of excellent reliability and proper shape. It was confirmed using shadowgraph photos and careful velocity measurements that the repeatability of the shock generation from shot to shot was excellent. Furthermore, the propagation velocity of the shock wave was measured to be approximately 510 m/s as the shock came into contact with the instrumented blades (numbered 4 and 5 on Fig. 3). This translates to a Mach number of approximately 1.5, indicating that the shock was sufficiently strong to simulate unsteady shock passage. Experimentation with varying amounts of shotgun powder in hand-packed shells was conducted, but these shells proved to be incapable of producing repeatable blast waves. Further discussion of this topic is included in the Master's thesis of Collie (1991). It is hoped that future work undertaken at Virginia Tech will include the capability to control the shock strength carefully so that weaker or stronger waves may be studied.

Instrumentation

In order to analyze the unsteady shock wave effects on the cascade blade row quantitatively, pressure instrumentation was utilized. Since the passage of the shock wave and its associated pressure fluctuation were very transient in nature, pressure transducers with extremely fast response characteristics were needed. Therefore, Kulite model XCQ-062 ultraminiature strain gage transducers were chosen for the study. The transducers were rated for 345 kPa maximum absolute pressure, and with protective screens in place, possessed natural frequencies of approximately 52 kHz.

Four Kulite transducers were flush-mounted in the surfaces of blades 4 and 5 (refer to Fig. 3 for the blade positions). Special care was taken in flush-mounting the transducers to avoid disruption of the normal flowfield. The actual transducer locations on the blades are indicated on Fig. 6. Each of the transducers was alternately staggered slightly off of the blade spanwise centerline to avoid possible flowfield disturbances produced by the other transducers. Due to the decreasing blade thickness toward the trailing edge, no transducers could be mounted downstream of #4.

Although the surface transducers could provide a reasonable indication of blade lift, measurements of loss had to be obtained downstream of the cascade. For this purpose, an additional Kulite XCQ-062 transducer, identical to the blade surface models, was mounted in the end of a small total pressure probe. This probe could be moved vertically downstream of the cascade in any horizontal location. The probe transducer will be referred to as Kulite #5 in the remainder of this paper. Further discussion of the use of Kulite #5 is included later.

Output of the Kulite transducers was recorded at a 200 kHz sampling frequency using a LeCroy Model 6810 stand-alone data acquisition system. Signal amplification was accomplished using Ektron Model 562 differential amplifiers. Since the Nyquist frequency was higher than the instrumentation response, no pre-filtering techniques were utilized in any of the testing. Some of the tests were repeated at a much higher sampling rate to verify this conclusion.

Experimental Results

This section contains the presentation and discussion of experimental data and shadowgraph photos. Data include unsteady blade surface pressures, approximate unsteady blade lift, downstream unsteady total pressure, unsteady wake pressure profiles, and estimated unsteady pressure loss. All data were recorded at a cascade exit isentropic Mach number of approximately 1.16. Comparisons are made with other related studies wherever applicable. It should be kept in mind that these data are an introductory step into the experimental analysis of shock effects on transonic turbine blade lift and loss. The rough estimates presented for unsteady "lift" and "loss" are not intended to uncover the full picture of blade lift and profile loss. However, they do provide extremely useful insight into the capabilities of analyzing these parameters in a transonic cascade facility with relatively simple shock generation equipment.

Zero Time Base. To facilitate comparison of all forms of data and shadowgraphs, a "zero time base" was established. As a matter of convenience, time-zero was chosen to be the time when the shotgun-generated shock wave first contacted Kulite #1. This time could easily be identified on the pressure data for all transducers since Kulite #1 data were recorded for every run and all data channels were sampled simultaneously by the LeCroy. In addition, the output from Kulite #1 was supplied to the shadowgraph system time-delay circuit, allowing the sudden shock-induced voltage spike to trigger the light source. Therefore, since the shadowgraph light source was triggered by Kulite #1, accurate calibration of the time-delay circuit allowed for establishment of a corresponding time-zero in all photos. Therefore, all time values appearing in the shadowgraphs and plots of this paper are based on the identical time-zero, permitting direct comparison of the entire set of results.

Shadowgraph Photos. Figure 7 is a sequence of 12 shadowgraphs, which capture the unsteady shock propagation through the cascade. The cascade isentropic exit Mach number was approximately 1.16 in all of these photos. In all cases, the two blades pictured fully are the instrumented blades (#4 and #5 as shown in Fig. 3). As presented previously, Fig. 4 shows the cascade under steady flow with no shock generation. The pair of trailing edge shock waves from each blade are clearly evident. Furthermore, the pair of thick dark lines positioned vertically and passing through each of the passages is unfortunately a scratch in the plexiglass cascade endwall. (Be careful not to confuse this scratch with any of the shock waves shown in the Fig. 7 pictures.) Finally, a discontinuity in the suction surface of blade #5 at approximately $X/C_{ax}=0.5$ produces a Mach wave, which appears in all shadowgraphs of Figs. 4 and 7. Please avoid confusion of this wave with the unsteady shotgun-generated shock wave.

In order to facilitate discussion of the unsteady shock propagation shown in Fig. 7, the illustration of Fig. 8 is included. Adapted directly from the shadowgraphs of Fig. 7, Fig. 8 provides a clearer representation of the shock propagation. It is especially helpful considering the complexity of the propagation patterns. In all the Fig. 8 sketches, the blades shown are the instrumented blades #4 and #5. Only one blade passage is shown in Fig. 8 to avoid confusion. However, it should be kept in mind while studying Fig. 8 that shock activity does occur simultaneously above and below these blades, as shown in Fig. 7. In fact, due to excellent periodicity between passages, information from passages E and F (refer to Fig. 3) is actually incorporated into Fig. 8. Therefore, frames *l*–*q* of Fig. 8 are actually "extrapolated" from the shock patterns of the upper passages shown in earlier frames. The small arrows included in Fig. 8 illustrate the direction of shock movement within each frame.

Figure 8(*a*) shows the earliest position in the propagation sequence that could be captured by the shadowgraph system. The primary shock wave, labeled *a*, is positioned within the passage, and a small reflection *b* is formed at the pressure surface impingement point. The shock that branches from the primary shock at the left of Fig. 8(*a*), labeled *d*, is a reflected wave and will be discussed below. In Fig. 8(*b*), the primary shock *a* has now moved down into contact with the suction surface crown of the lower blade. As indicated, a reflected wave *d* is formed, which begins to move in the direction opposite to the primary shock. At this point, the primary shock has been divided, with segment *a* moving along the suction surface toward the leading edge and segment *e* toward the trailing edge.

Figure 8(*c*) shows the shock positions 25 ms later. The primary wave *a* is now positioned at the blade leading edge with the reflected wave *d* having moved back fully into the passage. The second segment *e* of the primary shock has now propagated to nearly the end of the passage, with its pressure surface reflection *b* seemingly larger at this time. At time = 108 ms, Fig. 8(*d*) shows the primary shock *a* to have moved around the leading edge of the lower blade. A shock bifurcation *f*, as discussed thoroughly by Johnson et al. (1989b, 1990), is clearly evident. This bifurcation developed as the angle of the reflected shock *d* with the blade suction surface grew dramatically near the leading edge. Also in Fig. 8(*d*), the reflected wave *d* has moved completely across the passage and is now in contact with the pressure surface of the upper blade at *g*. A second reflection *h* occurs at the pressure surface and is shown to move back in the direction of the lower blade. Segment *e* of the primary shock wave has moved out of the passage and is shown at the rear suction surface of the lower blade, approaching the trailing edge.

Figure 8(*d*) also indicates the development of a small region of interest, labeled *i*, on the pressure surface near the upper blade leading edge. This region is consistent with the "vortical bubble" formation as discussed fully by Johnson et al. (1990). As described by Johnson, the shock wave bifurcation at the leading edge produces a vortex sheet which rolls up and attaches to the blade leading edge. Depending on the leading edge blade geometry and other factors, this vortical region is convected back along either the pressure or suction surface. Johnson proposed the vortical bubble idea as an explanation of the large heat transfer spikes found in earlier studies (Doorly and Oldfield, 1985a; Ashworth et al., 1985; Johnson et al., 1989a, 1989b). The powerful vortex contained within the vortical region acts to pull hot gases from the free-stream flow into the boundary layer. This argument was in contrast to earlier explanations by Doorly and Oldfield (1985a), which described the region as a "separation bubble."

Figure 8(*e*), at time = 121 ms, shows the primary shock *a* approximately one complete blade spacing below its location in Fig. 8(*a*). The reflected shock *d*, which began at the crown of the suction surface in 8(*b*) has moved almost completely out of the passage, with its second reflection *h* shown almost

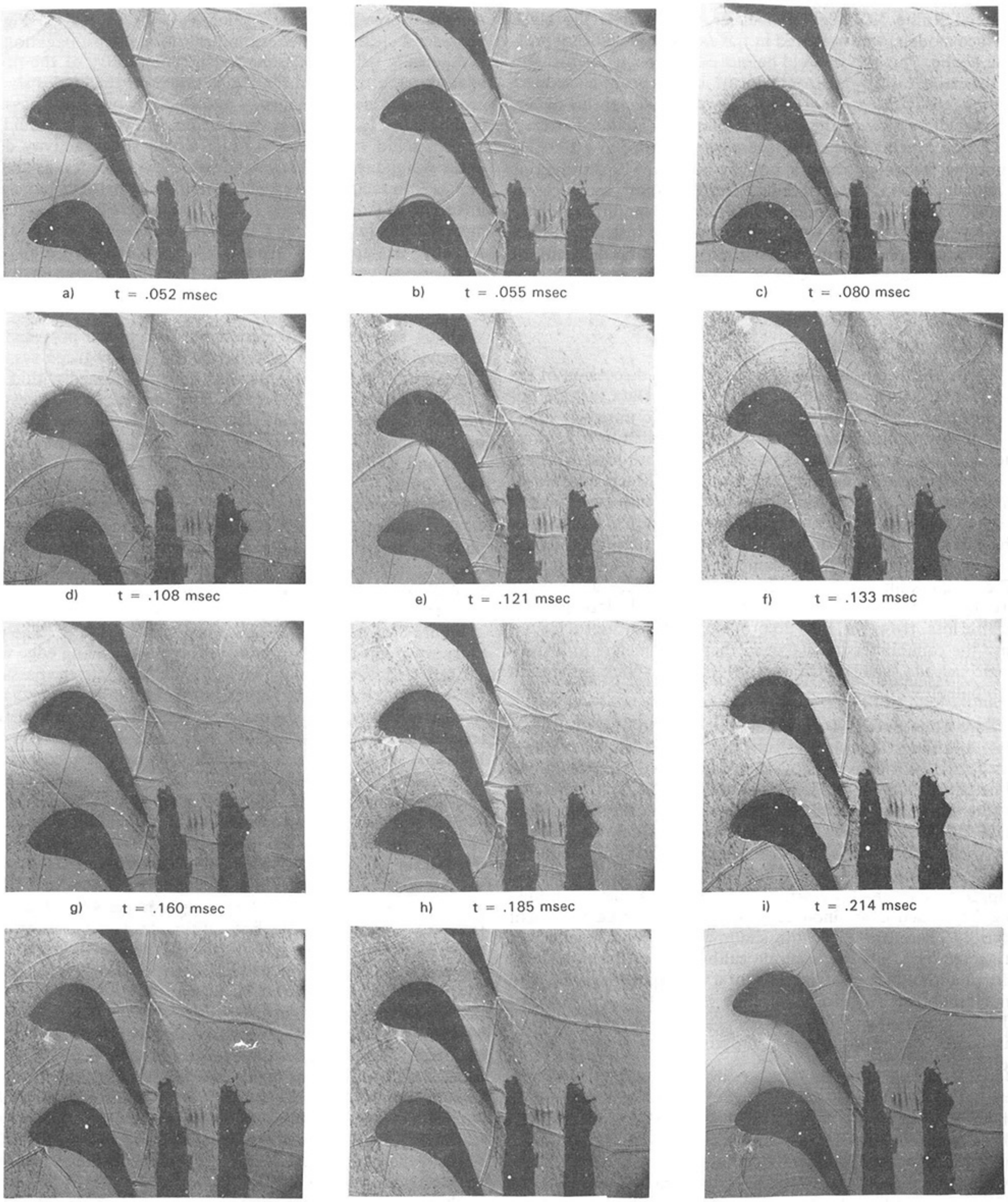

a) t = .052 msec

b) t = .055 msec

c) t = .080 msec

d) t = .108 msec

e) t = .121 msec

f) t = .133 msec

g) t = .160 msec

h) t = .185 msec

i) t = .214 msec

j) t = .243 msec

k) t = .270 msec

l) t = .295 msec

Fig. 7 Shadowgraphs: cascade unsteady shock passage

in contact with the suction surface once more. Figure 8(*e*) also indicates the first unsteady shock effects on the steady-state trailing edge shock waves. It appears that the steady shock *j*, which impinges on the suction surface of the lower blade, has begun to bend out toward the rear of the passage. This trend continues in the succeeding frames.

It may have become evident to the reader that the vortical region *i* shown in Fig. 8(*e*) does not appear in the corresponding shadowgraph of Fig. 7(*e*). In fact, the vortical region does not reappear in the shadowgraphs until Fig. 7(*h*). However, a set of shadowgraphs taken with an optical interference filter indicates presence of the region clearly throughout this time. Although these shadowgraphs were not of high enough quality to permit inclusion in this paper, they did provide the information necessary to illustrate the vortical region location in Figs. 8(*e*)–8(*g*).

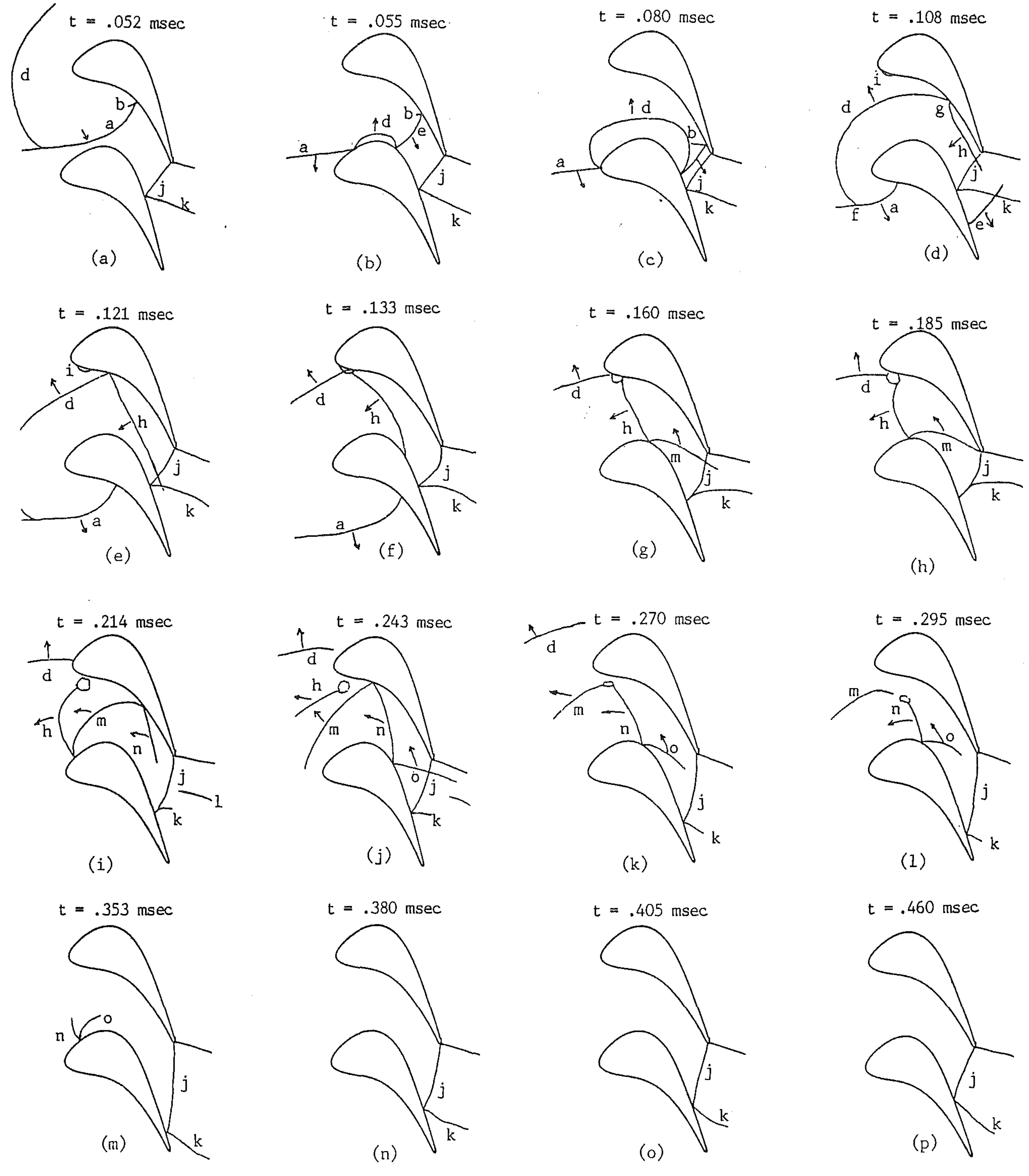

Fig. 8 Shock wave propagation through blade passage

Subsequent shock reflections and re-reflections are apparent in the blade passage until a time of approximately 353 ms (Fig. 8*m*). A description of this shock activity is not included in lieu of the detailed illustrations of Fig. 8. However, several characteristics of the shock behavior that are particularly notable include:

1 The movement of the vortical region away from the pressure surface and into the blade passage as shown in Figs. 8(*i*)–8(*l*);

2 the repeated reflection of shock waves across the blade passage with continually decreasing shock strength;

3 the continuing movement of the lower steady-state trailing edge shock *j* toward the rear of the cascade. This shock becomes almost vertical, as shown in Fig. 8(*m*), and finally recovers back to its original position at time = 510 ms. Furthermore, as shown in Fig. 8(*i*), the reflected steady-state shock *k* actually divides, with segment *i* soon disappearing from view.

Overall, the results presented in Figs. 7 and 8 agree fairly well with the findings of Johnson et al. (1989b). It should be kept in mind while comparing the two studies that the results from Oxford University were obtained using the rotating bar

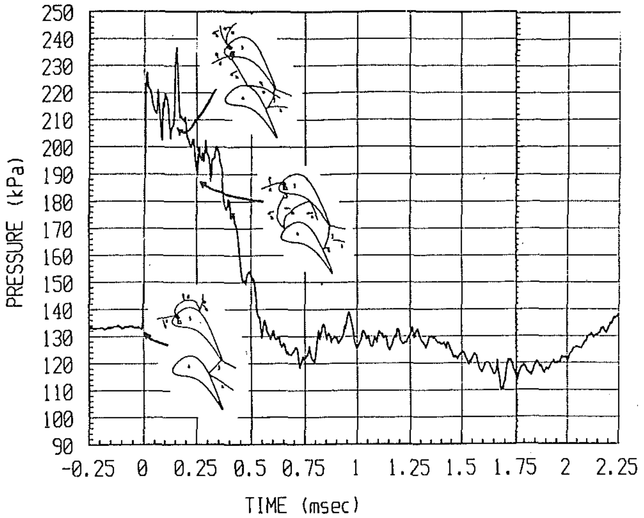

Fig. 9 Absolute pressure versus time for Kulite #1

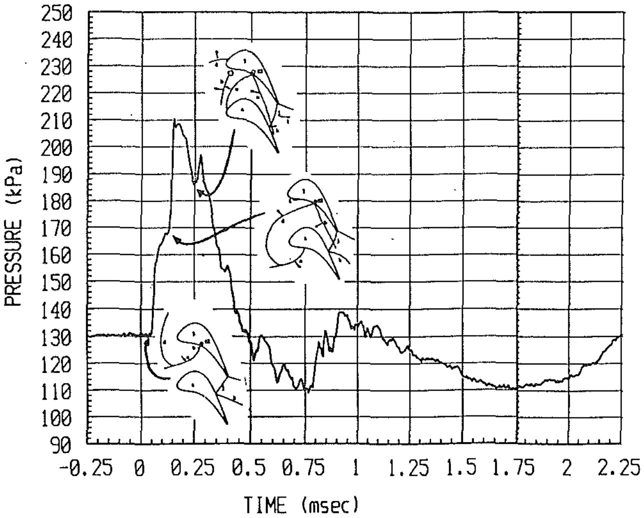

Fig. 10 Absolute pressure versus time for Kulite #2

shock generator, which produces two separate shock waves for each bar. The shotgun method employed in the Virginia Tech study generates only a single shock wave. Several differences do exist between results of the present study and those of Johnson et al. (1989b). First, the "lambda"-type shock reflection introduced by Johnson et al. (1989b) and discussed more fully by Johnson et al. (1990) is not apparent in the results of the Virginia Tech study. Although a reflection *b* is evident in Figs. 8(*a*)-8(*c*) of this paper, it appears to be a regular reflection rather than a lambda shock. However, no "zoomed" shadowgraphs of the pressure surface region were obtained in the Virginia Tech study as they were at Oxford; it is quite possible that the lambda reflection may actually be present and could be apparent in a higher-resolution shadowgraph. These reflections behave otherwise similarly between the two studies.

Other discrepancies occur due to the differences in leading edge geometry of the two studies. Comparing the shock propagation patterns of Fig. 8 with those presented by Johnson et al. (1989b), it is evident that differences do exist in the shock behavior near the blade leading edges. Specifically, the reflected wave *h* of Fig. 8 behaves quite differently than the corresponding shock shown by Johnson et al. (1989b). Furthermore, Johnson et al. (1990) identify the presence of the "vortical bubble," as mentioned previously, but give no indication that it moves off of the pressure surface and into the passage free-stream flow. Results of the Virginia Tech study clearly indicate separation of the vortical region from the pressure surface, as illustrated in Figs. 8(*i*)-8(*l*). It is quite possible that the difference in leading edge geometry may again be responsible for the apparent variation.

Another notable difference between results of the Oxford and Virginia Tech studies concerns the unsteady effects on the behavior of the steady-state trailing edge shock wave. Johnson et al. (1989b, 1990) make no reference to any fluctuation in the trailing edge shock waves during the unsteady shock passage. As noted previously, results of the present study indicate strong effect on the trailing edge shock wave *j* in Fig. 8. However, discussion included in the Oxford reports is limited to a shorter portion of the shock passage cycle than that contained in Figs. 7 and 8 of this paper.

No other experimentally based detailed illustrations or pictures of the unsteady shock propagation could be located in previously published literature. Giles (1990), however, presents numerically generated results based on the unsteady inviscid Euler equations. Giles' illustrations show reasonable agreement with the results of this paper as presented in Figs. 7 and 8. Giles' results do show somewhat fewer shock reflections within the blade passage during the unsteady shock cycle. Furthermore, Giles makes no mention of the vortical region, the lambda shock, or any trailing edge shock fluctuations. Further discussion of Giles' results is contained in sections to follow.

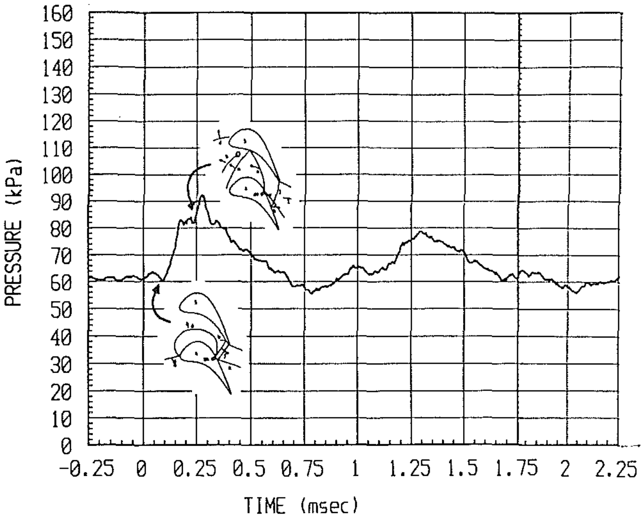

Fig. 11 Absolute pressure versus time for Kulite #4

Unsteady Blade Surface Pressures

Surface Pressure Traces. As explained, unsteady blade surface pressure measurements were obtained at the locations as specified in Fig. 6. Data from Kulite #3, however, are not presented due to spurious electrical fluctuations, which rendered then useless. Figures 9-11 are plots of the surface pressures from Kulites 1, 2, and 4, respectively. In each of these plots, *absolute* pressure is plotted in kPa and time in milliseconds. As described earlier, time-zero is identical in all plots as well as in the shadowgraphs and illustrations of Figs. 7 and 8. Figures 9-11 each show pressure from time = −0.25 ms to time = 3.75 ms. No significant data fluctuations occurred at times greater than 3.75 for any of the transducers.

Due to the consistency in time-zero throughout the data, the pressure histories from Figs. 9-11 can be correlated with the illustrations of Fig. 8 to aid in identifying the various pressure peaks. Therefore, appropriate illustrations have been included on Figs. 9-11, identifying the shock positions responsible for the specific pressure spikes noted. All data presented in Figs.

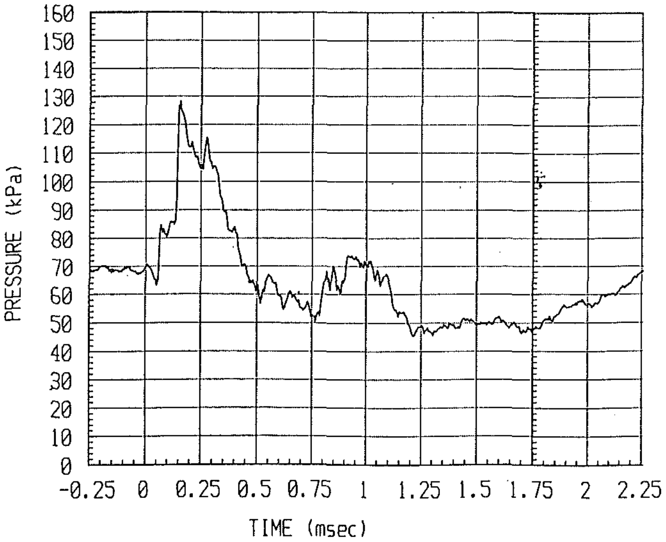

Fig. 12 Estimated lift versus time

9-11 has been ensemble-averaged over 15 separate runs to reduce signal noise. This averaging procedure was accomplished using a point-by-point averaging code created by the author. Although pressure data for each run were very similar, the averaging technique certainly altered the absolute pressure peak magnitudes found in individual traces. However, the ensemble-averaged plots of Figs. 9-11 perform extremely well in isolating specific shock wave phenomena, which appear somewhat less clearly in the individual pressure traces.

As indicated on Fig. 9, data from Kulite #1 reveal three distinct shock-induced pressure fluctuations. The first spike, occurring at time = 0.0 ms, results from the passage of the primary shock *a* directly over the transducer face. Subsequent impingement of the reflected shocks *h* and *d* result in two additional pressure spikes of much smaller magnitude as noted. The various other pressure spikes evident on Fig. 9 may be due to actual flow phenomena, but they could not be directly identified with a particular shock position from Fig. 8. Also evident from Fig. 9 is the relatively long period of the unsteady shock effect on the Kulite #1 pressure. The "steady-state" pressure apparent prior to time-zero in Fig. 9 does not recover until approximately 3.5 ms. (To provide some feel for this time duration, it may be informative to note that a fluid particle passing continuously through the blade passage at the cascade inlet velocity of M = 0.2 would travel through the cascade in approximately 0.5 ms. Therefore, the shock effects continue for roughly seven times this period.) Recalling the illustrations of Fig. 8, no shock activity could be identified in the passage after approximately 0.35 ms. Obviously, considerable flow disruption continues well past the last indication of actual shock wave presence in the blade passage.

Figure 10 provides the pressure history recorded by Kulite #2. Again, three distinct pressure spikes can be directly identified with particular shock locations. This first of these, occurring at approximately 0.05 ms, is due to the primary shock *a* as it moves along the pressure surface. A second spike occurs approximately 75 ms later when the reflected wave *d* reaches the pressure surface at Kulite #2. The third distinguishable spike occurs when the reflected wave *m* reaches Kulite #2. As in the case of Kulite #1, the steady-state pressure level does not recover until approximately 3.75 ms. Maximum pressure for Kulite #2 is slightly less than for Kulite #1, as is the minimum pressure level. Overall trends in data are comparable between Kulites 1 and 2.

As expected, the pressure levels for Kulite #4, as shown in Fig. 11, are somewhat lower than either of the other two transducers. Two pressure spikes are apparent: the first due to passage of the primary shock segment *e* over Kulite #4 and the second from reflected shock *n*. It was at first somewhat surprising that no pressure fluctuation could be associated with impingement of reflected wave *h* on Kulite #4 at a time of approximately 0.13 ms. However, upon examination of Figs. 8(*e*) and 8(*f*), it is apparent that the nearly zero angle between shock *h* and the blade surface at Kulite #4 prevents any shock-induced pressure fluctuation. In contrast to the curves of Figs. 9 and 10, Fig. 11 shows Kulite #4 to recover to its steady-state pressure level in only 1.75 ms, nearly twice as quickly as the other two transducers. Furthermore, it is apparent that the pressure drops only slightly below the steady-state value, also in contrast to Kulite #1 and Kulite #2.

Researchers at Oxford University have presented numerous unsteady blade surface pressure traces (Doorly and Oldfield, 1985a; Ashworth et al., 1985; Johnson et al, 1989a, 1989b, 1990). Each of these plots was based on the shock wave effects as generated by the rotating bar generator. As discussed earlier, the rotating bar actually generates a pair of shock waves with an expansion region in between. Therefore, since the shotgun generates a single shock, comparison of the Oxford pressure results with those of the present study is severely limited. Perhaps the only safe comparison between the two is that both do contain shock-induced pressure spikes.

Unsteady Blade Lift. Obviously, a complete picture of the unsteady lift during the shock passage cannot be obtained from only three surface transducer locations. However, project restrictions precluded full instrumentation of the blade surfaces. Therefore, a rough estimate of the unsteady lift fluctuation was composed from the unsteady pressure difference between Kulites 2 and 4. (It is worth mentioning that, from an incompressible viewpoint, a line through the locations of Kulites 2 and 4 on a single blade approximately parallels the direction of mean blade lift.) Figure 12 is a plot of the unsteady pressure difference between Kulites 2 and 4, including the pressure difference from time = −0.25 ms to 3.75 ms. The trace of Fig. 12 is actually the difference between the plots of Figs. 10 and 11 and therefore also represents an ensemble average. Additionally, the appropriate 80 ms time offset was applied to the data of Kulite #4 to compensate for the fact that Kulites 2 and 4 were mounted on different blades. Evident from Fig. 12 is the approximately 120 percent peak variation in "lift." Furthermore, abrupt changes in lift occur at several times during the shock passage.

Although no other experimental data concerning unsteady lift were located in previously published literature, Giles (1990) presents a curve of unsteady rotor lift based on his numerically generated inviscid code results. Giles notes a 40 percent peak-peak variation in lift with several abrupt changes also present. He proposes that an additional loss mechanism may be directly attributable to the unsteady blade lift. As described by Giles, an unsteady vortex sheet would be associated with the variation in lift. The kinetic energy contained in this unsteady vortex is eventually dissipated downstream of the blade row, leading to additional losses. Giles proposes that this loss is proportional to the square of the unsteady lift, and thus may be a substantial contributor to overall unsteady profile loss.

Although the experimental unsteady lift presented in Fig. 12 is certainly a rough approximation to the actual blade lift, it nevertheless conclusively indicates that strong variations in lift do exist. It is also evident in Fig. 12 that the lift does not recover to its steady-state value until approximate time = 2.25 ms. As Giles (1990) adds, the possible structural excitation that may be induced by the cyclically varying lift could also become detrimental to turbine performance.

Downstream Pressure Measurements

Traversing Probe Pressure Traces. The other form of pres-

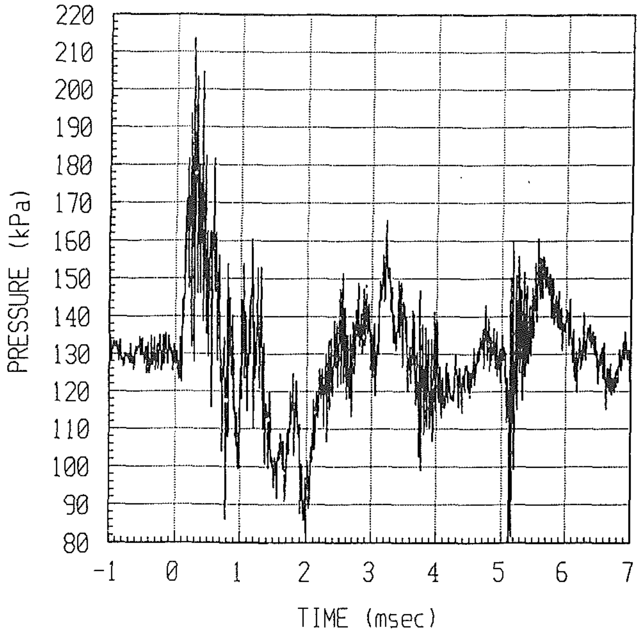

Fig. 13 Raw absolute pressure versus time for Kulite #5, position 0

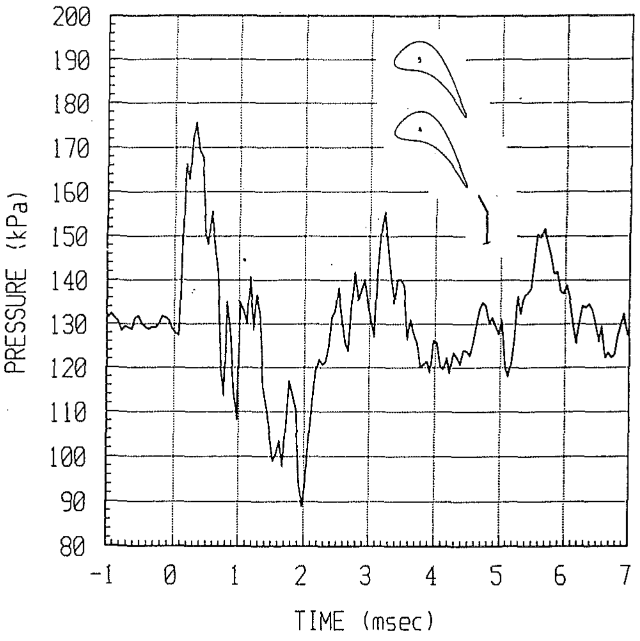

Fig. 14 Boxcar-averaged absolute pressure versus time for Kulite #5, position 0

sure data recorded in the wind tunnel during unsteady shock passage was the downstream total pressure from Kulite #5, situated 6.35 mm behind the cascade. As described previously, the Kulite #5 probe could be traversed vertically downstream of the cascade and was therefore used to record data in ten vertical locations over one complete blade spacing. Figure 13 is a plot of raw absolute pressure data from Kulite #5 in the position as noted on the Fig. 14 inset. Again, time-zero corresponds exactly to that of all previous data and shadowgraphs. Obviously, signal noise is relatively high in the data of Fig. 13. Therefore, a code was written to boxcar-average the Kulite #5 data. A running ten-point average, as shown in Fig. 14, proved to be the best compromise between high noise and loss of meaningful pressure behavior. Admittedly, the data as presented in Fig. 14 may not represent a totally accurate picture of the downstream total pressure: Prefiltering may be a better alternative for future work. However, it is felt that the ten-point average has preserved the major trends in pressure fluctuation and serves well the purposes of this introductory study.

At this point, it should be mentioned that interpretation of the Kulite #5 data should be subject to additional scrutiny. Since the probe was positioned in supersonic flow, a bow shock existed at the transducer face. No correction for the pressure drop associated with this bow shock has been made for the Kulite #5 data. Furthermore, Merritt and Aronson (1967) have shown that the behavior of a blast wave/bow wave interaction is indeed quite complicated. Therefore, the interaction between the unsteady shock wave and the probe bow shock may have influenced the pressure readings somewhat. Although the extent of influence was impossible to predict from the information obtained in this experiment, it is safe to say that rarefaction waves were most likely generated by the blast wave reflection. These rarefaction waves would have resulted in pressure drops not ordinarily present in the flowfield. An extensive analysis of this blast wave/bow wave interaction was not in the scope of this project, but will be considered if future work involves this method of pressure measurement.

Evident from Fig. 14, the downstream total pressure undergoes severe variations during the unsteady shock passage. As indicated on the Fig. 14 inset, the probe was positioned just above the wake of blade #4. Small fluctuations in the total pressure are still evident after 7 ms, considerably longer than the effects seen on the blade surfaces in Figs. 9–11. The data shown in Fig. 15 was obtained with the probe situated exactly one blade spacing above that of Fig. 14. The reasonable periodicity between the two is clearly evident. Refer to the Master's thesis of Collie (1991) for the full series of plots showing the probe at ten locations within the blade spacing. Similar trends can be found in all of these curves.

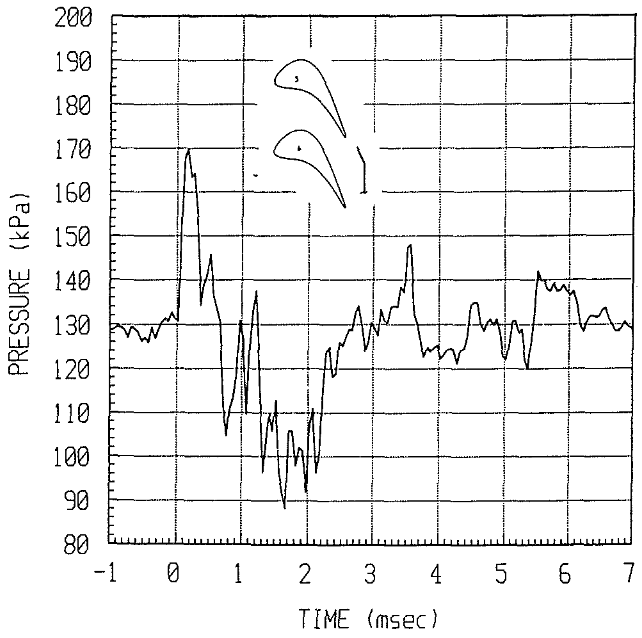

Fig. 15 Boxcar-averaged absolute pressure versus time for Kulite #5, position 9

Wake plots were generated by "time-slicing" the unsteady total pressure traces at the ten vertical locations, again numbered 0 to 9 from bottom to top. This procedure consisted of extracting the data point corresponding to a specific time from each of the ten pressure curves to construct a single trace for that specific time. Figure 16 presents the wake plots corresponding to three distinct times: time = −0.03 ms, 0.22 ms, and 1.47 ms. The first of these represents the steady-state wake

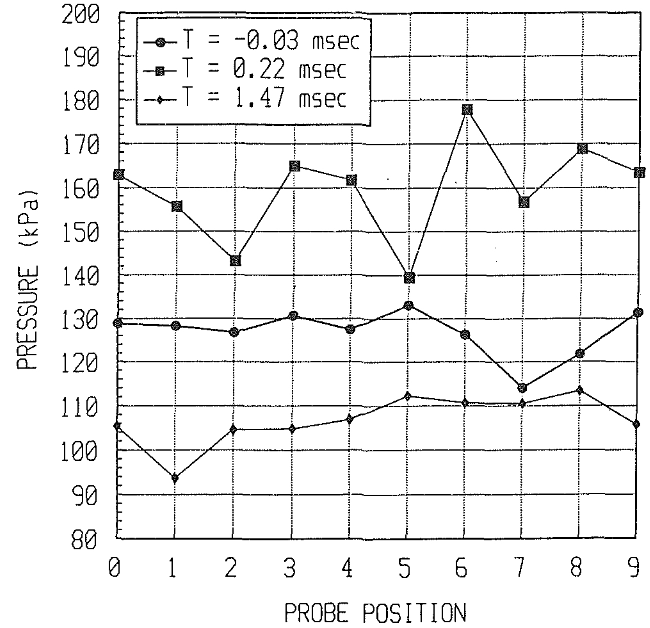

Fig. 16 Wake absolute pressure profiles: steady-state, maximum, and minimum

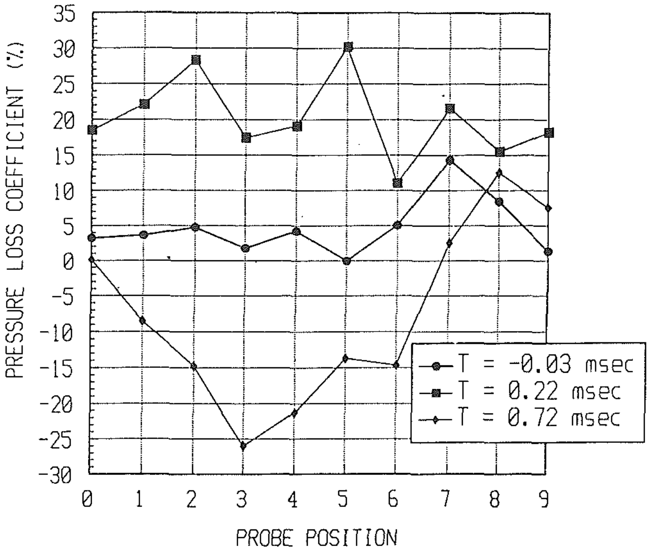

Fig. 17 Pressure loss profiles: steady-state, maximum, and minimum

profile, whereas the other two show the overall maximum and minimum variations, respectively. The steady-state profile (time = −0.03 ms) indicates trends as expected: The minimum pressure appears at position #7, directly in the blade wake. However, at other times shown, the trend of the steady-state profile has obviously disappeared. In fact, the minimum pressures at 0.22 ms and 1.45 ms occur near the center of the blade passage. A more complete set of wake plots from time = −0.03 ms to 6.97 ms is included by Collie (1991). These curves indicate the continuing variation in wake profile throughout this time period.

Unsteady Cascade Loss. In order to approximate the unsteady blade profile loss, estimates were made for the cascade pressure loss coefficient as defined by $(P_{t,\text{inlet}} - P_{t,\text{exit}})/P_{t,\text{inlet}}$. Although actual unsteady inlet total pressure was not recorded during the tests, an approximation was made using the unsteady, ensemble-averaged Kulite #1 data as plotted in Fig. 9. This was considered to be a reasonable estimate since Kulite #1 was located very close to the blade leading edge stagnation point. Data from the Kulite #5 probe were utilized as an approximation to $P_{t,\text{exit}}$. As mentioned previously, no correction was made for the Kulite #5 bow shock pressure loss. Therefore, cascade pressure loss estimates based on Kulite #5 data would be generally higher than expected. However, since it was the unsteady loss variation that was most desired, these approximations were considered to be quite appropriate.

Figure 17 includes plots of pressure loss coefficient (as a percentage) versus Kulite #5 probe position. Three loss profiles are shown, corresponding to the steady-state curve (−0.03 ms), maximum positive variation (0.22 ms), and maximum negative variation (0.72 ms). As indicated on Fig. 17, the pressure loss distribution across the passage certainly varies with time. Furthermore, variations in pressure loss coefficient of as much as 40 percent peak-peak appear between times 0.22 ms and 0.72 ms. It is also worth mentioning that the widest time-dependent variation in loss seems to occur near the center of the blade passage rather than in the wake regions. A more complete set of pressure loss coefficient curves is included by Collie (1991).

The pressure and loss data presented in Figs. 9–17 have certainly confirmed the suspicions of strong unsteady shock-induced fluctuations on the transonic flowfield. These results are not intended to be viewed as extremely accurate representations of absolute lift and loss values. However, they do clearly indicate that, from an introductory perspective, unsteady shock wave interaction does have a significant impact on blade performance. Visual evidence of shock-induced blade passage unsteadiness has also been presented in Figs. 7 and 8. It is hoped that these advances in the quantitative and qualitative understanding of unsteady shock effects has provided the impetus for more detailed investigations in the near future.

Conclusions and Recommendations

This project has successfully met the objectives set forth to provide capability for assessment of unsteady shock wave effects in the VPI Wind Tunnel Facility. A shock-generating system has been developed that is fully compatible with the existing transonic cascade test sections. Specialized optical systems and high-performance pressure instrumentation were developed and utilized to obtain qualitative and quantitative evidence of shock effects. Results indicate that significant variations in blade performance occur during the unsteady shock wave passage over the cascade. Specifically, a 120 percent peak-peak variation in estimated blade lift was found. Furthermore, an approximated loss coefficient was determined to fluctuate as much as 40 percent near the blade passage center. Visual evidence of unsteady shock effects was obtained in the form of shadowgraph photos. A previously unseen trailing edge shock wave distortion was also identified in the shadowgraphs.

It is hoped that experimental information such as that presented in this thesis will be of great benefit to the turbine blade designer. Previous industry assessment of turbine performance as based on steady-flow assumptions certainly does not represent important phenomena that actually exist during transonic operation. The growing movement toward unsteady, viscous numerical codes will certainly demand further experimental results to verify predictions. This study has also served as a springboard for further, more detailed investigations of unsteady shock wave effects currently being undertaken at Virginia Tech.

References

Ashworth, D. A., Lagraff, J. E., Schultz, D. L., and Grindrod, K. J., 1985, "Unsteady Aerodynamic and Heat Transfer Processes in a Transonic Turbine Stage," ASME *Journal of Engineering for Gas Turbines and Power*, Vol. 107, pp. 1022–1030.

Bertsch, R., 1990, "An Experimental Examination of the Influence of Trailing Edge Injection on Blade Losses in Transonic Turbine Cascades," Master's Thesis, Virginia Polytechnic Institute and State University, Blacksburg, VA.

Collie, J. C., Moses, H. L., and Kiss, T., 1991, "The Effect of Blunt Trailing Edge on Turbine Blade Performance," AIAA Paper No. 91-2130.

Collie, J. C., 1991, "Unsteady Shock Wave Effects on Transonic Turbine Cascade Performance," Master's Thesis, Virginia Polytechnic Institute and State University, Blacksburg, VA.

Doorly, D. J., 1983, "The Effects of Wake-Passing on Turbine Blades," PhD Thesis, Oxford University, Oxford, UK.

Doorly, D. J., and Oldfield, M. L. G., 1985a, "Simulation of the Effects of Shock Wave Passing on a Turbine Rotor Blade," ASME *Journal of Engineering for Gas Turbines and Power*, Vol. 107, pp. 998-1006.

Doorly, D. J., and Oldfield, M. L. G., 1985b, "Simulation of Wake Passing in a Stationary Turbine Rotor Cascade," *AIAA J. of Propulsion*, Vol. 1, No. 4, pp. 316-318.

Doughty, R. L., 1991, "The Effect of Blade Solidity on the Aerodynamic Loss of a Transonic Turbine Cascade," Master's Thesis, Virginia Polytechnic Institute and State University, Blacksburg, VA.

Doughty, R. L., Moses, H. L., and Gregory, B. A., 1992, "The Effect of Blade Solidity on the Aerodynamic Loss of a Transonic Turbine Cascade," AIAA Paper No. 91-0393, submitted for the 30th Aerospace Sciences Meeting, Reno, NV, Jan. 6-9, 1992.

Giles, M. B., 1990, "Stator/Rotor Interaction in a Transonic Turbine," *AIAA J. Propulsion*, Vol. 6, No. 5, pp. 621-627.

Johnson, A. B., Rigby, M. J., Oldfield, M. L. G., Ainsworth, R. W., and Oliver, M. J., 1989a, "Surface Heat Transfer Fluctuations on a Turbine Rotor Blade Due to Upstream Shock Wave Passing," ASME JOURNAL OF TURBOMACHINERY, Vol. 111, pp. 105-115.

Johnson, A. B., Rigby, M. J., and Oldfield, M. L. G., 1989b, "Unsteady Aerodynamic Phenomena in Simulated Wake and Shock Wave Passing Experiment," AGARD-CP-468.

Johnson, A. B., Oldfield, M. L. G., Rigby, M. J., and Giles, M. B., 1990, "Nozzle Guide Vane Shock Wave Propagation and Bifurcation in a Transonic Turbine Rotor," ASME Paper No. 90-GT-310.

Merritt, D. L., and Aronson, P. M., 1967, "Wind Tunnel Simulation of Head-On Bow Wave-Blast Wave Interactions," Report No. 67-123, United States Naval Ordnance Laboratory, White Oak, MD, Aug. 9.

Moses, H. L., Kiss, T., Bertsch, R., and Gregory, B. A., 1991a, "Aerodynamic Losses Due to Pressure Side Coolant Ejection in a Transonic Turbine Cascade," AIAA Paper No. 91-2032.

Moses, H. L., Schetz, J. A., and Gregory, B. A., 1991b, "Cooled, Transonic Turbine Cascade Testing," submitted for the *Proceedings of the ISABE Conference*, Nottingham, UK, Sept.

Pfeil, H., Herbst, R., and Schröder, T., 1983, "Investigation of the Laminar-Turbulent Transition of Boundary Layers Disturbed by Wakes," ASME JOURNAL OF TURBOMACHINERY, Vol. 105, pp. 130-137.

Priddy, W. J., and Bayley, F. J., 1985, "Effects of Free-Stream Turbulence on the Distribution of Heat Transfer Around Turbine Blade Sections," *Int. J. Heat Fluid Flow*, Vol. 6, No. 3, pp. 181-191, Sept.

Priddy, W. J., and Bayley, F. J., 1988, "Turbulence Measurements in Turbine Blade Passages and Implications for Heat Transfer," ASME JOURNAL OF TURBOMACHINERY, Vol. 110, pp. 73-79.

ERRATA

To the paper "Measurement and Prediction of Tip Clearance Flow in Linear Turbine Cascades" by F. J. G. Heyes and H. P. Hodson, published in the ASME JOURNAL OF TURBOMACHINERY, Vol. 115, No. 3, July 1993, pp. 376–382:

Page 376, column 2: $T\sqrt{\tau}$ should be T/τ.

Page 378, Fig. 3 caption: T/C should be τ/C.

Page 382, column 1: Sentence beginning "In the case of a turbine cascade . . ." should end with "is more difficult to predict with such codes."

Analysis of Steady and Unsteady Turbine Cascade Flows by a Locally Implicit Hybrid Algorithm

C. J. Hwang

J. L. Liu

Institute of Aeronautics and Astronautics,
National Cheng Kung University,
Tainan, Taiwan

For the two-dimensional steady and unsteady turbine cascade flows, the Euler/Navier-Stokes equations with Baldwin-Lomax turbulence model are solved in the Cartesian coordinate system. A locally implicit hybrid algorithm on mixed meshes is employed, where the convection-dominated part in the flow field is studied by a TVD scheme to obtain high-resolution results on the triangular elements, and the second- and fourth-order dissipative model is introduced on the O-type quadrilateral grid in the viscous-dominated region to minimize the numerical dissipation. When the steady subsonic and transonic turbulent flows are investigated, the distributions of isentropic Mach number on the blade surface, exit flow angle, and loss coefficient are obtained. Comparing the present results with the experimental data, the accuracy and reliability of the current approach are confirmed. By giving a moving wake-type total pressure profile at the inlet plane in the rotor-relative frame of reference, the unsteady transonic inviscid and turbulent flows calculations are performed to study the interaction of the upstream wake with a moving blade row. The Mach number contours, perturbation component of the unsteady velocity vectors, shear stress, and pressure distributions on the blade surface are presented. The physical phenomena, which include periodic flow separation on the suction side, bowing, chopping and distortion of incoming wake, negative jet, convection of the vortices and wake segments, and vortex shedding at the trailing edge, are observed. It is concluded that the unsteady aerodynamic behavior is strongly dependent on the wake/shock/boundary layer interactions.

Introduction

In recent years, substantial efforts have been expended in developing reliable and accurate computational or experimental procedures for predicting the flow behavior within turbine blade passages. A lot of the calculations or experiments for the flows in turbomachinery are based on the approximation that the flow in each blade row is steady in the reference frame of the stator or rotor. Due to the significant progress in computational fluid dynamics (CFD), several numerical methods have been presented to study the cascade flows. These methods include three major approaches: (*a*) inviscid flow field analysis (Delaney, 1983; Denton, 1983), (*b*) coupled analyses between inviscid and viscous flow fields (Hansen et al., 1980; Nakahashi et al., 1989), and (*c*) full viscous flow field analyses (Shamroth et al., 1984; Weinberg et al., 1986; Kwon, 1988; Furukawa et al., 1991). In many cases, inviscid analyses are capable of giving good predictions of the blade pressure distributions. When considering the shear-induced and heat transfer phenomena, approaches (*b*) and (*c*) are employed. The features of those two approaches were described by Shamroth et al. (1984). In this work, the complete Navier-Stokes equations are solved to analyze the full viscous flow fields.

In a real turbomachine, the unsteadiness of the flow arises due to the relative motion of the alternatively stationary and rotating annular blade rows. The unsteady phenomenon that occurs in the passages of an axial turbomachine is the focus and interest of current research efforts and engine design. The principal components of the unsteadiness for turbine cascade flows, which have been investigated by Doorly (1988), Hodson (1985a), Sharma et al. (1988), Yang et al. (1988), Jorgenson and Chima (1989), Rai and Madavan (1990), and Giles (1990), can be summarized as wake passing, shock wave passing (for transonic stages only), potential flow interactions and upstream high-energy turbulence. Although the simultaneous calculations of rotor and stator flows can provide reasonable results, which coincide with physical phenomena, the individual effect of components of the unsteadiness is difficult to identify. Also, this kind of approach takes a lot of computer time. From the results of Hodson (1985a), Rai and Madavan (1990), and Yang et al. (1988), the amplitude of flow fluctuation in the downstream rotor is generally larger than that in the upstream stator. By using the Euler solutions with suitable inflow conditions, the unsteadiness generated by wake with a single blade passage of the rotor is appropriately modeled to provide further insight into the mechanism of wake/rotor interactions for the subsonic cascade flows (Hodson, 1985b;

Contributed by the International Gas Turbine Institute and presented at the 37th International Gas Turbine and Aeroengine Congress and Exposition, Cologne, Germany, June 1-4, 1992. Manuscript received by the International Gas Turbine Institute February 11, 1992. Paper No. 92-GT-127. Associate Technical Editor: L. S. Langston.

Giles, 1988; Liu and Sockol, 1989). Although results associated with low-speed wake/rotor interactions indicate that the flow phenomena are dominated by an inviscid effect, it is desirable to predict the high-speed turbine cascade flow behaviors due to wake/rotor/shock/boundary layer interactions. For the unsteady transonic inviscid and turbulent flows, the Euler and Navier–Stokes equations are presently solved in the rotor-relative frame of reference, and the analytical function of total pressure for the moving wake is specified at the inlet plane.

The flow passages in turbomachinery are in general highly constrained by blade geometries. The periodic restriction sometimes causes difficulty in the grid generation, especially for turbine cascades with high stagger angle. As mentioned by Nakahashi et al. (1989) and Furukawa et al. (1991), a grid skewing problem in the midpassage and trailing edge regions produces large truncation errors of the numerical scheme. To overcome this problem, zonal approaches with the composite or overlaid grid system (quadrilateral or triangular meshes) are developed. Because purely triangular meshes are inefficient in boundary layers where the flow gradients are strongly one dimensional, a mixed grid system is employed in this work. The O-type quadrilateral mesh is placed near the blade surface to facilitate the one-dimensional stretched requirement for the efficient resolution of viscous effect, and the unstructured triangular meshes are constructed elsewhere. In the present calculations, the Baldwin–Lomax turbulence model is implemented on the structured quadrilateral grids. Even though this kind of treatment requires additional efforts to generate the mixed grids, the interpolation techniques, such as those presented by Mavriplis (1990) for the turbulent calculation on the purely triangular elements, are avoided.

Recently, TVD methods have been developed and applied to study the viscous cascade flows, such as that presented by Furukawa et al. (1991). As mentioned by Yee (1989), the TVD-type schemes for viscous flows may cause an adverse effect on the viscosity terms in the boundary layer region. To overcome this numerical problem and accurately simulate the viscous turbine cascade flows, a locally implicit hybrid algorithm, which has been developed by Hwang and Liu (1992), is introduced to solve the Navier–Stokes equations. For the steady turbulent subsonic and transonic flows passing through one advanced turbine cascade, which has been extensively tested in four European wind tunnels (Kiock et al., 1986), the numerical accuracy is confirmed by comparing the present results with the related experimental data. The distributions of isentropic Mach number on the blade surface, exit flow angle, and loss coefficient are presented. To study the physical phenomena of unsteady transonic inviscid and turbulent wake/rotor interaction flows, the Mach number contours, perturbation component of the unsteady velocity vectors, pressure and shear stress distributions on the blade surface are evaluated. It is observed that vortices are shed from the trailing edge and the unsteady aerodynamic behaviors are dominated by the wake/shock/boundary layer interactions.

Numerical Approaches

The two-dimensional unsteady Reynolds-averaged full Navier–Stokes equations in dimensionless conservation-law form are solved in the x–y Cartesian coordinate system. The molecular viscosity is determined by Sutherland's law, and the two-layer algebraic turbulence model of Baldwin and Lomax (1978) is adopted to estimate the eddy viscosity. To simulate the physical phenomena of viscous cascade flows accurately, which include the wake/shock/boundary layer interactions and flow recirculation, a locally implicit hybrid finite volume algorithm on the mixed meshes (Hwang and Liu, 1992) is employed. In this algorithm, the second- and fourth-order dissipative model is applied on the structured O-type quadrilateral cells to minimize the numerical dissipation in the boundary layer region, and the improved symmetric TVD scheme on the triangular elements is used to obtain high-resolution results in the convective dominated part. The steady-state flow calculations are first-order accurate in time, and the scheme becomes second-order accurate in time for the unsteady flow computations. As mentioned by Hwang and Liu (1992), the present method is locally implicit, but globally explicit and is unconditionally stable.

At the blade surface, no-penetration and no-slip conditions are imposed for the inviscid and viscous flows, respectively. The adiabatic wall condition is assumed in this work. At inlet, the total pressure, total temperature, and flow angle are specified, and the magnitude of velocity is obtained from the characteristic boundary treatment (Chima, 1985). Scott and Hankey (1986) used a similar boundary approach to achieve the Navier–Stokes solutions of unsteady flow in a compressor rotor. On the exit plane, the static pressure is prescribed, and the density and velocity components are extrapolated from the adjacent interior cells. By using similar treatments, several numerical solutions, such as those given by Jorgenson and Chima (1989), Liu and Sockol (1989), and Rai and Madavan (1990), were presented. Because the aforementioned boundary conditions are reflective and may influence the unsteady results, the development or employment of nonreflective boundary treatment is the way to understand the effects of the present boundary conditions in the future work. In addition, the no-lagged periodicity condition is assumed in the present calculations. This condition is easily satisfied by considering the points outside the calculation domain to have the same values as those of corresponding points, which are located at one pitch distance and are within the domain.

The flow solver is coupled with a mesh generation procedure that is capable of generating structured quadrilateral and unstructured triangular cells. The O-type quadrilateral meshes are constructed by solving the Poisson equation (Sorenson, 1980), and the triangular meshes are generated based on the advancing front concept (Lo, 1985). In this work, the quadrilateral meshes were generated first and then the interface nodes are set as boundary points for the triangular elements. The grid generation processes for triangular meshes include the placement and triangulation of grid points. Also, a smoothing technique (Lo, 1985) is employed after triangulation, and it is done by shifting each interior generated node to the center of the surrounding polygon.

Results and Discussion

Steady Turbulent Subsonic and Transonic Turbine Cascade Flows. The subsonic and transonic flows passing through a plane turbine rotor cascade (Kiock et al., 1986) have been investigated in four European wind tunnels at VKI Rhode-St.-Genese (RG), Belgium; DFVLR Goettingen (GO), Germany; DFVLR Braunschweig (BS), Germany; and Oxford (OX) University, United Kingdom. In this section, the subsonic turbulent flow is studied first. The values of exit Mach number (M_{exit}), Reynolds number (Re_{exit}) and incident flow angle (β_{inlet}) are equal to 0.788, 8×10^5, and 30 deg. As depicted in Fig. 1, the grid system contains the structured O-type quadrilateral grids around the blade and unstructured triangular elements elsewhere. Near the downstream boundary, a clustering of grid points is used to reduce the numerical errors arising due to the extrapolation of flow properties at the exit plane. The minimum grid spacing between the first cell and the surface of blade is 1.33×10^{-5} chord length. From the isentropic Mach number distributions on the blade surface which are plotted in Fig. 2(a), the present numerical method gives satisfactory results. The oscillatory behaviors at 25 and 80 percent axial chord on pressure side are due to the blade definition, where the blade coordinates are obtained by linear interpolation from the data given by Kiock et al. (1986). The flow is characterized by rapid acceleration along the suction side up to $x/c \simeq 0.6$

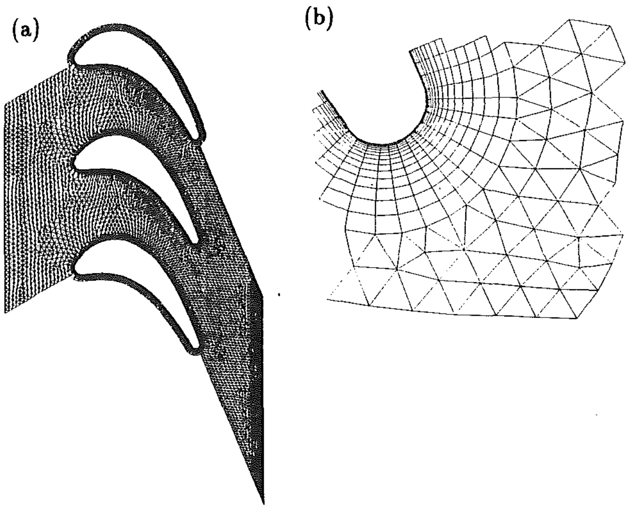

Fig. 1 (*a*) Mixed meshes (3875 elements and 155 × 21 grid points; Hwang and Liu, 1992) and (*b*) mesh around the trailing edge for turbine cascade flows

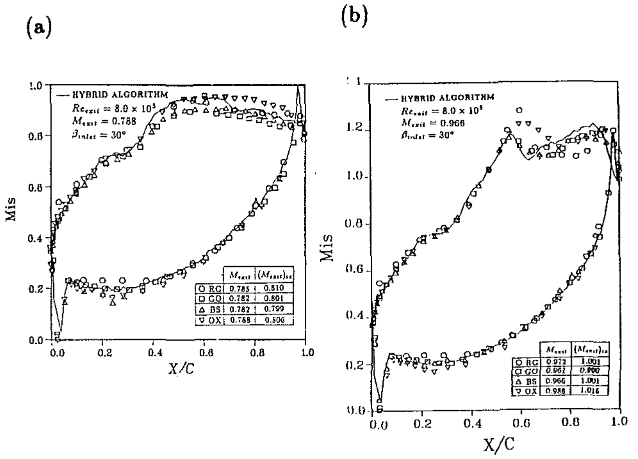

Fig. 2 Isentropic Mach number distributions for (*a*) subsonic and (*b*) transonic turbulent flows (Hwang and Liu, 1992) passing through the turbine cascade

and followed by moderate deceleration in the downstream. On the pressure side, the significant acceleration of the flow is obtained from $x/c \simeq 0.4$ to 0.98 and followed by a heavy deceleration. As mentioned by Kiock et al. (1986), although the exit Mach numbers in the four facilities are in the band of $\Delta M_{exit} = 0.006$, the surface isentropic Mach number distributions differ considerably in the rear half of the suction side. These differences are believed to be due to a discrepancy in the measurement of the exit static pressure. Except that different values of Mach number ($M_{exit} = 0.966$ and 0.988) on the exit plane are employed, the transonic turbulent flows with the same grid system (Fig. 1) and inflow conditions as those of subsonic turbine cascade flow are investigated. For the flow with M_{exit} equal to 0.966, the isentropic Mach number distribution on the blade surface (Fig. 2(*b*)), which was presented by Hwang and Liu (1992), agrees well with the experimental data (Kiock et al., 1986). This fact demonstrates that the present locally implicit hybrid algorithm can correctly predict the shock positions and resulting pressure distribution for the transonic cascade flow. To evaluate the reliability of present method further, the exit angle (β_{exit}) and loss coefficient ($\zeta = 1 - |\mathbf{V}_{exit}|^2/|\mathbf{V}_{exit,is}|^2$) for the subsonic and transonic flows are calculated. As shown in Fig. 3, reasonable agreement exists between the computed and measured cascade performances of wind tunnel testing (Kiock et al., 1986).

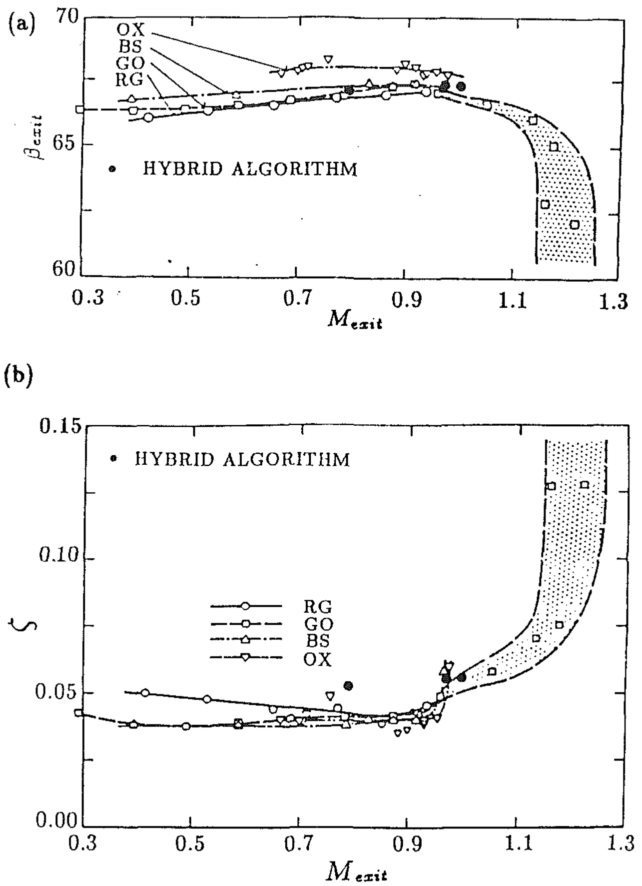

Fig. 3 Distributions of (*a*) exit flow angle and (*b*) loss coefficient for subsonic and transonic turbulent flows passing through the turbine cascade

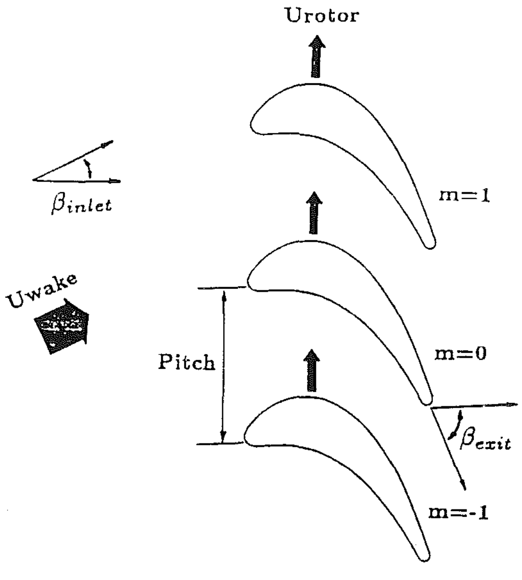

Fig. 4 Schematic of unsteady wake/rotor interaction flow

Inviscid Unsteady Transonic Wake/Rotor Interaction Flow. In this section, the numerical solutions are obtained for the wake flow passing through the turbine rotor cascade (Fig. 4). This simulation is performed by giving the wake total pressure profile at the inlet plane as follows (Liu and Sockol, 1989):

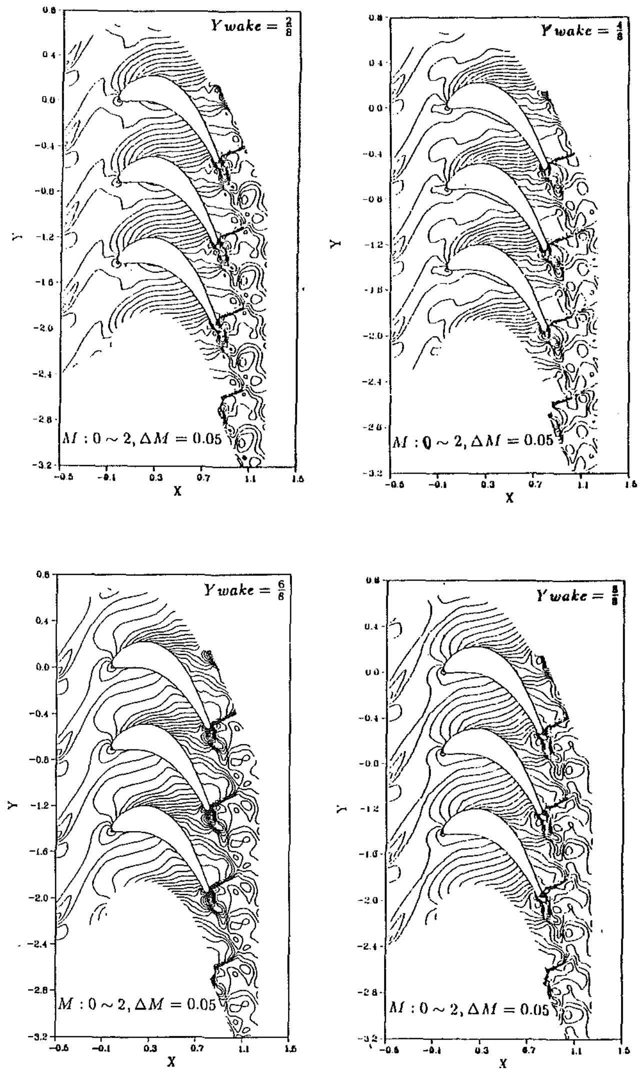

Fig. 5 The sequences of Mach number contours for inviscid unsteady transonic wake/rotor interaction flow

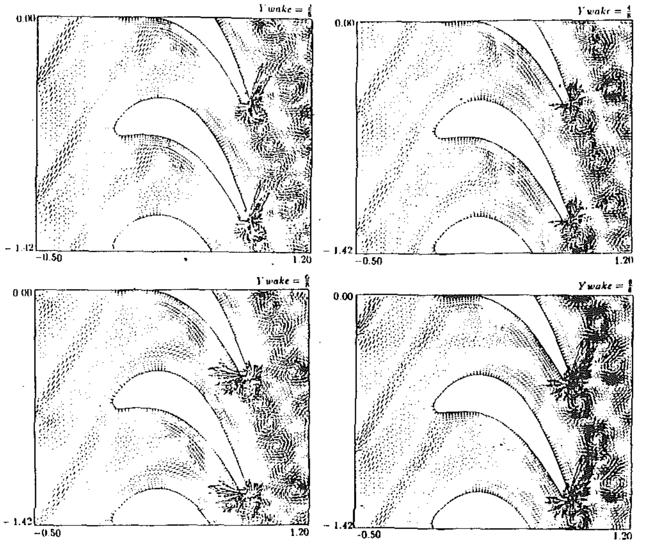

Fig. 6 The sequences of perturbation component of unsteady velocity vectors for inviscid unsteady transonic wake/rotor interaction flow

$$P_t = \begin{cases} (P_t)_{\text{inlet}} - P_{\text{amp}}\left[1-\left(\dfrac{|y'-Y_{\text{wake}}|}{W_{\text{band}}}\right)^{1.5}\right]^2 & \text{if } |y'-Y_{\text{wake}}| \le W_{\text{band}}; \\ (P_t)_{\text{inlet}} & \text{otherwise.} \end{cases} \qquad (1)$$

where the total pressure value, $(P_t)_{\text{inlet}}$, is the same as that of transonic flow ($M_{\text{exit}} = 0.988$ and $\beta_{\text{inlet}} = 30$ deg) with uniform inlet conditions. The P_{amp} and y' are the amplitude of total pressure disturbance and the normalized pitchwise distance of the blade passage ($0 \le y' \le 1$). The Y_{wake} is the location of the wake centerline, and W_{band} is the half width of the wake ($W_{\text{band}} = 0.15$). This analytical profile repeats when y' increases or decreases by an amount of the rotor pitch. In the present calculation, the total pressure defect (P_{amp}) associated with the incoming wake is specified as 10 percent of the uniform inlet total pressure $(P_t)_{\text{inlet}}$. The upward velocity of the rotor blade (U_{rotor}) is equal to the wake inlet velocity (U_{wake}), and this corresponds to a flow condition in which the incidence of inlet perturbation velocity of the wake is equal to 60 deg in the rotor-relative frame of reference. As mentioned by Hodson (1985b) and Giles (1988), the predicted results associated with low-speed wake/rotor interactions are dominated by inviscid effects. Even though the full viscous simulation is necessary in order to predict accurately the viscous phenomena for the high-speed turbine cascade flow, it is worthwhile that the inviscid flow is conducted first to understand the unsteady flow phenomena due to the interaction of time-varying wake and shock. Choosing the steady-state inviscid solution of the transonic flow (uniform inflow, $M_{\text{exit}} = 0.988$, and $\beta_{\text{inlet}} = 30$ deg) as the initial condition, the calculation is started by introducing the wake total pressure profile (Eq. (1)) on the inlet plane. According to the magnitude of U_{rotor}, the locations of wake centerline, Y_{wake}, are imposed through the unsteady inflow boundary in the range from zero to one. To increase the computing efficiency, the number of quadrilateral grids that are located around the blade surface (Fig. 1), is reduced to 155 × 8 grid points.

When the incoming wake moves across ten pitches, the computation is stopped. The sequences of unsteady Mach number contours are displayed in Fig. 5. From the unsteady results, incoming wakes and complex flow phenomena around the trailing edge and downstream of the rotor are indicated. To investigate the insight mechanism of wake/rotor interaction further, the perturbation component of unsteady velocity vectors at several instants during one cycle are studied. These unsteady perturbation velocity vectors were obtained by subtracting the time-averaged (over one cycle) velocity vectors at each grid point from the instantaneous velocity vectors. As plotted in Fig. 6, the direction of inlet perturbation velocity of wake is inclined with 60 deg to the horizontal line. It should be mentioned that the wake can be represented as "negative jets" (Lefcourt, 1965) superimposed upon an otherwise steady free stream (Hodson, 1985b). As a wake moves into a rotor blade passage, it becomes bowed because the midpassage convection velocity is larger than that on the forward part of the pressure surface. A pair of large vortices with opposite sign is observed. After the wake has been chopped by a rotor blade, the newly formed wake segment becomes distorted. The negative jet draws wake fluid away from the pressure surface and onto the suction surface. For the wake/rotor interaction flow in Hodson's low-speed turbine without shock effect, the above flow phenomena were also mentioned by Hodson (1985b) and Giles (1988). Furthermore, these wake segments and vortices are convected along the passage and finally interact with the shock near the trailing edge. Besides the phenomena described above, one of the dominant mechanisms of unsteadiness in

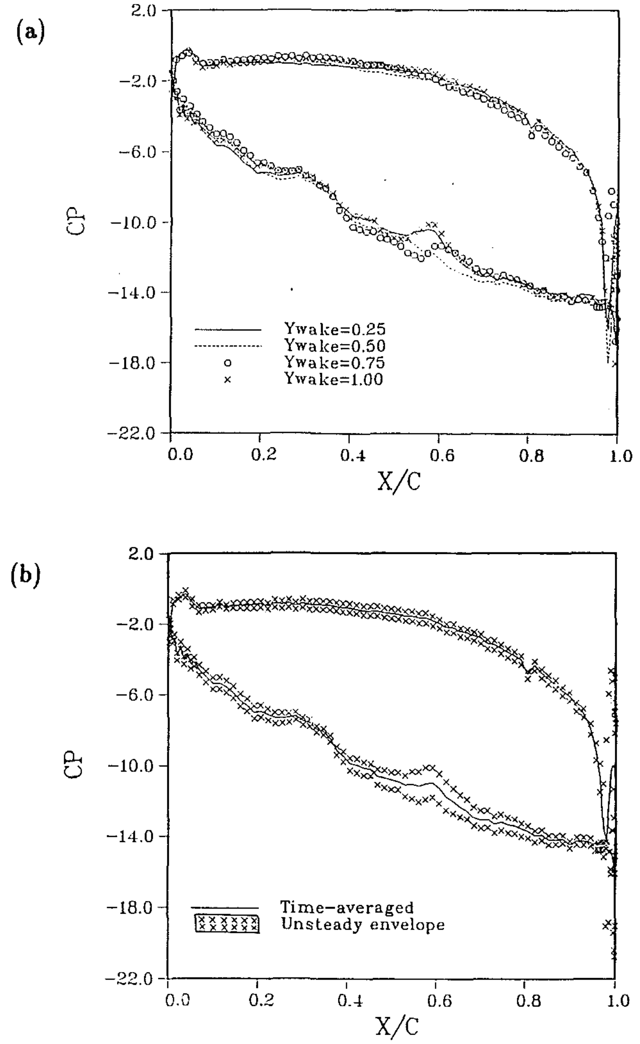

Fig. 7 Distributions of (*a*) temporal and (*b*) time-averaged and unsteady envelope pressure coefficients for inviscid unsteady transonic wake/rotor interaction flow

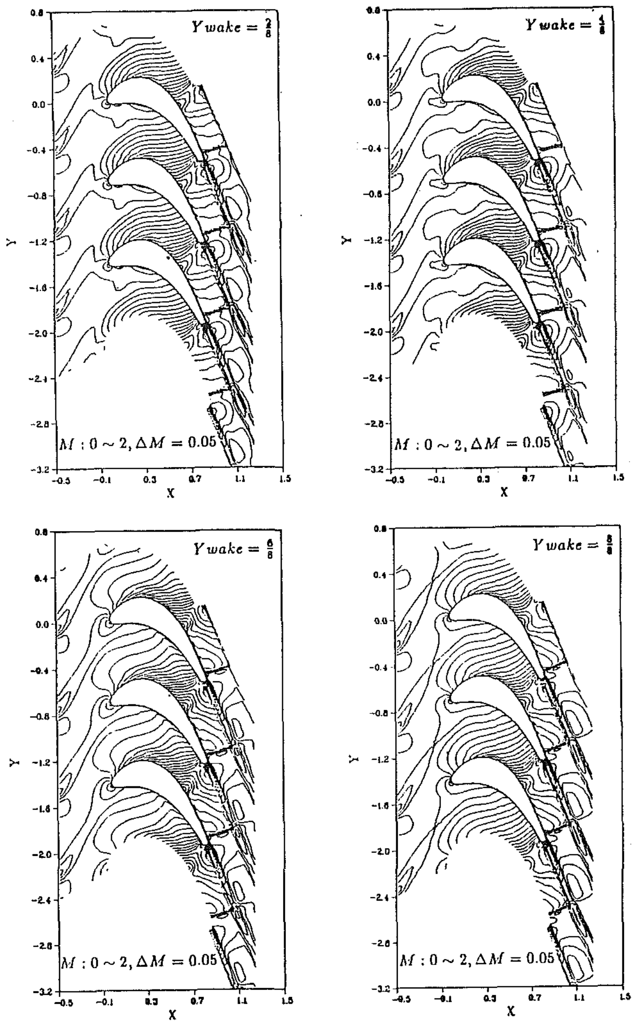

Fig. 8 The sequences of Mach number contours for turbulent unsteady transonic wake/rotor interaction flow

the flow field is vortex shedding at the trailing edge. Due to the wake/shock/vortex interaction, the unsteady fluctuations of velocity are enlarged around the trailing edge.

It is known that the motion of vortices in the rotor passage produces pressure fluctuations and thus results in periodic aerodynamic loading on the rotor blades. To understand the characteristics of the unsteady aerodynamic loading on the blade surface, the pressure coefficient is defined as

$$C_p = \frac{P - (P_t)_{\text{inlet}}}{\frac{1}{2}\rho_{\text{inlet}} U_{\text{rotor}}^2} \tag{2}$$

where the subscript "inlet" represents the flow condition at the inlet plane with the state of uniform inflow, and P is the instantaneous static pressure on the blade surface during one cycle. As shown in Fig. 7(*a*), the unsteady fluctuations of pressure over the entire blade surface are obtained, and larger variations happen around the weak shock ($x/c \simeq 0.55 \sim 0.60$) and strong shock ($x/c \simeq 0.98$) regions. Depending on the wake positions, the locations and strengths of the shocks are significantly changed. Replacing the pressure P expressed in Eq. (2) by the averaged, maximum, or minimum pressure values over one cycle, the time-averaged profile and unsteady envelope of pressure coefficient as a function of the axial distance along blade surface are plotted in Fig. 7(*b*). The maximum-minimum area represents the range of fluctuating pressure in a cycle, and the flow is really unsteady over the entire rotor surface. Due to the unsteady wake/shock interaction, the envelope is enlarged around the weak and strong shock regions.

Turbulent Unsteady Transonic Wake/Rotor Interaction Flow. To understand the wake/shock/boundary layer interaction further, the unsteady transonic wake/rotor interaction turbulent flow is investigated. This study is conducted by giving the wake total pressure profile at inlet plane, which has been expressed in Eq. (1). The values of P_{amp}, W_{band}, and $U_{\text{rotor}}/U_{\text{wake}}$ are the same as those of the inviscid flow case. Choosing the steady-state turbulent solutions (uniform inflow, $M_{\text{exit}} = 0.988$, $\beta_{\text{inlet}} = 30$ deg, and $Re_{\text{exit}} = 8 \times 10^5$) as the initial and exit boundary conditions, the calculation is started. In this case, the computation is stopped when the incoming wake moves across six pitches. The sequences of unsteady Mach number contours are displayed in Fig. 8, where the flow phenomena arising from incoming wake and wake/shock/boundary layer interaction are indicated. Except around the shocks and wake region behind the rotor, the flow structure is almost the same as that of the inviscid flow case. This means that the viscous boundary layer significantly affects wake/shock interaction and the mechanism of vortex shedding near the blunt trailing edge. To investigate the physical behaviors of wake/rotor interaction flow further, the perturbation component of unsteady velocities at several instants during one cycle are

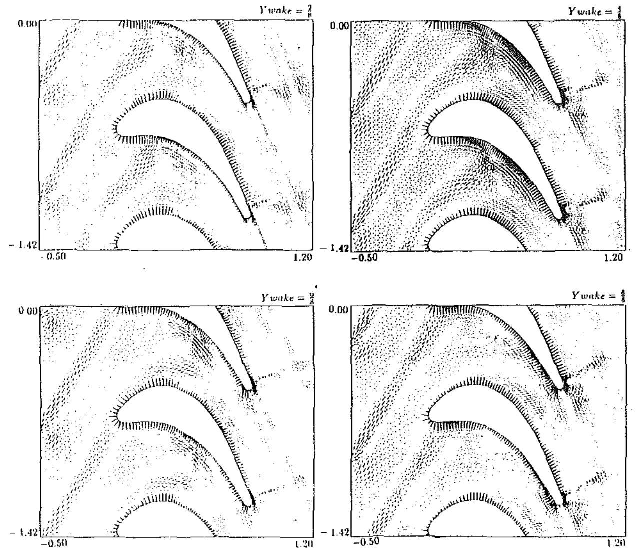

Fig. 9 The sequences of perturbation component of unsteady velocity vectors for turbulent unsteady transonic wake/rotor interaction flow

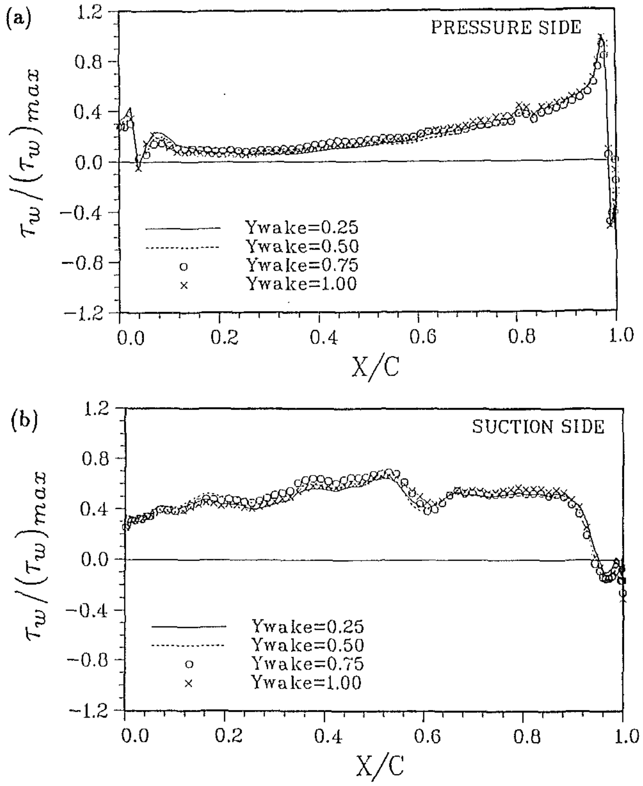

Fig. 10 Distributions of temporal shear stress on (*a*) pressure side and (*b*) suction side for turbulent unsteady transonic wake/rotor interaction flow

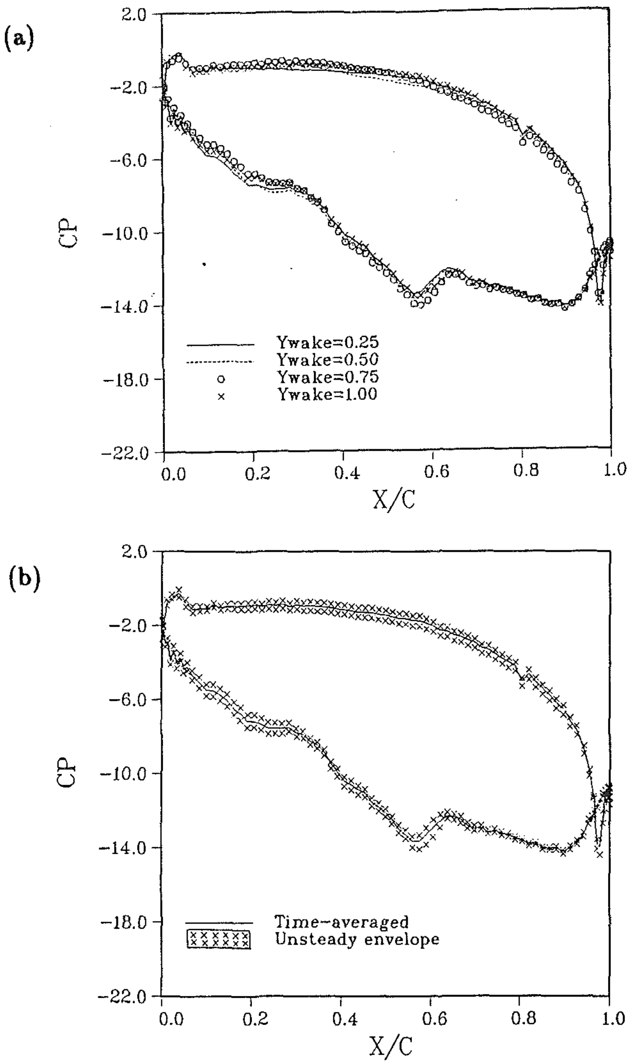

Fig. 11 Distributions of (*a*) temporal and (*b*) time-averaged and unsteady envelope pressure coefficients for turbulent unsteady transonic wake/rotor interaction flow

calculated. As shown in Fig. 9, the flow phenomena, which include the convection of a bowed wake into a rotor blade passage, and the transport of a pair of large vortices with opposite sign, are observed. After the wake was chopped by a rotor blade, the two halves of the cut wake segment are distorted. The negative jet draws wake fluid away from the pressure surface and toward the suction surface. Further, these wake segments and vortices are convected along the passage and finally interact with the shock near the trailing edge. The results of Fig. 9 also demonstrate that the unsteady perturbation velocities are significantly enlarged around the strong shock region due to the wake/shock/boundary layer interaction. As shown in Figs. 5, 6, 8, and 9, the flow behavior after the trailing edge of the rotor blade is completely different for the inviscid and turbulent unsteady wake/rotor interaction flows. It is apparent that the viscous turbulent effect tends to suppress and change the structure of the shedding vortices.

To obtain the viscous forces on the blade surface for the different positions of the incoming wake, the shear stresses on the pressure and suction sides are computed. From the distributions shown in Fig. 10, the incoming wake will affect the shear stress on the blade surface especially around the shock regions and the midportion of the suction side in the range of $x/c \simeq 0.1$–0.64. The separation point on the suction side oscillates in a small range around $x/c \simeq 0.94$–0.95. However, the locations of the stagnation and separation points on the pressure side are almost not changed. To understand the characteristics of the unsteady aerodynamic loading on the blade surface further, the distributions of the pressure coefficient (Eq. (2)) are calculated. From Fig. 11, unsteady fluctuations of pressure over the entire blade surface are observed. Except for the region $x/c > 0.35$ on the suction side and the region of the trailing edge, the quantities of the pressure coefficient at various wake locations are almost the same as those of the inviscid flow case (Fig. 7). The variations of location and strength for the weak shock are smaller than those of the inviscid flow case. The pressure fluctuations around the trailing

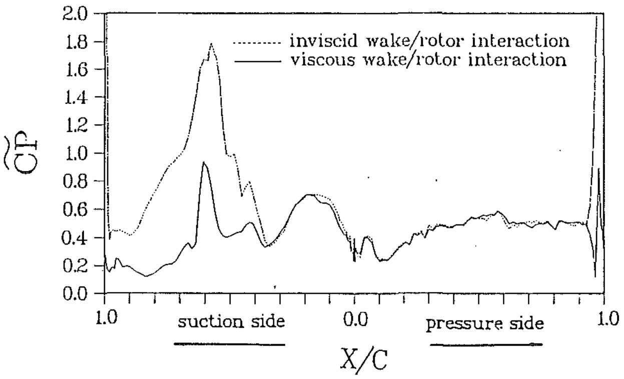

Fig. 12 Distributions of pressure fluctuation for inviscid and turbulent unsteady transonic wake/rotor interaction flows

edge are not significant, and this is consistent with the flow phenomenon that the shedding vortex is suppressed by the viscous turbulent effect.

Further, to achieve more detailed insight and quantitative analysis of the variation of aerodynamic loading, the temporal pressure fluctuation, $\tilde{C}_p$, along the blade surface is plotted in Fig. 12. The quantity $\tilde{C}_p$ is defined as

$$\tilde{C}_p=\frac{P_{\max}-P_{\min}}{\frac{1}{2}\rho_{\text{inlet}}U^2_{\text{rotor}}} \tag{3}$$

where $P_{\max}$ and $P_{\min}$ represent the maximum and minimum pressures over a cycle at a given point, respectively. As shown in Fig. 12, the peak values, which are due to the unsteady wake/shock/boundary layer interaction, are demonstrated for the inviscid and turbulent flows. In the inviscid flow, except near the trailing edge, the values of $\tilde{C}_p$ on the pressure side are smaller than those on the suction side. This is due to the fact that the combined interaction of wake/rotor/shock occurs on the suction side, while only wake/rotor interaction happens on the pressure side. For the viscous turbulent flow, the distribution of $\tilde{C}_p$ on the pressure side, where no shock exists, is similar to that of inviscid flow. This physical phenomenon is consistent with the fact that the low-speed wake/rotor interaction flows are dominated by inviscid effect (Hodson, 1985b; Giles, 1988; Liu and Sockol, 1989). On the other hand, significant variations of the results for the inviscid and turbulent flows are observed around the shock regions and trailing edge. Due to the boundary layer effect, the unsteady pressure variations in the shock regions are dissipated. From the above discussion, it is concluded that the characteristics of unsteady aerodynamic loading are dominated by the shock/boundary layer interaction. In this calculation, the present method requires approximately 6.5 × 10^{-3} s/iteration/cell on the computer, VAX8600. Also, about 5000 time steps per cycle are processed.

Conclusions

For the two-dimensional steady and unsteady turbine cascade flows, the Euler/Navier-Stokes equations with Baldwin-Lomax turbulence model are solved by using a locally implicit hybrid algorithm. In the viscous-dominated region, the second- and fourth-order dissipative model on the structured O-type quadrilateral meshes is employed to minimize the numerical dissipation. To obtain the high-resolution results in the convection-dominated flow fields, a TVD formulation on unstructured triangular elements is introduced. Considering the uniform inlet conditions (β_{inlet} = 30 deg) for the steady subsonic and transonic turbulent flows (M_{exit} = 0.788, 0.966, and 0.988), the numerical accuracy is confirmed by comparing the computed values of isentropic Mach number distributions, exit angle, and loss coefficient with the experimental data. When the unsteady inviscid and turbulent transonic wake/rotor interaction flows are investigated, the flow behaviors, which include periodic flow separation on the suction side, bowing, chopping, and distortion of incoming wake, negative jet, convection of the vortices and wake segments, and vortex shedding at the trailing edge, are observed. From the sequences of Mach number contours and perturbation component of unsteady velocity vectors, it is shown that the viscous turbulent effect tends to suppress and change the structure of shedding vortices. Due to the convection of vortices and wake segments, periodically unsteady loading on the blade is observed. The unsteady pressure fluctuations are clearly demonstrated over the entire rotor. Around the shock regions, the values of $\tilde{C}_p$ are larger. For the turbulent flow, the distribution of $\tilde{C}_p$ on the pressure side is similar to that of inviscid flow. Around the trailing edge and shocks on the suction side, the values of $\tilde{C}_p$ are significantly decreased in the turbulent flow calculation. From the above discussion, it is apparent that the shock and boundary layer play important roles in the transonic wake/rotor interaction flow problems.

References

Baldwin, B. S., and Lomax, H., 1978, "Thin Layer Approximation and Algebraic Model for Separated Turbulent Flows," AIAA Paper No. 78-257.

Chima, R. V., 1985, "Inviscid and Viscous Flows in Cascades With an Explicit Multiple-Grid Algorithm," *AIAA Journal*, Vol. 23, No. 10, pp. 1556-1563.

Delaney, R. A., 1983, "Time-Marching Analysis of Steady Transonic Flow in Turbomachinery Cascades Using the Hopscotch Method," ASME *Journal of Engineering for Power*, Vol. 105, pp. 272-279.

Denton, J. D., 1983, "An Improved Time-Marching Method for Turbomachinery Flow Calculation," ASME *Journal of Engineering for Power*, Vol. 105, pp. 514-524.

Doorly, D. J., 1988, "Modeling the Unsteady Flow in a Turbine Rotor Passage," ASME JOURNAL OF TURBOMACHINERY, Vol. 110, pp. 27-37.

Furukawa, M., Yamasaki, M., and Inoue, M., 1991, "A Zonal Approach for Navier-Stokes Computations of Compressible Cascade Flow Fields Using a TVD Finite Volume Method," ASME JOURNAL OF TURBOMACHINERY, Vol. 113, pp. 573-582.

Giles, M. B., 1988, "Calculation of Unsteady Wake/Rotor Interactions," *Journal of Propulsion and Power*, Vol. 4, pp. 356-362.

Giles, M. B., 1990, "Stator/Rotor Interaction in a Transonic Turbine," *Journal of Propulsion and Power*, Vol. 6, pp. 621-627.

Hansen, E. C., Serovy, G. K., and Sockol, P. M., 1980, "Axial-Flow Compressor Turning Angle and Loss by Inviscid-Viscous Interaction Blade-to-Blade Computation," ASME *Journal of Engineering for Power*, Vol. 102, pp. 28-34.

Hodson, H. P., 1985a, "Measurements of Wake-Generated Unsteadiness in the Rotor Passages of Axial Flow Turbines," ASME *Journal of Engineering for Gas Turbines and Power*, Vol. 107, pp. 467-476.

Hodson, H. P., 1985b, "An Inviscid Blade-to-Blade Prediction of a Wake-Generated Unsteady Flow," ASME *Journal of Engineering for Gas Turbines and Power*, Vol. 107, pp. 337-344.

Hwang, C. J., and Liu, J. L., 1992, "Locally Implicit Hybrid Algorithm for Steady and Unsteady Viscous Flows," *AIAA Journal*, Vol. 30, No. 5, pp. 1228-1236.

Jorgenson, P. C. E., and Chima, R. V., 1989, "Explicit Runge-Kutta Method for Unsteady Rotor/Stator Interaction," *AIAA Journal*, Vol. 27, No. 6, pp. 743-749.

Kiock, R., Lehthaus, F., Baines, N. C., and Sieverding, C. H., 1986, "The Transonic Flow Through a Plane Turbine Cascade as Measured in Four European Wind Tunnels," ASME *Journal of Engineering for Gas Turbines and Power*, Vol. 108, pp. 277-284.

Kwon, O. K., 1988, "Navier-Stokes Solution for Steady Two-Dimensional Transonic Cascade Flows," ASME JOURNAL OF TURBOMACHINERY, Vol. 110, pp. 339-346.

Lefcourt, M. D., 1965, "An Investigation Into Unsteady Blade Forces in Turbomachines," ASME *Journal of Engineering for Power*, Vol. 87, pp. 345-354.

Liu, J. S., and Sockol, P. M., 1989, "Unsteady Euler Cascade Analysis," AIAA Paper No. 89-0322.

Lo, S. H., 1985, "A New Mesh Generation Scheme for Arbitrary Planar Domains," *International Journal for Numerical Methods in Engineering*, Vol. 21, pp. 1403-1426.

Mavriplis, D. J., 1990, "Algebraic Turbulence Modeling for Unstructured and Adaptive Meshes," AIAA Paper No. 90-1653.

Nakahashi, K., Nozaki, O., Kikuchi, K., and Tamura, A., 1989, "Navier-Stokes Computations of Two- and Three-Dimensional Cascade Flowfields," *Journal of Propulsion and Power*, Vol. 5, No. 3, pp. 320-326.

Rai, M. M., and Madavan, N. K., 1990, "Multi-airfoil Navier-Stokes Simulations of Turbine Rotor-Stator Interaction," ASME JOURNAL OF TURBOMACHINERY, Vol. 112, pp. 377-384.

Scott, J. N., and Hankey, W. L., Jr., 1986, "Navier-Stokes Solutions of Unsteady Flow in a Compressor Rotor," ASME JOURNAL OF TURBOMACHINERY, Vol. 108, pp. 206-215.

Shamroth, S. J., McDonald, H., and Briley, W. R., 1984, "Prediction of Cascade Flow Fields Using the Averaged Navier-Stokes Equations," ASME *Journal of Engineering for Gas Turbines and Power*, Vol. 106, pp. 383-390.

Sharma, O. P., Butler, T. L., Renand, E., Milsaps, K., Jr., Dring, R. P., and Joslyn, H. D., 1988, "Rotor-Stator Interaction in Multi-stage Axial-Flow Turbines," AIAA Paper No. 88-3013.

Sorenson, R. L., 1980, "A Computer Program to Generate Two-Dimensional Grids About Airfoils and Other Shapes by the Use of Poisson's Equations," NASA TM 81198.

Weinberg, B. C., Yang, R. J., McDonald, H., and Shamroth, S. J., 1986, "Calculations of Two and Three Dimensional Transonic Cascade Flow Fields Using the Navier-Stokes Equations," ASME *Journal of Engineering for Gas Turbines and Power*, Vol. 108, pp. 93-102.

Yang, R. J., Lin, S. J., and Rai, M. M., 1988, "Unsteady Aerodynamics of Rotor-Stator Interaction in a Turbine Stage," AIAA Paper No. 88-0360.

Yee, H. C., 1989, "A Class of High-Resolution Explicit and Implicit Shock-Capturing Methods," NASA TM-101088.

Unsteady Boundary-Layer Transition in Flow Periodically Disturbed by Wakes

U. Orth[1]
Thermal Turbomachinery Department,
Technische Hochschule Darmstadt,
64287 Darmstadt,
Federal Republic of Germany

Boundary layers on turbomachinery blades develop in a flow that is periodically disturbed by the wakes of upstream blade cascades. These wakes have a significant effect upon laminar-turbulent boundary-layer transition. In order to study these effects, detailed velocity measurements using hot-wire probes were performed within the boundary-layer of a plate in flow periodically disturbed by wakes produced by bars moving transversely to the flow. The measurements were evaluated using the ensemble-averaging technique. The results show how the wake disturbance enters the boundary-layer and leads to a turbulent patch, which grows and is carried downstream. In favorable pressure gradients, transition due to wake turbulence occurred much earlier than predicted by linear stability theory. Between two wakes, laminar becalmed regions were observed far beyond the point at which the undisturbed boundary-layer was already turbulent.

1 Introduction

Due to the alternating arrangement of stationary and rotating blade rows in turbomachines, the boundary layer developing on a blade is periodically subjected to the wakes of upstream blades. The wakes exhibit a defect in mean velocity and a superimposed high level of turbulence intensity. These conditions have a significant influence upon boundary-layer transition behavior.

Knowledge of the boundary layer transition process is important for the design of turbomachinery blades. The boundary layer state, laminar or turbulent, greatly influences skin friction, and therefore drag losses and boundary layer separation. Since heat transfer coefficients are much higher in turbulent boundary layers, the location of transition is of importance for the sizing of blade cooling in gas turbine engines.

Various authors have published correlations predicting the onset of transition as a function of turbulence intensity and pressure gradient, e.g., Abu-Ghannam and Shaw (1980), whose correlation is based on measurements in strong adverse and favorable pressure gradients at different levels of isotropic free-stream turbulence produced by grids.

The present investigation was performed in a low-speed wind tunnel test rig on a plate where the boundary layer was sufficiently thick to permit hot-wire measurements. The flow was disturbed by wakes produced by bars crossing the flow upstream of the measuring section, in order to simulate realistic turbomachinery conditions. It was the same arrangement as employed by Pfeil and Pache (1977), Pfeil and Herbst (1979), Herbst (1980), and Pfeil et al. (1983).

In order to study the unsteady boundary-layer reaction in detail, hot-wire measurements were taken within the boundary layer and evaluated to visualize the temporal development. The results were compared with the boundary-layer development in undisturbed flow. The measurements presented in this paper are excerpts from a more extensive measurement series taken by Orth (1991).

2 Experimental Setup

The measurements presented here were carried out in a low-velocity wind tunnel with a rotating cascade upstream of the testing section, where a flat plate of 700 mm length and d = 20 mm thickness was mounted at half height, Fig. 1. The leading edge of the plate was carefully rounded with continuous curvature to prevent separation at positive angles of attack. The plate was set to different angles in order to adjust various adverse and favorable pressure gradients. Two rows of 30 pressure taps each were distributed along the centerline of the plate to measure the pressure distribution.

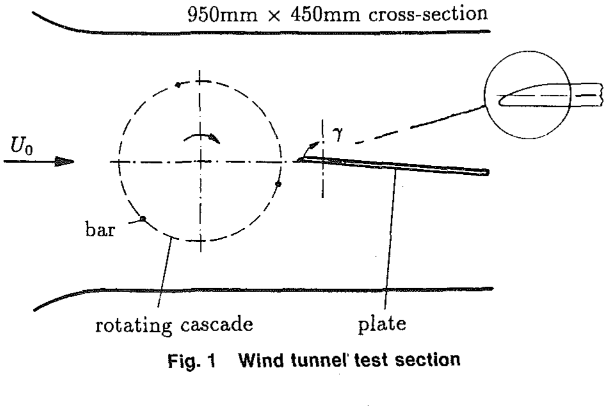

Fig. 1 Wind tunnel test section

---

[1] Present address: Allied-Signal Aerospace GmbH, 65479 Raunheim, Federal Republic of Germany.

Contributed by the International Gas Turbine Institute and presented at the 37th International Gas Turbine and Aeroengine Congress and Exposition, Cologne, Germany, June 1-4, 1992. Manuscript received by the International Gas Turbine Institute February 20, 1992. Paper No. 92-GT-283. Associate Technical Editor: L. S. Langston.

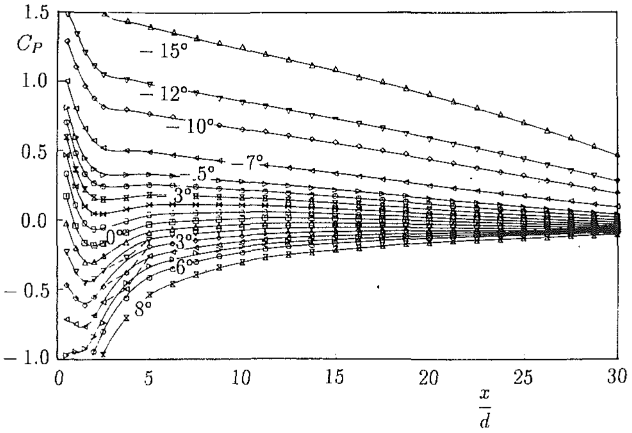

Fig. 2 Pressure distribution over the plate at various angles of attack, d = 20 mm, $U_0d/\nu = 2.09 \times 10^4$

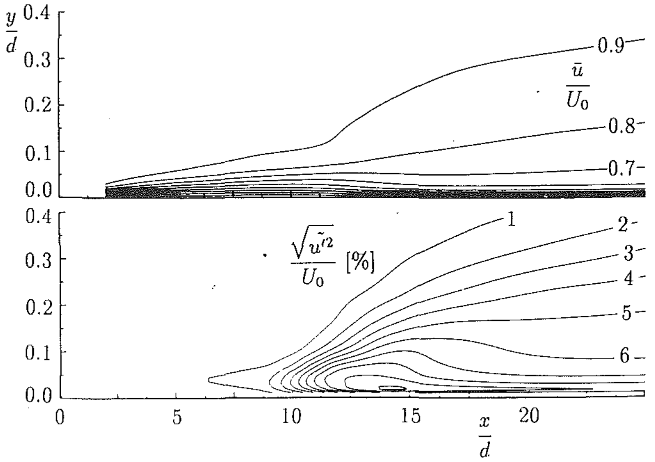

Fig. 3 Contours of mean velocity and turbulence intensity in undisturbed flow, γ = 0 deg, $U_0d/\nu = 2.09 \times 10^4$

The rotating cascade consists of two disks, which were driven and covered from the flow. Three bars of 2 mm diameter were fixed between the disks. The bars moved on a circular path with a radius of 300 mm perpendicular to the flow in front of the plate, so that their wakes hit the plate periodically. At the nearest position, the bars were 50 mm upstream of the plate leading edge. This setup was chosen to simulate conditions in turbomachines, where the blades are often subjected to periodic wakes of upstream blade rows.

Experiments were carried out in flow periodically disturbed by wakes and in an undisturbed flow, with a wind-tunnel turbulence intensity of 0.6 percent, for comparison. The Mach number was 0.05, so that compressibility effects are negligible.

3 Measurement Technique

The velocity measurements within the boundary layer were performed with single-hot-wire probes. Probe positioning was computer controlled using high precision stepper motors. The wall distance was adjusted with an accuracy of 0.005 mm.

Instantaneous hot-wire voltages were recorded by a digital data acquisition system (PDP11) and stored on magnetic tape for later evaluation. The rate of sampling and analog-digital conversion was between 5 and 50 kHz, the highest rate being used when a Fourier transform was to be carried out. A low-pass filter at 20 kHz was installed to prevent aliasing.

For experiments without periodic disturbances in the flow, five traces containing 4096 hot-wire voltages each were taken at each measuring position. For every single value, the corresponding velocity was calculated using King's law, and finally the mean velocity $\bar{u}$ and the turbulence intensity $\sqrt{\overline{u'^2}}$ were determined. In certain cases, frequency spectra were determined as well. Measurements in periodically disturbed flow were taken at a sampling rate of 10 kHz. At each position, 100 phase-locked bursts consisting of 1024 samples each were recorded. The data were used to calculate ensemble-averaged distributions of $\tilde{u}(t)$ and $\sqrt{\tilde{u'^2}}(t)$.

4 Measurements in Steady Flow

All measurements were taken in a free-stream velocity of 16.5 m/s. The Reynolds number was 7.31×10^5 using the plate length of 700 mm and 2.09×10^4 using the plate thickness of 20 mm.

The pressure distribution over the plate was measured for different angles of attack, as shown in Fig. 2. The rounded leading edge had a noticeable influence down to about $x/d = 5$, causing a pressure drop followed by a gradual pressure rise. $\gamma = 0$ deg corresponds to pressure gradient zero. The distributions for $\gamma = 2$ deg, 3 deg and 4 deg each show a point at $x/d = 3.75$, which lies lower than expected. This indicates the presence of a short separation bubble at these angles.

Hot-wire measurements were taken in the x-y plane on an array of positions within the boundary layer. Contours of constant mean velocity and constant turbulence intensity were calculated and are plotted in Fig. 3. An increase in turbulence intensity of more than 1 percent over the largely constant level within the laminar boundary layer is regarded as the onset of transition. This is observed near $x/d = 9$, which marks the beginning of a steep turbulence increase. A peak in turbulence intensity is encountered at $x/d = 14$, caused by the superposition of high-frequency turbulence and the slower intermittency between the laminar and turbulent states of the boundary layer.

Nomenclature

A = amplitude
C_P = pressure coefficient = $(p-p_0)/\frac{\rho}{2}U_0^2$
d = thickness of the plate = 20 mm
f = frequency
H_{12} = boundary-layer shape factor = δ_1/δ_2
p = static pressure
p_0 = free-stream pressure upstream of plate
Re = Reynolds number
u = velocity component parallel to surface
U_0 = free-stream velocity upstream of plate
U_∞ = velocity at the edge of the boundary layer
t = time
T = period of bar passing = 50 ms
Tu = turbulence intensity outside the boundary layer = $\sqrt{\overline{u'^2}}/U_0$
x = distance along plate surface
y = distance normal to surface
δ_1 = displacement thickness
δ_2 = momentum thickness
λ_2 = pressure gradient parameter = $\frac{\delta_2^2}{\nu}\frac{dU_\infty}{dx}$
ν = kinematic viscosity
ρ = density

Superscripts

$'$ = fluctuating component
$\bar{}$ = time-averaged quantity
$\tilde{}$ = ensemble-averaged quantity

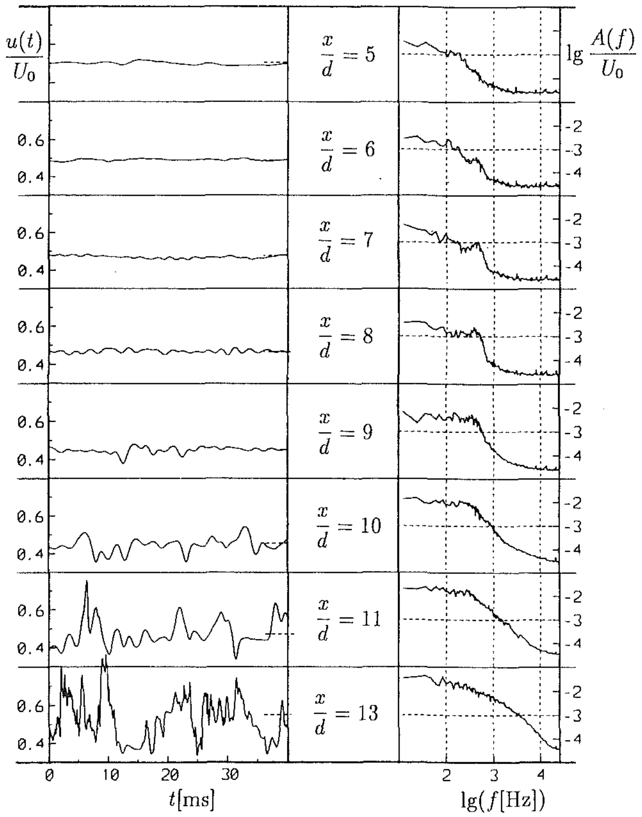

Fig. 4 Velocity traces and frequency spectra taken within the boundary layer at $y/d = 0.02$, undisturbed flow, $\gamma = 0$ deg, $U_0 d/\nu = 2.09 \times 10^4$

The upcome of turbulent shear stress leads to a deformation of the mean velocity profile. The comparison of laminar and turbulent boundary layer profiles with the same momentum thickness shows that the turbulent profile has a higher velocity at small wall distances but a lower velocity at greater wall distances. During transition, contours of low velocities therefore move toward the wall, and contours of high velocities move away from it. The contours of mean velocity show this clearly.

Velocity traces and frequency spectra are shown in Fig. 4 for eight flow positions at a wall distance of $y/d = 0.02$, where the amplification of fluctuations is most evident. In spite of a free-stream turbulence intensity of 0.6 percent, Tollmien-Schlichting waves appear at $x/d = 6$ and become amplified. They are clearly visible in the velocity traces and the spectra. The observed frequencies are in good agreement with results of stability calculations by Obremski et al. (1969), based on Falkner-Skan Profiles. The boundary layer is almost turbulent at $x/d = 13$, where the velocity traces exhibit high-frequency stochastic fluctuations and the spectrum shows increased amplitudes for all frequencies.

Detailed results of measurements at other angles of attack were published by Orth (1991) and are not shown here. As expected, the onset of transition moved towards the leading edge in adverse pressure gradients. In favorable pressure gradients, the boundary-layer remained laminar.

Boundary-layer transition on a cylinder in crossflow, where transitional separation bubbles appear at certain Reynolds numbers and turbulence intensities, was investigated by Pfeil and Orth (1990) based on a series of measurements performed in the same wind tunnel. As in the attached boundary-layer on the plate, Tollmien-Schlichting waves were clearly identified in the separated laminar boundary-layer prior to transition and subsequent reattachment.

5 Measurements in Periodically Disturbed Flow

Three bars of 2 mm diameter were mounted in the cascade rotating at 400 rpm. At every revolution, each bar generated two wakes, one in the near position (50 mm) and one in the far position (650 mm) from the plate leading edge. Therefore, 40 wakes per second hit the plate, 20 each from the near bar position and from the far bar position. The process repeats after $T = 50$ ms, and the Strouhal number, the nondimensional frequency, is $2\pi d/(T/2)U_0 = 0.30$, a value that is within the range found in turbomachinery.

Schröder (1985) studied the decay of unsteady wakes using measurements carried out in the same wind tunnel, Fig. 1, but without the plate. The maximum mean velocity defect within a plane wake, and also the maximum level of turbulence intensity, decreases proportional to $s^{-0.5}$, s being the flow distance from the bar. At the same time, the wake width increases proportional to $s^{0.5}$. Applied to the measurements presented here, Schröder's correlations yield a momentary flow angle deviation, at the plate leading edge, of -7.2 deg for the near wake, and $+1.4$ deg for the far wake. Maximum mean velocity defects are 14 percent and 3.2 percent of free-stream velocity, respectively. The maximum turbulence intensity $\sqrt{\widetilde{u'^2}}/U_0$ within the wake was 3.0 percent for the near wake and 1.5 percent for the far wake, based on hot-wire measurements on the plate outside the boundary layer near $x/d = 5$.

Measurements comparing the effect of a stationary wake with that of rotating wakes had showed that transition occurs at the same position for both cases. This indicates that it is the high level of turbulence intensity within the wake, and not the periodic fluctuation in mean velocity, that initiates transition. Addison and Hodson (1990b) also concluded that the high-frequency disturbances, and not velocity fluctuations of the wake jet, led to transition on the blades of their axial-flow turbine. The interaction of the wake turbulence with the boundary layer is therefore quasi-steady in typical turbomachinery conditions. These observations are in agreement with the work of Obremski and Fejer (1967), who defined a nonsteady Reynolds number $\mathrm{Re}_{NS} = (U_\infty \Delta U)/(2\pi f \nu)$ to describe the effect of oscillating flow on transition. Their study showed that periodic fluctuations force transition only if Re_{NS} is above 26,000. For the current measurements, Re_{NS} was only about 600.

As in undisturbed flow, hot-wire measurements were taken on an array of x and y positions. At each position, 100 phase-locked velocity traces were taken and evaluated to yield time-dependent distributions of ensemble-averaged turbulence intensities. Each plot shown in Fig. 5 represents a phase-lock-averaged distribution.

The wakes of the bar in the near position ($Tu = 3$ percent) and in the far position ($Tu = 1.5$ percent) can clearly be identified as they move over the plate. At $t/T = 0.4$, the near wake hits the plate. The reaction of the boundary layer is already visible at $t/T = 0.5$. A turbulent patch appears and convects downstream, its leading edge almost at free-stream velocity and its trailing edge significantly slower. Later, the growing turbulent patch clearly separates from the wake, which moves on outside the boundary layer.

A similar phenomenon occurs with the far wake, which hits the boundary layer at $t/T = 0.8$. In this case, a clear reaction of the boundary layer and the appearance of a turbulent patch can first be seen at $t/T = 0.2$ and at $x/d = 7.5$. At this time, the outside wake has already moved on, and no longer has any connection to the turbulent patch in the boundary layer.

Two things become evident when evaluating this sequence of contour plots: First, the disturbance caused by the wake is introduced into the boundary layer very early on, when the boundary layer is still thin. It does not lead to transition immediately. Instead, the disturbance convects within the bound-

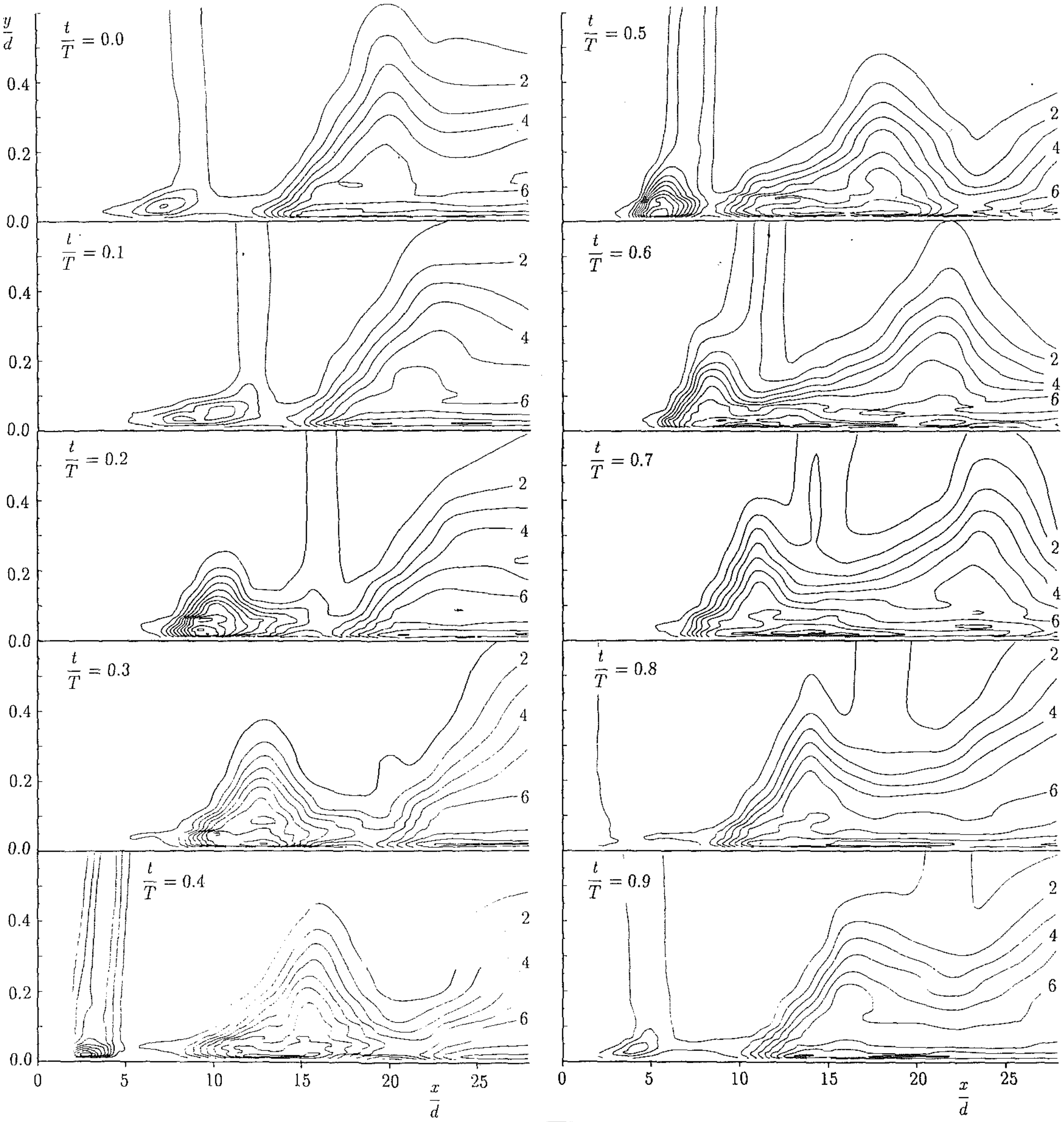

Fig. 5 **Phase-lock-averaged contours of turbulence intensity $\sqrt{\overline{u'^2}}/U_0$ [percent], $\gamma = 0$ deg, $U_0 d/\nu = 2.09 \times 10^4$, flow periodically disturbed by wakes, $TU_0/d = 41.3$**

ary layer and leads to transition sooner or later, depending on its intensity.

Secondly, a connection between the outer wake and the turbulent patch within the boundary layer, as suggested by Pfeil et al. (1983) and Addison and Hodson (1990a), apparently does not exist. Figure 5 clearly shows that the wake and the turbulent patch in the boundary layer move separately at their respective speeds. After disturbing the boundary layer very early on, the wake apparently has no further effect on the transition process.

The same data were used for the distance-time plots in Fig. 6. Ensemble-averaged distributions of turbulence intensity are shown for two wall distances. At $y/d = 0.12$, it again becomes evident that the disturbance within the boundary layer propagates at a slower rate than the wake outside the boundary layer, and that the wake completely separates from the turbulent patch, especially for the far wake, hitting the plate at $t/T = 0.8$.

The turbulent patch due to near-wake disturbance first appears at $t/T = 0.4$ or $t/T = 1.4$. The start of transition is marked at $x/d = 3.5$ for the near wake and $x/d = 7.5$ for the far wake. As before, an increase in turbulence intensity of more than 1 percent over the relatively stable level in the laminar boundary layer, at the wall distance where this first occurs, is viewed as the onset of transition. At $y/d = 0.03$ wall distance, the turbulent patches extend furthest in flow direction.

The dashed lines indicate the $0.5U_\infty$ trailing edge and 0.88 U_∞ leading edge propagation velocity of the turbulent patch, as first proposed by Schubauer and Klebanoff (1956), and recently verified for periodic forced turbulent patches by LaGraff et al. (1989). Measurements of turbulent patch propagation velocities at different angles of attack showed that they are basically independent of pressure gradient. However, the trailing edge velocity of 0.5 U_∞ increased by up to 10 percent in accelerated flow.

Figure 6 also reveals the existence of becalmed regions, as proposed by Schubauer and Klebanoff (1956) and discussed in detail by Pfeil et al. (1983). The propagation of Tollmien-Schlichting waves, at $0.29U_\infty$, is inhibited by the faster-moving turbulent patches. Therefore, natural transition does not occur

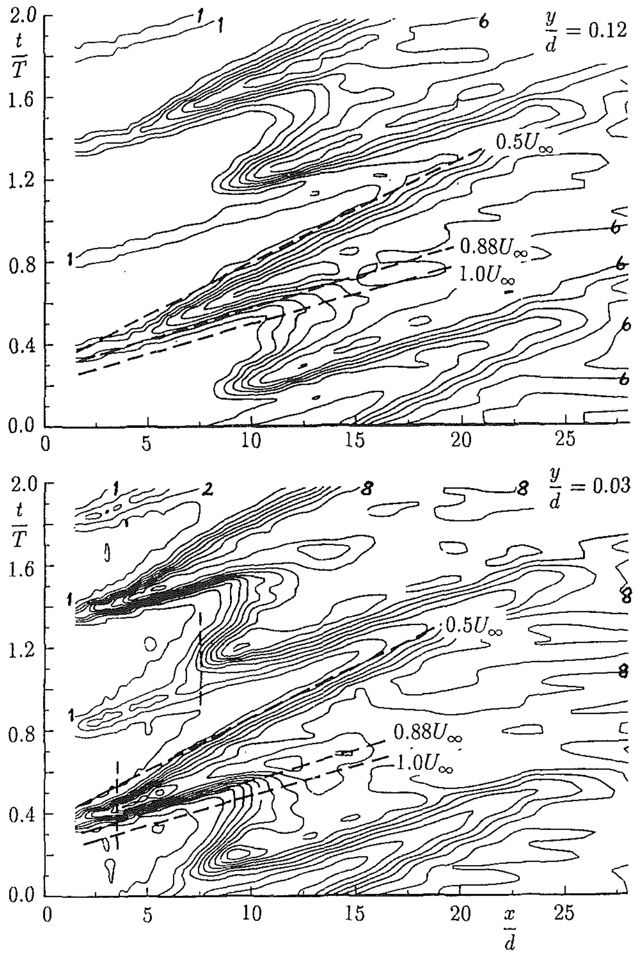

Fig. 6 Contours of turbulence intensity $\sqrt{\overline{u'^2}}/U_0$ [percent] in the distance-time plane, γ = 0 deg, $U_0 d/\nu = 2.09 \times 10^4$, flow periodically disturbed by wakes, $TU_0/d = 41.3$

behind a turbulent patch, creating a becalmed region. Laminar zones are still evident down to $x/d = 20$, whereas transition begins at $x/d = 9$ and ends at $x/d = 18.5$ in undisturbed flow.

Figure 7 shows the temporal development of boundary layer profiles of mean velocity and turbulence intensity when subjected to wakes. At $x/d = 2$, the wakes are clearly visible but the boundary layer has not yet reacted. At $x/d = 6$, the boundary layer has reacted to the turbulence input of the near wake, causing a brief increase in turbulence intensity and a deformation of the mean profile. At $x/d = 12$, the far-wake disturbance has also caused transition.

The turbulent patches grow and merge in flow direction, although short laminar becalmed regions are still visible at $x/d = 20$. These have disappeared at $x/d = 28$, although the boundary layer profiles are still not uniform in time at this position.

It again becomes evident, especially at $x/d = 12$, how the turbulent boundary layer separates from, and lags behind, the wake that caused it. The depictions also show that the turbulent boundary layer profiles are skewed in time. The maximum value of du/dy, indicating a turbulent profile close to the wall, occurs later than the time at which the outer boundary layer exhibits a typical turbulent profile.

An evaluation of the phase-lock-averaged boundary layer profiles yields the temporal development of the integral boundary layer parameters δ_2 and H_{12}. These are shown in Fig. 8. A short dip in the shape parameter H_{12} as a wake hits the boundary layer confirms that there is in fact no flow separation even with the far wake disturbance with its momentary flow angle increase of 1.4 deg. Again, we recognize the momentary onset of transition at $x/d = 3.5$ for the near-wake disturbance and at $x/d = 7.5$ for the far-wake disturbance, and the independent development of the outer wake and turbulent patch. At the last measurement point, $x/d = 28$, it is remarkable that although the boundary layer is almost fully turbulent, as indicated by H_{12}, the distribution of δ_2 shows a significant temporal variation in boundary layer thickness.

These investigations highlight the considerably different boundary layer development in periodically disturbed flow as compared to undisturbed flow. One effect is that the high turbulence intensity of the wake momentarily leads to an earlier onset of transition. Perhaps more remarkable is the fact that the effect of the periodic wakes extends far beyond the point at which the transition process is completed in the undisturbed boundary layer. Laminar zones extend far downstream, and an unsteadiness is still observed even when the boundary layer is finally fully turbulent.

6 Onset of Transition in Boundary Layers Disturbed by Wakes

Boundary layer measurements in undisturbed and disturbed flow, as previously described for γ = 0 deg, were also carried out at several other angles of attack in adverse and favorable pressure gradients. Figure 9 shows the development of the boundary layer of each angle of attack in a depiction of the Reynolds number based on displacement thickness Re_{δ_2}, versus the pressure gradient parameter λ_2. The characteristic shape of the curves due to pressure gradient is caused by the rounded leading edge, as mentioned in the discussion of Fig. 1.

At each angle, transition was registered in undisturbed flow (Tu = 0.6 percent), for the far-wake disturbance (Tu = 1.5 percent), and for the near-wake disturbance (Tu = 3.0 percent), and marked in Fig. 9. Also shown is the stability limit for Falkner-Skan profiles. The results of the measurements indicate that at sufficiently high turbulence intensities, the transition Reynolds number is almost independent of the pressure gradient. At favorable pressure gradients, transition is therefore encountered far earlier than could be expected according to stability theory.

Other authors have published transition criteria considering the effects of pressure gradient and free-stream turbulence, e.g., Driest and Blumer (1963), Dunham (1972), Seyb as published by Arnal (1984), and Abu-Ghannam and Shaw (1980). Of these correlations, that of Abu-Ghannam and Shaw is probably most reliable since it is based on a large number of measured points in favorable and adverse pressure gradients. At 3 percent turbulence intensity, it predicts the onset of transition of $\mathrm{Re}_{\delta_2} \approx 215$ for favorable pressure gradients. The flow was disturbed by grids producing a homogeneous and isotropic turbulence.

The new measurements presented in this paper show that the onset of transition occurs earlier than predicted by the correlations. This must be due to the structure of the wake turbulence, which can have a more severe influence on transition than the isotropic turbulence of grids as used by the other authors, and may also be attributed in part to the pressure gradient near the leading edge of the plate.

7 Conclusions

Investigations of boundary layer transition in undisturbed flow and in flow periodically disturbed by wakes were carried out based on extensive new hot-wire measurements.

In undisturbed flow (Tu = 0.6 percent), Tollmien-Schlichting waves were observed, which were amplified and led to transition. At high turbulence levels, transition can occur via a high intensity bypass mechanism as discussed by Morkovin (1977) without the amplification of Tollmien-Schlichting waves.

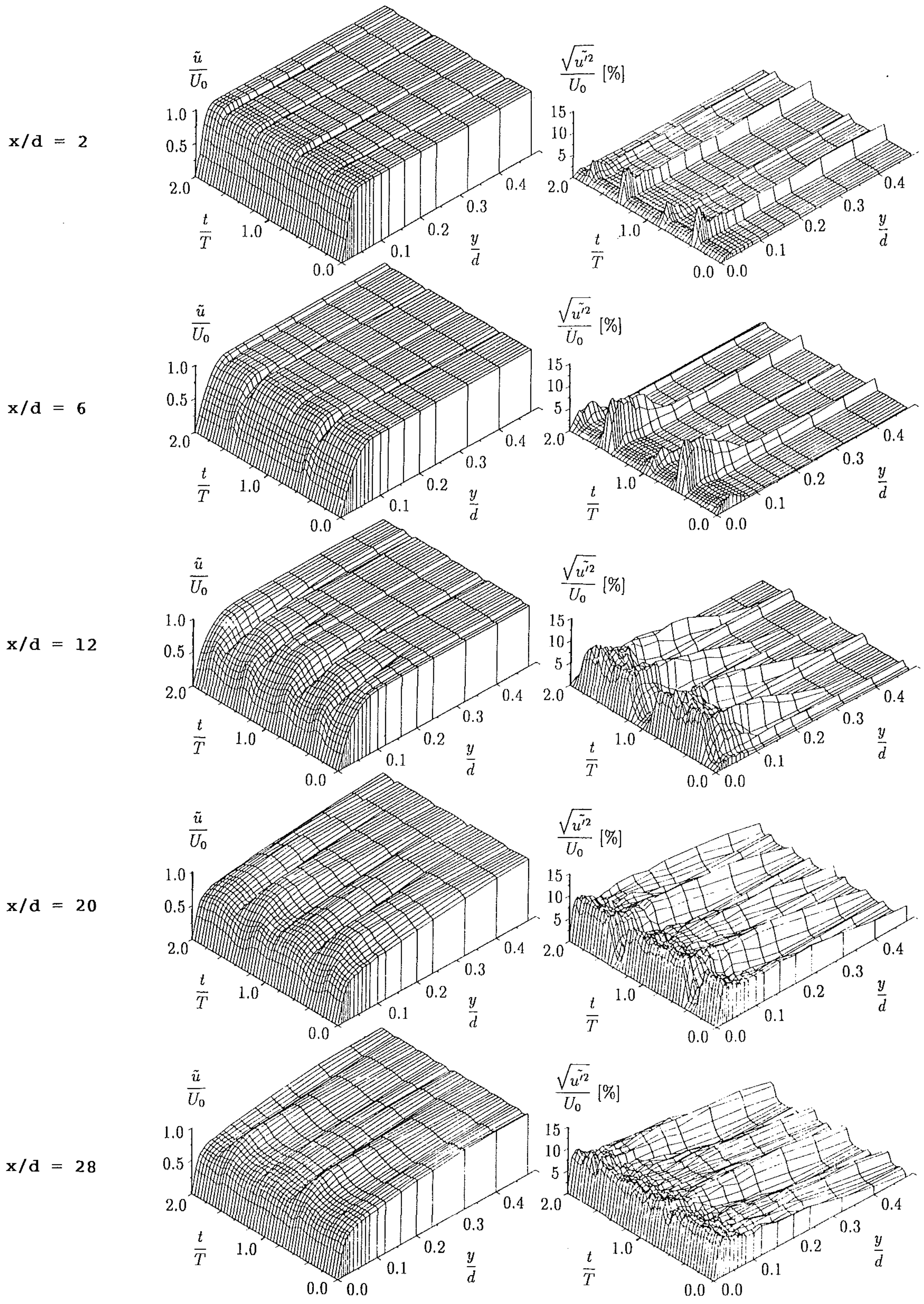

Fig. 7 Temporal development of boundary layer profiles of mean velocity and turbulence intensity, $\gamma = 0$ deg, $U_0 d/\nu = 2.09 \times 10^4$, flow periodically disturbed by wakes, $TU_0/d = 41.3$

Under periodic flow conditions as found in turbomachinery, the observed early onset of transition is likely to be caused by the high intensity of stochastic turbulence, and not by the periodic fluctuations.

The phase-lock-averaged contours of turbulence intensity in periodically disturbed flow have shown how the boundary layer reacts to the disturbance input. The disturbance enters the boundary layer very early on, and convects within it before leading to transition, sooner or later depending on turbulence intensity. Meanwhile, the wake passes over the boundary layer without noticeably influencing it again.

The boundary layer in flow periodically disturbed by wakes

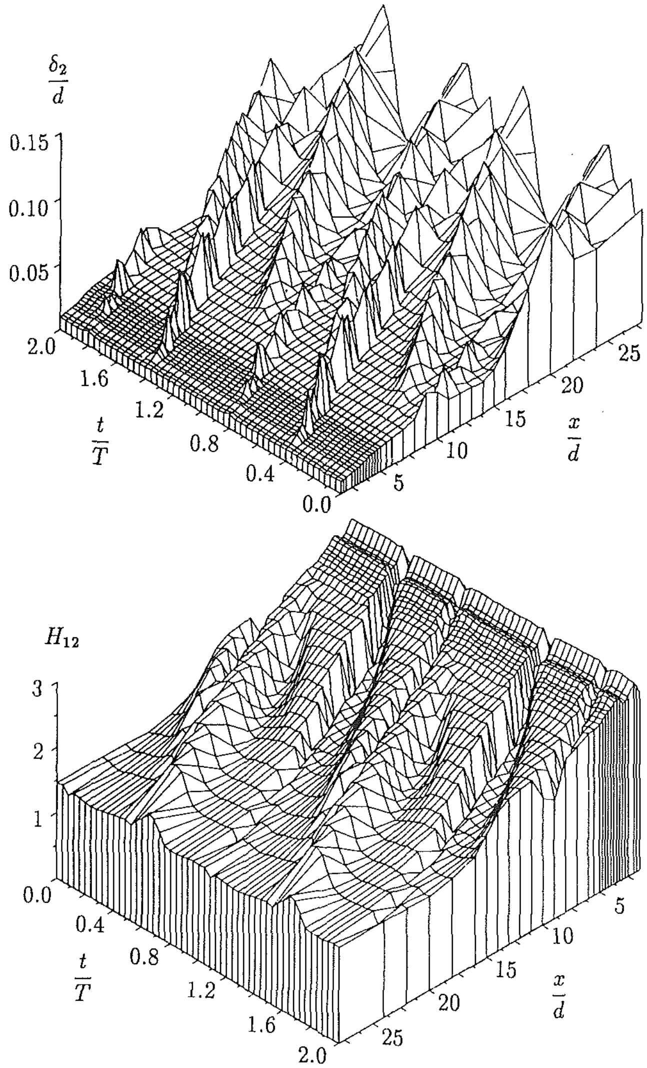

Fig. 8 Temporal development of boundary layer momentum thickness δ_2 and shape parameter H_{12}, γ = 0 deg, U_0d/ν = 2.09 × 10^4, flow periodically disturbed by wakes, TU_0/d = 41.3

differs in two ways from a boundary layer developing in undisturbed flow. First, an early onset of transition is observed momentarily as the high turbulence level of the wake disturbs the boundary layer and leads to the formation of a turbulent patch. Second, laminar becalmed regions are formed behind the turbulent patches, so that brief periods of laminar flow are still observed far beyond the location at which the undisturbed boundary layer is fully turbulent.

The results also show that with increasing turbulence intensity, the onset of transition shifts to lower Reynolds numbers, and the effect of pressure gradient almost disappears. The wake turbulence leads to an earlier transition than observed by other authors in isotropic grid turbulence.

Dedication

This paper is dedicated to Prof. Dr.-Ing. H. Pfeil, who initiated and greatly supported this work, but died before the preparation of this manuscript.

Acknowledgments

The financial support provided by the Deutsche Forschungsgemeinschaft (DFG) is gratefully acknowledged by the author.

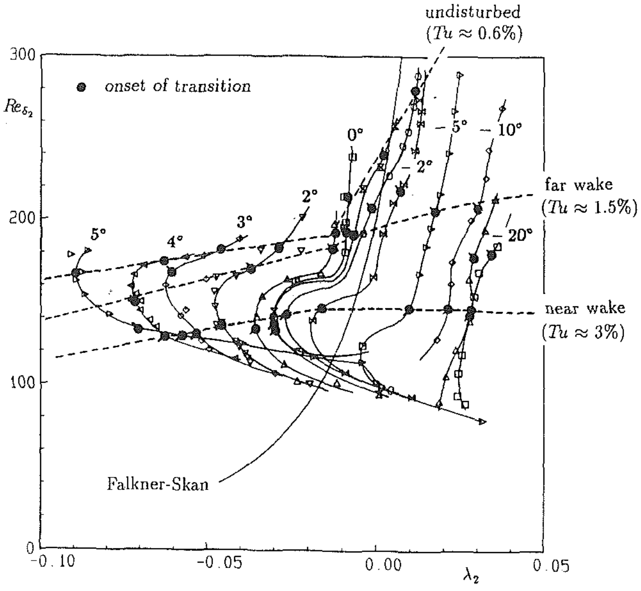

Fig. 9 Onset of transition in flow disturbed by wakes and in undisturbed flow, for various angles of attack, compared with Falkner-Skan profile linear stability theory

References

Abu-Ghannam, B. J., and Shaw, R., 1980, "Natural Transition of Boundary Layers—the Effects of Turbulence, Pressure Gradient and Flow History," *J. Mech. Engin. Sci.*, Vol. 22, pp. 213-228.

Addison, J. S., and Hodson, H. P., 1990a, "Unsteady Transition in an Axial-Flow Turbine: Part 1—Measurements on the Turbine Rotor," ASME JOURNAL OF TURBOMACHINERY, Vol. 112, pp. 206-214.

Addison, J. S., and Hodson, H. P., 1990b, "Unsteady Transition in an Axial-Flow Turbine: Part 2—Cascade Measurements and Modeling," ASME JOURNAL OF TURBOMACHINERY, Vol. 112, pp. 215-221.

Arnal, D., 1984, "Description and Prediction of Transition in Two-Dimensional Incompressible Flow," AGARD-R-709.

Driest, E. R. van, and Blumer, C. B., 1963, "Boundary-Layer Transition: Freestream Turbulence and Pressure Gradient Effect," *AIAA Journal*, Vol. 1, pp. 1303-1306.

Dunham, J., 1972, "Predictions of Boundary Layer Transition on Turbomachinery Blades," AGARD-ograph 164.

Herbst, R., 1980, "Entwicklung von Grenzschichten bei instationärer Zuströmung," Doctoral Thesis, TH Darmstadt, Federal Republic of Germany.

LaGraff, J. E., Ashworth, D. A., and Schulz, D. L., 1989, "Measurement and Modeling of the Gas Turbine Blade Transition Process as Disturbed by Wakes," ASME JOURNAL OF TURBOMACHINERY, Vol. 111, pp. 315-322.

Morkovin, M. V., 1977, "Instability, Transition to Turbulence and Predictability," AGARD-ograph 236.

Obremski, H. J., and Fefer, A. A., 1967, "Transition in Oscillating Boundary Layer Flows," *Journal of Fluid Mechanics*, Vol. 29, pp. 93-111.

Obremski, H. J., Morkovin, M. V., Landahl, M., Wazzan, A. R., Okamura, T. T., and Smith, A. M. O., 1969, "A Portfolio of Stability Characteristics of Incompressible Boundary Layers," AGARD-ograph 134.

Orth, U., 1991, "Untersuchung des Umschlagvorganges von Platten- und Zylindergrenzschichten bei ungestörter und stationär oder periodisch gestörter Zuströmung," Doctoral Thesis, TH Darmstadt, Federal Republic of Germany.

Pfeil, H., and Pache, W., 1977, "Messungen von Strömungsgrenzschichten unter Turbomaschinenbedingungen," *Z. Flugwiss. Weltraumforsch.*, Vol. 1, pp. 267-277.

Pfeil, H., and Herbst, R., 1979, "Transition Procedure of Instationary Boundary Layers," ASME Paper No. 79-GT-128.

Pfeil, H., Herbst, R., and Schröder, T., 1983, "Investigation of the Laminar-Turbulent Transition of Boundary Layers Disturbed by Wakes," ASME *Journal of Engineering for Power*, Vol. 105, pp. 130-137.

Pfeil, H., and Orth, U., 1990, "Boundary-Layer Transition on a Cylinder With and Without Separation Bubbles," *Experiments in Fluids*, Vol. 10, pp. 23-32.

Schröder, T., 1985, "Entwicklung des instationären Nachlaufs hinter quer zur Strömungsrichtung bewegten Zylindern und dessen Einfluss auf das Umschlagverhalten von ebenen Grenzschichten stromabwärts angeordneter Versuchskörper," Doctoral Thesis, TH Darmstadt, Federal Republic of Germany.

Schubauer, G. B., and Klebanoff, P. S., 1956, "Contributions on the Mechanics of Boundary-Layer Transition," NACA Report 1289.

T. Cebeci
Aerospace Engineering Department,
California State University, Long Beach,
Long Beach, CA 90840

M. F. Platzer
Department of Aeronautics and Astronautics,
Naval Postgraduate School,
Monterey, CA 93943

H. M. Jang[1]

H. H. Chen

Aerospace Engineering Department,
California State University, Long Beach,
Long Beach, CA 90840

An Inviscid-Viscous Interaction Approach to the Calculation of Dynamic Stall Initiation on Airfoils

An interactive boundary-layer method is described for computing unsteady incompressible flows over airfoils, including the initiation of dynamic stall. The inviscid unsteady panel method developed by Platzer and Teng is extended to include viscous effects. The solutions of the boundary-layer equations are obtained with an inverse finite-difference method employing an interaction law based on the Hilbert integral, and the algebraic eddy-viscosity formulation of Cebeci and Smith. The method is applied to airfoils subject to periodic and ramp-type motions and its abilities are examined for a range of angles of attack, reduced frequency, and pitch rate.

1.0 Introduction

The effect of unsteady motion of an airfoil on its stall behavior is of considerable interest regarding propellers, helicopter rotors, and compressors. Experiments with oscillating airfoils (Carr, 1988) have shown that the flow remains attached for angles of attack greater than those that cause stall on a steady airfoil. In addition, the onset of dynamic stall depends on the airfoil geometry, the flow Reynolds number and Mach number, and the degree of flow unsteadiness (reduced frequency). Hence there is a great need to develop calculation methods that can predict this phenomenon.

In principle there are two approaches to the calculation of viscous unsteady flows, one based on the solution of the Reynolds-averaged Navier-Stokes equations or their reduced forms and the other on the solution of a combination of inviscid and boundary-layer equations, often referred to as the interactive boundary-layer approach. Both calculation approaches have merit when applied to airfoil and wing flows, though the more complete Navier-Stokes equations are likely to represent better those flows in which cross-stream convection and diffusion are important, as in fully stalled conditions, whereas the interactive approach offers the possibility of more accurate numerical solutions with considerable savings of computer time and storage. An appraisal of either calculation method must also be viewed in the context of the physical processes they are to represent. Thus, in the case of unsteady airfoil flows, we are concerned with boundary layers that are comparatively thin at moderate angles of attack, thicker at higher angles of attack, with regions of separation on the upper surface of the airfoil, formation of a vortex at much higher angles of attack followed by rather thick and separated flow. Transition, with its complicated dependence upon geometry, becomes increasingly more important with increasing angle of attack and with decreasing chord Reynolds number. All these effects occur close to a surface so that the calculation method must represent a comparatively thin layer with high accuracy.

This paper presents an efficient and accurate approach for calculating unsteady flows over airfoils. It is based on the interactive boundary-layer approach that has been explored extensively for steady airfoil flows by Cebeci et al. (1986, 1990, 1991). Comparisons between the predictions of this method for steady flows include experimental data and solutions of the Navier-Stokes equations by Mehta et al. (1986) and Chang et al. (1988). Recently Jang et al. (1991) extended the interactive approach to the calculation of blade boundary layers and compared its predictions with Navier-Stokes calculations. In the present paper, in Section 2, we provide a complete description of this method including its extension to the prediction of dynamic stall onset on airfoils subject to ramp-type or harmonic oscillation motions. Results are presented in the third section and the paper ends with a summary of the more important conclusions.

2.0 Interactive Method for Unsteady Flows

As in two-dimensional steady flows, the interactive method for unsteady flows is based on the solutions of the inviscid and boundary-layer equations so as to ensure that each influences the other. The inviscid flow equations are solved by a panel method in which the airfoil is defined by a set of points with neighboring points connected by straight-line panels that have source density q_j ($j = 1, 2, \ldots, n$) and vorticity γ. The

---

[1] Present address: Mechanical Engineering Department, Chinese Culture University, Taiwan.

Contributed by the International Gas Turbine Institute and presented at the 37th International Gas Turbine and Aeroengine Congress and Exposition, Cologne, Germany, June 1-4, 1992. Manuscript received by the International Gas Turbine Institute February 11, 1992. Paper No. 92-GT-128. Associate Technical Editor: L. S. Langston.

inviscid method, developed by Platzer and Teng (Teng, 1987) is essentially an extension of the well-known Hess–Smith panel method for steady flows (Hess and Smith, 1966). The induced velocities caused by the elementary flows corresponding to source and vortex flows satisfy the irrotationality condition and the boundary conditions at infinity. In the approach adopted by Hess and Smith (1966), the source strength is assumed to be constant over each panel and is adjusted to give zero normal velocity over the airfoil and the vorticity strength is taken to be constant on all panels with its single value adjusted to satisfy the condition associated with the specification of circulation. The Kutta condition is used for this purpose, and although several properties of the flow at the trailing edge have been used in lieu of this condition, in the Hess–Smith method it is assumed that the upper and lower surface tangential velocities approach a common limit at the trailing edge.

In the extension of this method to unsteady flows, it is again necessary to determine the surface singularity distributions of source q_j and vorticity γ. We have the same number of unknowns, $(n + 1)$, but they are time dependent. We, therefore, introduce a subscript k as the time-step counter so that the unsteady flow problem is postulated to be solved at successive intervals of time, starting from $t_o = 0$. At each time step, t_k $(k = 1, 2, \ldots)$, the airfoil is represented by surface singularity distributions consisting of source and vorticity distributions $(q_j)_k$ $(j = 1, 2, \ldots, n)$ and γ_k. Again the source strengths vary from panel to panel but the vorticity strength remains the same for all panels.

The overall circulation Γ_k at time-step t_k is γ_k multiplied by the airfoil perimeter, l, and since the total circulation must be conserved according to the Helmholtz theorem of conservation of vorticity, any changes in the circulation at the airfoil surface must be balanced by an equal and opposite change in the vorticity leaving the airfoil. This vortex shedding process takes place through an element attached as an additional panel at the trailing edge with uniform vorticity distribution $(\gamma_w)_k$. This shed vorticity panel is established if its length Δ_k and inclination to the x axis of the airfoil-fixed coordinate system θ_k are determined. These are determined with the procedure of Basu and Hancock (1987) and the shedding process from the trailing edge is represented by a series of free vortices, each of constant vorticity determined by the time history of the circulation about the airfoil.

The viscous effects are included in the inviscid method through a blowing velocity, v_n

$$v_n = \frac{d}{dx}(u_e\delta^*) \tag{1}$$

which replaces the zero normal velocity at the airfoil surface and through the application of the Kutta condition. The blowing velocity displaces the dividing streamline outward from the surface of the airfoil to the location of the displacement thickness. The blowing velocity applied on the airfoil is replaced by suction velocity placed on the wake dividing streamline, as is the case for steady flows. Experience has shown that best results are obtained when surface pressures are calculated with a Kutta condition applied on the displacement surface rather than on the surface panels.

The boundary-layer equations for two-dimensional incompressible laminar and turbulent flows are well known and, with the eddy viscosity (ϵ_m) concept, can be expressed in the following form:

$$\frac{\partial u}{\partial x} + \frac{\partial v}{\partial y} = 0 \tag{2}$$

$$\frac{\partial u}{\partial t} + u\frac{\partial u}{\partial x} + v\frac{\partial u}{\partial y} = \frac{\partial u_e}{\partial t} + u_e\frac{\partial u_e}{\partial x} + \nu\frac{\partial}{\partial y}\left(b\frac{\partial u}{\partial y}\right) \tag{3}$$

where $b = 1 + \epsilon_m/\nu$. The usual wall boundary conditions on the airfoil are

$$y = 0, \quad u = v = 0 \tag{4a}$$

For an external velocity distribution specified by the panel method, $u_e^o(x, t)$, the edge boundary condition is

$$y = \delta, \quad u = u_e^o(x, t) \tag{4b}$$

The boundary conditions in the wake, as in steady flows, require the definition of a dividing line, $y = 0$, which in our study is assumed to correspond to the instantaneous wake dividing streamline. This may not be a good choice for severe unsteady motions but is likely to be appropriate for mild unsteady motions. The resulting boundary conditions in the wake are

$$y = 0, \quad v = 0 \tag{5a}$$

$$y \to \pm\infty, \quad u \to u_e^o(x, t) \tag{5b}$$

To calculate flows with separation, the external velocity must be computed as part of the solution. In the present study, as in steady flows, this is achieved with the formulation recommended by Veldman (1981), according to which the perturbation velocity due to viscous effects, namely, $\delta u_e(x, t)$ will be assumed to be given by the so-called Hilbert integral,

$$\delta u_e(x, t) = \frac{1}{\pi}\int_{x_a}^{x_b} \frac{\mathrm{d}}{\mathrm{d}\sigma}(\mathrm{u}_e\delta^*)\frac{d\sigma}{x - \sigma} \tag{6}$$

in the interaction region confined to the range $x_a \le x \le x_b$ so that the edge boundary condition is written as

$$u_e(x, t) = u_e^o(x, t) + \delta u_e(x, t) \tag{7}$$

In addition to the above boundary conditions, the solutions of Eqs. (2) and (3) require initial and upstream conditions. We generate the former by assuming that at $t = 0$ steady conditions prevail and solve the steady-flow equations. There is no problem in generating the upstream conditions for the steady-flow equations since the calculations start at the stagnation point. However, the situation is somewhat different for unsteady flows since the stagnation point is not fixed and, although u_e is zero, we cannot assume a priori that u is also zero. A convenient and accurate procedure to calculate the first velocity profile (the upstream condition) at the new time step has been developed by Cebeci and Carr (1983). This procedure involves the characteristic box scheme developed by Cebeci and Stewartson, as described by Bradshaw et al. (1981) and is used to generate the upstream conditions.

A detailed description of the solution procedure will be reported separately. Briefly, the above equations employing the algebraic eddy-viscosity formulation of Cebeci and Smith (1974) are first expressed in transformed coordinates; these provide significant advantages over the physical coordinates by allowing the calculations to be performed with larger steps in the streamwise and time directions. In addition, they remove the singularity the equations have in physical coordinates at the stagnation point of the airfoil. Two sets of coordinate transformations are employed, one for the direct problem when the equations are solved for the prescribed pressure distribution and the other for the inverse problem with the inviscid velocity updated during the iterations. In the direct mode we use the Falkner–Skan transformation given by

$$\eta = \sqrt{u_e/\nu x}\,y, \quad \psi = \sqrt{u_e \nu x}\,F(x, \eta, t) \tag{8}$$

and write Eqs. (2) and (3) in the following form:

$$(bF'')' + \frac{m+1}{2}FF'' + m[1 - (F')^2] + m_3(1 - F') - \frac{\eta}{2}m_3F'' = x\left(\frac{1}{u_e}\frac{\partial F'}{\partial t} + F'\frac{\partial F'}{\partial x} - F''\frac{\partial F}{\partial x}\right) \tag{9}$$

Here a prime denotes differentiation with respect to η and m and m_3 are dimensionless pressure gradient parameters given by

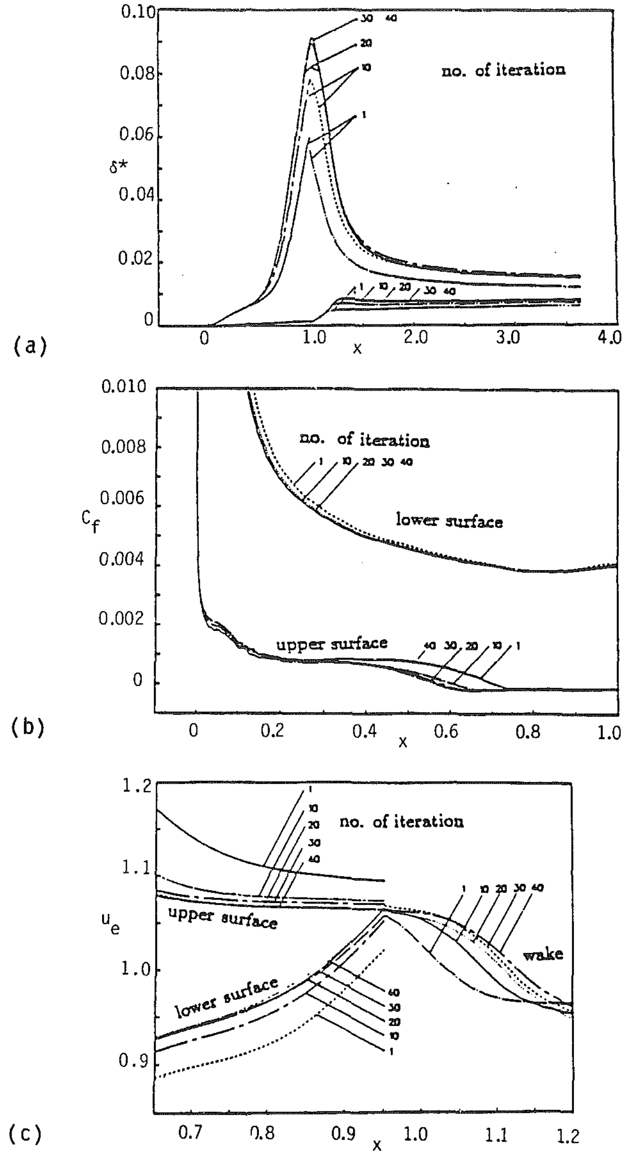

Fig. 1 The variation of (*a*) displacement-thickness, (*b*) local skin-friction coefficient, and (*c*) boundary-layer edge velocity (only the trailing-edge regions are shown) distributions with iteration number: steady, α = 15 deg, $R_c = 2 \times 10^6$

$$m=\frac{x}{u_e}\frac{\partial u_e}{\partial x}, \quad m_3=\frac{x}{u_e^2}\frac{\partial u_e}{\partial t} \tag{10}$$

In the inverse mode, we use a modified form of the transformation given by Eq. (8),

$$Y=\sqrt{u_0/\nu x}\,y, \quad \psi=\sqrt{u_0\nu x}\,f(x, y, t) \tag{11}$$

and, with a prime now denoting differentiation with respect to Y, write Eqs. (2) and (3) in the following form, with all the dimensional quantities properly normalized:

$$(bf'')'+\frac{1}{2}ff''+xu_e\frac{\partial u_e}{\partial x}+x\frac{\partial u_e}{\partial t} = x\left(\frac{\partial f'}{\partial t}+f'\frac{\partial f'}{\partial x}-f''\frac{\partial f}{\partial x}\right) \tag{12}$$

In the direct mode, the boundary conditions for Eq. (9) are straightforward and follow from those given by Eqs. (4) and (5). For airfoil calculations, they are

$$\eta=0, \quad F=F'=0; \quad \eta=\eta_e, \quad F'=1 \tag{13a}$$

and for wake calculations, they are

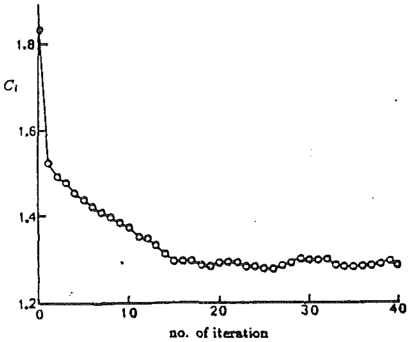

Fig. 2 The variation of lift-coefficient with iteration number: steady, α = 15 deg, $R_c = 2 \times 10^6$

$$\eta=0, \quad F=0; \quad \eta\to\pm\infty, \quad F'\to 1 \tag{13b}$$

In the inverse mode, after applying a discrete approximation to the Hilbert integral, those on the airfoil are

$$Y=0, \quad f=f'=0 \tag{14a}$$

$$Y=Y_e, \quad u_e-\tilde{c}_{ii}(Y_e u_e-f_e)=g_i \tag{14b}$$

and in the wake

$$Y=\pm Y_e, \quad u_e-\tilde{c}_{ii}[u_e(Y_e-Y_{-e})-(f_e-f_{-e})]=(g_w)_i \tag{15a}$$

$$Y=0, \quad f=0 \tag{15b}$$

In the above equations, the subscript e denotes quantities at the edge of the wall boundary layer and the upper edge of the wake; $-e$ denotes quantities at the lower edge of the wake; $\tilde{c}_{ii}$ is defined as

$$\tilde{c}_{ii}=c_{ii}\left(\frac{\nu x}{u_o}\right)^{1/2} \tag{16}$$

The parameters g_i and $(g_w)_i$ are given by

$$g_i=(u_e^o)_i^k+\sum_{j=i_a^I}^{i-1} C_{ij}[D_j^I-(D_j^I)^k] - C_{ii}(D_i^I)^k+\sum_{j=i+1}^{i_b} C_{ij}[DB_j^I)\,(D_j^I)^k] \tag{17a}$$

$$(g_w)_i=(u_e^o)_i^k+\frac{1}{2}\sum_{I=u\&l}\left\{\sum_{j=i_a^I}^{i-1} C_{ij}[D_j^I-(D_j^I)^k] - C_{ii}(D_i^I)^k+\sum_{j=i+1}^{i_b} C_{ij}[DB_j^I-(D_j^I)^k]\right\} \tag{17b}$$

where the superscript $I = u$ refers to upper side quantities or l to lower side quantities, with

$$D\equiv\sqrt{\nu x/u_o}\,(Y_e u_e-f_e)$$

Depending on the complexity of the flowfield, two forms of the box scheme are employed. In regions where u is positive, the regular box scheme is used. In regions of negative u velocity, the characteristic box scheme is used with the FLARE approximation, discussed by Bradshaw et al. (1981) in which the convective term in the momentum equation, $f''(\partial f'/\partial x)$ is set equal to zero in regions of negative velocity. Further details will be provided by Cebeci and Khattab (1992).

3 Results and Discussion

For a given inviscid velocity distribution provided by the panel method, the solutions of the boundary-layer equations described in the previous section involve an iteration process in which the downstream effects are accounted for by performing a series of calculations (sweeps) on the airfoil and in the wake starting first on the stagnation point of the airfoil.

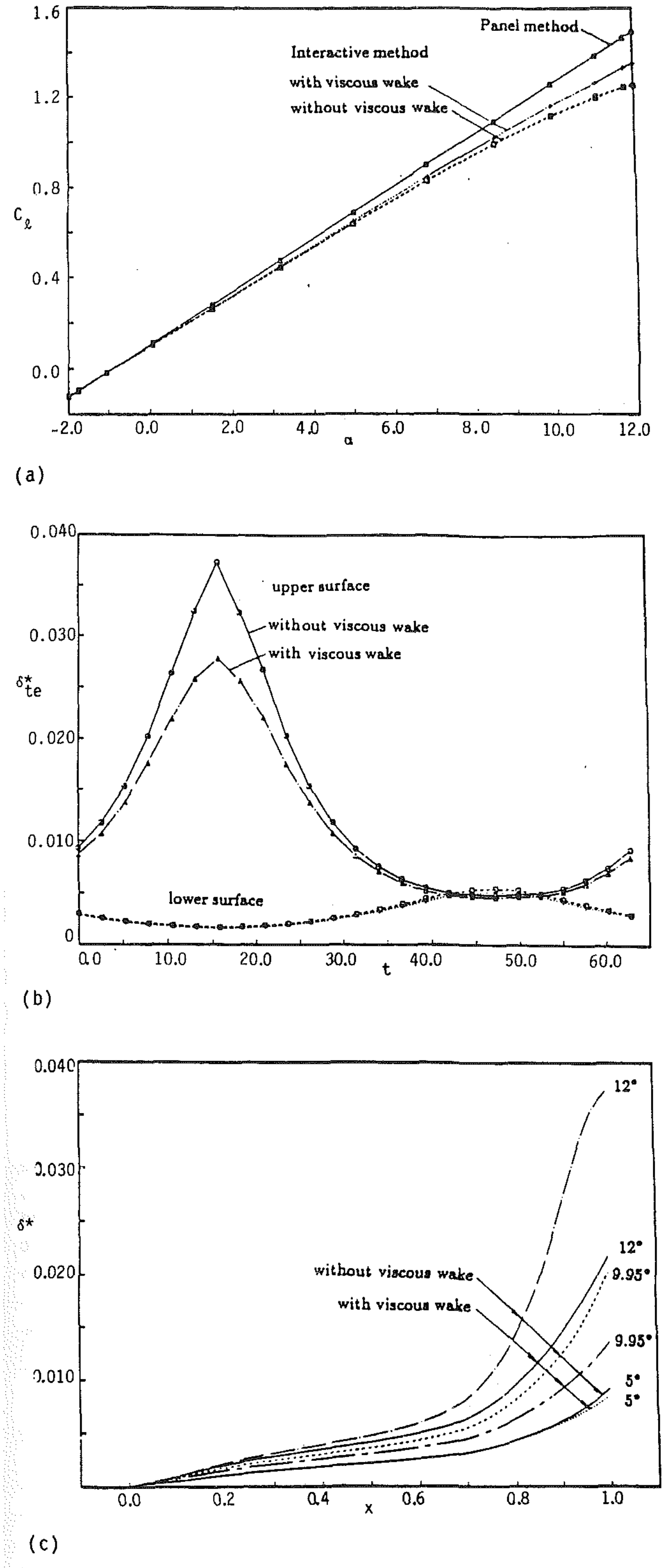

Fig. 3 The effect of viscous wake on (*a*) lift-coefficient and (*b*) displacement-thickness distribution at trailing edge and (*c*) displacement-thickness distribution on the upper surface. $\alpha(t)$ = 5 deg + 7 deg sin(ωt), k = 1 × 10^{-5}, R_c = 2 × 10^6.

After each sweep, the displacement thickness is updated so that the upstream and downstream viscous effects can be included in the next sweep. In addition to improving the boundary-layer calculations in this way, the effect of viscous effects on the pressure distribution are also accounted for via the blowing velocity in the panel method. Moreover, for the flow over a lifting body, the Kutta condition and wake-vorticity effects are related to the pressure distribution on the body surface.

The calculations start with the steady-state conditions and upon the convergence of the solutions, the same iterative procedure shifts to the next time step with the solutions at previous time as initial guesses. A typical evolution of the solutions during the inviscid-viscous iteration procedure is shown in Figs. 1 and 2. The calculations were performed for the Sikorsky SSC-A09 airfoil section at a chord Reynolds number of 2 × 10^6 and an angle of attack of 15 deg, which is beyond that of maximum lift. In order to improve the rate of convergence, the calculations began with displacement thickness and blowing-velocity distributions from a converged solution at an angle of attack of 14 deg so that the solutions indicated by iteration 1 in Fig. 1 include viscous effects. Figure 1(*a*) shows the upper surface, lower surface, and wake displacement-thickness distributions. The displacement thickness on the lower surface and for the forward 0.4 of chord on the upper surface do not change with the iterations, whereas the trailing-edge displacement thickness on the upper surface increases by 50 percent during the computation. Figure 1(*b*) illustrates the change in local skin-friction coefficients with iteration number on the two surfaces; the only important changes are in the vicinity of separation. The variation of the velocity distribution, u_e, with iteration is shown in Fig. 1(*c*), and it should be noted that the discontinuities in the u_e and δ^* distributions at the trailing edge are gradually eliminated as the iteration number increases.

For the results presented in this paper, 20 inviscid-viscous iterations were assumed to be sufficient for flows involving stall, and fewer iterations were sufficient where stall did not occur. The variation of lift coefficient with iterations is shown in Fig. 2, and the large change in the first iteration is due to the initial guess.

The interactive boundary-layer calculations can be performed for an airfoil with and without consideration of its wake. Before we present results for an airfoil operating under unsteady flow conditions, we first consider the wake effect on the solutions. To this end, we examine the Sikorsky SSC-A09 airfoil undergoing a harmonic oscillation, α = 5 deg + 7 deg sin(ωt), at a very low reduced frequency, $k(\equiv \omega c/u_\infty)$ = 1 × 10^{-5}. The lift coefficients of Fig. 3(*a*) show that for a chord Reynolds number, R_c of 2 × 10^6, the roles of wall boundary layer and viscous wake are opposite so that the former reduces the lift coefficient while the latter increases it, and the magnitudes of the effects increase at high angles of attack. Figure 3(*b*) shows the displacement thicknesses on the upper and lower surfaces at the trailing edge for one cycle of motion, and Fig. 3(*c*) shows the displacement thickness distribution on the upper surface at various angles of attack. Both figures show that the viscous wake reduces the displacement thickness, which is built up by the viscous effects in the wall boundary layer.

The study of the viscous wake effects in the slow motion cases, as described above, provides a quantitative standard for evaluating the viscous wake effects in more severe unsteady flows. When the airfoil performs slow movements, the vorticities shed to the wake are weak and the wake, due to the viscosity, behaves like a distribution of sinks along the dividing line. Increasing the severity of the unsteady motion increases the strength of the vorticities shed to the wake. The wake of a real flow over an airfoil can, therefore, be described as including vorticities and sinks that mix and interact with each other.

To model the unsteady wake by a viscous-inviscid interactive method, some assumptions are necessary. In the present method we have assumed that the two elements of the unsteady wake model, vortices and sinks, are distinct and do not influence each other. This means that the vortices shed via the potential flow go downstream according to their own local velocities

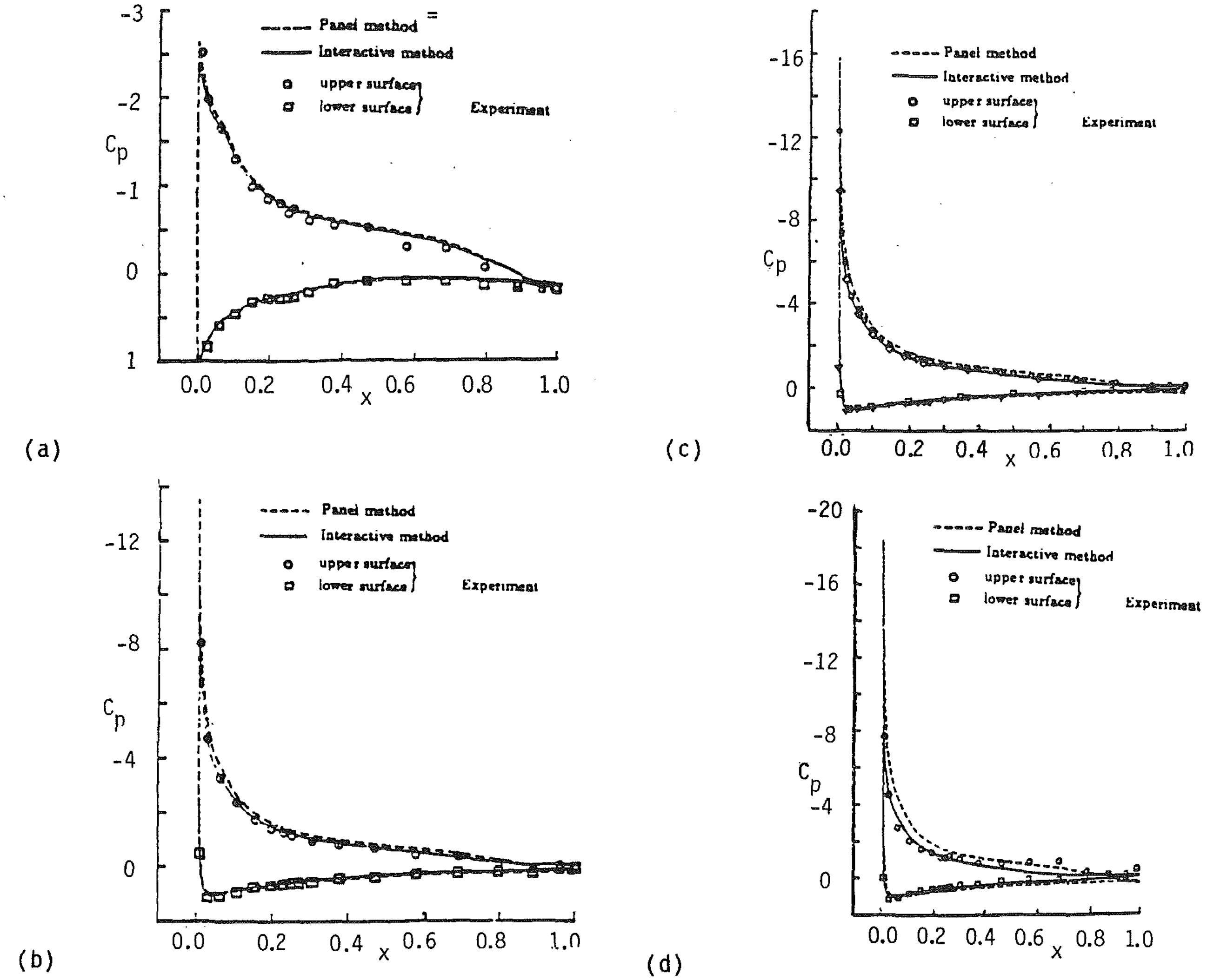

Fig. 4 Pressure-coefficient distributions at α = (*a*) 6 deg, (*b*) 13 deg, (*c*) 14 deg, (*d*) 15 deg; steady, $R_c = 2 \times 10^6$

without the influence of sinks, and the sinks computed from the viscous wake distribute on the instantaneous wake dividing line, the location of which is evaluated without the influence of vorticities. This model satisfies the steady-flow condition as the unsteady motion approaches zero and should capture most of the characteristics of the wake as the unsteady motion of the airfoil increases.

3.1 Results for Steady Flows. Steady-flow calculations including the wake effect were performed for a Sikorsky SSC-A09 airfoil at a chord Reynolds number of 2×10^6 with transition fixed on the upper and lower surfaces at locations two stations behind the stagnation point. These results have been described before by Cebeci and Jang (1990) and therefore only a few additional comparisons with the measurements of Lorber and Carta (1988) are presented here.

Pressure-coefficient distributions on the airfoil surface are displayed in Figs. 4(*a*) to 4(*d*). At low angles of attack, the boundary-layer effects are negligible and the results of both the panel and interactive methods agree with experiment. When the angles of attack are higher than 13 deg, the boundary-layer effects become more important, and Figs. 4(*c*) and 4(*d*) show that the interactive solutions agree with experimental data better than those of inviscid-flow equations.

3.2 Results for Unsteady Flows. The accuracy of an interactive method for simulating the unsteady flow depends on several factors, which include the inviscid-flow method, the modification of the inviscid-flow method to accept viscous effects, the boundary-layer scheme as well as the numerical scheme used to solve the equations, and the coupling procedure between the inviscid- and viscous-flow calculations. The results in the previous subsection described for steady flows show that these factors are properly represented in the steady-flow calculations so that the steady-flow model can now be used as a base for extension to unsteady-flow calculations.

The overall features of a subsonic flow over an airfoil executing an unsteady motion are primarily characterized by the extent of flow reversal (or separation). For testing the performance of our method, calculations are performed in the order of increasing levels of flow complexity, starting first with flows without and then with reversal and in subsection 3.3 are followed by flows with substantial regions of flow separation.

Flows Without Reversal Region. We again consider the same Sikorsky airfoil in which the change in angle of attack takes place according to

$$\alpha(t) = 5 \text{ deg} + 5 \text{ deg} \sin \omega t$$

at three reduced frequencies, $k = 1 \times 10^{-4}$, 0.1, and 0.5 for a chord Reynolds number of 2×10^6. The interactive flow calculations are performed with the unsteady panel method and the inverse boundary-layer method described in Section 2.0.

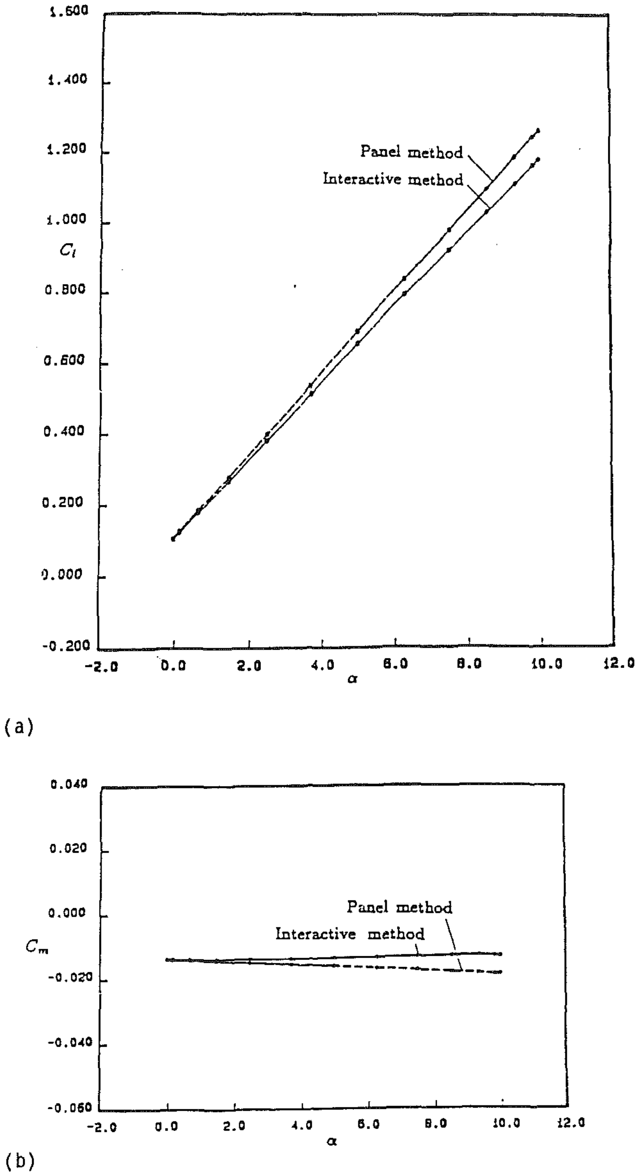

Fig. 5 Variations of (*a*) lfit and (*b*) pitching moment coefficients with angle of attack for the SSC-A09 airfoil; $\alpha(t) = 5$ deg + 5 deg $\sin(\omega t)$, $k = 10^{-4}$

The results with the interactive method shown in Fig. 5 were first obtained with the inverse boundary-layer calculations performed for steady flow calculations. Even though at each time the inviscid flow was calculated with the unsteady panel method, the viscous effects were calculated with the boundary-layer equations in which the time-dependent terms, $\partial u/\partial t$ and $\partial u_e/\partial t$ were neglected. This quasi-steady model is valid when

$$\frac{\partial u}{\partial t} \text{ and } \frac{\partial u_e}{\partial t} \ll u_e \frac{\partial u_e}{\partial x}$$

Repeating the calculations in which the viscous effects are computed with the unsteady boundary-layer equations and comparing the results with those obtained with the quasi-steady model showed that (Fig. 5) the solutions of both interactive methods were identical.

Figures 6 and 7 show the lift and pitching moment coefficient curves for the other two frequencies, all computed with viscous effects obtained from the solutions of the unsteady boundary-layer equations. We can see from the results that the hysteresis effects increase with the increase of the reduced frequency. Since the boundary-layer calculation started from steady state and suddenly joined the inviscid flow calculation, the viscous-inviscid results showed a little discontinuity at the beginning and the end of the cycle. One very interesting aspect of the lift coefficient curve is that at $k = 0.1$ the lift coefficient of the upward stroke is lower than that of the downward stroke, but it is just opposite at $k = 0.5$. This phenomenon can be explained by comparing the pressure coefficient distributions in the upward and downward strokes at a certain angle of attack ($\alpha = 7.5$ deg purely inviscid flow, for example), as shown in Fig. 8 for different frequencies. At $k = 10^{-4}$, no hysteresis effects appear and the pressure-coefficient distributions of upward and downward strokes are identical to the steady one. Increasing k to 0.1, the hysteresis effects appear mainly on the fore part of the airfoil. The pressure peak at $\alpha = 7.5$ deg ↑ is lower than the corresponding steady one, whereas that at $\alpha = 7.5$ deg ↓ is higher, so that the lift coefficient in the downward stroke is higher than that in the upward stroke. Increasing k generates more unsteady motion of the airfoil aft (since it is farther from the pivot point) so that the effects on the pressure distribution there are more enhanced, as shown in Fig. 8(*c*), for $k = 0.5$. From the pressure distribution, we can see that in the downward stroke the negative contribution to the lift coefficient in the aft part cannot be balanced by the

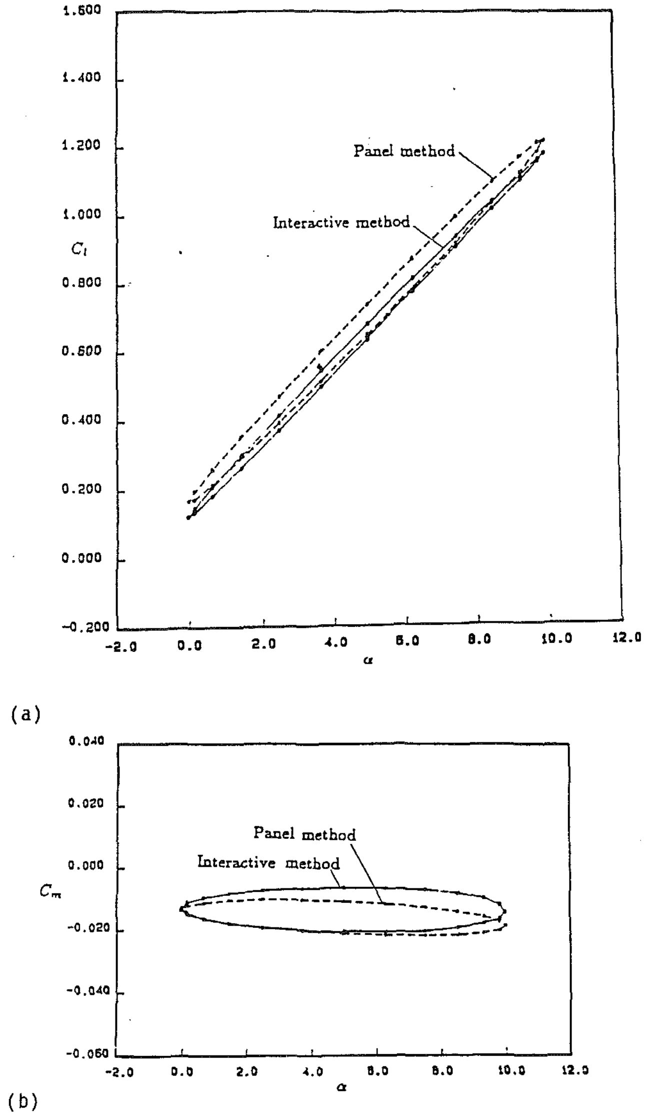

Fig. 6 Variations of (*a*) lift and (*c*) pitching moment coefficients of the SSC-A09 airfoil with angle of attack; $\alpha(t) = 5$ deg + 5 deg $\sin(\omega t)$, $k = 0.1$

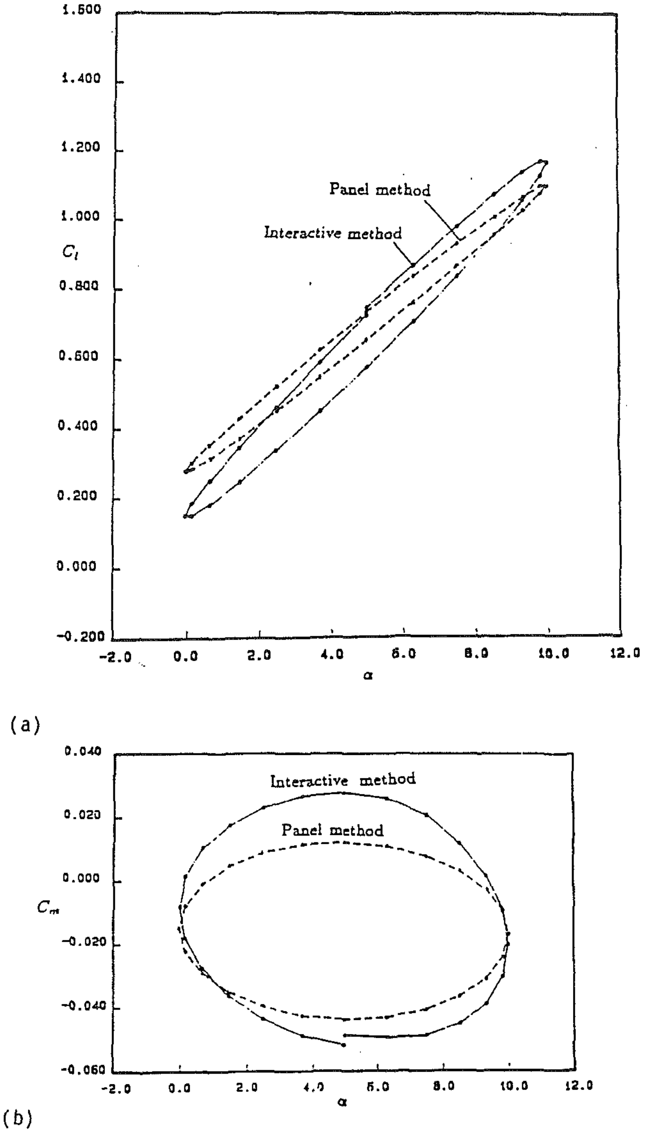

Fig. 7 Variations of (*a*) lift and (*b*) pitching moment coefficients of the SSC-A09 airfoil with angle of attack; unsteady, $\alpha(t)$ = 5 deg + 5 deg sin (ωt), k = 0.5

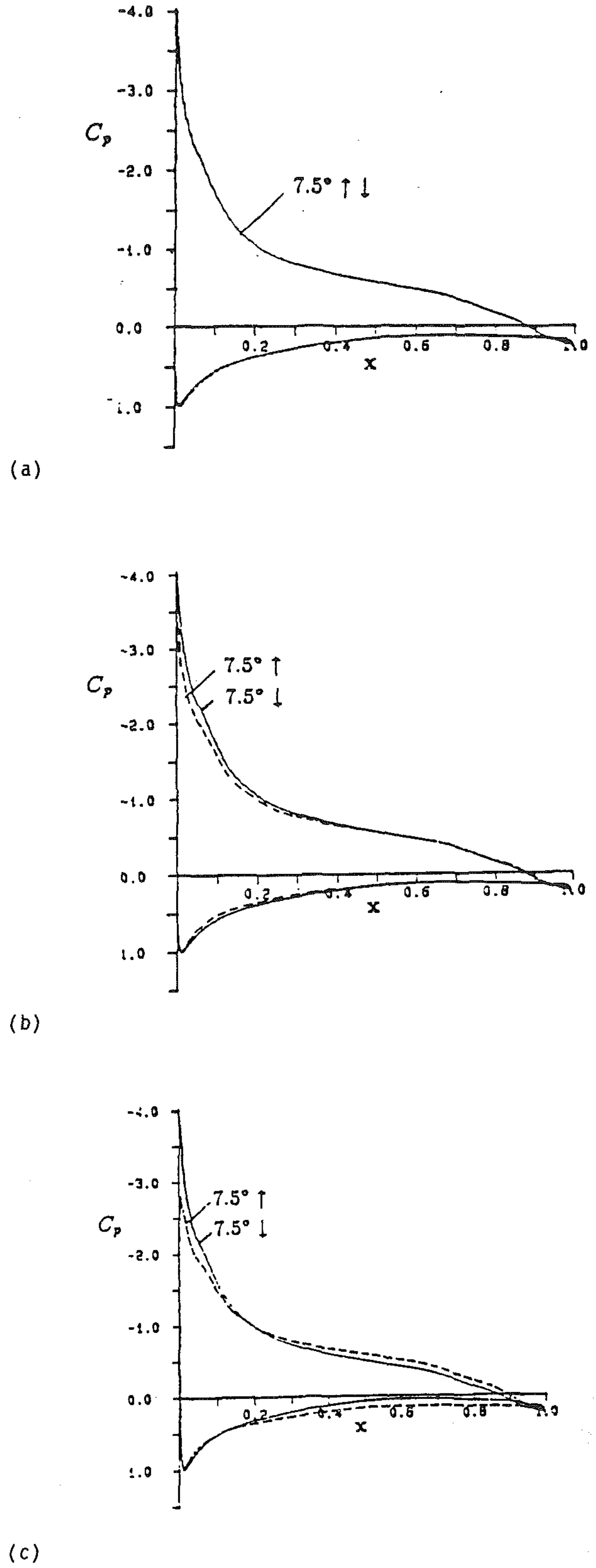

Fig. 8 The inviscid-flow pressure-coefficient distributions for the SSC-A09 airfoil at α = 7.5 deg of the harmonic oscillation, $\alpha(t)$ = 5 deg + 5 deg sin (ωt), with k = (*a*) 10^{-4}, (*b*) 0.1, and (*c*) 0.5

positive contribution from the fore part so that the C_l in the downward stroke is lower.

When an airfoil performs an unsteady motion, there is energy transfer between the airfoil and its surrounding fluid, and this energy transfer is indicated by the pitching moment. The pitching moment at $k = 0.1$ within one cycle of motion is shown in Fig. 6(*b*). The negative pitch moment in the upward stroke indicates that the airfoil motion is against the aerodynamic moment induced by the surrounding fluid, whereas in the downward stroke the aerodynamic moment is favorable to the airfoil motion. Therefore, the energy is transferred to and absorbed from the fluid in the upward and the downward strokes, respectively. The area enclosed by the pitch-moment curve indicates the net energy transferred to the fluid in each cycle of harmonic oscillation. The viscosity enhances the hysteresis effects, Fig. 6(*b*), so that more energy is required to execute a cycle of motion. In the very slow pitching case, $k = 10^{-4}$, both the inviscid and the viscous-inviscid interactive curves show almost no hysteresis effects, Fig. 5(*b*), so that the energy transferred to the fluid in one cycle is negligible. At $k = 0.5$, the pitch moment in most of the downward stroke becomes positive, which indicates that the airfoil motion is against the aerodynamic moment not only in the upward stroke but also in most of the downward stroke. In this case, the viscosity also increases the hysteresis effects and the energy transferred to the surrounding fluid in one cycle of motion.

The boundary-layer development can be represented by the

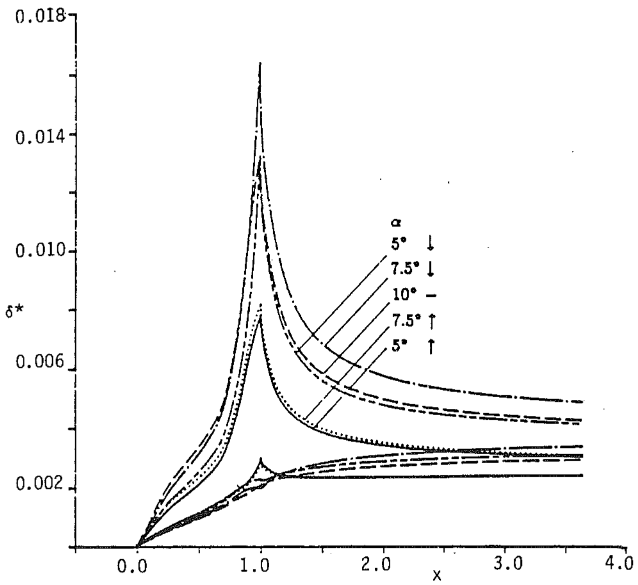

Fig. 9 Comparison of the displacement-thickness distributions of the SSC-A09 airfoil in the upward and downward strokes

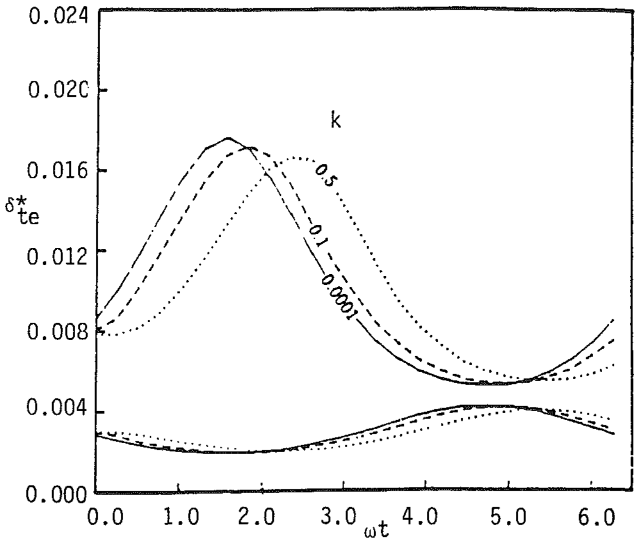

Fig. 10 The effect of reduced frequency on the trailing-edge displacement thicknesses of the SSC-A09 airfoil.

displacement thickness distributions; some features of them are displayed in Figs. 9 and 10. The displacement thickness distributions on the upper and lower sides of the airfoil and wake at angles of attack α = 5, 7.5, and 10 deg in the upward and downward strokes are shown in Fig. 9 for $k = 0.5$. At a certain angle of attack, the upper-side displacement thickness in the downward stroke is higher than that in the upward stroke. The influence of the reduced frequency on the displacement-thickness distribution can be clearly represented by the trailing-edge value, as shown in Fig. 10. The maximum displacement thickness shifts to the downward stroke as the reduced frequency increases.

Flows With Reversal Region. In the upward stroke of the harmonic oscillation, the pitch rate decreases when the airfoil approaches the maximum angle. At high angles of attack, decreasing the pitch rate speeds up the rate of expansion of the trailing-edge reversal or separation region. To suppress this region and delay the occurrence of stall, a high pitch rate must be maintained at high angles of attack. To study the behavior of an airfoil under these conditions we consider the same airfoil executing a ramp-type motion from 5 deg to 16 deg with a constant pitch rate of A $(\dot{\alpha}\ c/u_\infty) = 0.02$.

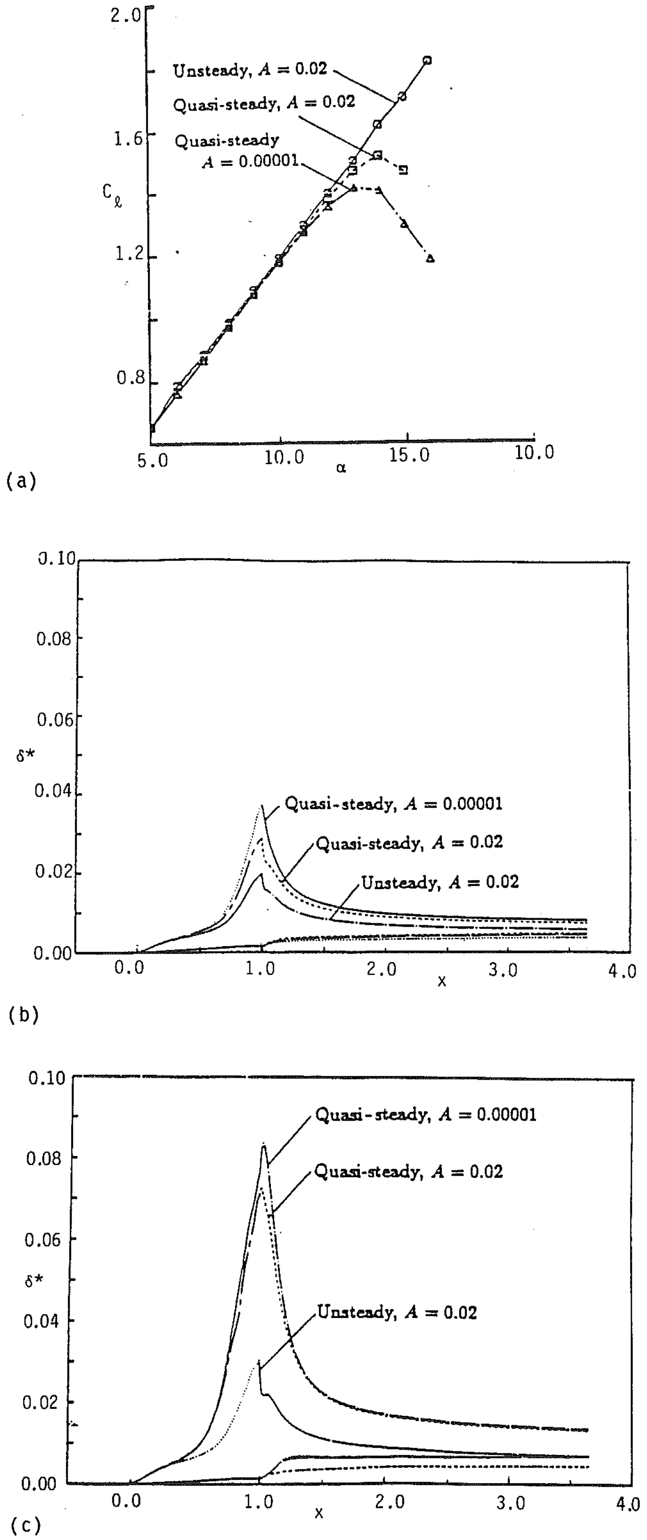

Fig. 11 The effects of pitch rate and the boundary-layer approach on the (*a*) lift-coefficient and (*b*) α = 13 deg, (*c*) α = 15 deg distributions of the SSC-A09 airfoil subject to ramp-type motion with constant pitch rate

In Fig. 11, the lift-coefficient curves computed by using the unsteady and quasi-steady approaches for $A = 0.02$ are compared with the solution computed by the quasi-steady approach

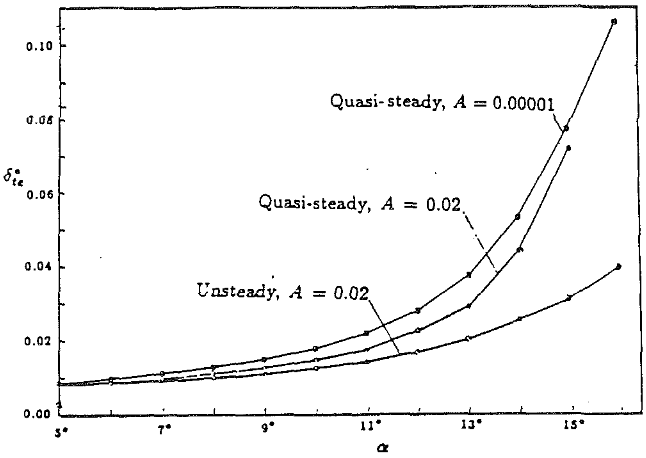

Fig. 12 The effects of pitch rate and the boundary-layer approach on the trailing-edge displacement-thickness distribution of the SSC-A09 airfoil subject to a ramp-type motion with constant pitch rate

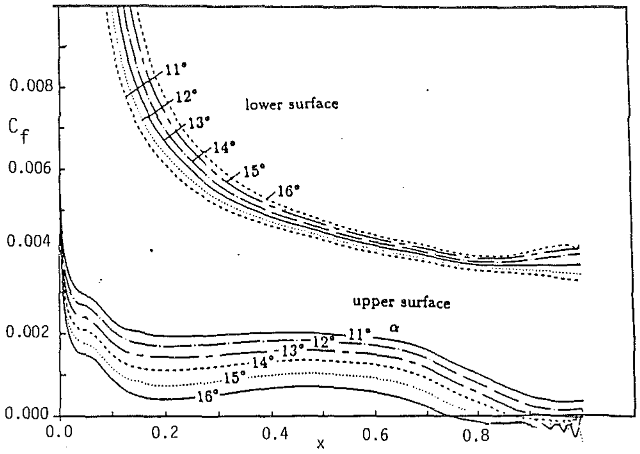

Fig. 14 The friction-coefficient distributions of the SSC-A09 airfoil subject to a ramp-type motion with constant pitch rate, $A = 0.02$

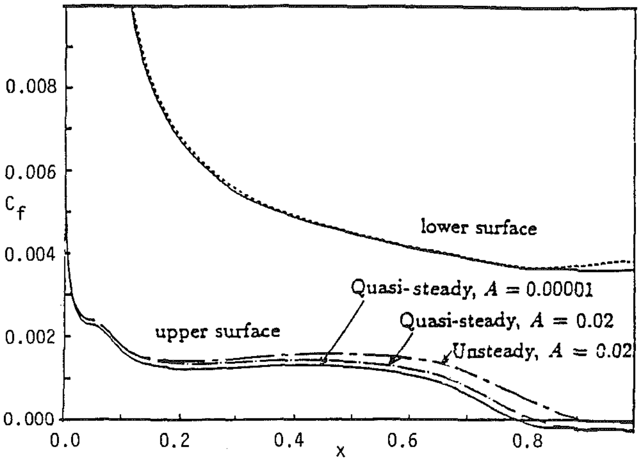

Fig. 13 The effects of pitch rate and the boundary-layer approach on the local skin-friction coefficient distribution of the SSC-A09 airfoil subject to a ramp-type motion with constant pitch rate

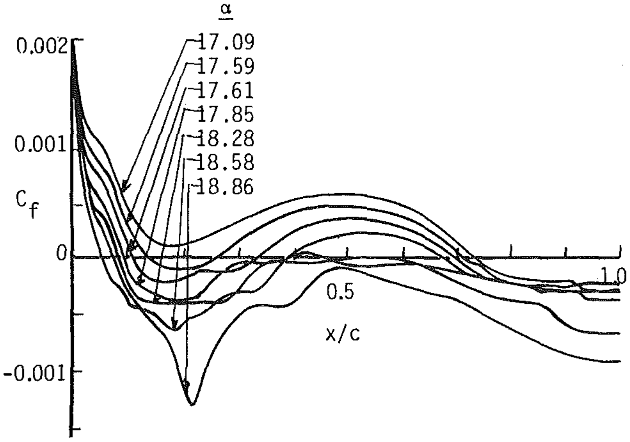

Fig. 15 Initiation of leading-edge vortex with trailing-edge separation on the Sikorsky airfoil subject to ramp-type motion with a pitch rate of 0.02, $R_c = 2 \times 10^6$, α varies from 0 deg to 30 deg

for $A = 10^{-5}$. The quasi-steady solution at $A = 0.02$ has a higher maximum lift at higher angle of attack than that at $A = 10^{-5}$. Due to the retarding effects from the lower angle of attack and smaller streamwise pressure gradient, the unsteady-flow solution shows no stall within the angles of attack computed. Figures 11(*b*) and 11(*c*) display the displacement-thickness distributions for two angles of attack. At an angle of attack before static stall, $\alpha = 13$ deg, the differences between the three distributions of Fig. 11(*b*) are much less than those shown in Fig. 11(*c*) for the solutions after static stall at $\alpha = 15$ deg. The variation of displacement thickness with the reduced frequency can be represented by the trailing edge values, Fig. 12. From Figs. 11(*b*), 11(*c*), and 12, we can conclude that increasing the pitch rate reduces the displacement thickness on the upper side of the flowfield and hence the boundary-layer effects on the outer inviscid flow.

The local skin-friction coefficient distributions on the upper and lower surfaces of the airfoil computed with the quasi-steady approach at $\alpha = 13$ deg are shown in Fig. 13. The C_f distribution on the lower surface are influenced very little with pitch rate, but those on the upper surface are influenced with the reversal region suppressed by the increasing pitch rate. Figure 14 shows the results in which the boundary-layer calculations are performed with unsteady mode for $A = 0.02$. With increase in angle of attack, the friction coefficient on the upper surface decreases, whereas on the lower surface it increases, and a reversal flow region starts growing from the trailing edge at the angle of attack of 12.7 deg. The wiggle on the C_f distribution near the trailing edge is enhanced as the reversal region increases. The extension of the calculation method requires a procedure that is able to avoid the wiggles in the solutions. This will be discussed in the next subsection.

3.3 Initiation of Dynamic Stall on a Pitching Airfoil. The numerical solution of the unsteady boundary-layer equations for two-dimensional flows is a relatively easy task provided there are not flow reversals in the streamwise velocity component u. Keller's box scheme used in this paper, or any other finite-difference method such as the Crank-Nicolson scheme, can be used to solve the equations for a prescribed pressure distribution. This is not the case, however, when the streamwise velocity component contains negative velocities. While there are some remedies to circumvent the difficulties in the solution procedure caused by flow reversals in u, they are not satisfactory when there are substantial regions of flow reversals. As discussed by Cebeci (1986), their calculation requires a numerical method which follows the physics of the flow and proper choice of step sizes in time and x directions. An appropriate scheme that can be used to satisfy these requirements is the characteristic box scheme developed by Cebeci and Stewartson, described by Bradshaw et al. (1981), and used here to extend the unsteady flow calculations of the previous subsection to higher angles of attack.

The results using this scheme with special attention to the choice of step lengths are presented for the Sikorsky airfoil subject to the ramp-type of motion with a pitch rate of 0.02. The experimental data, which are due to Lorber and Carta (1988), indicate that the vortex initiates around 17 degrees of angle of attack. The calculations confirm this and indicate how the trailing-edge separation causes the initiation of the vortex. To elaborate further on this point, let us consider the distribution of the local skin-friction values on the upper surface of this airfoil at several angles of attack, Fig. 15. It is clear from Fig. 14 that for $\alpha < 12$ deg, there is no flow separation on the airfoil, which has a steady stall angle of around 14 deg. The unsteadiness causes the stall angle to increase to around 20 deg, according to experiments. The flow behavior on the airfoil begins to change quickly, however, once the trailing-edge separation takes place for $\alpha > 12$ deg, see Fig. 14. At $\alpha = 17.09$, there is no leading-edge flow separation but only a trailing-edge separation, which occurs around 72 percent. At the next angle of attack, $\alpha = 17.61$, leading-edge separation takes place close to 12 percent chord with a bubble reattaching around 33 percent and is followed by a trailing-edge separation at 70 percent. The explosive nature of the leading-edge separation bubble, which is all turbulent, becomes more obvious at the next $\alpha = 17.85$, where leading-edge separation takes place around 10 percent but the reattachment of the bubble moves to 50 percent chord, a bubble of 40 percent in extent, followed by trailing-edge separation moving to 60 percent chord. Very shortly thereafter, less than one degree increase in angle of attack, the leading-edge separation bubble disappears with complete flow separation taking place at around 5 percent chord.

4.0 Concluding Remarks

An interactive boundary-layer method for computing unsteady incompressible flows over airfoils, including the initiation of dynamic stall, is described. The inviscid unsteady panel method, developed by Platzer and Teng, is further extended to include viscous effects. The boundary-layer method uses an inverse finite-difference technique based on Keller's box schemes and the algebraic turbulence model of Cebeci and Smith. Following the description of the method, it has been applied to unsteady flows in order to investigate the abilities of the method and compare the calculations with available experimental data. The study shows that: (*a*) In the harmonic oscillation cases, hysteresis effects are evident as the reduced frequency increases. The hysteresis phenomena appear in the solutions of both viscous and inviscid flows and are qualitatively represented by the present method. (*b*) In the case of ramp-type motion with a high constant pitch rate, the solutions correctly show that the thick trailing-edge separation region in steady flow is suppressed to a thin reversal region and, at the same time, stall is delayed. (*c*) Due to the neglect of unsteady terms, $\partial u/\partial t$ and $\partial u_e/\partial t$, the quasi-steady approach does not properly simulate unsteady flows at high pitch rates. (*d*) The prediction of the onset of dynamic stall with the present method agrees with the data of Lorber and Carta for the Sikorsky airfoil and shows that for this airfoil, the initiation of dynamic stall is caused by the trailing-edge separation.

Acknowledgments

This work was performed under Grant No. AFOSR-900262.

References

Basu, B. C., and Hancock, G. J., 1987, "The Unsteady Motion of a Two-Dimensional Airfoil in Incompressible Inviscid Flow," *Journal of Fluid Mechanics*, Vol. 87, pp. 157-168.

Bradshaw, P., Cebeci, T., and Whitelaw, J. H., 1981, *Engineering Calculation Methods for Turbulent Flows*, Academic Press, New York.

Carr, L. W., 1988, "Progress in Analysis and Prediction of Dynamic Stall," *Journal of Aircraft*, Vol. 25, No. 1, pp. 6-17.

Cebeci, T., and Smith, A. M. O., 1974, *Analysis of Turbulent Boundary Layers*, Academic Press, New York.

Cebeci, T., and Carr, L. W., 1983, "Calculation of Boundary Layer Near the Stagnation Point of an Oscillating Airfoil," NASA TM 84350.

Cebeci, T., 1986, "Unsteady Boundary Layers With an Intelligent Numerical Scheme," *Journal of Fluid Mechanics*, Vol. 163, pp. 129-140.

Cebeci, T., Clark, R. W., Chang, K. C., Halsey, N. D., and Lee, K., 1986, "Airfoils With Separation and the Resulting Wakes," *Journal of Fluid Mechanics*, No. 163, pp. 323-347.

Cebeci, T., and Jang, H. M., 1990, "Interactive Boundary-Layer Method for Unsteady Airfoil Flows: Quasi-Steady Model," *Journal of Aircraft*, Vol. 27, pp. 673-678.

Cebeci, T., Jau, J., Vitiello, D., and Chang, K. C., 1990, "Prediction of Post-stall Flows on Airfoils," in: *Numerical and Physical Aspects of Aerodynamic Flows IV*, T. Cebeci, ed., Springer-Verlag, Heidelberg, p. 93.

Cebeci, T., McIlvaine, M., Chen, H. H., and Liebeck, R. H., 1991, "Calculation of Low Reynolds Number Flows at High Angles of Attack," *Journal of Aircraft*, Vol. 28, No. 4, pp. 246-252.

Cebeci, T., and Khattab, A. A., 1992, "Numerical Solution of the Unsteady Boundary-Layer Equations With Extensive Regions of Flow Separation," paper in preparation.

Chang, K. C., Alemdaroglu, N., Mehta, U., and Cebeci, T., 1988, "Further Comparisons of Interactive Boundary-Layer and Thin-Layer Navier-Stokes Procedures," *Journal of Aircraft*, Vol. 25, pp. 897-903.

Hess, J. L., and Smith, A. M. O., 1966, "Calculation of Potential Flow About Arbitrary Bodies," in: *Progress in Aeronautical Sciences*, Pergamon Press, Oxford, Vol. 8, p. 1-138.

Jang, H. M., Ekaterinaris, J. A., Platzer, M. F., and Cebeci, T., 1991, "Essential Ingredients for the Computation of Steady and Unsteady Blade Boundary Layers," ASME JOURNAL OF TURBOMACHINERY, Vol. 13, pp. 608-616.

Lorber, P. F., and Carta, F. O., 1988, "Airfoil Dynamic Stall at Constant Pitch Rate and High Reynolds Number," *Journal of Aircraft*, Vol. 25, pp. 548-556.

Mehta, U., Chang, K. C., and Cebeci, T., 1986, "Relative Advantages of Interactive and Thin Navier-Stokes Procedures," in: *Numerical and Physical Aspects of Aerodynamic Flows III*, T. Cebeci, ed., Springer-Verlag, New York.

Teng, N. H., 1987, "The Development of a Computer Code (U2DIIF) for the Numerical Solution of Unsteady, Inviscid and Incompressible Flow Over an Airfoil," M.S. Thesis, Naval Postgraduate School, Monterey, CA.

Veldman, A. E. P., 1981, "New, Quasi-Simultaneous Method to Calculate Interacting Boundary Layers," *AIAA Journal*, Vol. 154, pp. 79-85.

Unsteady Aerodynamics and Gust Response in Compressors and Turbines

S. R. Manwaring
Engineer.

D. C. Wisler
Manager.
Mem. ASME

Aerodynamics Research Laboratory,
GE Aircraft Engines,
Cincinnati, OH 45215

A comprehensive series of experiments and analyses was performed on compressor and turbine blading to evaluate the ability of current, practical, engineering/analysis models to predict unsteady aerodynamic loading of modern gas turbine blading. This is part of an ongoing effort to improve methods for preventing blading failure. The experiments were conducted in low-speed research facilities capable of simulating the relevant aerodynamic features of turbomachinery. Unsteady loading on compressor and turbine blading was generated by upstream wakes and, additionally for compressors, by a rotating inlet distortion. Fast-response hot-wire anemometry and pressure transducers embedded in the airfoil surfaces were used to determine the aerodynamic gusts and resulting unsteady pressure responses acting on the airfoils. This is the first time that gust response measurements for turbines have been reported in the literature. Several different analyses were used to predict the unsteady component of the blade loading: (1) a classical flat-plate analysis, (2) a two-dimensional linearized flow analysis with a "frozen gust" model, (3) a two-dimensional linearized flow analysis with a "distorted gust" model, (4) a two-dimensional linearized Euler analysis, and (5) a two-dimensional nonlinear Euler analysis. Also for the first time, a detailed comparison of these analyses methods is made and the importance of properly accounting for both vortical and potential disturbances is demonstrated. The predictions are compared with experiment and their abilities assessed to help guide designers in using these prediction schemes.

1.0 Introduction and Background

Turbomachinery blade rows in both compressors and turbines are subject to the periodic unsteady flow commonly generated by wakes from the upstream blade rows and, additionally for compressors, by rotating stall cells and inlet distortions. When the blades and vanes encounter these disturbances, unsteady forces result on their surfaces. This can produce not only very significant airfoil vibration when the frequency of these unsteady forces equals the airfoil natural frequency, but also failure if the material endurance limit is exceeded. To predict the airfoil vibration to prevent failure, one must determine these induced unsteady forces.

Historically, periodic unsteady flows have been modeled as small perturbation gusts superimposed on a uniform flow field. Classical thin-airfoil theory was used to calculate induced unsteady pressures generated on the airfoil surfaces by the gusts. The airfoils were considered to be flat plates at zero incidence; thus, the unsteady pressures were decoupled from the uniform steady-flow solution and didn't interact with the steady flow field. Whitehead's (1970) subsonic LINSUB and Nagashima and Whitehead's (1977) supersonic LINSUP compressible-flow codes used these very simplified assumptions. Goldstein and Atassi's (1976) model included the effect of a gust interacting with incompressible flow over an isolated airfoil. Caruthers' (1980) analysis provided unsteady interaction for a cascade.

More recently, significant progress in modeling has been made. Verdon and Hall (1990) developed a two-dimensional, linearized flow analysis with two different gust-modeling capabilities. Holmes and Chuang (1991) and Hall and Crawley (1987) both used a two-dimensional linearized Euler analysis to predict unsteady pressures due to gusts. Giles (1988, 1991a), Jorgenson and Chima (1988), Oden and Bass (1989), and Janus and Whitfield (1989) have developed two-dimensional, nonlinear Euler analyses. A three-dimensional, unsteady Navier–Stokes solver was developed by Rai (1987).

On the experimental side, Fleeter has directed gust-response experiments using low-speed compressors. Fleeter et al. (1978, 1980) investigated airfoil camber and axial spacing effects on the gust response of a stator. Capece et al. (1986) and Capece and Fleeter (1987) investigated the effect of steady aerodynamic loading and waveform shape of the forcing function on gust response. Manwaring and Fleeter (1990, 1991, 1993) investigated rotor response to inlet distortions and wake-type disturbances.

Gallus et al. (1980) obtained gust-response measurements at the midspan of a low-camber vane in a single-stage compressor. Hardin et al. (1987) measured oscillating airfoil aerodynamics

---

Contributed by the International Gas Turbine Institute and presented at the 37th International Gas Turbine and Aeroengine Congress and Exposition, Cologne, Germany, June 1–4, 1992. Manuscript received by the International Gas Turbine Institute October 1992. Paper No. 92-GT-422. Associate Technical Editor: H. Lukas.

on the rotor of a single-stage compressor. They also performed inlet distortion experiments, but the results were not published. Caruthers and Dalton (1993) made comparisons of Caruthers' (1980) analysis with the data of Fleeter et al. (1978).

Several authors have presented measurements of the unsteady aerodynamic loading on turbomachinery blade rows, but their data analysis did NOT include harmonic decomposition to obtain the gust response of the airfoil row. For these studies, the reader is referred to the work of Adachi and Murakami (1979), O'Brien et al. (1980), and the turbine work of Dring et al. (1982) and Doorly (1988).

In all the gust-response experiments described above, the comparisons with data were mostly confined to predictions from classical flat-plate analyses. No comprehensive comparisons using the more recent models have been reported. In addition, no experimental investigations of gust response for turbines have been reported.

Consequently, the question for the design engineer still remains: How well do the various models predict gust response for the airfoil geometries encountered? Our paper addresses this issue.

2.0 Objectives and Approach

2.1 Objectives. The overall objective of this work is to evaluate the ability of current, practical models to predict the gust response of modern gas turbine blading to unsteady aerodynamic excitation. This includes (1) obtaining experimental measurements of the unsteady aerodynamic flow and the resulting gust response for both compressor and turbine blading, (2) computing gust response using current models, and (3) assessing the appropriateness and practicality of the models by comparing predictions with experimental data.

We seek, in part, to answer the following questions:

Can linearized analysis methods, in which the unsteady part of the flow is linearized about a steady, nonlinear mean flow, yield reasonably accurate predictions of unsteady loading in modern turbomachinery blading?

Does the assumption that the gust does not interact with the mean flow (i.e., frozen gust) seriously reduce the accuracy of the predictions?

Do both vortical and potential disturbances need to be included in the forcing function?

Can the same models adequately predict gust response for both compressor and turbine blading over a wide range of vector diagrams, loading levels and reduced frequencies?

Are these codes practical to set up and run and thus usable for iterating designs before hardware is released?

2.2 Approach. The overall approach used to achieve the objectives combines experimentation and computational analyses as described in Sections 3.0 and 4.0.

The unsteady aerodynamic excitation of the turbomachinery blading considered in the present paper is produced by periodic velocity disturbances from upstream airfoil wakes and compressor distortion. These periodic disturbances are decomposed into harmonic components via a Fourier analysis since most unsteady aerodynamic codes assume all time unsteadiness is purely harmonic. For our purposes, the "gust" is taken as the magnitude and phase of the first Fourier coefficient in this harmonic decomposition, as illustrated in Appendix I. It will also be referred to as the "forcing function." A gust is termed "frozen" if it does not interact with the mean flow and "distorted" if it does.

The unsteady aerodynamic loading produced on the blading due to this unsteady aerodynamic excitation is also decomposed into harmonic components. "Gust response" is taken to be the first Fourier coefficient in the harmonic decomposition of the unsteady pressures acting on the airfoil surfaces.

The unsteady excitation velocities contain two parts: a rotational (vortical) part associated with vorticity variations, and an irrotational (potential) part associated with pressure variations. The experimental evaluations reported to date have considered only vortical disturbances. However, certain analysis models distinguish between these types of disturbances. This is important because vortical disturbances do not decay axially while potential disturbances decay exponentially in the axial direction. Consequently we resolved the measured unsteady velocities into these two parts in a manner suggested by Giles (1991b) to obtain input for some of the models. In the analysis given in Appendix II, the coefficients D and A are derived. They give respectively the contributions of vortical

Nomenclature

A = coefficient of harmonic potential disturbance
b = semichord = $c/2$
c = chord, 0 percent = leading edge
$C_{p,i}$ = ith harmonic unsteady pressure coefficient
D = coefficient of harmonic vortical disturbance
DP = design point
H = amplitude of gust
HL = high loading
IGV = inlet guide vane
k = reduced frequency = $\omega b/\overline{V}$
L = 2π/disturbance pitch
LL = low loading
M = Mach number
$N1$ = first-stage nozzle row
$N2$ = second-stage nozzle row
p = periodic unsteady pressure on airfoil surfaces
$\hat{p}_i$ = ith harmonic unsteady pressure on airfoil surfaces
PS = pressure surface
$R1$ = first-stage rotor row
SS = suction surface
t = time
u^+ = streamwise component of periodic unsteady velocity
$\hat{u}_i^+$ = ith harmonic streamwise gust
U = wheel speed
U_∞ = steady uniform flow
v^+ = transverse component of periodic unsteady velocity
$\hat{v}_i^+$ = ith harmonic transverse gust
V = periodic unsteady absolute velocity
$\overline{V}$ = time-mean absolute velocity
$\overline{V}_1$ = time-mean absolute velocity at airfoil row inlet
W = periodic unsteady relative velocity
$\overline{W}$ = time-mean relative velocity
α = periodic unsteady absolute air angle
$\overline{\alpha}$ = time-mean absolute air angle
β = interblade phase angle or relative air angle
$\overline{\beta}$ = time-mean relative air angle
$\Delta C_{p,i}$ = coefficient of unsteady pressure difference, ith harmonic
ΔP = pressure rise across compressor or drop across turbine
ΔP_{RD} = constant pressure difference in rotating distortion predictions
ΔV = unsteady absolute velocity
ΔW = unsteady relative velocity
$\Delta\alpha$ = difference in periodic unsteady absolute flow angle from time-mean value
$\Delta\beta$ = difference in periodic unsteady relative flow angle from time-mean value
ρ = air density
ϕ = phase of complex unsteady pressure
ω = gust frequency

Subscripts

i = harmonic number
S = streamwise component
T = transverse component
z = axial component
θ = tangential component

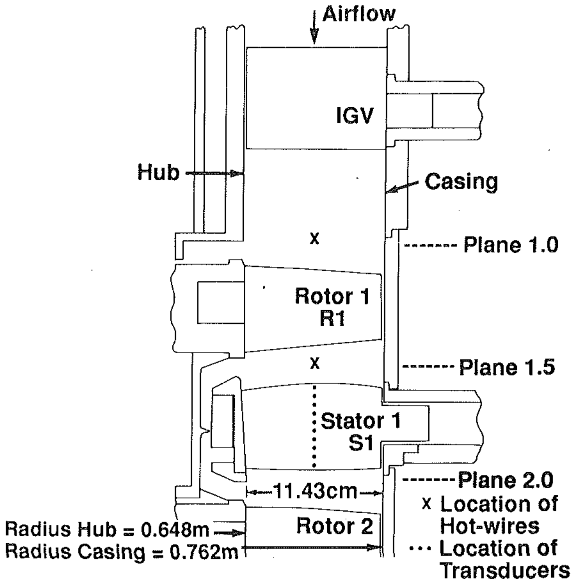

Fig. 1 Compressor test stage

Table 1 Pitchline blading parameters

	Compressor			Turbine		
	IGV	R1	S1	N1	R1	N2
Solidity	1.40	1.14	1.43	1.64	1.48	1.68
Aspect Ratio	1.36	1.20	1.34	3.97	3.87	5.10
Chord, cm	8.38	9.55	8.53	7.62	7.87	5.97
Stagger, Deg.	19.6	50.4	32.7	39.8	34.9	22.9
Camber, Deg.	3.0	31.8	39.0	60.0	96.9	102.4
No. of Airfoils	74	54	74	82	72	108
Axial Gap, cm	9.80	2.79		2.54	2.54	

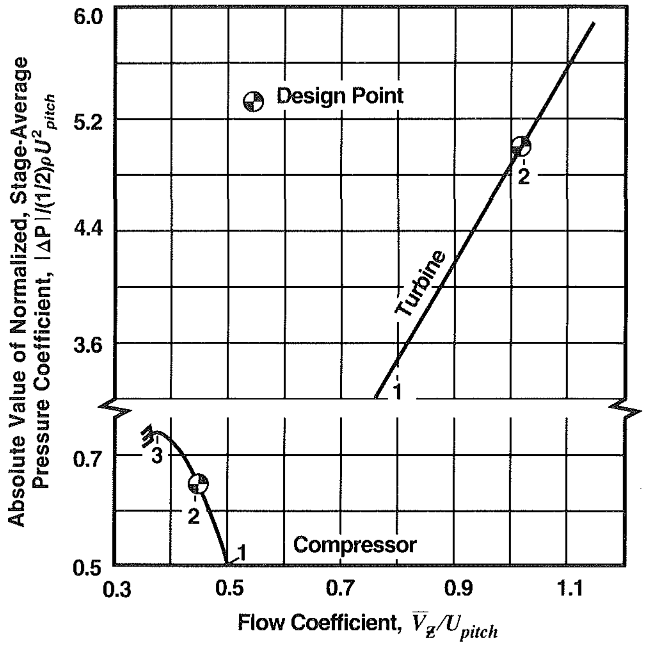

Fig. 2 Comparison of compressor and turbine performance/loading levels (note break in ordinate)

and potential disturbances to the forcing function. By examining the relative magnitudes of D and $A\,(L/\overline{V})$, we determine where potential effects also need to be incorporated into the analysis.

3.0 Experimental Test Program

A test program is described for measuring: (1) the unsteady velocities that are generated by upstream airfoil wakes or distortions that enter the downstream airfoil row and from which the gust or forcing functions are computed; and (2) the resulting unsteady pressures on the downstream airfoils from which the gust response is computed.

3.1 Test Vehicles

Low-Speed Research Compressor (*LSRC*). The LSRC is an experimental facility that duplicates the essential features of smaller, high-speed compressor flow fields in a large, low-speed machine, where very detailed investigations of the flow can be made. The facility, which has a constant casing diameter of 1.524 m (60.0 in.), is described by Wisler (1985).

Typical of modern designs, the compressor had a high-hub/tip-ratio (0.85) and highly loaded, low-aspect-ratio, high-solidity blading with shrouded stators and inlet guide vanes. The design and test of the blading, which is a low-speed model of a midstage of the 10-stage, 23:1 pressure ratio, E^3 compressor, are described by Wisler (1985). The geometry of the test stage is shown in Fig. 1 and blading parameters are given in Table 1. The first stage of four identical stages was the test stage. Tests were conducted at 800 rpm for low loading (*LL*), the design point (*DP*), and high loading/near stall (*HL*) conditions shown as test Points 1, 2, and 3, respectively, in Fig. 2.

The LSRC has the capability of testing with a rotating inlet distortion. Such a distortion pattern could be generated by a fan operating in rotating stall ahead of an unstalled HP compressor. For these studies, a 120 deg segment of a radially uniform perforated plate having 42 percent solidity was located ten annulus heights above the first rotor. Tests were conducted with the distortion counterrotating at 30 percent of rotor speed.

Low-Speed Research Turbine (*LSRT*). Being similar to the LSRC in modeling concept, the LSRT is an experimental facility that duplicates certain essential features of a high-speed-turbine flow field in a large, low-speed machine. This vertical facility has a constant annulus area with a casing diameter of 1.524m (60.0 in.). Ambient air is pulled through the LSRT from the inlet at the top into a large plenum beneath the turbine. This air, being drawn through the blading by a large centrifugal blower, causes the turbine to rotate. Bleed air into the plenum and IGVs on the blower allow various turbine operating points to be set.

The two and one-half stage low-pressure turbine, having outlet guide vanes, is a low-speed, aerodynamic model of a generic high-speed LP turbine. A cross section of the 0.60 hub/tip-ratio blading is given in Fig. 3 and design parameters are given in Table 1. Tests on Nozzle Two (*N*2) were conducted at 600 rpm for low loading (*LL*) and the design point (*DP*) shown as test Points 1 and 2 in Fig. 2. Importantly, the much higher loading levels per stage of the turbine relative to the compressor are seen in the figure.

Two Dimensionality of the Flow Field. The steady and unsteady flow field of the compressor and turbine were determined to be two dimensional at the midspan location chosen for the measurements. For the compressor, hot-wire measurements of the inlet flow to the stator at the design flow coefficient gave radial profiles of axial velocity and absolute flow angle that were nearly flat from 20 to 65 percent span. The radial profile of centerline deficit of the rotor wakes was nearly flat from 35 to 80 percent span. For the turbine, flow angle measurements of the nozzle inlet flow showed the radial profile to be nearly flat from 15 to 70 percent span.

3.2 Instrumentation and Data Sampling

Hot-Wire Anemometry. Measurements of the steady and

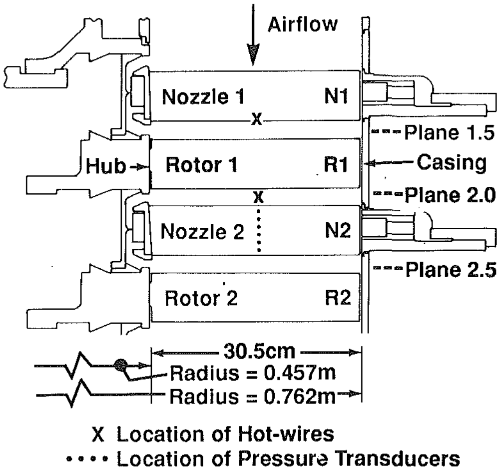

Fig. 3 Turbine test stage

periodic unsteady velocities and flow angles entering the airfoil rows were made with a TSI IFA 100 anemometer system using both 45 deg, slanted hot wires and cross hot wires. The hot wires were calibrated in a free jet, with measurement accuracy being ±1.25 percent for velocity and ±0.5 deg for flow angle.

The hot wires were located radially at 50 percent immersion and axially at halfway between the rotor trailing edge and stator or nozzle leading edge. Circumferentially, they were located at midpitch between the two instrumented vanes for the compressor. For the turbine they were aligned along the leading edge streamline of an instrumented nozzle for circumferential indexing purposes to be described later. The hot wires were retracted from the flow field after their use to avoid aerodynamic interference with the airfoil surface instrumentation. Measurements were taken at Plane 1.5 for the compressor shown in Fig. 1 and Plane 2.0 for the turbine shown in Fig. 3.

Airfoil Surface Static Taps. The steady pressures on the airfoil surfaces were measured at the midspan with static taps machined in chordwise arrays. Each array had 14 taps on the suction surface and 10 on the pressure surface for the compressor and 13 and 11 respectively for the turbine. Each tap was ported through a Scanivalve pressure multiplex to a pressure transducer accurate to 0.015 percent of full scale.

Airfoil Surface Pressure Transducers. The periodic unsteady pressures acting on the airfoil surfaces were measured at midspan with ultraminiature, high-response, Kulite model LQ-125 pressure transducers embedded inside the airfoil surfaces. Small pressure ports pneumatically connected the sensor to the measurement surface. The port diameters were sized properly and the lengths were small enough as defined by Doebelin 1975 so as not to attenuate periodic unsteady pressures. The instrumented airfoils, having 10 transducers per surface for the compressor and 12 for the turbine, were arranged so that suction and pressure surface measurements were made in the same passage.

The transducers were calibrated after installation in the airfoils by using both a pressurized/evacuated chamber and a dynamic frequency-response calibrator. The transducer accuracy is ±1.00 percent as determined by a least-squares fit of the static calibration data. The response was unattenuated or phase-shifted up to 1400 Hz or two times blade passing frequency.

Data Sampling. The hot-wire and pressure transducer signals were digitized and ensemble-averaged. A Kinetic Systems analog-to-digital converter was used at digitization rates of up to 50 kHz to give at least 70 equally spaced increments across any one period of unsteadiness, for example, one blade spacing. The 200 ensemble averages, used for each of these 70 increments, greatly reduced the effects of time-unresolved unsteadiness. A one-per-rev pulse from an optical encoder on a blade tip triggered the data gathering. The data-sampling process described above was repeated to obtain data for all 54 compressor blades and 72 turbine blades to give better frequency resolution for Fourier decomposition.

Upstream IGV/Nozzle Indexing. The blading configurations shown in Figs. 1 and 3 have, respectively, an IGV ahead of the first compressor rotor and a nozzle (*N*1) immediately upstream of the first turbine rotor. These IGVs and nozzles were indexed circumferentially to determine any effect of their wakes on the measurements. No effect was found for IGV indexing probably because the IGVs were relatively far upstream. A significant effect was found for the closely coupled *N*1 turbine nozzles. Consequently, all hot-wire and pressure transducer measurements for the turbine were circumferentially averaged over 11 equally spaced positions of the *N*1 nozzle to remove the effect of the *N*1 wakes on the measurements.

3.3 Data Analyses.

The procedures for analyzing the experimental data to obtain the unsteady aerodynamic forcing functions and resulting gust response on the airfoil surfaces are described.

Steady and Periodic Unsteady Velocities. The time-mean velocity was determined by arithmetically averaging the ensemble-averaged velocities for all of the equally spaced time increments across all of the blade spacings. From this, a single time-mean vector diagram was constructed for the compressor and turbine as shown by the solid lines in Figs. 4(*a*) and 4(*b*). Then for EACH time increment, an instantaneous vector diagram was computed as shown by the dashed lines in Fig. 4. From the one steady and the many instantaneous vector diagrams, the periodic unsteady velocities u^+ (streamwise) and v^+ (transverse) were computed as seen in the circular inset in Fig. 4.

Harmonic Decomposition to Obtain the Gusts. The periodic unsteady velocities computed above, u^+ and v^+, were harmonically decomposed to obtain the gust components $\hat{u}_i^+$ and $\hat{v}_i^+$. A Fast Fourier Transform (FFT) algorithm was used to obtain the Fourier coefficients at the fundamental harmonic ($i = 1$ is blade passing frequency for rotor wakes) and higher harmonics ($i = 2, 3, \ldots$). The first harmonic gusts, $\hat{u}_1^+$ and $\hat{v}_1^+$, are reported in this paper. The phase of the gust is referenced so that the transverse component is 0 deg at the airfoil leading edge.

Gust Response. The digitized, ensemble-averaged, periodic unsteady pressures measured on the airfoil surfaces by the transducers constitute the unsteady aerodynamic loading. These were harmonically decomposed as described above to obtain the Fourier coefficients. The first harmonic coefficient was taken as the gust response on the airfoil surface at the transducer locations. This coefficient was normalized and referenced in the classical manner using the time-mean velocity, $\bar{V}$, and transverse gust component, $\hat{v}_1^+$, as defined in Eq. (1). This normalized coefficient is accurate to within ±3.5 percent. The normalized Fourier coefficients are complex arithmetic vectors having real and imaginary components, e.g., amplitude and phase. The normalized, unsteady pressure difference acting on the airfoil is calculated as shown in Eq. (2). The unsteady lift on the airfoil was then determined by integrating the unsteady pressure difference along the airfoil:

$$C_p = \frac{\hat{p}}{\rho \bar{V} \hat{v}^+} = C_{p,\text{real}} + iC_{p,\text{imag}} \qquad (1)$$

$$\Delta C_p = C_{p,\text{pressure}} - C_{p,\text{suction}} = |C_{p,p}| e^{i\phi_p} - |C_{p,s}| e^{i\phi_s} \qquad (2)$$

where

$$|C_p| = \sqrt{C^2_{p,\text{real}} + C^2_{p,\text{imag}}} \text{ and } \phi = \tan^{-1}(C_{p,\text{imag}}/C_{p,\text{real}}).$$

4.0 Computational Analyses

Several different computational analysis techniques were evaluated. They each have the same capability of computing the response of an airfoil to an imposed aerodynamic gust.

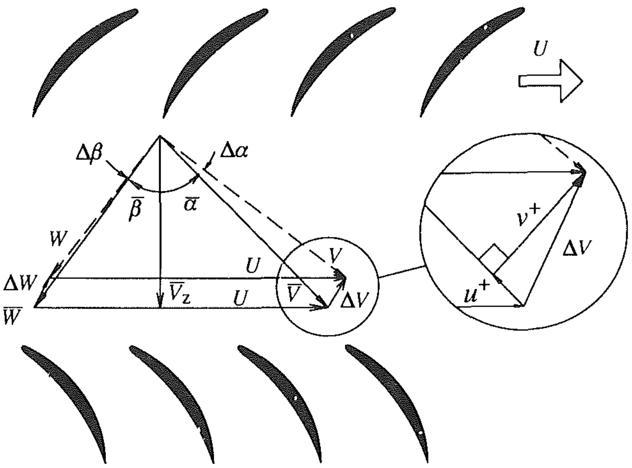

a) Compressor Vector Diagram

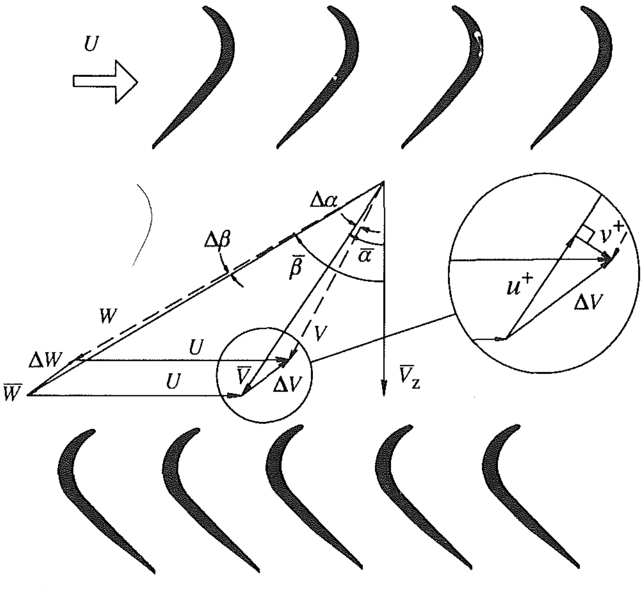

b) Turbine Vector Diagram

Fig. 4 Velocity vector diagrams showing streamwise and transverse unsteady velocities u^+ and v^+

Generally speaking, they all follow these common steps summarized in Table 2: (1) compute steady flow solution, (2) model wake unsteadiness as a harmonic gust, and (3) compute unsteady flow solution. An exception is UNSFLO, which does not take the above linearization steps but solves the entire nonlinear flow field at once. However, even for those taking the common steps, they achieve their objective in different manners as described below. The frozen gust listed in Table 2 is one that remains constant in amplitude and shape as it convects through an airfoil row, while the distorted gust interacts with the mean flow and changes amplitude and shape in the process.

4.1 Computational Models Being Evaluated

LINSUB. This is a classical method of linearized flat-plate analysis, which assumes the steady flow to be uniform in Step 1 of Table 2, uses a frozen gust model in Step 2, and applies an integral method to solve for the linearized unsteady potential flow in Step 3. Unlike the other models, LINSUB doesn't compute gust response on individual suction and pressure surfaces. It computes only unsteady pressure difference between these surfaces. This method was developed by Whitehead (1970).

LINFLO. This analysis technique solves the nonlinear steady flow in Step 1 using a potential flow CFD method. It uses a distorting (interacting) gust model in Step 2 and a linearized unsteady Euler flow in Step 3. A structured H-grid is used for a global analysis and a structured C-grid for local analysis. The model is referred to in this paper as LINFLO, although other users may recognize it as LINFLO 1.3. The method was developed by Verdon and Hall (1990).

They also produced an ad hoc version of LINFLO, which we have called LINFG in our paper (others will recognize it as LINFLO 1.2). It uses a frozen gust model in Step 2 and a linearized, unsteady, potential flow in Step 3. We include LINFG solutions in this paper only because they have proven extremely valuable to us as a learning tool about frozen gusts.

LEAP2D. This CFD analysis solves the nonlinear steady flow as Euler flow instead of potential flow in Step 1, uses the distorted gust model in Step 2, and solves the linearized unsteady Euler flow in Step 3. It uses an adaptive triangular mesh grid. The method was developed by Holmes and Chuang (1991).

UNSFLO. This methodology is different from those described above. The nonlinear Euler analysis uses a generalized wake interaction model and solves for the total steady and unsteady flow field with time-marching replacing the general approach described above. An unstructured, rectangular computational grid is used. The methodology was developed by Giles (1988).

4.2 Running the Codes. We set up a procedure for blind, unbiased running of the codes by either the code developer himself or a recognized overseer of the code and associate of the developer. Credit is given in the acknowledgments. This gave assurance that the codes were set up and run properly to give expert-validated solutions. Some details are given below.

Table 2 Computational/analytical models

ANALYSES	STEP 1. STEADY FLOW	STEP 2. MODEL WAKE AND UNSTEADINESS	STEP 3. UNSTEADY FLOW
LINSUB	Uniform Flow	Frozen Gust ($\hat{v}^+$ only)	Linearized Potential Flow
LINFG	Potential Flow	Frozen Gust ($\hat{v}^+$ & $\hat{u}^+$)	Linearized Potential Flow
LINFLO	Potential Flow	Distorted Gust ($\hat{v}^+$ & $\hat{u}^+$)	Linearized Euler Flow
LEAP2D	Euler Flow	Distorted Gust ($\hat{v}^+$ & $\hat{u}^+$)	Linearized Euler Flow
UNSFLO	Non-linear Euler Flow using generalized wake		

Table 3 Time-mean and gust parameters

		M	$\overline{\alpha}$	$\overline{\beta}$	k	$\hat{v}_1^+/\overline{V}$	$\hat{u}_1^+/\hat{v}_1^+$		D		AL/$\overline{V}$	
						Mag.	Mag.	Phase	Mag.	Phase	Mag.	Phase
Compressor Wakes	**LL**	0.133	41.6	-42.9	4.02	0.121	0.126	158.7	0.124	-179.1	0.006	-112.3
	DP	0.126	46.0	-45.8	4.28	0.053	0.246	-148.3	0.048	-164.7	0.014	-16.0
	HL	0.120	50.7	-49.0	4.53	0.051	0.174	-67.1	0.045	-174.9	0.009	16.2
Compressor Distortion	**DP**	0.132	46.7	-45.5	0.02	0.036	0.730	169.0	–	–	–	–
Turbine Wakes	**LL**	0.104	-35.1	-63.2	3.65	0.009	2.791	99.6	0.019	125.2	0.014	-143.9
	DP	0.130	-39.2	-61.9	2.89	0.009	2.342	114.2	0.017	129.7	0.009	-151.9

The input to the codes consists of the airfoil row geometry and the parameters listed in Table 3, which were obtained from the hot-wire measurements. Although the airfoil coordinates cannot be presented, geometry parameters are listed in Table 1. For the steady flow calculations, the input conditions are the absolute flow angle and the inlet Mach number. For the unsteady flow calculations, the inputs are the reduced frequency, the interblade phase angle (obtainable from Table 1), and the forcing function.

The forcing functions as listed in Table 3 are specified in different ways for the various codes. LINSUB, LINFG, and LINFLO require magnitude of $\hat{v}_1^+/\overline{V}$, LEAP2D requires both magnitude and phase of $\hat{u}_1^+/\hat{v}_1^+$, and UNSFLO requires both magnitude and phase of D and A, the coefficients used for inputting the contributions of vortical and potential disturbances, respectively. LEAP2D determines the vortical and potential parts of the input boundary conditions from the magnitude and phase of $\hat{u}_1^+/\hat{v}_1^+$. LINFG and LINFLO were run with only vortical-type input conditions and thus required only the magnitude of $\hat{v}_1^+/\overline{V}$.

For each of the codes, a sufficient number of grid points were used to achieve grid independent solutions to within a few percent. Specifically, LINFLO used a 21 × 90 H-grid and a 21 × 70 C-grid. LEAP2D used an adaptive mesh of 4200 cells for the compressor and 4900 cells for the turbine. UNSFLO used a 25 × 100 grid.

5.0 Forcing Function

The forcing functions or gusts, computed from our hot-wire measurements, are presented in this section. The relevant differences between the compressor and turbine unsteady velocities and gusts are documented. The gusts are used in Step 2 of Table 2 to model the wakes and other unsteadiness in the various models.

5.1 Gusts From Compressor Rotor Wakes. The periodic unsteadiness generated by the rotor wakes is shown in Fig. 5(*a*–*f*) for design-point operation. The rotor wakes shown in Fig. 5(*a*) are classically asymmetric with a wake deficit of about 15 percent of the free-stream velocity. There is a small change in relative air angle in the wake as seen in Fig. 5(*b*). In the absolute frame, there are large changes in both air angle and transverse unsteady velocity, α and v^+ (Figs. 5*d* and 5*f*), while there are small changes in both absolute velocity and streamwise unsteady velocity, V and u^+ (Fig. 5*c* and 5*e*).

The results described above are explained by examining the vector diagram typical for compressors in Fig. 4(*a*). Note that the sum of the mean relative and absolute air angles, listed in Table 3 and depicted in Fig. 4(*a*), is about 90 deg. Thus, a large change in relative velocity in the rotor wake (ΔW), coupled with small changes in relative air angle ($\Delta\beta$), will generate large unsteadiness in the absolute frame of reference mainly in absolute air angle, $\Delta\alpha$, (and thus incidence) and in transverse unsteady velocity, v^+. Changes in absolute velocity, V, and in streamwise unsteady velocity, u^+, will be small by comparison.

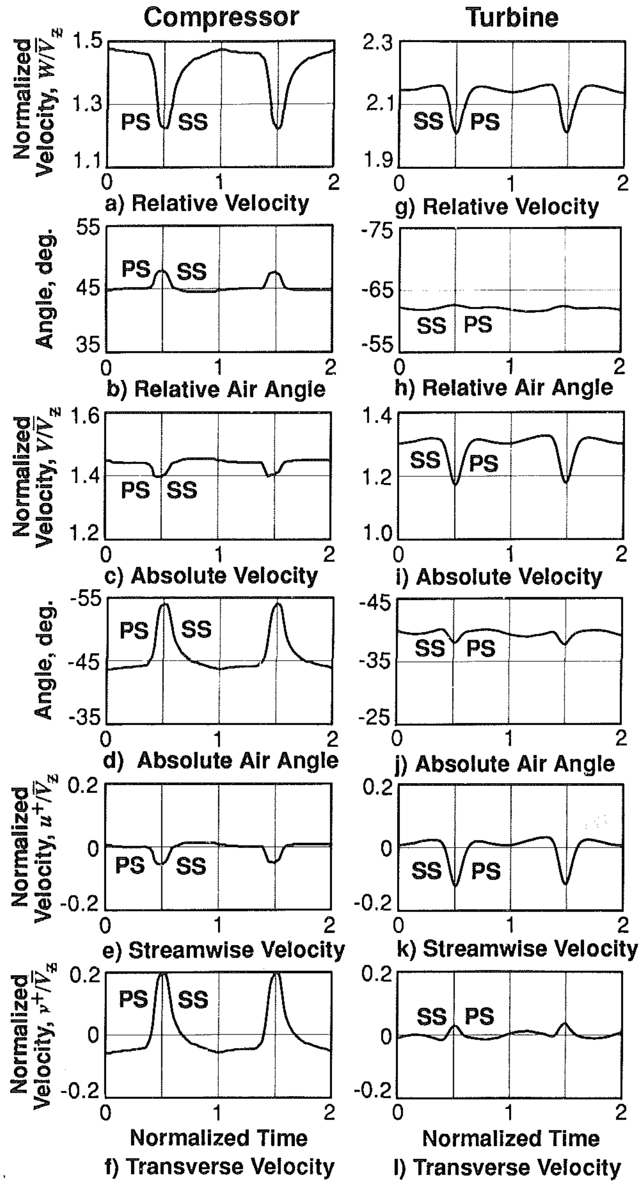

Fig. 5 Measured properties of compressor rotor wakes compared with those for turbine rotor wakes

The streamwise and transverse gusts, $\hat{u}_1^+$ and $\hat{v}_1^+$, are presented in Fig. 6(*a*) and 6(*b*) for the first five harmonics. The transverse gust dominates the unsteadiness as seen in the first

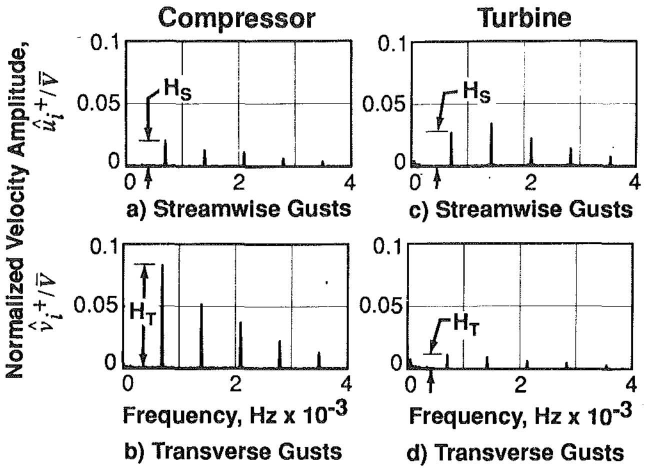

a) Streamwise Gusts c) Streamwise Gusts

b) Transverse Gusts d) Transverse Gusts

Fig. 6 Comparison of the first five harmonics of the gusts measured in the compressor and turbine

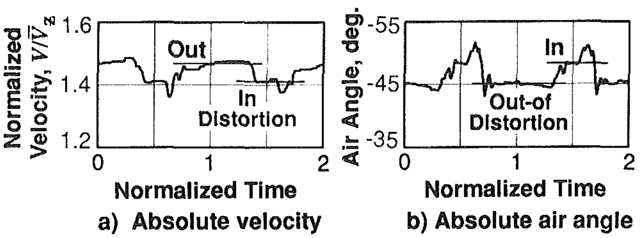

a) Absolute velocity b) Absolute air angle

Fig. 7 Unsteadiness in the compressor due to 120 deg distortion counterrotating at 30 percent of rotor speed

harmonic where the amplitude of the transverse gust, H_T, is four times that of the streamwise gust, H_S. The gusts are tabulated in Table 3.

5.2 Gusts From Rotating Inlet Distortions. The 120 deg rotating inlet distortion produces in-distortion and out-of-distortion velocity fluctuations, shown in Fig. 7, that are almost twice those generated by the rotor wakes seen in Fig. 5(*c*). Angle fluctuations are about one-half of those shown in Fig. 5(*d*). Compared to values for the rotor wake, the streamwise and transverse unsteady velocities are now more nearly equal.

Properties of the gusts are listed in Table 3.

5.3 Gusts From Turbine Rotor Wakes. The periodic unsteadiness generated by the turbine rotor wakes is shown in Figs. 5(*g*–*l*) for design-point operation. Comparing these measurements with their respective compressor equivalents shown in Figs. 5(*a*–*f*) gives the relevant differences below.

The relative velocity defect in the turbine wake shown in Fig. 5(*g*) is only 5 percent of the free-stream velocity compared with 15 percent for the compressor wake shown in Fig. 5(*a*). The relative flow angle shown in Fig. 5(*h*) for the turbine remains nearly constant, even through the wake. In the absolute frame of reference, wake-generated unsteadiness now gives large changes in both absolute velocity and steamwise unsteady velocity, V and u^+ (Figs. 5*i* and 5*k*), while changes in air angle (incidence) and transverse unsteady velocity, α and v^+ (Fig. 5*j* and 5*l*), are small. These results are opposite to those seen for the compressor.

The results described above are explained by examining the vector diagram typical for LP turbines in Fig. 4(*b*). Now the mean relative and absolute air angles are separated by only about 25 deg based on the data listed in Table 3. This is in contrast to 90 deg for the compressor. Consequently, large changes in relative flow velocity with small changes in relative angle now produce large changes in absolute velocity and streamwise unsteady velocity. Changes in absolute air angle (incidence) and transverse unsteady velocity are small.

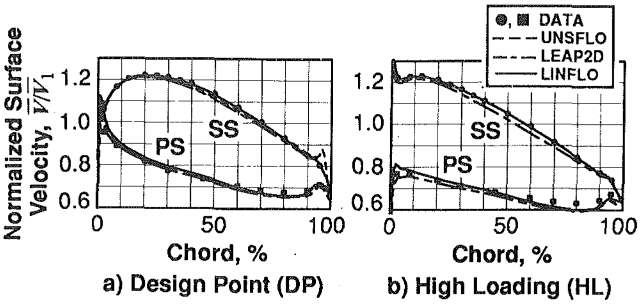

a) Design Point (DP) b) High Loading (HL)

Fig. 8 Time-mean distributions of surface velocity for the compressor stator at (*a*) design point and (*b*) high loading; experiment compared with various models

The amplitude of the first harmonic streamwise gust, H_S for $\hat{u}_1^+$, is two and one-half times that of the transverse gust, H_T for $\hat{v}_1^+$, as seen in Figs. 6(*c*) and 6(*d*). Again, this is the reverse of the compressor results.

Properties of the gusts are listed in Table 3.

5.4 Contributions of the Vortical and Potential Disturbances to the Forcing Function. The evaluation of whether vortical and potential disturbances need to be incorporated in UNSFLO is now made.

For the compressor, it is clear from Table 3 that vortical disturbances dominate since the magnitudes of $\bar{D}$ are at least four to five times larger than those for $A(L/\bar{V})$ as computed from Eq. (12) in the Appendix. Potential effects, although present, should not contribute significantly.

For the turbine, however, the magnitudes of $\bar{D}$ and $A(L/\bar{V})$ in Table 3 are more nearly equal, indicating that potential effects are now important. This results because turbine D values are lower than compressor values. It will be shown in Section 8.3 that incorporating both vortical and potential disturbances as input into UNSFLO improves turbine predictions.

6.0 Gust Response Due to Compressor Rotor Wakes

The measured gust response of the stator due to the compressor rotor wakes is compared to predictions for the low-loading (*LL*), design-point (*DP*), and high-loading (*HL*) cases. The rotor wakes generated high values of reduced frequency of approximately four to five.

6.1 Steady and Unsteady Loading

Steady Loading. The measured time-mean loading on the airfoil surfaces is compared with the predictions from the models in Figs. 8(*a*) and 8(*b*) for the design-point and high-loading conditions, respectively. Agreement is very good with especially good descriptions of the loading change as the compressor is throttled to high loading. In Fig. 8(*b*), there is somewhat more loading predicted on the rear portion of the pressure surface than measured.

At low loading (not shown), the velocity distributions near the leading edge were not predicted quite as well by the inviscid models, probably due to a small pressure-surface separation at −10.4 deg incidence angle.

Unsteady Loading. The unsteady loading of the stator, produced by the passing rotor wakes, is presented in Figs. 9(*a*) and 9(*b*) for the design-point case and in Figs. 9(*c*) and 9(*d*) for the increased loading case. For each case the instantaneous distributions of surface velocity are shown for two of approximately 70 pitchwise locations of the upstream rotor blade. These correspond to the maximum and minimum loading levels as the wakes pass. A time-mean prediction is also plotted for reference.

The instantaneous increase in stator loading due to the increase in absolute air angle (incidence) as the wake passes is

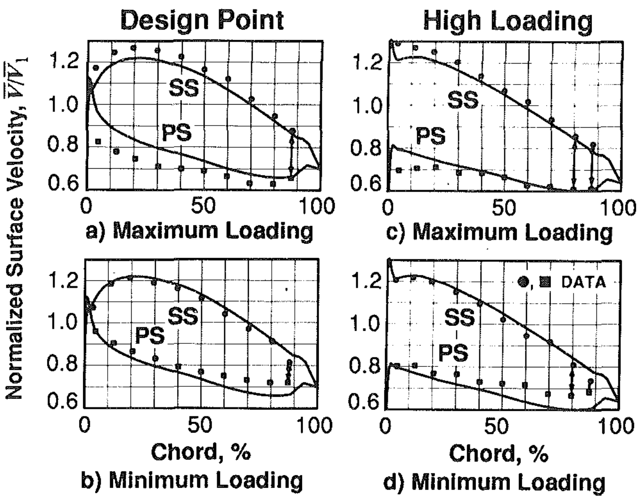

Fig. 9 Snapshots of measured unsteady loading on the compressor stator for two instantaneous circumferential positions of the rotor wake relative to the stator; solid curve is time-mean loading shown for reference

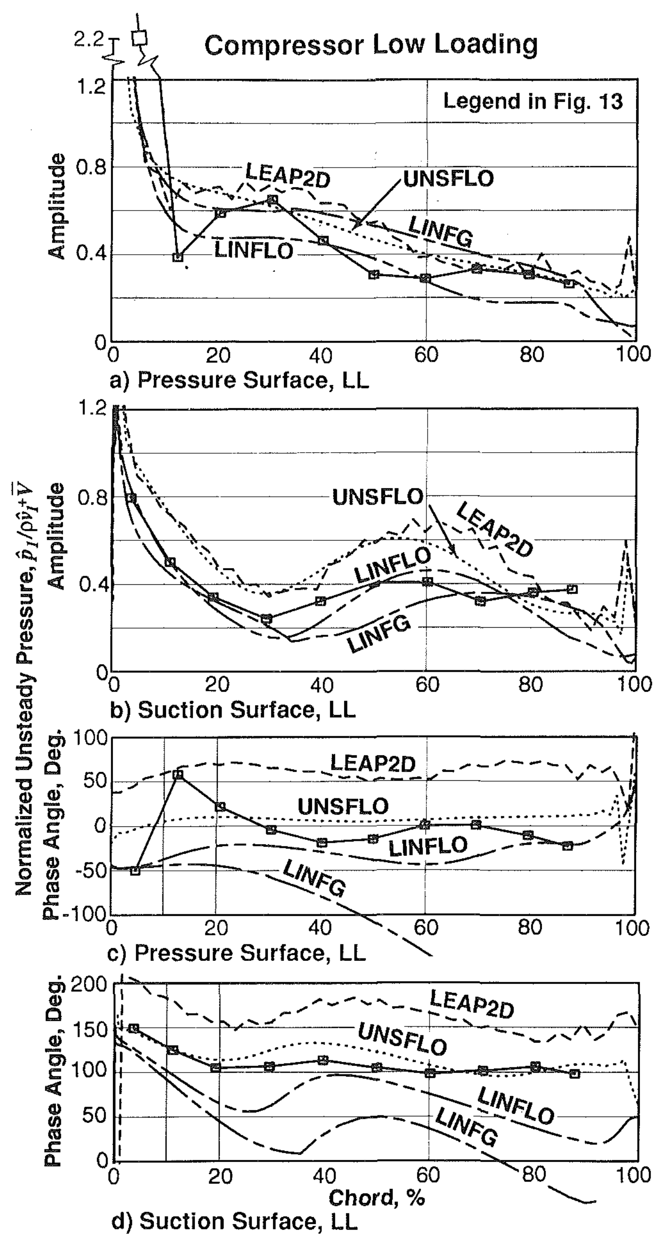

Fig. 10 Comparison of the measured and predicted response of a stator to compressor rotor wakes for low loading; first harmonic is shown

clearly seen in Fig. 9(*a*) and 9(*c*). At the design point, Fig. 9(*a*), the instantaneous change in incidence of 10 deg (see Fig. 5*d*) produces a loading change about equal to that shown in Fig. 8 for the 5 deg time-mean change in incidence from the design point to high loading. At these high reduced frequencies the system responds to about one-half of the change in incidence. This is explained aerodynamically as follows.

Potential flow studies for flow over an airfoil show that when incidence angle is changed without allowing a change in airfoil circulation, the resulting movement of the leading edge stagnation point (and hence change in local loading) is only one-half of what would occur if the circulation were permitted to change. In the present case, the rotor wake produces a large local change in airfoil incidence. However, because the wake is narrow compared to the chord, it cannot produce a global change in circulation for the whole airfoil. Hence only about one-half of the change in leading edge loading is realized.

Attention is drawn to the large fluctuations about the time-mean prediction measured at 88 percent chord for the design point in Figs. 9(*a*) and 9(*b*) and at 80 and 88 percent chord for increased loading in Figs. 9(*c*) and 9(*d*). This increased unsteadiness, seen by the change in length of the arrows in the figure, is probably due to the chordwise unsteady motion of a suction surface separation over these measurement locations brought about by the increased turbulence level of the rotor wakes passing through the passage.

6.2 Gust Response. The normalized amplitude and phase of the first harmonic of the measured unsteady pressures at each transducer location on the airfoil are compared to predictions in Figs. 10–12 for the low-loading, the design-point, and the high-loading cases, respectively. The resultant first-harmonic pressure differences are shown in Fig. 13.

Amplitude of Surface Unsteady Pressures. All of the analysis codes (LINFG, LINFLO, LEAP2D, and UNSFLO) do a good job in predicting both the level and trend of the unsteady pressure amplitudes on the pressure surface for the low-loading case in Fig. 10(*a*). At the design point in Fig. 11(*a*), the data trend flattens, while the analyses, which have a small negative chordwise slope, slightly overpredict the data over the first half of chord and underpredict it over the latter half. This over/underprediction feature becomes more apparent in Fig. 12(*a*) as loading increases. We offer three possible explanations:

1 The unsteadiness on the suction surface at increased loading (Fig. 12*b*) could affect the pressure surface unsteadiness, although we do note that pressure surface phase angles in Fig. 12(*c*) do not change over the last 50 percent of chord while suction surface phase in Fig. 12(*d*) does.

2 The downstream potential field of Rotor 2 could affect Stator 1. Our measurements and analysis indicate that this effect is not large. At the design point, the fluctuation in flow velocity from the potential field of Rotor 2 at 75 percent of Stator 1 chord is about ±0.4 percent of free-stream velocity or about 5 percent of the rotor wake defect. This effect does increase by 50 percent at high loading.

3 Kerrebrock and Mikolajczak (1970) show that the low-energy fluid from the rotor wakes collects on the pressure surface. The increase in wake turbulence levels that occurs in compressors as loading increases could effect unsteadiness levels in the pressure surface boundary layers. This is not modeled.

Very near the leading edge (5 percent chord), a large-amplitude unsteadiness (spike) was measured at low loading as shown in Fig. 10(*a*). Our analysis indicates a small pressure-

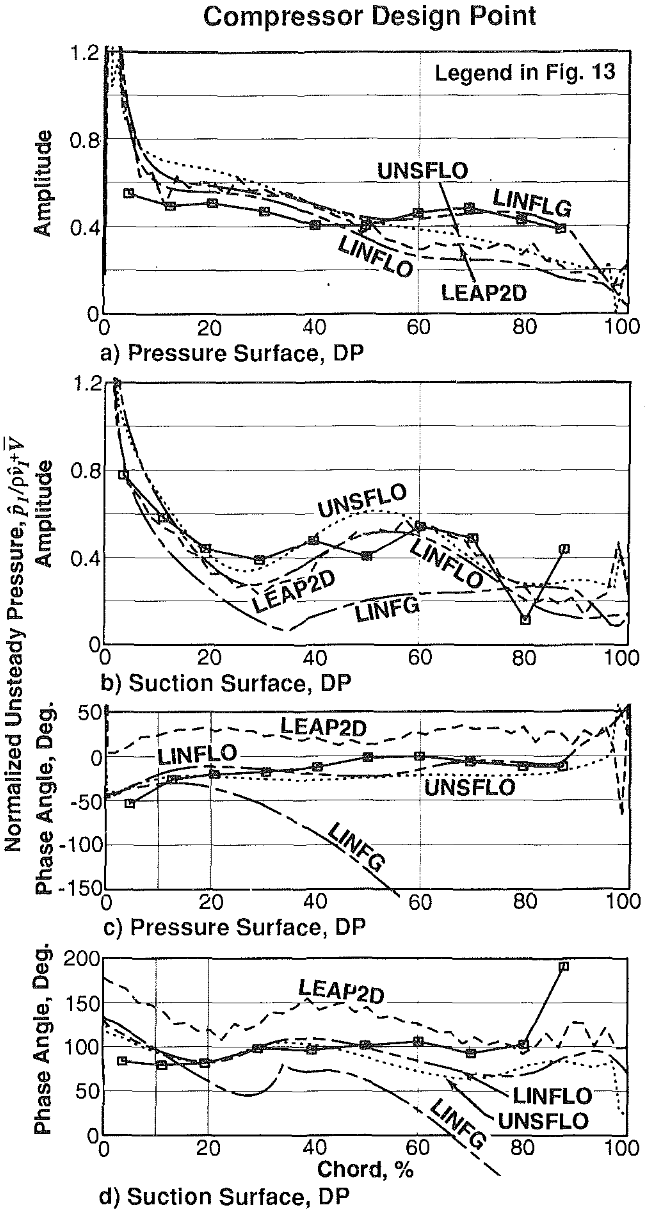

a) Pressure Surface, DP

b) Suction Surface, DP

c) Pressure Surface, DP

d) Suction Surface, DP

Fig. 11 Comparison of the measured and predicted response of a stator to compressor rotor wakes for design point; first harmonic is shown

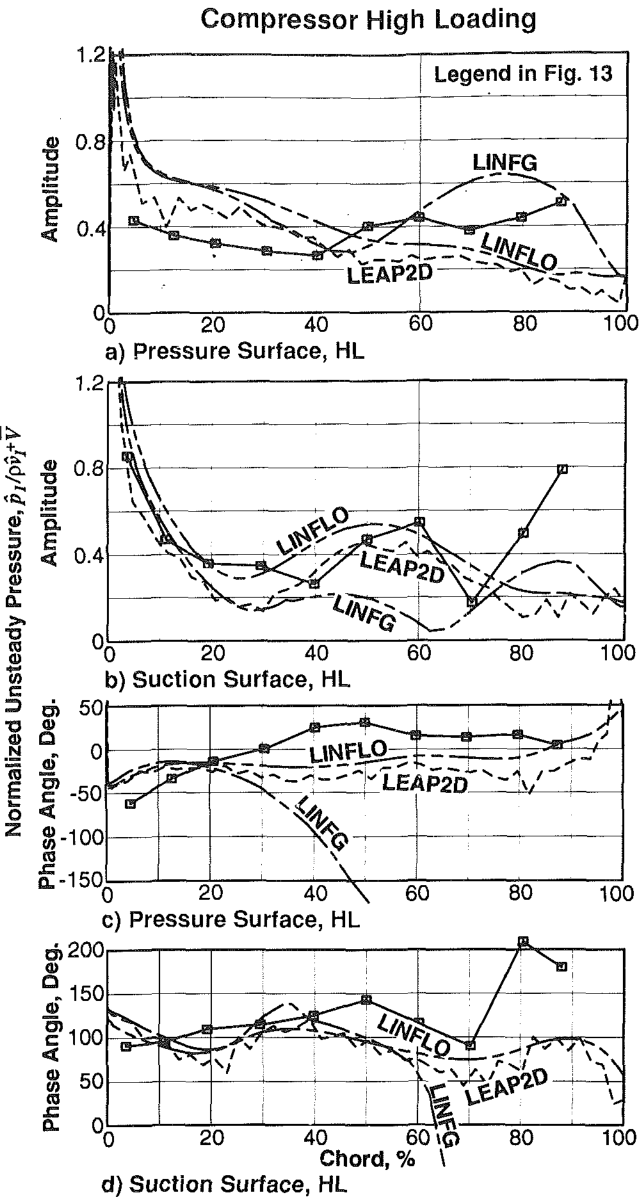

a) Pressure Surface, HL

b) Suction Surface, HL

c) Pressure Surface, HL

d) Suction Surface, HL

Fig. 12 Comparison of the measured and predicted response of a stator to compressor rotor wakes for high loading; first harmonic is shown

surface separation at this low incidence. The 5 percent chord location is probably just ahead of the separation bubble in the high-gradient flow region around the leading edge. Thus as the stagnation point moves due to passage of the wakes, the pressure acting on this transducer will vary greatly. Farther downstream the low-amplitude unsteadiness at 12.5 percent chord is probably measured inside the separation bubble before reattachment of the boundary layer. Pressure would not vary greatly inside the bubble as its location fluctuates. At 5 percent chord in Figs. 11(*a*) and 12(*a*) for the design and high-loading cases, respectively, the data were probably not in the high-acceleration region near the leading edge.

On the suction surface, LINFLO, LEAP2D, and UNSFLO do very good jobs in predicting chordwise trend at all three loading levels, Figs. 10(*b*), 11(*b*), and 12(*b*). They do exceptionally well in both magnitude and trend over the first 80 percent of chord for the design-point and high-loading cases, Figs. 11(*b*) and 12(*b*), respectively. The leading edge region is well predicted at all loading levels. Near the trailing edge, the models do not predict the sharp rise in the data as loading increases. This rise is probably caused by the forward and aft motion of a separation region on the suction surface that results as the rotor wakes pass through. Inviscid codes would not predict these effects.

By comparison, LINFG does not do as well on the suction surface in predicting either magnitude or trend from about 30 percent chord to the trailing edge. The differences between LINFG and both the data and the other predictions increase as loading levels increase, as shown in Figs. 10(*b*) to 11(*b*) to 12(*b*). This is not surprising because LINFG assumes that a frozen gust is convected through the vane row; therefore, it cannot accurately predict amplitudes when stronger steady/unsteady flow field interactions begin to occur as loading increases.

Phase Angles. The measured phase angles in Figs. 10–12 are generally well predicted by LINFLO and UNSFLO, especially at the design point shown in Figs. 11(*c*) and 11(*d*). The LEAP2D predictions are shifted from the data by approximately 60 deg at low loading and 35 deg at the design point. Possible reasons for this will be addressed in the dis-

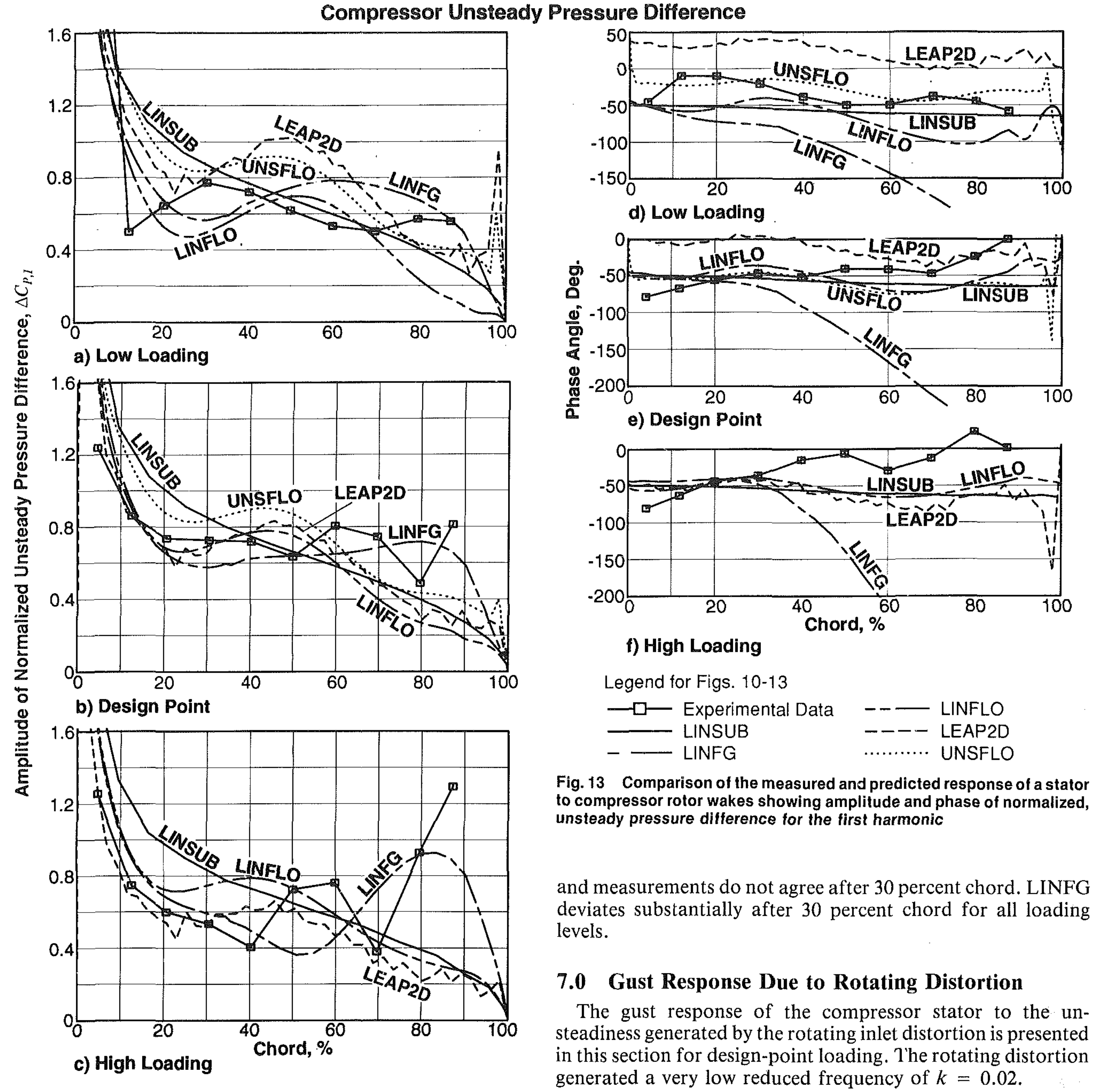

Fig. 13 Comparison of the measured and predicted response of a stator to compressor rotor wakes showing amplitude and phase of normalized, unsteady pressure difference for the first harmonic

cussion. LINFG, with its frozen gust assumption, does not predict phase angle well after 30 to 40 percent chord.

Unsteady Pressure Difference. LINFLO, LEAP2D, and UNSFLO do a good job in predicting magnitude and trend of the amplitude of the unsteady pressure difference over most of the airfoil, especially in Figs. 13(*b*) and 13(*c*). LINFG, although doing well over the first 60 percent of chord, breaks away from the other models over the aft portion of the airfoil as loading increases. This is not surprising in view of its frozen gust assumption. The LINSUB predictions, although not unreasonable, are the poorest of the group. Of course none of these inviscid models can predict the previously described increase in unsteadiness near the trailing edge of the suction surface as loading increases.

Agreement between predictions and measurements of the magnitude and trend of phase angles shown in Figs. 13(*d*) and 13(*e*) is good for LINSUB, LINFLO, and UNSFLO. LEAP2D is shifted in magnitude about 50 deg at low and design-point loading. At high loading shown in Fig. 13(*f*), the predictions and measurements do not agree after 30 percent chord. LINFG deviates substantially after 30 percent chord for all loading levels.

7.0 Gust Response Due to Rotating Distortion

The gust response of the compressor stator to the unsteadiness generated by the rotating inlet distortion is presented in this section for design-point loading. The rotating distortion generated a very low reduced frequency of $k = 0.02$.

7.1 Steady and Unsteady Loading

Steady Loading. The shapes of the time-mean velocity distributions on the airfoil surfaces and their agreement with the predictions are nearly identical to those shown in Fig. 8(*a*).

Unsteady Loading. In Figs. 7(*a*) and 7(*b*), two levels of both absolute velocity and flow angle are seen that corresponded to the out-of-distortion and in-distortion cases, respectively. After analysis, the instantaneous set of unsteady velocity distributions on the airfoil surface for the out-of-distortion case was in excellent agreement with time-mean predictions computed using out-of-distortion levels of absolute velocity and air angle taken from Figs. 7(*a*) and 7(*b*). Similarly, the instantaneous data for the in-distortion case were in excellent agreement with time-mean predictions computed using in-distortion levels of absolute velocity and air angle taken from Figs. 7(*a*) and 7(*b*).

Apparently the circumferential extent of the distortion is large enough to support a static pressure difference and a global change in circulation for each quasi-steady region despite the

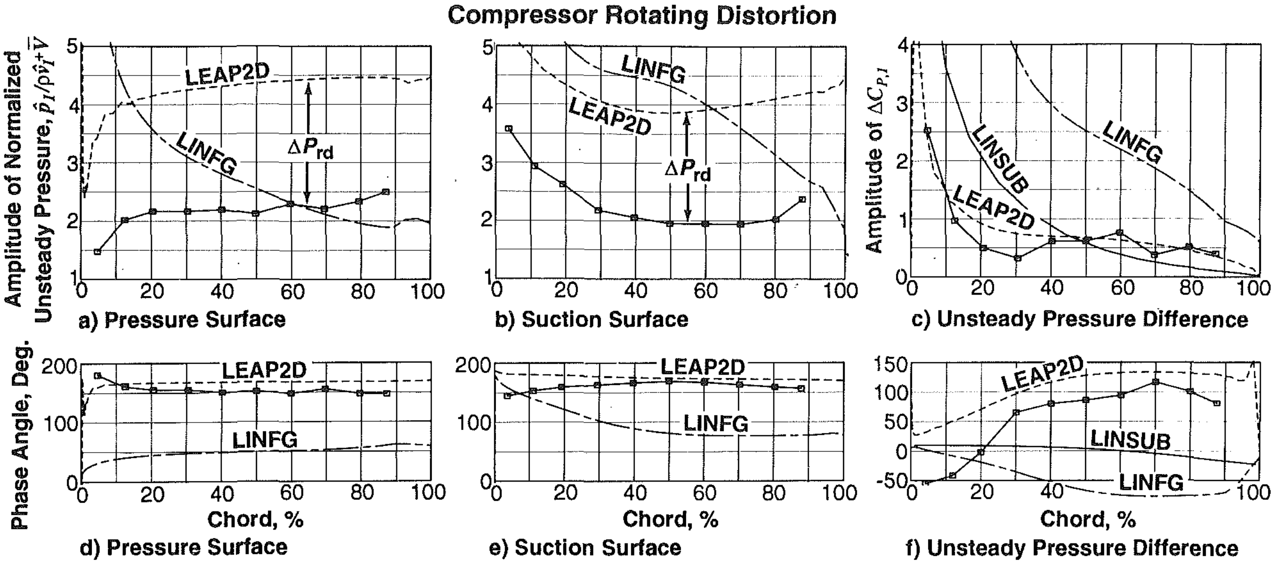

Fig. 14 Comparison of the measured and predicted response of a stator to a rotating inlet distortion at the design point; first harmonic is shown, counterrotation rate is 30 percent of rotor speed

relatively high rate of screen rotation of −30 percent of rotor speed.

7.2 Gust Response. The amplitude and phase of the first harmonics of the unsteady pressures are presented in Fig. 14 along with LINSUB, LINFG, and LEAP2D predictions. The other models were not run because of time limitations.

LINSUB and LINFG are poor predictors of the data in both level and trend.

LEAP2D, on the other hand, predicts the trends of the suction and pressure surface amplitudes and both the levels and trends of the phase angles very well. The predicted levels of the unsteady pressure are shifted by a constant pressure, ΔP_{RD}, as marked in Figs. 14(*a*) and 14(*b*). This shift results because the predictions do not account for the change in pressure levels for the in-distortion and out-of-distortion cases. However, the amplitude of the unsteady pressure difference in Fig. 14(*c*) is predicted very well because ΔP_{RD} subtracts out when the complex difference is computed (since the pressure and suction surface phases are nearly equal). LEAP2D gives good predictions of unsteady pressure difference even at very low reduced frequencies.

8.0 Gust Response Due to LP Turbine Rotor Wakes

The nozzle response to gusts generated by turbine rotor wakes is compared with predictions for low loading (*LL*) and the design point (*DP*). The rotor wakes generated moderately high values of reduced frequency of three.

8.1 Steady and Unsteady Loading

Steady Loading. The time-mean loading on the airfoil surfaces is presented in Figs. 15(*a*) and 15(*b*) for low loading and design point, respectively.

The various models do reasonably well in predicting the design-point loading seen in Fig. 15(*a*). However, at low flow (low incidence) shown in Fig. 15(*b*), the models are not able to predict the pressure surface loading over the first 30 percent of chord. These data reflect a suspected pressure-surface separation resulting from the large negative incidence of −16 deg. The inviscid models would not be able to predict this separated flow.

Unsteady Loading. As the rotor wake passes, the instantaneous distributions of surface velocity on the turbine nozzle (not shown) are virtually identical to the time-mean data shown in Fig. 15. This is in contrast to the large changes shown in Fig. 9 for the compressor. The reasons for this are: (1) the unsteadiness in the turbine does not produce the large changes in air angle (incidence) that were seen for the compressor (compare Figs. 5*j* and 5*d*), and (2) relatively speaking, the turbine rotor wakes are a smaller fraction of free-stream velocity than those of the compressor while turbine nozzle loading is much larger than compressor stator loading. Thus any unsteadiness would be a smaller fraction of the average level.

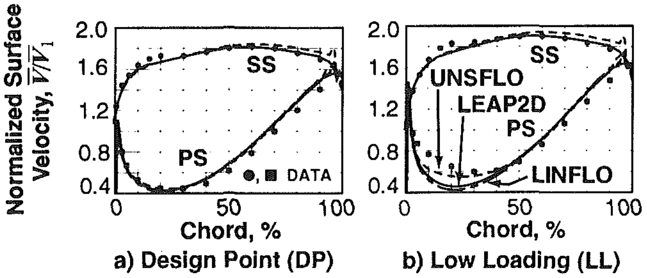

Fig. 15 Time-mean distributions of surface velocity for the turbine nozzle; experiment compared with CFD models

8.2 Gust Response. The measured, first harmonic gust response of the nozzle to turbine rotor wakes is compared to predictions in Figs. 16–18.

Amplitude of Surface Unsteady Pressure. At the design point, LINFLO, LEAP2D, and UNSFLO do reasonably well in predicting data trends on the pressure surface, Fig. 17(*a*). For the suction surface, Fig. 17(*b*), they do an excellent job in predicting trend. LINFG, using a frozen gust, predicts trend poorly on both suction and pressure surfaces.

With respect to predicting magnitude of unsteady pressure at the design point, UNSFLO does well on the first half of the pressure surface as seen in Fig. 17(*a*); LINFLO and LEAP2D are about 30 percent high. Over the second half of the airfoil UNSFLO is about 30 percent low and LINFLO and LEAP2D are quite good. On the suction surface, LINFLO, LEAP2D, and UNSFLO are seen in Fig. 17(*b*) to do excellent jobs. Once again, LINFG predicts magnitudes poorly for both pressure and suction surfaces.

At low loading seen in Fig. 16(*a*), the data show that the pressure unsteadiness becomes very low on the forward region of the pressure surface from 10 to 30 percent chord. The

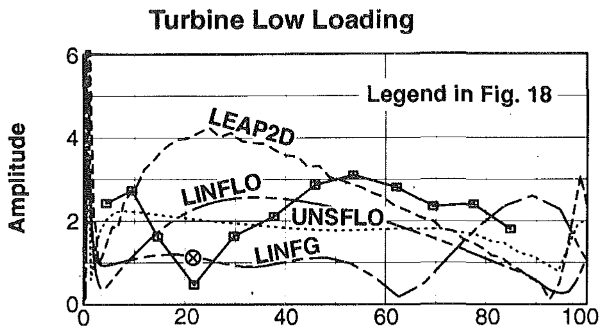

a) Pressure Surface, LL

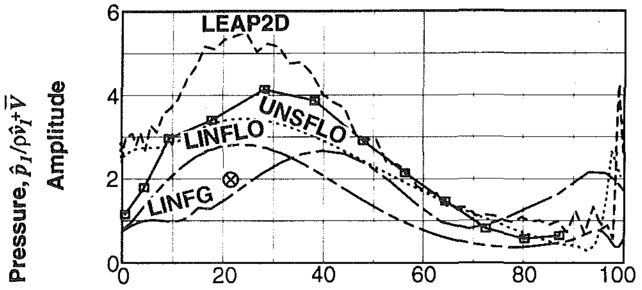

b) Suction Surface, LL

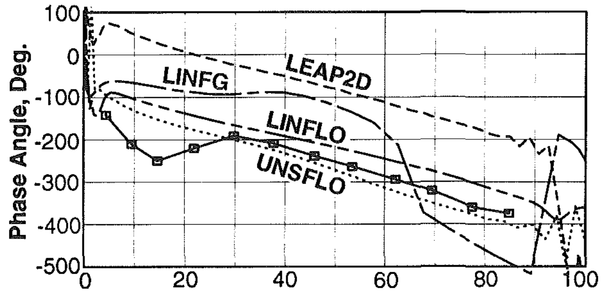

c) Pressure Surface, LL

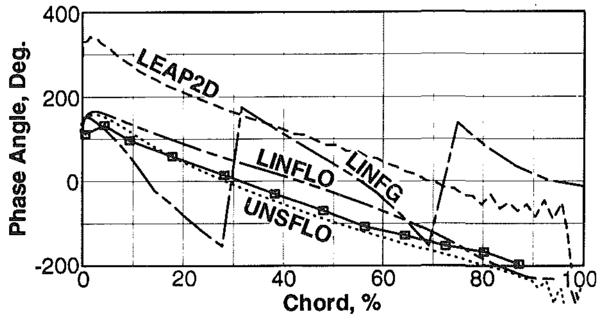

d) Suction Surface, LL

Fig. 16 Comparison of the measured and predicted response of a turbine nozzle to rotor wakes for low loading; first harmonic is shown

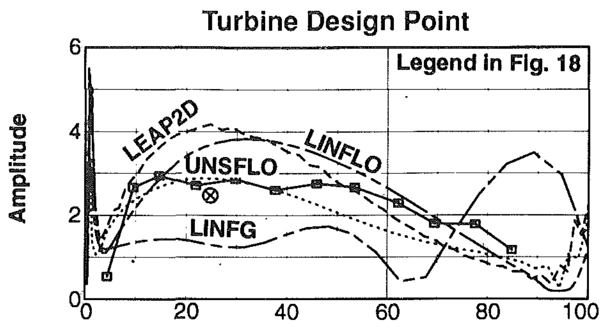

a) Pressure Surface, DP

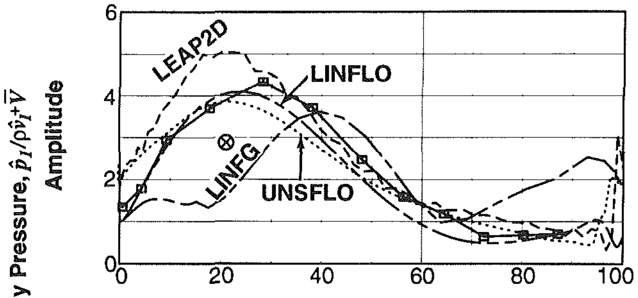

b) Suction Surface, DP

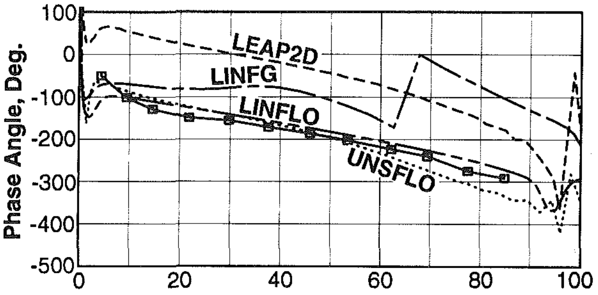

c) Pressure Surface, DP

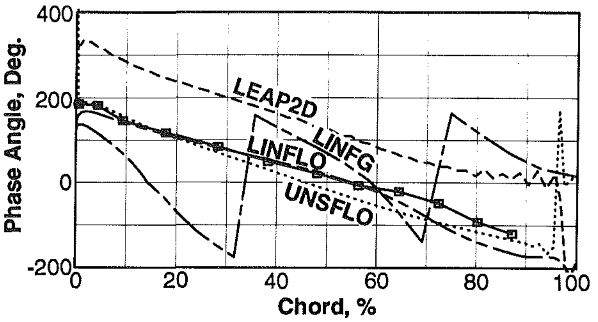

d) Suction Surface, DP

Fig. 17 Comparison of the measured and predicted response of a turbine nozzle to rotor wakes for design point; first harmonic is shown

transducers are located inside a suspected, low-incidence, pressure-surface separation described for the time-mean data in Fig. 15(*b*). A time-mean flow separation could shield the surface from wake-generated unsteadiness until the flow reattaches. Inviscid models would not be expected to predict this.

For the suction surface at low loading shown in Fig. 16(*b*), LEAP2D and UNSFLO do reasonably well in predicting both magnitude and trend of the data. LINFLO predicts trend well but underpredicts the data. LINFG does poorly in predicting both magnitude and trend.

Phase Angle. LINFLO and UNSFLO do outstanding jobs in predicting both the magnitude and trend of the phase angle data on the suction and pressure surfaces as shown in Figs. 16(*c*, *d*) and Figs. 17 (*c*, *d*).

LEAP2D predicts trend very well but is shifted in magnitude from the data by about 150 deg. LINFG, with its frozen gust assumption, is not able to predict phase angle. These discrepancies will be addressed in the discussion.

Unsteady Pressure Difference. The unsteady pressure differences (pressure minus suction surface unsteady pressures) are presented in Fig. 18 for the two loading levels. UNSFLO does exceptionally well in predicting the amplitude and trend of the design-point data shown in Fig. 18(*b*). LEAP2D and LINFLO overpredict the data by about 30 and 20 percent, respectively at 25 percent chord but do exceptionally well from 40 percent chord to the trailing edge. LINFG does poorly and LINSUB does very poorly.

At low loading shown in Fig. 18(*a*), all of these inviscid

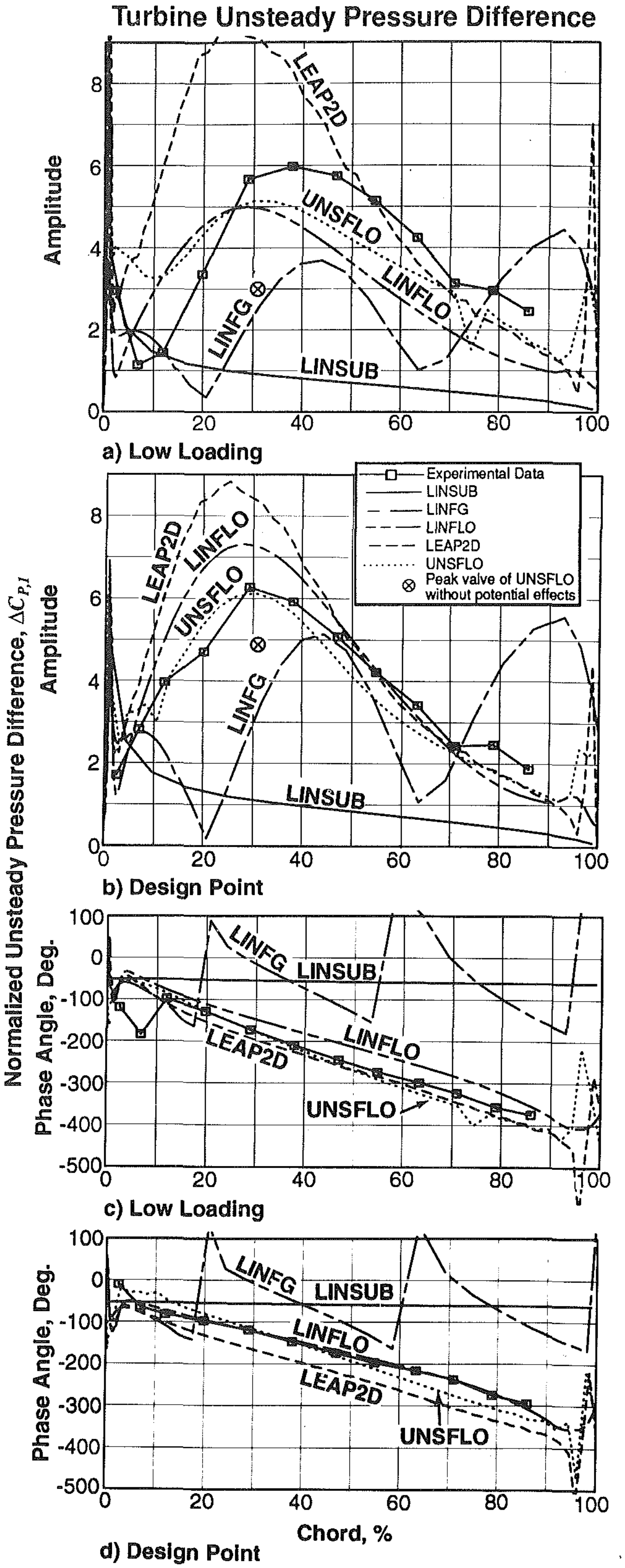

a) Low Loading

b) Design Point

c) Low Loading

d) Design Point

Fig. 18 Comparison of the measured and predicted response of a turbine nozzle to rotor wakes showing amplitude and phase of normalized unsteady pressure difference; first harmonic is shown

models have difficulty predicting the effects of the pressure-surface separation on the forward portion of this airfoil. On average LINFLO and UNSFLO do reasonably. LEAP2D does well over the latter half of the airfoil but overpredicts loading on the forward portion. LINFG and LINSUB do poorly.

Table 4 Comparison of predictions of amplitude of unsteady pressure

			DATA	LINSUB	LINFG	LINFLO	LEAP2D	UNSFLO
Cray Equivalent Time, Secs				1	10	10	100	1200
Development Year				1970	1986	1989	1991	1988
			Int.-Ave.	%	%	%	%	%
Compressor Rotor Wakes	Low Loading	PS	0.51	–	**5***	-25*	**6***	**3***
		SS.	0.38	–	**-19***	**-9***	42*	31*
		ΔP	0.71	**8**	**5**	**-17***	**19**	**17**
	Design	PS	0.46	–	**12***	**-12***	**-5***	**7***
		SS	0.45	–	-44	**-7***	**-8***	**6***
		ΔP	0.74	**1**	**-4***	**-11***	**-8***	**8***
	High Loading	PS	0.37	–	35*	**12***	**-13***	NC
		SS	0.42	–	-41*	**0***	-28*	NC
		ΔP	0.68	**7**	**-1**	**-1***	-23*	NC
Compr. Distortion	Design	PS	2.17	–	33	NC	98*	NC
		SS	2.25	–	97	NC	83*	NC
		ΔP	0.66	76	449	NC	**19***	NC
Turbine Rotor Wakes	Low Loading	PS	2.20	–	-53	**-13**	33	**-14**
		SS	2.44	–	-34	-38*	26*	**-6***
		ΔP	4.01	-80	-47	**-19***	41	**-5***
	Design	PS	2.37	–	-40	**16***	**15***	**-12***
		SS	2.35	–	**-14**	**-10***	**16***	**-4***
		ΔP	4.09	-76	-30	**12***	25*	**-3***

a. Bold, large numbers show agreement within ±20% of data
b. * Predictions show good trendwise agreement with data
c. Experimental data are integrated-averages obtained from Eq. 3
d. Values under code acronyms are percent differences using Eq. 4
e. "NC" means not computed, "–" means model cannot compute this

LINFLO, LEAP2D, and UNSFLO do outstanding jobs in predicting phase angle in Fig. 18(*c*) and 18(*d*). LINSUB and LINFG are not able to predict phase angles well.

8.3 Importance of Including Potential Disturbances. The importance of including both the vortical and potential disturbances into the UNSFLO analysis is clearly demonstrated in Figs. 16(*a*, *b*), 17(*a*, *b*), and 18(*a*, *b*). The peak amplitude of the unsteady pressure predicted by UNSFLO without potential effects is indicated by the "⊗" symbol in the figures. Including potential effects raises the UNSFLO solution by about 40 percent for low loading and 20 percent for the design point to give much better agreement with the data.

9.0 Discussion

9.1 Arrangement of Tables. In order to get a more quantitative assessment of the ability of the various models to predict unsteady aerodynamic loading, we constructed Table 4 as follows. For each of the Figs. 10–14 and 16–18, the experimentally measured amplitudes of unsteady pressures and pressure differences were integrated along the chord using Eq. (3) from the first to the last measurement location. This average amplitude is listed in Table 4 under the column "Data" for each test condition. An integrated average value of amplitude of unsteady pressure was also computed for each of the predictions in the figures. The chord length of integration was identical to that for the experimental data.

$$\overline{P}=\frac{\int_{i=1}^{N} P_i dc}{\int_{i=1}^{N} dc} \qquad (3)$$

Table 5 Comparison of predictions of phase of unsteady pressure

			DATA	LINSUB	LINFG	LINFLO	LEAP2D	UNSFLO
			Int.-Ave.	Δ *deg*	Δ *deg*	Δ *deg*	Δ *deg*	Δ *deg*
Compressor Rotor Wakes	Low Loading	PS	-1	–	-111	-29	64	**9**
		SS	109	–	-77	-36*	54*	**-7***
		Δ*P*	-35	-23	-86	-34*	56*	**-6***
	Design	PS	-14	–	-112	**-1***	38*	**-10***
		SS	99	–	-63	**-10***	27*	**-13***
		Δ*P*	-45	**-13**	-86*	**-8***	32*	**-14***
	High Loading	PS	4	–	-146	**-19***	-32*	NC
		SS	126	–	-85	-35	-41	NC
		Δ*P*	-24	-34	-120	-29	-37	NC
Compr. Distortion	Design	PS	154	–	-105*	NC	**13***	NC
		SS	162	–	-65	NC	**14***	NC
		Δ*P*	60	-54	-111	NC	47*	NC
Turbine Rotor Wakes	Low Loading	PS	-259	–	78	54*	-152*	**5***
		SS	-44	–	67	35*	-116*	**-10***
		Δ*P*	-234	160	195	41*	-44*	**0***
	Design	PS	-188	–	104	**14***	-195*	**0***
		SS	-35	–	**-10**	**-12***	158*	**-20***
		Δ*P*	-165	98	121	**3***	**7***	**-3***

a. Bold, large numbers show agreement within ±20° of data
b. * Predictions show good trendwise agreement with data
c. Experimental data are integrated-averages obtained from Eq. 3
d. Values under code acronyms are differences from data in degrees
e. "NC" means not computed, "–" means model cannot compute this

The percent difference between these predicted and measured values of average unsteady pressure was computed from Eq. (4) and listed for each model under the appropriate column in Table 4. When the prediction agrees with the measurement within 20 percent, the numbers in the table are larger and boldfaced. When predictions show good trendwise agreement with the measurements, an asterisk appears.

$$\text{percent difference} = \frac{\overline{P}_{\text{predicted}} - \overline{P}_{\text{measured}}}{\overline{P}_{\text{measured}}} \times 100 \tag{4}$$

The same type of integration procedure was used to find average phase angle for both the data and the predictions. For the data, the average values of phase angle are listed in degrees in Table 5 while, for the predictions, the differences between the data and the predictions are listed in degrees. Large boldfaced numbers indicate agreement with data within ±20 deg and asterisks indicate good trendwise agreement with measurements.

9.2 Discussion of the Predictive Capability of the Models. Our discussion on the predictive ability of the models focuses on nonlinear effects and restrictive assumptions; the importance of vortical and potential effects in the forcing function; amplitude and phase of the gust response; and computing practicality.

Nonlinear Effects and Restrictive Assumptions. An evaluation of whether nonlinearity played an important role in the analyses was made by examining the predictions of gust response obtained from the nonlinear UNSFLO model. In response to forcing functions consisting only of the first harmonic of the rotor wakes, the amplitudes of the second harmonics of the surface unsteady pressures were computed by UNSFLO to be at most only 2 percent of the amplitudes of the first harmonics for the compressor and 7 percent for the turbine. If nonlinear effects were significant, these second harmonics would be much larger. Thus it was concluded that nonlinear effects could be neglected and linearized analysis methods were applicable for all of our data needs, even for the more highly loaded LP turbine.

The second harmonics, which are seen in the gust response of the compressor experimental data, resulted from the second harmonics in the periodic unsteadiness of the wakes and not from nonlinearity effects.

Turning to the frozen gust assumption, we note that the accuracy of the predictions of the models that use this assumption deteriorates rapidly as loading increases. This is seen by examining Tables 4 and 5. LINSUB and LINFG do make accurate predictions of the magnitude of unsteady pressure for the compressor at low loading and the design point. However, at high loading for the compressor and for the much higher loading levels for the turbine seen in Fig. 2, they make poor predictions. Phase angles are predicted poorly at all loading levels. On the other hand, the models such as LINFLO, LEAP2D, and UNSFLO, which use the distorted gust or generalized wake along with modern CFD methods, make much more accurate predictions as loading increases.

Importance of Vortical and Potential Effects in the Forcing Function. The need, not only to have accurate models but also to incorporate all relevant features of the forcing function into the analysis, has been amply demonstrated by our results.

Henderson and Fleeter (1991) first reported an interesting finding with respect to the phase angle of the ratio of streamwise-to-transverse gusts $\hat{u}_1^+/\hat{v}_1^+$. They reported for their tests using uncambered airfoils that when this phase angle was 0 or 180 deg, they got excellent correlations of gust response data with LINSUB. When this phase angle was not 0 to 180 deg, their correlations were poorer. For the latter case they measured *static pressure variations just upstream of the airfoils.* They concluded that, when the phase angle of $\hat{u}_1^+/\hat{v}_1^+$ was not 0 or 180 deg, effects were present that linear theory did not model.

An assessment of the phase angles of $\hat{u}_1^+/\hat{v}_1^+$ for our data in Table 3 does not tend to support the conclusions described above. Some of our phase angles are well away from 0 or 180 deg and yet linear theory is still applicable in all of our cases.

However when we focused on the phase angle of the vortical parameter D, we found a relevant correlation. It is seen in Appendix II that the numerator of the magnitude of the potential parameter A in Eq. (12*b*) is identical to the numerator of the phase angle of D in Eq. (12*a*). Thus when there are no potential effects, i.e., $|A| = 0$, then the phase angle of D is 0 or 180 deg. As potential effects come into play ($|A| \neq 0$), the phase angle of D differs from 0 or 180 deg.

The above is clearly seen in our data in Table 3. For the low-loading and high-loading compressor cases, the phase angles of D are 179.1 and 174.9 deg (very close to 180 deg). At the design point the phase angle is within 15 deg or 180 deg. For these three compressor cases, vortical effects were previously shown to dominate. For the turbine cases the phase angles of D are 125.2 and 129.7 deg (well away from 180 deg) and important potential effects are present. This was shown previously by comparing magnitudes of D and $A(L/\overline{V})$ in Table 3 and examining Figs. 16–18 as discussed in section 8.3. This is part of the physics of the flow that has improved turbine predictions of the data.

Nonlinear effects were previously shown to be small for our tests cases. Consequently we conclude that our phase angles of D being equal to or different from 0 to 180 deg are related to vortical and potential effects rather than to a linearization feature of the model.

Amplitude and Phase of the Gust Response. By examining the number of occurrences of bold-faced numbers and asterisks in Tables 4 and 5, one can get an assessment of how often the

Table 6 Percent of total number of cases in which predictions and data agree within ±20 percent of amplitude or ±20 deg of phase

	Amplitude		Phase	
	Magnitude	Trend	Magnitude	Trend
LINSUB	50%	0%	17%	0%
LINFG	39%	28%	6%	6%
LINFLO	87%	87%	47%	80%
LEAP2D	50%	83%	17%	83%
UNSFLO	92%	83%	100%	92%

predictions and the data are in agreement. To this end, we constructed Table 6 as follows: For each model listed in Tables 4 and 5, we counted the number of times that the model made accurate predictions and divided this by the total number of times that predictions were attempted. Using UNSFLO in Table 4 as an example, we find 11 accurate predictions of amplitude of unsteady pressure (bold-faced numbers) in 12 attempts. Thus, UNSFLO made accurate predictions in 11/12, or 92 percent, of its attempts. This value is listed in Table 6 under the appropriate column. The process was repeated for the magnitude and trend of the amplitude and phase for all of the models.

Although we caution the reader about carrying this statistical approach too far, we do learn the following from Table 6:

LINFLO, LEAP2D, and UNSFLO predict data trends for both compressors and turbines very well in about 85 percent of all cases tested. LINFLO and UNSFLO predict amplitude of unsteady pressure well in about 90 percent of all cases, and LEAP2D in about 50 percent. UNSFLO predicts phase angle well in 100 percent of the cases and LINFLO in about 50 percent. LEAP2D has more difficulty predicting phase angle. LINSUB and LINFG use frozen gusts and do not predict the data accurately in very many cases. LINSUB does not predict data trends in any cases. Although LINSUB seemingly predicts magnitude for all three compressor cases, it does so by overpredicting unsteady loading on the forward half of the airfoil by as much as it underpredicts it in the aft half and thus gets the correct answer for the wrong reason.

The process of circumferentially averaging the turbine data, to remove the effects of upstream $N1$ wakes, produced results that the models were able to predict. This may mean that the models could be used in the multistage environment if proper averaging techniques were used.

We now address the discrepancy between LEAP2D's prediction and the measurements. For example, the average discrepancy between the data and prediction of phase angle is about 150 deg for the turbine and about 35-60 deg for the compressor. We checked to be sure that this discrepancy did not occur from LEAP2D's use of one-dimensional nonreflecting boundary conditions (1D NRBC) at these low Mach numbers. The Mach numbers were doubled and LEAP2D was run with both 1-D NRBC and 2-D NRBC. Minimal differences were seen between any of the results. The discrepancy could be in pre- or postprocessing of the phase angle reference. The numerics of the code are known to be sound. The developers of LEAP2D are currently addressing this situation.

Computer Practicality. The predictions described above have been made with models that do not require extremely large CPU computing times. This practical aspect is important for certain design applications. LINFLO converged in 10 seconds of equivalent Cray time; LEAP2D achieved a solution in less than 100 seconds, and UNSFLO reached convergence for our data in approximately 1200 seconds. Obviously, computing time for LINFLO is very appealing in design applications where large numbers of computational runs are necessary.

The initial setup time by an expert user is about two hours for any of the CFD models. The complexity of the setup is also about the same for any of the models.

10 Conclusions

The following conclusions about the ability of current models to predict unsteady aerodynamics and gust response in compressors and LP turbines are drawn.

1 Linear analysis methods, in which the unsteady part of the flow is linearized about a steady, nonlinear mean flow, yield reasonably accurate predictions of the unsteady loading in many turbomachinery applications. Nonlinear unsteady effects were found to be negligible for all cases tested, even at the higher loading levels and camber of the LP turbine. Blading with very large wake defects may require nonlinear analysis.

2 The frozen gust assumption is not appropriate for analyzing our data at higher loading levels. Models that use this assumption, e.g., LINSUB and LINFG, gave poorer predictions at higher compressor loading and at all turbine loading levels. Models that use the distorted gust or generalized wake along with modern CFD methods, e.g., LINFLO, LEAP2D, and UNSFLO, make much more accurate predictions as loading increases.

3 The importance of properly including both vortical and potential disturbances in the forcing function has been demonstrated experimentally for the first time.

- By examining the relative magnitudes of the properly normalized parameters called D and $A(L/\overline{V})$, one can determine whether potential effects need to be incorporated. If D dominates $A(L/\overline{V})$, then only vortical effects are needed and the phase angle of D is near 0 or 180 deg. As these parameters become more nearly equal, both effects must be considered and the phase angle of D differs substantially from 0 or 180 deg.
- By including potential disturbances with vortical ones when needed, UNSFLO turbine predictions increased by 20 to 40 percent and yielded better agreement with data.

4 UNSFLO and LINFLO do very well in predicting the data as seen in Table 6. LEAP2D does reasonably in predicting amplitude but has some difficulty predicting phase angle at this stage of its development. Considering the complexities of the issues, we think that these are significant accomplishments for the models.

5 The computational models can be run within reasonable computer CPU and setup times. LINFLO has the appeal of running in 10 seconds. Quick running is of practical importance in many design applications.

6 The success of our circumferential averaging technique may guide the application of these codes in the multistage environment.

7 From the designer's perspective, this work has demonstrated that these state-of-the-art codes yield useful predictions of unsteady flow response for compressors and turbines over a wide range of operating conditions and reduced frequencies. Consequently, we see the potential that designs could be evaluated before hardware is manufactured yielding large savings in time and cost.

Acknowledgments

The authors are deeply indebted to the following people for their considerable efforts in support of this paper: to Dr. David Chiang, GE Aircraft Engines, for much discussion about the paper and for help with LINFLO; to Dr. Andrew Chuang, GE Aircraft Engines, and Dr. Graham Holmes, GE Corporate R&D Center, for their advice, discussions, and running of LEAP2D; to Prof. Michael Giles, Massachusetts Institute of Technology, for his advice, ideas, discussions and running of UNSFLO; to Dr. Daniel Hoyniak, NASA Lewis Research Center, and to Dr. Joseph Verdon, United Technologies Research Center, for their discussions and help with LINFLO. Also, much thanks goes to Dr. Hyoun-Woo Shin and Mr. David Halstead for their help in the acquisition of hot-wire data. The authors also wish to thank GE Aircraft Engines for permission to publish this paper.

References

Adachi, T., and Murakami, Y., 1979, "Three-Dimensional Velocity Distribution Between Stator Blades and Unsteady Force on a Blade Due to Passing Wakes," *Bull. JSME*, Vol. 22, No. 170, pp. 1074–1082.

Capece, V. R., Manwaring, S. R., and Fleeter, S., 1986, "Unsteady Blade Row Interactions in a Multi-stage Compressor," *AIAA Journal of Propulsion*, Vol. 2, No. 2, pp. 168–174.

Capece, V. R., and Fleeter, S., 1987, "Unsteady Aerodynamic Interactions in a Multistage Compressor," ASME JOURNAL OF TURBOMACHINERY, Vol. 109, pp. 420–428.

Caruthers, J. E., 1980, "Aerodynamic Analysis of Cascaded Airfoils in Unsteady Rotational Flow," presented at the Second Symposium on Aeroelasticity in Turbomachines, Lausanne, Switzerland.

Caruthers, J. E., and Dalton, W. N., 1993, "Unsteady Aerodynamic Response of a Cascade to Nonuniform Inflow," ASME JOURNAL OF TURBOMACHINERY, Vol. 115, pp. 76–84.

Doebelin, E. O., 1975, *Measurement Systems*, McGraw-Hill, New York, pp. 398–401.

Doorly, D. J., 1988, "Modeling the Unsteady Flow in a Turbine Rotor Passage," ASME JOURNAL OF TURBOMACHINERY, Vol. 110, pp. 27–37.

Dring, R. P., Joslyn, H. D., Hardin, L. W., and Wagner, J. H., 1982, "Turbine Rotor-Stator Interaction," ASME *Journal of Engineering for Power*, Vol. 104, No. 4, pp. 729–742.

Fleeter, S., Jay, R. L., and Bennett, W. A., 1978, "Rotor Wake Generated Unsteady Aerodynamic Response of a Compressor Stator," ASME *Journal of Engineering for Power*, Vol. 100, pp. 664–675.

Fleeter, S., Bennett, W. A., and Jay, R. L., 1980, "The Time-Variant Aerodynamic Response of a Stator Row Including the Effects of Airfoil Camber," ASME *Journal of Engineering for Power*, Vol. 102, pp. 334–343.

Gallus, H. E., Lambertz, J., and Wallman, Th., 1980, "Blade-Row Interaction in an Axial-Flow Subsonic Compressor Stage," ASME *Journal of Engineering for Power*, Vol. 102, pp. 169–177.

Giles, M. B., 1988, "Calculation of Unsteady Wake/Rotor Interaction," *AIAA Journal of Propulsion and Power*, Vol. 4, No. 4, pp. 356–362.

Giles, M. B., 1991a, "UNSFLO: A Numerical Method for the Calculation of Unsteady Flow in Turbomachinery," Massachusetts Institute of Technology GTL Report #205.

Giles, M. B., 1991b, private communication.

Goldstein, M. E., and Atassi, H., 1976, "A Complete Second-Order Theory for the Unsteady Flow About an Airfoil Due to a Periodic Gust," *J. Fluid Mech.*, Vol. 74, pt. 4, pp. 741–765.

Hall, K., and Crawley, E., 1987, "Calculation of Unsteady Flows in Turbomachinery Using the Linearized Euler Equations," *Proceedings of the 4th Symposium on Unsteady Aerodynamics and Aeroelasticity of Turbomachines and Propellors*, Aachen, West Germany.

Hardin, L. W., Carta, F. O., and Verdon, J. M., 1987, "Unsteady Aerodynamic Measurements on a Rotating Compressor Blade Row at Low Mach Number," ASME JOURNAL OF TURBOMACHINERY, Vol. 109, No. 4, pp. 499–507.

Henderson, G., and Fleeter, S., 1991, "Forcing Function Effects on Low Solidity Cascade Gust Response Unsteady Aerodynamics," *Proceedings of the 6th International Symposium on Unsteady Aerodynamics, Aeroacoustics and Aeroelasticity of Turbomachines and Propellers*, University of Notre Dame, IN.

Holmes, D. G., and Chuang, H. A., 1991, "Two Dimensional Linearized Harmonic Euler Flow Analysis for Flutter and Forced Response," *Proceedings of the 6th International Symposium on Unsteady Aerodynamics, Aeroacoustics and Aeroelasticity of Turbomachines and Propellers*, University of Notre Dame, IN.

Janus, J. M., and Whitfield, D. L., 1989, "A Simple Time-Accurate Turbomachinery Algorithm With Numerical Solutions of an Uneven Blade Count Configuration," AIAA Paper No. 89-0206.

Jorgenson, P. C. E., and Chima, R. V., 1988, "An Explicit Runge–Kutta Method for Unsteady Rotor/Stator Interaction," AIAA Paper No. 88-0049.

Kerrebrock, J. L., and Mikolajczak, A. A., 1970, "Intra-rotor Transport of Rotor Wakes and Its Effect on Compressor Performance," ASME *Journal of Engineering for Power*, Vol. 92, pp. 359–368.

Manwaring, S. R., and Fleeter, S., 1990, "Inlet Distortion Generated Periodic Aerodynamic Rotor Response," ASME JOURNAL OF TURBOMACHINERY, Vol. 112, pp. 298–307.

Manwaring, S. R., and Fleeter, S., 1991, "Forcing Function Effects on Rotor Periodic Aerodynamic Response," ASME JOURNAL OF TURBOMACHINERY, Vol. 112, pp. 312–319.

Manwaring, S. R., and Fleeter, S., 1993, "Rotor Blade Unsteady Aerodynamic Gust Response to Inlet Guide Vane Wakes," ASME JOURNAL OF TURBOMACHINERY, Vol. 115, pp. 197–206.

Nagashima, T., and Whitehead, D. S., 1977, "Linearized Supersonic Unsteady Flow in Cascades," Aeronautical Research Council, Reports and Memoranda 3811.

O'Brien, W. F., Cousins, W. T., and Sexton, M. R., 1980, "Unsteady Pressure Measurements and Data Analysis Techniques in Axial-Flow Compressors," *Measurements in Rotating Components of Turbomachinery*, ASME, pp. 195–201.

Oden, J. T., and Bass, J. M., 1989, "Adaptive Computation Methods for Fluid-Structure Interaction in Internal Flow," NASA SBIR Contracts NAS3-24849.

Rai, M., 1987, "Unsteady 3D Navier–Stokes Simulations of Turbine Rotor–Stator Interaction," AIAA Paper No. 87-2038.

Verdon, J. M., and Hall, K. C., 1990, "Development of a Linearized Unsteady Aerodynamic Analysis for Cascade Gust Response Predictions," NASA Contract, NAS3-25425.

Whitehead, D. S., 1970, "Vibration and Sound Generation in a Cascade of Flat Plates in Subsonic Flow," Aeronautical Research Council, Reports and Memoranda 3865.

Wisler, D. C., 1985, "Loss Reduction in Axial-Flow Compressor Through Low-Speed Model Testing," ASME *Journal of Engineering for Gas Turbines and Power*, Vol. 107, pp. 354–363.

APPENDIX I

The measured, periodic wakes from the rotor blades are decomposed into harmonic components via a Fourier analysis as shown in Fig. 19. The reconstructed waveform from harmonics one through ten is in excellent agreement with the measurements. The "gust" is taken as the amplitude, H_T in Fig. 19, and phase of the first harmonic of this Fourier decomposition. These values of the amplitude H_T are plotted in Figs. 6, 10–14 and 16–18.

APPENDIX II

Vortical and Potential Disturbances

The following incompressible analysis of vortical and potential disturbances is made to allow easy evaluation of their relative magnitudes. This approach, provided by Giles (1991b), is particularly important for determining the input conditions for UNSFLO.

Vortical disturbances, $\hat{u}_v$ and $\hat{v}_v$, can be expressed by

$$\overline{u}_v = \overline{V}_z D e^{-iL(\theta - \overline{W}_\theta / \overline{V}_z z)} \text{ and } \tilde{v}_y = \overline{W}_\theta D e^{-iL(\theta - \overline{W}_\theta / \overline{V}_z z)} \tag{5}$$

Note that they are sinusoidal in nature and do not decay in the axial direction.

Potential disturbances are expressed by the classical velocity potential, ϕ, as

$$\phi = A e^{(-iL\theta - Lz)} \tag{6}$$

They are sinusoidal in nature but decay exponentially in the axial direction.

By taking appropriate derivatives of the velocity potential in Eq. (6), one obtains the velocities due to potential disturbances,

$$\tilde{u}_p = -LAe^{(-iL\theta - Lz)} \text{ and } \tilde{v}_p = -iLAe^{(-iL\theta - Lz)} \tag{7}$$

The harmonic pressure fluctuations are then computed from the Bernoulli equation

$$\tilde{p} = -\rho(\overline{V}_z \tilde{u}_p + \overline{W}_\theta \tilde{v}_p) = -\rho(\overline{V}_z L + i\overline{W}_\theta L) A e^{(-iL\theta - Lz)} \tag{8}$$

By combining the velocity fluctuations due to the vortical and potential disturbances at the hot-wire location defined to be $z = 0$, the following equations are obtained:

$$\tilde{u}_c = \tilde{u}_v + \tilde{u}_p = (\overline{V}_z D - LA) e^{-iL\theta} = \hat{u} e^{-iL\theta} \tag{9a}$$

$$\tilde{v}_c = \tilde{v}_v + \tilde{v}_p = (\overline{W}_\theta D - iLA) e^{-iL\theta} = \hat{v} e^{-iL\theta} \tag{9b}$$

where

$$\hat{u} \equiv (\overline{V}_z D - LA) \text{ and } \hat{v} \equiv (\overline{W}_\theta D - iLA) \tag{10}$$

The values of D and A are then computed by simultaneous solution of Eq. (10) as

$$D = \frac{i\hat{u} - \hat{v}}{i\overline{V}_z - \overline{W}_\theta} \text{ and } A = \frac{\overline{V}_z \hat{v} - \overline{W}_\theta \hat{u}}{L(i\overline{V}_z - \overline{W}_\theta)} \tag{11}$$

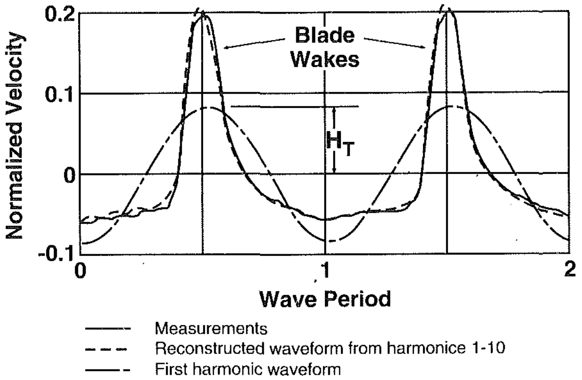

Fig. 19 Comparison of Fourier decomposed wake profiles with measurements

which can also be expressed in terms of magnitude and phase as

$$|D| = \frac{(\hat{u}^2 + \hat{v}^2)^{1/2}}{\overline{W}} \text{ and } \theta_D = \tan^{-1} \frac{\overline{V}_z \hat{v} - \overline{W}_\theta \hat{u}}{\overline{V}_z \hat{u} + \overline{W}_\theta \hat{v}} \qquad (12a)$$

$$|A| = \frac{\overline{V}_z \hat{v} - \overline{W}_\theta \hat{u}}{L\overline{W}} \text{ and } \theta_A = \tan^{-1} \frac{\overline{W}_\theta \overline{V}_z \hat{u} - \overline{V}_z^2 \hat{v}}{\overline{W}_\theta^2 \hat{u} - \overline{V}_z \overline{W}_\theta \hat{v}} \qquad (12b)$$

Values of $\hat{u}$ and $\hat{v}$ are computed from our measured streamwise and transverse gusts, $\hat{u}_i^+$ and $\hat{v}_i^+$, by using the coordinate transformation

$$\begin{pmatrix} \hat{u} \\ \hat{v} \end{pmatrix} = \begin{pmatrix} \cos a & -\sin a \\ \sin a & \cos a \end{pmatrix} \begin{pmatrix} \hat{u}_i^+ \\ \hat{v}_i^+ \end{pmatrix} \qquad (13)$$

Additional Nomenclature

$\tilde{p}$ = harmonic unsteady static pressure
$\tilde{u}$, $\tilde{v}$ = axial and tangential harmonic unsteady velocity

Subscripts

c = combined
p = potential
v = vortical

Forcing Function Effects on Unsteady Aerodynamic Gust Response: Part 1—Forcing Functions

G. H. Henderson[1]

S. Fleeter

School of Mechanical Engineering,
Purdue University,
West Lafayette, IN 47907

The fundamental gust modeling assumption is investigated by means of a series of experiments performed in the Purdue Annular Cascade Research Facility. The unsteady periodic flow field is generated by rotating rows of perforated plates and airfoil cascades. In this paper, the measured unsteady flow fields are compared to linear-theory vortical gust requirements, with the resulting unsteady gust response of a downstream stator cascade correlated with linear theory predictions in an accompanying paper. The perforated-plate forcing functions closely resemble linear-theory forcing functions, with the static pressure fluctuations small and the periodic velocity vectors parallel to the downstream mean-relative flow angle over the entire periodic cycle. In contrast, the airfoil forcing functions exhibit characteristics far from linear-theory vortical gusts, with the alignment of the velocity vectors and the static pressure fluctuation amplitudes dependent on the rotor-loading condition, rotor solidity, and the inlet mean-relative flow angle. Thus, these unique data clearly show that airfoil wakes, both compressor and turbine, are not able to be modeled with the boundary conditions of current state-of-the-art linear unsteady aerodynamic theory.

Introduction

In a multistage turbomachine, downstream blade rows are periodically in upstream blade row wakes. As a result, the inlet flow field to the downstream blade row varies periodically with time. The upstream rotating reference frame spatial flow nonuniformities are a temporal aerodynamic forcing function, a gust, causing a fluctuating pressure response on the stationary downstream blades. Such blade-row-wake interactions are the most common and least understood source of unsteady aerodynamic excitation causing high-cycle blade fatigue. The a priori prediction of flow-induced vibration stresses cannot be made with current technology due to the inadequacy of unsteady aerodynamic models. Thus costly redesigns are necessary when engine development testing reveals unacceptable blade stress levels.

State-of-the-art unsteady aerodynamic models are essentially limited to two-dimensional linearized perfect-fluid theory analyses. In the absolute reference frame, the steady flow past flat-plate airfoils is uniform, with a small perturbation unsteady flow resulting from the upstream rotor blade wake flow field resolved into streamwise and transverse components. Advanced analyses that allow the potential field of the downstream airfoils to distort the wake by linearizing about the nonuniform mean flow near the blade row instead of the much simpler upstream uniform mean flow are currently being developed by, for example, Goldstein and Atassi (1976), Scott and Atassi (1990), Hall and Verdon (1989), Fang (1991). In all of these models, the forcing function is defined in terms of its harmonics, with each harmonic forcing function modeled as a vortical gust forcing function boundary condition in the prediction of the resulting blade row unsteady aerodynamics. Thus, even though forcing functions can be generated by a wide variety of fundamentally different phenomena, all forcing functions are modeled as being equivalent, with the resulting predicted blade row response independent of the particular wake generator. The assumption that all gusts are equivalent is referred to herein as the fundamental gust modeling assumption.

A number of experiments have been directed at the verification of such mathematical models and the determination of their applicability and limitations (Frank and Henderson, 1980; Fleeter et al., 1978, 1980, 1981; Gallus et al., 1980; Capece et al., 1986; Capece and Fleeter, 1987, 1989). Of particular interest are the experiments that investigated the unsteady aerodynamic response of a research compressor rotor performed by Manwaring and Fleeter (1991). The first harmonic gust response of the first-stage rotor generated by two 2-per-revolution unsteady forcing functions were measured: an inlet flow distortion and the wakes behind flat plate airfoils. The two first harmonic unsteady aerodynamic forcing functions had similar

---

[1] Advanced Product Development, Cummins Engine Company, Columbus, IN.

Contributed by the International Gas Turbine Institute and presented at the 37th International Gas Turbine and Aeroengine Congress and Exposition, Cologne, Germany, June 1–4, 1992. Manuscript received by the International Gas Turbine Institute February 17, 1992. Paper No. 92-GT-174. Associate Technical Editor: L. S. Langston.

gust characteristics including the ratio of the streamwise-to-normal gust components u^+/v^+ and reduced frequency values. The first harmonic gust response of the first-stage rotor generated by these two different forcing functions were shown to be dependent on the particular forcing function. However, because the two first harmonic forcing functions are equivalent in terms of the classical unsteady aerodynamic theory boundary conditions, these results cannot be predicted.

In the above experiments, the unsteady response comparisons with linear theory were made without considering the fundamental gust modeling assumptions. In fact, no investigations have been conducted to examine forcing function characteristics for consistency with the linear-theory profile. This clearly needs to be addressed in order to assess the validity of current unsteady aerodynamics models and to direct the development of more advanced models.

This research is directed at this needed fundamental investigation of the forcing function characteristics and their effect on the resulting blade row gust unsteady aerodynamic response. In this paper, the fundamental vortical gust modeling assumption is experimentally investigated, with the resulting blade row gust unsteady aerodynamic response considered in an accompanying paper (Henderson and Fleeter, 1993). These experiments are performed in the Purdue Annular Cascade Research Facility, which features a single rotor-stator stage and experimentally reproduces the fundamental unsteady flow phenomena inherent in axial flow turbomachines. The unsteady periodic forcing functions are generated with rotating rows of perforated plates and airfoil cascades, Fig. 1. These geometries were selected because the wakes from these objects originate by fundamentally different phenomena. Thus, the fundamental gust modeling assumption is directly investigated by comparing the measured gust characteristics to those modeled by linear vortical gust theory.

Linear Theory Vortical Gust Characteristics

In classical linear perfect-fluid theory, the wake flow field is composed of a uniform mean flow and a superimposed sinusoidal vortical gust **w** propagating according to the wave-number vector **k**. The resulting blade-row flow field schematic is presented in Fig. 2. For convenience, the rotor wake periodic shape is Fourier decomposed with the fundamental harmonic shown. Thus, the nonuniform rotor-wake flow field is made up of the harmonic wake velocity distribution superimposed on the uniform downstream mean-relative flow field. The downstream relative velocity decreases from the mean in the rotor wake regions and increases from the mean in the free stream by the amplitude of the vortical gust w^+. It is this harmonic velocity that is the unsteady aerodynamic forcing function to the downstream stationary airfoils.

In the stationary reference frame of the downstream airfoil row, the propagation of the harmonic wake velocity field is defined by considering periodicity requirements in the axial-circumferential coordinate system. As a consequence of this periodicity, the downstream mean-relative flow W_2 and the gust propagation vector **k** are perpendicular.

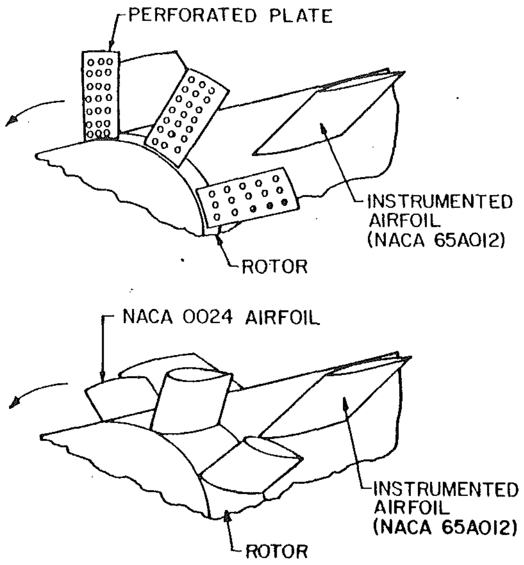

Fig. 1 Test section with wake generators

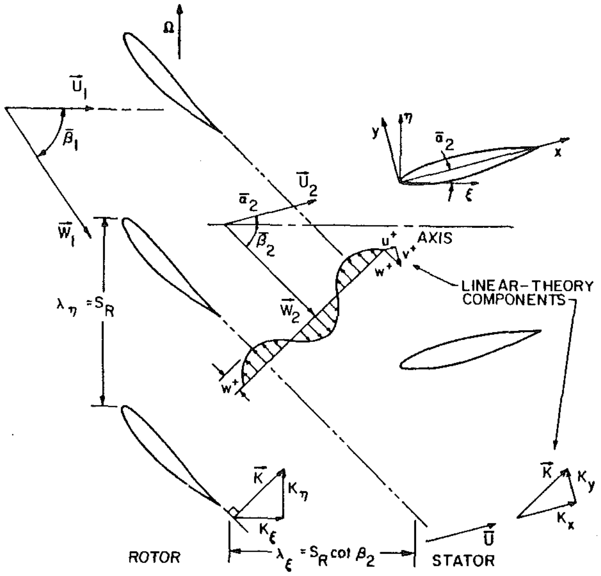

Fig. 2 Turbomachine gust propagation

Nomenclature

$\mathbf{k}$ = gust propagation wave-number vector
p = perturbation pressure
P_S = unsteady static pressure
P_V = unsteady velocity pressure
r = frequency ratio
S_R = rotor blade-to-blade spacing
u = streamwise gust component
u^+ = streamwise gust amplitude
$\mathbf{u}$ = velocity perturbation vector
$\mathbf{U}$ = absolute velocity

$\bar{U}$ = mean absolute velocity
v = transverse gust component
v^+ = transverse gust amplitude
$\mathbf{w}$ = gust velocity perturbation
w^+ = gust amplitude
$\mathbf{w}^+$ = gust amplitude vector
W = relative velocity
$\bar{W}$ = mean-relative velocity
α = angle of attack
$\bar{\alpha}$ = mean absolute flow direction
$\bar{\beta}$ = mean-relative flow angle

β_w = gust velocity vector direction
ϕ_w = gust component phase angle
ϕ_s = unsteady static pressure phase angle
ϕ_v = unsteady velocity pressure phase angle
Ω = rotor velocity
Ω_f = free-rotation rotor velocity

Subscripts

1 = rotor inlet
2 = rotor exit

The stator row flow field is modeled as being compressible and isentropic. For a uniform steady flow, the linearized continuity and momentum equations describing the perturbation velocity and pressure are

$$\frac{1}{\rho_o c_o^2}\frac{D_o p}{Dt}+\nabla\cdot\mathbf{u}=0 \qquad (1)$$

$$\frac{D_o\mathbf{u}}{Dt}=\frac{1}{\rho_o}\nabla p \qquad (2)$$

where $\frac{D_o}{Dt}=\frac{\partial}{\partial t}+\overline{U}\frac{\partial}{\partial x}$.

This inviscid flow is analyzed by superpositioning of rotational and irrotational flow fields. Thus the unsteady velocity perturbation $\mathbf{u}$ is considered to consist of a rotational velocity component $\mathbf{w}$ and an irrotational component, represented by a potential gradient $\nabla\phi$. The rotational and irrotational components satisfy continuity independently (Goldstein, 1978).

The unsteady aerodynamic loading on an airfoil is determined by solving the velocity potential equation using standard techniques subject to the Kutta condition and the solid boundary condition at the airfoil surface. The airfoil surface boundary condition introduces the effect of the forcing function rotational flow or gust into the unsteady pressure field. This requires the specification of the rotational flow field generated by the gust $\mathbf{w}$. The propagation of the gust is written as

$$\mathbf{w}=\mathbf{w}^+e^{i(\mathbf{k}\cdot\mathbf{x}-k_xt)}=0 \qquad (3)$$

where the gust component amplitude vector is $\mathbf{w}^+=u^+\mathbf{i}+v^+\mathbf{j}$, the gust propagation vector is $\mathbf{k}=k_x\mathbf{i}+k_y\mathbf{j}$ and $x=x\mathbf{i}+y\mathbf{j}$.

The gust velocity perturbation and the gust propagation vector must be perpendicular for all time and space $\mathbf{W}\cdot\mathbf{k}=0$ for the rotational wake flow field to satisfy continuity. Thus, two constraints are imposed by continuity on the downstream rotational forcing function wake flow field. The primary constraint is the requirement that the gust-component phase angle ϕ_w, i.e., the phase angle between the streamwise and transverse gust component harmonics, be either 0 deg or 180 deg. If this primary constraint is satisfied then the secondary constraint stipulates that the gust-component amplitude vector must be parallel to the downstream mean-relative flow $\mathbf{w}^+ \parallel \mathbf{W}_2$. When the primary constraint is satisfied, the gust amplitude simplifies to $w^+=\sqrt{u^{+2}+v^{+2}}$, with the periodic velocity vectors parallel over the entire periodic cycle.

Gust profiles are completely defined by specifying $\mathbf{k}$, w^+, β_w and ϕ_w, where β_w is the gust-amplitude angle. If the primary gust constraint is violated, the gust-amplitude angle β_w is distinct from the velocity vector angle β_w', the angle of any velocity vector, and w^+ is not equal to $\sqrt{u^{+2}+v^{+2}}$. Note that the velocity vector angle β_w' is the angle of any velocity vector and varies with time and space whereas the gust-amplitude angle β_w is the angle of the maximum gust magnitude or gust amplitude w^+ and is a constant. For a gust that violates the primary constraint, the gust amplitude and gust-amplitude angle are found by maximizing the velocity vector magnitude, leading to

$$w^+=\{u^{+2}\cos^2[P_{\max}+\phi_w]+v^{+2}\cos^2[P_{\max}]\}^{1/2} \qquad (4)$$

$$\beta_w=\tan^{-1}\left[\frac{u^+\cos[P_{\max}+\phi_w]}{v^+\cos[P_{\max}]}\right]-\overline{\alpha}_2 \qquad (5)$$

where $P_{\max}$ indicates the point in time and space where the gust magnitude is maximized. Note that if the primary constraint is satisfied, $\phi_w=0$ deg or 180 deg, then the gust amplitude and gust amplitude angle reduce to $w^+=\sqrt{u^{+2}+v^{+2}}$ and $\beta_w=\beta_w'$ since $P_{\max}=0$.

The parameters ϕ_w and β_w are important indicators of how closely an actual periodic wake flow field is modeled by a linear-theory vortical gust profile, with ϕ_w the indicator of the primary constraint and β_w the indicator of the secondary constraint. Thus β_w and ϕ_w are defined as the linear-gust parameters and are used to characterize the wake flow fields created by the wake generators. For a linear-theory vortical gust, the primary constraint is that $\phi_w=0$ deg or 180 deg, with the secondary constraint requiring that $\beta_w=\overline{\beta}_2$.

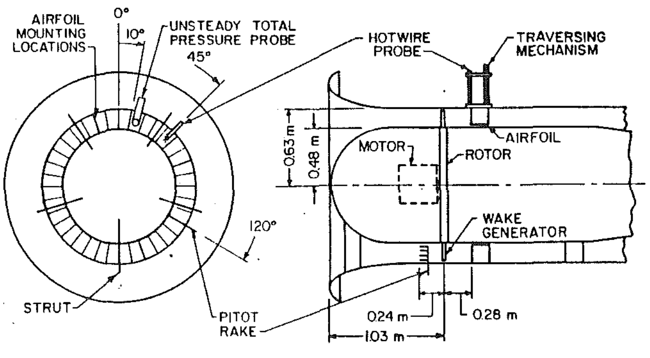

Fig. 3 Annular test section schematic

Research Facility

The Purdue Annular Cascade Research Facility is an open-loop draw-through type wind tunnel capable of test section velocities of 70 m/s (220 ft/sec). The inlet flow, conditioned first by a honeycomb section and then a settling chamber, accelerates into the annular test section via a bellmouth inlet. The test section exit flow is diffused into a large plenum. The 224 kW (300 hp) centrifugal fan located downstream of the plenum draws the air through the facility, with the guide vanes at the fan inlet allowing flow rate adjustment through the facility. The annular test section, Fig. 3, houses a rotor independently driven by a 7.5 kW (10 hp) A-C motor controlled by a variable frequency drive to create the desired unsteady flow field together with a downstream stator row. The separate drive motors on the rotor and system fan uncouple the rotor speed from the throughflow velocity. Thus, independent control over unsteady aerodynamic parameters, for example the reduced frequency, is possible since the system flow rate is independent of the rotor speed and rotor configuration.

Basic measurements include the test-section velocity profile upstream of the rotor and the test-section air stagnation temperature and static pressure. A pitot tube rake provides the test-section inlet velocity profile. The test-section air stagnation temperature is measured using a thermocouple. The pitot rake is an assembly of 10 total pressure tubes equally spaced across the annular test section and aligned with the annulus axis. Two test-section static taps, located on the outer annulus wall, are utilized, one near the pitot rake and the other 3.18 cm (1.25 in.) upstream of the airfoil leading edge. The inlet velocities are calculated from isentropic compressible flow theory using the pitot rake air stagnation pressure, the test-section air static pressure measurement, and the test-section air stagnation temperature measurements as the input parameters.

Forcing Functions

The unsteady periodic forcing functions are generated with rotating rows of perforated plates and airfoil cascades, Fig. 1. The perforated plates were fabricated from 56 percent porosity aluminum sheet mounted on the rotor such that the plate width was normal to the rotor axis. The airfoils have a 7 deg twist from the hub to the tip to achieve a constant spanwise angle-of-attack and are mounted on the rotor at 35 percent chord and set to stagger angles measurable to within ±0.5 deg.

Instrumentation. Unsteady data define the forcing function or gust generated by the rotating rows of perforated plates and airfoil cascades. These data are determined by the midspan unsteady velocity and static pressure fluctuations downstream of these rotors. The rotor-exit flow-field unsteady total pressure is measured with a hemispherical-nosed total pressure pitot tube fitted with an unsteady pressure transducer. The amplitude of the incident flow angle is a function of the wake generator, with the angle of the pitot tube set to minimize the flow angle variations. The criterion presented by Becker and Brown (1974) shows that the errors produced by the incidence flow angle fluctuations should be no more than 6 percent when the perforated plates are installed and less than 1 percent when the airfoils are installed. A cross hot-wire anemometer located on the downstream stator vane row leading edge line is used to measure the stator cascade inlet flow field. The absolute velocity magnitude and flow angle errors are estimated at 4 percent and 0.5 deg, respectively. The wake velocity deficits are decomposed into streamwise and transverse velocity components.

Stator Inlet Flow Field. A spanwise survey of the stator cascade inlet flow field generated independently by eight perforated plates and eight airfoils was performed to insure proper two dimensionality. This survey showed excellent two dimensionality of the time-averaged flow field for both wake generators. From 20 to 80 percent span, the absolute velocity magnitude and flow angle were within 2 percent and 1 deg, respectively, of the midspan value. The perforated plate-generated fundamental harmonics were also highly two dimensional near the midspan, with the gust amplitude within 5 percent of the midspan value from 33 to 67 percent span. The twisted rotor blades also produced a two-dimensional fundamental harmonic, with the gust amplitude within 5 percent of the midspan value from 33 to 67 percent span.

Data Acquisition and Analysis. The time variant signals are digitized over one rotor revolution using approximately 2000 samples. The number of ensemble averages necessary to obtain clean periodic time traces was investigated. Ensemble averaging the hot-wire and pressure transducer signals 150 and 100 times, respectively, produces very clean periodic time traces with the random fluctuations averaged away. The Fourier components of the ensemble-averaged time traces are numerically determined with Fast Fourier Transform software. The sample frequency is set and the number of samples is adjusted to produce time records of exactly one rotor rotation period to eliminate frequency leakage problems in Fourier Transform analysis. The sample frequency and number of digitizations are set based upon an accurate rotor rotational speed. The rotor rotational speed is measured by digitizing the shaft trigger signal at the maximum sample frequency and counting the number of samples between shaft triggers.

Results

To investigate the fundamental forcing function gust modeling assumptions, a series of experiments directed at understanding the relevant aerodynamic forcing function characteristics were conducted. The periodic flow fields downstream of rotating rows of perforated plates and airfoil cascades were measured and analyzed for consistency with constraints of linear theory. These experiments were conducted with a constant axial velocity corresponding to a Mach number of approximately 0.15. The velocity and pressure fields were measured 0.28 m (1.8 stator airfoil chords) downstream of the rotor center plane. With the wake-generating rotor airfoils installed, the measurement location was separated from the rotor-airfoil trailing edge by an axial distance of 1.6 rotor-airfoil chords.

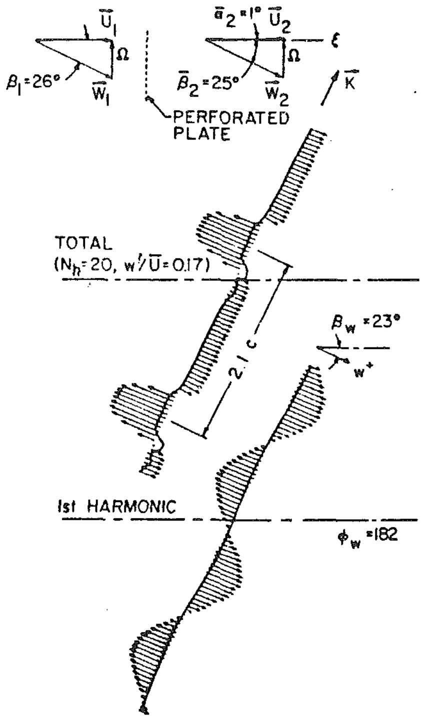

Fig. 4 *Low rotor speed effect on perforated plate forcing functions*

Forcing Function Data. A low rotor speed perforated-plate generated aerodynamic forcing function is presented in Fig. 4. The stator row was empty for these measurements. The periodic velocity vector profile and static pressure distribution define the forcing function. A complete forcing function composed of N_h harmonics is shown together with the forcing function fundamental harmonic. The mean velocity triangles represent the inlet and downstream steady flow fields, denoted by subscripts 1 and 2. The mean velocity triangles include the absolute **U** relative **W** and rotor Ω velocity vectors normalized by the mean axial velocity and the absolute and relative flow angles, $\bar{\alpha}$ and $\bar{\beta}$. The inlet flow enters the test section in a purely axial direction. Thus the (rotor speed)-to-(axial velocity) ratio determines the inlet mean-relative flow angle $\tan \bar{\beta}_1 = \Omega/\bar{U}_1$. The inlet mean-relative flow angle increases and decreases with rotor speed and is characteristic of the operating point of the facility.

Forcing Function Scaling. The unsteady velocity vector and static pressure measurements are scaled so that an unsteady velocity vector of unit length represents a velocity pressure fluctuation equal to a unit pressure fluctuation. The velocity and static pressure scale factors, $w_{\rm rms}$ and $p_{\rm rms}$ for small perturbations, are linearly related by

$$p_{\rm rms}=\rho\bar{U}_2 w_{\rm rms} \tag{6}$$

where $w_{\rm rms}$ is the root-mean-square of the velocity fluctuations and $p_{\rm rms}$ is calculated from Eq. (6). Since $w_{\rm rms}$ and $p_{\rm rms}$ are linearly related by the constant $\rho\bar{U}_2$, scaling in this manner allows the direct determination of the relative proportions of the velocity and static pressure fluctuations.

Perforated Plate Forcing Functions. The low rotor speed perforated-plate forcing function presented in Fig. 4 closely resembles a linear-theory vortical gust. In particular, the periodic gust velocity vectors are parallel to $\mathbf{W}_2$ and the static pressure distribution is very small, with the fundamental-harmonic linear gust parameters ϕ_w and β_w very near the linear theory values, with ϕ_w = 182 deg and $\beta_w \approx \bar{\beta}_2$.

The effect of rotor speed on the perforated-plate forcing

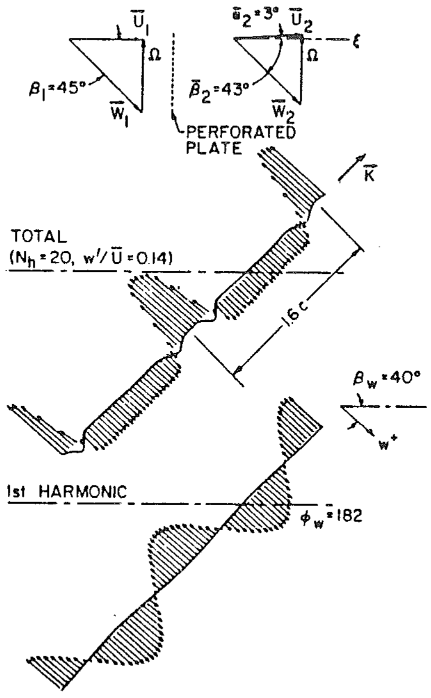

Fig. 5 High rotor speed effect on perforated plate forcing functions

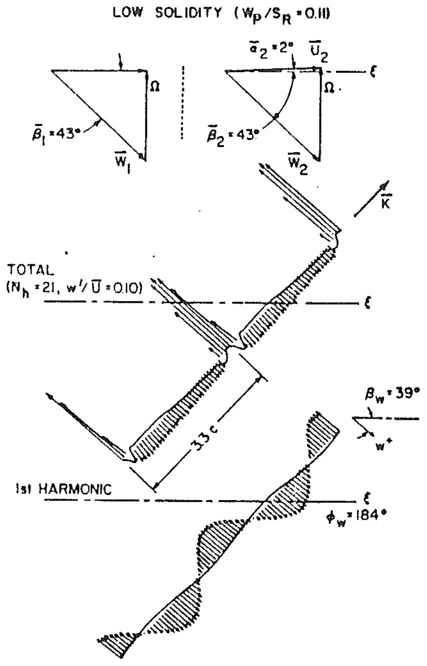

Fig. 6 Low solidity effect on perforated plate forcing functions

function is seen by comparing Figs. 4 and 5. The higher-rotor speed is twice that of the lower. The steady velocity triangles show an increase with rotor speed in the inlet and downstream mean-relative flow angles, $\bar{\beta}_1$ and $\bar{\beta}_2$, respectively. Note the corresponding adjustment in the gust propagation direction to a more axial direction, which is required for $\mathbf{k} \perp \mathbf{W}_2$. Both the total and fundamental-harmonic forcing functions portray linear-theory characteristics as the periodic velocity vectors are parallel to $\mathbf{W}_2$ and periodic static pressure fluctuations are small.

The effect of reduced frequency, i.e., rotor solidity, on the perforated-plate forcing functions is shown in Figs. 6 and 7. The rotor solidity was varied by changing the number of plates, i.e., the rotor circumferential spacing. For the lower-solidity rotor, five plates were utilized, resulting in a circumferential plate spacing of approximately ten times the plate width. For the higher-solidity rotor, 20 plates were used, resulting in a gap between the plates approximately equal to the plate width. With equal mean axial velocities and rotor speeds, equal mean velocity triangles for the two cases are obtained. Very different forcing function total profiles due to the very different wake width-to-circumferential spacing ratios. However, when these profiles are Fourier decomposed, the fundamental harmonics are very similar. Both forcing functions exhibit the characteristics of a linear vortical gust, with the periodic velocity vectors parallel to the downstream mean-relative flow and the static pressure variations small.

Perforated-plate fundamental-harmonic vortical linear-gust parameter data β_w and ϕ_w, as a function of rotor solidity and inlet mean-relative flow angle $\beta_w - \bar{\beta}_2$, are presented in Fig. 8. In the upper plots, the difference between the gust-amplitude angle and downstream mean-relative flow angle, $\beta_w - \bar{\beta}_2$, is presented. For a linear vortical gust $(\beta_w - \bar{\beta}_2)$ is zero. The linear-gust parameters closely match the linear-theory values indicating fundamental-harmonic profiles closely resembling a linear-theory vortical profile. The perforated plates generate linear-theory vortical gust profiles independent of the inlet mean-relative flow angle (i.e., rotor speed), rotor solidity, and plate width.

Airfoil-Cascade Forcing Functions. Low-solidity airfoil-cascade forcing functions illustrating the effects of steady rotor loading are presented in Figs. 9, 10, and 11. The rotor cascade was comprised of five airfoils, resulting in a low rotor solidity value of 0.16. The rotor-airfoil steady loading was varied by changing the angle-of-attack. Three rotor-airfoil angles-of-attack were investigated, produced by changing the stagger angle while maintaining the same inlet mean-relative flow angle $\bar{\beta}_1$.

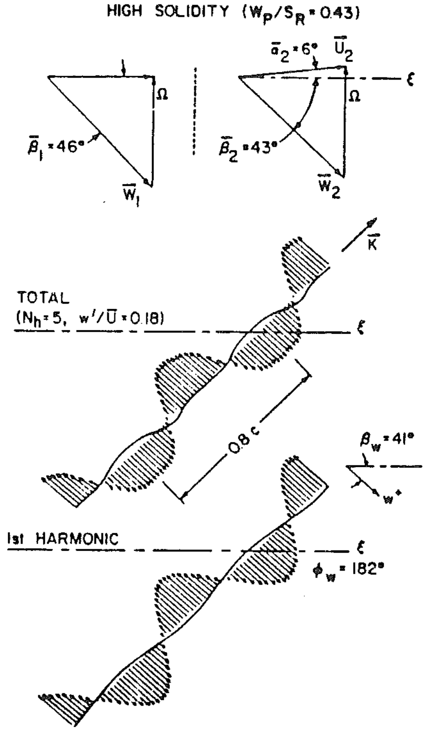

Fig. 7 High solidity effect on perforated plate forcing functions

For the neutral-loading condition, power to the rotor motor was switched off allowing the rotor to rotate freely in the flow provided independently by the large downstream centrifugal

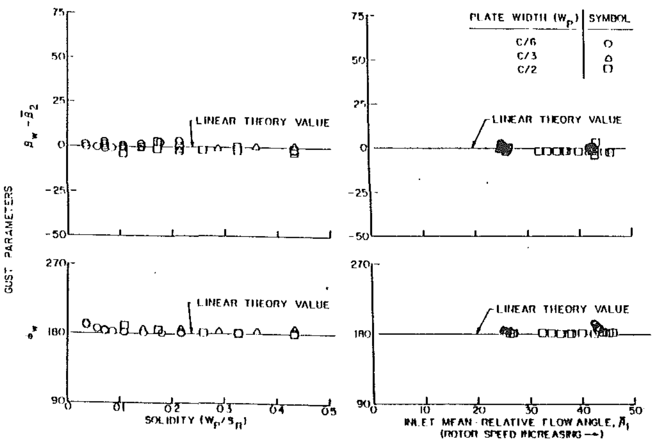

Fig. 8 Solidity and rotor speed effect on fundamental harmonic perforated plate linear gust parameters

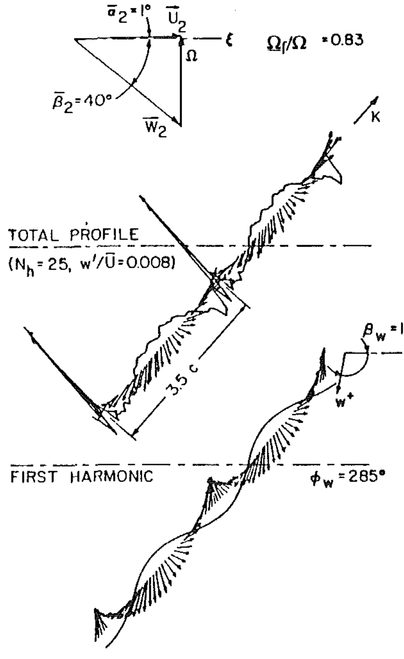

Fig. 9 Compressor loading effect on airfoil forcing function; low solidity rotor and high rotational speed

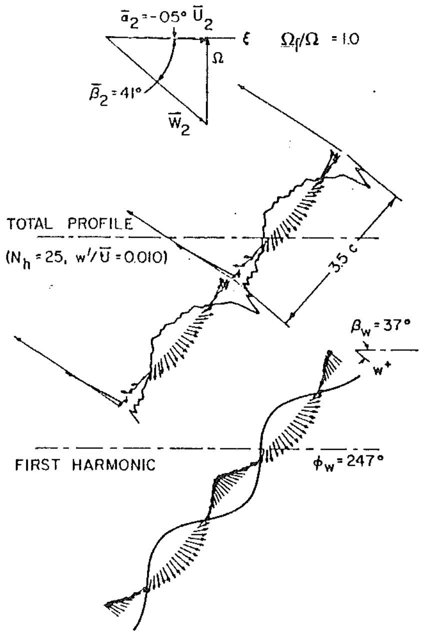

Fig. 10 Neutral loading effect on airfoil forcing function; low solidity rotor and high rotational speed

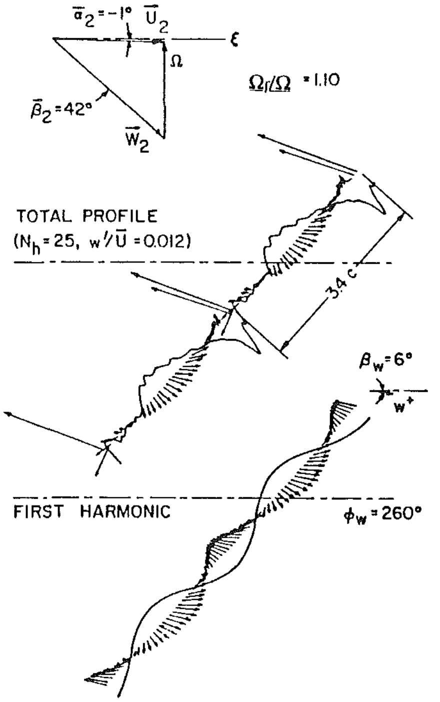

Fig. 11 Turbine loading effect on airfoil forcing function; low solidity rotor and high rotational speed

fan. The friction opposing the rotor rotation is very small, with the rotor mounted directly to the motor shaft that turns in ball-bearings. Thus, the only friction producing components in the drive system are the motor ball-bearings. A frictionless rotor fitted with flat plate airfoils rotates at the speed required to align the chord line with the inlet measure-relative flow, i.e., the no load condition. Thus the stagger angle determines the free-rotation speed in an constant speed flow.

To achieve compressor-loading conditions, the stagger angle was set lower than the neutral-case stagger angle. Power to the drive system was applied to increase the rotor speed to the neutral-load rotor speed. Thus shaft energy input was required for this rotor loading condition—hence the description "compressor" loading. To achieve turbine-loading conditions, the stagger angle was set higher than the neutral-case stagger angle. The rotor motor and speed controller were set to slow the rotor rotation to match the neutral-load rotor speed. Thus the rotor drive system dissipated energy from the flow, hence the description "turbine" loading. Also presented is the rotor speed ratio Ω_f/Ω. This parameter is the ratio of the free-rotation rotor speed, i.e., rotor motor off, to the rotor speed under loaded conditions and is used to characterize the degree of rotor loading. This ratio is less than unity for compressor loading since the free-rotation speed is less than the loaded speed, whereas for the turbine-loading condition the rotor speed ratio is greater than unity.

The forcing functions presented in Figs. 9–11 show gust characteristics far from linear-theory vortical gusts. Not only are the wake region velocity vectors misaligned with the downstream mean-relative flow $\bar{\beta}_2$, the free-stream velocity vectors are nonparallel and misaligned with the downstream mean-relative flow. In contrast, the perforated-plate free-stream velocity vectors were parallel to $\bar{\beta}_2$. Also, the airfoil forcing

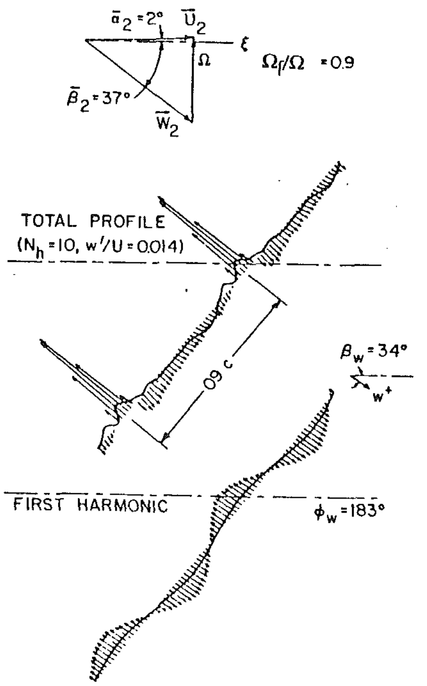

Fig. 12 Compressor loading effect on airfoil function; high solidity rotor and high rotational speed

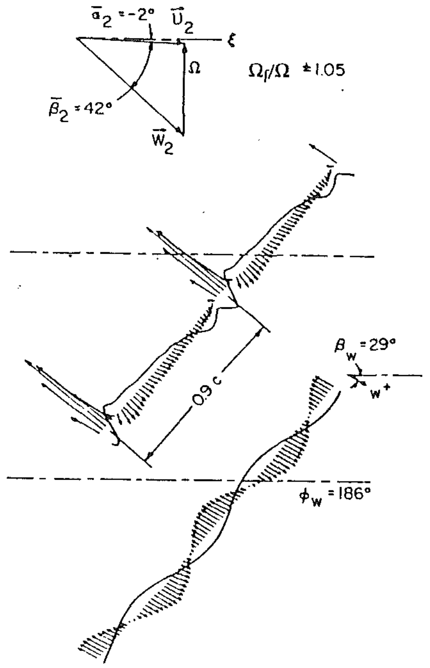

Fig. 13 Neutral loading effect on airfoil forcing function; high solidity rotor and high rotational speed

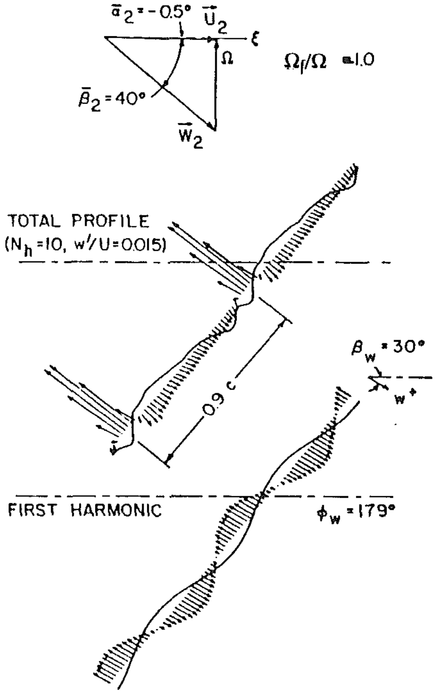

Fig. 14 Turbine loading effect on airfoil forcing function; high solidity rotor and high rotational speed

functions exhibit sizable static pressure fluctuations that are not considered in linear theory and are not present in the perforated-plate forcing functions.

The wake-region velocity vectors respond to the rotor loading condition by slanting in the direction of the lift force. The lift force is directed normal to the inlet mean-relative flow and under compressor-loading conditions pushes on the fluid in the general direction of the gust propagation direction. Under turbine-loading conditions the airfoil pushes on the fluid in the opposite direction since the lift force has reversed direction 180 deg due to the change in sign of the rotor-airfoil angle-of-attack. A large change in the direction of the wake-region velocity vectors with rotor loading occurs, seen by comparing the compressor and turbine forcing functions. The effect of the changing lift force direction is reflected by the large variation in the fundamental-harmonic gust-amplitude angle β_w. The value of β_w changes from a value much greater than the linear-theory value, $\bar{\beta}_2 \approx 41$ deg, under compressor-loading conditions, $\beta_w = 101$ deg, to a value much less than the linear-theory value under turbine-loading conditions, $\beta_w = 6$ deg.

Airfoil forcing functions for a high-solidity rotor, $C_R/S_R = 0.49$, are presented in Figs. 12, 13, and 14. Similar mean-velocity flow fields existed for these experiments and the low-solidity rotor experiments of Figs. 9–11. The velocity vectors for the high-solidity rotor forcing functions are near parallel to one another but not necessarily parallel to $\mathbf{W}_2$. The static pressure fluctuations are sizable for the neutral and turbine cases, but much smaller for the compressor case. The response of the wake-region velocity-vector angles due to the lift force is very weak. The fundamental-harmonic gust-amplitude angles β_w decrease somewhat as the rotor loading varies from compressor to turbine conditions but the β_w values are only 3 deg and 13 deg from the linear-theory $\bar{\beta}_2$ values in the compressor and turbine cases, respectively. The fundamental-harmonic gust-component phase angles are all near 180 deg, thereby satisfying the primary linear-gust constraint.

Figures 9–11 and 12–14 enable a comparison of low and high-solidity airfoil forcing functions to be made. The high-solidity velocity vectors are more parallel and aligned with $\bar{\beta}_2$. Additionally, the wake-region velocity vectors are much less responsive to the rotor lift force variations with the static pressure fluctuations also smaller. The fundamental-harmonic β_w value decreases as the rotor loading varies from compressor to turbine conditions for both the high-solidity and low-solidity cases but the variation of β_w is much greater for the low-solidity rotor. The fundamental-harmonic gust-component phase angles are near the linear-theory value for all the high-solidity airfoil forcing functions, which is in sharp contrast to the low-solidity forcing functions where ϕ_w deviated greatly from the linear-theory vortical value. The argument cannot be made that these differences are the result of different loadings on

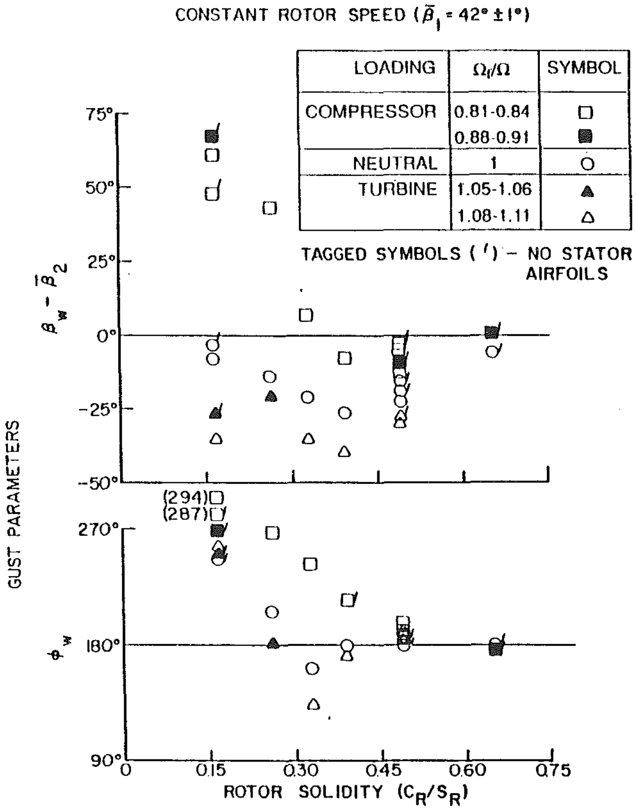

Fig. 15 Rotor loading and solidity effect on airfoil fundamental-harmonic linear-gust parameters; constant rotor speed

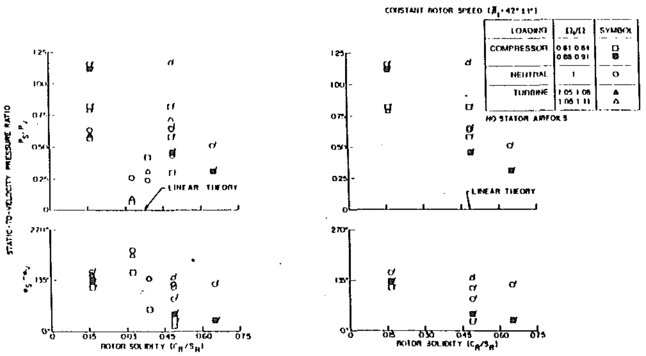

Fig. 16 Rotor loading and solidity effect on airfoil fundamental-harmonic static-to-velocity pressure ratio; constant rotor speed and empty stator row

individual rotor blades since the neutral-case blade loading is the same. Thus these variations are due to the change in rotor solidity.

Figure 15 shows the effect of rotor solidity on the fundamental-harmonic vortical linear-gust parameters of airfoil-cascade forcing functions. The rotor speed, i.e., inlet mean-relative flow angle, was constant. The difference between the gust-amplitude angle and the downstream mean-relative flow angle $(\beta_w - \bar\beta_2)$ is plotted, with zero being the linear-theory value. The linear-gust parameters respond to rotor loading and rotor solidity with definite trends. On a vertical constant-rotor-solidity line, $(\beta_w - \bar\beta^2)$ is greatest with compressor loading and decreases with neutral and turbine loading conditions. For similar loading conditions, $(\beta_w - \bar\beta_2)$ decreases with rotor solidity for the lower-solidity values then increases at the higher-solidity values such that the data are near the linear-theory value or showing the tendency of approaching the linear-theory value at the high-rotor-solidity values. The trends of the gust-component phase angles also show that increasing the rotor solidity tends to produce linear-theory results. Under neutral and turbine-loading conditions, ϕ_w decreases with rotor solidity to values below 180 deg, then increases to the linear-theory value at the intermediate-solidity values. Under neutral-loading conditions, ϕ_w correlates well with linear theory for rotor solidities above 0.35. Under compressor-loading conditions, ϕ_w decreases uniformly with solidity until the linear-theory value is reached at the higher-rotor-solidity values. Thus high-solidity rotors tend to generate linear-theory-gust velocity profiles.

The unsteady velocity data of Fig. 15 were obtained with the research facility in two configurations: stator airfoils installed and no stator airfoils. For the installed stator cascade, the solidity of the stator cascade was very low, 0.17, being comprised of only the four instrumented airfoils. The hot-wire and total pressure probes were at least 1.5 stator chords circumferentially from the nearest stator airfoil. Repeated measurements obtained in both configurations show that the forcing function velocity measurements were negligibly affected by the presence of the stator airfoils.

The fundamental-harmonic static-to-velocity pressure ratio, P_s/P_v, of the forcing functions of Fig. 15 are presented in Figs. 16. The upper plot presents the magnitude ratio, $|P_s/P_v|$, and the lower plot the phase shift between the forcing function static and velocity pressure harmonics $\phi_s - \phi_v$. Referring to the repeated data obtained with and without the stator airfoils installed, the forcing function static-to-velocity pressure magnitude ratio is significantly less with the stator airfoils installed, particularly for the low-solidity value. Thus, the forcing function static pressure measurements are significantly affected by the presence of the stator airfoils since Fig. 15 shows the forcing function velocity measurements unaffected by the presence of the stator airfoils. To compare forcing functions, the forcing function characteristics in an undisturbed flow field are considered with the data obtained with no stator airfoils replotted in Fig. 16.

Figure 16 shows that the proportion of the forcing function static pressure-to-velocity pressure decreases with solidity for the compressor and neutral loading conditions whereas the two turbine-loading data points show an increase in the pressure ratio with solidity. The phase angle between the forcing function static pressure and velocity pressure fundamental harmonics are approximately equal at 135 deg for the low-solidity value. The neutral and turbine loading phase-shift data is relatively flat at 135 deg, whereas the compressor-loading data shows that the fundamental pressure harmonics are more in phase at the higher solidities. Under compressor and neutral-loading conditions the proportion of static-to-velocity pressure decreases with solidity, corresponding to better correlation of the linear-gust parameters with linear-theory values. Under turbine-loading conditions the proportion of static pressure in the forcing function is high, corresponding to the poorer correlation of the turbine-loading linear-gust parameters with linear-theory values.

Airfoil forcing functions are presented in Figs. 17–19 for a high-solidity rotor and low rotor speed (i.e., low inlet mean-relative flow angle). These forcing functions exhibit profile shapes that depend upon the rotor-loading condition. The velocity vectors are aligned with the downstream mean-relative flow angle in the compressor case, but are increasingly misaligned as neutral and turbine loading are introduced. The static pressure fluctuations are low in the compressor case and increase with neutral and turbine loading. The effect of rotor speed is illustrated by comparing both high-solidity forcing functions, Figs. 12–14 and 17–19. The velocity vectors of the lower-rotor-speed forcing functions respond much more to rotor loading. In the low-rotor-speed compressor forcing function, the fundamental-harmonic β_w value is slightly above the linear-theory value and decreases as neutral and turbine loading

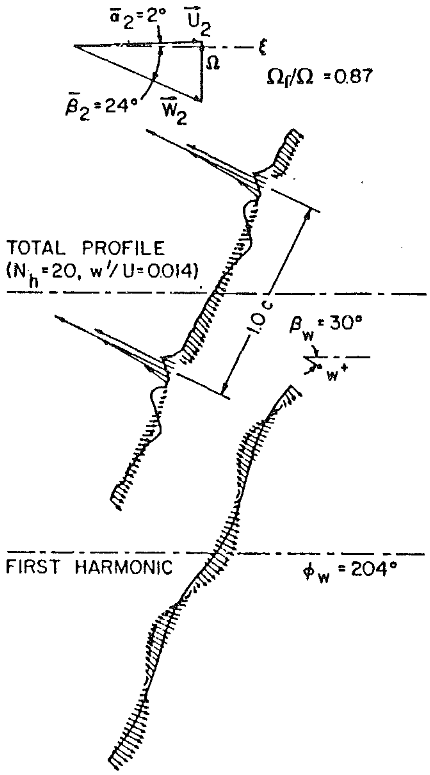

Fig. 17 Compressor rotor loading effect on airfoil forcing functions; high-solidity rotor and low rotational speed

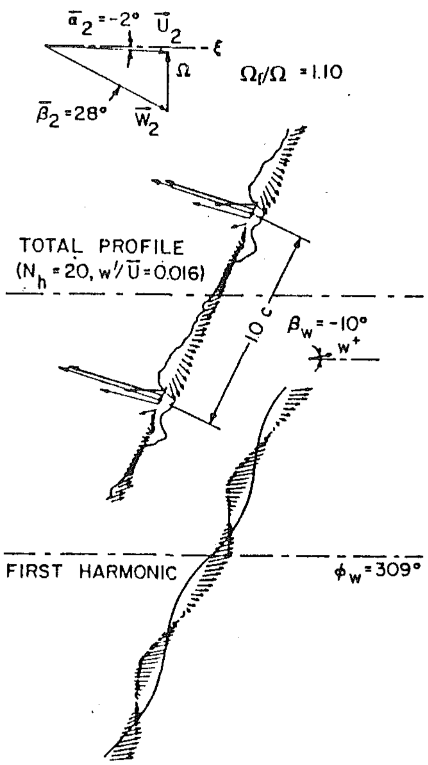

Fig. 19 Turbine rotor loading effect on airfoil forcing functions; high-solidity rotor and low rotational speed

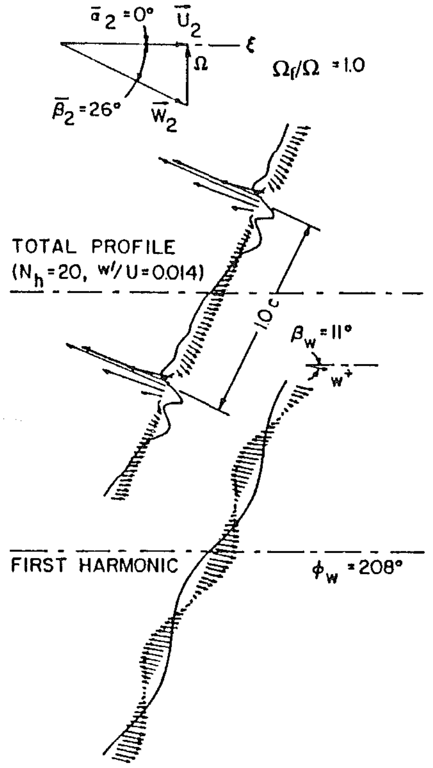

Fig. 18 Neutral rotor loading effect on airfoil forcing functions; high-solidity rotor and low rotational speed

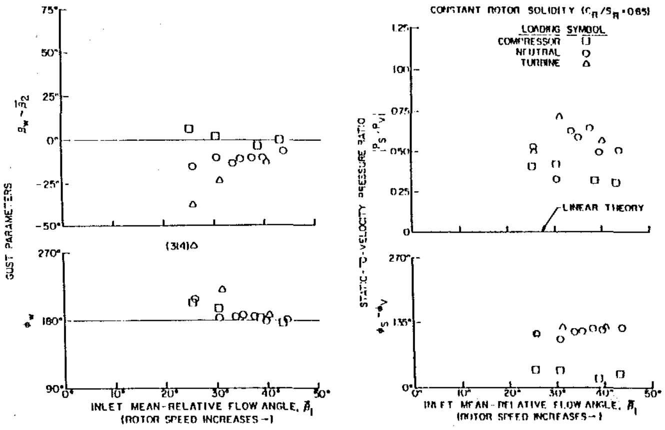

Fig. 20 Rotor loading and speed effect on airfoil fundamental-harmonic linear gust parameters and static-to-velocity pressure ratio; constant rotor solidity

are introduced. The turbine β_w value is much lower than the linear-theory value. The high-rotor-speed fundamental-harmonic β_w value decreases as the rotor loading changes from compressor to turbine conditions but to a much lesser extent. The low-rotor-speed fundamental-harmonic gust-component phase angle, ϕ_w, is also more a function of loading. Under compressor and neutral-loading conditions, ϕ_w values are approximately equal at a value 25 deg greater than the linear-theory value. The turbine-loaded fundamental-harmonic ϕ_w value is much greater, 129 deg above the linear-theory value. In contrast, the high-rotor-speed ϕ_w values are near the linear-theory value and a much weaker function of rotor loading.

The effect of rotor speed on the fundamental-harmonic linear-gust parameters of the airfoil-cascade forcing functions is presented in Fig. 20. The rotor solidity is constant at a high value, $C_R/S_R = 0.65$. These data were obtained with no stator airfoils in the research facility. Definite trends due to rotor loading and inlet mean-relative flow angle are evident. Comparing constant $\bar{\beta}_1$ cases, compressor $(\beta_w - \bar{\beta}_2)$ values near the linear theory results are found with $(\beta_w - \bar{\beta}_2)$ values increasingly below the linear-theory line for the neutral and turbine loading conditions, respectively. The $(\beta_w - \bar{\beta}_2)$ values approach the linear-theory value as the rotor speed increases. The gust-component phase angle values ϕ_w are similar for the compressor and neutral cases, approximately 25 deg above the linear-theory value for the low-$\bar{\beta}_1$ value. Under turbine-loading conditions, the ϕ_w value is much higher at the lowest rotor speed. For all loading conditions, ϕ_w approaches the linear-theory value for increasing rotor speeds. Thus, high inlet mean-relative flow angles or high rotor speeds tend to generate linear-theory-gust velocity profiles.

The effect of rotor speed on the fundamental-harmonic static-to-velocity pressure ratios for the constant-solidity airfoil-cascade forcing functions are also presented in Fig. 20. The proportion of static-to-velocity pressure in the forcing functions is approximately 0.5 for each loading condition at the low-$\bar{\beta}_1$ value. The proportion of static pressure to velocity pressure under neutral and turbine-loading conditions is higher than under compressor conditions at the higher rotor speeds. The lower plot shows that the phase shift between the static pressure and velocity pressure fundamental harmonics is a weak function for rotor speed, but displays definite trends as a function of the rotor-loading condition. The phase angle values under the neutral and turbine-loading conditions are approximately equal at a value of 125 deg, whereas the phase angle values in the compressor loading conditions are near 30 deg, indicating that the static and velocity pressures are much more in phase for compressor loading conditions. Comparing the linear-gust parameter and pressure ratio plots, no clear relationship is evident relating the presence of the static pressure distribution in the forcing function to the deviation of the linear-gust parameters from the vortical linear-theory values.

Summary and Conclusions

The fundamental gust modeling assumptions have been investigated by means of a series of experiments performed in the Purdue Annular Cascade Research Facility. The unsteady periodic flow field, measured via hot-wire anemometer and total pressure probes, was generated by rotating rows of perforated plates and airfoil cascades. The measured unsteady flow fields were analyzed harmonically according to the constraints of linear theory.

The perforated-plate forcing functions closely resemble linear-theory vortical forcing functions. The static pressure fluctuations are small and the periodic velocity vectors are parallel to the downstream mean-relative flow angle over the entire periodic cycle. The correlation of the gust parameters β_w and ϕ_w with linear-theory vortical values is excellent.

Unfortunately for the turbomachine designer, airfoil-cascade forcing functions are much more complex. The airfoil forcing functions display characteristics far from linear-theory vortical gusts. The alignment of the velocity vectors and the static pressure fluctuation amplitudes are dependent upon the rotor-loading condition, rotor solidity, and the inlet mean-relative flow angle. The velocity vectors are aligned closer to the downstream mean-relative flow angle and the static pressure fluctuations are smaller for compressor-loading conditions, high-solidity rotors, and high rotor speeds. The velocity vectors become increasingly misaligned and the static pressure fluctuations increase for neutral and turbine loading conditions, respectively, and when rotor solidity or rotor speed decreases. The wake-region velocity vectors are much more responsive to the lift force in low-solidity rotors or at low rotor speeds. Changing the rotor loading from compressor to turbine conditions degrades the linear-gust parameter correlation. For similar loading conditions, increasing the rotor solidity or rotor speed improves the linear-gust parameters correlation. The fundamental-harmonic static-to-velocity pressure ratios are nearly the same for all rotor loading conditions when the rotor solidity or the rotor speed is low. The static-to-velocity pressure ratio increases as the rotor loading varies from the compressor to turbine conditions when the rotor solidity or rotor speed is high. The static and velocity pressure fundamental harmonics are relatively in phase for compressor-loading conditions and out-of-phase for neutral and turbine-loading conditions when the rotor solidity or rotor speed is high.

In summary, these unique data clearly show that airfoil wakes, both compressor and turbine, are not able to be modeled by the boundary conditions of current state-of-the-art linear vortical gust unsteady aerodynamic theory. Modeling the static pressure fluctuations as arising from the rotor airfoil potential field and incorporating the rotor potential into the analysis may improve the data-theory correlation.

Acknowledgments

This research was sponsored, in part, by the NASA Lewis Research Center. Both the financial support and the technical interchanges with Dr. Daniel Hoyniak are most gratefully acknowledged.

References

Becker, H. A., and Brown, A. P. G., 1974, "Response of Pitot Probes in Turbulent Streams," *Journal of Fluid Mechanic*, Vol. 62, part 1, pp. 85–114.

Capece, V. R., Manwaring, S. R., and Fleeter, S., 1986, "Unsteady Blade Row Interactions in Multistage Compressor," *AIAA Journal of Propulsion*, Vol. 2, No. 2, pp. 168–174.

Capece, V. R., and Fleeter, S., 1987, "Unsteady Aerodynamic Interactions in a Multi-stage Compressor," ASME JOURNAL OF TURBOMACHINERY, Vol. 109, No. 3, pp. 420–428.

Capece, V. R., and Fleeter, S., 1989, "Experimental Investigation of Multistage Interaction Gust Aerodynamics," ASME JOURNAL OF TURBOMACHINERY, Vol. 111, pp. 409–417.

Fang, J., 1991, "Compressible Flows With Vortical Disturbances Around Cascades of Airfoils," Ph.D. Thesis, University of Notre Dame.

Fleeter, S., Jay, R. L., and Bennett, W. A., 1978, "Rotor Wake Generated Unsteady Aerodynamic Response of a Compressor Stator," ASME *Journal of Engineering for Power*, Vol. 100, pp. 664–675.

Fleeter, S., Jay, R. L., and Bennett, W. A., 1980, "The Time-Variant Aerodynamic Response of a Stator Row Including the Effects of Airfoil Camber," ASME *Journal of Engineering for Power*, Vol. 102, pp. 334–343.

Fleeter, S., Jay, R. L., and Bennett, W. A., 1981, "Wake Induced Time-Variant Aerodynamics Including Rotor-Stator Axial Spacing Effects," ASME *Journal of Fluids Engineering*, Vol. 103, pp. 59–66.

Franke, G. F., and Henderson, R. E., 1980, "Unsteady Stator Response to Upstream Rotor Wakes," *AIAA Journal of Aircraft*, Vol. 17, No. 1, pp. 500–506.

Gallus, H. E., Lambertz, J., and Wallmann, Th., 1980, "Blade-Row Interaction in an Axial-Flow Subsonic Compressor Stage," ASME *Journal of Engineering for Power*, Vol. 102, pp. 169–177.

Goldstein, M. E., and Atassi, H., 1976, "A Complete Second-Order Theory for the Unsteady Flow About an Airfoil Due to Periodic Gust," *Journal of Fluid Mechanics*, Vol. 74, part 4, pp. 741–765.

Goldstein, M. E., 1978, "Unsteady Vortical and Entropic Distortions of Potential Flows Round Arbitrary Obstacles," *Journal of Fluid Mechanics*, Vol. 89, part 3, pp. 433–468.

Hall, K. C., and Verdon, J. M., 1989, "Gust Response Analysis for Cascades Operating in Nonuniform Mean Flows," AGARD Conference—Unsteady Aerodynamic Phenomena in Turbomachines, AGARD CPP-468.

Henderson, G. H., and Fleeter, S., 1993, "Forcing Function Effects on Unsteady Aerodynamic Gust Response: Part 2—Low Solidity Airfoil Row Response," ASME JOURNAL OF TURBOMACHINERY, Vol. 115, this issue, pp. 751–761.

Manwaring, S. R., and Fleeter, S., 1991, "Forcing Function Effects on Rotor Periodic Aerodynamic Response," ASME JOURNAL OF TURBOMACHINERY, Vol. 113, pp. 312–319.

Scott, J. S., and Atassi, H. M., 1990, "Numerical Solutions of the Linearized Euler Equations for Unsteady Vortical Flows Around Lifting Airfoils," AIAA Paper 90-0694.

Forcing Function Effects on Unsteady Aerodynamic Gust Response: Part 2—Low Solidity Airfoil Row Response

G. H. Henderson[1]

S. Fleeter

School of Mechanical Engineering,
Purdue University,
West Lafayette, IN 47907

The fundamental gust modeling assumption is investigated by means of a series of experiments performed in the Purdue Annular Cascade Research Facility. The unsteady periodic flow field is generated by rotating rows of perforated plates and airfoil cascades, with the resulting unsteady periodic chordwise pressure response of a downstream low-solidity stator row determined by miniature pressure transducers embedded within selected airfoils. When the forcing function exhibited the characteristics of a linear-theory vortical gust, as was the case for the perforated-plate wake generators, the resulting response on the downstream stator airfoils was in excellent agreement with the linear-theory models. In contrast, when the forcing function did not exhibit linear-theory vortical gust characteristics, i.e., for the airfoil wake generators, the resulting unsteady aerodynamic responses of the downstream stators were much more complex and correlated poorly with the linear-theory gust predictions. Thus, this investigation has quantitatively shown that the forcing function generator significantly affects the resulting gust response, with the complexity of the response characteristics increasing from the perforated-plate to the airfoil-cascade forcing functions.

Introduction

A number of experiments have been directed at the verification of unsteady aerodynamic models appropriate for blade row forced response prediction and the determination of their applicability and limitations (for example, Franke and Henderson, 1980; Fleeter et al., 1978, 1980, 1981; Gallus et al., 1980; Dring et al., 1982; Hodson, 1985; Capece et al., 1986; Capece and Fleeter, 1987, 1989). In these, the unsteady airfoil row response comparisons with linear theory were made without considering the fundamental gust modeling assumptions. However, it has been found experimentally that the harmonic gust response generated by different but fundamentally equivalent forcing functions are dependent on the particular forcing function (Manwaring and Fleeter, 1991; Kim and Fleeter, 1991).

In an accompanying paper, the fundamental vortical gust modeling assumption was investigated by means of a series of experiments performed in the Purdue Annular Cascade Research Facility (Henderson and Fleeter, 1992). The unsteady periodic flow field was generated by rotating rows of perforated plates and airfoil cascades. The perforated-plate forcing functions were shown to resemble closely linear-theory vortical forcing functions, with the static pressure fluctuations small and the periodic velocity vectors parallel to the downstream mean-relative flow angle over the entire periodic cycle. In contrast, the airfoil forcing functions exhibited characteristics far from linear-theory vortical gusts, with the alignment of the velocity vectors and the static pressure fluctuation amplitudes dependent on the rotor-loading condition, rotor solidity, and the inlet mean-relative flow angle.

In this paper, the resulting effect of the perforated plate and airfoil wake forcing functions, which exhibit fundamentally different modeling features on the resulting downstream airfoil row unsteady aerodynamic gust response, are presented. The unsteady periodic chordwise pressure response of the downstream stator vanes are determined by miniature pressure transducers embedded within selected symmetric airfoils.

These experiments have been performed in the Purdue Annular Cascade Research Facility, which features a single rotor–stator stage and experimentally reproduces the fundamental unsteady flow phenomena inherent in axial flow turbomachines. The unsteady periodic forcing functions are generated with rotating rows of perforated plates and airfoil cascades, Fig. 1. The reader is referred to the accompanying paper for a discussion of the research facility and forcing function measurement and analysis (Henderson and Fleeter, 1992).

---

[1] Current address: Advanced Product Development, Cummins Engine Company, Columbus, IN.

Contributed by the International Gas Turbine Institute and presented at the 37th International Gas Turbine and Aeroengine Congress and Exposition, Cologne, Germany, June 1–4, 1992. Manuscript received by the International Gas Turbine Institute February 17, 1992. Paper No. 92-GT-175. Associate Technical Editor: L. S. Langston.

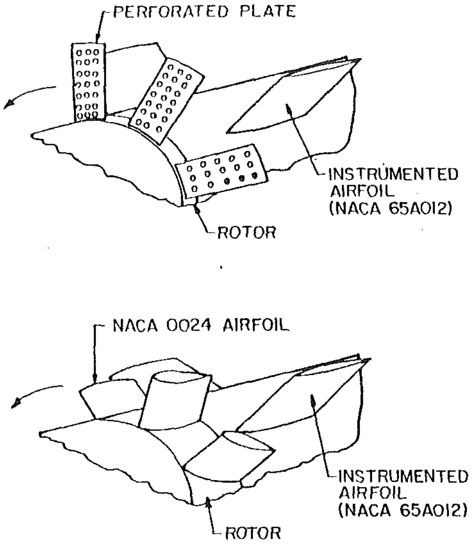

Fig. 1 Test section configurations with wake generators

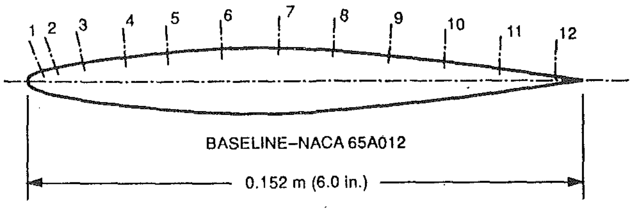

PRESSURE MEASUREMENT LOCATIONS

TAP NO.	1	2	3	4	5	6	7	8	9	10	11	12
% CHORD	2.5	5.0	10.0	17.5	25	35	45	55	65	75	85	95

Fig. 2 Stator airfoil profile

Stator Vane Row and Instrumentation

The low-solidity stator row was comprised of the four instrumented airfoils, two for static and two for dynamic data, resulting in a low solidity value of 0.17. Reduced frequency variations were accomplished by changing both the number of wake generators and the rotor speed. The hot-wire probe was outside the potential field of the lightly loaded stator airfoils. Thus the velocity measurements obtained with the stator airfoils installed were used to nondimensionalize the unsteady pressure measurements.

Figure 2 presents the symmetric stator airfoil profiles. The profile coordinates were taken from Abbott and Von Doenhoff (1959). The airfoil chord and span are equal at 0.152 m (6.0 in.). The instrumented airfoils were assembled from three 0.051 m (2.0 in.) wide spanwise sections fabricated from solid aluminum. The center section houses static pressure taps or dynamic pressure transducers. The twelve chordwise tap locations provide highly detailed spatial resolution of the midspan chordwise pressure distributions. The stator airfoils are mounted through holes in the outer diameter of the test section by trunnions attached at the 35 percent chord. The stator airfoil stagger angle can be set to within ±0.5 deg.

Both steady and unsteady rotor blade row data are required. The steady data quantify the detailed stator-airfoil steady surface aerodynamic loading distribution, defined by the static surface pressure distribution and the stator-cascade mean inlet flow field, defined by the mean velocity downstream of the rotor. With the unsteady velocity and static pressure fluctuations downstream of the rotor, i.e., the stator vane forcing function specified per the accompanying paper, the unsteady data define the detailed stator-airfoil surface periodic aerodynamic loading distribution as specified by the periodic surface pressure distribution.

Static pressure taps and high-response pressure transducers embedded in the stator airfoils are used to obtain the detailed airfoil-surface steady and unsteady pressure data. Four instrumented airfoils are required, two to obtain static pressure distributions on each surface and two to obtain the periodic pressure distributions on each surface. The stator-cascade steady and unsteady velocity fields are measured using a cross hot-wire probe. The total pressure fluctuations downstream of the rotor are measured with an unsteady total pressure probe. The static pressure distributions are calculated by subtracting the velocity (i.e., dynamic) pressure, $\rho_0 \overline{U}_2^2/2$, from the total pressure.

The airfoil unsteady surface pressures are measured with PCB Piezotronics model 103A piezoelectric pressure transducers. The transducers have a nominal sensitivity of 0.22 mV/Pa (1500 mV/psi) and a natural frequency of 13 kHz. After the transducers were installed in the airfoil, the dynamic response of each airfoil transducer-passage system was experimentally determined to correct for any passage effects.

Unsteady Data Acquisition and Analysis

All time-variant signals are digitized over one rotor revolution using approximately 2000 samples. The number of ensemble averages necessary to obtain clean periodic time traces was investigated. Ensemble averaging the hot-wire and pressure transducer signals 150 and 100 times, respectively, produces very clean periodic time traces with the random fluctuations

Nomenclature

C = stator airfoil chord length
$\hat{C}_L$ = unsteady lift coefficient
$\hat{C}_{M,C/4}$ = unsteady quarter chord moment coefficient
$\overline{C}_p$ = steady surface pressure coefficient
$\overline{C}_{\Delta p}$ = steady differential pressure coefficient
$\hat{C}_p$ = unsteady surface pressure coefficient
$\hat{C}_{\Delta p}$ = unsteady differential pressure coefficient
k_b = reduced frequency based on semichord
k_c = reduced frequency based on chord
N = number of rotor wake generators
p = perturbation pressure
S = blade spacing
$\mathbf{U}$ = absolute velocity
v^+ = transverse gust amplitude
w^+ = gust amplitude
α = angle of attack
$\overline{\alpha}_1$ = rotor inlet mean absolute flow direction
$\overline{\alpha}_2$ = rotor exit mean absolute flow direction
$\overline{\beta}_1$ = rotor inlet mean-relative flow angle
$\overline{\beta}_2$ = rotor exit mean-relative flow angle
β_w = gust amplitude angle
γ = stagger angle
ρ_0 = free-stream density
σ = interblade phase angle
Ω = rotor velocity
Ω_f = free-rotation rotor velocity

averaged away. The Fourier components of the ensemble-averaged time traces are numerically determined with Fast Fourier Transform software. The sample frequency is set and the number of samples is adjusted to produce time records of exactly one rotor rotation period to eliminate frequency leakage problems in Fourier Transform analysis. The sample frequency and number of digitizations are set based upon an accurate rotor rotational speed. The rotor rotational speed is measured by digitizing the shaft trigger signal at the maximum sample frequency and counting the number of samples between shaft triggers.

Pressure Coefficients. The chordwise pressure response data are presented as nondimensional pressure coefficients and are correlated with a steady linear-theory analysis. The unsteady-response data are correlated with Smith's (1972) compressible flow analysis. Both of these analyses account for the cascade stagger angle γ and the solidity C/S, with Smith's unsteady analysis also considering the reduced frequency k_c and the interblade phase angle σ.

The steady data are nondimensionalized by calculating a steady surface pressure coefficient

$$\overline{C}_p(x)=\frac{\overline{p}(x)-p_\infty}{\frac{1}{2}\rho_0\overline{U}^2} \qquad (1)$$

where $\overline{p}$ is the time-averaged airfoil surface pressure and p_∞ is the free-stream pressure measured on the test-section outer diameter just upstream of the stator cascade.

The steady differential pressure coefficient is defined by

$$\overline{C}_{\Delta p}=\overline{C}_{p,l}-\overline{C}_{p,u} \qquad (2)$$

where the subscripts l and u refer to the lower and upper airfoil surfaces, respectively.

The unsteady periodic signals are Fourier decomposed and each pressure harmonic nondimensionalized by calculating an unsteady surface pressure coefficient

$$\hat{C}_p(x)=\frac{\hat{p}(x)}{\rho\overline{U}\hat{v}} \qquad (3)$$

where $\hat{p}$ and $\hat{v}$ represent the harmonic surface pressure and transverse gust component, respectively.

The harmonic differential pressure coefficient is defined by

$$\hat{C}_{\Delta p}=\hat{C}_{p,l}-\hat{C}_{p,u}. \qquad (4)$$

Direct comparison of the experimental and theoretical steady and unsteady lift coefficients is accomplished by integrating the experimental and theoretical chordwise differential pressure coefficients over the airfoil chord.

$$C_L=\frac{1}{C}\int_{0.025C}^{0.95C} C_{\Delta p}dx. \qquad (5)$$

The trapezoidal rule is used to evaluate the integral from the discrete differential pressure coefficient data and theoretical predictions. The differential pressure distributions were integrated from the leading edge tap location, 0.025C, to the trailing edge tap location, 0.95C. In a similar manner experimental and theoretical quarter-chord moment coefficients are calculated.

$$C_{M,c/4}=\frac{1}{C^2}\int_{0.025C}^{0.95C} C_{\Delta p}(x-0.25)dx. \qquad (6)$$

The complex valued unsteady pressure coefficients, lift coefficients, and moment coefficients contain both amplitude and phase angle information. These quantities are referenced to the transverse gust sinusoid measured by the cross hot-wire on the airfoil leading edge plane. To obtain pressure coefficients for a single equivalent airfoil, the pressure signals are phase corrected to account for the circumferential locations of the instrumented airfoils. The uncertainty of the measured surface pressure coefficients is estimated at 10 percent where the response is large near the leading edge.

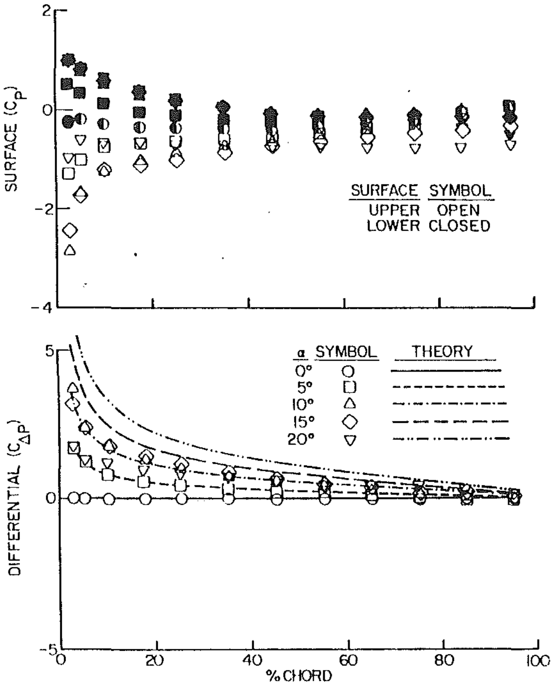

Fig. 3 Steady chordwise pressure distributions

Results

A series of experiments were performed to investigate the unsteady aerodynamic gust response of a downstream symmetric-airfoil stator cascade to perforated-plate and airfoil-cascade forcing functions. A similar axial velocity was utilized in these experiments corresponding to a Reynolds number of approximately 500,000 based on the stator-airfoil chord length. The stator-airfoil steady loading was small for the entire forcing function experimental investigation due to the small angle-of-attack between the axially aligned (zero stagger angle) symmetric stator airfoils and the nearly axial rotor exit flow. The rotor exit flow was very close to axial due to the small swirl angles, $\overline{\alpha}_2$ less than 5 deg, imparted by the wake generators.

Airfoil Surface Static Pressures. Figure 3 presents the airfoil steady chordwise surface and differential pressure coefficients obtained in a steady flow field. The correlation with linear theory is excellent for angles-of-attack less than 15 deg. At $\overline{\alpha}$ = 0 deg the surface pressures are coincident, resulting in zero differential pressure coefficients. For angles-of-attack greater than 10 deg, stalling is evident. For all of the unsteady gust response experiments, the angle-of-attack was less than 5 deg.

Perforated-Plate-Generated Response. The unsteady aerodynamic gust response of a low-solidity symmetric-airfoil cascade to wide perforated-plate forcing functions is shown in Fig. 4 in terms of the unsteady fundamental-harmonic lift and moment coefficients $\hat{C}_L$ and $\hat{C}_{M,C/4}$. The upper two plots present the lift and quarter-chord moment coefficient magnitudes and the lower two plots the lift and quarter-chord moment coefficient phase angles. The reduced frequency is varied by changing the number of perforated plates or changing the rotor speed. Also presented are the theoretical predictions from Smith's linearized compressible cascade analysis. Changing the number of perforated plates changes the interblade phase angle, but only four interblade phase angles σ are possible with

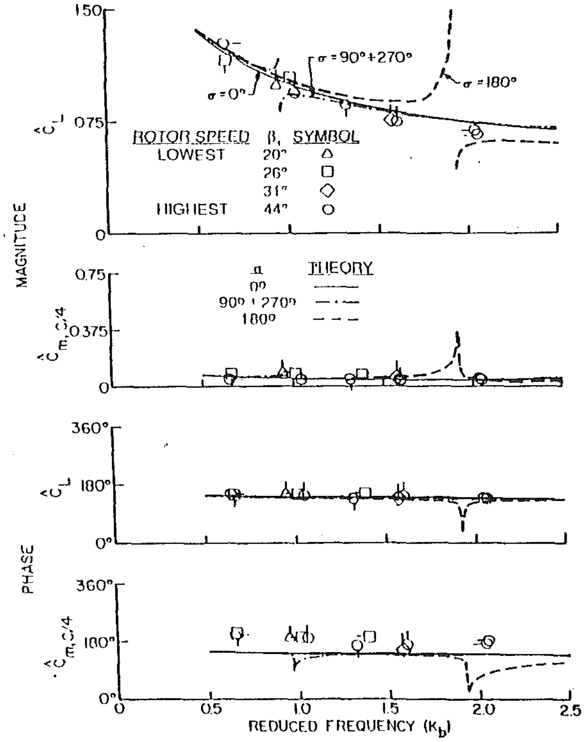

Fig. 4 Perforated plate forcing function harmonic lift and moment coefficients

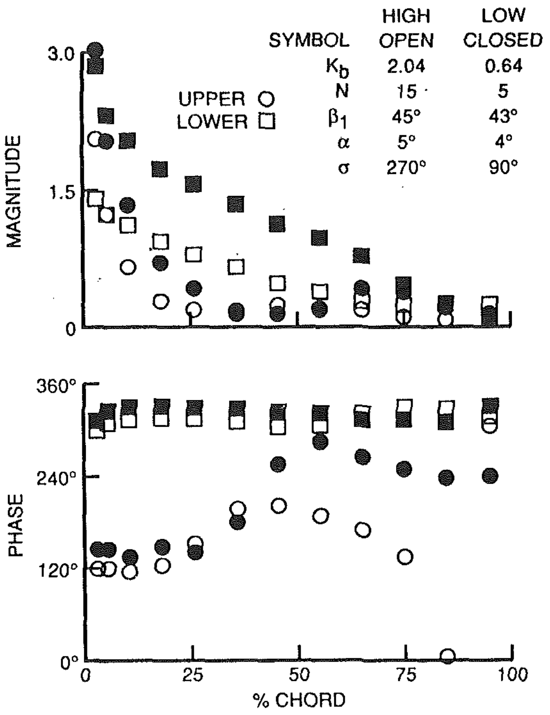

Fig. 5 Reduced frequency effect on perforated plate generated harmonic airfoil surface chordwise pressure

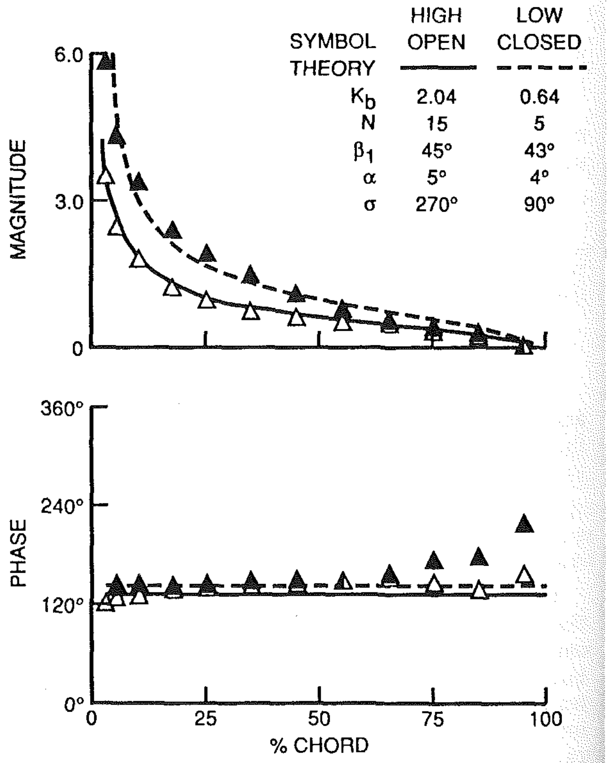

Fig. 6 Reduced frequency effect on perforated plate generated harmonic airfoil surface chordwise pressure difference

four airfoils comprising the stator cascade. However, the $\sigma = 90$ and 270 deg predictions are the same for an unstaggered cascade. The discontinuities in the predictions result from the acoustic resonance condition. The interblade phase angle of each data point is indicated by the location of a tick mark on the symbol. Tick marks at the 12-o'clock, 3-o'clock, 6-o'clock, and 9-o'clock position designate interblade phase angles of 0, 90, 180, and 270 deg, respectively. Note that the perforated-plate forcing functions closely match linear theory vortical gusts of these experiments.

The measured unsteady lift coefficients correlate almost exactly with the theoretical predictions in both the magnitude and phase plots. The quarter-chord unsteady moment coefficient magnitudes are very small and also correlate well with the theoretical predictions. The moment coefficient phase angles deviate from theory when the lift-coefficient phase-angle corelation is used as a basis of judgment. However, note that the quarter-chord moment-coefficient phase angles are of little consequence because of the very small moment coefficient magnitudes.

The effect of reduced frequency on the chordwise unsteady pressure gust response of the airfoil cascade to perforated-plate forcing functions is illustrated in Figs. 5 and 6. The same rotor speed was utilized in each experiment with the reduced frequency changed by increasing the number of plates (i.e., increasing rotor solidity) from five to fifteen. The upper and lower surfaces correspond to the suction and pressure surfaces for positive mean angles-of-attack.

The lower-surface response magnitude decreases monotonically from the leading to trailing edge, whereas the upper-surface response magnitude decreases rapidly over the leading quarter chord, then increases slightly, so that a relative minimum, a dip, in the data trend is predominant near the quarter chord. The dip moves forward with reduced frequency. The lower-surface response phase angle is relatively flat, with the upper-surface response phase angle more a function of chord location. The upper and lower-surface responses are approximately equal in magnitude and approximately 180 deg out of phase at the leading edge. At the trailing edge, the Kutta condition is approached as the upper and lower-surface pressure coefficients are again approximately equal in magnitude and are now nearly in phase. The differential-pressure coefficients are in excellent agreement with the theoretical vortical gust predictions in both magnitude and phase.

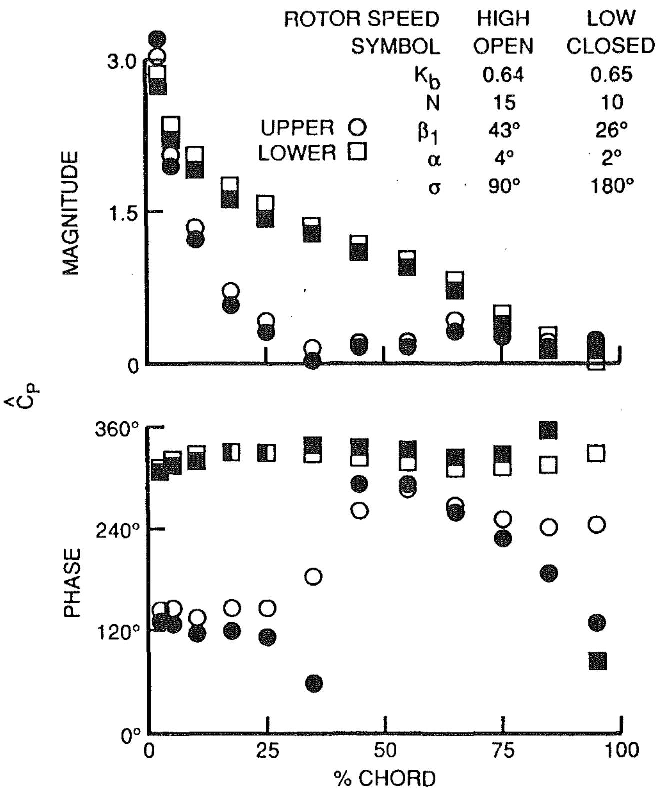

Fig. 7 Rotor speed effect on perforated plate generated harmonic airfoil surface chordwise pressure

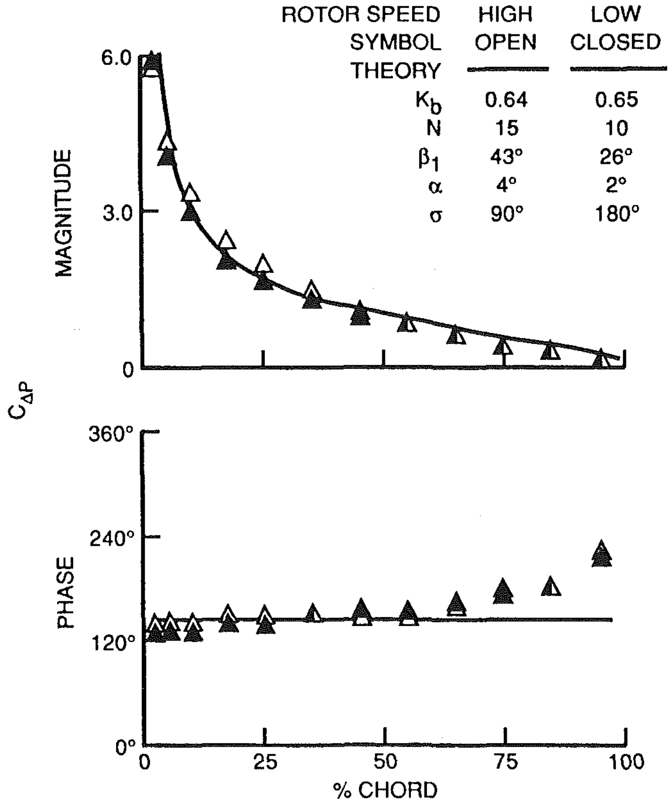

Fig. 8 Rotor speed effect on perforated plate generated harmonic airfoil surface chordwise pressure difference

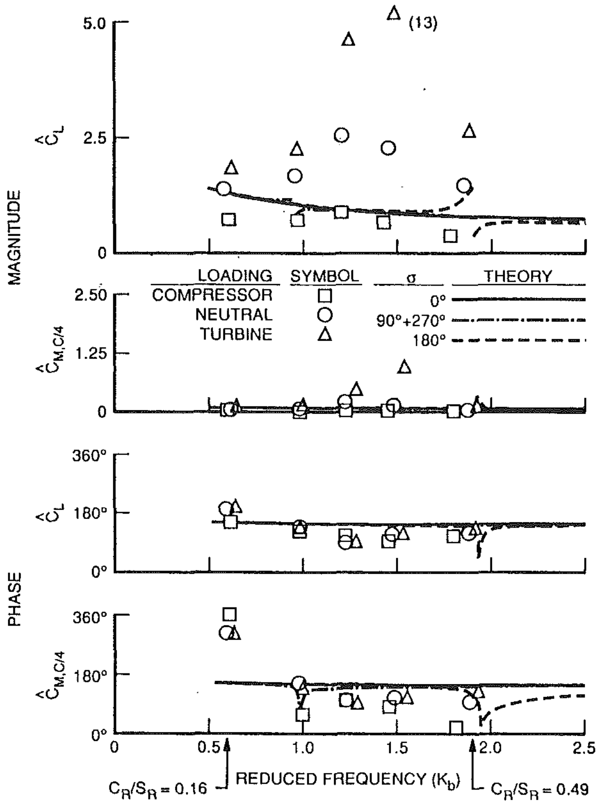

Fig. 9 Airfoil cascade forcing function harmonic lift and moment coefficients

The effect of rotor speed on the chordwise pressure response of a low-solidity symmetric-airfoil cascade is presented in Figs. 7 and 8. A low and high-rotor-speed setting were utilized, with the higher-rotor speed twice that of the lower. The reduced frequency was held constant at the lowest value by using half as many wake generators in the higher-rotor-speed experiment. The forcing function investigation showed that doubling the rotor speed approximately doubles the transverse gust amplitude by decreasing the angle between the downstream mean flow and the gust propagation direction (Henderson and Fleeter, 1993). However, there are only small differences in the surface unsteady pressure response or differential-pressure coefficients between the two cases. The upper-surface response phase angles deviate near the midchord, but only where the magnitudes are small. Thus, for these symmetric airfoils, the correct classical linear theory pressure measurement scaling factor is the transverse gust-component amplitude.

Airfoil-Cascade-Generated Response. The unsteady aerodynamic gust response of the low-solidity symmetric-airfoil cascade to airfoil-cascade wake forcing functions is presented in terms of the unsteady fundamental-harmonic lift and moment coefficients in Fig. 9. The rotor speed was held constant with the reduced frequency increased by adding airfoils, i.e., increased rotor solidity. Rotor-solidity values are indicated on the abscissa.

The trends of the unsteady aerodynamic coefficients do not follow the linear-theory vortical gust predictions. The unsteady lift-coefficient magnitude correlation is poor for all rotor loading conditions, with the turbine-loading conditions producing the poorest correlations. The quarter-chord unsteady moment coefficients, both predicted and measured, are small compared to the unsteady lift coefficient magnitudes. However, the forcing functions are far from linear theory vortical gusts, i.e., the static pressure fluctuations are high and the linear-gust parameter correlation is poor (Henderson and Fleeter, 1993), which coincides with the poor response correlation. The issue of relating the vortical gust-parameter correlation to the response correlation is confused by the competing characteristics

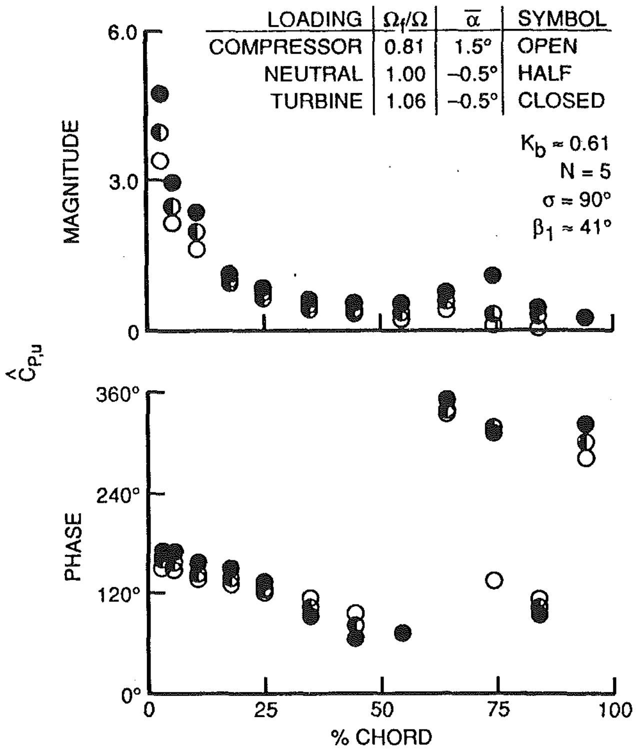

Fig. 10 Low reduced frequency rotor loading effect on airfoil cascade generated harmonic upper airfoil surface chordwise pressure

of the forcing function such as the unsteady velocity profile and the large static pressure fluctuations. The only clear trend evident in the response data is based on rotor-loading conditions. Considering each set of constant-solidity data, the unsteady lift coefficient magnitudes increase as the rotor loading is changed from compressor to turbine conditions. This behavior corresponds with the decreasing $(\beta_w - \bar{\beta}_2)$ values (Henderson and Fleeter, 1993), as the rotor loading changes from compressor to turbine conditions.

The effect of rotor-loading conditions on the chordwise unsteady response of the low-solidity symmetric-airfoil cascade is presented in Figs. 10, 11, and 12 for the lowest reduced frequency value. The response trends on the upper surface are similar for all rotor-loading conditions from the leading edge to 65 percent chord. The upper-surface responses decrease monotonically from the leading edge to the midchord then increase slightly. The upper-surface phase angles are relatively equal for each loading condition and slope downward from the leading edge to 65 percent chord. Over the aft quarter chord the upper-surface response trends are functions of rotor-loading conditions. The lower-surface response trends are also similar from the leading edge to 65 percent chord. The lower-surface response magnitudes decrease monotonically from the leading edge to the midchord. The lower-surface response phase angles are weak functions of chord position from the leading edge to 65 percent chord. Over the aft quarter chord the lower-surface response trends are functions of rotor-loading conditions.

Comparing the two surfaces shows that the upper-surface unsteady response magnitudes are greater than the lower-surface values for compressor-loading conditions. As neutral and turbine loading conditions are introduced, the lower-response magnitudes increase greatly from the leading edge to the 65 percent chord so that the lower-surface response magnitudes are greater than the upper-surface values. The upper-surface response magnitudes also increase near the leading edge but to a much lesser extent. The upper-surface response magnitudes remain small near the 35 percent chord for all rotor loading conditions. Near the leading edge the surface response phase angles are approximately 180 deg apart. The surface response satisfies the Kutta condition as the magnitudes and phase angles are nearly equal at the trailing edge.

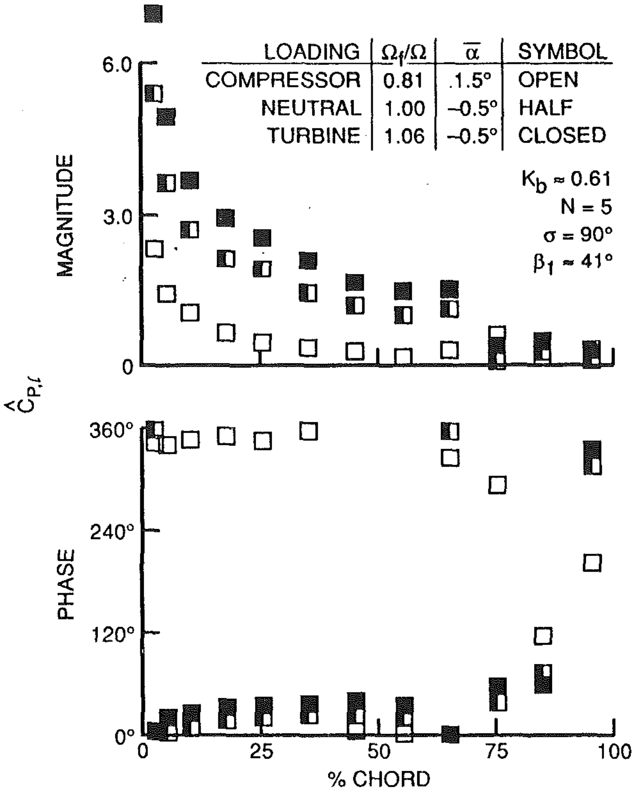

Fig. 11 Low reduced frequency rotor loading effect on airfoil cascade generated harmonic lower airfoil surface chordwise pressure

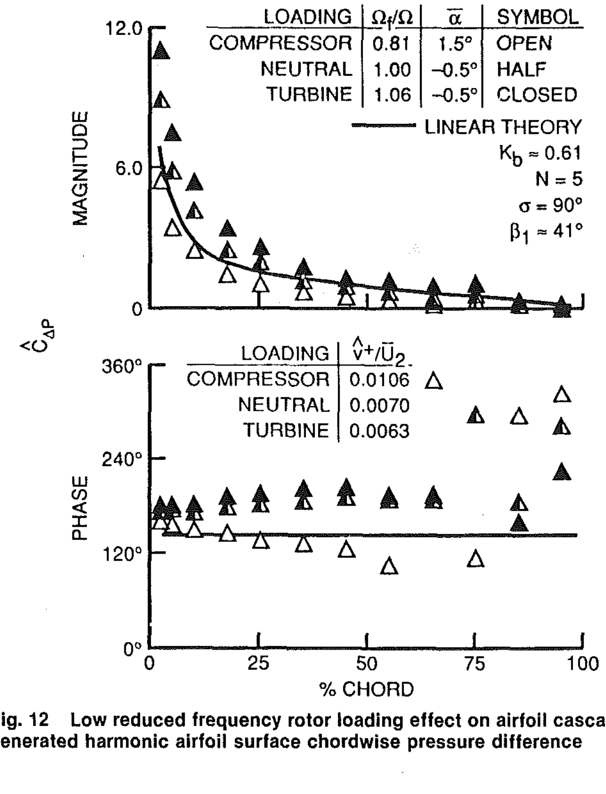

Fig. 12 Low reduced frequency rotor loading effect on airfoil cascade generated harmonic airfoil surface chordwise pressure difference

The unsteady differential-pressure-coefficient magnitudes

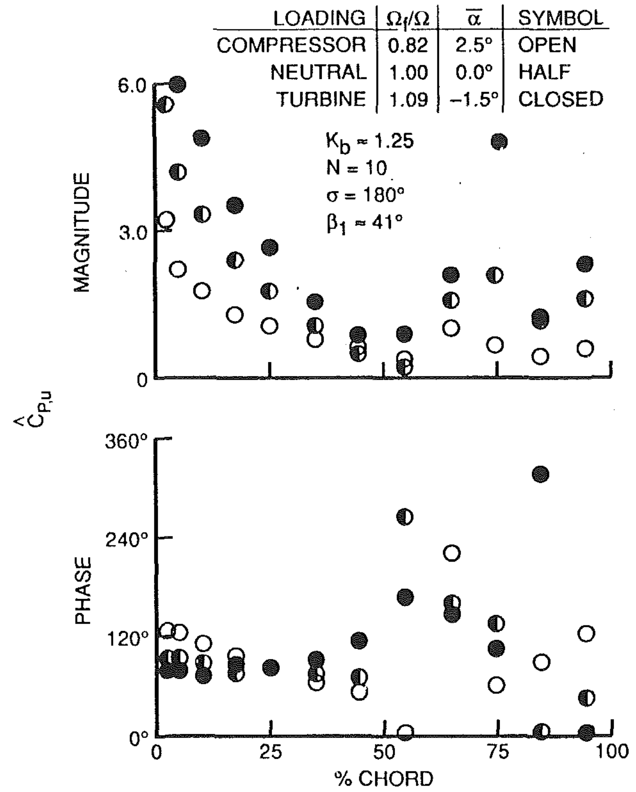

Fig. 13 Intermediate reduced frequency rotor loading effect on airfoil cascade generated harmonic upper airfoil surface chordwise pressure

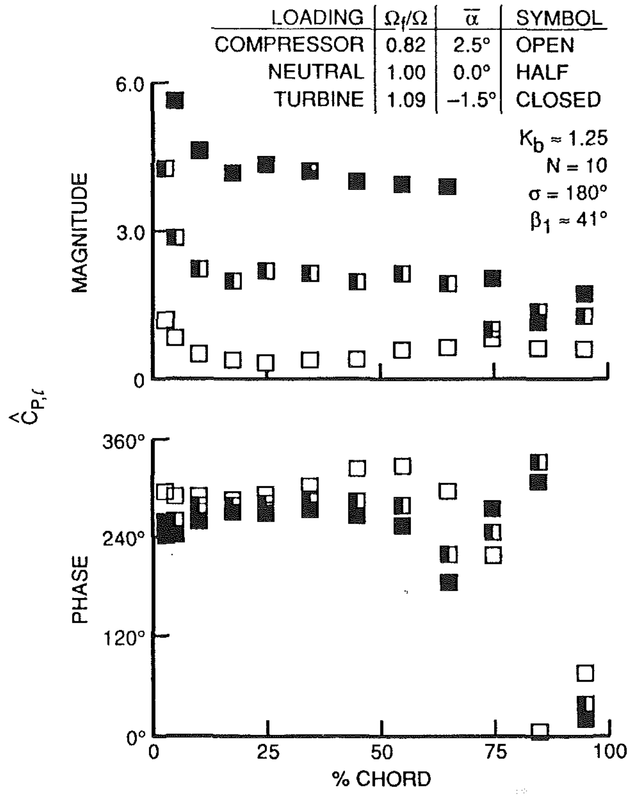

Fig. 14 Intermediate reduced frequency rotor loading effect on airfoil cascade generated harmonic lower airfoil surface chordwise pressure

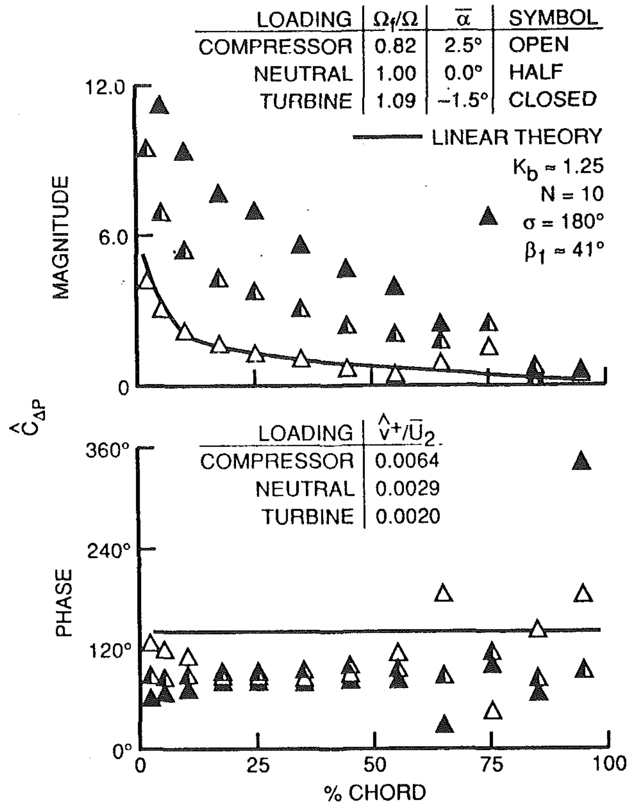

Fig. 15 Intermediate reduced frequency rotor loading effect on airfoil cascade generated harmonic airfoil surface chordwise pressure difference

follow the trend of the linear-theory predictions, but the data are shifted to higher values as the rotor-loading changes from turbine to compressor conditions. The response magnitude correlation is poorest for the turbine loading. The differential-pressure-coefficient phase angles for the neutral and turbine-loading cases are relatively flat from the leading edge to the 65 percent chord. The flat phase angle response trend is consistent with the linear-theory predictions, but the data are larger in value than the predicted values. The compressor-case phase angles slope slightly downward from the leading edge to 55 percent chord but are near the linear theory prediction. The variation in the unsteady differential-pressure-coefficient magnitudes and lift coefficients is obviously due to some rotor-loading dependent characteristic of the forcing function, which affects the lower surface more than the upper surface by greatly increasing the response magnitude.

The effect of the rotor-loading condition on the chordwise pressure response of the low-solidity symmetric-airfoil stator cascade is presented in Figs. 13, 14, and 15 for an intermediate reduced frequency value. The upper-surface response magnitude trends are similar for all rotor-loading conditions from the leading edge to the midchord. The response magnitudes decrease monotonically from the leading edge to midchord. Near the trailing edge the response magnitude trends are a function of rotor-loading conditions. Note the dramatic increase in response magnitude at 75 percent chord as the rotor loading changes from compressor to turbine conditions. The upper-surface response phase angles are very flat for neutral and turbine loading conditions from the leading edge to the 35 percent chord, whereas the compressor-case response phase angles decrease over the same portion of the chord. Over the aft half chord, the upper-surface response trends are strong functions of rotor-loading conditions.

The lower-surface response magnitudes exhibit very different chordwise trends. The response magnitudes decrease from the leading edge to 17 percent chord, then remain relatively constant to 65 percent chord. The turbine and neutral-case response phase angles increase slightly, then decrease slightly from the leading edge to the midchord, whereas the reverse

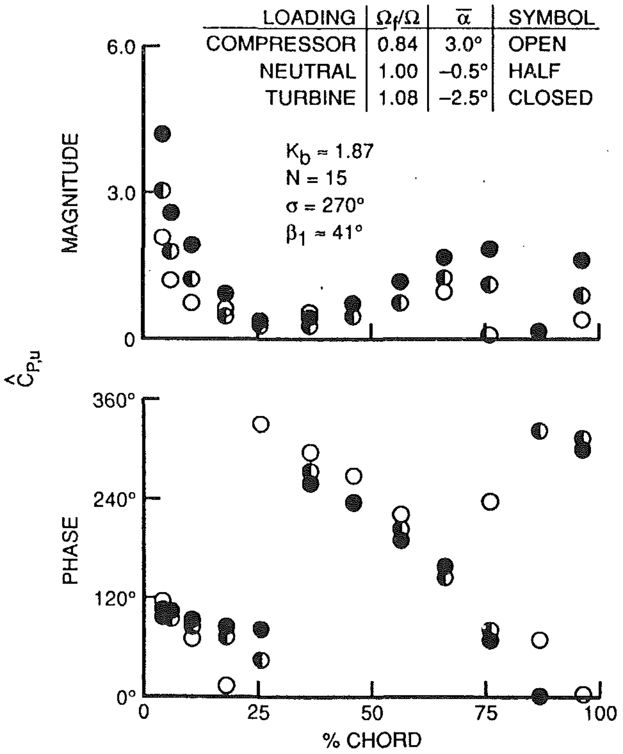

Fig. 16 High reduced frequency rotor loading effect on airfoil cascade generated harmonic upper airfoil surface chordwise pressure

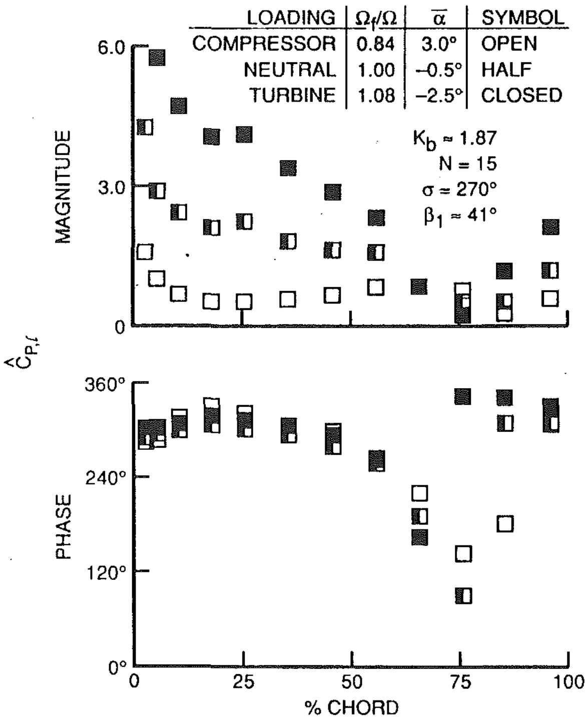

Fig. 17 High reduced frequency rotor loading effect on airfoil cascade generated harmonic lower airfoil surface chordwise pressure

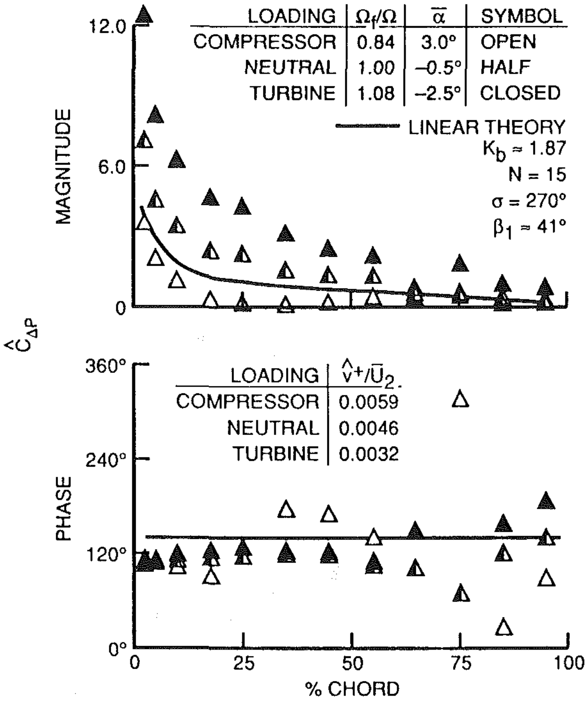

Fig. 18 High reduced frequency rotor loading effect on airfoil cascade generated harmonic airfoil surface chordwise pressure difference

occurs for the compressor-case. The lower-surface response trends are much weaker functions of rotor-loading conditions near the trailing edge as compared to the upper-surfaces responses.

Both surface unsteady pressure response magnitudes are affected by rotor-loading conditions. Under compressor loading conditions, the lower-surface response magnitudes are smaller than the upper-surface values over the leading half chord. As the rotor loading changes from compressor to turbine conditions the response magnitudes increase greatly near the leading edge on the upper surface but remain relatively constant near midchord. The lower-surface response magnitudes are affected over a much larger portion of the chord, from the leading edge to 65 percent chord, and to a greater extent. Under turbine-loading conditions the response magnitudes of each surface are similar near the leading edge. The response phase angles are not greatly affected by rotor loading over the leading half chord and are approximately 180 deg out of phase near the leading edge. The response magnitudes and phase angles are approximately equal on each surface near the trailing edge, thus satisfying the Kutta condition.

The unsteady differential-pressure-coefficient magnitudes correlate well with the linear-theory predictions under compressor-loading conditions over the leading half chord. As neutral and turbine loading conditions are introduced the unsteady differential-pressure coefficients increase in magnitude and slope dramatically from the leading edge to the 65 percent chord. This behavior is dominated by the drastic increases in the lower-surface response. The abrupt increase in the 75 percent chord unsteady differential-pressure-coefficient magnitude is linked to the upper-surface response. The differential-pressure-coefficient phase angles are constant over the entire airfoil chord for neutral loading and constant over the leading half chord for turbine loading. The compressor unsteady differential-pressure-coefficient phase angles depend more upon chordwise position, decreasing with chord location over the leading half chord. The differential coefficients are strong functions of rotor-loading conditions near the trailing edge, which is linked to the more varied upper-surface response.

The effect of rotor-loading condition on the chordwise pressure response of the low-solidity symmetric-airfoil stator cascade is shown in Figs. 16, 17, and 18 for the high-reduced-frequency value. The upper-surface response trends are similar for all loading conditions from the leading edge to 65 percent chord. The response magnitudes decrease monotonically from the leading edge to the quarter chord then increase to 65 percent chord. Similar to the perforated-plate responses, the dip in the upper-surface response magnitude moves forward with reduced frequency, demonstrated by comparing Figs. 13-15 and 16-19. The upper-surface response phase angles are very similar for neutral and turbine loading conditions from the leading edge to 75 percent chord and are relatively constant near the leading edge. The upper-surface compressor-loading phase angles decrease near the leading edge. The upper-surface response phase angles are very similar for all rotor loading conditions from 45 percent chord to 65 percent chord. Over the aft quarter chord, the upper surface response trends are functions of rotor-loading conditions.

The lower-surface response magnitude trends are very similar for neutral and turbine-loading conditions. The response magnitudes decrease monotonically from the leading edge to the quarter chord, with a slight increase occurring at 35 percent chord followed by a monotonic decrease to 65 percent chord. The compressor-loading response magnitudes decrease monotonically from the leading edge to the quarter chord, then increase slightly to 75 percent chord. The lower-surface response phase angles are very similar for all rotor-loading conditions from the leading edge to 65 percent chord. Over the aft quarter chord, the response trends are functions of rotor-loading conditions.

The lower-surface unsteady pressure response magnitude is much more a function of rotor-loading than the upper-surface response magnitude. The lower-surface response magnitude increases greatly from the leading edge to the midchord as the rotor loading changes from compressor to turbine conditions. The upper-surface increases near the leading edge but to a much lesser extent. The upper-surface response magnitude is unaffected by rotor loading near the quarter chord. The response phase angles are relatively weak functions of rotor loading from the leading edge to 65 percent chord.

Under compressor loading conditions, the trend of the unsteady differential-pressure-coefficient magnitude data departs from the linear-theory prediction as evident by the dip at 25 percent chord. The compressor unsteady differential-pressure-coefficient phase angles are a strong function of chord position and also depart from the flat phase-angle prediction. The neutral and turbine unsteady differential-pressure-coefficient magnitude data follow the trend of the linear-theory prediction but are shifted to higher values for turbine-loading conditions. The unsteady differential-pressure-coefficient phase angles are relatively flat over the first 65 percent of the chord for neutral and turbine-loading conditions. Similar to the other chordwise response results, the changes in the unsteady differential pressure coefficients due to rotor-loading conditions are dominated by the response behavior of the lower surface.

Summary and Conclusions

The fundamental vortical gust modeling assumption has been investigated by means of a series of experiments performed in the Purdue Annular Cascade Research Facility. The unsteady periodic flow field is generated by rotating rows of perforated plates and airfoil cascades, with the resulting unsteady periodic chordwise pressure response of a downstream low solidity stator row determined by miniature pressure transducers embedded within selected airfoils. In an accompanying paper, it was shown that the perforated-plate forcing functions closely resemble linear-theory vortical gust forcing functions. In contrast, however, airfoil forcing functions exhibit characteristics far from linear-theory vortical gusts.

In this paper, the unsteady aerodynamic response of a low-solidity stator vane row was determined experimentally, with these data correlated with linear theory predictions. It was found that when the forcing function exhibited the characteristics of a linear-theory vortical gust, as was the case for the perforated-plate wake generators, the resulting response on the downstream stator airfoils was in excellent agreement with the linear-theory models. In contrast, when the forcing function did not exhibit linear-theory vortical gust characteristics, i.e., for the airfoil wake generators, the resulting unsteady aerodynamic responses of the downstream were much more complex and correlated poorly with the linear-theory vortical gust predictions.

Thus, this investigation has quantitatively shown that the forcing function generator significantly affects the resulting gust response, with the complexity of the response characteristics increasing from the perforated-plate to the airfoil-cascade forcing functions.

Acknowledgments

This research sponsored, in part, by the NASA Lewis Research Center. Both the financial support and the technical interchanges with Dr. Daniel Hoyniak are most gratefully acknowledged.

References

Abbott, I., and Von Doenhoff, A., 1959, *Theory of Wing Sections*, Dover Publications, New York.

Capece, V. R., Manwaring, S. R., and Fleeter, S., 1986, "Unsteady Blade Row Interactions in Multistage Compressor," *AIAA Journal of Propulsion*, Vol. 2, No. 2, pp. 168-174.

Capece, V. R., and Fleeter, S., 1987, "Unsteady Aerodynamic Interactions in a Multi-stage Compressor," ASME JOURNAL OF TURBOMACHINERY, Vol. 109, pp. 420-428.

Capece, V. R., and Fleeter, S., 1989, "Experimental Investigation of Multistage Interaction Gust Aerodynamics," ASME JOURNAL OF TURBOMACHINERY, Vol. 111, pp. 409-417.

Dring, R. P., Joslyn, H. D., Hardin, L. W., and Wagner, J. H., 1982, "Turbine Rotor-Stator Interaction," ASME *Journal of Engineering for Power*, Vol. 104, pp. 729-742.

Fleeter, S., Jay, R. L., and Bennett, W. A., 1978, "Rotor Wake Generated Unsteady Aerodynamic Response of a Compressor Stator," ASME *Journal of Engineering for Power*, Vol. 100, pp. 664-675.

Fleeter, S., Jay, R. L., and Bennett, W. A., 1980, "The Time-Variant Aerodynamic Response of a Stator Row Including the Effects of Airfoil Camber," ASME *Journal of Engineering for Power*, Vol. 102, pp. 334-343.

Fleeter, S., Jay, R. L., and Bennett, W. A., 1981, "Wake Induced Time-Variant Aerodynamics Including Rotor-Stator Axial Spacing Effects," ASME *Journal of Fluids Engineering*, Vol. 103, No. 1, pp. 59-66.

Franke, G. F., and Henderson, R. E., 1980, "Unsteady Stator Response to Upstream Rotor Wakes," *AIAA Journal of Aircraft*, Vol. 17, No. 7, pp. 500-506.

Gallus, H. E., Lambertz, J., and Wallmann, Th., 1980, "Blade-Row Interaction in an Axial-Flow Subsonic Compressor Stage," ASME *Journal of Engineering for Power*, Vol. 102, pp. 169-177.

Henderson, G. H., and Fleeter, S., 1993, "Forcing Function Effects on Unsteady Aerodynamic Gust Response, Part 1: Forcing Functions," ASME JOURNAL OF TURBOMACHINERY, Vol. 115, this issue, pp. 741-750.

Hodson, H. P., 1985, "An Inviscid Blade-to-Blade Prediction of a Wake-Generated Unsteady Flow," ASME *Journal of Engineering for Gas Turbines and Power*, Vol. 107, pp. 337-344.

Kim, K. H., and Fleeter, S., 1991, "Compressor Blade Gust Response to Attached & Separated Flow Forcing Functions," Notre Dame Report No. XX.

Manwaring, S. R., and Fleeter, S., 1991, "Forcing Function Effects on Rotor Periodic Aerodynamic Response," ASME JOURNAL OF TURBOMACHINERY, Vol. 113, pp. 312-319.

Smith, S. N., 1972, "Discrete Frequency Sound Generation in Axial Flow Turbomachines," R&M 3709, Aeronautical Research Council, United Kingdom.

chord. Similar to the perforated-plate responses, the dip in the upper-surface response magnitude moves forward with reduced frequency, demonstrated by comparing Figs. 13-15 and 16-19. The upper-surface response phase angles are very similar for neutral and turbine loading conditions from the leading edge to 75 percent chord and are relatively constant near the leading edge. The upper-surface compressor-loading phase angles decrease near the leading edge. The upper-surface response phase angles are very similar for all rotor loading conditions from 45 percent chord to 65 percent chord. Over the aft quarter chord, the upper surface response trends are functions of rotor-loading conditions.

The lower-surface response magnitude trends are very similar for neutral and turbine-loading conditions. The response magnitudes decrease monotonically from the leading edge to the quarter chord, with a slight increase occurring at 35 percent chord followed by a monotonic decrease to 65 percent chord. The compressor-loading response magnitudes decrease monotonically from the leading edge to the quarter chord, then increase slightly to 75 percent chord. The lower-surface response phase angles are very similar for all rotor-loading conditions from the leading edge to 65 percent chord. Over the aft quarter chord, the response trends are functions of rotor-loading conditions.

The lower-surface unsteady pressure response magnitude is much more a function of rotor-loading than the upper-surface response magnitude. The lower-surface response magnitude increases greatly from the leading edge to the midchord as the rotor loading changes from compressor to turbine conditions. The upper-surface increases near the leading edge but to a much lesser extent. The upper-surface response magnitude is unaffected by rotor loading near the quarter chord. The response phase angles are relatively weak functions of rotor loading from the leading edge to 65 percent chord.

Under compressor loading conditions, the trend of the unsteady differential-pressure-coefficient magnitude data departs from the linear-theory prediction as evident by the dip at 25 percent chord. The compressor unsteady differential-pressure-coefficient phase angles are a strong function of chord position and also depart from the flat phase-angle prediction. The neutral and turbine unsteady differential-pressure-coefficient magnitude data follow the trend of the linear-theory prediction but are shifted to higher values for turbine-loading conditions. The unsteady differential-pressure-coefficient phase angles are relatively flat over the first 65 percent of the chord for neutral and turbine-loading conditions. Similar to the other chordwise response results, the changes in the unsteady differential pressure coefficients due to rotor-loading conditions are dominated by the response behavior of the lower surface.

Summary and Conclusions

The fundamental vortical gust modeling assumption has been investigated by means of a series of experiments performed in the Purdue Annular Cascade Research Facility. The unsteady periodic flow field is generated by rotating rows of perforated plates and airfoil cascades, with the resulting unsteady periodic chordwise pressure response of a downstream low solidity stator row determined by miniature pressure transducers embedded within selected airfoils. In an accompanying paper, it was shown that the perforated-plate forcing functions closely resemble linear-theory vortical gust forcing functions. In contrast, however, airfoil forcing functions exhibit characteristics far from linear-theory vortical gusts.

In this paper, the unsteady aerodynamic response of a low-solidity stator vane row was determined experimentally, with these data correlated with linear theory predictions. It was found that when the forcing function exhibited the characteristics of a linear-theory vortical gust, as was the case for the perforated-plate wake generators, the resulting response on the downstream stator airfoils was in excellent agreement with the linear-theory models. In contrast, when the forcing function did not exhibit linear-theory vortical gust characteristics, i.e., for the airfoil wake generators, the resulting unsteady aerodynamic responses of the downstream were much more complex and correlated poorly with the linear-theory vortical gust predictions.

Thus, this investigation has quantitatively shown that the forcing function generator significantly affects the resulting gust response, with the complexity of the response characteristics increasing from the perforated-plate to the airfoil-cascade forcing functions.

Acknowledgments

This research sponsored, in part, by the NASA Lewis Research Center. Both the financial support and the technical interchanges with Dr. Daniel Hoyniak are most gratefully acknowledged.

References

Abbott, I., and Von Doenhoff, A., 1959, *Theory of Wing Sections*, Dover Publications, New York.

Capece, V. R., Manwaring, S. R., and Fleeter, S., 1986, "Unsteady Blade Row Interactions in Multistage Compressor," *AIAA Journal of Propulsion*, Vol. 2, No. 2, pp. 168-174.

Capece, V. R., and Fleeter, S., 1987, "Unsteady Aerodynamic Interactions in a Multi-stage Compressor," ASME JOURNAL OF TURBOMACHINERY, Vol. 109, pp. 420-428.

Capece, V. R., and Fleeter, S., 1989, "Experimental Investigation of Multistage Interaction Gust Aerodynamics," ASME JOURNAL OF TURBOMACHINERY, Vol. 111, pp. 409-417.

Dring, R. P., Joslyn, H. D., Hardin, L. W., and Wagner, J. H., 1982, "Turbine Rotor-Stator Interaction," ASME *Journal of Engineering for Power*, Vol. 104, pp. 729-742.

Fleeter, S., Jay, R. L., and Bennett, W. A., 1978, "Rotor Wake Generated Unsteady Aerodynamic Response of a Compressor Stator," ASME *Journal of Engineering for Power*, Vol. 100, pp. 664-675.

Fleeter, S., Jay, R. L., and Bennett, W. A., 1980, "The Time-Variant Aerodynamic Response of a Stator Row Including the Effects of Airfoil Camber," ASME *Journal of Engineering for Power*, Vol. 102, pp. 334-343.

Fleeter, S., Jay, R. L., and Bennett, W. A., 1981, "Wake Induced Time-Variant Aerodynamics Including Rotor-Stator Axial Spacing Effects," ASME *Journal of Fluids Engineering*, Vol. 103, No. 1, pp. 59-66.

Franke, G. F., and Henderson, R. E., 1980, "Unsteady Stator Response to Upstream Rotor Wakes," *AIAA Journal of Aircraft*, Vol. 17, No. 7, pp. 500-506.

Gallus, H. E., Lambertz, J., and Wallmann, Th., 1980, "Blade-Row Interaction in an Axial-Flow Subsonic Compressor Stage," ASME *Journal of Engineering for Power*, Vol. 102, pp. 169-177.

Henderson, G. H., and Fleeter, S., 1993, "Forcing Function Effects on Unsteady Aerodynamic Gust Response, Part 1: Forcing Functions," ASME JOURNAL OF TURBOMACHINERY, Vol. 115, this issue, pp. 741-750.

Hodson, H. P., 1985, "An Inviscid Blade-to-Blade Prediction of a Wake-Generated Unsteady Flow," ASME *Journal of Engineering for Gas Turbines and Power*, Vol. 107, pp. 337-344.

Kim, K. H., and Fleeter, S., 1991, "Compressor Blade Gust Response to Attached & Separated Flow Forcing Functions," Notre Dame Report No. XX.

Manwaring, S. R., and Fleeter, S., 1991, "Forcing Function Effects on Rotor Periodic Aerodynamic Response," ASME JOURNAL OF TURBOMACHINERY, Vol. 113, pp. 312-319.

Smith, S. N., 1972, "Discrete Frequency Sound Generation in Axial Flow Turbomachines," R&M 3709, Aeronautical Research Council, United Kingdom.

DISCUSSION

D. C. Wisler[1]

Dr. Henderson and Prof. Fleeter have conducted careful research in a difficult area that is of great importance to turbomachinery designers. Having read the paper with interest and having noted the novel method for presenting forcing functions in Part 1, we offer the following additional data and comments for the authors to consider.

---

[1] Aerodynamics Research Laboratory, GE Aircraft Engines, Cincinnati, OH 45215-6301.

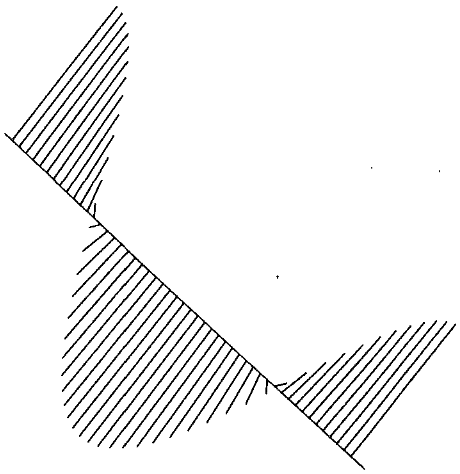

a) Low Loading, $\Phi_W=158.7^0$, $\Phi_D=-179.1^0$

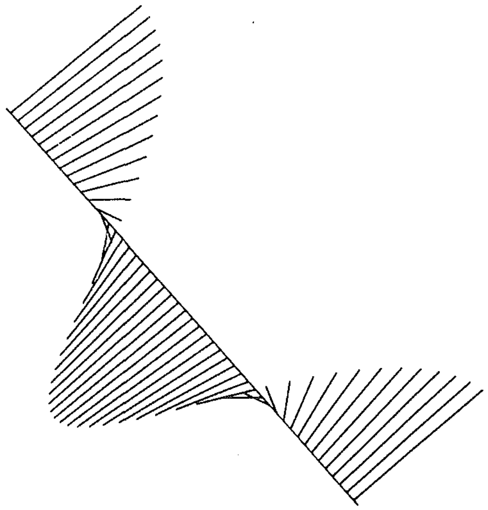

b) High Loading, $\Phi_W=-67.1^0$, $\Phi_D=-174.9^0$

Fig. 19 Vector representation of forcing function for the compressor, Φ_D nearly 180 deg, vectors parallel, gust vortical

Table 1 Gust characteristics

	LOADING	LINEAR ANALYSIS VALID	VORTICAL EFFECT PRESENT	POTENTIAL EFFECTS PRESENT	$\lvert\phi_W-180\rvert$ OR $\lvert\phi_W-0\rvert$	$\lvert\phi_D-180\rvert$ OR $\lvert\phi_D-0\rvert$
	LOW	YES	YES	NO	21.3	0.9
COMPRESSOR	DESIGN	YES	YES	NO	36.7	15.3
WAKES	HIGH	YES	YES	NO	67.1	5.1
TURBINE	LOW	YES	YES	YES	80.4	54.8
WAKES	DESIGN	YES	YES	YES	65.8	50.3

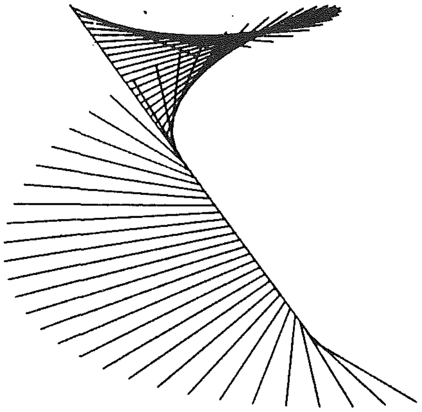

Fig. 20 Vector representation of forcing function for the turbine, design point, Φ_w = 114.2 deg, Φ_D = 129.7 deg (far from 180 deg), vectors not parallel, gust both vortical and potential

We reprocessed our data, which were presented recently in Manwaring and Wisler (1993), to display vector representations of the forcing function in the same manner as the authors do in their Part 1 Figs. 4–7, 9–14 and 17–19. The results are shown in Table 1 and Figs. 19 and 20.

The angles shown are: (1) ϕ_w, the phase angle between the streamwise and transverse gusts, and (2) ϕ_D, the phase angle of the coefficient D that gives the contribution of vortical disturbances to the forcing function, as described by Manwaring and Wisler (1993).

Dr. Henderson and Prof. Fleeter state that "For a linear-theory gust, the primary constraint is that $\phi_w = 0$ or 180 deg . . .". They then observe that when the primary constraint is satisfied, their gust vectors are parallel and their data are in good agreement with linear theory. When it is not satisfied, the gust vectors are not parallel, but misaligned, and agreement with linear theory is poor. This leads them to draw the following conclusions: ". . . airfoil wakes, both compressor and turbine, are not able to be modeled with the boundary conditions of current state-of-the-art linear unsteady aerodynamic theory" and "unfortunately for the turbomachine designer, airfoil-cascade forcing functions are much more complex. The airfoil forcing functions display characteristics far from linear-theory gusts."

Our data shown in Table 1 and in Figs. 19 and 20 and in our paper do not tend to support the conclusions described by Henderson and Fleeter. We found that current, state-of-the-art, linear, unsteady aerodynamic models do reasonably well in predicting the unsteady loading for the compressor and turbine cases we tested. This finding did not depend upon whether ϕ_w was near 0 or 180 deg, as shown in Table 1, or whether the gust vectors were parallel. In fact the linear theory was valid for the nonparallel vectors of Fig. 20.

However, we did find a relevant correlation between the phase angle ϕ_D and the shape of the vector representation of the forcing function. When ϕ_D was near 0 or 180 deg as seen for the compressor wakes in Table 1, only vortical effects were present in the forcing function and the vectors were nearly parallel, as seen in Fig. 19. When ϕ_D was not near 0 or 180 deg, as seen for the turbine wakes in Table 1, *both* vortical and potential effects were present in the forcing function and the vectors were not parallel but misaligned, as seen in Fig. 20. Note that our Fig. 19 is similar to the authors' Figs. 4–7 and our Fig. 20 is similar to their Fig. 9.

Consequently we come to different conclusions than the authors. We find that linear analysis of the unsteady flowfield yields reasonably accurate predictions of unsteady loading in many turbomachinery cases. We think that the differences in question are related to vortical and potential effects in the forcing function and to the need to use appropriate models rather than to a linearization feature of the unsteady model.

References

Manwaring, S. R., and Wisler, D. C., 1993, "Unsteady Aerodynamics and Gust Response in Compressors and Turbines," ASME JOURNAL OF TURBOMACHINERY, Vol. 115, this issue, pp. 724–740.

N. A. Cumpsty[2]

The estimation of unsteady forces and moments on blades remains one of the difficult problems in turbomachinery and

---

[2] Whittle Laboratory, Cambridge University, Cambridge, United Kingdom.

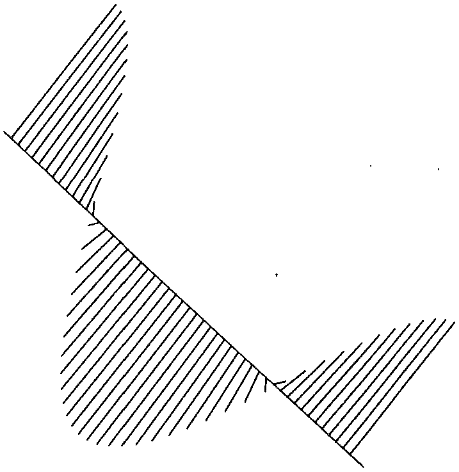

a) Low Loading, $\Phi_W=158.7^0$, $\Phi_D=-179.1^0$

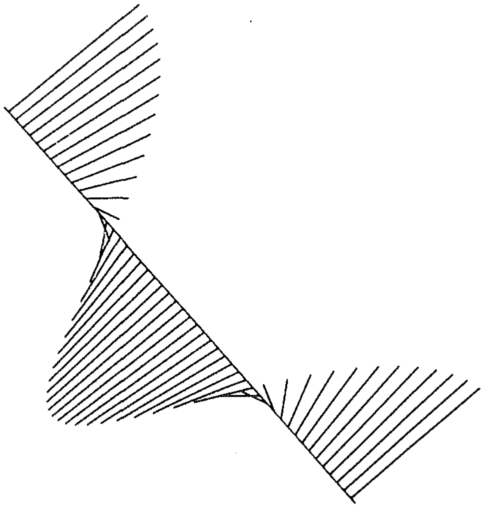

b) High Loading, $\Phi_W=-67.1^0$, $\Phi_D=-174.9^0$

Fig. 19 Vector representation of forcing function for the compressor, Φ_D nearly 180 deg, vectors parallel, gust vortical

We reprocessed our data, which were presented recently in Manwaring and Wisler (1993), to display vector representations of the forcing function in the same manner as the authors do in their Part 1 Figs. 4–7, 9–14 and 17–19. The results are shown in Table 1 and Figs. 19 and 20.

The angles shown are: (1) ϕ_w, the phase angle between the streamwise and transverse gusts, and (2) ϕ_D, the phase angle of the coefficient D that gives the contribution of vortical disturbances to the forcing function, as described by Manwaring and Wisler (1993).

Dr. Henderson and Prof. Fleeter state that "For a linear-theory gust, the primary constraint is that ϕ_w = 0 or 180 deg . . .". They then observe that when the primary constraint is satisfied, their gust vectors are parallel and their data are in good agreement with linear theory. When it is not satisfied, the gust vectors are not parallel, but misaligned, and agreement with linear theory is poor. This leads them to draw the following conclusions: ". . . airfoil wakes, both compressor and turbine, are not able to be modeled with the boundary conditions of current state-of-the-art linear unsteady aerodynamic theory" and "unfortunately for the turbomachine designer, airfoil-cascade forcing functions are much more complex. The airfoil forcing functions display characteristics far from linear-theory gusts."

Table 1 Gust characteristics

	LOADING	LINEAR ANALYSIS VALID	VORTICAL EFFECT PRESENT	POTENTIAL EFFECTS PRESENT	$\lvert\phi_W-180\rvert$ OR $\lvert\phi_W-0\rvert$	$\lvert\phi_D-180\rvert$ OR $\lvert\phi_D-0\rvert$
	LOW	YES	YES	NO	21.3	0.9
COMPRESSOR	DESIGN	YES	YES	NO	36.7	15.3
WAKES	HIGH	YES	YES	NO	67.1	5.1
TURBINE	LOW	YES	YES	YES	80.4	54.8
WAKES	DESIGN	YES	YES	YES	65.8	50.3

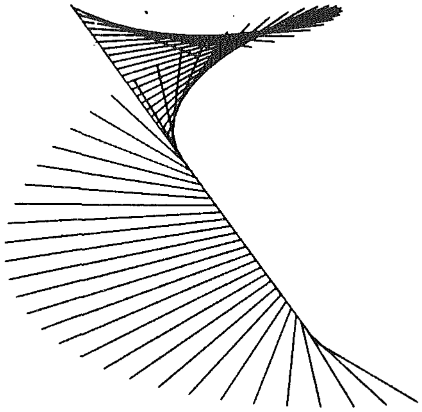

Fig. 20 Vector representation of forcing function for the turbine, design point, Φ_w = 114.2 deg, Φ_D = 129.7 deg (far from 180 deg), vectors not parallel, gust both vortical and potential

Our data shown in Table 1 and in Figs. 19 and 20 and in our paper do not tend to support the conclusions described by Henderson and Fleeter. We found that current, state-of-the-art, linear, unsteady aerodynamic models do reasonably well in predicting the unsteady loading for the compressor and turbine cases we tested. This finding did not depend upon whether ϕ_w was near 0 or 180 deg, as shown in Table 1, or whether the gust vectors were parallel. In fact the linear theory was valid for the nonparallel vectors of Fig. 20.

However, we did find a relevant correlation between the phase angle ϕ_D and the shape of the vector representation of the forcing function. When ϕ_D was near 0 or 180 deg as seen for the compressor wakes in Table 1, only vortical effects were present in the forcing function and the vectors were nearly parallel, as seen in Fig. 19. When ϕ_D was not near 0 or 180 deg, as seen for the turbine wakes in Table 1, *both* vortical and potential effects were present in the forcing function and the vectors were not parallel but misaligned, as seen in Fig. 20. Note that our Fig. 19 is similar to the authors' Figs. 4–7 and our Fig. 20 is similar to their Fig. 9.

Consequently we come to different conclusions than the authors. We find that linear analysis of the unsteady flowfield yields reasonably accurate predictions of unsteady loading in many turbomachinery cases. We think that the differences in question are related to vortical and potential effects in the forcing function and to the need to use appropriate models rather than to a linearization feature of the unsteady model.

References

Manwaring, S. R., and Wisler, D. C., 1993, "Unsteady Aerodynamics and Gust Response in Compressors and Turbines," ASME JOURNAL OF TURBOMACHINERY, Vol. 115, this issue, pp. 724–740.

N. A. Cumpsty[2]

The estimation of unsteady forces and moments on blades remains one of the difficult problems in turbomachinery and

---

[2] Whittle Laboratory, Cambridge University, Cambridge, United Kingdom.

the two papers by Henderson and Fleeter contain the fruits of much hard work and careful experimentation. The approach adopted, in which simple disturbances are allowed to interact with a downstream blade row, may be termed traditional. The analytical method with which the measurements are compared was written by Smith (1972) more than twenty years ago. The authors were therefore most unfortunate to publish these papers when the work by Manwaring and Wisler (1993) was about to appear, since they were unable to adapt their papers to either the new measurements and computation methods used by Manwaring and Wisler or to the conclusions drawn. Manwaring and Wisler, in a very extensive and impressive paper, showed unsteady measurements made in a low-speed compressor and turbine, each of which had geometry and loading representative of current aeroengine practice. These measurements were compared with a total of five different unsteady prediction methods, several very recent and one of which is nonlinear. Most significantly it appears that a linear approximation for the unsteady flow is good in a wide range of flows and the discrepancies found in the past are not associated with linearization, even for the interaction of closely spaced blade rows. It seems to me that the entire topic has been altered by Manwaring and Wisler's paper.

I therefore wonder whether Dr. Henderson and Professor Fleeter would like to modify the abstracts and conclusions of their papers in the light of Manwaring and Wisler. Would they, for example, like to modify their conclusion in Part 1 concerning the ability of linear unsteady aerodynamic theory to predict the unsteady behavior. Similarly the conclusion regarding the linear theory in Part 2 could with advantage be altered. I would also like to suggest that the term "linear-gust" be dropped. As Manwaring and Wisler show, the cases that allow reasonable prediction with the very simple theory are those having a primarily vortical inlet perturbation and the amplitude of the perturbation does not seem to be the limiting quantity. When potential interactions are present, as they generally are with loaded blade rows closely spaced, a more complete specification of the inlet conditions is necessary, but linear theory can still predict reasonably well what is measured.

The presence of a significant potential velocity perturbation is revealed by the phase angle between the streamwise and normal components of the combined velocity perturbation (the sum of the potential and vortical perturbations). A purely vortical disturbance corresponds to a perturbation in velocity parallel to the undisturbed flow; such a disturbance requires that the streamwise and normal components to be either in phase or in antiphase, i.e., 0 or 180 deg apart. The streamwise and normal components for a potential perturbation are 90 deg apart. If the amplitude of the potential disturbance is very small the phase angle between the streamwise and normal components of the combined velocity perturbation will approximate 0 or 180 deg.

Authors' Closure

The authors concur with the intent of the statements of Wisler and Cumpsty. The confusion is a matter of semantics. At the time of our paper, Giles decomposition of the forcing function into a vortical and potential part had not been published and classical linear unsteady aerodynamic theories did not include provisions for decomposing measured forcing functions into vortical and potential components. The authors were certainly aware of linear theories that modeled vortical disturbances and potential disturbances.

However, the method of decomposing a measured forcing function into these components was not widely known. At the time, the authors and much of the unsteady aerodynamics community considered theories that modeled only wakes or vortical disturbances as the state-of-the-art since this was considered to be the dominant forcing function for a downstream blade row. Giles provided a much needed contribution: a method of decomposing a measured forcing function, thereby enabling the unsteady force acting on a downstream blade row to be calculated from the individual vortical and potential parts.

The objective of our research was to point out the shortcomings of the vortical-only analyses. Henderson and Fleeter (1991) introduced the importance of the gust or disturbance component phase, and showed experimentally that when this phase angle was 0 or 180 deg, the velocity vectors were parallel to the time-averaged flow field and that no static pressure gradient, i.e., potential field, was present, the requirement for a vortical-only disturbance. When the disturbance component phase angle is neither 0 or 180 deg, the disturbance velocity vectors were not parallel to the time-averaged flow field and a static pressure gradient, i.e., potential field, was measured. Our results show that linear theories that model vortical disturbances are valid when a pure vortical disturbance is present, but the vortical-only linear theory is lacking when the disturbance contains a potential component. In fact, we suggested that the analysis could be improved by modeling the potential component of the gust and incorporating it into the analysis. Had we been privy to the Giles decomposition method, a better correlation of the resulting unsteady pressure and lift on the downstream vane row would have been obtained by superpositioning of the vortical and potential solutions, obtained for example from Smith (1972) or other unsteady aerodynamic analyses.

It should be noted that Giles splitting of the measured gust into vortical and potential components was implemented by Manwaring and Wisler utilizing unsteady velocity data only. However, although vortical gusts only involve velocity fluctuations, potential gusts are characterized by static pressure fluctuations as well. Thus the data analysis technique of Manwaring and Wislers attributed any violation of the vortical gust constraints to the presence of an unsteady potential perturbation. However, these constraints can be violated by effects not modeled by linear theory, such as momentum diffusion in the wake. In addition, any experimental error that affects the measured unsteady velocity field directly affects the calculated unsteady potential field. Thus, linear theory gusts reconstructed from the components calculated using only velocity fluctuations may yield erroneous static pressure perturbations.

References

Henderson, G., and Fleeter, S., 1991, "Forcing Function Effects on Low Solidity Cascade Gust Response Unsteady Aerodynamics," *Proceedings of the 6th International Symposium on Unsteady Aerodynamics, Aeroacoustics and Aeroelasticity of Turbomachines and Propellers*, University of Notre Dame, IN.

the two papers by Henderson and Fleeter contain the fruits of much hard work and careful experimentation. The approach adopted, in which simple disturbances are allowed to interact with a downstream blade row, may be termed traditional. The analytical method with which the measurements are compared was written by Smith (1972) more than twenty years ago. The authors were therefore most unfortunate to publish these papers when the work by Manwaring and Wisler (1993) was about to appear, since they were unable to adapt their papers to either the new measurements and computation methods used by Manwaring and Wisler or to the conclusions drawn. Manwaring and Wisler, in a very extensive and impressive paper, showed unsteady measurements made in a low-speed compressor and turbine, each of which had geometry and loading representative of current aeroengine practice. These measurements were compared with a total of five different unsteady prediction methods, several very recent and one of which is nonlinear. Most significantly it appears that a linear approximation for the unsteady flow is good in a wide range of flows and the discrepancies found in the past are not associated with linearization, even for the interaction of closely spaced blade rows. It seems to me that the entire topic has been altered by Manwaring and Wisler's paper.

I therefore wonder whether Dr. Henderson and Professor Fleeter would like to modify the abstracts and conclusions of their papers in the light of Manwaring and Wisler. Would they, for example, like to modify their conclusion in Part 1 concerning the ability of linear unsteady aerodynamic theory to predict the unsteady behavior. Similarly the conclusion regarding the linear theory in Part 2 could with advantage be altered. I would also like to suggest that the term "linear-gust" be dropped. As Manwaring and Wisler show, the cases that allow reasonable prediction with the very simple theory are those having a primarily vortical inlet perturbation and the amplitude of the perturbation does not seem to be the limiting quantity. When potential interactions are present, as they generally are with loaded blade rows closely spaced, a more complete specification of the inlet conditions is necessary, but linear theory can still predict reasonably well what is measured.

The presence of a significant potential velocity perturbation is revealed by the phase angle between the streamwise and normal components of the combined velocity perturbation (the sum of the potential and vortical perturbations). A purely vortical disturbance corresponds to a perturbation in velocity parallel to the undisturbed flow; such a disturbance requires that the streamwise and normal components to be either in phase or in antiphase, i.e., 0 or 180 deg apart. The streamwise and normal components for a potential perturbation are 90 deg apart. If the amplitude of the potential disturbance is very small the phase angle between the streamwise and normal components of the combined velocity perturbation will approximate 0 or 180 deg.

Authors' Closure

The authors concur with the intent of the statements of Wisler and Cumpsty. The confusion is a matter of semantics. At the time of our paper, Giles decomposition of the forcing function into a vortical and potential part had not been published and classical linear unsteady aerodynamic theories did not include provisions for decomposing measured forcing functions into vortical and potential components. The authors were certainly aware of linear theories that modeled vortical disturbances and potential disturbances.

However, the method of decomposing a measured forcing function into these components was not widely known. At the time, the authors and much of the unsteady aerodynamics community considered theories that modeled only wakes or vortical disturbances as the state-of-the-art since this was considered to be the dominant forcing function for a downstream blade row. Giles provided a much needed contribution: a method of decomposing a measured forcing function, thereby enabling the unsteady force acting on a downstream blade row to be calculated from the individual vortical and potential parts.

The objective of our research was to point out the shortcomings of the vortical-only analyses. Henderson and Fleeter (1991) introduced the importance of the gust or disturbance component phase, and showed experimentally that when this phase angle was 0 or 180 deg, the velocity vectors were parallel to the time-averaged flow field and that no static pressure gradient, i.e., potential field, was present, the requirement for a vortical-only disturbance. When the disturbance component phase angle is neither 0 or 180 deg, the disturbance velocity vectors were not parallel to the time-averaged flow field and a static pressure gradient, i.e., potential field, was measured. Our results show that linear theories that model vortical disturbances are valid when a pure vortical disturbance is present, but the vortical-only linear theory is lacking when the disturbance contains a potential component. In fact, we suggested that the analysis could be improved by modeling the potential component of the gust and incorporating it into the analysis. Had we been privy to the Giles decomposition method, a better correlation of the resulting unsteady pressure and lift on the downstream vane row would have been obtained by superpositioning of the vortical and potential solutions, obtained for example from Smith (1972) or other unsteady aerodynamic analyses.

It should be noted that Giles splitting of the measured gust into vortical and potential components was implemented by Manwaring and Wisler utilizing unsteady velocity data only. However, although vortical gusts only involve velocity fluctuations, potential gusts are characterized by static pressure fluctuations as well. Thus the data analysis technique of Manwaring and Wislers attributed any violation of the vortical gust constraints to the presence of an unsteady potential perturbation. However, these constraints can be violated by effects not modeled by linear theory, such as momentum diffusion in the wake. In addition, any experimental error that affects the measured unsteady velocity field directly affects the calculated unsteady potential field. Thus, linear theory gusts reconstructed from the components calculated using only velocity fluctuations may yield erroneous static pressure perturbations.

References

Henderson, G., and Fleeter, S., 1991, "Forcing Function Effects on Low Solidity Cascade Gust Response Unsteady Aerodynamics," *Proceedings of the 6th International Symposium on Unsteady Aerodynamics, Aeroacoustics and Aeroelasticity of Turbomachines and Propellers*, University of Notre Dame, IN.

An Analysis System for Blade Forced Response

Hsiao-Wei D. Chiang

R. E. Kielb

GE Aircraft Engines,
Cincinnati, OH 45215

A frequent cause of turbomachinery blade failure is excessive resonant response. The most common excitation source is the nonuniform flow field generated by inlet distortion, wakes and/or pressure disturbances from adjacent blade rows. The standard method for dealing with this problem is to avoid resonant conditions using a Campbell diagram. Unfortunately, it is impossible to avoid all resonant conditions. Therefore, judgments based on past experience are used to determine the acceptability of the blade design. A new analysis system has been developed to predict blade forced response. The system provides a design tool, over and above the standard Campbell diagram approach, for predicting potential forced response problems. The incoming excitation sources are modeled using a semi-empirical rotor wake/vortex model for wake excitation, measured data for inlet distortion, and a quasi-three-dimensional Euler code for pressure disturbances. Using these aerodynamic stimuli, and the blade's natural frequencies and mode shapes from a finite element model, the unsteady aerodynamic modal forces and the aerodynamic damping are calculated. A modal response solution is then performed. This system has been applied to current engine designs. A recent investigation involved fan blade response due to inlet distortion. An aeromechanical test had been run with two different distortion screens. The resulting distortion entering the fan was measured. With this as input data, the predicted response agreed almost exactly with the measured response. In another application, the response of the LPT blades of a counterrotating supersonic turbine was determined. In this case the blades were excited by both a wake and a shock wave. The shock response was predicted to be three times larger than that of the wake. Thus, the system identified a new forcing function mechanism for supersonic turbines. This paper provides a basic description of the system, which includes: (1) models for the wake excitation, inlet distortion, and pressure disturbance; (2) a kernel function solution technique for unsteady aerodynamics; and (3) a modal aeroelastic solution using strip theory. Also, results of the two applications are presented.

Introduction

Preventing turbomachinery blade failures is a necessary goal for the engine manufacturer. The benefits are decreased development time and cost, lower maintenance costs, and fewer operational restrictions. To this end, it is essential to prevent excessive vibration in turbomachinery blading due to forced response. The current state-of-the-art design technique for estimating the forced response of turbomachinery blading is deficient in terms of quantitatively predicting blade response levels. The Campbell diagram method of estimating the occurrence of forced response problems can only indicate the likelihood of encountering a significant resonant condition. Therefore, a forced response prediction system that can predict the actual level of vibratory stress is key for improved advanced turbomachinery blade design.

Forced response is caused primarily by turbomachinery blading operating in nonuniform flow fields. As a result, unsteady aerodynamic forces and moments are generated on the blading. When the frequency of these aerodynamic forces and moments is equal to a blade's natural frequency, a marked increase in blade vibratory response usually occurs. When the vibration levels exceed the material endurance limits, high cycle fatigue failure soon results.

The standard method for dealing with blade forced response is to avoid resonant conditions. A Campbell diagram is used to determine when the blade natural frequency is coincident with the excitation frequency. This system would be entirely adequate if all resonant conditions could be avoided. Unfortunately, this is impossible. Therefore, judgments based on past experience must be used to determine the acceptability of a blade design. To help remedy this situation a forced response prediction system was developed. The objective was to provide a design tool, in addition to Campbell diagrams, for analyzing forced response problems.

The forced response prediction system consists of three parts: (1) flow defect modeling, (2) unsteady aerodynamics for gust response and aerodynamic damping, and (3) aeroelastic modal

---

Contributed by the International Gas Turbine Institute and presented at the 37th International Gas Turbine and Aeroengine Congress and Exposition, Cologne, Germany, June 1-4, 1992. Manuscript received by the International Gas Turbine Institute February 17, 1992. Paper No. 92-GT-172. Associate Technical Editor: L. S. Langston.

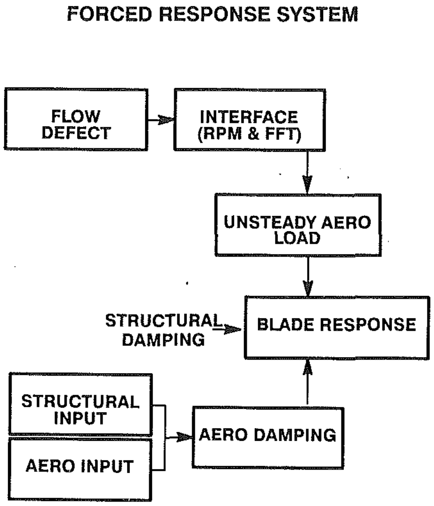

Fig. 1 Flow chart for forced response analysis system

solution for blade response. The flow chart for the system is shown in Fig. 1.

Flow defects due to wake disturbances can be determined from measured wake data, empirical curve-fit wake modeling, or analytical CFD viscous wake modeling. Examples of wake data can be found in: Durali (1980); Gallus et al. (1980); Hobbs et al. (1982); Shreeve and Neuhoff (1983); Binder et al. (1985); Pfeil and Sieber (1986); Lakshminarayana and Zhang (1987); Manwaring and Fleeter (1993); and Gallus et al. (1991). Empirical models are from Mugridge and Morfey (1972), Raj and Lakshminarayana (1973), Kemp and Sears (1955), Korakianitis (1988b), and Majjigi and Gliebe (1984). Warfield and Lakshminarayana (1987) used a Navier–Stokes program with a turbulence model to predict the wake formation behind an airfoil cascade. Potential disturbances have been modeled either with classical small disturbance theory (Kemp and Sears, 1953; Osborne, 1973; Taylor and Ng, 1987; Korakianitis, 1988a) or with CFD methods using potential, Euler, and Navier–Stokes solutions. Taylor and Ng showed good agreement between experiment and analytical predictions.

In this paper, the incoming excitation sources are modeled using a semi-empirical rotor wake/vortex model (Majjigi and Gliebe, 1984) for wake excitation, measured data for inlet distortion, and a quasi-three-dimensional Euler code (Holmes et al., 1988) for pressure disturbances. Using these aerodynamic stimuli, the unsteady aerodynamic modal forces are calculated using unsteady gust response models.

For unsteady gust response aerodynamic models, most of the classical approaches assume a vortical gust being convected through the cascade undisturbed by the surrounding flow (referred to as the "frozen gust" assumption). Whitehead's (1970) subsonic code, Fleeter's (1973) subsonic code, and Nagashima and Whitehead's (1977) supersonic code all use the frozen gust assumption. Goldstein and Atassi (1976) extended the frozen gust assumption to a "distorted" gust model, i.e., the gust interacts with the surrounding flow; however, this was limited to an isolated airfoil in an incompressible flow. Recent CFD approaches to gust response range from linearized Euler codes (Verdon and Hall, 1990; Verdon et al., 1991; Hall and Verdon, 1990; Hall and Clark, 1991; Holmes and Chuang, 1991; Kahl and Klose, 1991), to full nonlinear Euler methods (Giles, 1986; Fransson and Pandolfi, 1986; Gerolymos, 1988; Jorgenson and Chima, 1988; Oden and Bass, 1989; Janes and Whitfield, 1989), to a full nonlinear Navier–Stokes method (Rai, 1987).

Aerodynamic damping analyses commonly utilize the same models as the gust analyses. One of the first investigations of classical motion-dependent unsteady aerodynamics was reported by Whitehead (1960) for incompressible flow. Atassi and Akai (1978) extended the Whitehead model to include steady loading effects. Later extensions were Whitehead (1970) for subsonic flow and Nagashima and Whitehead (1977), Adamczyk and Goldstein (1978), and Verdon and McCune (1975), for supersonic flow. Bendiksen (1986) included steady loading and shock motion. Williams and Hwang (1986) extended the two-dimensional assumption to three dimensions for subsonic propellers. CFD approaches to motion-dependent unsteady aerodynamics include linearized potential codes (Ni and Sisto, 1976; Verdon and Caspar, 1984; Whitehead, 1982), linearized Euler codes (Hall and Crawley, 1987; Hall and Clark, 1991; Holmes and Chuang, 1991; Kahl and Klose, 1991), full nonlinear Euler methods (Fransson and Pandolfi, 1986; Gerolymos, 1988), and a full nonlinear Navier–Stokes method (Sankar and Tang, 1985).

The CFD models provide improved accuracy; however, they are less desirable for a design analysis system due to the excessive computational time and memory required. In this paper, both the gust response and the motion-dependent unsteady aerodynamic models are based on Kirsch's (1990) classical two-dimensional kernel function approach for subsonic, transonic, and supersonic unsteady aerodynamics. This method is similar to Whitehead (1970) for subsonic flow and Nagashima and Whitehead (1977) for supersonic flow but includes small steady loading effects, strong shock effects, and uses the "frozen-gust" assumption (Holt and Kirsch, 1981).

Until 1980, the aeroelastic models were mainly based on energy methods (Carta, 1967; Snyder and Commerford, 1974; Mikolajczak et al., 1975), where the blades were assumed to vibrate in a single-degree-of-freedom mode. However, during the 1980s, the lumped parameter two-degree-of-freedom model became a common approach for aeroelastic analysis. This approach uses a typical section along the span of a blade with one bending and one torsional degree of freedom (Bendiksen and Friedmann, 1980). Later Kaza and Kielb (1984, 1985) introduced a beam structural dynamic model to incorporate the three-dimensional properties of a blade including centrifugal stiffening effects. Aeroelastic modal analysis based on the finite element method was introduced by Turnberg (1983). He used the mode shapes and frequencies from the finite element modal analysis to determine the unsteady aerodynamic forces acting at several strips along the span of a blade. Crawley (1988) summarized an aeroelastic formulation for both tuned and mistuned rotors using a modal analysis approach. Kaza et al. (1989) extended the modal analysis to include a three-

Nomenclature

b = blade semichord
$\{F_m(t)\}$ = motion-dependent unsteady aerodynamic forces
$\{F_g(t)\}$ = gust response unsteady aerodynamic forces
$[G]$ = blade damping matrix
$[G_m]$ = generalized damping matrix
$[K]$ = blade stiffness matrix
$[K_m]$ = generalized stiffness matrix
k = reduced frequency $= \omega b/U$
$[M]$ = blade mass matrix
$[M_m]$ = generalized mass matrix
$\{Q(t)\}$ = modal displacement
U = uniform mean flow velocity
$\{X\}$ = physical displacements
β = interblade phase angle
$[\phi]$ = $n \times m$ mode shape matrix
ω = blade natural frequency

dimensional unsteady aerodynamic theory. Srinivasan and Fabunmi (1984) and Smith (1990) developed modal solutions, which couple finite element models with two-dimensional linearized unsteady aerodynamic theories.

The aeroelastic models described above assume all blades of a bladed disk are identical. However, this is not the case in practice. The simplest method for considering the mistuning effect is to conduct a tuned forced response analysis and to use previous experience to define a mistuning magnification factor. For modeling a mistuned blade disk many of the methods described above for tuned systems have been extended. Some examples are Whitehead (1965, 1966), Huang (1982), Srinivasan and Fabunmi (1984), Kaza and Kielb (1984), Afolabi (1988), and Griffin (1988).

In this paper, a modal aeroelastic model was utilized to simulate the three-dimensional aeroelastic effects by calculating the unsteady aerodynamic loads on two-dimensional strips, which are stacked from hub to tip along the span of the blade. This model assumes a "tuned" rotor such that all the blades in the rotor have identical frequencies and mode shapes (i.e., no mistuning effects are included).

This forced response prediction system has been applied to current engine designs. A recent study was made involving fan blade response due to inlet distortion. An aeromechanical test had been run with two different distortion screens. The resulting distortions entering the fan were measured. A finite element model was used to determine the blade's natural frequencies and mode shapes. The structural damping was estimated from measured data. Another application was to determine the response of the LPT blades of a counterrotating supersonic turbine. In this case the blades were excited by both a wake and a shock wave.

Analysis System

Dynamic Equations of Motion. The well-known dynamic equations of motion can be expressed as a system of equations for the n degrees of freedom of the system:

$$[M]\{\ddot{X}\} + [G]\{\dot{X}\} + [K]\{X\} = \{F_m(t)\} + \{F_g(t)\} \tag{1}$$

The $[M]$, $[G]$, and $[K]$ matrices represent the inertia, damping, and stiffness properties of the blade with $\{X\}$ being the n-degree-of-freedom displacements. In this equation, we assume that all the blades in a blade row are vibrating as a tuned rotor such that every blade has identical frequencies and mode shapes. (Refer to Kaza and Kielb, 1984, 1985, for the dynamic equations of motion for a mistuned rotor.) The forcing terms on the right-hand side of Eq. (1) represent the motion-dependent unsteady aerodynamic forces $\{F_m(t)\}$ and the gust response unsteady aerodynamic forces $\{F_g(t)\}$.

The solution of the undamped homogeneous form of Eq. (1) results in the set of modal properties, which are the frequencies and mode shapes for m modes. Using these modal properties, the displacements $\{X\}$ can be expressed as

$$\{X(t)\} = [\phi]\{Q(t)\} \tag{2}$$

$[\phi]$ is the $n \times m$ mode shape matrix and $\{Q(t)\}$ is the modal displacement. Substitution of Eq. (2) into Eq. (1), and premultiplying by $[\phi]^T$, the transpose of the modal matrix, results in the modal equation of motion below:

$$[M_m]\{\ddot{Q}\} + [G_m]\{\dot{Q}\} + [K_m]\{Q\} = [\phi]^T(\{F_m(t)\} + \{F_g(t)\}) \tag{3}$$

$[M_m]$ and $[K_m]$ are the generalized mass and stiffness matrices. $[G_m]$ is the generalized damping matrix, which, in general, is a full matrix. Here, this damping matrix is assumed to be a diagonal matrix consisting of modal damping coefficients.

By assuming simple harmonic motion, the modal displacement $\{Q(t)\}$ can be expressed as

$$\{Q(t)\} = \{\bar{Q}\}e^{i\omega t} \tag{4}$$

The motion-dependent unsteady aerodynamic forces $\{F_m(t)\}$ and the gust response unsteady aerodynamic forces $\{F_g(t)\}$ can be put in the form

$$\{F_m(t)\} = [A]\{\bar{Q}\}e^{i\omega t} \tag{5}$$

$$\{F_g(t) = \{\bar{F}_g\}e^{i\omega t} \tag{6}$$

where $[A]$ represents the unsteady aerodynamic forces due to harmonic motion of the blade and $\{\bar{F}_g\}$ represents the unsteady aerodynamic forces acting on the rigid blade due to a sinusoidal gust.

After substituting Eqs. (4), (5), and (6) into (3) and dividing by $e^{i\omega t}$,

$$-\omega^2[M_m]\{\bar{Q}\} + i\omega[G_m]\{\bar{Q}\} + [K_m]\{\bar{Q}\} = [\phi]^T([A]\{\bar{Q}\} + \{\bar{F}_g\}) \tag{7}$$

where $[A]$ can be obtained using the unsteady aerodynamic program with input of mode shapes and frequencies provided by a finite element vibratory analysis. $\{\bar{F}_g\}$ is calculated using the same unsteady aerodynamic program with input from a flow defect model.

Flow Defect Models. To predict dynamic stress levels, flow fields must be identified and analyzed. The three major types of aerodynamic forcing functions that cause forced response problems in turbomachinery blading are inlet distortions, wake disturbances, and potential disturbances.

Inlet distortion is usually caused by cross wind, atmospheric gusts, wakes from upstream wings and pylons, and nonuniform inlets. These distortions are mainly total pressure distortions, which can be measured or modeled using CFD methods. In the application shown herein, the distortions due to the screens are determined from measured data.

Wake disturbance is also a total pressure distortion, usually from upstream blade trailing edge wakes. Wake disturbances can be obtained from measured data, from empirical curve-fit wake modeling, or from analytical CFD viscous wake modeling. In this paper, a semi-empirical rotor wake/vortex analysis program is utilized to model the upstream wakes including the tip vortex (Majjigi and Gliebe, 1984). In particular, the Mugridge and Morfey (1972) wake model, and Kemp and Sears model (1955), and a linear rational model by Majjigi and Gliebe (1984) are available in this program. Based on a comparison of the three model predictions with experimental data conducted by Kim (1991), the linear rational model shows somewhat better agreement, and therefore is used in this paper. Also available in this program is a tip clearance vortex model, which consists of a forced vortex core and surrounding free vortex for the tip vortices.

Potential disturbances are static pressure distortions and can be reasonably modeled using inviscid CFD methods (like an Euler code) or also can be from measured data. Unlike inlet distortions and wake disturbances, which always come from upstream, potential disturbances can be from either upstream or downstream. However, in this paper, the potential disturbance due to upstream trailing edge shocks is considered, and is modeled using a quasi-three-dimensional Euler code that includes stream tube contraction (Holmes et al., 1988).

Once these circumferential flow defects are obtained, they are transformed into the rotating blade coordinate system, and Fourier transformed for the desired harmonic. For inlet distortion, with the total pressure distortion data as input, an inlet distortion harmonic analysis program is run to Fourier transform the distortion into unsteady velocity perturbations for the harmonic components of interest. This program uses an empirical correlation between the static pressure distortion and the total pressure distortion based on Mokelke (1979). The distortion-induced tangential velocity can be calculated using the tangential static pressure distribution and the momentum equation. The unsteady velocity perturbation (gust) is then

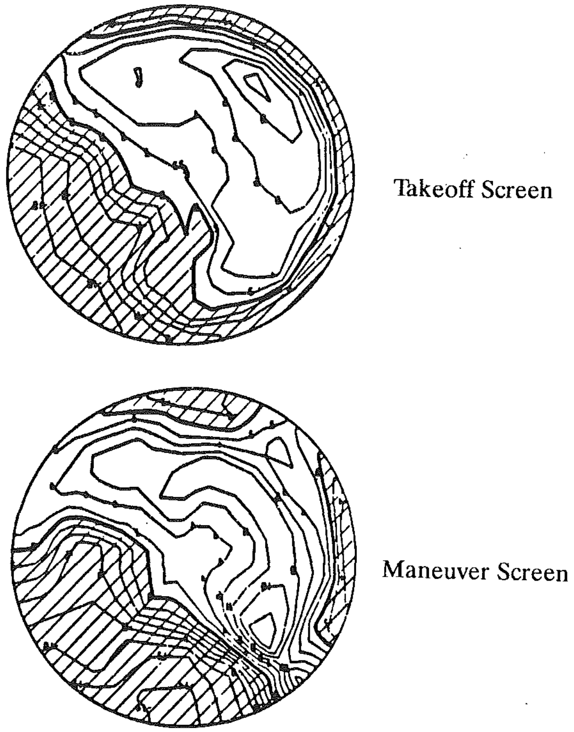

Fig. 2 Total pressure contours for takeoff and maneuver screens

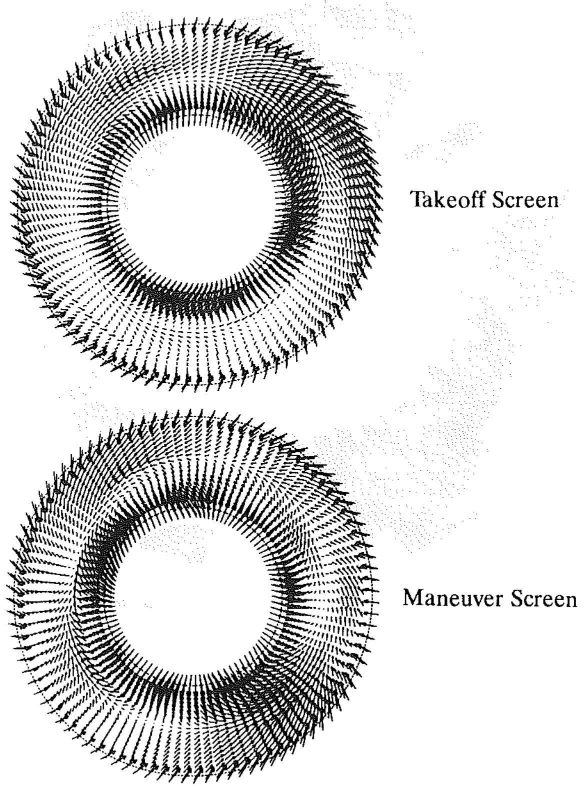

Fig. 3 Tangential velocity vector plots for takeoff and maneuver screens

calculated and input to an unsteady aerodynamic program to calculate the gust-induced unsteady loading.

Unsteady Aerodynamics. Both the unsteady aerodynamic loading $\{\bar{F}_g\}$ and the motion-dependent unsteady aerodynamic forces $[A]$ are calculated utilizing classical two-dimensional kernel functions in a strip theory calculation for subsonic, transonic, and supersonic flows (Kirsch, 1990). With the velocity perturbation provided by flow defect models and the blade mode shapes and frequencies provided by a finite element model, the system calculates the modal unsteady aerodynamic loading due to the flow defects as well as the aerodynamic damping. For the unsteady aerodynamic loading, the unsteady aerodynamic model assumes the velocity perturbation (gust) is convected by the free stream and is not deformed by the blade row (i.e., the frozen gust assumption).

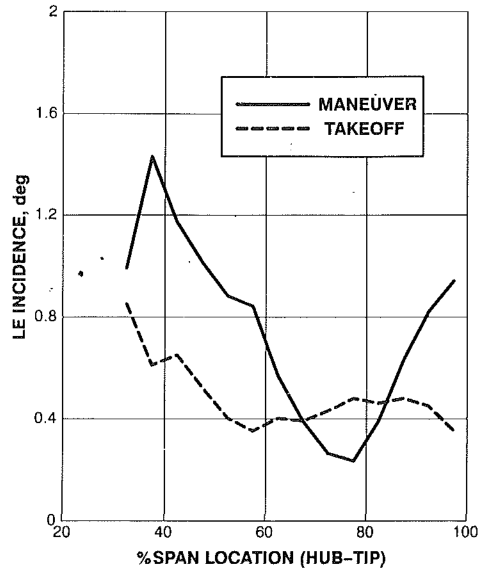

Fig. 4 Three per rev velocity perturbations for takeoff and maneuver screens

Modal Aeroelastic Solution. The structural damping $[G_m]$ can be estimated from previous experience or with measured data. With the above unsteady aerodynamic loading $\{\bar{F}_g\}$, the motion-dependent unsteady aerodynamic forces $[A]$, and the structural damping $[G_m]$ as input, the blade modal response can be calculated using Eq. (7), and is

$$\{\bar{Q}\} = [-\omega^2[M_m] + i\omega[G_m] + [K_m] - [\phi]^T[A]]^{-1}[\phi]^T\{\bar{F}_g\} \quad (8)$$

The blade modal response $\{\bar{Q}\}$ can be used to calculate the vibratory blade stress using the modal stress information.

Application I—Fan Inlet Distortion

An aeromechanical test was run with two different distortion screens. The two distortion screens were installed upstream of the fan inlet to simulate takeoff and maneuver conditions.

Inlet Distortion. These distortions were measured near the fan inlet with total pressure probes. There are 24 circumferential readings and 5 radial readings to provide the total 120 readings for the inlet distortion. Figure 2 shows the total pressure contours. With the total pressure distortion data as input, the inlet distortion harmonic analysis program was run to Fourier transform the distortion into unsteady velocity perturbations for the harmonic components of interest, which, in this case, is the third harmonic component (3 per rev). Figure 3 presents the tangential velocity component vector plots for the two distortion screens. The 3 per rev velocity perturbations in terms of incidence amplitude are shown in Fig. 4 for both takeoff and maneuver conditions. These velocity perturbations are used as input to the unsteady aerodynamic gust response program to obtain the unsteady loading.

Finite Element Model. Since the fan has a tip shroud design, a cyclic symmetry model was used to simulate the first system mode, which crosses 3 per rev at 92 percent speed. The finite element model is shown in Fig. 5. The Campbell diagram of this blade in Fig. 6 shows how the first system modes crosses 3, 4, and 5 per rev at different speeds. The cosine and sine

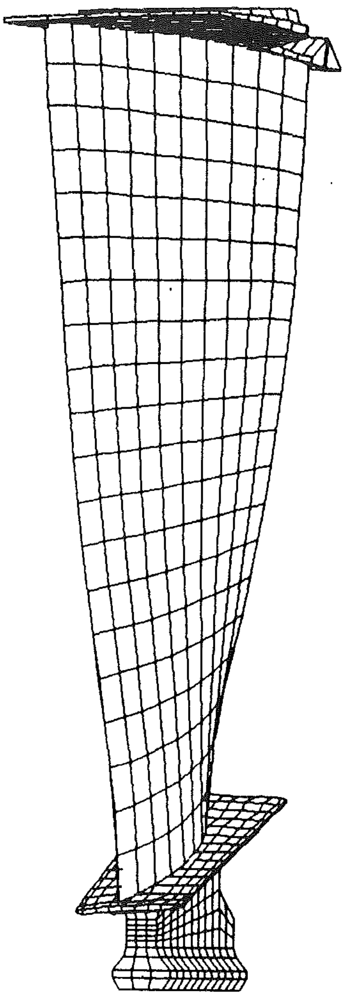

Fig. 5 Finite element model of fan blade

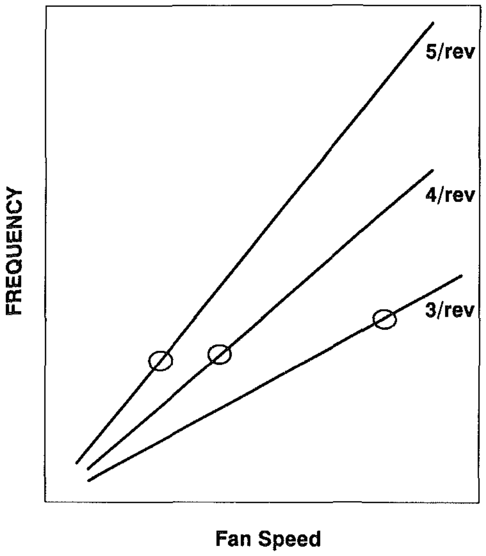

Fig. 6 Campbell diagram for fan blade

mode shapes of the blades are shown in Fig. 7. These two mode shapes define the standing wave of the entire assembly (Fig. 8). However, two standing waves with a 90-deg temporal phase can be combined to form a three-nodal diameter backward traveling wave mode. (Refer to Crawley, 1988, for a summary of the standing and traveling wave modes.) These mode shapes are input to the motion-dependent unsteady aerodynamic program to calculate the aerodynamic damping.

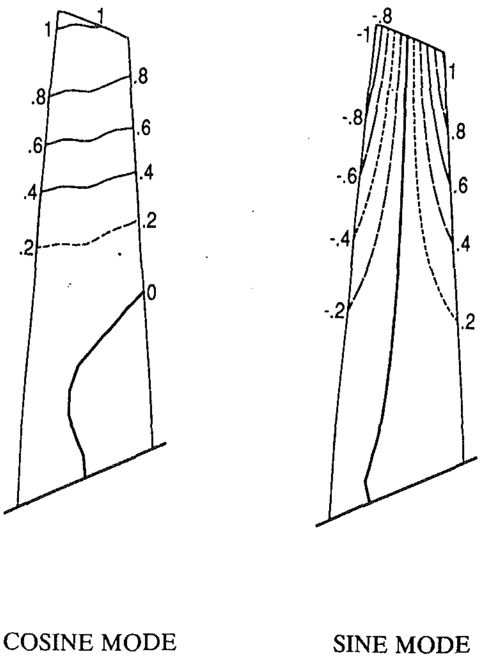

Fig. 7 Cyclic symmetry cosine and sine mode shapes for fan blade

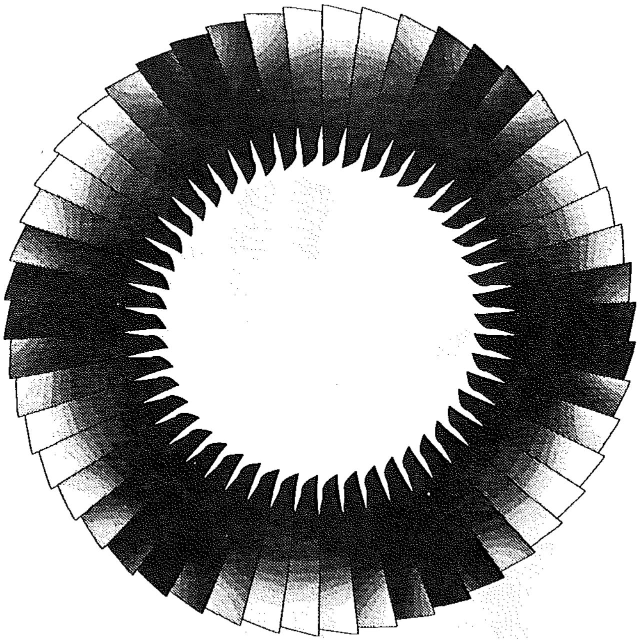

Fig. 8 First system mode mode shape for fan rotor

Unsteady Aerodynamics. The relative flow field for the fan blade is supersonic at the tip and subsonic near the hub. A strong trailing edge shock is assumed for the supersonic flow portion. The reduced frequency is calculated to be 0.254 to 0.282 for the first system mode and the interblade phase angle is 338.4 deg for the 3 per rev backward traveling wave. However, due to an acoustic resonance encountered at 3 per rev, we calculated the 0 and 7 per rev modal unsteady aerodynamic loading and aerodynamic damping to interpolate for the 3 per rev case.

Blade Response. By using structural damping estimated from previous engine data, the blade modal response was cal-

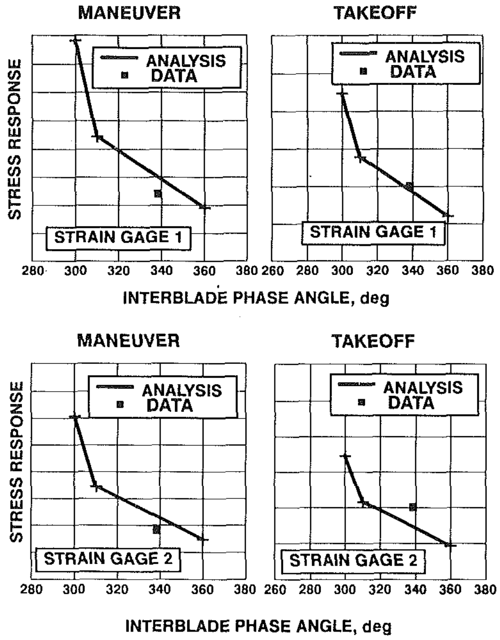

Fig. 9 Fan inlet distortion response prediction versus data

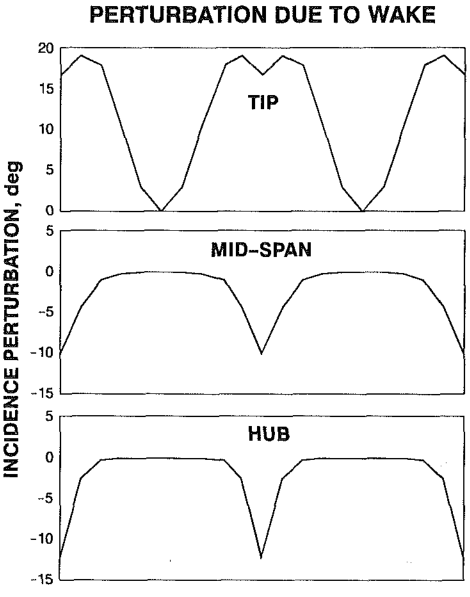

Fig. 10 HPT wake disturbance at LPT blade leading edge

culated for both screen conditions. These modal responses were then combined with the finite element dynamic stress solution to predict the blade stresses at two strain gage locations for the two screen cases. These predicted stresses are plotted versus the strain gage data in Fig. 9. As can be seen, the predicted (tuned) stresses agree very well with the strain gage data. Note that only a few blades were instrumented during the test. We have shown the data from the blades with the highest response. As expected for a system mode of a tip shrouded fan, the blade-to-blade response variation is relatively small.

Application II—Counterrotating Supersonic Turbine

In a second application, this analysis system was used to determine the response of the LPT blades of a counterrotating supersonic turbine. The HP turbine inlet Mach number is subsonic, but the exit Mach number is well into the supersonic region. The LP turbine inlet Mach number is subsonic and the exit Mach number is transonic. In this case the LPT blades were excited by both a wake and a shock wave emanating from the upstream HPT blades.

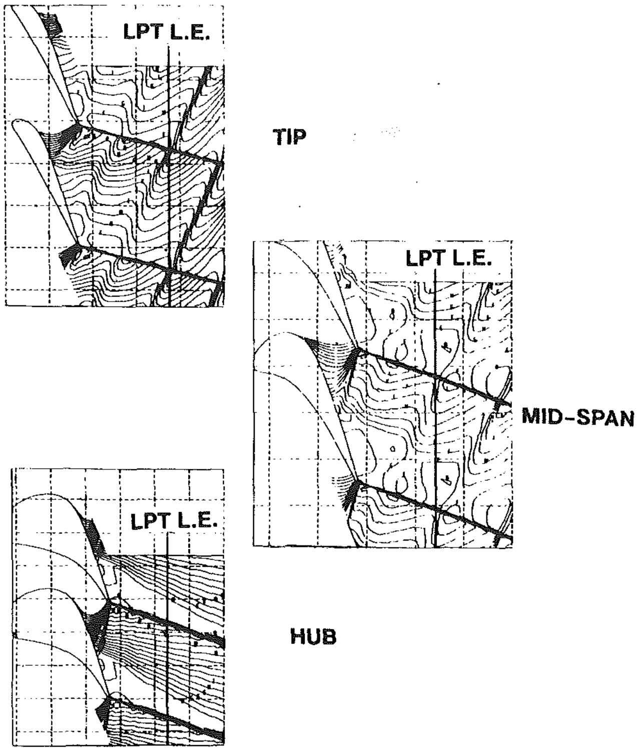

Fig. 11 Shock disturbance static pressure contour

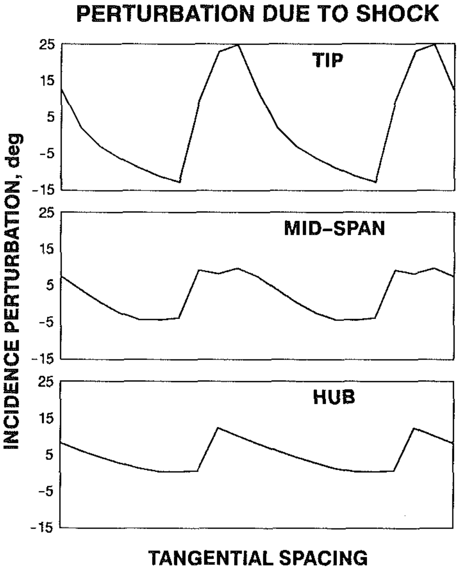

Fig. 12 LPT leading edge flow angle distortion due to shock disturbance

Wake and Shock Excitation. The previously discussed wake model (Majjigi and Gliebe, 1984) was used to simulate the HPT rotor wakes. Also, the previously mentioned tip vortex model was included. The predicted incidence perturbation at the LPT leading edge is shown in Fig. 10. The shock excitation from the HPT trailing edge shocks was modeled using a quasi-three-dimensional Euler code. The predicted static pressure contour plots for the shocks are shown in Fig. 11. The pressure distortion due to the shocks was converted into the flow angle

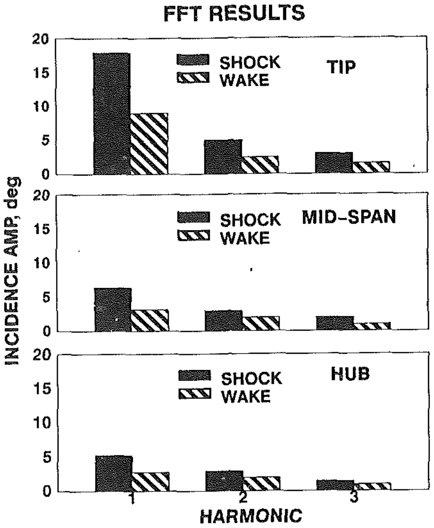

Fig. 13 Comparison of wake and shock velocity perturbations

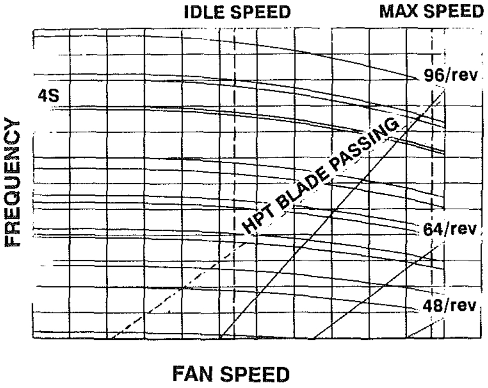

Fig. 14 LPT blade Campbell diagram

distortion shown in Fig. 12. Both the wake and shock excitations were Fourier transformed into velocity perturbations, which are compared in Fig. 13. As can be seen, the shock excitation is predicted to be almost twice as large.

Unsteady Aerodynamics. Figure 14 shows a Campbell diagram of this LPT blade with HPT blade excitation crossing the four-strip (4S) mode. Shown in Fig. 15 is the 4S mode shape used to calculate the aerodynamic damping.

The flow field for the LPT blade is transonic at the tip and subsonic near the hub. The reduced frequency is 4.0 to 7.0 for the 4S mode and the interblade phase angle is 66.7 deg for the HPT blade passing. As expected, the aerodynamic damping is negligible for the 4S mode.

Wake Versus Shock Response. Using the above information and structural damping estimated from previous data, the wake and shock induced blade responses were predicted. Although the shock excitation is predicted two times larger than that of the wake, due to the different spanwise phase distribution between the shock and the wake excitations, the shock response is predicted to be almost three times larger than the wake response, as shown in Fig. 16. Therefore, using this forced response prediction system, we have identified the shock excitation as a new forcing function mechanism for advanced supersonic turbines.

Summary and Conclusions

An analysis system developed to predict turboblading forced response is presented. A modal aeroelastic solution is implemented. This solution models the three-dimensional aeroelastic effects by calculating unsteady aerodynamic loads on two-dimensional strips, which are stacked along the span of the blade from hub to tip. A classical two-dimensional kernel function theory is utilized to calculate the subsonic, transonic, and supersonic unsteady aerodynamics due to both the incoming flow defects and the blade motion. A finite element method is used to provide the mode shape and frequency. The descriptions of flow defects, including inlet distortions, wake disturbances, and potential disturbances, are obtained either from data or analytical models. With structural damping estimated from previous data, the system predicts the blade forced response.

The analysis system was applied to two engine applications. A fan inlet distortion was analyzed with measured distortion

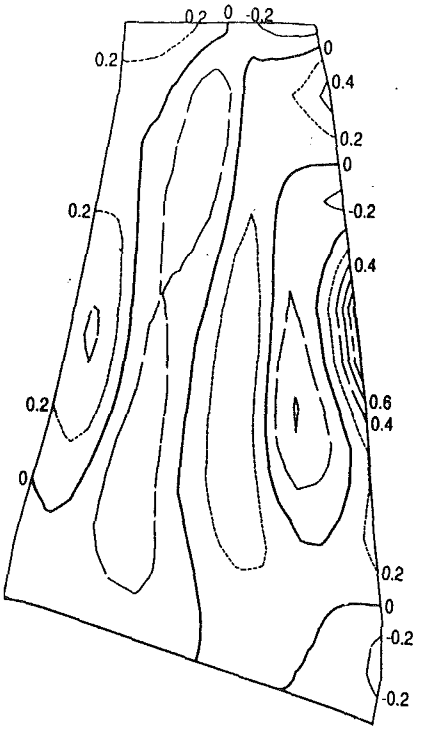

Fig. 15 LPT blade four-stripe (4S) mode shape

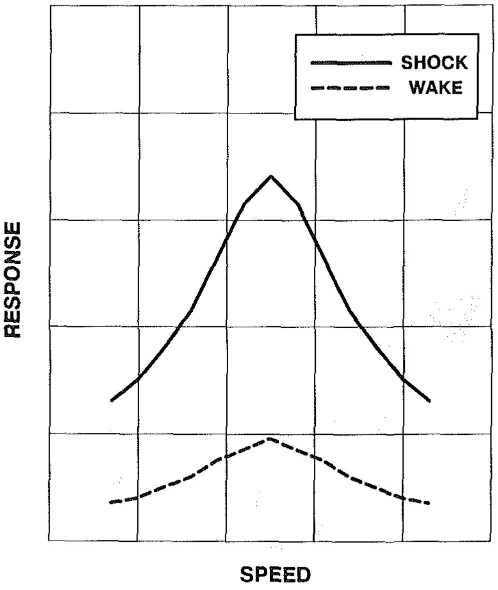

Fig. 16 Comparison of shock and wave induced response

and the predicted response agreed very well with the measured response. In a second application, LPT blades of a supersonic counterrotating turbine were excited by both a wake and a shock wave. The wake disturbance was modeled using a semi-empirical wake/vortex model. A quasi-three-dimensional Euler code was used to model the shock excitation. The shock-induced LPT blade response is predicted to be three times larger than that induced by the wake. Therefore, we have identified the shock excitation as an important forcing function mechanism.

In summary, this analysis system has been demonstrated to be a useful design tool, over and above the standard Campbell diagram approach, for predicting potential forced response problems.

Acknowledgments

The authors would like to thank Joe Grenier who performed the finite element analysis and to General Electric Aircraft Engines for permission to publish this paper. Special thanks go to Al Kirsch, who developed the modal aeroelastic solution and the two-dimensional kernel function unsteady aerodynamics, and provided guidance and support throughout this work.

References

Adamczyk, J. J., and Goldstein, M. E., 1978, "Unsteady Flow in a Supersonic Cascade With Subsonic Leading-Edge Locus," *AIAA Journal*, Vol. 16, No. 12, pp. 1248–1254.

Afolabi, D., 1988, "Vibration Amplitudes of Mistuned Blades," ASME JOURNAL OF TURBOMACHINERY, Vol. 110, pp. 251–257.

Atassi, H., and Akai, T. J., 1978, "Aerodynamic Force and Moment on Oscillating Airfoils in Cascade," ASME Paper No. 78-GT-181.

Bendiksen, O. O., and Friedmann, P., 1980, "Coupled Bending-Torsion Flutter in Cascades," *AIAA Journal*, Vol. 18, No. 2.

Bendiksen, O. O., 1986, "Role of Shocks in Transonic/Supersonic Compressor Flutter," *AIAA Journal*, Vol. 24, No. 7.

Binder, A., Foster, W., Kruse, H., and Rogge, H., 1985, "An Experimental Investigation Into the Effects of Wakes on the Unsteady Turbine Rotor Flow," ASME *Journal of Engineering for Gas Turbines and Power*, Vol. 107, pp. 458–566.

Carta, F. O., 1967, "Coupled Blade-Disk-Shroud Flutter Instabilities in Turbojet Engine Rotors," ASME *Journal of Engineering for Power*, Vol. 89, pp. 419–426.

Crawley, E. F., 1988, "Aeroelastic Formulation for Tuned and Mistuned Rotors," *AGARD Manual on Aeroelasticity in Axial-Flow Turbomachines, Vol. 2, Structural Dynamics and Aeroelasticity.*

Durali, M., 1980, "Rotor Wake Behavior in a Transonic Compressor Stage and Its Effect on the Loading and Performance of the Stator," MIT GT&PDL Report No. 149.

Fleeter, S., 1973, "Fluctuating Lift and Moment Coefficients for Cascaded Airfoils in a Non-uniform Compressible Flow," *J. Aircraft*, Vol. 10, No. 2, pp. 93–98.

Fransson, T., and Pandolfi, M., 1986, "Numerical Investigation of Unsteady Subsonic Compressible Flows Through an Oscillating Cascade," ASME Paper No. 86-GT-304.

Gallus, H. E., Lambertz, J., and Wallmann, T., 1980, "Blade-Row Interaction in an Axial-Flow Subsonic Compressor Stage," ASME *Journal of Engineering for Power*, Vol. 102, pp. 169–177.

Gallus, H. E., Poensgen, C. A., and Zeschky, J., 1991, "Three-Dimensional Unsteady Flow in Single Stage Axial Turbine and Compressor Stages," *Proceedings of the 6th International Symposium on Unsteady Aerodynamics, Aeroacoustics and Aeroelasticity of Turbomachines and Propellors*, Notre Dame, IN.

Gerolymos, G. A., 1988, "Numerical Integration of the Blade-to-Blade Surface Euler Equations in Vibrating Cascades," *AIAA Journal*, Vol. 26, No. 12, pp. 1483–1492.

Giles, M. B., 1986, "UNSFLO: a Numerical Method for Unsteady Inviscid Flow in Turbomachinery," Technical Report CFDL-TR-86-6, Massachusetts Institute of Technology, Cambridge, MA.

Goldstein, M. E., and Atassi, H., 1976, "A Complete Second-Order Theory for the Unsteady Flow About an Airfoil Due to a Periodic Gust," *J. Fluid Mech.*, Vol. 74, Pt. 4, pp. 741–765.

Griffin, J. H., 1988, "On Predicting the Resonant Response of Bladed-Disk Assemblies," ASME *Journal of Engineering for Gas Turbines and Power*, Vol. 110, pp. 45–50.

Hall, K. C., and Crawley, E. F., 1989, "Calculation of Unsteady Flows in Turbomachinery Using the Linearized Euler Equations," *AIAA Journal*, Vol. 27, pp. 777–787.

Hall, K. C., and Verdon, J. M., 1990, "Gust Response Analysis for Cascades Operating in Nonuniform Mean Flows," presented at AGARD Specialists Meeting on Unsteady Aerodynamic Phenomena in Turbomachines, Luxembourg, Paper No. 10 in AGARD-CP-468.

Hall, K. C., and Clark, W. S., 1991, "Calculation of Unsteady Linearized Euler Flows in Cascades Using Harmonically Deforming Grids," *Proceedings of the 6th International Symposium on Unsteady Aerodynamics, Aeroacoustics and Aeroelasticity of Turbomachines and Propellors*, Notre Dame, IN.

Hobbs, D. E., Wagner, J. H., Dannenhoffer, J. F., and Dring, R. P., 1982, "Experimental Investigation of Compressor Wakes," ASME Paper No. 82-GT-299.

Holmes, D. G., Lamson, S. H., and Connell, S. D., 1988, "Quasi-3D Solutions for Transonic Inviscid Flows by Adaptive Triangulation," ASME Paper No. 88-GT-83.

Holmes, D. G., and Chuang, H. A., 1991, "Two Dimensional Linearized Harmonic Euler Flow Analysis for Flutter and Forced Response," *Proceedings of the 6th International Symposium on Unsteady Aerodynamics, Aeroacoustics and Aeroelasticity of Turbomachines and Propellers*, Notre Dame, IN.

Holt, R. F., and Kirsch, A. A., 1981, "Experimental Analysis of Blade Instability—Steady Aeroelastic Prediction Program and User's Manual," GE-TIS R81AEG283, AF Contract F33615-76-C-2035.

Huang, W. H., 1982, "Vibration of Some Structures With Periodic Random Parameters," *AIAA Journal*, Vol. 20, No. 7, pp. 1001–1008.

Janes, J. M., and Whitfield, D. L., 1989, "A Simple Time-Accurate Turbomachinery Algorithm With Numerical Solutions for an Uneven Blade Count Configuration," AIAA Paper No. 89-0206.

Jorgenson, P. C. E., and Chima, R. V., 1988, "An Explicit Runge-Kutta Method for Unsteady Rotor/Stator Interaction," AIAA Paper No. 88-0049.

Kahl, G., and Klose, A., 1991, "Time Linearized Euler Calculations for Unsteady Quasi-3D Cascade Flows," *Proceedings of the 6th International Symposium on Unsteady Aerodynamics, Aeroacoustics and Aeroelasticity of Turbomachines and Propellers*, Notre Dame, IN.

Kaza, K. R. V., and Kielb, R. E., 1984, "Flutter of Turbofan Rotors With Mistuned Blades," *AIAA Journal*, Vol. 22, No. 11, pp. 1618–1625.

Kaza, K. R. V., and Kielb, R. E., 1985, "Vibration and Flutter of Mistuned Bladed-Disk Assemblies," *AIAA Journal of Propulsion and Power*, Vol. 1, No. 5, pp. 336–344.

Kaza, K. R. V., Mehmed, O., Narayanan, G. V., and Murthy, D. V., 1989, "Analytical Flutter Investigation of a Composite Propfan Model," *AIAA Journal of Aircraft*, Vol. 26, No. 8, pp. 772–780.

Kemp, N. H., and Sears, W. R., 1953, "Aerodynamic Interference Between Moving Blade Rows," *J. Aeronaut. Sci.*, Vol. 20, No. 9, pp. 585–597.

Kemp, N. H., and Sears, W. R., 1955, "The Unsteady Forces Due to Viscous Wakes in Turbomachines," *J. Aeronaut. Sci.*, Vol. 22, No. 7, pp. 478–483.

Kielb, R. E., and Ramsey, J. K., 1989, "Flutter of a Fan Blade in Supersonic Axial Flow," ASME JOURNAL OF TURBOMACHINERY, Vol. 111, pp. 462–467.

Kim, K. H., 1991, GE Aircraft Engines, unpublished work.

Kirsch, A. A., 1990, General Aeroelastic Program—GE Proprietary Analysis.

Korakianitis, T. P., 1988a, "On the Prediction of Unsteady Forces on Gas-Turbine Blades. Part 1: Typical Results and Potential Flow Interaction Effects," ASME Paper No. 88-GT-89.

Korakianitis, T. P., 1988b, "On the Prediction of Unsteady Forces on Gas-Turbine Blades. Part 2: Viscous Wake Interaction and Axial Gap Effects," ASME Paper No. 88-GT-90.

Lakshminarayana, B., and Zhang, J., 1987, "Analysis of 3D Turbulence Wakes by Momentum Integral Technique," AIAA Paper No. 87-1437.

Majjigi, R. K., and Gliebe, P. R., 1984, "Development of a Rotor Wake/Vortex Model," NASA Contract NAS3-23681, NASA-CR-174849.

Manwaring, S. R., and Fleeter, S., 1993, "Rotor Blade Unsteady Aerodynamic Gust Response to Inlet Guide Vane Wakes," ASME JOURNAL OF TURBOMACHINERY, Vol. 115, pp. 197–206.

Mikolajczak, A. A., Arnoldi, R. A., Snyder, L. E., and Stargardter, H., 1975, "Advances in Fan and Compressor Blade Flutter Analysis and Predictions," *AIAA Journal of Aircraft*, Vol. 12, No. 4, pp. 325–332.

Mokelke, H., 1979, "The Prediction of Steady Circumferential Pressure and Temperature Distortions in the Multistage Axial Flow Compressor," ASME Paper No. 79-GT-184.

Mugridge, B. D., and Morfey, C. L., 1972, "Sources of Noise in Axial Flow Fans," *Journal of the Acoustical Society of America*, Vol. 51, No. 5, Part 1, pp. 1411–1426.

Nagashima, T., and Whitehead, D. S., 1977, "Linearized Supersonic Unsteady Flow in Cascades," Aeronautical Research Council, Reports and Memoranda 3811.

Ni, R. H., and Sisto, F., 1976, "Numerical Computation of Nonstationary Aerodynamics of Flat Plate Cascades in Compressible Flow," ASME *Journal of Engineering for Power*, Vol. 98, pp. 165–170.

Oden, J. T., and Bass, J. M., 1989, "Adaptive Computation Methods for Fluid-Structure Interaction in Internal Flow," NASA SBIR Contract, NAS3-24849.

Osborne, C., 1973, "Compressible Unsteady Interactions Between Blade Rows," *AIAA J.*, Vol. 11, No. 3, pp. 340–346.

Pfeil, H., and Sieber, J., 1986, "Velocity Distribution and Decay Characteristics of Wake Behind a Compressor Rotor-Blade," ASME Paper No. 86-GT-115.

Rai, M., 1987, "Unsteady 3D Navier-Stokes Simulations of Turbine Rotor-Stator Interaction," AIAA Paper No. 87-2038.

Raj, R., and Lakshminarayana, B., 1973, "Characteristics of the Wake Behind a Cascade of Airfoils," *J. Fluid Mech.*, Vol. 61, Pt. 4, pp. 707–730.

Sankar, N. L., and Tang, W., 1985, "Numerical Solution of Unsteady Viscous Flow Past Rotor Sections," AIAA Paper No. 85-0129.

Shreeve, R. P., and Neuhoff, F., 1983, "Measurement of the Flow From a High Speed Compressor Rotor Using a Dual Probe Digital Sampling Technique," ASME Paper No. 83-GT-215.

Smith, E. T., 1990, "Aeroelastic Stability Analysis of a High-Energy Turbine Blade," AIAA Paper No. 90-2351.

Snyder, L. E., and Commerford, G. E., 1974, "Supersonic Unstalled Flutter in Fan Rotors, Analytical and Experimental Results," ASME *Journal of Engineering for Power*, Vol. 96, pp. 379–386.

Srinivasan, A. V., and Fabunmi, J. A., 1984, "Cascade Flutter Analysis of Cantilever Blades," ASME *Journal of Engineering for Gas Turbines and Power*, Vol. 106, pp. 34–43.

Taylor, A. C., and Ng, W. F., 1987, "Analytical Prediction of the Unsteady Lift on a Rotor Caused by Downstream Struts," ASME Paper No. 87-GT-145.

Turnberg, J. 1983, "Classical Flutter Stability of Swept Propellers," AIAA/ASME/ASCE/AHS 24th Structures, Structural Dynamics and Materials Conference, 83-0847-CP.

Verdon, J. M., and McCune, J. E., 1975, "Unsteady Supersonic Cascade in Subsonic Axial Flow," *AIAA Journal*, Vol. 13, No. 2, pp. 193–201.

Verdon, J. M., and Caspar, J. R., 1984, "A Linearized Unsteady Aerodynamic Analysis for Transonic Flows," *J. Fluid Mech.*, Vol. 149, pp. 403–429.

Verdon, J. M., and Hall, K. C., 1990, "Development of a Linearized Unsteady Aerodynamic Analysis for Cascade Gust Response Predictions," NASA Contract Report 4308.

Verdon, J. M., Barnett, M., Hall, K. C., and Ayer, T. C., 1991, "Development of Unsteady Aerodynamic Analyses for Turbomachinery Aeroelastic and Aeroacoustic Applications," NASA Contract Report 4405.

Warfield, M. J., and Lakshminarayana, B., 1987, "Calculation of a 3D Turbomachinery Rotor Flow With a Navier-Stokes Code," ASME Paper No. 87-GT-232.

Whitehead, D. S., 1960, "Force and Moment Coefficients for Vibrating Aerofoils in Cascade," Aeronautical Research Council, Reports and Memoranda 3254.

Whitehead, D. S., 1965, "Torsional Flutter of Unstalled Cascade Blades at Zero Deflection," Aeronautical Research Council, Reports and Memoranda 3429.

Whitehead, D. S., 1966, "Effect of Mistuning on the Vibration of Turbomachine Blades Induced by Wakes," *Journal of Mechanical Engineering Science*, Vol. 8, No. 1, pp. 15–21.

Whitehead, D. S., 1970, "Vibration and Sound Generation in a Cascade of Flat Plates in Subsonic Flow," Aeronautical Research Council, Reports and Memoranda 3865.

Whitehead, D. S., 1982, "The Calculation of Steady and Unsteady Transonic Flow in Cascades," CUED/A-Turbo/TR 118, University of Cambridge.

Williams, M. H., and Hwang, C. C., 1986, "3D Unsteady Aerodynamic and Aeroelastic Response of Advanced Turboprops," AIAA Paper No. 86-0846.

M. P. Mignolet
Associate Professor.

C.-C. Lin
Research Assistant.

Dept. of Mechanical and
Aerospace Engineering,
Arizona State University,
Tempe, AZ 85287-6106

The Combined Closed Form-Perturbation Approach to the Analysis of Mistuned Bladed Disks

A two-step method is presented for the determination of reliable approximations of the probability density function of the forced response of a randomly mistuned bladed disk. Under the assumption of linearity, an integral representation of the probability density function of the blade amplitude is first derived. Then, deterministic perturbation techniques are employed to produce simple approximations of this function. The adequacy of the method is demonstrated by comparing several approximate solutions with simulation results.

Introduction

The accurate prediction of the dynamic behavior of turbomachines has been and still represents an important issue in the design of gas turbines. This continuous interest is in part due to the complexity of the fluid-structure interaction problem involved but also to the ever increasing sophistication of the components of the disk such as blade geometry, presence of shrouds, lacing wires, blade-to-blade or blade-to-ground dampers, ... The difficulty of the analysis has naturally led to the formulation of simplified models based on physical assumptions. In particular, it has often been assumed that the blades were identical or equivalently that small differences in blade geometry and mechanical properties arising during the manufacturing process could be neglected. This hypothesis appears only logical at first in view of the quality control inspections that are performed during the manufacturing process. However, such models have been unable to explain some blade failures, the so-called rogue blades.

In search for an explanation, some early investigators (Whitehead, 1966; Dye and Henry, 1969; Ewins, 1969) found that small variations in blade mechanical properties across the disk could result in a much larger increase in the forced vibration response of some blades. This lack of symmetry of the disk, traditionally referred to as mistuning, has since been investigated by quite a few researchers (Huang, 1982; Dugundji and Bundas, 1984; Ewins and Han, 1984; Kielb and Kaza, 1984; Basu and Griffin, 1986; Sinha, 1986; Griffin, 1988; Sinha and Chen, 1988, 1989; Wei and Pierre, 1988a, 1988b; Mignolet and Christensen, 1990 and references therein). In these investigations, it has been found that distributions of blade frequencies remaining within 5 percent or less of the design value can lead to amplitudes of vibration of certain blades that are as large as 2.43 times (Basu and Griffin, 1986) the tuned value, which is computed on the basis of identical blades. In fact, a theoretical study of this phenomenon (Whitehead, 1966) has shown that the increase in amplitude can be as large as $(1+\sqrt{N})/2$ where N denotes the number of blades. Clearly, the fatigue life of the high response blades will be substantially lower than the corresponding value predicted for the tuned system.

The influence of mistuning on the free vibration of the disk has also been investigated, especially in connection with the determination of the flutter boundary (Bendiksen, 1984; Dugundji and Bundas, 1984; Kaza and Kielb, 1984; Kielb and Kaza, 1984; Srinivasan and Fabunmi, 1984; Crawley and Hall, 1985; Kaza and Kielb, 1985; Nissim, 1985; Valero and Bendiksen, 1986 and references therein). Paradoxically, these studies have shown that mistuning has a beneficial effect on flutter; it pushes the appearance of this phenomenon to higher flow velocities. In particular, it was shown that a distribution of blades that alternatively have a high and a low natural frequency (alternate mistuning) is quite effective in raising the flutter velocity. From a practical point of view, this result is very interesting since such a mistuning is readily achieved by selecting the blades from two distinct groups of identical components. However, it should be noted that the corresponding disk consists of a tuned assembly of identical subsystems, each composed of two adjacent blades. Thus, its forced vibration response is likely to be highly influenced by small variations in the mechanical properties of the subsystem that might occur during the manufacturing process.

The main difficulty encountered in the assessment of the effects of the unavoidable manufacturing mistuning lies in the lack of precise knowledge of the distribution of blade natural frequencies. In fact, it was recognized very early that the most appropriate model represents the blades' mechanical properties, mass and/or stiffness, as random variables whose means coincide with the design values. Further, their small standard deviations yield measures of quality of the manufacturing process. This characterization provides a well-defined mathematical frame, namely the theory of random vibrations, for the quantification of the effects of mistuning, in particular for the determination of the minimum and mean values of the fatigue

---

Contributed by the International Gas Turbine Institute and presented at the 37th International Gas Turbine and Aeroengine Congress and Exposition, Cologne, Germany, June 1-4, 1992. Manuscript received by the International Gas Turbine Institute February 11, 1992. Paper No. 92-GT-125. Associate Technical Editor: L. S. Langston.

life. To perform this analysis, it is first necessary to obtain the probability density function of the amplitude of response of the bladed disk. This prior computation, which has already been considered by several researchers (Huang, 1982; Sinha, 1986; Sinha and Chen, 1988, 1989; Mignolet and Christensen, 1990; Wei and Pierre, 1990), represents the object of the present investigation.

Sinha (1986), Sinha and Chen (1988, 1989) and Wei and Pierre (1990) have relied on perturbation techniques to derive approximate expressions for the response of the disk that are accurate to first order in the small variations of the blade properties. The central limit theorem has then been invoked (Sinha, 1986) to obtain an approximation of the required probability density function of the amplitude of vibration. An alternative approach, which is somewhat of a dual of the above technique, has been sketched by Mignolet and Christensen (1990) in the context of a two-bladed disk. This method, termed the combined closed form–perturbation approach, requires first the derivation of an exact integral representation of the probability density function. Then, a deterministic perturbation analysis is performed to obtain a simple and reliable approximation of the probability density function. The goal of the present investigation is first to extend the theoretical basis of the method to account for an arbitrary number of blades and then to discuss in detail the implementation aspects of the technique.

The Model and Its Deterministic Response

Neglecting the effects of the nonlinearities associated with the structure, the fluid, and their interaction, it is found that a bladed disk can be modeled as a linear multi-degree-of-freedom system whose equations of motion can be written in the compact form

$$M\ddot{\mathbf{X}}+C\dot{\mathbf{X}}+K\mathbf{X}=\mathbf{F}. \tag{1}$$

In the above relation, the symbol $\mathbf{X}$ denotes the time-dependent vector whose components are the displacements of the N degrees of freedom. Further, M, C, and K represent the corresponding $N\times N$ mass, damping, and stiffness matrices. Finally, the N-component vector $\mathbf{F}$ denotes the external forces acting on the disk.

When the system is tuned, that is, when all the blades are perfectly identical, the matrices M, C, and K possess a special structure that reflects the invariance of the disk under a rotation by an angle $2\pi/N$. Interestingly, this property can be utilized to derive simple, closed form expressions for the natural frequencies, the mode shapes, and the steady-state response of the disk to the harmonic excitation (Thomas, 1979; Mignolet and Christensen, 1990)

$$\mathbf{F}(t)=\mathbf{F}_0^{(c)}\cos\omega t+\mathbf{F}_0^{(s)}\sin\omega t \tag{2}$$

The introduction of mistuning in the system, for example in the form of small blade-to-blade variations in the mass distribution and natural frequencies, destroys the rotational symmetry of the disk and prevents the use of the corresponding closed form results in the determination of its dynamic response.

This analysis must then be accomplished by using standard techniques. In particular, the steady-state response of the disk to the excitation vector given by Eq. (2) can be sought in the form

$$\mathbf{X}(t)=\mathbf{U}\cos\omega t+\mathbf{V}\sin\omega t \tag{3}$$

Then, it is readily shown that the components U_i and V_i of the constant vectors $\mathbf{U}$ and $\mathbf{V}$ satisfy the linear equations

$$H\mathbf{Z}=\tilde{\mathbf{F}} \tag{4}$$

with

$$\mathbf{Z}^T=[U_1V_1U_2V_2\cdots U_NV_N] \tag{5}$$

and

$$\tilde{\mathbf{F}}^T=[F_{01}^{(c)}\,F_{01}^{(s)}\,F_{02}^{(c)}\,F_{02}^{(s)}\cdots F_{0N}^{(c)}\,F_{0N}^{(s)}] \tag{6}$$

where the superscript T designates the operation of matrix transposition and H is a $2N\times 2N$ matrix whose block elements are composed of the terms $K_{il}-\omega^2M_{il}$ and ωC_{il}, i, $l=1, \ldots, N$.

The lack of precise knowledge of the values of the mass and of the natural frequencies of the blades has led to the modeling of these quantities as random variables whose means correspond to the design specifications and whose small variances are representative of the manufacturing process. The presence of nondeterministic blade characteristics, M_{il}, C_{il}, and/or K_{il} in Eqs. (1) and (4) implies in turn that the components of the corresponding vectors $\mathbf{U}$ and $\mathbf{V}$ are also random variables. Their probabilistic properties must be determined for an accurate assessment of the vibration response of the mistuned bladed disk, in particular of the fatigue life.

Random Response: Combined Closed Form–Perturbation Approach

Probability Density Function of Amplitude: A Closed Form Expression. In this section, a closed form expression will be derived for the probability density function of the response of an arbitrary degree-of-freedom of a randomly mistuned bladed disk subjected to the harmonic excitation given by Eq. (2). For clarity of the presentation, assume that a total of m elements of the matrices M, C, and K vary from a set of n blades to another one to such extent that they should be considered as random variables. Further, denote these parameters and their specified joint probability density function by Λ_i, $i=1, \ldots, m$ and $p_\Lambda(\lambda)=p_{\Lambda_1\Lambda_2\ldots\Lambda_m}(\lambda_1, \lambda_2, \ldots, \lambda_m)$, respectively.

Clearly, given a realization of the random blade parameters Λ_i, the matrices M, C, and K can be determined and the dynamic response of the disk, in particular the elements U_i and V_i, can be computed from Eqs. (4)–(6). Then, a sample realization of the amplitude A_i corresponding to the specified values of Λ_i is readily obtained as

$$A_i=\sqrt{U_i^2+V_i^2}. \tag{7}$$

Viewed in this manner, the system of Eqs. (4)–(7) appears as a transformation of the blade characteristics Λ_i into the amplitude of vibration A_i.

Thus, following the rules of changes of random variables, a closed form expression can be derived for the probability density function of the amplitude $p_{A_i}(a)$. Specifically, introducing the random variables $\tilde{\Lambda}_j$, $j=1, \ldots, m$, defined as

$$\tilde{\Lambda}_1=A_i \tag{8a}$$

and

$$\tilde{\Lambda}_j=\Lambda_j \quad j=2, \ldots, m, \tag{8b}$$

it is readily shown that their joint probability density function $p_{\tilde{\Lambda}}(\tilde{\lambda})$ is

$$p_{\tilde{\Lambda}}(\tilde{\lambda})=\frac{p_\Lambda(\lambda)}{J(\lambda, \tilde{\lambda})} \tag{9}$$

where $J(\lambda, \tilde{\lambda})$ denotes the Jacobian of the transformation $\Lambda_i\rightarrow\tilde{\Lambda}_i$. It is straightforward to prove that this function reduces to

$$J(\lambda, \tilde{\lambda})=\left|\frac{\partial a}{\partial\lambda_1}\right|=\frac{1}{2a}\left|\frac{\partial(a^2)}{\partial\lambda_1}\right| \tag{10}$$

where a designates the realized value of A_i corresponding to the selections $\Lambda_i=\lambda_i$, $i=1, \ldots, m$.

Finally, the probability density function $p_{A_i}(a)$ is obtained by integrating the joint density $p_{\tilde{\Lambda}}(\tilde{\lambda})$ over the domain of the variables $\tilde{\lambda}_i=\lambda_i$, $i=2, \ldots, m$, that is

$$p_{A_i}(a)=2a\int_{-\infty}^{+\infty}\cdots\int_{-\infty}^{+\infty}\frac{p_\Lambda(\lambda)}{\left|\dfrac{\partial(a^2)}{\partial\lambda_1}\right|}d\lambda_2\cdots d\lambda_m. \qquad (11)$$

To complete the closed form determination of $p_{A_i}(a)$, it remains to derive an expression for the derivative $|\partial(a^2)/\partial\lambda_1|$. To this end, denote by $\mathbf{e}_i$ the $2N$-component vector whose elements are all zero except the ith one, which equals one. Then, it is found from Eqs. (4) and (5) that

$$U_i=\mathbf{e}_{2i-1}^T\mathbf{Z}=\mathbf{e}_{2i-1}^T H^{-1}\tilde{\mathbf{F}} \qquad (12)$$

and

$$V_i=\mathbf{e}_{2i}^T\mathbf{Z}=\mathbf{e}_{2i}^T H^{-1}\tilde{\mathbf{F}} \qquad (13)$$

so that

$$a^2=U_i^2+V_i^2=\mathbf{e}_{2i-1}^T H^{-1}\tilde{\mathbf{F}}\tilde{\mathbf{F}}^T H^{-T}\mathbf{e}_{2i-1}+\mathbf{e}_{2i}^T H^{-1}\tilde{\mathbf{F}}\tilde{\mathbf{F}}^T H^{-T}\mathbf{e}_{2i}. \qquad (14)$$

In order to compute $|\partial(a^2)/\partial\lambda_1|$, note that the derivatives with respect to a parameter α of an arbitrary matrix D and of its inverse D^{-1} are related through the equation (Noble and Daniel, 1988)

$$\frac{d(D^{-1})}{d\alpha}=-D^{-1}\left(\frac{dD}{d\alpha}\right)D^{-1} \qquad (15)$$

Thus, combining Eqs. (14) and (15), it is found that

$$\left|\frac{\partial(a^2)}{\partial\lambda_1}\right|=2\left|\mathbf{e}_{2i-1}^T H^{-1}\left(\frac{\partial H}{\partial\lambda_1}\right)H^{-1}\tilde{\mathbf{F}}\tilde{\mathbf{F}}^T H^{-T}\mathbf{e}_{2i-1}+\mathbf{e}_{2i}^T H^{-1}\left(\frac{\partial H}{\partial\lambda_1}\right)H^{-1}\tilde{\mathbf{F}}\tilde{\mathbf{F}}^T H^{-T}\mathbf{e}_{2i}\right| \qquad (16)$$

where the derivative $(\partial H/\partial\lambda_1)$ is readily obtained by first determining which of the matrices M, C, and K involve λ_1 and then locating these block elements in H according to Eqs. (4)–(6).

Note finally that the procedure described in this section could also be employed to derive the joint probability density function of two, three, or more amplitudes.

Probability Density Function of Amplitude: Perturbation Solution. From a purely mathematical point of view, Eqs. (11), (14), and (16) form a complete and exact representation of the probability density function of the amplitude A_i for any number of blades n and random characteristics Λ_i. Indeed, Eq. (14) can be seen either as an expression for the squared amplitude a^2 in terms of $\lambda_1, \ldots, \lambda_m$ or as an implicit definition of the variable λ_1 as a function of $a^2, \lambda_2, \ldots, \lambda_m$. This result can then be combined with Eq. (16) to provide an expression for $|\partial(a^2)/\partial\lambda_1|$ involving only $a^2, \lambda_2, \ldots, \lambda_m$, which in turn can be introduced in the denominator of the integrand of Eq. (11). Finally, upon evaluation of the $m-1$ fold integral, the probability density function $p_{A_i}(a)$ is evaluated in closed form.

It should be recognized, however, that a *direct* application of the step by step procedure enunciated above involves simple mathematical operations that are computationally difficult to perform. The determination of the functional form of λ_1 in terms of $a^2, \lambda_2, \ldots, \lambda_m$ and the evaluation of the inverse H^{-1} are typical examples of this situation. In this context, note that quality control inspections lead to the rejection of blades whose characteristics are too different from the design specifications so that the standard deviation of the random variable Λ_i, σ_i, is small in comparison to its mean value, $\overline{\Lambda}_i$. Thus, the variables of integration λ_i can be written in the form

$$\lambda_i=\overline{\Lambda}_i+\sigma_i\delta\lambda_i \quad i=1, \ldots, m \qquad (17)$$

where $\sigma_i\,\delta\lambda_i$ represents a small mistuning of the blade property Λ_i satisfying

$$\sigma_i\delta\lambda_i \ll \overline{\Lambda}_i \quad i=1, \ldots, m. \qquad (18)$$

The above inequality suggests a perturbation approach to the evaluation of the probability density function $p_{A_i}(a)$. Specifically, decomposing the matrix H into a mean component $\overline{H}$ corresponding to the design values $\overline{\Lambda}_i$ and a mistuned term δH, it is found that

$$H^{-1}=(\overline{H}+\delta H)^{-1}=\overline{H}^{-1}[I+\delta H\overline{H}^{-1}]^{-1}=\overline{H}^{-1}[I-\delta H\overline{H}^{-1}+(\delta H\overline{H}^{-1})^2+\cdots] \qquad (19)$$

where I denotes the $2N\times 2N$ unit matrix. Further, under the assumption that the design specifications correspond to a tuned bladed disk, the matrix H possesses a special structure, which can be exploited to derive efficient techniques for the evaluation of $\overline{H}^{-1}$ and of H^{-1} through Eq. (19) (see Sinha and Chen, 1988, for an example).

Note that the representation of H^{-1} given by Eq. (19) is valid only when the series $I-\delta H\overline{H}^{-1}+(\delta H\overline{H}^{-1})^2+..$ converges, that is, provided that all of the eigenvalues of $\delta H\overline{H}^{-1}$ belong to the open interval $(-1, +1)$. Other series approximations of H^{-1} must be used if the domain of integration in Eq. (11) contains values of the deterministic parameters $\lambda_1, \lambda_2, \ldots, \lambda_m$ to which corresponds a matrix $\delta H\overline{H}^{-1}$ possessing at least one eigenvalue larger than one in modulus. In particular, note that the expansion

$$H^{-1}=(\overline{H}+\delta H)^{-1}=\delta H^{-1}[I+\overline{H}\delta H^{-1}]^{-1}=\delta H^{-1}[I-\overline{H}\delta H^{-1}+(\overline{H}\delta H^{-1})^2+\cdots] \qquad (20)$$

is valid when all of the eigenvalues of $\delta H\overline{H}^{-1}$ are outside the domain $(-1, +1)$.

Introducing an appropriate limited Taylor expansion, such as Eq. (19) or (20), into Eqs. (14) and (16), approximate expressions of λ_1 and $|\partial(a^2)/\partial\lambda_1|$ can be derived in terms of $a^2, \lambda_2, \ldots, \lambda_m$ and a perturbation-like representation of $p_{A_i}(a)$ can be obtained from Eq. (11).

The series expansion shown in Eq. (19) has already been suggested for the determination of the dynamic response of a mistuned bladed disk. Specifically, Sinha (1986) and Sinha and Chen (1988, 1989) have used this representation in connection with the *random* matrix H to derive the series solution of Eq. (4)

$$\mathbf{Z}=\overline{H}^{-1}\tilde{\mathbf{F}}-\overline{H}^{-1}\delta H\overline{H}^{-1}\tilde{\mathbf{F}}+\cdots \qquad (21)$$

In the above equation, the tuned matrix $\overline{H}$ corresponds as before to the design specifications $\overline{\Lambda}_i$ while δH involves the random variations of blade characteristics $\Lambda_i-\overline{\Lambda}_i$ as opposed to the deterministic differences $\lambda_i-\overline{\Lambda}_i$ considered in the present approach. The convergence of the series solution (21) requires that the random terms $\Lambda_i-\overline{\Lambda}_i$ be "small" enough so that the eigenvalues of $\delta H\overline{H}^{-1}$ all belong to the open interval $(-1, +1)$. The term "small" should be used carefully in connection with random variables since such quantities can take on arbitrarily large values even for arbitrarily small variances provided that their probability density function extends to infinity.

Thus, the validity of Eq. (21) is limited to random blade characteristics Λ_i whose probability density is defined over a finite domain such that the eigenvalues of $\delta H\overline{H}^{-1}$ all belong to the interval $(-1, +1)$. This condition can be quite restrictive when the lowest eigenvalue of $\overline{H}$ is very small, as occurs for example when the frequency of the excitation is close to a natural frequency of the tuned bladed disk.

Example

Model. The modalities of application of the combined closed form–perturbation approach will now be demonstrated by considering the simple, yet realistic, model of a bladed disk shown in Fig. 1, which represents an extension of the dynamic system considered in particular by Griffin and Sinha (1985), Sinha (1986), Sinha and Chen (1988, 1989). The stiffness k_C

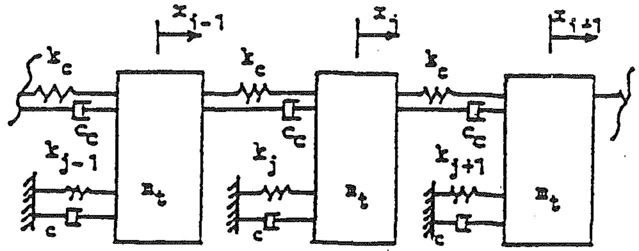

Fig. 1 Model of bladed disk

and the damping coefficient c_C are selected to account for the interblade coupling due to both the aerodynamic effects and the flexibility of the disk. Further, it is assumed that the masses and damping coefficients of the blades are all identical so that the mistuning is restricted to the blade-disk stiffnesses whose variations from the mean value are denoted by k_i, $i=1, \ldots, n$. Thus, it is found that

$$m=n=N \tag{22}$$

and

$$\Lambda_i=k_i+k_t \quad i=1, \ldots, n \tag{23}$$

where k_t designates the mean blade-disk stiffness common to all blades.

Closed-Form Expression. To exemplify the derivation of the different terms present in Eq. (11), consider the evaluation of the probability density function of the first blade $p_{A_1}(a)$. The identification of the matrix H is achieved first by rewriting the equations of motion of the bladed disk, Fig. 1, in the form of Eq. (4). It is readily found that (Lin, 1991)

$$H=\begin{bmatrix} h_1+k_1 & h_3 & -h_2 & h_4 & 0 & 0 & \cdot & -h_2 & h_4 \\ -h_3 & h_1+k_1 & -h_4 & -h_2 & 0 & 0 & \cdot & -h_4 & -h_2 \\ -h_2 & h_4 & h_1+k_2 & h_3 & -h_2 & h_4 & \cdot & 0 & 0 \\ -h_4 & -h_2 & -h_3 & h_1+k_2 & -h_4 & -h_2 & \cdot & 0 & 0 \\ \cdot & \cdot & \cdot & \cdot & \cdot & \cdot & \cdot & \cdot & \cdot \\ -h_2 & h_4 & 0 & 0 & 0 & 0 & \cdot & h_1+k_n & h_3 \\ -h_4 & -h_2 & 0 & 0 & 0 & 0 & \cdot & -h_3 & h_1+k_n \end{bmatrix} \tag{24}$$

where the deterministic parameters h_1, h_2, h_3, and h_4 are defined as

$$h_1=k_t-m\,\omega^2+2\,k_C \tag{25}$$

$$h_2=k_C \quad n>2 \tag{26a}$$

$$h_2=2\,k_C \quad n=2 \tag{26b}$$

$$h_3=-(c+c_C)\omega. \tag{27}$$

$$h_4=c_C\omega \quad n>2 \tag{28a}$$

$$h_4=2c_C\omega \quad n=2 \tag{28b}$$

The squared amplitude, a^2, of response of the blade 1 corresponding to a set of stiffness variations k_i is seen from Eq. (14) to be

$$a^2=\mathbf{e}_1^TH^{-1}\tilde{\mathbf{F}}\tilde{\mathbf{F}}^TH^{-T}\mathbf{e}_1+\mathbf{e}_2^TH^{-1}\tilde{\mathbf{F}}\tilde{\mathbf{F}}^TH^{-T}\mathbf{e}_2. \tag{29}$$

The evaluation of the Jacobian $|\partial(a^2)/\partial k_1|$ requires first the computation of the derivative $\partial H/\partial k_1$, which is readily achieved from Eq. (24) in the form

$$\frac{\partial H}{\partial k_1}=\begin{bmatrix} 1 & 0 & 0 & 0 & 0 & 0 & \cdot & 0 & 0 \\ 0 & 1 & 0 & 0 & 0 & 0 & \cdot & 0 & 0 \\ 0 & 0 & 0 & 0 & 0 & 0 & \cdot & 0 & 0 \\ 0 & 0 & 0 & 0 & 0 & 0 & \cdot & 0 & 0 \\ \cdot & \cdot & \cdot & \cdot & \cdot & \cdot & \cdot & \cdot & \cdot \\ 0 & 0 & 0 & 0 & 0 & 0 & \cdot & 0 & 0 \\ 0 & 0 & 0 & 0 & 0 & 0 & \cdot & 0 & 0 \end{bmatrix}=\mathbf{e}_1\mathbf{e}_1^T+\mathbf{e}_2\mathbf{e}_2^T. \tag{30}$$

Then, introducing the above result in Eq. (16) and noting that (see Appendix I for a proof)

$$\mathbf{e}_1^TH^{-1}\mathbf{e}_1=\mathbf{e}_2^TH^{-1}\mathbf{e}_2 \tag{31}$$

and

$$\mathbf{e}_1^TH^{-1}\mathbf{e}_2=-\mathbf{e}_2^TH^{-1}\mathbf{e}_1, \tag{32}$$

it can be shown that the Jacobian reduces to

$$\left|\frac{\partial(a^2)}{\partial k_1}\right|=2\,a^2\,|\mathbf{e}_1^TH^{-1}\mathbf{e}_1|. \tag{33}$$

In order to isolate the dependency of $|\partial(a^2)/\partial k_1|$ on the stiffness k_1, introduce the following partitions

$$H=\begin{bmatrix} H_{11} & H_{12} \\ H_{21} & H_{22} \end{bmatrix} \tag{34}$$

and

$$H^{-1}=\begin{bmatrix} L_{11} & L_{12} \\ L_{21} & L_{22} \end{bmatrix} \tag{35}$$

where the submatrices H_{11}, H_{12}, H_{21}, and H_{22}, or L_{11}, L_{12}, L_{21}, and L_{22}, have dimensions 2×2, $2\times(2n-2)$, $(2n-2)\times 2$, and $(2n-2)\times(2n-2)$, respectively. Then, using the Frobenius-Schur formula for the inverse of a partitioned matrix, it is found that

$$L_{11}=G^{-1} \tag{36}$$

and

$$L_{12}=-G^{-1}H_{12}H_{22}^{-1}=-L_{11}H_{12}H_{22}^{-1} \tag{37}$$

where

$$G=H_{11}-H_{12}H_{22}^{-1}H_{21}=\begin{bmatrix} g_{11}+k_1 & g_{12} \\ -g_{12} & g_{11}+k_1 \end{bmatrix}. \tag{38}$$

In the above equation, the symbols g_{11} and g_{12} designate two functions of the stiffnesses $k_2, \ldots, k_n$ defined by the relations

$$g_{11}=h_1-\mathbf{e}_1^TH_{12}H_{22}^{-1}H_{21}\mathbf{e}_1 \tag{39}$$

and

$$g_{12}=h_3-\mathbf{e}_1^TH_{12}H_{22}^{-1}H_{21}\mathbf{e}_2. \tag{40}$$

Finally, introducing the partitioned vector $\mathbf{W}$ in the form

$$\mathbf{W}=[I_2 \quad -H_{12}H_{22}^{-1}]\tilde{\mathbf{F}} \tag{41}$$

it is found that (Lin, 1991)

$$a^2=\frac{W^2}{(g_{11}+k_1)^2+g_{12}^2} \tag{42}$$

$$k_1=-g_{11}\pm\left[\frac{W^2}{a^2}-g_{12}^2\right]^{1/2} \tag{43}$$

and

$$\left|\frac{\partial(a^2)}{\partial k_1}\right|=2\frac{a^4}{W^2}\left[\frac{W^2}{a^2}-g_{12}^2\right]^{1/2} \tag{44}$$

where W^2 denotes the squared norm of the vector $\mathbf{W}$, that is $\mathbf{W}^T\mathbf{W}$. Equations (11) and (42)-(44) form a complete and exact representation of the probability density of the amplitude A_1. Note finally that this function can also be written in the form

$$p_{A_1}(a)=\frac{1}{a^3}E\left[\frac{W^2 p_{k_1}(k_1)}{\left[\dfrac{W^2}{a^2}-g_{12}^2\right]^{1/2}}\right] \tag{45}$$

where the expectation, $E[\cdot]$, is taken with respect to the variables k_j, $j=2, \ldots, N$ under the constraint that $-\tau \leq k_1 \leq \tau$ or equivalently that

$$-\tau \leq -g_{11} \pm \left[\frac{W^2}{a^2}-g_{12}^2\right]^{1/2} \leq \tau. \tag{46}$$

where $-\tau$ and τ are the limits of variation of the variables k_i.

To complete the formulation of the problem, it remains to specify the joint probability density function of the stiffness variation k_i. For the sake of illustration, it has been assumed that these random variables are independent and identically, uniformly distributed so that

$$p_{k_1k_2\ldots k_n}(k_1, k_2, \ldots, k_n)=\frac{1}{(2\tau)^n}$$

$$\text{for } (k_1, k_2, \ldots, k_n)\in[-\tau, \tau]\times[-\tau, \tau]\cdots[-\tau, \tau] \tag{47}$$

and 0 otherwise. Note that any other bona fide probability density function could have been selected since the combined closed form-perturbation method is valid for all probabilistic models of the blade's properties.

It can be shown that the rotational symmetry of both the system and the excitation implies that

$$p_{A_1}(a)=p_{A_2}(a)=\cdots=p_{A_n}(a) \tag{48}$$

so that Eqs. (11) and (42)–(46) can in fact be used in connection with any blade.

Finally, to demonstrate the derivation of an approximate expression for the probability density function of the amplitude in both resonant and off-resonant conditions, the components of the force vector $\mathbf{F}(t)$ are chosen in the form

$$F_i(t)=F_0\cos(\omega t+\Psi_i) \tag{49}$$

where

$$\Psi_i=\frac{2\pi r}{n}(i-1). \tag{50}$$

When the parameter ω is selected as the rth natural frequency of the system given by

$$\omega_r=\left[\frac{k_t+4k_C\sin^2\left(\dfrac{\pi r}{n}\right)}{m}\right]^{1/2} \qquad r=0, \ldots, n-1 \tag{51}$$

the excitation $\mathbf{F}(t)$ corresponds to the rth engine order and is proportional to the rth mode shape of the system. Off-resonant conditions can also be simulated from Eqs. (49)–(50) by letting ω be different from the values ω_r, Eq. (51).

Near-Resonant Excitation. The effects of mistuning are known to be especially important when the system is excited at or near one of its natural frequencies. Since the derivation of a reliable approximation of the probability density function of the response is simpler in the former case ($\omega \approx \omega_0$) than in the latter ($\omega=\omega_0$), a near-resonant excitation will first be considered. Further, the case of a small variance of the mistuned stiffnesses, or equivalently $\tau/k_t \ll 1$, is of particular importance in this study since it corresponds to bladed disks manufactured under a tight quality control. Then, following a previous discussion, an approximate expression for the probability density function $p_{A_1}(a)$ will be sought by expanding the matrix H_{22}^{-1} according to Eq. (19) where $\overline{H}_{22}$ is given by Eq. (24) and (34) with $k_2=k_3=\cdots=k_n=0$ and

$$\delta H_{22}=\mathrm{diag}[k_2, k_2, k_3, k_3, \cdots k_n, k_n]. \tag{52}$$

Keeping only the terms involving zeroth and first powers in δH_{22}, it is found that

$$g_{11}=(h_1-\mathbf{e}_1^T H_{12}\overline{H}_{22}^{-1}H_{21}\mathbf{e}_1)+\mathbf{e}_1^T H_{12}\overline{H}_{22}^{-1}\delta H_{22}\overline{H}_{22}^{-1}H_{21}\mathbf{e}_1$$
$$+O(\delta H_{22}^2)=g_{11}^0+\mathbf{g}_{11}^L\delta H_{22}\mathbf{g}_{11}^R+O(\delta H_{22}^2) \tag{53}$$

$$g_{12}=(h_3-\mathbf{e}_1^T H_{12}\overline{H}_{22}^{-1}H_{21}\mathbf{e}_2)+\mathbf{e}_1^T H_{12}\overline{H}_{22}^{-1}\delta H_{22}\overline{H}_{22}^{-1}H_{21}\mathbf{e}_2$$
$$+O(\delta H_{22}^2)=g_{12}^0+\mathbf{g}_{12}^L\delta H_{22}\mathbf{g}_{12}^R+O(\delta H_{22}^2) \tag{54}$$

where the scalars g_{11}^0, g_{12}^0 and vectors $\mathbf{g}_{11}^L$, $\mathbf{g}_{11}^R$, $\mathbf{g}_{12}^L$, $\mathbf{g}_{12}^R$ are given in Appendix II. Proceeding in a similar manner in connection with the term W^2 leads to the expression

$$W^2=w_0+\mathbf{w}_1\delta H_{22}\mathbf{w}_2 \tag{55}$$

where the scalar w_0 and the vectors $\mathbf{w}_1$, $\mathbf{w}_2$ are given in Appendix II.

Finally, using Eqs. (45), (53)–(55), a first-order approximation of the probability density function can be expressed in the form

$$p_{A_1}(a)=\frac{w_0}{2\tau a^2\sqrt{w_0-a^2 g_{12}^{0\,2}}}$$
$$+\frac{E\left[\left[\dfrac{w_0}{2a^2}-g_{12}^{0\,2}\right]\mathbf{w}_1\delta H_{22}\mathbf{w}_2+w_0 g_{12}^0\mathbf{g}_{12}^L\delta H_{22}\mathbf{g}_{12}^R\right]}{2\tau[w_0-a^2 g_{12}^{0\,2}]^{3/2}} \tag{56}$$

where the expectation $E[\cdot]$ is taken with respect to the variables k_2, k_3, …, k_n, under the linearized version of the constraint (46), that is

$$-\tau \leq \left[-g_{11}^0 \pm \sqrt{\frac{w_0}{a^2}-g_{12}^{0\,2}}\right]$$
$$+\left[-\mathbf{g}_{11}^L\delta H_{22}\mathbf{g}_{11}^R \pm \frac{\mathbf{w}_1\delta H_{22}\mathbf{w}_2-2a^2 g_{12}^0\mathbf{g}_{12}^L\delta H_{22}\mathbf{g}_{12}^R}{2a\sqrt{w_0-a^2 g_{12}^{0\,2}}}\right] \leq \tau. \tag{57}$$

According to Eqs. (56) and (57), the first-order approximation of the probability density function $p_{A_1}(a)$ can be expressed as the expected value of a linear combination of the random variables k_2, k_3, …, k_n under the linear inequality constraints given by Eq. (57). Thus, the value of $p_{A_1}(a)$ can readily be evaluated by relying on the algorithm recently developed by Mignolet and Lin (1992). For completeness, a summary of this computational technique is presented in Appendix III.

Resonant Excitation. The evaluation of the probability density function $p_{A_1}(a)$ according to Eq. (11) or (45) is rendered more delicate in the case of a resonant excitation by the possible presence in the domain of integration, or in its neighborhood, of a singularity of the integrand. This situation is depicted in Fig. 2 in the simple, illustrative example of a three-blade disk (the corresponding figure in the case of a 24-blade

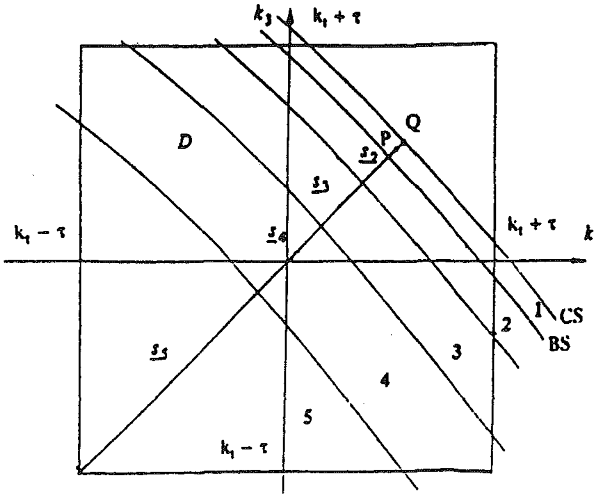

Fig. 2 Domain of integration, resonant case

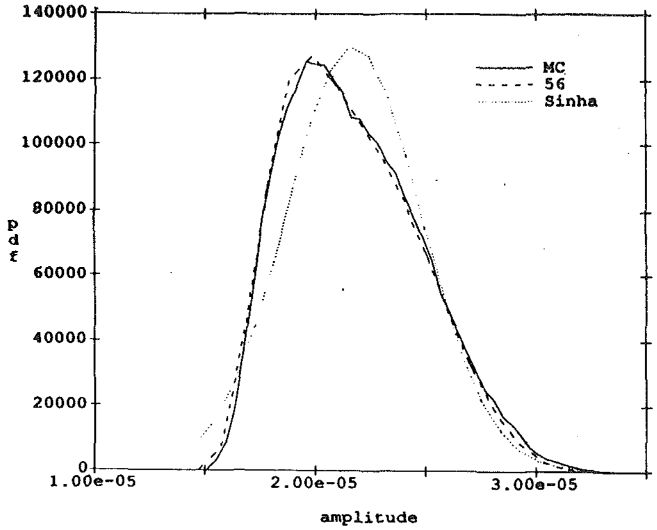

Fig. 3 Probability density of blade amplitude, $\omega = 6000$ rad/s

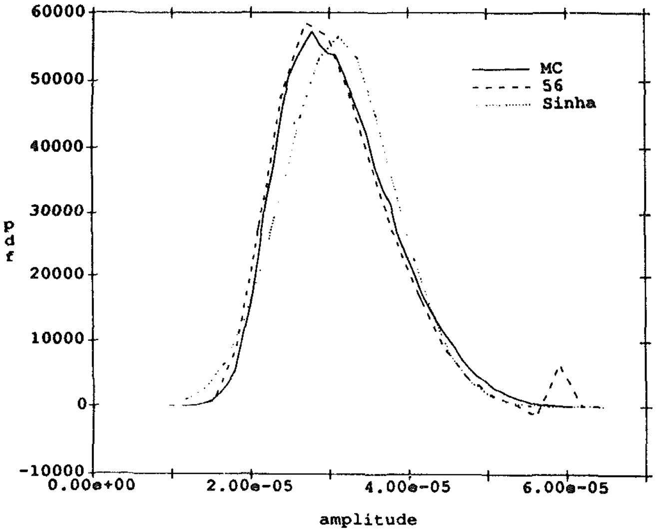

Fig. 4 Probability density of blade amplitude, $\omega = 6100$ rad/s

disk would be 23-dimensional). The surfaces denoted by *CS* and *BS* will be termed the critical and bound surfaces, respectively. They correspond to the conditions

$$\frac{W^2}{a^2} - g_{12}^2 = 0 \quad \text{for } CS \tag{58}$$

and

$$k_1 = -g_{11} \pm \left[\frac{W^2}{a^2} - g_{12}^2\right]^{1/2} = \pm\tau \quad \text{for } BS. \tag{59}$$

The region labeled 1 in Fig. 2 and located between the bound and critical surfaces is, for some values of r and n, part of the domain of integration D corresponding to Eq. (46). This fact can be ascertained by computing the value of the stiffness variation k_1, Eq. (43), corresponding to any point P located between the bound and critical surfaces. Then, the region 1 is an integral part of the domain D if and only if the computed value of k_1 lies between $-\tau$ and τ.

When necessary, the integration over the singular region 1 is accomplished in three steps (see Appendix IV for details). First, the functions W^2 and $(W^2/a^2) - g_{12}^2$ are expanded in Taylor series of $k_2, k_3, \ldots, k_n$ keeping respectively two and three terms (linear and quadratic approximations). Then, the function $W^2/\sqrt{(W^2/a^2) - g_{12}^2}$ is integrated in the direction perpendicular to the critical surface. This operation effectively removes the singularity of the problem. The third and final step of the computation, which consists in the integration over the $n-2$ tangential coordinates, is accomplished by relying, as in the off-resonant case, on the algorithm described in Appendix III.

Although the integrand is well behaved in the remaining domain, i.e., the regions labeled 2-5, it should be noted that the singularity on the critical surface has a global effect on the function $W^2/\sqrt{(W^2/a^2) - g_{12}^2}$, producing in particular rapid, nonlinear changes in the normal direction to the critical surface. This behavior motivated the division of the domain of integration into a number of smaller regions, labeled 2-5 in Fig. 2. Further, the contribution of each of these regions to the probability density function $p_{A_1}(a)$ has been obtained by relying first on a local linearization of the integrand with respect to the corresponding midpoint $\mathbf{s}_i$, see Fig. 2, and then on the algorithm described in Appendix III.

Numerical Example

To demonstrate the effectiveness of the proposed combined closed form-perturbation (CFP) method, a bladed disk has been considered whose parameters are as follows (Sinha and Chen, 1988):

$$m = 0.0114 \text{ kg} \tag{60}$$

$$k_C = 45430 \text{ N/m} \tag{61}$$

$$k = 430000 \text{ N/m} \tag{62}$$

$$c_C = 0 \tag{63}$$

$$c = 1.433 \text{ N}\cdot\text{s/m} \tag{64}$$

$$r = 3. \tag{65}$$

Further, it has been assumed that the mistuning originates in the stiffnesses, which are modeled as random variables uniformly distributed in the interval $k_j \in [-8000\sqrt{3}, 8000\sqrt{3}]$ in N/m. Shown in Figs. 3 and 4 are the probability density functions obtained by a thorough Monte Carlo simulation (curves labeled MC, 100,000 samples generated) and by Eq. (56) (curves labeled 56) corresponding to a 24-blade disk subjected to periodic excitations of frequencies $\omega = 6000$ and 6100 rad/s, respectively. These excitation frequencies are close to the value ω_0, Eq. (51), which is readily found to be 6141.60 rad/s. Clearly, the matching between the exact (Monte Carlo) and approximate (CFP) results is excellent in both cases. Note the presence on Fig. 4 of a small fluctuation in the CFP curve in the large amplitude tail of the distribution. This undulation is, from a numerical point of view, symptomatic of the proximity of the critical surface, Eq. (58), to the domain of integration and justifies the need for a separate investigation of the resonant conditions. Physically, the fluctuation indicates that some of the blades are undergoing resonance, and thus, display large amplitudes of response.

Also shown in Figs. 3 and 4 are the probability density functions obtained by relying on a three-term approximation of the equations of motion, as discussed by Sinha and Chen (1988, 1989). A comparison of these results clearly indicates that the combined closed form-perturbation approach provides a closer fit of the exact probability density function of the response.

Shown in Figs. 5-8 are the probability density functions, exact (through Monte Carlo simulation) and approximate (through the present approach), corresponding to 16, 18, 20, and 24-blade disks. It is seen that reliable approximations of $p_{A_i}(a)$ can also be obtained in the resonant case in spite of its aforementioned difficulties and peculiarities. It should be noted that the accuracy of the approximation obtained by the CFP method varies with the engine order. In particular, it appears

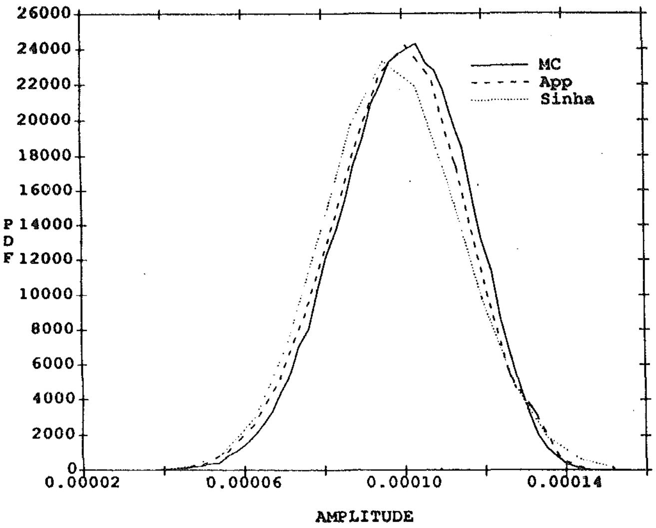

Fig. 5 Probability density, 16 blades, third engine order

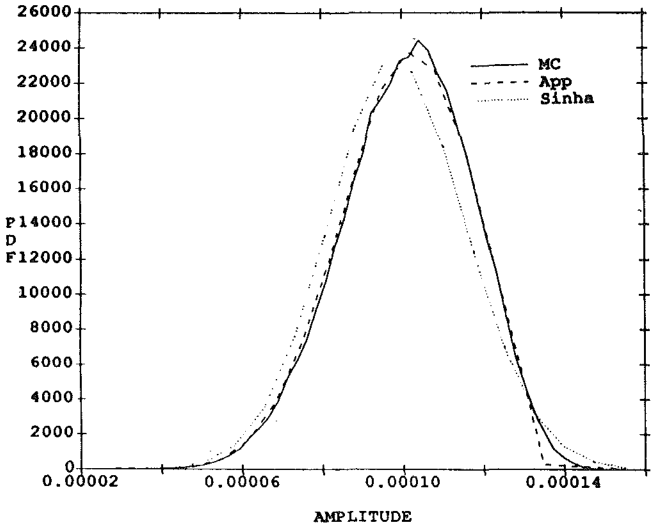

Fig. 6 Probability density, 18 blades, third engine order

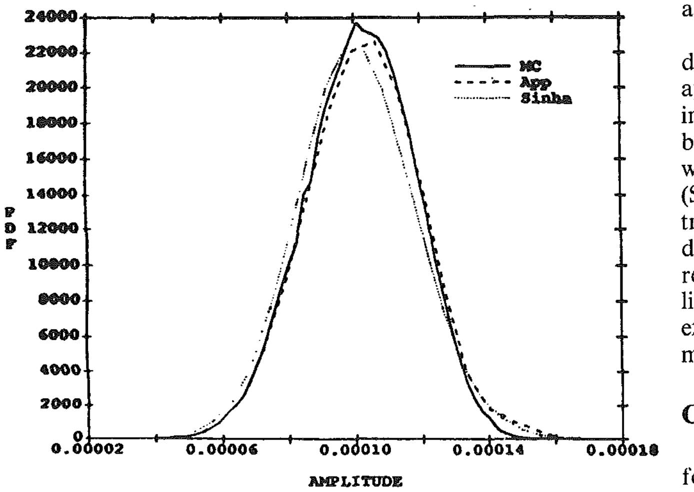

Fig. 7 Probability density, 20 blades, third engine order

that the zeroth engine order, which corresponds to excitation forces on the different blades which are in phase with each other, leads to the poorest matching between simulation and CFP results. This situation is depicted in Fig. 9 in context with a 24-blade disk. Finally, note that the ordinates in Figs. 5–9 have been scaled to satisfy the requirement that the total probability be equal to one.

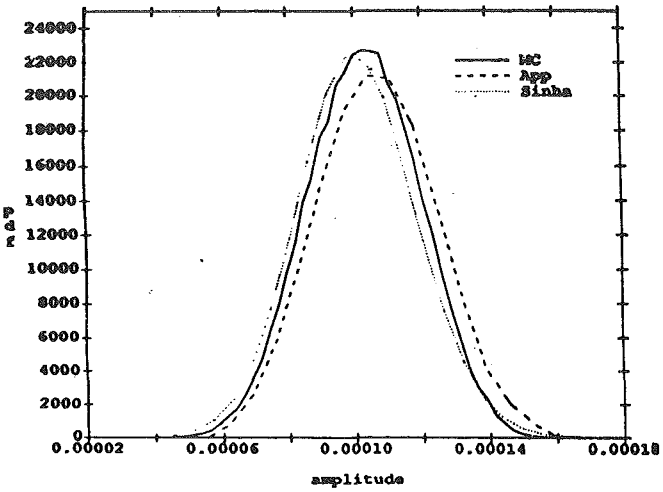

Fig. 8 Probability density, 24 blades, third engine order

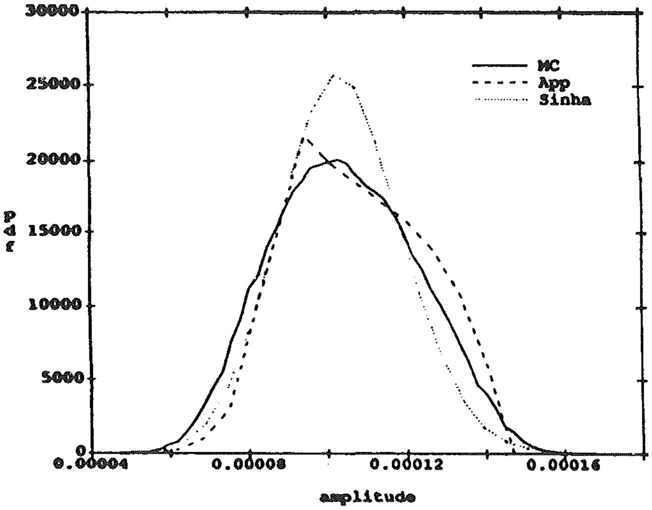

Fig. 9 Probability density, 24 blades, zeroth engine order

Also shown in Figs. 5–9 are the approximate probability density functions obtained by relying on Sinha and Chen's approach. A comparison of these curves with the corresponding results derived by the CFP method indicates that the combined closed form-perturbation technique performs always as well as and very often better than Sinha and Chen's approach (Sinha and Chen, 1988, 1989) in modeling the probability distribution of the amplitude of response of mistuned bladed disks. This conclusion is reinforced by noting that the CFP results shown in Figs. 3–9 have been obtained by relying on linear approximations of W^2 and either linear or quadratic expansions of $(W^2/a^2)-g_{12}^2$ as opposed to the cubic polynomial model of Sinha and Chen (1988, 1989).

Conclusions

In this paper, the determination of approximate expressions for the probability density function of the amplitude of response of randomly mistuned bladed disk has been addressed. A new computational method, termed the combined closed form-perturbation approach, has been suggested. First, it was recognized that the equations describing the steady-state response of the disk, Eqs. (4)–(6), represent a transformation between the set of random blade properties and the corresponding amplitudes of vibration. On the basis of this remark, an exact multifold integral representation of the probability density function of the blade amplitude was derived, Eq. (11), which is valid for any number of blades and any type of mistuning. Next, the computational aspects of the determination of the probability density function from this representation were investigated. In particular, it was found that the small magnitude of the variance of the blade properties could lead to simple perturbation-like approximations by relying on Eq. (19).

The modalities of application of the combined closed form-perturbation approach were demonstrated by considering a simple model of the disk in which each blade is represented by a one-degree-of-freedom system. Accurate approximations of the probability density function of the amplitude of response were sought first for near-resonant excitations. A reliable approximation of the probability density function was derived on the basis of a small mistuning, Eq. (56), through a series expansion of the integral representation in powers of the mistuned variables. An excellent matching between this approximation and simulation results was obtained in all cases considered. In the case of a resonant excitation, it was found that a similar approximation technique led in general to reliable approximations of the simulation results. A comparison of near-resonance and resonance results with the corresponding curves obtained by Sinha and Chen (1988, 1989) illustrates the advantages of the present approach.

Acknowledgments

The partial support of this work by a grant from the Allied-Signal Aerospace Company is gratefully acknowledged.

References

Basu, P., and Griffin, J. H., 1986, "The Effects of Limiting Aerodynamic and Structural Coupling in Models of Mistuned Bladed Disk Vibration," ASME *Journal of Vibration, Acoustics, Stress, and Reliability in Design*, Vol. 108, pp. 132-139.

Bendiksen, O. O., 1984, "Flutter of Mistuned Turbomachinery Rotors," ASME *Journal of Engineering for Gas Turbines and Power*, Vol. 106, pp. 25-33.

Crawley, E. F., and Hall, K. C., 1985, "Optimization and Mechanisms of Mistuning in Cascades," ASME *Journal of Engineering for Gas Turbines and Power*, Vol. 107, pp. 418-426.

Dugundji, J., and Bundas, D. J., 1984, "Flutter and Forced Response of Mistuned Rotors Using Standing Wave Analysis," *AIAA Journal*, Vol. 22, No. 11, pp. 1652-1661.

Dye, R. C. F., and Henry, T. A., 1969, "Vibration Amplitudes of Compressor Blades Resulting From Scatter in Blade Natural Frequencies," ASME *Journal of Engineering for Power*, Vol. 91, pp. 182-188.

Ewins, D. J., 1969, "The Effects of Detuning Upon the Forced Vibrations of Bladed Disks," *Journal of Sound and Vibration*, Vol. 9, No. 1, pp. 65-79.

Ewins, D. J., and Han, Z. S., 1984, "Resonant Vibration Levels of a Mistuned Bladed Disk," ASME *Journal of Vibration, Acoustics, Stress, and Reliability in Design*, Vol. 106, pp. 211-217.

Gradshteyn, I. S., and Ryzhik, I. M., 1980, *Table of Integrals, Series, and Products*, Academic Press, New York.

Griffin, J. H., and Sinha, A., 1985, "The Interaction Between Mistuning and Friction in the Forced Response of Bladed Disk Assemblies," ASME *Journal of Engineering for Gas Turbines and Power*, Vol. 107, pp. 205-211.

Griffin, J. H., 1988, "On Predicting the Resonant Response of Bladed Disk Assemblies," ASME *Journal of Engineering for Gas Turbines and Power*, Vol. 110, pp. 45-50.

Huang, W.-H., 1982, "Vibration of Some Structures With Periodic Random Parameters," *AIAA Journal*, Vol. 20, No. 7, pp. 1001-1008.

Kaza, K. R. V., and Kielb, R. E., 1984, "Flutter of Turbofan Rotors With Mistuned Blades," *AIAA Journal*, Vol. 22, No. 11, pp. 1618-1625,

Kaza, K. R. V., and Kielb, R. E., 1985, "Vibration and Flutter of Mistuned Bladed-Disk Assemblies," *Journal of Propulsion*, Vol. 1, No. 5, pp. 336-344.

Kielb, R. E., and Kaza, K. R. V., 1984, "Effects of Structural Coupling on Mistuned Cascade Flutter and Response," ASME *Journal of Engineering for Gas Turbines and Power*, Vol. 106, pp. 17-24.

Lin, C. C., 1992, "The Combined Closed Form-Perturbation Approach to the Analysis of Mistuned Bladed Disks," M.S. Thesis, Arizona State University, Tempe, AZ.

Mignolet, M. P., and Christensen, K. R., 1990, "Probabilistic Analysis of Mistuned Bladed Disks: A Combined Closed Form-Perturbation Approach," ASME Paper No. 90-GT-191.

Mignolet, M. P., and Lin, C. C., 1992, "Probability and Conditional Moments of Multivariate Uniform Random Variables Satisfying a Linear Inequality Constraint," *Probabilistic Engineering Mechanics*, Vol. 7, pp. 65-74.

Nissim, E., 1985, "Optimization of Cascade Blade Mistuning, Part I: Equations of Motion and Basic Inherent Properties," *AIAA Journal*, Vol. 23, No. 8, pp. 1213-1222.

Noble, B., and Daniel, J., 1988, *Applied Linear Algebra*, Prentice-Hall, Englewood Cliffs, NJ.

Sinha, A., 1986, "Calculating the Statistics of Forced Response of a Mistuned Bladed Disk Assembly," *AIAA Journal*, Vol. 24, No. 11, pp. 1797-1801.

Sinha, A., and Chen, S., 1988, "Probabilistic Analysis of Forced Response of a Bladed Disk Assembly With Various Mistuning Distributions," *Proceedings of the 29th Structures, Structural Dynamics and Materials Conference*, Williamsburg, VA, Part III, pp. 1487-1494.

Sinha, A., and Chen, S., 1989, "A Higher Order Technique to Compute the Statistics of Forced Response of a Mistuned Bladed Disk," *Journal of Sound and Vibration*, Vol. 130, No. 2, pp. 207-221.

Srinivasan, A. V., and Fabunmi, J. A., 1984, "Cascade Flutter Analysis of Cantilevered Blades," ASME *Journal of Engineering for Gas Turbines and Power*, Vol. 106, pp. 34-43.

Thomas, D. L., 1979, "Dynamics of Rotationally Periodic Structures," *International Journal for Numerical Methods in Engineering*, Vol. 14, pp. 81-102.

Valero, N. A., and Bendiksen, O. O., 1986, "Vibration Characteristics of Mistuned Shrouded Blade Assemblies," ASME *Journal of Engineering for Gas Turbines and Power*, Vol. 108, pp. 293-299.

Wei, S.-T., and Pierre, C., 1988a, "Localization Phenomena in Mistuned Assemblies With Cyclic Symmetry—Part I: Free Vibrations," ASME *Journal of Vibration, Acoustics, Stress, and Reliability in Design*, Vol. 110, pp. 429-438.

Wei, S.-T., and Pierre, C., 1988b, "Localization Phenomena in Mistuned Assemblies With Cyclic Symmetry—Part II: Forced Vibrations," ASME *Journal of Vibration, Acoustics, Stress, and Reliability in Design*, Vol. 110, pp. 439-449.

Wei, S.-T., and Pierre, C., 1990, "Statistical Analysis of the Forced Response of Mistuned Cyclic Assemblies," *AIAA Journal*, Vol. 28, No. 5, pp. 861-868.

Whitehead, D. S., 1966, "Effect of Mistuning on the Vibration of Turbomachines Blades Induced by Wakes," *Journal of Mechanical Engineering Science*, Vol. 8, No. 1, pp. 15-21.

APPENDIX I

The special structure of the matrices H and δH provides a series of simplifications in the determination of the Jacobian, Eq. (33). Specifically, partitioning $(H+\delta H)$, as an $N\times N$ block matrix, it is readily seen that each of its 2×2 block elements, denoted here by $\{H+\delta H\}_{jl}$, can be written in the form

$$\{H+\delta H\}_{jl}=\begin{bmatrix} d & e \\ -e & d \end{bmatrix} \tag{A.1}$$

for some values of the coefficients d and e. Such 2×2 matrices, termed here anticentrosymmetric, are characterized by the condition

$$P_2^T\{H+\delta H\}_{jl}P_2=\{H+\delta H\}_{jl} \tag{A.2}$$

where

$$P_2=\begin{bmatrix} 0 & 1 \\ -1 & 0 \end{bmatrix}. \tag{A.3}$$

In fact, it is readily shown that Eq. (A.2) is a necessary and sufficient condition for the existence of the representation (A.1) of the matrix $\{H+\delta H\}_{jl}$. Since the property (A.2) is valid for all 2×2 block elements of $(H+\delta H)$, it is readily shown that this matrix satisfies the equation

$$P_N^T(H+\delta H)P_N=(H+\delta H) \tag{A.4}$$

where

$$P_N=\begin{bmatrix} P_2 & 0 & \cdot & \cdot & 0 \\ 0 & P_2 & \cdot & \cdot & 0 \\ \cdot & \cdot & \cdot & \cdot & \cdot \\ \cdot & \cdot & \cdot & \cdot & \cdot \\ 0 & 0 & \cdot & \cdot & P_2 \end{bmatrix}. \tag{A.5}$$

It is now possible to show that the matrix $(H+\delta H)^{-1}$ also satisfies Eq. (A.4). To this end, note first that

$$(H+\delta H)(H+\delta H)^{-1}=I_{2N} \tag{A.6}$$

and

$$P_N^T P_N = P_N P_N^T = I_{2N} \tag{A.7}$$

where I_{2N} denotes the $2N \times 2N$ identity matrix. Then, rewrite Eq. (A.6) in the form

$$P_N^T[(H+\delta H)(P_N P_N^T)(H+\delta H)^{-1}]P_N = P_N^T I_{2N} P_N = I_{2N} \tag{A.8}$$

or equivalently as

$$[P_N^T(H+\delta H)P_N][P_N^T(H+\delta H)^{-1}P_N] = I_{2N} \tag{A.9}$$

In view of the property (A.4), it is found that

$$(H+\delta H)[P_N^T(H+\delta H)^{-1}P_N] = I_{2N} \tag{A.10}$$

so that

$$P_N^T(H+\delta H)^{-1}P_N = (H+\delta H)^{-1}. \tag{A.11}$$

The last equation shows that $(H+\delta H)^{-1}$ also satisfies Eq. (A.4) and thus, that each of its 2×2 block elements $\{(H+\delta H)^{-1}\}_{jl}$ is anticentrosymmetric. Equations (31) and (32) then follow by considering in particular $\{(H+\delta H)^{-1}\}_{11}$.

APPENDIX II

It is readily seen from Eqs. (53)–(55) that

$$g_{11}^0 = k_t - m\omega^2 + 2k_C - \mathbf{e}_1^T H_{12}\overline{H}_{22}^{-1}H_{21}\mathbf{e}_1 \tag{A.12}$$

$$\mathbf{g}_{11}^R = \overline{H}_{22}^{-1}H_{21}\mathbf{e}_1 \tag{A.13}$$

$$\mathbf{g}_{11}^L = \mathbf{g}_{12}^L = \mathbf{e}_1^T H_{12}\overline{H}_{22}^{-1} \tag{A.14}$$

$$g_{12}^0 = -c\omega - \mathbf{e}_1^T H_{12}\overline{H}_{22}^{-1}H_{22}\mathbf{e}_2 \tag{A.15}$$

$$\mathbf{g}_{12}^R = \overline{H}_{22}^{-1}H_{21}\mathbf{e}_2. \tag{A.16}$$

Further, introducing the partition

$$\tilde{\mathbf{F}} = \begin{bmatrix} \tilde{\mathbf{F}}_1 \\ \tilde{\mathbf{F}}_2 \end{bmatrix} \tag{A.17}$$

where $\tilde{\mathbf{F}}_1$ is a two-component vector, it is found from Eq. (41) that

$$\begin{aligned}\mathbf{W} = \tilde{\mathbf{F}}_1 - H_{12}H_{22}^{-1}\tilde{\mathbf{F}}_2 &= [\tilde{\mathbf{F}}_1 - H_{12}\overline{H}_{22}^{-1}\tilde{\mathbf{F}}_2] \\ &\quad + H_{12}\overline{H}_{22}^{-1}\delta H_{22}\overline{H}_{22}^{-1}\tilde{\mathbf{F}}_2 + O(\delta H_{22}^2)\end{aligned} \tag{A.18}$$

so that

$$\begin{aligned}W^2 = \mathbf{W}^T\mathbf{W} &= [\tilde{\mathbf{F}}_1 - H_{12}\overline{H}_{22}^{-1}\tilde{\mathbf{F}}_2]^T[\tilde{\mathbf{F}}_1 - H_{12}\overline{H}_{22}^{-1}\tilde{\mathbf{F}}_2] \\ &\quad + 2[\tilde{\mathbf{F}}_1 - H_{12}\overline{H}_{22}^{-1}\tilde{\mathbf{F}}_2]^T H_{12}\overline{H}_{22}^{-1}\delta H_{22}\overline{H}_{22}^{-1}\tilde{\mathbf{F}}_2 + O(\delta H_{22}^2).\end{aligned} \tag{A.19}$$

The above expression can be written in the form of Eq. (55) by selecting

$$w_0 = [\tilde{\mathbf{F}}_1 - H_{12}\overline{H}_{22}^{-1}\tilde{\mathbf{F}}_2]^T[\tilde{\mathbf{F}}_1 - H_{12}\overline{H}_{22}^{-1}\tilde{\mathbf{F}}_2] \tag{A.20}$$

$$\mathbf{w}_1 = 2[\tilde{\mathbf{F}}_1 - H_{12}\overline{H}_{22}^{-1}\tilde{\mathbf{F}}_2]^T H_{12}\overline{H}_{22}^{-1} \tag{A.21}$$

and

$$\mathbf{w}_2 = \overline{H}_{22}^{-1}\tilde{\mathbf{F}}_2. \tag{A.22}$$

APPENDIX III

The evaluation of the moments

$$E\left[k_j^p \,\middle|\, \sum_{j=1}^{n} b_j k_j \le b_0\right]$$

of uniform random variables k_j satisfying a linear inequality constraint of the form

$$\sum_{j=1}^{n} b_j k_j \le b_0$$

has recently been investigated by Mignolet and Lin (1992). It was shown in particular that

$$\begin{aligned}E\left[\sum_{j=1}^{n} a_j k_j \,\middle|\, \sum_{i=1}^{n} b_i k_i \le b_0\right] &= \sum_{j=1}^{n} a_j E\left[k_j \,\middle|\, \sum_{i=1}^{n} b_i k_i \le b_0\right] \\ &= \frac{1}{\left[\prod_{i=1}^{n} b_i\right] n!}\left[d_0 b_0^n - \sum_{i=1}^{n}(d_0 - d_i)\lfloor b_0 - b_i \rfloor^n\right. \\ &\quad \left. + \sum_{\substack{i,j=1 \\ i>j}}^{n}(d_0 - d_i - d_j)\lfloor b_0 - b_i - b_j \rfloor^n - \cdot\cdot\right]\end{aligned} \tag{A.23}$$

where the notation $\lfloor u \rfloor$ denotes the maximum of u and 0. Further,

$$d_0 = \frac{b_0}{n+1}\sum_{j=1}^{n}\frac{a_j}{b_j} \tag{A.24a}$$

and

$$d_i = -a_i + \frac{b_i}{n+1}\sum_{j=1}^{n}\frac{a_j}{b_j}. \tag{A.24b}$$

A reduction of the number of computations required to evaluate

$$E\left[\sum_{j=1}^{n} a_j k_j \,\middle|\, \sum_{j=1}^{n} b_j k_j \le b_0\right]$$

according to Eq. (A.23) can be achieved when some of the coefficients b_j are small. Then, separating the parameters b_j into two groups, the large coefficients b_j, $j=1, \ldots, n-m$ and the small ones

$$c_j = b_{n-m+j} \quad j=1, \ldots, m, \tag{A.25}$$

it is found that

$$\begin{aligned}E\left[\sum_{j=1}^{n} a_j k_j \,\middle|\, \sum_{i=1}^{n} b_i k_i \le b_0\right] &= \frac{1}{\left[\prod_{i=1}^{n-m} b_i\right](n-m)!} \\ &\quad \times \left[e_0^{(1)} b_0^{n-m} - \sum_{i=1}^{n-m}(e_0^{(1)} - e_i^{(1)})\lfloor b_0 - b_i \rfloor^{n-m}\right. \\ &\quad \left. + \sum_{\substack{i,j=1 \\ i>j}}^{n-m}(e_0^{(1)} - e_i^{(1)} - e_j^{(1)})\lfloor b_0 - b_i - b_j \rfloor^{n-m} - \cdot\cdot\right] \\ &\quad - \frac{1}{2\left[\prod_{i=1}^{n-m} b_i\right](n-m-1)!}\left[e_0^{(2)} b_0^{n-m-1} - \sum_{i=1}^{n-m}(e_0^{(2)} - e_i^{(2)})\right. \\ &\quad \times \lfloor b_0 - b_i \rfloor^{n-m-1} + \sum_{\substack{i,j=1 \\ i>j}}^{n-m}(e_0^{(2)} - e_i^{(2)} - e_j^{(2)}) \\ &\quad \left. \times \lfloor b_0 - b_i - b_j \rfloor^{n-m-1} - \cdot\cdot\right]\end{aligned} \tag{A.26}$$

where

$$e_0^{(1)} = \frac{b_0}{n-m+1}\sum_{j=1}^{n-m}\frac{a_j}{b_j} + \frac{1}{2}\sum_{j=n-m+1}^{n} a_j \tag{A.27a}$$

$$e_i^{(1)} = -a_i + \frac{b_i}{n-m+1}\sum_{j=1}^{n-m}\frac{a_j}{b_j} \quad i=1, \ldots, n-m \tag{A.27b}$$

and

$$\begin{aligned}e_0^{(2)} &= \left(\sum_{i=1}^{m} c_i\right)\left[\frac{b_0}{n-m}\sum_{j=1}^{n-m}\frac{a_j}{b_j} + \frac{1}{2}\sum_{j=n-m+1}^{n} a_j\right] \\ &\quad + \frac{1}{12}\sum_{i=1}^{m} c_i a_{n-m+i}\end{aligned} \tag{A.28a}$$

$$e_i^{(2)} = -a_i + \frac{b_i}{n-m} \sum_{j=1}^{n-m} \frac{a_j}{b_j} \quad i=1, \ldots, n-m. \tag{A.28b}$$

Note that higher order approximate expressions of

$$E\left[\sum_{j=1}^{n} a_j k_j \,\middle|\, \sum_{j=1}^{n} b_j k_j \le b_0 \right]$$

are readily derived and that the above results can be extended to the case of nonuniform random variables k_j.

A detailed derivation of the above results and a thorough analysis of the computational and implementation aspects of Eqs. (A.23) and (A.26) can be found in Mignolet and Lin (1992).

APPENDIX IV

Let $\mathbf{K} = [k_2, k_3, \ldots, k_n]^T$ be the position vector of an arbitrary point P in the region labeled 1 (see Fig. 2). Similarly, let $\mathbf{K}_Q$ denote the position vector of a point Q located on the critical surface. Then, expanding in Taylor series the function W^2 and $(W^2/a^2) - g_{12}^2$ with respect to the point $\mathbf{K}_Q$, it is found that

$$W^2 \approx \mu_0 + \mu_1^T(\mathbf{K} - \mathbf{K}_Q) + (\mathbf{K} - \mathbf{K}_Q)^T B_1 (\mathbf{K} - \mathbf{K}_Q) \tag{A.29}$$

$$\frac{W^2}{a^2} - g_{12}^2 \approx \mu_2^T(\mathbf{K} - \mathbf{K}_Q) + (\mathbf{K} - \mathbf{K}_Q)^T B_2 (\mathbf{K} - \mathbf{K}_Q) \tag{A.30}$$

where μ_0 is the value of W^2 corresponding to $\mathbf{K}_Q$. Further, μ_1, μ_2 and B_1, B_2 are the gradients and Hessians of the functions W^2 and $(W^2/a^2) - g_{12}^2$ corresponding to the point $\mathbf{K}_Q$. Note that the vector μ_2 is in the direction normal to the surface $(W^2/a^2) - g_{12}^2 = 0$ at the point $\mathbf{K}_Q$. Further, define the matrix D as

$$D = \begin{bmatrix} u_2 & u_3 & u_4 & \cdot & u_n \\ u_3 & -u_2 & 0 & \cdot & 0 \\ u_4 & 0 & -u_2 & \cdot & 0 \\ \cdot & \cdot & \cdot & \cdot & \cdot \\ \cdot & \cdot & \cdot & \cdot & \cdot \\ u_n & 0 & 0 & \cdot & -u_2 \end{bmatrix} \tag{A.31}$$

with

$$\mu_2 = [u_2, u_3, \ldots, u_n]^T \tag{A.32}$$

and introduce the new position vector $\boldsymbol{\alpha} = [\alpha_2, \alpha_3, \ldots, \alpha_n]^T$ defined by

$$\mathbf{K} = \mathbf{K}_Q + D\boldsymbol{\alpha}. \tag{A.33}$$

Then, the contribution of the domain 1 to the probability density function can be expressed as a multifold integral over the variables $\alpha_2, \alpha_3, \ldots, \alpha_n$. A Taylor expansion of the corresponding integrand with respect to the normal variable α_2 yields the following approximate contribution

$$\det(D) \int \cdot\cdot \int \left[\int_0^{\epsilon/|\mu_2|} \frac{d_1\alpha_2 + d_2}{\sqrt{d_3\alpha_2^2 + d_4\alpha_2 + d_5}} d\alpha_2 \right] d\alpha_3 \cdot\cdot d\alpha_n \tag{A.34}$$

where ϵ is the small distance between the critical and the first bound surfaces. Further, the functions d_1, d_2, d_3, d_4, and d_5 are quadratic in the variables α_i, $i = 3, 4, \ldots, n$. The integration over α_2 can be evaluated by standard techniques as (Gradshteyn and Ryzhik, 1980)

$$\int \frac{d_1\alpha_2 + d_2}{\sqrt{d_3\alpha_2^2 + d_4\alpha_2 + d_5}} d\alpha_2 = \frac{d_1\sqrt{R}}{d_3} + \left(d_2 - \frac{d_4 d_1}{2d_3}\right) \frac{1}{\sqrt{d_3}} \ln(2\sqrt{d_3 R} + 2d_3\alpha_2 + d_4) \quad \text{when } d_3 > 0 \tag{A.35a}$$

and

$$\int \frac{d_1\alpha_2 + d_2}{\sqrt{d_3\alpha_2^2 + d_4\alpha_2 + d_5}} d\alpha_2 = \frac{d_1\sqrt{R}}{d_3} + \left(d_2 - \frac{d_4 d_1}{2d_3}\right) \frac{-1}{\sqrt{-d_3}} \sin^{-1}\left(\frac{2d_3\alpha_2 + d_4}{\sqrt{d_4^2 - 4d_3 d_5}}\right) \quad \text{when } d_3 < 0 \tag{A.35b}$$

where $R = d_3\alpha_2^2 + d_4\alpha_2 + d_5$. A final linearization of Eq. (A.35) with respect to the variables $\alpha_3, \alpha_4, \cdots, \alpha_n$ yields the following approximation

$$\int_0^{\epsilon/|\mu_2|} \frac{d_1\alpha_2 + d_2}{\sqrt{d_3\alpha_2^2 + d_4\alpha_2 + d_5}} d\alpha_2 \approx E_0 + \sum_{i=3}^{n} E_i \alpha_i. \tag{A.36}$$

It remains then to return to the original variables k_i and to compute the remaining integral. The first step is readily accomplished by noting that

$$\boldsymbol{\alpha}' = D'(\mathbf{K} - \mathbf{K}_Q) \tag{A.37}$$

where

$$\boldsymbol{\alpha}' = [\alpha_3, \alpha_4, \cdots, \alpha_n]^T \tag{A.38}$$

and

$$D' = \begin{bmatrix} \text{2nd row of } D^{-1} \\ \text{3rd row of } D^{-1} \\ \cdot \\ \cdot \\ \text{last row of } D^{-1} \end{bmatrix} \tag{A.39}$$

while the evaluation of the integral over the variables $k_3, \cdots, k_n$ is achieved by relying on the algorithm described in Appendix III.

G. A. Gerolymos
Université Pierre & Marie Curie,
Paris, France

Advances in the Numerical Integration of the Three-Dimensional Euler Equations in Vibrating Cascades

In the present work an algorithm for the numerical integration of the three-dimensional unsteady Euler equations in vibrating transonic compressor cascades is described. The equations are discretized in finite-volume formulation in a mobile grid using isoparametric brick elements. They are integrated in time using Runge-Kutta schemes. A thorough discussion of the boundary conditions used and of their influence on results is undertaken. The influence of grid refinement on computational results is examined. Unsteady convergence of results is discussed.

Introduction

Methods for numerically integrating the unsteady Euler equations in vibrating cascades have been developed by various authors, in two or two and a half dimensions (e.g., Gerolymos, 1988a; He, 1990; Kau and Gallus, 1989; Huff et al., 1991). These methods compare very well with linearized flat-plate cascade theory, and give satisfactory agreement with experiment, in the supersonic flutter region, at least up to the shock-wave/boundary-layer interaction region (Gerolymos et al., 1990). Recently He and Denton (1993a, 1993b) used viscous-inviscid interaction for predicting attached flows around vibrating cascades, including shock-wave/boundary-layer interaction, where it is shown that the phase error introduced by inviscid methods can be accounted for by viscous effects. Sidén (1991) solved the Reynolds-averaged Navier-Stokes equations using a mixing-length turbulence closure, for subsonic flows around oscillating cascades.

In a recent review paper on aeroelastic problems in turbomachines Bendiksen (1990) points out that "a real rotor would have a three-dimensional shock structure that would differ from the corresponding two-dimensional cascade shock structure" (cf. Epstein et al., 1979; Kerrebrock, 1981) and remarks that "in the aeroelastic problems, there is a general consensus that viscous effects can be neglected except in stall and choke flutter problems." In view of current CFD (Computational Fluid Dynamics) status (e.g., MacCormack, 1985; Jameson, 1988, 1989; Hussaini, 1989), and of computer hardware and software development (Neves, 1988a, 1988b), three-dimensional unsteady Euler solvers for turbomachinery flows can be readily industrialized. Furthermore, Navier-Stokes algorithm structure can be considered as an extension of Euler solvers (e.g., Gerolymos, 1990), and consequently, the development of three-dimensional unsteady Euler solvers is the first step toward three-dimensional unsteady Navier-Stokes solvers.

The present work is a development of the vibrating cascades three-dimensional Euler solver presented by Gerolymos (1988b), in which the MacCormack explicit scheme (MacCormack, 1971) was used. It is concerned with using more advanced numerical techniques, both with respect to computational efficiency and to robustness, viz. Runge-Kutta schemes (Jameson et al., 1981; Jameson, 1983; Venkatakrishnan and Jameson, 1988) in finite-volume formulation based on isoparametric brick elements (Zienkiewicz, 1977; Oden, 1972); it is also concerned with discussing in detail the numerical boundary conditions used and their effect on computational results, and with investigating unsteady convergence of results.

2 Numerics

2.1 Governing Equations. The flow field is modeled by the unsteady three-dimensional Euler equations (e.g., Vavra, 1960),

$$\frac{\partial\rho}{\partial t}+\nabla\cdot(\rho\mathbf{W})=0$$

$$\frac{\partial\rho\mathbf{W}}{\partial t}+\nabla\cdot(\rho\mathbf{W}\otimes\mathbf{W}+p\mathbb{I})+2\rho\boldsymbol{\Omega}\times\mathbf{W}+\rho\nabla(-\Omega^2R^2/2)=0$$

$$\frac{\partial\rho E}{\partial t}+\nabla\cdot(\rho\mathbf{W}H)=0 \qquad (1)$$

completed by the perfect-gas equation of state,

$$p=\rho R_g T \qquad (2)$$

where ρ is the density, t the time, ∇ the gradient operator, $\mathbf{W}$ the relative flow velocity, H the rothalpy ($H = h + W^2/2 - (\Omega R)^2/2$), h the static enthalpy, E the total energy in the rotating frame ($E = H - p/\rho$), $\boldsymbol{\Omega}$ the rotational velocity

---

Contributed by the International Gas Turbine Institute and presented at the 37th International Gas Turbine and Aeroengine Congress and Exposition, Cologne, Germany, June 1-4, 1992. Manuscript received by the International Gas Turbine Institute February 17, 1992. Paper No. 92-GT-170. Associate Technical Editor: L. S. Langston.

vector, R the radius with respect to the rotation axis, p the static pressure, T the static temperature, R_g the gas constant, and $\mathbb{I}$ the identity 3×3 tensor.

2.2 Space Discretization. The Euler equations are discretized in a moving structured grid, whose displacement velocity field is determined by the blade vibration (cf. Gerolymos, 1988a, 1988b). The flow variables are stored at the vertices of the grid. The space discretization of the equations uses the finite-volume technique (cf. the review by Vinokur, 1989). Integrating the Euler equations in a mobile control volume $\mathcal{V}(t)$ defined by each grid cell, and applying the divergence theorem (Vavra, 1960), the following finite-volume equations are obtained:

$$\frac{\partial}{\partial t}\left(\iiint_{\mathcal{V}} \rho d\mathcal{V}\right)+\iiint_{\partial\mathcal{V}} \rho(\mathbf{W}-\mathbf{V}_g)\mathbf{n}dS=0$$

$$\frac{\partial}{\partial t}\left(\iiint_{\mathcal{V}} \rho\mathbf{W}d\mathcal{V}\right)+\iint_{\partial\mathcal{V}} (\rho(\mathbf{W}-\mathbf{V}_g)(\mathbf{W}\cdot\mathbf{n})+p\mathbf{n})dS$$
$$+\iiint_{\mathcal{V}} \rho(2\boldsymbol{\Omega}\times\mathbf{W}+\nabla(-\Omega^2R^2/2))d\mathcal{V}=0$$

$$\frac{\partial}{\partial t}\left(\iiint_{\mathcal{V}} (\rho H-p)d\mathcal{V}\right)+\iint_{\partial\mathcal{V}}$$
$$\times((\rho H-p)(\mathbf{W}-\mathbf{V}_g)\cdot\mathbf{n}+p\mathbf{n})dS=0 \quad (3)$$

where $\mathcal{V}(t)$ is the control-volume, $\partial\mathcal{V}$ is the control-volume boundary surface, and $\mathbf{V}_g$ is the grid displacement velocity.

The surface integrals that appear in the finite-volume equations (Eqs. (2)) must be approximated using some numerical procedure. Usually (e.g., Ni, 1982; Denton, 1983; Koeck, 1985; Holmes and Tong, 1985; Venkatakrishnan and Jameson, 1988) they are computed as the mean value of the integrand (1/4 of the sum of the values of the integrand at the corresponding vertices) times the area of the surface (summed over the six hexahedron surfaces). In the present work it was preferred to use isoparametric brick elements (Zienkiewicz, 1977; Oden, 1972), with trilinear interpolation, for computing the surface integrals in Eq. (2). This type of elements is widely used in finite-volume computations for computing the volume of the grid cells (e.g., Kordulla and Vinokur, 1983; Davies and Salmond, 1985; Dukowicz, 1988). Computer implementation consists in computing the operator

$$\mathrm{DIV}(\mathbf{f})=\frac{1}{\mathcal{V}}\iint_{\partial\mathcal{V}} \mathbf{f}\cdot\mathbf{n}dS \quad (4)$$

There results a computing-time overhead of ~10 percent with respect to standard divergence computations.

2.3 Time Discretization. Time stepping is based on the Runge-Kutta procedure, initially introduced by Jameson et al. (1981), and extensively used by many authors, both for steady and unsteady flow problems (e.g., Jameson, 1983; Chima, 1985, 1987; Jameson and Mavriplis, 1986; Venkatakrishnan and Jameson, 1988; He, 1990; Chima and Yokota, 1990; Batina, 1991).

Denoting $\mathbf{U}\in\mathbb{R}^5$ the vector of unknowns

$$\mathbf{U}=[\rho,\ \rho W_1,\ \rho W_2,\ \rho W_3,\ \rho H-p]^T \quad (5)$$

the Euler equations may be concisely written in the following semi-discrete form

$$\frac{\partial\mathbf{U}}{\partial t}+\mathbf{DIV}\{\mathbf{F}(\mathbf{U})\}+\mathbf{S}(\mathbf{U})=\mathbf{DIS}(\mathbf{U}) \quad (6)$$

where $\mathbf{F}\in\mathbb{R}^3\times\mathbb{R}^5$ denotes the corresponding fluxes (cf. Eqs. (1) and (3)), and $\mathbf{DIV}$: $\mathbb{R}^3\times\mathbb{R}^5\rightarrow\mathbb{R}^5$ is a numerical approximation to the divergences of the fluxes; $\mathbf{S}\in\mathbb{R}^5$ are source terms. If overscores denote mean values over a control volume, $\mathfrak{T}$ is a transfer operator from volume centers to vertices, and **DIS(U)** is the artificial dissipation operator (to be discussed in the following), a NRG-order Runge-Kutta time-stepping scheme is

$$^0\mathbf{U}={}^n\mathbf{U}$$
$$\overline{^1\Delta\mathbf{U}}=-\alpha_1\Delta t\{\mathbf{DIV}[\mathbf{F}(^0\mathbf{U})]+\mathbf{S}(^0\mathbf{U})-\mathbf{DIS}(^0\mathbf{U})\}$$
$$^1\mathbf{U}={}^0\mathbf{U}+\mathfrak{T}[\overline{^1\Delta\mathbf{U}}]$$
$$\overline{^2\Delta\mathbf{U}}=-\alpha_2\Delta t\{\mathbf{DIV}[\mathbf{F}(^1\mathbf{U})]+\mathbf{S}(^1\mathbf{U})-\mathbf{DIS}(^1\mathbf{U})\}$$
$$^2\mathbf{U}={}^0\mathbf{U}+\mathfrak{T}[\overline{^2\Delta\mathbf{U}}]$$
$$\vdots$$
$$\overline{^{\mathrm{NRG}}\Delta\mathbf{U}}=-\alpha_{\mathrm{NRG}}\Delta t\{\mathbf{DIV}[\mathbf{F}(^{\mathrm{NRG}-1}\mathbf{U})]$$
$$+\mathbf{S}(^{\mathrm{NRG}-1}\mathbf{U})-\mathbf{DIS}(^{\mathrm{NRG}-1}\mathbf{U})\}$$
$$^{\mathrm{NRG}}\mathbf{U}={}^0\mathbf{U}+\mathfrak{T}[\overline{^{\mathrm{NRG}}\Delta\mathbf{U}}]$$
$$^{n+1}\mathbf{U}={}^{\mathrm{NRG}}\mathbf{U} \quad (7)$$

Table 1 Coefficients for Runge-Kutta schemes

NRG	2	3	4	5
α_1	$\frac{1}{2}$	$\frac{6}{10}$	$\frac{1}{4}$	$\frac{1}{4}$
α_2	1	$\frac{1}{2}$	$\frac{1}{3}$	$\frac{1}{6}$
α_3		1	$\frac{1}{2}$	$\frac{3}{8}$
α_4			1	$\frac{1}{2}$
α_5				1
CFL	0·95	1·5	2·5	3·5

Transfer of residuals from volume centers to vertices is done by volume-weighted-averaging, which as noted by Jameson (1983) preserves conservation of mass, momentum, and energy. Various schemes may be represented by the previous time stepping depending on the choice of NRG and of the α coefficients. Higher-order (larger NRG) schemes are stable for larger CFL numbers (e.g., Jameson et al., 1981; Chima et al., 1987). The α coefficients and corresponding CFL numbers used in the present study are summarized in Table 1. As noted by Venkatakrishnan and Jameson (1988) $\alpha_{\mathrm{NRG}}=1$ for consistency, and $\alpha_{\mathrm{NRG}-1}=1/2$ for second-order time accuracy. No particular treatment of the source terms was found necessary for the cases studied.

2.4 Artificial Dissipation. Artificial dissipation (cf. Roache, 1972) was used in order to damp parasitic oscillations and capture shock waves (operator **DIS**: $\mathbb{R}^5\rightarrow\mathbb{R}^5$). It consists of a fourth-order smoothing $^4\mathbf{DIS}$ and a second-order nonlinear shock-capturing diffusionlike operator $^2\mathbf{DIS}$ (Lapidus, 1967). The nonlinear operator is applied only on velocity components. Both these operators are applied in a split sequential fashion in every grid direction. Symbolically

$$\mathbf{DIS}(\mathbf{U})={}^2\mathbf{DIS}_i(\mathbf{U})+{}^2\mathbf{DIS}_j(\mathbf{U})+{}^2\mathbf{DIS}_k(\mathbf{U})+{}^4\mathbf{DIS}_i(\mathbf{U})$$
$$+{}^4\mathbf{DIS}_j(\mathbf{U})+{}^4\mathbf{DIS}_k(\mathbf{U}) \quad (8a)$$

$$^4\mathbf{DIS}(\mathbf{U})=\frac{q_4}{\Delta t}\{-\mathbf{U}_{i+2}+4\mathbf{U}_{i+1}-6\mathbf{U}_i+4\mathbf{U}_{i-1}-\mathbf{U}_{i-2}\} \quad (8b)$$

$$^2\mathbf{DIS}(\mathbf{U})=[0,\ ^2\mathrm{DIS}(\rho W_1),\ ^2\mathrm{DIS}(\rho W_2),\ ^2\mathrm{DIS}(\rho W_3),\ 0]^T \quad (8c)$$

$$ {}^2\mathrm{DIS}(\rho W)=\frac{q_2}{\Delta l}\{(\rho_{i+1}+\rho_i)(W_{i+1}-W_i)\,|W_{i+1}-W_i| + (\rho_{i-1}+\rho_i)(W_{i-1}-W_i)\,|W_{i-1}-W_i|\} \quad (8d) $$

where Δl is a mean cell length, defined in the same way as in Gerolymos (1988b).

The boundary treatment of the dissipation operators is essential for the quality of the results, and sometimes for the global numerical stability of the scheme itself. For the Lapidus-type second-order nonlinear operator (Lapidus, 1967), applied only to the velocity components, one-sided differences were used at boundary points. This boundary treatment was found to be important for the overall scheme stability at three-dimensional-corner supersonic expansion regions. This presumably explains the problems encountered by He (1990), who did not use such a treatment. For the fourth-order operator ^{4}**DIS** the treatment mentioned by Pulliam (1986a, 1986b), Swanson and Turkel (1987), and Olsson and Johnson (1989) was used. The corresponding differencing stencil may be described in matrix notation as

$$ {}^4\mathbf{DIS}\begin{bmatrix} \mathbf{U}_1 \\ \mathbf{U}_2 \\ \mathbf{U}_3 \\ \cdot \\ \cdot \\ \cdot \\ \cdot \\ \cdot \\ \mathbf{U}_{Ni-2} \\ \mathbf{U}_{Ni-1} \\ \mathbf{U}_{Ni} \end{bmatrix} = \begin{bmatrix} -1+2-1\;\;0 & 0 & 0 & 0 & \\ +2-5+4-1 & 0 & 0 & 0 & \\ -1+4-6+4 & -1 & 0 & 0 & \\ 0-1+4-6 & +4 & -1 & 0 & \\ & \ddots & & & \\ & & \ddots & & \\ & & & \ddots & \\ & 0 & -1 & +4 & -6+4-1\;\;0 \\ & 0 & 0 & -1 & +4-6+4-1 \\ & 0 & 0 & 0 & -1+4-5+2 \\ & 0 & 0 & 0 & 0-1+2-1 \end{bmatrix} \begin{bmatrix} \mathbf{U}_1 \\ \mathbf{U}_2 \\ \mathbf{U}_3 \\ \cdot \\ \cdot \\ \cdot \\ \cdot \\ \cdot \\ \mathbf{U}_{Ni-2} \\ \mathbf{U}_{Ni-1} \\ \mathbf{U}_{Ni} \end{bmatrix} \quad (9) $$

It should be noted that Eq. (43*b*) of Pulliam (1986a) was not used because it was found to be excessively dissipative. In the present work the values $q_2 = 0.7$ and $q_4 = 0.004$ were used.

2.5 Grid Generation and Displacement. The computational grid is generated algebraically and is displaced in order to conform with the vibrating blades. Both grid generation and grid displacement procedures are the same as those used by Gerolymos (1988a, 1988b), and will therefore not be detailed here.

2.6 Boundary Conditions

2.6.1 General Remarks. Boundary conditions are applied using the theory of characteristics. The particular numerical implementation follows closely the work of Viviand and Veuillot (1978), Brochet (1980), Veuillot and Cambier (1984), and Cambier et al. (1981, 1985, 1988). It should be noted that when using Runge–Kutta schemes boundary conditions (and particularly nonpenetration) should be applied at the end of every stage of the Runge–Kutta cycle, and not only at the end of the cycle, in order to avoid extrapolation problems (Gottlieb and Turkel, 1978).

2.6.2 Blade and Solid Wall Conditions. On the blade surface $\partial\mathbb{B}$ the unsteady nonpenetration condition is applied

$$ \mathbf{W}(t,\mathbf{x})\cdot\mathbf{n}(t,\mathbf{x})=\frac{\partial\mathbf{q}(t,\mathbf{x})}{\partial t}\cdot\mathbf{n}(t,\mathbf{x}) \quad \forall\mathbf{x}\in\partial\mathbb{B} \quad (10) $$

where **n** is the unit normal vector on the blade surface, **x** is the position vector, **q** is the blade surface position vector (mean position + instantaneous vibratory displacement). The same condition with zero normal-to-the-wall velocity is applied on the tip and hub surfaces. At intersections of solid surfaces the velocity vector is forced parallel to the intersection line, following Brochet (1980).

2.6.3 Inflow and Outflow Conditions. At the inflow boundary a one-dimensional nonreflecting boundary condition was applied, following the theory by Hedstrom (1979), which for the present case may be summarized as:

$$ \begin{gathered} \frac{\partial p}{\partial t}+\rho a\,\frac{\partial(\mathbf{W}\cdot\mathbf{n})}{\partial t}=0 \\ \frac{\partial S}{\partial t}=0 \\ \frac{\partial[\angle(\mathbf{V},\mathbf{e}_u)]}{\partial t}=0 \\ \frac{\partial[\angle(\mathbf{V},\mathbf{e}_r)]}{\partial t}=0 \end{gathered} \quad (11) $$

where $\angle(\mathbf{a}_1, \mathbf{a}_2)$ is the angle between the two vectors $\mathbf{a}_1$ and $\mathbf{a}_2$, **n** is the ingoing unit normal vector at the upstream boundary (invariably the positive axial direction), p the static pressure, ρ the static density, a the sound velocity, **W** the relative flow velocity, S the entropy, **V** the absolute flow velocity, **W** the relative flow velocity, $\mathbf{e}_u$ the unit vector in the tangential direction, and $\mathbf{e}_r$ the unit vector in the radial direction. The last two conditions in Eqs. (11) imply that the absolute flow angles are fixed.

At the outflow boundary again a one-dimensional nonreflecting boundary condition, following Hedstrom (1979), is applied,

$$ \frac{\partial p}{\partial t}+\rho a\,\frac{\partial(\mathbf{W}\cdot\mathbf{n})}{\partial t}=0 \quad (12) $$

where **n** is the ingoing unit normal vector at the outflow boundary (invariably the negative axial direction), p the static pressure, ρ the static density, a the sound velocity, **W** the relative flow velocity.

The above boundary conditions are valid in the case of conventional subsonic throughflow machinery where the normal to the boundary Mach number is subsonic ($|\mathrm{M}_n| < 1$). In the supersonic throughflow case, lately drawing much attention (cf. Wood et al., 1988, for steady flow analysis and design, Kielb and Ramsey, 1989, for aeroelastic studies) all variables are fixed at the inflow boundary, and are extrapolated at the outflow. The unsteady problem is indeed much simpler, since no upstream-propagating waves appear, as can be seen for example in the work of Lane (1957).

It should be remarked that the present boundary conditions *are not* nonreflecting in the three-dimensional case. Results using the boundary condition of Eq. (11) or a classical reservoir boundary condition are identical insofar as blade pressures are concerned, as shown by Gerolymos et al. (1990). The problem of multidimensional nonreflecting boundary conditions is a subject of research by many workers (cf. the review by Givoli, 1991). A detailed study of the effects of inflow and outflow boundary conditions for vibrating cascade configurations, especially with comparison to theoretical farfield considerations (cf. Verdon, 1989) seems necessary.

2.6.4 Cut Condition. At the permeable pitchwise boundaries, a matching condition between adjacent channels is applied, following Cambier et al. (1985, 1989). The problem of reconstructing the flow on the two neighboring channels, making use of chorochronic periodicity conditions, is discussed in Section 2.7. The matching condition is applied by discretizing the characteristic equations on the surface that separates the two channels and taking only upwind information, in the sense of information propagation along characteristics.

2.6.5 Slipsurface Fitting. Downstream of the trailing plane of the blades, a simple matching condition between adjacent channels might be looked upon with some suspicion, concerning the correct simulation of shed vorticity and of the unsteady Kutta condition (cf. McCroskey, 1977; Crighton, 1985). One solution is to attach a slipsurface to the trailing plane of the blades. This is not so difficult, as it would be in external three-dimensional aerodynamics, because of the existence of the hub and tip surfaces, which provide material limits to the slipsurface, thus limiting roll-up problems. As explained by Cambier et al. (1985) for the computation of this contact discontinuity all compatibility relations (in both domains) are used; the matching conditions apply the equality of pressure and normal velocity, and allow for differences in tangential velocities and entropy (computed separately in each domain, using the corresponding characteristic equations). The flow velocity normal to the contact discontinuity and relative to it (normal flow velocity, $\mathbf{W} \cdot \mathbf{n}$, minus normal slipsurface displacement velocity, $\mathbf{W}_{ss} \cdot \mathbf{n}$) must be 0 (cf. Lax, 1954, 1957). Therefore, at every iteration, the slipsurface is displaced using the computed flow velocity. In order for the slipsurface to remain a smooth surface, and for no instabilities to occur during the displacement procedure, the grid points on the slipsurface are displaced in a purely circumferential direction (with a velocity whose projection on the normal to the slipstream gives the displacement velocity $\mathbf{W}_{ss}$), and *slopes on the slipsurface are always upstream-biased.*

A typical slipsurface plot, for Fan A, which is described in section 3, "Results," is presented in Fig. 1. It represents the slipsurface, for the steady-flow computation, at nominal speed and moderately high pressure ratio. It should be observed that the variation of flow angles with radial position introduces a tendency to stretch the slipsurface, and, at the same time, to roll it round the hub. For this reason (quite representative of reality) numerical computations may become unstable, due to grid degeneracy, if the outflow-boundary is positioned very far downstream. This problem does not appear in 2.5-dimensional computations, where the whole blade-to-blade surface is unrolled and mapped onto a plane (e.g., Gerolymos, 1988a). Positioning the outflow boundary near the trailing edge might be unattractive, especially when the cascade and vibration parameters correspond to propagating waves (cf. Whitehead, 1987). Therefore studies are presented in section 3 examining the use of a simple matching condition in lieu of a fitted slipsurface. However, one must note the enhanced robustness induced by slipstream fitting, especially in supersonic-through-flow machinery computations.

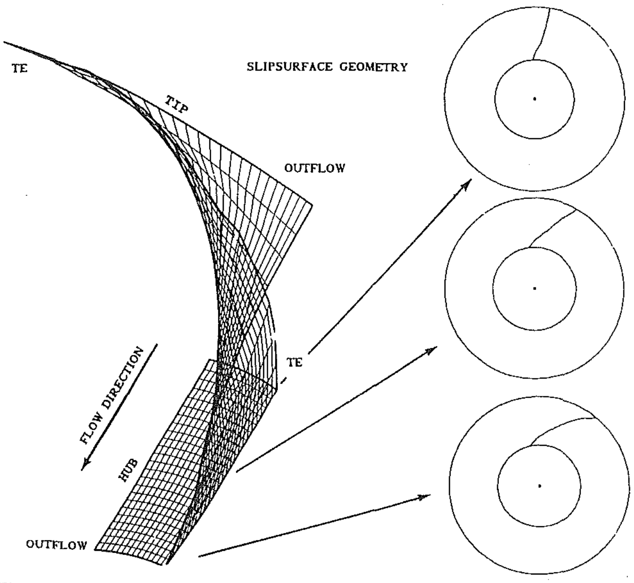

Fig. 1 **Illustration of slipsurface geometry for a typical wide-chord fan; the circles are (R, θ) planes**

2.7 Chorochronic Periodicity. When one is concerned with the response of the flow field to a traveling-wave vibration of the bladed disk, spectacular gains in computing time are obtained by computing only one interblade channel, making use of the chorochronic periodicity of the flow. Chorochronic periodicity is introduced because, as shown by Lane (1956), the aeroelastic eigenmodes of a perfectly tuned (with perfect cyclic symmetry) bladed disk are traveling waves, decaying, propagating, or amplifying, depending on the aeroelastic stability of the system (under the sole assumption that the coupled aeromechanical system is linear), viz. that the vibration of the bladed disk is of the form,

$$\mathbf{q}(t, x, R, \theta+2k\pi/N) = e^{-\zeta\omega t}\,\Re e\{\mathbf{q}_0(t, x, R, \theta)e^{i(\omega t+k\beta_r)}\} \quad (13)$$

where $\mathbf{q}$ is the vibratory displacement vector, t the time, x the coordinate along the engine axis, R the radius, θ the azimuthal angle of a reference sector ($0 \leq \theta < 2\pi/N$), $\mathbf{q}_0$ the vibratory displacement vector of the reference sector, ω the angular vibration frequency, ζ the damping factor, β_r the interblade phase angle, N the number of blades, and $k \in \mathbb{Z}$. Equation (13) is the symbolic representation of the traveling-wave mode, where all the blades vibrate in the same way as their neighbor, but with a phase-difference β_r one from another, and an amplitude varying as $e^{-\zeta\omega t}$ with time.

In practice aerodynamic computations are done for a constant-amplitude traveling-wave vibration input ($\zeta = 0$). For such an input it is assumed (and has been verified through comparison with full annular cascade computations by Gerolymos, 1988c) that the same chorochronic periodicity holds for the flowfield. Hence, computations are performed on a single channel, applying the following chorochronic periodicity conditions at the permeable pitchwise boundaries:

$$F(t, x, R, \theta) = F(t-k\omega^{-1}\beta_r, x, R, \theta+2k\pi/N) \quad (14)$$

for every aeromechanical quantity F, where t is the time, x the coordinate along the engine axis, R the radius, θ the azimuthal angle, ω the vibration frequency, β_r the interblade phase angle, N the number of blades, and $k \in \mathbb{Z}$.

There are two different ways for the numerical treatment of chorochronic periodicity, either the Time-Inclining (TI) method, introduced by Giles (1988, 1990), or the Signal-Storage-and-Reconstruction (SSR) technique, introduced by Erdos et al. (1977), and used by various authors (e.g., Hodson, 1985; Koya and Kotake, 1985; Gerolymos, 1988a, 1988b; He, 1990; Lewis et al., 1989). In the present work the SSR technique was used, with storage of a discretized temporal signal and reconstruction using piecewise quintic interpolation. Details are given in the appendix.

3 Results

3.1 Configuration. Results are presented for Fan A, a wide chord transonic fan (Fan A in Gerolymos, 1988b), and ONERA Cascade A in Gerolymos et al. (1990). Fan A is unshrouded, has 22 blades, and has a design rotation speed of 9551 rpm. The operating map of Fan A is shown in Fig. 3 of Gerolymos (1988b). Results are presented for a point on the nominal speed line, at moderately high pressure ratio, with started flow at the tip sections.

3.2 Grid Influence

3.2.1 Steady-State Flow. Results are presented for three computational grids, an 80 × 15 × 15 grid (axial × radial × pitchwise), an 100 × 21 × 21 grid, and an 120 × 30 × 30 grid. The blade planform (projection on the (x, R) plane, with x the engine axis and R the radius) for the three grids used is schematically depicted in Fig. 2 (only the grid points on the surface of the blade are shown, corresponding to 30 × 15, 38 × 21,and 46 × 30 points, respectively). One can remark the coarseness of the 80 × 15 × 15 grid, in the radial direction near the tip. This has a marked influence on steady flow results as may be seen in Fig. 3 where the steady-state Mach number distribution on the blade surface for the three grids is shown. The insufficient radial resolution of the 80 × 15 × 15 grid introduces a marked smearing of the shock-wave surface, and a substantial error both at the tip section (associated with parasitic entropy production by the coarse grid), and near the sonic radius. On the other hand the differences between the 100 × 21 × 21 and 120 × 30 × 30 grid are not easily discernible in Fig. 3. Detailed comparisons of Mach number distribution versus axial distance for the two coarser grids are presented in Fig. 4. The conclusions drawn from Fig. 3 are confirmed. It is seen that the coarse grid introduces a 0.1 error in Mach number, which is not acceptable for steady flow computations. Detailed examination of results has shown that this is caused solely by parasite entropy production, the results for mass flow rate and rotor pressure ratio being quite the same for the two grids. Detailed comparisons of Mach number distributions versus axial distance for the two finer grids are shown in Fig. 5, confirming that there is little difference in the results using the two finer grids, and that for practical purposes the 100 × 21 × 21 grid is adequate. Therefore the effect of grid refinement on unsteady results will be assessed through comparison between the 80 × 15 × 15 grid and the 100 × 21 × 21 grid.

It is remarked that the prediction of relative fan performance (performance compared to design point in terms of mass flow rate and pressure ratio) is quite satisfactory using the Euler code (cf. Gerolymos, 1988b).

3.2.2 Vibration Mode. Unsteady results are presented for the first torsional mode (1T) of Fan A (which is mode No. 3 of the blade, the first two modes being the bending 1F and 2F modes). The computations are performed at nominal speed with standard ISA inflow conditions (1 bar of absolute total pressure and 18°C), for which the mechanical speed is 9551 rpm, and the vibration frequency of the 1T mode is 707 Hz.

The vibrational modes are quite pure (small bending/torsion coupling), due to the fact that the fan is unshrouded. Also, the disk is quite rigid, so that various traveling-wave modes have small, indeed negligible, influence on the blade mode-shape and frequency so that the difference in aeroelastic modes comes only from the interblade-phase-angle effect on unsteady aerodynamic pressures). A plot illustrating the vibration mode used for the unsteady computations is presented in Fig. 6,

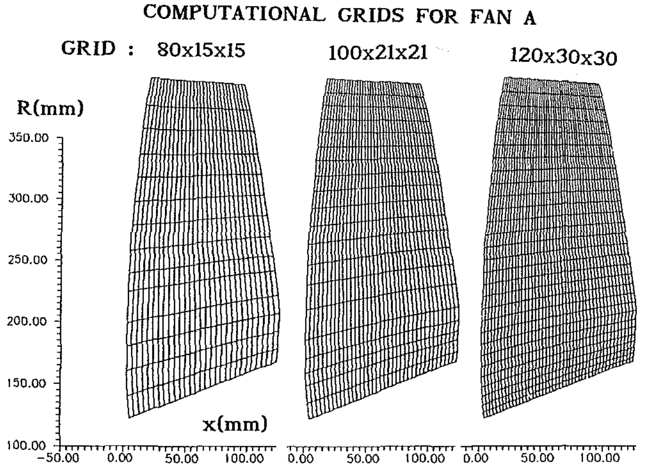

Fig. 2 Projection of the blade on the (*x*, *R*) plane, illustrating the three grids used

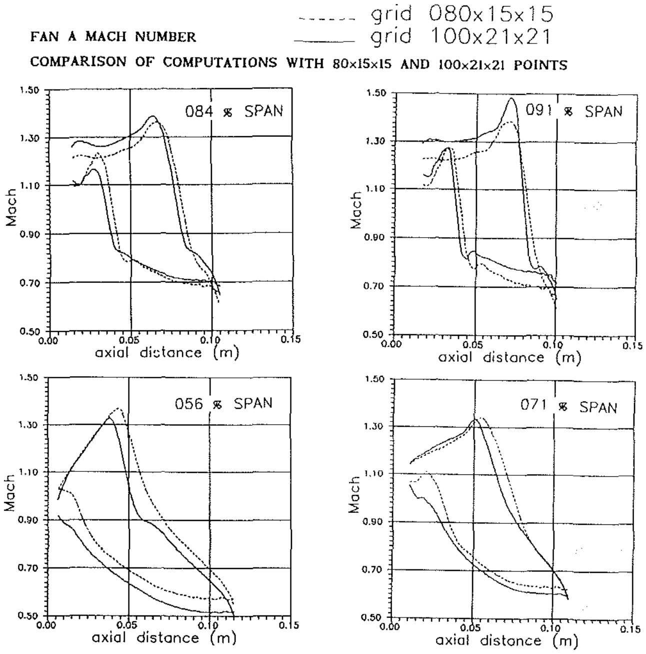

Fig. 4 Mach number level on Fan A blade, for computations with an 80 × 15 × 15 grid and an 100 × 21 × 21 grid

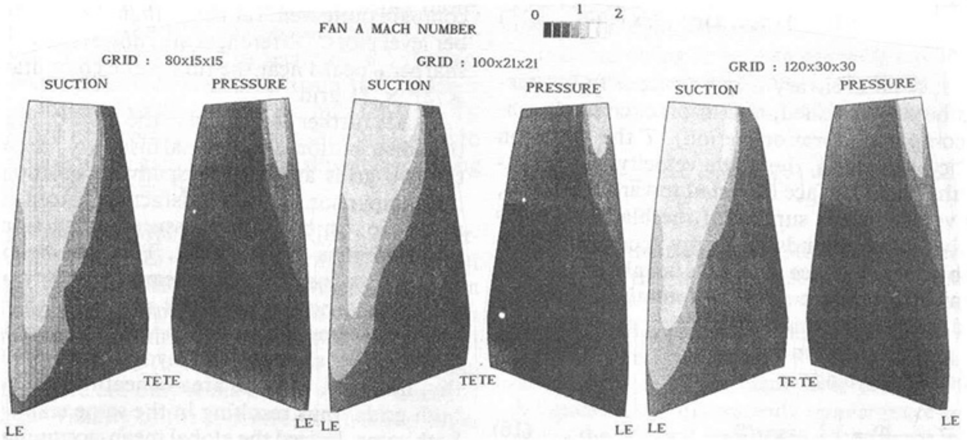

Fig. 3 Mach number level on Fan A blade, for three different grids

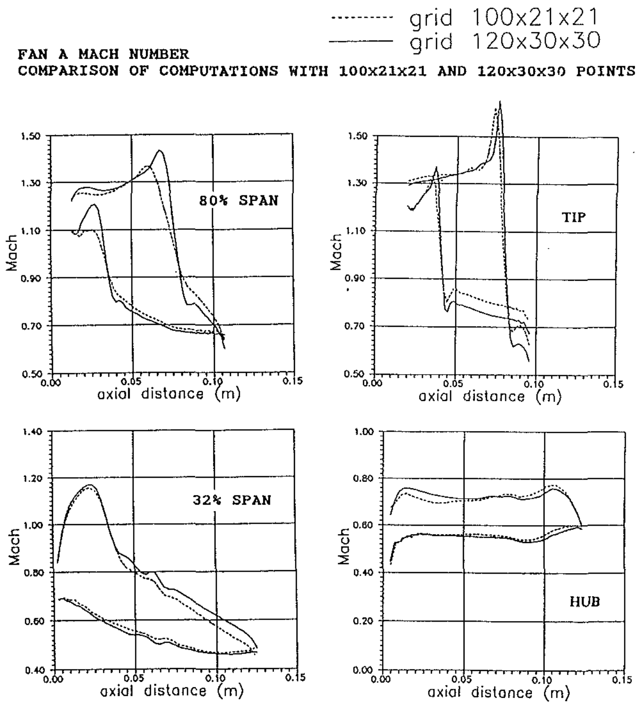

Fig. 5 **Mach number level on Fan A blade, for computations with a 100 × 21 × 21 grid and a 120 × 30 × 30 grid**

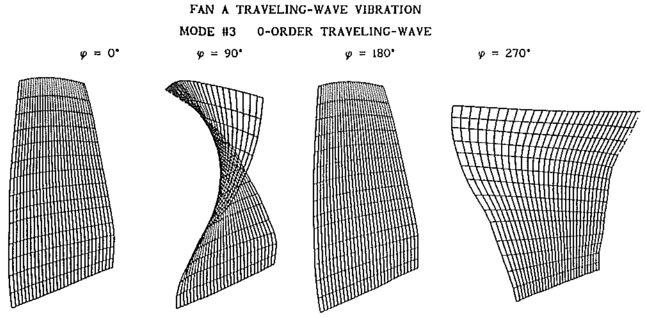

Fig. 6 **Vibration mode shape for Fan A blade torsional vibration**

which shows the planform vibratory deformation of the blade at various instants of the vibration period (the mechanical computations were done by Mascarell, 1986, using the finite-element code SAMCEF of SAMTech [B]).

3.2.3 Unsteady Results. Unsteady results are presented in Fig. 7, where the mean-accumulated-power level on the blade surface for the two grids used is presented. The mean-accumulated-power $\mathfrak{p}$ is defined by

$$\mathfrak{p}(\mathbf{x}) = \frac{1}{T}\int_{t_0}^{t_0+T} p(t)\mathbf{q}_t(\mathbf{x},t)\cdot\mathbf{n}(\mathbf{x},t)dt \quad \forall \mathbf{x}\in\partial\mathbb{B} \qquad (15)$$

where t is the time, t_0 an arbitrary origin (once a fully time-periodic flow has been established, and in practice the beginning of the last computed vibration period), T the vibration period, p the static pressure, $\mathbf{q}_t$ the blade velocity, $\mathbf{n}$ the outgoing normal on the blade surface (directed toward the fluid), and $\mathbf{x}$ a position vector on the surface of the blade $\partial\mathbb{B}$. It is clear that a positive $\mathfrak{p}$ corresponds to energy accumulated, in the mean, by the blade, and hence promotes instability. Global stability is determined, for uncoupled computations (coupled computations and the determination of damping are the subject of a companion paper (Gerolymos, 1993)) by the integral $\mathcal{P}$ of $\mathfrak{p}$ on the surface of the blade

$$\mathcal{P} = \iint_{\partial\mathbb{B}} \mathfrak{p}(\mathbf{x})dS \qquad (16)$$

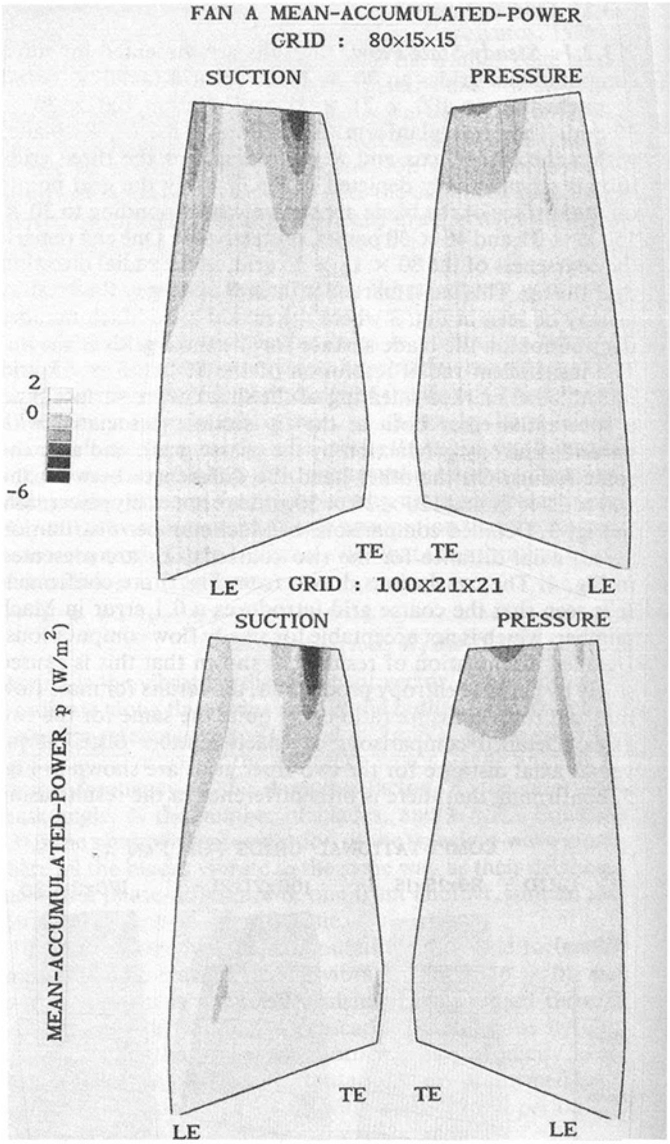

Fig. 7 **Mean-accumulated-power level on Fan A blade, for torsional vibration at 707 Hz and 0 interblade-phase-angle, for two different grids**

The knowledge of $\mathcal{P}$ permits the computation of the aerodynamic damping δ_{aero} that is defined in the energy method of Carta (1967).

The mean-accumulated-power level on the blade surface for the two grids considered is presented in Fig. 7, for the torsional vibration mode of Fig. 6, at 707 Hz. The results of Fig. 7 compare quite well, far better than the steady-state Mach number level plots. Differences are, however, observed in the much sharper $\mathfrak{p}$ peaks near the tip for the computations with the 100 × 21 × 21 grid.

This is further elucidated in the plots of Fig. 8, which present the $\mathfrak{p}$ distributions versus axial distance, for computations using the two grids at different spanwise positions. It is seen that the comparison is quite satisfactory, except at the shock foot, at the tip, on both the pressure and suction sides. The finer grid exhibits a sharper peak. This is to be expected, since the shock wave is artificially smeared over a fixed number of grid points, and hence the shock profile is sharper for the finer grid. The same phenomenon was observed in the two-dimensional comparisons of Gerolymos et al. (1990). It is noteworthy, however, that the area beneath the peaks is the same for both grids, thus resulting in the same stability predictions for both cases. Indeed the global mean-accumulated-power $\mathcal{P}$ (Eq. (16)) is −16.8 W for the 100 × 21 × 21 grid and −17.9 W

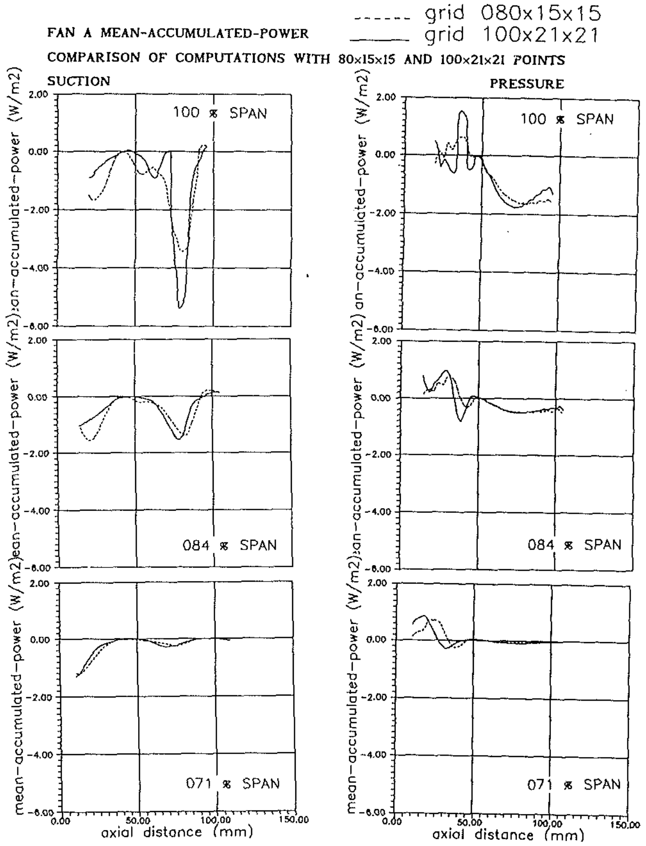

Fig. 8 Mean-accumulated-power $\mathfrak{p}$ on Fan A blade for vibration in model No. 3 (1T at 707 Hz and 0 interblade phase angle), for computations with an 80 × 15 × 15 grid and a 100 × 21 × 21 grid

for the 80 × 15 × 15 grid, i.e., a difference of only 5 percent. As a general conclusion of this comparison of results between the two grids it should be remarked that comparisons of unsteady results are much more in agreement than comparisons of steady results, a conclusion also drawn by Gerolymos et al. (1990) in connection with comparisons of computations with experimental results.

3.3 Importance of Slipsurface-Fitting

3.3.1 General Remarks. Previous computations reported by this author had always used a fitted slipsurface (Gerolymos, 1988a, 1988b; Gerolymos et al., 1990). This is the case for the results in section 3.2 as well. The systematic use of slipsurface fitting was suggested by the results of Pandolfi (1980) who reported one of the very first unsteady time-marching Euler computations in vibrating cascades and found important differences in results with and without slipstream fitting (note, however, that Pandolfi used a very coarse grid in the circumferential direction). It was remarked in section 2.6.5 that serious computational difficulties may arise from the tendency of the fitted slipsurface to wrap around the hub (cf. Fig. 1), which may cause grid degeneracy. It is interesting therefore to examine whether there is any gain from using slipsurface fitting in three-dimensional Euler computations.

3.3.2 Steady-State Results. Computations were performed on the same 80 × 15 × 15 grid with and without slipsurface fitting. The axial distributions of Mach number on the blade surface at various spanwise stations are plotted in Fig. 9. It is seen that the results with fitted slipsurface (solid line) and without slipsurface fitting (symbols) are practically indistinguishable. There are only some minor discrepancies at the tip section in the vicinity of the pressure-side trailing edge.

3.3.3 Unsteady Results. Unsteady computations were run

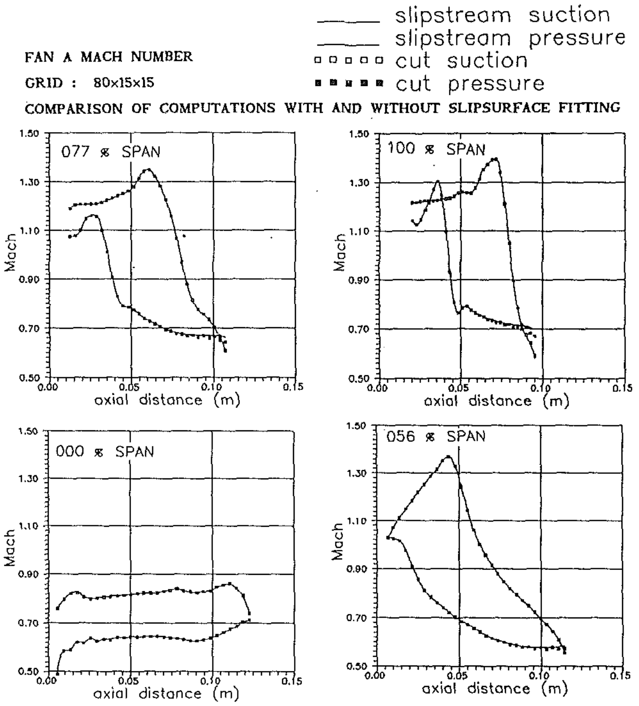

Fig. 9 Mach number level on Fan A blade, for computations with and without slipsurface fitting, for an 80 × 15 × 15 grid

for the torsional mode at 707 Hz and 0-order traveling wave. Comparisons of axial distribution of $\mathfrak{p}$ at various spanwise stations (Fig. 10) show excellent agreement between the two methods, results being practically identical. It seems that slipsurface fitting is not at all necessary for such computations, even for a coarse 80 × 15 × 15 grid. This has been confirmed by a number of two-dimensional numerical experiments for a wide Mach number range.

3.4 Unsteady Convergence. Unsteady time-marching computations are run for a prescribed number of periods until convergence in the sense of harmonics is attained. The number of periods required for convergence is examined in the following.

In Fig. 11 are presented the axial distributions of the amplitude and phase of the first-harmonics of pressure on the surface of the blade, for the tip section, for the usual torsional mode at 707 Hz and 0 interblade phase angle. Results obtained at the end of four, eight, and ten periods are presented. It is seen that phase angles both on suction and pressure surface are practically converged in four periods. Convergence of the amplitude, at the shock foot, both on the suction and the pressure sides is slower, but eventually attained after the simulation of eight periods.

It is interesting to have an unsteady convergence norm. Since harmonics at every grid point in the flow field are not computed (for economy of storage), the following error L2-norm is used:

$$\text{error} = \frac{1}{TS_B}\sqrt{\iint_{\partial \mathbb{B}} dS \int_{t_0}^{t_0+T} dt \left\{\frac{p(t)-p(t-T)}{p(t-T)}\right\}^2} \qquad (17)$$

where t_0 is the time at the start of the period, T the vibration period, $\partial\mathbb{B}$ the blade surface of area S_B, and p the static pressure. Hence the error is defined as the rms relative variation of pressure during the last vibration period. A similar criterion, but at a small number of chosen points and not everywhere on the surface of the blade, was used by Lewis et al. (1989). A typical result of unsteady convergence is shown in Fig. 12, where the decimal logarithm of the error is plotted versus the number of periods. As a general rule engineering accuracy is

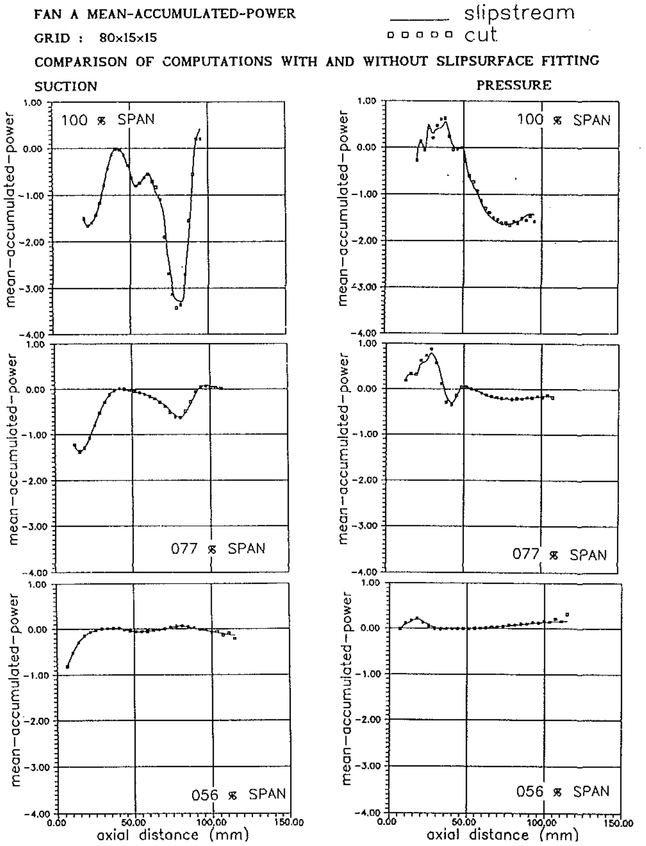

Fig. 10 Mean accumulated power ${}_p$ on Fan A blade for vibration in model No. 3 (1T at 707 Hz and 0 interblade phase angle), for computations with and without slipsurface fitting for an 80 × 15 × 15 grid

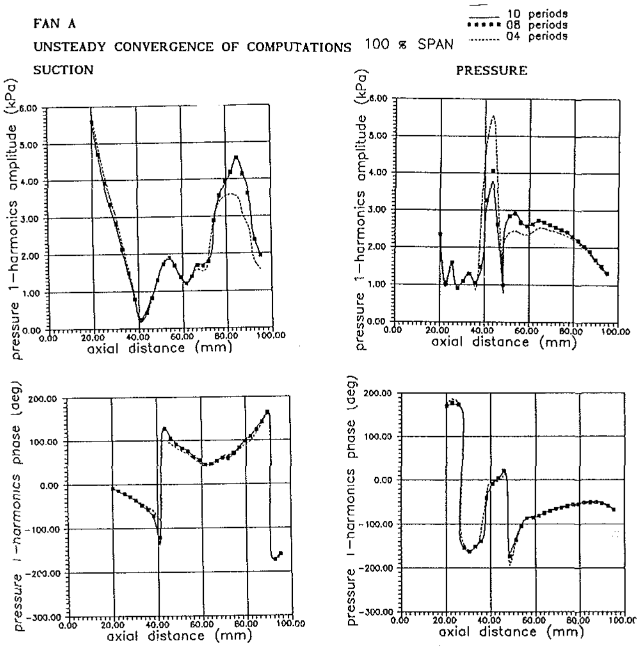

Fig. 11 Convergence of pressure first-harmonics at the tip section of Fan A, for an 80 × 15 × 15 grid, with fitted slipsurface

obtained within six periods, and even sooner if only global results (aerodynamic damping) are required.

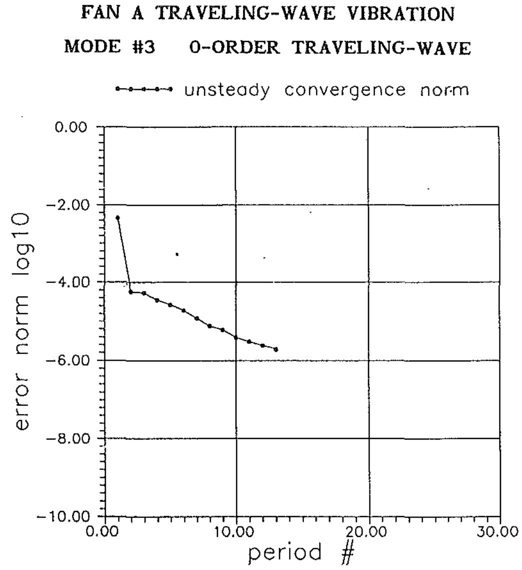

Fig. 12 Unsteady convergence for Fan A blade torsional vibration

Table 2 Computing time per iteration*

NRG	CFL	μs/iteration/ /gridpoint	μs/iteration/ /gridpoint/CFL
2	0·95	23·8	25·0
3	1·50	32·3	21·5
4	2·50	40·9	16·4
5	3·50	49·4	14·1

* for a 80×15×15 grid on a FUJITSU VP-200 computer

In order to have an idea of the computing time requirements of a configuration, computing times on a VP-200 Fujitsu computer are given in Table 2. Typically 1/4 *h*-1 *h* is required on a supercomputer, for one of the first modes of a fan blade. Since the stability time step depends mostly on the corresponding steady-state flow and the scheme's CFL number and since for a given frequency the number of iterations to simulate one period is equal to the period divided by the time step, computing time is proportional to f^{-1} where f is the vibration period.

3.5 Remarks. It is noted that results with the Jameson schemes used in the present work are similar, for Fan A, to those obtained by Gerolymos (1988b). Therefore, the results presented above were mostly concerned with influence of various numerical parameters on results.

4 Conclusions

In the present work, a method for the time-marching numerical computation of the Euler equations in cascades vibrating in a constant amplitude traveling-wave mode was described. Sample results and a number of studies on the influence of numerical parameters were presented. It was shown that using slipsurface fitting is not necessary, thus allowing the use of typical grids with inflow and outflow boundaries far from the blades. Unsteady convergence of results was studied showing that convergence to engineering accuracy is obtained after approximately six vibration periods have been simulated.

5 Discussion

There are three points concerning future research need, viz., methodology validation, taking account of shrouds and other geometry complications, and reducing computing time requirements.

1 There are extremely few three-dimensional data (experimental or analytical) in vibrating cascades. To this author's knowledge, the only existing data are those used by Halliwell et al. (1984) to validate their stacked 2.5-dimensional time-

linearized potential flow computations, based on the method of Whitehead (1982). Unfortunately these data (geometry + mode shapes + unsteady pressures) are not available in the open literature. There exist, however, theoretical semi-analytic studies by Namba and Ishikawa (1983) and Chi (1993). The comparison of the present three-dimensional Euler code with these studies has been undertaken recently, and will be reported in a future paper.

2 The present version of the Euler code does not provide for the modeling of shrouds. This is a major drawback of the method, especially since shrouded fans are instability prone in the supersonic flutter region (due to the torsion/bending coupling that is introduced mechanically by the shroud). It is planned to update the Euler code in a multiblock version taking into account the shroud effects, following the work of Derrien (1986).

3 Further possible improvements should concern the reduction of computing time. To this end, time-consistent multigrid or quasi-multigrid schemes (e.g., Couailler and Peyret, 1985; Fung and Fu, 1987; Anderson et al., 1989) are a very attractive possibility. Another possibility is the use of a time-linearized three-dimensional Euler method, with shock-capturing capabilities (Hall and Crawley, 1989, have developed a two-dimensional time-linearized Euler method, in nonconservative formulation, with shock fitting).

Acknowledgments

This work was conducted under contract with SNECMA, with Alex Ribère and Didier Nicoud as technical monitors, and is published by permission. The computations were performed on the Fujitsu VP-200 computer of CIRCE and on the Cray-2 computer of CCVR, at the Ecole Polytechnique.

References

Akima, H., 1970, "A New Method of Interpolation and Smooth Curve Fitting Based on Local Procedures," *J. Assoc. Comp. Mach.*, Vol. 17, pp. 589-602.

Anderson, W. K., Thomas, J. L., and Rumsey, C. L., 1989, "Extensions and Applications of Flux-Vector Splitting to Unsteady Calculations on Dynamic Meshes," *AIAA J.*, Vol. 27, pp. 673-674.

Batina, J. T., 1991, "Unsteady Euler Algorithm With Unstructured Dynamic Mesh for Complex-Aircraft Aerodynamic Analysis," *AIAA J.*, Vol. 29, pp. 327-333.

Bendiksen, O. O., 1990, "Aeroelastic Problems in Turbomachines," AIAA Paper No. 90-1157.

Brochet, J., 1980, "Calcul Numérique d'Écoulements Internes 3-D Transsoniques," *Rech. Aérosp.*, Vol. 1980•5, pp. 301-305.

Cambier, L., Ghazzi, W., Veuillot, J. P., and Viviand, H., 1981, "Une Approche par Domaines Pour le Calcul dÉcoulements Compressibles," ONERA TP 1981-143.

Cambier, L., Dusson, F., and Veuillot, J. P., 1985, "Méthode Multi-domaines Pour les Équations d'Euler—Applications Pour des Sous-Domaines Avec Recouvrement," *Rech. Aérosp.*, Vol. 1985•3, pp. 181-186.

Cambier, L., Veuillot, J. P., and Vuillot, A. M., 1988, "Développements Récents sur les Méthodes de Calcul d'Écoulements Internes par Résolution des Équations d'Euler ou de Navier-Stokes," *Rev. Franç. Méc.*, Vol. 1988•4, pp. 11-26.

Carta, F. O., 1967, "Coupled Blade-Disk-Shroud Flutter Instabilities in Turbojet Engine Rotors," ASME *Journal of Engineering for Power*, Vol. 89, pp. 419-426.

Chi, R. M., 1993, "An Unsteady Lifting Surface Theory for Ducted Fan Blades," ASME JOURNAL OF TURBOMACHINERY, Vol. 115, pp. 175-188.

Chima, R. V., 1985, "Inviscid and Viscous Flows in Cascades With an Explicit Multiple-Grid Algorithm," *AIAA J.*, Vol. 23, pp. 1556-1563.

Chima, R. V., 1987, "Explicit Multigrid Algorithm for Quasi-3-D Viscous Flows in Turbomachinery," *AIAA J. Prop. Power*, Vol. 3, pp. 397-405.

Chima, R. V., Turkel, E., and Schaffer, S., 1987, "Comparison of 3 Explicit Multigrid Methods for the Euler and Navier-Stokes Equations," NASA Tech. Mem. 88878.

Chima, R. V., and Yokota, J. W., 1990, "Numerical Analysis of 3-D Viscous Internal Flows," *AIAA J.*, Vol. 28, pp. 798-806.

Crighton, D. G., 1985, "The Kutta Condition in Unsteady Flow," *Ann. Rev. Fluid Mech.*, Vol. 17, pp. 411-445.

Couailler, V., and Peyret, R., 1985, "Étude Théorique et Numérique de la Méthode Multigrille de Ni," *Rech. Aérosp.*, Vol. 1985•5, pp. 285-300.

Davies, D. E., and Salmond, D. J., 1985, "Calculation of the Volume of a General Hexahedron for Flow Predictions," *AIAA J.*, Vol. 23, pp. 954-956.

Denton, J. D., 1983, "An Improved Time Marching Method for Turbomachinery Flow Calculation," ASME *Journal of Engineering for Power*, Vol. 105, pp. 514-524.

Derrien, T., 1986, "Calcul 3-D Dans les Aubages de Turbo-machines Avec Nageoire," *AGARD Conf. Proc.*, Vol. 401, pp. 14•1-14•15.

Dukowicz, J. K., 1988, "Efficient Volume Computation for 3-D Hexahedral Cells," *J. Comp. Phys.*, Vol. 74, pp. 493-496.

Epstein, A. H., Kerrebrock, J. L., and Thompkins, W. T., Jr., 1979, "Shock-Structure in Transonic Compressor Rotors," *AIAA J.*, Vol. 17, pp. 375-379.

Erdos, J. I., and Alzner, E., and McNally, W., 1977, "Numerical Solution of Periodic Transonic Flow Through a Fan Stage," *AIAA J.*, Vol. 15, pp. 1559-1568.

Fung, K. H., and Fu, J. K., 1987, "Computation of Unsteady Transonic Aerodynamics With Truncation Error Injection," *AIAA J.*, Vol. 25, pp. 1018-1020.

Gerolymos, G. A., 1988a, "Numerical Integration of the Blade-to-Blade Surface Euler Equations in Vibrating Cascades," *AIAA J.*, Vol. 26, pp. 1483-1492.

Gerolymos, G. A., 1988b, "Numerical Integration of the 3-D Unsteady Euler Equations for Flutter Analysis of Axial Flow Compressors," ASME Paper No. 88-GT-255; *Int. J. Turbo Jet Eng.*, Vol. 7, 1990, pp. 131-142.

Gerolymos, G. A., 1988c, "Periodicity Superposition and 3-D Effects in Supersonic Compressor Flutter Aerodynamics," ASME Paper No. 88-GT-136; *Int. J. Turbo Jet Eng.*, Vol. 7, 1990, pp. 143-152.

Gerolymos, G. A., 1990, "Implicit Multiple-Grid Computation of the Compressible Navier-Stokes Equations Using k-ϵ Turbulence Closure," *AIAA J.*, Vol. 28, pp. 1707-1717.

Gerolymos, G. A., Blin, E., and Quiniou, H., 1990, "Comparison of Inviscid Computations With Theory and Experiment in Vibrating Transonic Compressor Cascades," ASME Paper No. 90-GT-373; *Rech. Aérosp.*, Vol. 1991•6, 1991, pp. 63-82.

Gerolymos, G. A., 1993, "Coupled Three-Dimensional Aeroelastic Stability Analysis of Bladed Disks," ASME JOURNAL OF TURBOMACHINERY, Vol. 115, pp. 791-799.

Giles, M. B., 1988, "Calculation of Unsteady Wake/Rotor Interaction," *J. Prop. Power*, Vol. 4, pp. 356-362.

Giles, M. B., 1990, "Stator/Rotor Interaction in a Transonic Turbine," *J. Prop. Power*, Vol. 6, pp. 621-627.

Givoli, D., 1991, "Nonreflecting Boundary Conditions," *J. Comp. Phys.*, Vol. 94, pp. 1-29.

Gottlieb, D., and Turkel, E., 1978, "Boundary Conditions for Multistep Finite Difference Methods for Time-Dependent Equations," *J. Comp. Phys.*, Vol. 26, pp. 181-196.

Hall, K. C., and Crawley, E. F., 1989, "Calculation of Unsteady Flows in Turbomachinery Using the Linearized Euler Equations," *AIAA J.*, Vol. 27, pp. 777-787.

Halliwell, D. G., Newton, S. G., and Lit, K. S., 1984, "A Study of Unsteady Pressures Near the Tip of a Transonic Fan in Unstalled Supersonic Flutter," ASME *Journal of Vibration, Acoustics, Stress, and Reliability in Design*, Vol. 106, pp. 198-203.

Hedstrom, G. W., 1979, "Nonreflecting Boundary-Conditions for Nonlinear Hyperbolic Systems," *J. Comp. Phys.*, Vol. 30, pp. 222-237.

He, L., 1990, "An Euler Solution for Unsteady Flows Around Oscillating Blades," ASME JOURNAL OF TURBOMACHINERY, Vol. 112, pp. 714-722.

He, L., and Denton, J. D., 1993a, "Inviscid-Viscous Coupled Solution for Unsteady Flows Through Vibrating Blades: Part 1—Description of the Method," ASME JOURNAL OF TURBOMACHINERY, Vol. 115, pp. 94-100.

He, L., and Denton, J. D., 1993b, "Inviscid-Viscous Coupled Solution for Unsteady Flows Through Vibrating Blades: Part 2—Computational Results," ASME JOURNAL OF TURBOMACHINERY, Vol. 115, pp. 101-109.

Hodson, H. P., 1985, "An Inviscid Blade-to-Blade Prediction of a Wake-Generated Unsteady Flow," ASME *Journal of Engineering for Gas Turbines and Power*, Vol. 107, pp. 337-344.

Holmes, D. G., and Tong, S. S., 1985, "Three-Dimensional Euler Solver for Turbomachinery Blade-Rows," ASME JOURNAL OF TURBOMACHINERY, Vol. 107, pp. 258-264.

Huff, D. L., Swafford, T. W., and Reddy, T. S. R., 1991, "Euler Flow Predictions for an Oscillating Cascade Using a High Resolution Wave-Split Scheme," ASME Paper No. 91-GT-198.

Hussaini, M. Y., 1989, "Computational Fluid Dynamics—a Personal View," *Lect. Notes Phys.*, Vol. 323, pp. 3-17.

Jameson, A., Schmidt, W., and Turkel, E., 1981, "Numerical Solutions of the Euler Equations by Finite-Volume Methods Using Runge-Kutta Time-Stepping Schemes," AIAA Paper No. 81-1259.

Jameson, A., 1983, "Solution of the Euler Equations for 2-D Transonic Flow by a Multigrid Method," *Appl. Math. Comp.*, Vol. 13, pp. 327-355.

Jameson, A., and Mavriplis, D., 1986, "Finite-Volume Solution of the 2-D Euler Equations on a Regular Triangular Mesh," *AIAA J.*, Vol. 24, pp. 611-618.

Jameson, A., 1988, "Computational Transonics," *Comm. Pure Appl. Math.*, Vol. 41, pp. 507-549.

Jameson, A., 1989, "Computational Aerodynamics for Aircraft Design," *Science*, Vol. 245, pp. 361-371.

Kau, H. P., and Gallus, H. E., 1989, "Numerical Investigation of Unsteady Flow in Oscillating Turbine and Compressor Cascades," *AGARD Conf. Proc.*, Vol. 468, pp. 2•1-2•10.

Kerrebrock, J. L., 1981, "Flow in Transonic Compressors," *AIAA J.*, Vol. 19, pp. 4-19.

Kielb, R. E., and Ramsey, J. K., 1989, "Flutter of a Fan Blade in Supersonic Axial Flow," ASME JOURNAL OF TURBOMACHINERY, Vol. 111, pp. 462-467.

Koeck, C., 1985, "Computation of 3-D Flow Using the Euler Equations and Multiple-Grid Scheme," *Int. J. Num. Meth. Fluids*, Vol. 5, pp. 483-500.

Kordulla, W., and Vinokur, M., 1983, "Efficient Computation of Volume in Flow Predictions," *AIAA J.*, Vol. 21, pp. 917–918.

Koya, M., and Kotake, S., 1985, "Numerical Analysis of Fully 3-D Periodic Flows Through a Turbine Stage," ASME *Journal of Engineering for Gas Turbines and Power*, Vol. 107, pp. 945–952.

Lane, F., 1956, "System Mode Shapes in the Flutter of Compressor Blade Rows," *J. Aero Sci.*, Vol. 23, pp. 54–66.

Lane, F., 1957, "Supersonic Flow Past an Oscillating Cascade With Supersonic Leading-Edge Locus," *J. Aero Sci.*, Vol. 24, pp. 65–66.

Lapidus, A., 1967, "A Detached Shock Calculation by 2-Order Finite-Differences," *J. Comp. Phys.*, Vol. 2, pp. 154–177.

Lax, P. D., 1954, "Weak Solutions of Nonlinear Hyperbolic Equations and Their Computation," *Comm. Pure Appl. Math.*, Vol. 8, pp. 159–193.

Lax, P. D., 1957, "Hyperbolic Systems of Conservation Laws," *Comm. Pure Appl. Math.*, Vol. 10, pp. 537–566.

Lewis, J. P., Delaney, R. A., and Hall, E. J., 1989, "Numerical Prediction of Turbine Vane-Blade Aerodynamic Interaction," ASME JOURNAL OF TURBOMACHINERY, Vol. 111, pp. 387–393.

MacCormack, R. W., 1971, "Numerical Solution of the Interaction of a Shock-Wave With a Laminar Boundary-Layer," *Lect. Notes Phys.*, Vol. 8, pp. 151–163.

MacCormack, R. W., 1985, "Current Status of Numerical Solutions of the Navier-Stokes Equations," AIAA Paper 85-0032.

Mascarell, J. P., 1986, SNECMA Villaroche [F], private communication.

McCroskey, W. J., 1977, "Some Current Research in Unsteady Fluid Dynamics," ASME *Journal of Fluids Engineering*, Vol. 99, pp. 8–39.

Neves, K. W., 1988a, "Hardware Architecture," AGARDograph *311*, pp. 11–53.

Neves, K. W., 1988b, "Algorithm and General Software Considerations," AGARDograph 311, pp. 55–98.

Namba, M., and Ishikawa, A., 1983, "3-D Aerodynamic Characteristics of Oscillating Supersonic and Transonic Annular Cascades," ASME *Journal of Engineering for Power*, Vol. 105, pp. 138–146.

Ni, R. H., 1982, "A Multiple-Grid Scheme for Solving the Euler Equations," *AIAA J.*, Vol. 20, pp. 1565–1571.

Oden, J. T., 1972, *Finite Elements of Nonlinear Continua*, McGraw-Hill, New York, pp. 134–140.

Olsson, P., and Johnson, S. L., 1989, "Boundary Modifications of the Dissipation Operators for 3-D Euler Equations," *J. Sci. Comp.*, Vol. 4, pp. 159–195.

Pandolfi, M., 1980, "Numerical Experiments on Unsteady Flows Through Vibrating Cascades: 2," *Unsteady Aerodynamics and Aeroelasticity of Turbomachines and Propellers Symposium*, Lausanne [CH].

Pulliam, T. H., 1986a, "Artificial Dissipation Models for the Euler Equations," *AIAA J.*, Vol. 24, pp. 1931–1940.

Pulliam, T. H., 1986b, "Implicit Solution Methods in Computational Fluid Dynamics," *Appl. Num. Math.*, Vol. 2, pp. 441–447.

Rai, M. M., and Chaussee, D. S., 1984, "New Implicit Boundary Procedures—Theory and Applications," *AIAA J.*, Vol. 22, pp. 1094–1100.

Roache, P., 1972, "On Artificial Viscosity," *J. Comp. Phys.*, Vol. 10, pp. 169–184.

Sidén, L. D. G., 1991, "Numerical Simulation of Unsteady Viscous Compressible Flows Applied to Blade Flutter Analysis," ASME Paper No. 91-GT-203.

Swanson, R. C., and Turkel, E., 1987, "Artificial Dissipation and Central Difference Schemes for the Euler and the Navier-Stokes Equations," AIAA Paper 87-1107.

Vavra, M. H., 1960, *Aerothermodynamics and Flow in Turbomachines*, Wiley, New York, pp. 107–132.

Venkatakrishnan, V., and Jameson, A., 1988, "Computation of Unsteady Transonic Flows by the Solution of Euler Equations," *AIAA J.*, Vol. 26, pp. 974–981.

Verdon, J. M., 1989, "The Unsteady Flow in the Far Field of an Isolated Blade Row," *J. Fluids Struct.*, Vol. 3, pp. 123–149.

Veuillot, J. P., and Cambier, L., 1984, "A Subdomain Approach for the Computation of Compressible Inviscid Flows," ONERA TP 1984-61.

Vinokur, M., 1989, "An Analysis of Finite-Difference and Finite-Volume Formulations of Conservation Laws," *J. Comp. Phys.*, Vol. 81, pp. 1–52.

Viviand, H., and Veuillot, J. P., 1978, "Méthodes Pseudoinstationnaires Pour le Calcul d' Écoulements Transsoniques," ONERA Pub. 1978-4.

Whitehead, D. S., 1982, *The Calculation of Steady and Unsteady Transonic Flows in Cascades*, Cambridge University Engineering Department.

Whitehead, D. S., 1987, "Classical 2-D Methods," AGARDograph 298 pp. 3•1–3•30.

Wood, J. R., Schmidt, J. F., Steinke, R. J., Chima, R. V., and Kunik, W. G., 1988, "Application of Advanced Computational Codes in the Design of an Experiment for a Supersonic Throughflow Fan Rotor," ASME JOURNAL OF TURBOMACHINERY, Vol. 110, pp. 270–279.

Zienkiewicz, O. C., 1977, *The Finite Element Method*, McGraw-Hill, New York, pp. 148–210.

APPENDIX

Chorochronic Periodicity

The following chorochronic periodicity conditions apply at the permeable pitchwise boundaries:

$$\mathbf{U}(x, R, \theta_b+\frac{2\pi}{N}; t)=[\mathbf{R}]\mathbf{U}(x, R, \theta_b; t+\omega^{-1}\beta_r) \quad \text{(A1)}$$

$$\mathbf{U}(x, R, \theta_b; t)=[\mathbf{R}^{-1}]\mathbf{U}(x, R, \theta_b+\frac{2\pi}{N}; t-\omega^{-1}\beta_r) \quad \text{(A2)}$$

where $\mathbf{U} \in \mathbb{R}^5$ is the vector of unknowns, x is the axial coordinate, R the radius, $\theta_b(x, R)$ is the azimuthal coordinate of the boundary, N is the number of blades, t the time, β_r the interblade phase angle, ω is the vibration frequency, and $[\mathbf{R}]$ is a 5×5 square matrix rotating the Cartesian coordinates of the momentum vector $\rho\mathbf{W}$ by an angle $\psi = 2\pi/N$

$$[\mathbf{R}]=\begin{bmatrix} 1 & 0 & 0 & 0 & 0 \\ 0 & 1 & 0 & 0 & 0 \\ 0 & 0 & \cos\psi & -\sin\psi & 0 \\ 0 & 0 & \sin\psi & \cos\psi & 0 \\ 0 & 0 & 0 & 0 & 1 \end{bmatrix} \quad \text{(A3)}$$

In order to apply the chorochronic periodicity conditions on the permeable pitchwise boundaries, the values of $\mathbf{U}$ at $\theta_- = \theta_b$ and $\theta_+ = \theta_b + 2\pi/N$ are stored for a number L of instants per period ($L = 72$ was used in the present work)

$$^{\text{store}}\mathbf{U}^{\pm}(x, R) \leftarrow \mathbf{U}\left(x, R, \theta_{\pm}, \omega t=\frac{2\pi l}{L}\right) \quad l=1, \ldots, L \quad \text{(A4)}$$

The conditions described in Eqs. (A1) and (A2) are applied by reconstructing the signals using a piecewise quintic interpolation procedure denoted by the operator $\mathfrak{D}(\omega t)$

$$\mathbf{U}(x, R, \theta_{\pm}; t)=\mathfrak{D}(\omega t)\{^{\text{store}}\mathbf{U}^{\pm}(x, R)\} \quad \text{(A5)}$$

The interpolation operator $\mathfrak{D}$ is an extension of the work of Akima (1970) on piecewise cubic interpolation to piecewise quintic interpolation. Given the values $y_l \doteq y(x_l)$ of the real function $y(x)$ at L points ($l = 1, \ldots L$), the value at a required point x in the interval $x_l \leq x < x_{l+1}$ is given by

$$y(x) \sim \alpha\xi^5+\beta\xi^4+\gamma\xi^3+\delta\xi^2+\epsilon\xi+\zeta \quad \text{(A6)}$$

where $\xi \in [-1, 1]$ is defined by

$$\xi \doteq \frac{x-\dfrac{x_l+x_{l+1}}{2}}{\dfrac{x_{l+1}-x_l}{2}} \quad \text{(A7)}$$

and the interpolation coefficients depend on slopes and curvatures at x_l and x_{l+1} and are given by

$$\begin{bmatrix} \alpha \\ \beta \\ \gamma \\ \delta \\ \epsilon \\ \zeta \end{bmatrix} = \frac{1}{48}\begin{bmatrix} -9 & -9 & -3 & +9 & -9 & +3 \\ 0 & +3 & +3 & 0 & -3 & +3 \\ +30 & +30 & +6 & -30 & +30 & -6 \\ 0 & -18 & -6 & 0 & +18 & -6 \\ -45 & -21 & -3 & +45 & -21 & +3 \\ +24 & +15 & +3 & +24 & -15 & +3 \end{bmatrix}\begin{bmatrix} \eta_l \\ \eta_l' \\ \eta_l'' \\ \eta_{l+1} \\ \eta_{l+1}' \\ \eta_{l+1}'' \end{bmatrix} \quad \text{(A8)}$$

where

$$\eta_l=y_l; \quad \eta_l'=2y_l'/(x_{l+1}-x_l); \quad \eta_l''=4y_l''/(x_{l+1}-x_l)^2 \quad \text{(A9)}$$

Slopes and curvatures of y are estimated using fourth-order Taylor expansions. The ωt periodicity of the functions y considered in the present work is explicitly used at $l = 1$ and $l = L$, enabling the use of centered differences everywhere.

Coupled Three-Dimensional Aeroelastic Stability Analysis of Bladed Disks

G. A. Gerolymos
Université Pierre & Marie Curie,
Paris, France

In the present work an algorithm for the coupled aeromechanical computation of three-dimensional compressor cascades vibrating in a traveling-wave mode is presented and applied to the determination of aeroelastic stability of a transonic fan rotor. The initial vibratory modes are computed using a finite-element structural analysis code. The unsteady flow field response to blade vibration is estimated by numerical integration of the three-dimensional unsteady Euler equations. Coupling relations are formulated in the frequency domain, using a mode-modification technique, based on modal projection. The vibratory mode is updated at the end of the aerodynamic simulation of each period, and the updated mode is used for the simulation of the next period. A number of results illustrate the method's potential.

1 Introduction

Turbomachinery flutter is analyzed using one of a number of formulations, traveling-wave, standing-wave, or influence-wave (cf. Crawley, 1988). The developments in the field have been reviewed by, e.g., Platzer (1975, 1978), Sisto (1977), Fleeter (1979), Bendiksen (1988, 1990), and in the 2 volumes of AGARDograph 298 (1987, 1988).

Many studies of turbomachinery flutter have been based on a methodology proposed by Carta (1967). This method, which Bendiksen (1990) calls the *energy method*, is based on the assumption that flutter occurs in one of the natural modes of vibration of the rotor and computes the energy exchange between this vibration mode and the flow field. Any mode modification due to unsteady aerodynamic forces is neglected (but the steady-state aerodynamic forces are often included in the computation of the vibratory mode). As a consequence this methodology is essentially *uncoupled*, or more precisely *weakly coupled*, in the sense that no feedback of unsteady aerodynamic forces on mode shape and frequency is included. This methodology has been extensively used combined with aerodynamic models of varying complexity, mostly strip theories, based on spanwise stacking of two-dimensional aerodynamic models, and more recently fully three-dimensional methods. In the original work of Carta (1967), Theodorsen's (1935) isolated flat-plate airfoil theory was used (Bendiksen (1990) notes that "it appears that Carta's method is quite successful in estimating the *relative* stability of various fan designs, even if Theodorsen's isolated airfoil theory is used"). Flat-plate cascade theories (cf. Whitehead, 1987, for a comprehensive review of these theories) were used by, e.g., Mikolajczak et al. (1975), Halliwell (1980), Adamczyk et al. (1982). Halliwell et al. (1984) and Barton and Halliwell (1987) used Whitehead's (1982) unsteady linearized potential solver FINSUP in a strip theory model. Gerolymos (1988b) solved the three-dimensional Euler equations to compute the response and stability of modes computed by a three-dimensional finite-element method.

A number of other methods exist that compute the *coupled* aeroelastic eigenmodes and, eventually the flutter boundaries. Most authors have been interested in parametric studies using typical section models (Bisplinghoff and Ashley, 1962). Whitehead (1966, 1974) studied a torsional SDOF (Single-Degree-Of-Freedom) typical section model using the flat-plate theories of Whitehead (1962), for incompressible, and Smith (1973) for compressible subsonic flow. Bendiksen and Friedmann (1980, 1981, 1982) studied a typical section model coupled with flat-plate cascade theory (Whitehead, 1962, for incompressible flows, Bendiksen and Friedmann, 1981, for supersonic flows with subsonic leading-edge locus). Dugundji and Bundas (1984) used a standing-wave formulation for studying a typical section model using Whitehead's (1962) incompressible flat-plate cascade theory and Padé approximants (e.g., Edwards et al., 1979). Kaza and Kielb (1982) and Kielb and Kaza (1983, 1984) investigated the effects of mistuning on cascade flutter and response using a typical section model coupled with the flat-plate aerodynamic theories of Smith (1973), for subsonic flows, and of Adamczyk and Goldstein (1978) for supersonic flows with subsonic leading-edge locus. Kielb and Ramsey (1989) used a typical section model coupled with the flat-plate theory of Lane (1957) to study supersonic throughflow fan flutter. Sinha et al. (1986) used Whitehead's (1962) incompressible flat plate cascade theory coupled with a torsional SDOF typical section model to study the influence of friction dampers on torsional blade flutter (this work was an extension of previous investigations by Sinha and Griffin, 1983, 1985, and Griffin and Sinha, 1985, who simply used negative viscous damping to simulate the aerodynamic forces). Akai and Atassi (1980) computed flutter boundaries for a typical section model using their low Mach number loaded cascade model (Atassi and Akai, 1980).

Contributed by the International Gas Turbine Institute and presented at the 37th International Gas Turbine and Aeroengine Congress and Exposition, Cologne, Germany, June 1–4, 1992. Manuscript received by the International Gas Turbine Institute February 17, 1992. Paper No. 92-GT-171. Associate Technical Editor: L. S. Langston.

Other authors consider more realistic structural models. Kaza and Kielb (1984a) used a nonlinear elastic beam theory (Kaza and Kielb, 1984b) coupled with the flat-plate cascade theories of Smith (1973) and Adamczyk and Goldstein (1978); this model was extended to include disk flexibility by Kaza and Kielb (1985). Srinivasan and Fabunmi (1984) used an *assumed modes method* (Bisplinghoff and Ashley, 1962), with three coupled bending-torsion basic modes, coupled with Smith's (1973) flat-plate cascade theory in a strip theory fashion. White and Bendiksen (1987) used an assumed modes method coupled with a strip-theory computation based on the flat-plate cascade theory of Bendiksen and Friedman (1981) to compute the aeroelastic characteristics of metal and composite blades. Henry and Vincent (1990) used an assumed modes method (with basic modes obtained by a variety of structural methods) coupled with results from the 2.5-dimensional Euler method of Gerolymos (1988a); in this work the Euler method was used to generate tabulated force and moment results for various blade sections (intersections of steady flow streamsurfaces with the blade), i.e., to generate an *aerodynamic modal basis*.

The above review of the literature on coupled computation of aeroelastic eigenmodes leads to the following conclusions:

- The bulk of the literature is concerned with model parametric studies.
- Virtually all methods, including those using advanced structural models, are based on two-dimensional aerodynamic theories, mostly of the flat-plate type, in a strip theory fashion, with the exception of Henry and Vincent, who used a strip theory based on 2.5-dimensional computations; however, fully three-dimensional computations have proved to be indispensable, especially in transonic/supersonic compressors (e.g., Epstein et al., 1979; Kerrebrock, 1981; Karadimas, 1988), and are believed to be so for the unsteady case as well (cf. Bendiksen, 1990).

The purpose of this paper is to develop a coupling procedure, to compute aeroelastic vibration modes, frequency and damping, using the three-dimensional Euler solver developed by Gerolymos (1992) as aerodynamic operator (cf. Fig. 1 for a global description of the computational procedure). This paper will be concerned with the *tuned rotor* problem (Lane, 1956).

2 Problem Statement

2.1 Assumed Modes Method and Aerodynamic Operator. In the present work, the assumed modes method is used. First (cf. section 2.2) a set of basic structural modes (in which the static deformation and stiffening due to steady aerodynamic pressures have been included) is computed. These modes are computed for various traveling-wave orders ι (cf. Lane, 1956), of corresponding interblade phase angle $\beta_\iota = 2\pi r/N$ ($\iota = 0, 1, \ldots, N\text{-}1$), thus generating a *mechanical modal basis* (mechanical ≠ aeromechanical), which can be described by the set $\mathbb{M}$

$$\mathbb{M} = \left\{ \mathfrak{M}(m, \iota, \mathbf{P}) \;\middle|\; \begin{matrix} 1 \le m \le M & m \in \mathbb{Z} \\ 0 \le \iota \le N-1 & \iota \in \mathbb{Z} \end{matrix} \right\} \tag{1}$$

where m is the blade mode number, M the number of blade modes used for the subsequent modal synthesis, ι the traveling-wave order defining the interblade-phase-angle β_ι, N the number of blades, $\mathbb{Z}$ the set of integers, and $\mathbf{P}$ denotes the operating point under consideration, e.g.,

$$\mathbf{P} = [\pi_{T-T}, \overset{\circ}{m}, \text{rpm}, p_{t1}, T_{t1}]^T \tag{2}$$

where π_{T-T} is the total-to-total pressure ratio, $\overset{\circ}{m}$ the mass flow rate, rpm the rotation velocity, p_{t1} the inlet total pressure, and T_{t1} the inlet total temperature (all these parameters influence the *mechanical* modes through centrifugal stiffening and *steady aerodynamic effects*). These modes will be coupled, when excited, through *unsteady aerodynamic effects*, to yield *aeromechanical eigenmodes*

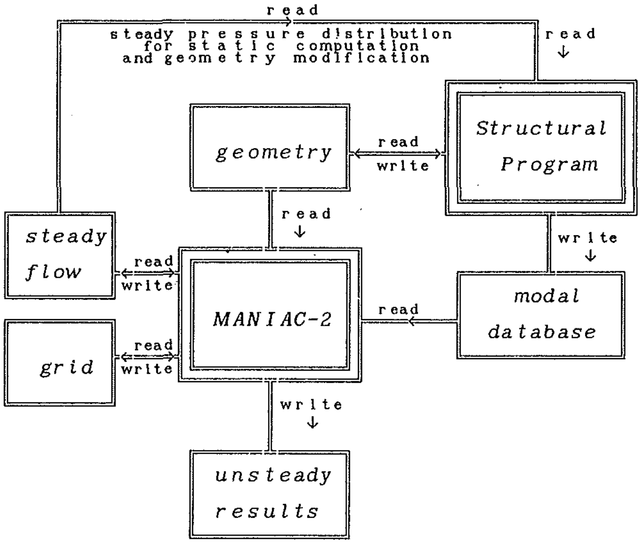

Fig. 1 Flow-diagram of the three-dimensional computer program MANIAC-2 (Methodology for Aeroelastic Numerical Instability Analysis in Compressors)

$$/\mathrm{A} = \left\{ \mathfrak{A}(m, \iota, \mathbf{P}) \;\middle|\; \begin{matrix} 1 \le m \le M & m \in \mathbb{Z} \\ 0 \le \iota \le N-1 & \iota \in \mathbb{Z} \end{matrix} \right\} \tag{3}$$

Based on the orthogonality of aeromechanical eigenmodes of different β_ι (cf. Thomas, 1979; Lane, 1956) the computation of the aeromechanical eigenmode $\mathfrak{A}(m = l, \iota = r, \mathbf{P})$ uses the modal basis $\mathbb{M}_r \subset \mathbb{M}$

$$\mathbb{M}_r = \left\{ \mathfrak{M}(m, \iota = r, \mathbf{P}) \;\middle|\; \begin{matrix} 1 \le m \le M & m \in \mathbb{Z} \\ \iota = r & \end{matrix} \right\} \tag{4}$$

for a fixed $r \in \{0, 1, \ldots, N-1\}$. This is an important reduction to the number of degrees of freedom, since an original problem for the search of $M \times N$ modes is reduced to N separate problems of M modes, as is usually the case in tuned rotor aeroelasticity. Then the aeromechanical mode l for the traveling wave r, $\mathfrak{A}(l, r, \mathbf{P})$ will be assumed to have a mode shape $\Phi(l, r, \mathbf{P})$ given by

$$\{\Phi(l, r, \mathbf{P})\} = \sum_{m=1}^{M} \{\eta_m \{\varphi(m, r, \mathbf{P})\}\} \tag{5}$$

where $\{\Phi\}$ denotes the aeromechanical mode shape, $\{\varphi\}$ the mechanical mode shape (cf. section 2.2), and η_m are the generalized coordinates. In order to formulate the aeroelastic problem and compute the coupling of the mechanical eigenmodes through unsteady aerodynamic effects two methods are encountered in the literature: the use of Padé approximants (e.g., Edwards et al., 1977; Dugundji and Bundas, 1984), or the use of an aerodynamic modal basis (e.g., Henry and Vincent, 1990). In either case, one would need to compute the aerodynamic operator, in the form of unsteady pressures on the surface of the blade, for *each of the assumed modes* used for the modal projection, vibrating at *various frequencies*, e.g., for the frequencies of each eigenmode. Hence the knowledge of an aerodynamic data base in the form

$$\mathbb{P}_r = \left\{ {}^1p(\mathbf{x}, \mathfrak{M}, f, \mathbf{P}) \;\middle|\; \begin{matrix} \mathfrak{M} \in \mathbb{M}_r \\ \mathbf{x} \in \partial\mathbb{B} \\ f \in \mathbb{F}_r \end{matrix} \right\} \tag{6}$$

where ${}^1p$ are the first-harmonics of pressure, $\mathbf{x}$ a position vector, $\partial\mathbb{B}$ the blade surface, and $\mathbb{F}_r = \{{}^rf_1, {}^rf_2, \ldots, {}^rf_M\}$ are

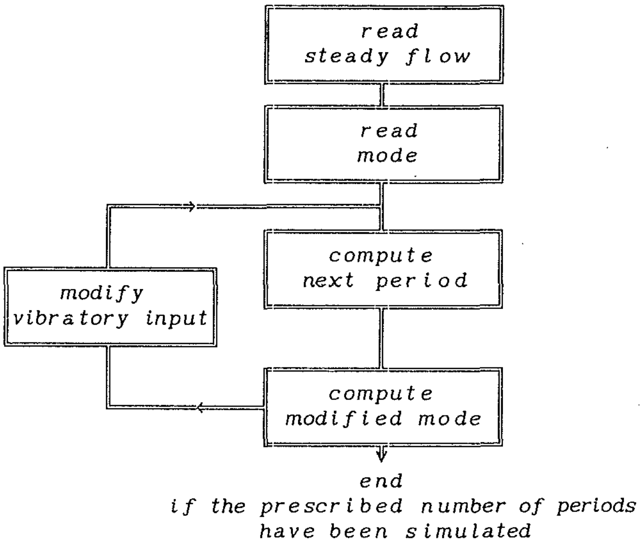

Fig. 2 Procedure for coupled aeromechanical computation

the frequencies of the mechanical modes $\mathbb{M}_r$ used in the assumed modes method. Hence the prediction of the coupled aeroelastic modes (and their stability or instability) for only one traveling wave order would require $M \times M$ aerodynamic computations. Since the stability of one operating point would require the computation of $L \sim 8$ (an arbitrary estimation) traveling waves, $L \times M \times M$ computations would be needed for the construction of the aerodynamic database at *each operating point.* Since most aeroelastic studies in the field of turbomachinery have used simple (and computationally rapid) methods, often analytical, the construction of $\mathbb{P}_r$, and often of $\mathbb{P} = \mathbb{P}_0 \cup \mathbb{P}_1 \cup \cdots \cup \mathbb{P}_{N-1}$ did not present a major problem. This is not the case, however, for three-dimensional time-marching Euler methods (and later solvers with viscous models), where the realistic representation of the steady and unsteady flow field requires substantial computing times. A typical time-marching Euler computation of the three-dimensional unsteady flow in a vibrating cascade requires from 1/4 h-1 h of CPU on a CRAY-XMP computer (depending on the frequency, cf. Gerolymos, 1992), say a typical ~1/2 h per computation (as a mean for the first six frequencies of a fan rotor). This computation is done for a given vibratory mode and a given interblade-phase-angle. Hence for a typical $M = 6$, 36 Euler computations would be required, resulting in unrealistic computing times, since this operation should be done $L \sim 8$ times at each operating point $\mathbf{P}$, for various operating points. *The purpose of the present work is to circumvent this problem by developing a coupling method using only one aerodynamic computation for each aeroelastic mode*, thus reducing the computing time per mode by a factor M.

To this purpose a method of *mode modification* during the time-marching iterations was developed. This procedure, which will be described in detail in section 3, is schematically described in Fig. 2. At the end of the aerodynamic simulation of each period of the *aeromechanical mode* $\mathfrak{A}(l, r, \mathbf{P})$, the aeromechanical mode is reactualized by the contributions of the modes of Eq. (5), computed on the basis of the unsteady pressures generated by $\mathfrak{A}(l, r, \mathbf{P})$ itself $\{{}^{l}p[\mathbf{x}, \mathfrak{A}(l, r, \mathbf{P})], \mathbf{x}\in\partial\mathbb{B}\}$, instead of an equivalent linear superposition of unsteady pressures generated by each assumed mode and interpolated to the frequency of interest. The frequency is now an unknown determined by the coupling procedure, $f = f[\mathfrak{A}(l, r, P)]$.

2.2 Basic Structural Modes. The *mechanical modes* are computed using the theory for rotationally periodic structures developed by Thomas (1974, 1979) and its extension to substructuring coupled with wave propagation developed by Henry (1980) and Henry and Ferraris (1984). The modes used in section 4, "Results," were computed by Mascarell and coworkers (1990) using the finite element computer program SAMCEF (SAMTech, Belgium) in which the aforementioned analysis method has been implemented by Lombard et al. (1986). In the following are summarized the basic hypotheses of the structural model:

- computation of undamped natural modes.
- inclusion of structural deformation and stiffening induced by centrifugal forces and steady aerodynamic pressures (e.g., from a three-dimensional Euler steady-state solution).
- modes in traveling-wave formulation for a basic blade + disk sector, with appropriate phase-shifted boundary conditions at disk and shroud interfaces.
- shroud interface modeled by appropriate boundary conditions (Mascarell, 1990).

The resulting eigenmodes (cf. Thomas, 1979) are complex, because of the phase-shifted boundary conditions, this being the only difference with classical undamped systems. The resulting generalized eigenvalue problem is hermitian (cf. Thomas, 1979; Henry and Ferraris,1984), i.e., the mass and stiffness matrices $[\mathbf{M}(r, \mathbf{P})]\in\mathbb{C}^{\mathrm{NDOF}\times\mathrm{NDOF}}$, and $[\mathbf{K}(r, \mathbf{P})]\in\mathbb{C}^{\mathrm{NDOF}\times\mathrm{NDOF}}$, dependent on interblade phase angle and operating point, are hermitian. This problem can be solved by decomposition to two real symmetric generalized eigenvalue problems (cf. Wilkinson, 1965). A number of properties of the solutions are of interest here, viz.,

- the eigenvalues are real, i.e., the modes are undamped.
- the modal mass and stiffness are real, i.e., defining

$$\left.\begin{array}{l} \mu(m, r, \mathbf{P}) \doteq \{\varphi(m, r, \mathbf{P})\}^* \ [\mathbf{M}(r, \mathbf{P})] \ \{\varphi(m, r, \mathbf{P}) \\ k(m, r, \mathbf{P}) \doteq \{\varphi(m, r, \mathbf{P})\}^* \ [\mathbf{K}(r, \mathbf{P})] \ \{\varphi(m, r, \mathbf{P})\} \end{array}\right| \begin{array}{l} 1\le m\le M \\ 0\le r\le N-1 \end{array} \quad (7)$$

where $\mu(m, r, \mathbf{P})$ is the modal mass, and $k(m, r, \mathbf{P})$ the modal stiffness, $\{\cdot\}^*$ denotes the transpose complex conjugate of a vector and $\{\varphi(m, r, \mathbf{P})\}\in\mathbb{C}^{\mathrm{NDOF}}$ the mode shape vector of the mode $\mathfrak{M}(m, r, \mathbf{P})$, it follows that

$$\mu(m, r, \mathbf{P})\in\mathbb{R};\ k(m, r\mathbf{P})\in\mathbb{R};\ 1\le m\le M;\ 0\le r\le N-1 \quad (8)$$

Furthermore Thomas (1979) shows that the traveling-wave modes appear in counterrotating pairs (waves r and $N-r$), with identical frequency ($f[\mathfrak{M}(m, r, \mathbf{P})] = f[\mathfrak{M}(m, N-r, \mathbf{P})]$) and whose mode shapes are complex conjugates (i.e., for a sector with NDOF degrees of freedom $\{\varphi(m, r, \mathbf{P})\} = \{\overline{\varphi}(m, N-r, \mathbf{P})\}\in\mathbb{C}^{\mathrm{NDOF}}$). Of importance for the coupling procedure used is that modal mass and stiffness are real and that mode shapes are orthogonal with respect to the mass and stiffness matrices, i.e.,

$$\left.\begin{array}{l} \{\varphi(l, r, \mathbf{P})\}^*[\mathbf{M}(r, \mathbf{P})]\varphi(m, r, \mathbf{P})\} = \delta_{ml}\mu(l, r, \mathbf{P}) \\ \{\varphi(l, r, \mathbf{P})\}^*[\mathbf{K}(r, \mathbf{P})]\varphi(m, r, \mathbf{P})\} = \delta_{ml}k(l, r, \mathbf{P}) \end{array}\right| \begin{array}{l} 1\le m, l\le M \\ 0\le r\le N-1 \end{array} \quad (9)$$

where δ_{ml} is Kronecker's δ.

3 Aeroelastic Coupling

Consider the computation of the coupled mode $\mathfrak{A}(l, r, \mathbf{P})$. As described in section 2.1 this mode is computed using an assumed modes method based on modes from $\mathbb{M}_r$. Since in the following the traveling wave order r and the operating point $\mathbf{P}$ are fixed the explicit functional dependence on $(r, \mathbf{P})$ of various properties will be dropped to simplify notation. Let $\lambda \in \mathbb{C}$ be the eigenvalue associated with the aeromechanical eigenmode $\mathfrak{A}_l = \mathfrak{A}(l, r, \mathbf{P})$

$$\lambda = -\zeta\omega + i\omega \tag{10}$$

where i is the imaginary unit, ω is the vibration frequency, and ζ is the damping factor. This definition is slightly different from the classic SDOF oscillator definition (e.g., Meirovitch, 1975), where the undamped natural frequency is used to define ζ. The mode shape Φ_l of the aeroelastic eigenmode $\mathfrak{A}_l$ is assumed to be represented by a finite number of mechanical modes M

$$\Re e[\{\Phi_l\}e^{\lambda t}] \sim \Re e\left[\sum_{m=1}^{M} \eta_m e^{\lambda t}\{\varphi_m\}\right] \tag{11}$$

where $\{\varphi_m\} = \{\varphi(m, r, \mathbf{P})\} \in \mathbb{C}^{\mathrm{NDOF}}$ are the mode shapes of modes $\mathfrak{M}(m, r, \mathbf{P}) \in \mathbb{M}_r$, $\eta_m \in \mathbb{C}$ are generalized coordinates in the modal space $\mathbb{M}_r$. Using Eq. (11), the aeroelastic equations of motion become (cf. Crawley, 1988)

$$\lambda^2[\mathbf{M}]\left(\sum_{m=1}^{M} \eta_m e^{\lambda t}\{\varphi_m\}\right) + [\mathbf{K}]\left(\sum_{m=1}^{M} \eta_m e^{\lambda t}\{\varphi_m\}\right) = \\ = \{\mathfrak{f}(\eta_1, \eta_2, \ldots, \eta_M; \lambda)\}e^{\lambda t} \tag{13}$$

where $\{\mathfrak{f}\} \in \mathbb{C}^{\mathrm{NDOF}}$ is the finite-element representation vector of the first-harmonics of pressure forces applied on each point of the blade surface (its elements being 0 at points of the structure that are not on the *wetted* surface). Note that although the aerodynamic code used in the present work is nonlinear, only the first-harmonics of the aerodynamic forces are considered in the coupling procedure, which is linearized. Instead of searching an explicit relation of $\{\mathfrak{f}\}$ with the generalized coordinates themselves and the frequency λ, its value is directly computed by the Euler solver following the diagram of Fig. 2. The aeroelastic computation of the mode $\mathfrak{A}_l$ starts with the simulation of one vibration period of the mode $\mathfrak{M}_l \in \mathbb{M}_r$ with $\lambda \leftarrow i\omega$. At the end of this period a first estimation (note that the aerodynamic simulation of $\mathfrak{M}_l$ is not continued until periodic convergence of the unsteady aerodynamic forces) of $\{\mathfrak{f}(0, \ldots, 0, 1, 0, \ldots, 0; i\omega)\}$, with $\eta_m = \delta_{ml}$ $(m = 1, \ldots, M)$ is obtained. These aerodynamic forces will not be orthogonal to the other mechanical mode shapes, and will excite them. With the procedure that will be described in the following, the generalized coordinates of Eq. (11) will be reactualized, and a new vibration period will be simulated by the Euler code, with the reactualized mode shape and frequency as input, which will furnish a new frequency and mode shape, and this procedure is continued until convergence.

In order to determine the coupling relations, consider the projection of the equations of motion (Eq. (12)) on the modal basis by premultiplying with $\{\varphi_n\}^*$

$$\{\varphi_n\}^*\lambda^2[\mathbf{M}]\left(\sum_{m=1}^{M} \eta_m e^{\lambda t}\{\varphi_m)\right) + \{\varphi_n\}^*[\mathbf{K}]\left(\sum_{m=1}^{M} \eta_m e^{\lambda t}\{\varphi_m)\right) = \\ = \{\varphi_n\}^*\{\mathfrak{f}(\eta_1, \eta_2, \ldots, \eta_M; \lambda)\}e^{\lambda t} \tag{13}$$

defining

$$f_n(\eta_1, \eta_2, \ldots, \eta_M; \lambda) \doteq \{\varphi_n\}^*\{\mathfrak{f}(\eta_1, \eta_2, \ldots, \eta_M; \lambda)\} \tag{14}$$

and rearranging the terms, after simplifying by $e^{\lambda t}$ yields

$$\sum_{m=1}^{N} ((\lambda^2\{\varphi_n\}^*[\mathbf{M}]\{\varphi_m\} + \{\varphi_n\}^*[\mathbf{K}]\{\varphi_m\})\eta_m\} \\ = f_n(\eta_1, \ldots, \eta_M; \lambda) \tag{15}$$

and using the orthogonality relations of Eq. (9) the following equations of motion are obtained (returning to the index m instead of n):

$$\lambda^2\eta_m\mu_m + \eta_m k_m = f_m(\eta_1, \eta_2, \ldots, \eta_M; \lambda) \ \forall m = 1, 2, \ldots, M \tag{16}$$

and since

$$\omega_m^2 \doteq k_m/\mu_m \ \forall m = 1, 2, \ldots, M \tag{17}$$

the equivalent expression of the equations of motion (Eq.(16)) is obtained:

$$\eta_m(\lambda^2 + \omega_m^2) = \frac{f_m(\eta_1, \eta_2, \ldots, \eta_M; \lambda)}{\mu_m} \ \forall m = 1, 2, \ldots, M \tag{18}$$

Equation (18) is the basis for formulating the coupling relations, described in the following.

Set $n \leftarrow 0$; ${}^0\eta_l = \delta_{ml}$; ${}^0\lambda = i\omega_l$

$\underline{0}$: $n \leftarrow n + 1$

$\underline{1}$: Compute ${}^n f_m = f_m({}^n\eta_1, {}^n\eta_2, \ldots, {}^n\eta_M; \lambda)$ $\forall m = 1, 2, \ldots, M$

$\underline{2}$: Update

$${}^{n+1}\eta_l = 1$$

$${}^{n+1}\lambda^2 = -\omega_l^2 + \frac{{}^n f_l}{\mu_l}$$

$${}^{n+1}\eta_m = \frac{{}^n f_m}{\mu_m({}^{n+1}\lambda^2 + \omega_m^2)} \ \forall m = 1, \ldots, l-1, \\ l+1, \ldots, M \tag{19}$$

$\underline{3}$: Repeat steps 0–2 until convergence.

The coupling relations are described as an iterative procedure with iteration count n the period simulated by the Euler code. The iterations are necessary for the computation of the generalized aerodynamic forces f_m. Since the coupling relations are linear, it was chosen invariably to set $\eta_l = 1$, thus interpreting η_m for $m \neq l$ as perturbations of the corresponding mechanical mode.

This iterative procedure has not presented problems in the applications. On inspection of step 2 of the iterative procedure (Eq. (19)) it is seen that because the steady stiffness k_l (structural + centrifugal + steady pressure field) is an order of magnitude higher than the unsteady aerodynamic stiffness f_l (for supersonic fan applications) the frequency perturbation is small. The stability of the second relation of step 2 of Eq. (19) requires that the eigenfrequencies be well separated; keeping in mind that the modal coordinates used are for a fixed interblade phase angle β_r, common for all the modes, this requirement is usually satisfied (e.g., frequencies closer than 60 Hz are not encountered in the first six blade modes of the shrouded Fan C examined in the Results section).

The aerodynamic damping δ_{aero} (logarithmic decrement) is computed for $\zeta = -\Re e(\lambda\omega^{-1}) \ll 1$ by the well-known approximate formula (Carta, 1967)

$$\delta \cong 2\pi\zeta \Big/ \sqrt{1 - \zeta^2} \tag{20}$$

A note concerning the computation and physical significance of f_m is in order here. The vector $\{\mathfrak{f}(\eta_1, \eta_2, \ldots, \eta_M; \lambda)\}$ is the vector of the first-harmonics of pressure forces applied at each point on the blade surface. Consequently if $\mathbf{q}_m(\mathbf{x}) \in \mathbb{C}^3$ is the complex displacement amplitude of the mode $\mathfrak{M}_m$ at the point $\mathbf{x}$ on the blade surface

$$f_m = \{\varphi_m\}^*\{\mathfrak{f}\} = \sum_{\mathbf{x} \in \partial\mathbb{B}} (-\bar{\mathbf{q}}_m(\mathbf{x}) \cdot \mathbf{n}(\mathbf{x})\ {}^1p(\mathbf{x})\Delta S) \sim \\ \sim \iint_{\partial\mathbb{B}} (-\bar{\mathbf{q}}_m(\mathbf{x}) \cdot \mathbf{n}(\mathbf{x})\ {}^1p(\mathbf{x})dS) \tag{21}$$

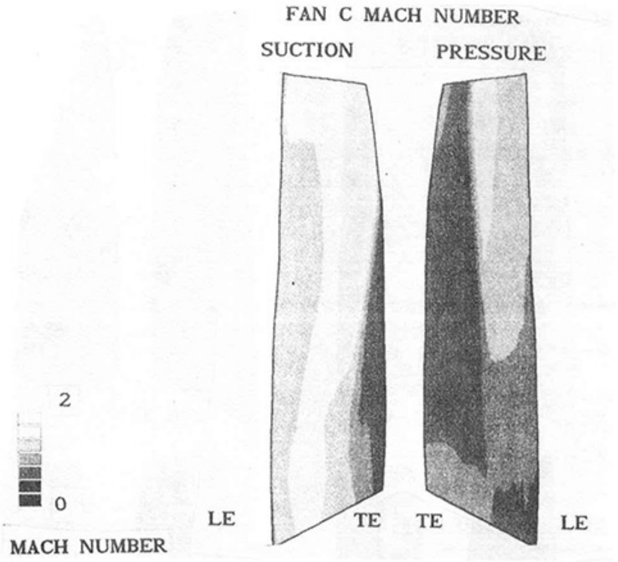

Fig. 3 Mach number level on Fan C blade, at 107 percent speed

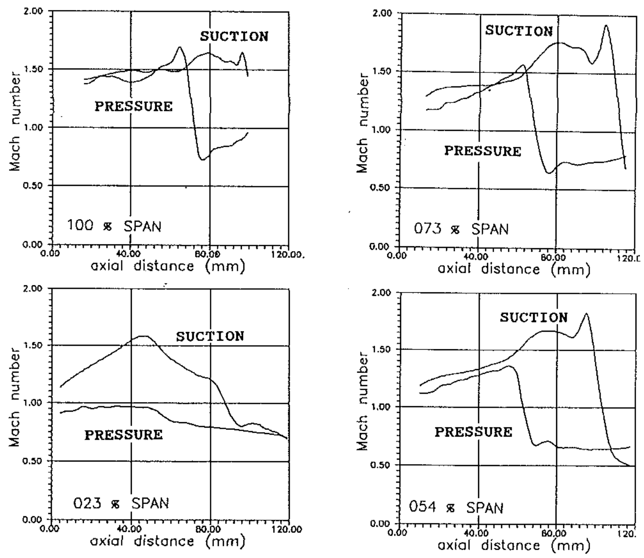

Fig. 4 Mach number axial distributions on Fan C blade

where **n** is the outgoing normal to the blade surface $\partial\mathbb{B}$, and ${}^1p$ is the first-harmonic of pressure on the blade surface, and $\sim$ means a numerical approximation of the integral. The physical significance of f_m is made clear by observing that

$$\mathfrak{Im}[f_m] \sim \mathfrak{Im}\left[\iint_{\partial\mathbb{B}} (-\bar{\mathbf{q}}_m(\mathbf{x})\bullet\mathbf{n}(\mathbf{x})\ {}^1p(\mathbf{x})dS\right] \sim$$

$$\sim \pi^{-1}\iint_{\partial\mathbb{B}}\left(\int_0^{2\pi\omega^{-1}} (-\mathbf{V}_m(\mathbf{x};\,\omega t)\bullet\mathbf{n}(\mathbf{x};\,\omega t)p(\mathbf{x};\,\omega t))dt\right)dS \quad (22)$$

i.e., $\pi\mathfrak{Im}[f_m]$ is the energy virtually accumulated by the blade during one period of vibration at frequency ω in the mode $\mathfrak{M}_m$ due to the composite unsteady pressure field (response to the resultant aeromechanical vibration mode $\mathfrak{A}_l$).

4 Results

4.1 Configuration and Steady Flow

4.1.1 Configuration. Results of the coupled aeromechanical method are given for Fan C at a point on the 107 percent speed line. Fan C has 38 blades and its design rotation speed is 4836 rpm. Fan C has a part-span shroud, which was not modeled during the aerodynamic simulations (it was, however, included in the mechanical model, where it has a great influence on vibration modes, as explained in the work of Carta, 1967). Although the shock-wave system of the rotor is influenced by the part-span shroud, with important effects on efficiency (cf. Derrien, 1986), it is expected that reasonably accurate results may be obtained for the unsteady aerodynamics of the vibrating cascade. The inclusion of the shroud into the aerodynamic model will be the subject of a future study (cf. Gerolymos, 1993).

4.1.2 Steady Flow. All the computations were run on an 80 × 15 × 15 grid. Although this grid is relatively coarse, it is believed, in view of the parametric studies on the influence of the computational grid on results, described in Gerolymos (1993), that reasonably accurate unsteady results may be obtained.

Steady flow results are shown in Fig. 3, where the Mach number level, on the surface of the blade, is plotted. Axial Mach number distribution at various spanwise stations is plotted in Fig. 4. It is seen that there is a strong shock-wave system on the suction surface. The operating point computed was at 107 percent speed and at a relatively low pressure ratio. Therefore, the shock waves on the suction surface and near the tip are very close to the trailing edge. The shock wave is well downstream into the interblade channel on the pressure surface as well. The shock system penetrates to the hub (cf. Fig. 4 at 54 and 23 percent span), on the suction surface, although this effect is probably exaggerated by the coarseness of the grid in the neighborhood of the hub.

Table 1 Frequencies of ± 4-order traveling-wave modes used in the assumed modes method

mode #	*frequency*
1	235. Hz
2	408. Hz
3	626. Hz
4	688. Hz
5	805. Hz
6	901. Hz

4.2 Unsteady Results and Aeroelastic Coupling

4.2.1 Mechanical Modes. Computations of the coupled aeroelastic eigenmodes were run for the ± 4-order traveling waves (the terms −4-order is used in the following for the ($N-4$)-order traveling wave).The frequencies of the mechanical modes used for the modal projection in the assumed modes method are given in Table 1 (note that the frequencies are the same for the ±4-order traveling waves, because undamped basic mechanical modes are considered).

The corresponding mode shapes are depicted in Fig. 5 for the +4-order traveling wave (the corresponding −4-order traveling-wave mechanical mode shapes are qualitatively similar). The presence of the shroud complicates the modes, introducing important bending/torsion coupling. Note that modes 3 and 4 are quite similar, and their frequencies are close (a difference of 60 Hz). It is expected that nonnegligible coupling between these two modes will occur through unsteady aerodynamic forces. Modes 5 and 6 are higher modes. Mode 5, especially, exhibits important amplitudes beneath the shroud. These six modes were used in the assumed modes method, for computing the first four coupled aeromechanical modes. Some

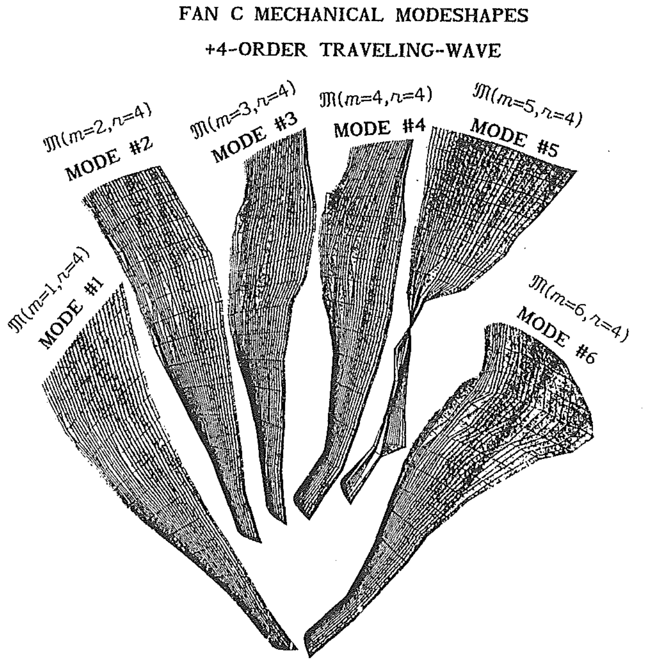

Fig. 5 Mechanical modes $\mathfrak{M}(m, 4)$ for Fan C at 107 percent speed, on the operating line, used in the assumed modes method

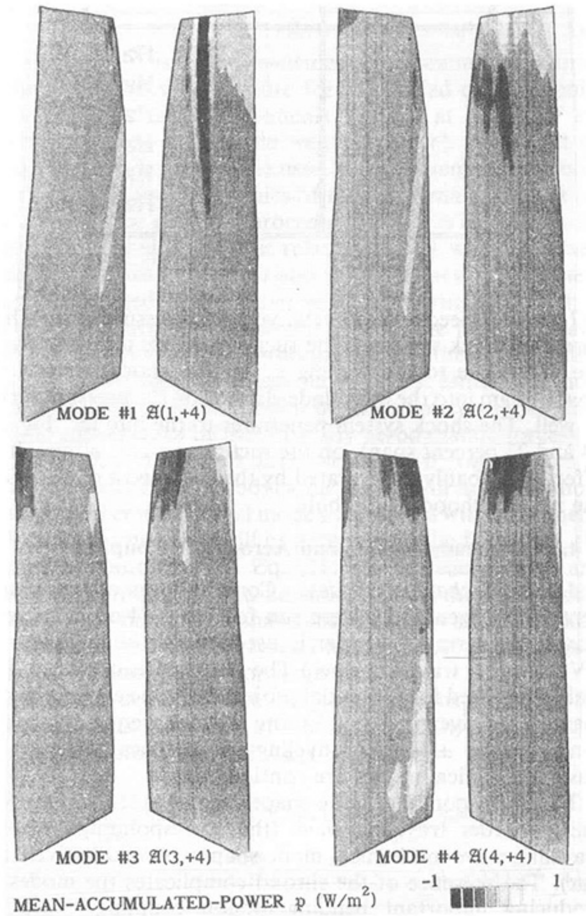

Fig. 6 Mean accumulated power on Fan C blade at 107 percent speed, for the first four coupled aeroelastic modes for +4 traveling wave

anomalies at the ~70 percent span neighborhood mark the position of the shroud (not shown).

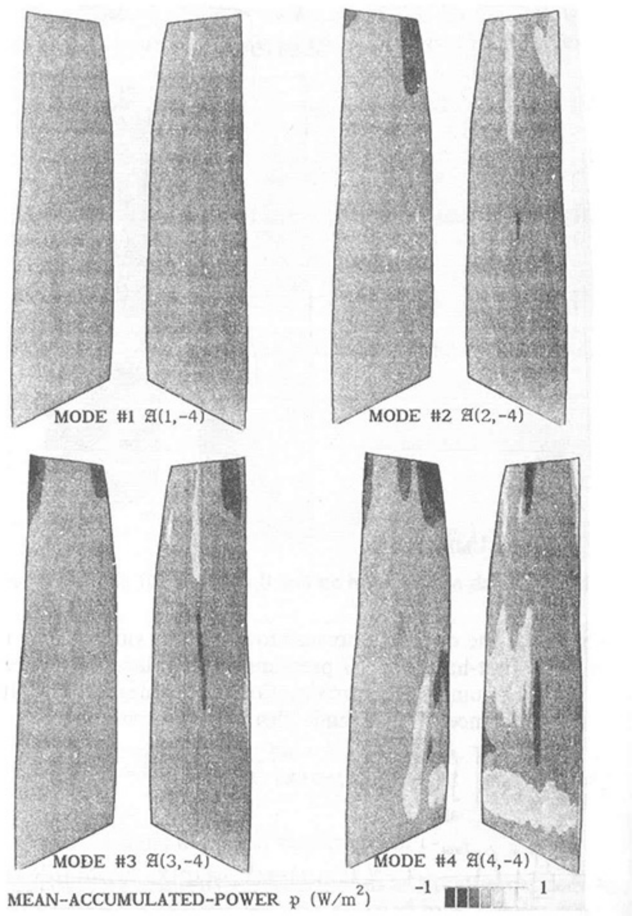

Fig. 7 Mean accumulated power on Fan C blade at 107 percent speed, for the first four coupled aeroelastic modes for −4 traveling wave

4.2.2 *Computation of Coupled Aeromechanical Modes.* Computations for the coupled aeromechanical eigenmodes will be presented for the ±4-order traveling waves. It is clear that this is not sufficient for examining the stability characteristics of the operating point under consideration, but it serves to illustrate the results obtained by the method, and to make a preliminary assessment on the importance of aerodynamic coupling of mechanical eigenmodes. The level of mean accumulated power $\mathfrak{p}$

$$\mathfrak{p} \doteq \frac{1}{2\pi}\int_0^{2\pi} p(\mathbf{x}, \omega t)\mathbf{V}(\mathbf{x}, \omega t)\mathbf{n}(\mathbf{x}, \omega t)d(\omega t) \quad \mathbf{x}\in\partial\mathbb{B} \qquad (23)$$

on the blade surface for the ±4-order traveling waves of the first four aeromechanical eigenmodes $\{\mathfrak{A}(l, \pm 4), l = 1, 2, 3, 4\}$ are depicted in Fig. 6 for the forward traveling wave and in Fig. 7 for the backward traveling wave. Note that the locations of the leading edge and trailing edge, on the suction surface, and the pressure surface are the same as explained in Fig. 3 where the steady-state isoMachs are plotted. In general, unsteady energy accumulation (positive or negative, i.e., unstable or stable, respectively) will take place near the tip. This is expected since $\mathfrak{p}$ denotes unsteady pressures weighted by local displacement velocity, and displacements are important at the tip sections. Modes $\mathfrak{A}(4, +4)$ and $\mathfrak{A}(4, -4)$ exhibit important power accumulation at near-hub sections, this mode being of the 2*F* type, although much more complicated due to the presence of the shroud (cf. Fig. 5).

4.2.3 *Stability and Aeroelastic Coupling.* Results concerning frequency modification, damping, ζ, and logarithmic decrement δ (computed from Eq. (20)) for the coupled aeromechanical modes computed in section 4.2.2 are given in Table 2. It is seen that in general frequency modifications are very

Table 2 Frequency modification, damping, and logarithmic decrement for the ± 4-order traveling wave coupled aeroelastic modes $\mathfrak{A}$

+4-order traveling-wave				
mode #	$\mathfrak{M}$ *frequency*	$\mathfrak{A}$ *frequency*	ζ	δ
1	234·8 Hz	235·4 Hz	+1·70%	+10·6%
2	408.3 Hz	406.6 Hz	-0·43%	-2·7%
3	626·1 Hz	615·8 Hz	+0·17%	+1·0%
4	688·1 Hz	679·4 Hz	+0·07%	+0·4%
-4-order traveling-wave				
mode #	$\mathfrak{M}$ *frequency*	$\mathfrak{A}$ *frequency*	ζ	δ
1	234·8 Hz	233·9 Hz	+0·15%	+0·9%
2	408.3 Hz	407.1 Hz	-0·04%	-0·2%
3	626·1 Hz	623·5 Hz	+0·10%	+0·6%
4	688·1 Hz	686·4 Hz	-0·07%	-0·4%

Table 3 Aeroelastic coupling of mechanical modes through unsteady aerodynamic effects for the ± 4-order traveling-wave coupled aeroelastic modes $\mathfrak{A}$

+4-order traveling-wave				
mode	$\mathfrak{A}(1,+4)$	$\mathfrak{A}(2,+4)$	$\mathfrak{A}(3,+4)$	$\mathfrak{A}(4,+4)$
$\mathfrak{M}(1,+4)$	1·000	0·049	0·010	0·009
$\mathfrak{M}(2,+4)$	0·014	1·000	0·009	0·006
$\mathfrak{M}(3,+4)$	0·010	0·035	1·000	0·130
$\mathfrak{M}(4,+4)$	0·025	0·023	0·089	1·000
-4-order traveling-wave				
mode	$\mathfrak{A}(1,-4)$	$\mathfrak{A}(2,-4)$	$\mathfrak{A}(3,-4)$	$\mathfrak{A}(4,-4)$
$\mathfrak{M}(1,-4)$	1·000	0·009	0·002	0·001
$\mathfrak{M}(2,-4)$	0·001	1·000	0·005	0·007
$\mathfrak{M}(3,-4)$	0·002	0·013	1·000	0·050
$\mathfrak{M}(4,-4)$	0·002	0·005	0·040	1·000

small. Indeed they are negligible, except for modes $\mathfrak{A}(3, +4)$ and $\mathfrak{A}(4, +4)$ that show a ~2 percent frequency modification due to aeroelastic coupling. Concerning damping it is seen that as expected from inspection of $\mathfrak{p}$ plots, mode $\mathfrak{A}(1, 4)$ is particularly stable. Modes $\mathfrak{A}(2, \pm 4)$ are both unstable. Also computed results for mode $\mathfrak{A}(4, -4)$ show instability. Examination of Fig. 8 shows that this instability is induced by near-hub sections. However, confidence in this result is small, due to insufficient near-hub resolution of the computational grid.

A detailed analysis of mechanical mode coupling is presented in Table 3, where the values of $\|\eta_m\|$ for the various aeroelastic modes is given, representing the participation of each mechanical mode $\mathfrak{M}$ to each aeromechanical mode $\mathfrak{A}$. This participation is normed to 1 for the mechanical mode corresponding to the aeromechanical one ($\mathfrak{M}(l, r)$ for $\mathfrak{A}(l, r)$), and as a consequence participation of other mechanical modes is given as a fraction of this mode. It is seen that generally coupling is quite weak, on the order of ~5 percent for most cases, with the exception of mode $\mathfrak{A}(4, +4)$, which has a 13 percent participation of mode $\mathfrak{M}(3, +4)$, a phenomenon justified by the proximity in frequency of the two modes. However, the coupling effect is dependent on the aeroelastic mass ratio (cf. Bendiksen,1990) and therefore the limited number of results presented here, for a particular fan blade, and a particular operating point are insufficient to substantiate any conclusion.

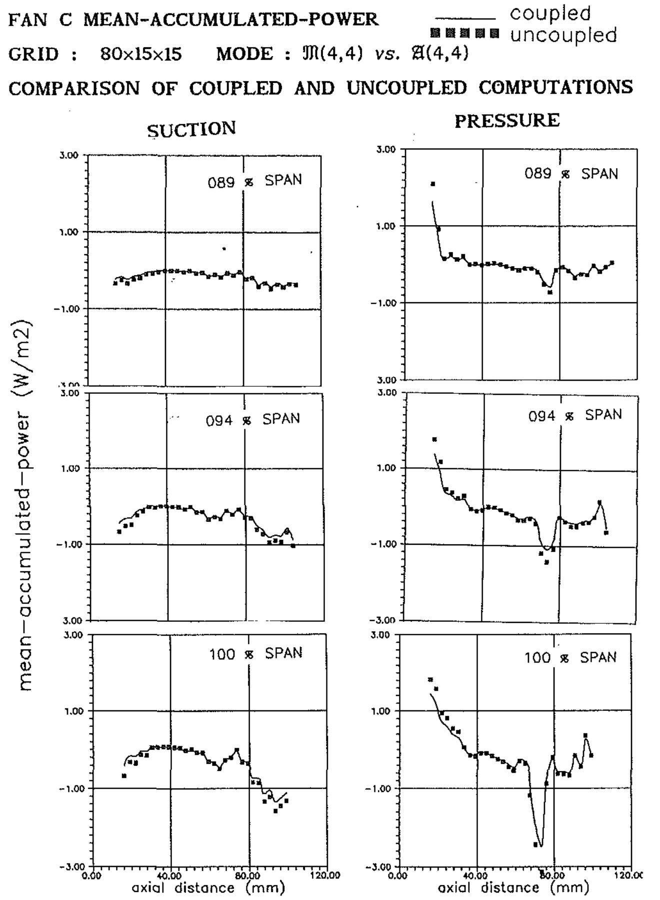

Fig. 8 Comparison of mean accumulated power on Fan C blade for coupled and uncoupled computations (modes $\mathfrak{M}(4, 4)$ and $\mathfrak{A}(4, 4)$)

4.3 Comparison of Coupled and Uncoupled Computations

4.3.1 Mean-Accumulated-Power $\mathfrak{p}$. A detailed comparison of $\mathfrak{p}$ distributions versus axial distance for coupled and uncoupled computations for modes $\mathfrak{M}(4, +4)$ and $\mathfrak{A}(4, +4)$ is presented in Fig. 8. This is interesting because $\mathfrak{M}(4, +4)$ is characterized by important coupling of mechanical modes 4 and 3. It is seen that there is very little difference between coupled and uncoupled computations, with the exception of the $\mathfrak{p}$ peaks at the shock-wave feet and in the neighborhood of the trailing edge.

4.3.2 Damping and Stability. Although the differences between coupled and uncoupled computations in Fig. 8 seem very small, they have an effect on aerodynamic damping. This is illustrated in Fig. 9(*a*), where the convergence of logarithmic decrement δ, for coupled $\mathfrak{A}(4, +4)$ and uncoupled computations is presented, as a function of the number of periods simulated by the Euler solver. It is seen that convergence of δ for both coupled and uncoupled computations is quite rapid, the level of damping being obtained already after the simulation of 3–4 periods. In Fig. 9(*b*) the convergence of the frequency of the coupled mode is presented. It is clear that already after simulating one vibration period the frequency of the coupled aeroelastic mode is obtained. What is remarkable is that the effects of aeroelastic coupling on damping are important. There is a ~30 percent difference in damping between

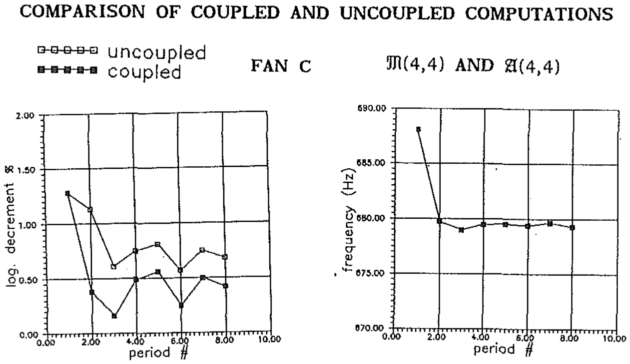

(a) (b)

Fig. 9 Unsteady convergence for Fan C coupled and uncoupled computations (*a*) logarithmic decrement in percent (*b*) vibration frequency

the coupled and the uncoupled computations, the effect of aeroelastic coupling being destabilizing. It is clear that small differences in p distributions, such as those of Fig. 8, can induce substantial changes in damping. This is due to the fact that aerodynamic damping is itself a small quantity, sensible to mode shape changes. It is again remarked that the number of computations run is not sufficient to draw general conclusions about aeroelastic coupling.

5 Conclusions

In the present work a methodology of mode modification was described, which is used in conjunction with an unsteady three-dimensional Euler solver for determining the aeroelastic eigenmodes of tuned rotors. The advantage of the methodology proposed is that it induces practically no computational overhead when compared to the aerodynamic operator computing time requirements. Sample results, illustrating the potential of the method, were presented. A limited number of studies on the importance of aeroelastic coupling showed that the effects of coupling are relatively small on unsteady flow response, but can have a nonnegligible effect on damping. The reader is reminded that the aerodynamic computations were performed with a rather coarse mesh. While this might lead to some scepticism regarding the exact values of results, it does not negate the importance and applicability of the coupling procedure.

6 Discussion

It is believed that the work presented in this paper offers interesting perspectives for the study of turbomachinery aeroelasticity, since it is the first attempt to include realistic three-dimensional aerodynamic computations in a coupled aeroelastic stability analysis. There certainly are several points that require further research, viz., methodology validation, evaluation of three-dimensional effects, evaluation of the influence of the shroud on the flow field (steady and unsteady), a systematic study of coupling effects. Further developments should include fully nonlinear computations in the time domain. Such a methodology in two dimensions is currently being developed by Bendiksen (1990).

Acknowledgments

This work was conducted under contract with SNECMA, with Alex Ribère and Didier Nicoud as technical monitors, and is published by permission. The contribution of J. P. Mascarell and co-workers who computed the mechanical eigenmodes for the results presented herein is also acknowledged. All the computations were performed on the Cray-2 computer of CCVR, at the Ecole Polytechnique.

References

Adamczyk, J. J., and Goldstein, M. E., 1978, "Unsteady Flow in a Supersonic Cascade With Subsonic Leading-Edge-Locus," *AIAA J.*, Vol. 16, pp. 1248-1254.

Adamczyk, J. J., Stevans, W., and Jutras, R., 1982, "Supersonic Stall Flutter of High-Speed Fans," ASME *Journal of Engineering for Power*, Vol. 104, pp. 675-682.

Akai, T. J., and Atassi, H., 1980, "Aerodynamic and Aeroelastic Characteristics of Oscillating Loaded Cascades at Low Mach Number: Part 2—Stability and Flutter Boundaries," ASME *Journal of Engineering for Power*, Vol. 102, pp. 352-356.

Atassi, H., and Akai, T. J., 1980, "Aerodynamic and Aeroelastic Characteristics of Oscillating Loaded Cascades at Low Mach Number: Part1—Pressure Distribution, Forces, and Moments," ASME *Journal of Engineering for Power*, Vol. 102, pp. 344-351.

Barton, H. A., and Halliwell, D. G., 1987, "Detailed On-Blade Measurements on a Transonic Fan in Unstalled Supersonic Flutter 4," presented at *Unsteady Aerodynamics & Aeroelasticity of Turbomachines & Propellers Symposium*, Aachen, Germany.

Bendiksen, O. O., and Friedmann, P. P., 1980, "Coupled Bending-Torsion Flutter in Cascades," *AIAA J.*, Vol. 18, pp. 194-201.

Bendiksen, O. O., and Friedmann, P. P., 1981, "Coupled Bending-Torsion Flutter in a Supersonic Cascade," *AIAA J.*, Vol. 19, pp. 774-781.

Bendiksen, O. O., and Friedmann, P. P., 1982, "The Effect of Bending-Torsion Coupling of Fan and Compressor Blade Flutter," ASME *Journal of Engineering for Power*, Vol. 104, pp. 617-623.

Bendiksen, O. O., 1988, "Recent Developments in Flutter Suppression Techniques for Turbomachinery Rotors," *J. Prop. Power*, Vol. 4, pp. 164-171.

Bendiksen, O. O., 1990, "Aeroelastic Problems in Turbomachines," AIAA Paper No. 90-1157.

Bisplinghoff, R. L., and Ashley, H., 1962, *Principles of Aeroelasticity*, Dover, pp. 59-60, 186-279.

Carta, F. O., 1967, "Coupled Blade-Disc Shroud Flutter Instabilities in Turbojet Engine Rotors," ASME *Journal of Engineering for Power*, Vol. 89, pp. 419-426.

Crawley, E. F., 1988, "Aeroelastic Formulation for Tuned and Mistuned Rotors," AGARDograph, Vol. 298, pp. 19.1-19.24.

Derrien, T., 1986, "Calcul 3-D Dans les Aubages de Turbo-machines Avec Mageoire," *AGARD Conf. Proc.*, Vol. 401, pp. 14.1-14.15.

Dugundji, J., and Bundas, D. J., 1984, "Flutter and Forced Response of Mistuned Rotors Using Standing Wave Analysis," *AIAA J.*, Vol. 22, pp. 1652-1660.

Edwards, J. W., Ashley, H., and Breakwell, J. V., 1979, "Unsteady Aerodynamic Modeling for Arbitrary Motions," *AIAA J.*, Vol. 17, pp. 365-374.

Epstein, A. H., Kerrebrock, J. L., and Thompkins, W. T., Jr., 1979, "Shock Structure in Transonic Compressor Rotors," *AIAA J.*, Vol. 17, pp. 375-379.

Fleeter, S., 1979, "Aeroelasticity Research for Turbomachinery Applications," *J. Aircraft*, Vol. 16, pp. 320-326.

Gerolymos, G. A., 1988a, "Numerical Integration of Blade-to-Blade Surface Euler Equations in Vibrating Cascades," *AIAA J.*, Vol. 26, pp. 1483-1492.

Gerolymos, G. A., 1988b, "Numerical Integration of the 3-D Unsteady Euler Equations for Flutter Analysis of Axial Flow Compressors," ASME Paper No. 88-GT-255; *Int. J. Turbo Jet Eng.*, Vol. 7, 1990, pp. 131-142.

Gerolymos, G. A., 1993, "Advances in the Numerical Integration of the Three-Dimensional Euler Equations in Vibrating Cascades," ASME JOURNAL OF TURBOMACHINERY, Vol. 115, pp. 781-790.

Griffin, J. H., and Sinha, A., 1985, "The Interaction Between Mistuning and Friction in the Forced Response of Bladed Disk Assemblies," ASME JOURNAL OF TURBOMACHINERY, Vol. 107, pp. 205-211.

Halliwell, D. G., 1980, "The Effect of Intake Conditions on Supersonic Flutter in Turbofan Engines," *J. Aircraft*, Vol. 17, pp. 300-304.

Halliwell, D. G., Newton, S. G., and Lit, K. S., 1984, "A Study of Unsteady Pressures Near the Tip of a Transonic Fan in Unstalled Supersonic Flutter," ASME *Journal of Vibration, Acoustics, Stress, and Reliability in Design*, Vol. 106, pp. 198-203.

Circulaires," *J. Méc. Appl.*, Vol. 4, pp. 61-82.

Henry, R., and Ferraris, G., 1984, "Substructuring and Wave Propagation—an Efficient Technique for Impeller Dynamic Analysis," ASME *Journal of Engineering for Gas Turbines and Power*, Vol. 106, pp. 2-10.

Henry, R., and Vincent, B., 1990, "Instabilité Aéroélastique dans les Moteurs d' Avions—Application à un Etage de Soufflante SNECMA," *Rev. Franc. Méc.*, Vol. 1990.1, pp. 23-32.

Karadimas, G., 1988, "Design of High Performance Fans Using Advanced Aerodynamics Codes," ASME JOURNAL OF TURBOMACHINERY, Vol. 110, pp. 419-425.

Kaza, K. R. V., and Kielb, R. E., 1982, "Flutter and Response of a Mistuned Cascade in Incompressible Flow," *AIAA J.*, Vol. 20, pp. 1120-1127.

Kaza, K. R. V., and Kielb, R. E., 1984a, "Flutter of Turbofan Rotors With Mistuned Blades," *AIAA J.*, Vol. 22, pp. 1618-1625.

Kaza, K. R. V., and Kielb, R. E., 1984b, "Effects of Warping and Pretwist on Torsional Vibration of Rotating Beams," ASME *Journal of Applied Mechanics*, Vol. 51, pp. 913-920.

Kaza, K. R. V., and Kielb, R. E., 1985, "Vibration and Flutter of Mistuned Bladed-Disk Assemblies," *J. Prop. Power*, Vol. 1, pp. 336-344.

Kerrebrock, J. L., 1981, "Flow in Transonic Compressors," *AIAA J.*, Vol. 19, pp. 4-19.

Kielb, R. E., and Kaza, K. R. V., 1983, "Aeroelastic Characteristics of a Cascade of Mistuned Blades in Subsonic and Supersonic Flows," ASME *Journal of Vibration, Acoustics, Stress, and Reliability in Design*, Vol. 105, pp. 425-433.

Kielb, R. E., and Kaza, K.R. V., 1984, "Effects of Structural Coupling on Mistuned Cascade Flutter and Response," ASME *Journal of Engineering for Gas Turbines and Power*, Vol. 106, pp. 17-24.

Kielb, R. E., and Ramsey, J. K., 1989, "Flutter of a Fan Blade in Supersonic Axial Flow," ASME JOURNAL OF TURBOMACHINERY, Vol. 111, pp. 462-467.

Lane, F., 1956, "System Mode Shapes in the Flutter of Compressor Blade Rows," *J. Aero. Sci.*, Vol. 23, pp. 54-66.

Lane, F., 1957, "Supersonic Flow Past an Oscillating Cascade With Supersonic Leading-Edge Locus," *J. Aero. Sci.*, Vol. 24, pp. 65-66.

Lombard, Y., Kill, N., and Geradin, M., 1986, "Analyse Modale des Structures á Périodicité Cyclique," Laboratoire de Techniques Aéronautiques & Spatiales de l' Université de Liège, Belgium.

Mascarell, J. P., 1990, private communication, SNECMA Villaroche, France.

Meirovitch, L., 1975, *Elements of Vibration Analysis*, McGraw-Hill, pp. 13-21.

Mikolajczak, A. A., Arnoldi, R. A., Snyder, L. E., and Stargardter, H., 1975, "Advances in Fan and Compressor Blade Flutter Analysis and Predictions," *J. Aircraft*, Vol. 12, pp. 325-332.

Platzer, M. F., 1975, "Transonic Blade Flutter—a Survey," *Shock Vibr. Dig.*, Vol. 7, pp. 97-106.

Platzer, M. F., 1978, "Unsteady Flows in Turbomachines—a Review of Current Developments," *AGARD Conf. Proc.*, Vol. 227, pp. 33.1-33.28.

Sinha, A., and Griffin, J. H., 1983, "Friction Damping of Flutter in Gas Turbine Engine Airfoils," *J. Aircraft*, Vol. 20, pp. 372-376.

Sinha, A., and Griffin, J. H., 1985, "Effects of Friction Dampers on Aerodynamically Unstable Rotor Stages," *AIAA J.*, Vol. 23, pp. 262-270.

Sinha, A., Griffin, J. H., and Kielb, R. E., 1986, "Influence of Friction Dampers on Torsional Blade Flutter," ASME *Journal of Engineering for Gas Turbines and Power*, Vol. 108, pp. 313-318.

Sisto, F., 1977, "Review—a Review of the Fluid Mechanics of Aeroelasticity in Turbomachines," ASME *Journal of Fluids Engineering*, Vol. 99, pp. 40-44.

Smith, S. N., 1973, "Discrete Frequency Sound Generation in Axial Flow Turbomachines," *Aero. Res. Counc.*, R&M 3709.

Srinivasan, A. V., and Fabunmi, J. A., 1984, "Cascade Flutter Analysis of Cantilevered Blades," ASME *Journal of Engineering for Gas Turbines and Power*, Vol. 106, pp. 34-43.

Theodorsen, Th., 1935, "General Theory of Aerodynamic Instability and the Mechanism of Flutter," NACA Rep. 496.

Thomas, D. L., 1974, "Standing-Waves in Rotationally Periodic Structures," *J. Sound Vibr.*, Vol. 37, pp. 288-290.

Thomas, D. L., 1979, "Dynamics of Rotationally Periodic Structures," *Int. J. Num. Meth. Eng.*, Vol. 14, pp. 81-102.

White, J. F., III, and Bendiksen, O. O., 1987, "Aeroelastic Behavior of Low-Aspect-Ratio Metal and Composite Blades," ASME *Journal of Engineering for Gas Turbines and Power*, Vol. 109, pp. 168-175.

Whitehead, D. S., 1962, "Force and Moment Coefficients for Vibrating Airfoils in Cascade," *Aero. Res. Counc.*, R&M 3254.

Whitehead, D. S., 1966, "Torsional Flutter of Unstalled Cascade Blades at O Deflection," *Aero. Res. Counc.*, R&M 3429.

Whitehead, D. S., 1974, "The Effect of Compressibility on Unstalled Torsional Flutter," *Aero. Res. Counc.*, R&M 3754.

Whitehead, D. S., 1982, "The Calculation of Steady and Unsteady Transonic Flows in Cascades," Cambridge University Engineering Department, United Kingdom.

Whitehead, D. S., 1987, "Classical 2-D Methods," *AGARDograph*, No. 298, pp. 3.1-3.30.

Wilkinson, J. H., 1965, *The Algebraic Eigenvalue Problem*, Oxford University Press, United Kingdom, pp. 174-176.

Calculation of Three-Dimensional Unsteady Flows in Turbomachinery Using the Linearized Harmonic Euler Equations

K. C. Hall

C. B. Lorence

Department of Mechanical Engineering
and Materials Science,
Duke University,
Durham, NC 27708

An efficient three-dimensional Euler analysis of unsteady flows in turbomachinery is presented. The unsteady flow is modeled as the sum of a steady or mean flow field plus a harmonically varying small perturbation flow. The linearized Euler equations, which describe the small perturbation unsteady flow, are found to be linear, variable coefficient differential equations whose coefficients depend on the mean flow. A pseudo-time time-marching finite-volume Lax-Wendroff scheme is used to discretize and solve the linearized equations for the unknown perturbation flow quantities. Local time stepping and multiple-grid acceleration techniques are used to speed convergence. For unsteady flow problems involving blade motion, a harmonically deforming computational grid, which conforms to the motion of the vibrating blades, is used to eliminate large error-producing extrapolation terms that would otherwise appear in the airfoil surface boundary conditions and in the evaluation of the unsteady surface pressure. Results are presented for both linear and annular cascade geometries, and for the latter, both rotating and nonrotating blade rows.

Introduction

The ability to predict the aeroelastic phenomena of flutter and forced response is critical to the development of future generations of turbomachinery components including traditional fans, compressor and turbine stages, and unducted propfans. The aeromechanical behavior of these devices is strongly dependent on the unsteady aerodynamic behavior of the blade rows. Furthermore, the unsteady flow fields in these devices are inherently three dimensional. New blade designs are becoming more three-dimensional with large amounts of twist and sweep. However, despite tremendous improvements in unsteady aerodynamic analyses over the past three decades, the accurate and efficient prediction of the unsteady aerodynamic behavior of realistic three-dimensional turbomachinery blade rows and propellers remains largely an unsolved problem.

Numerous two-dimensional analyses have been developed for flat-plate two-dimensional cascades operating in the incompressible (Whitehead, 1960, 1962), subsonic (Smith, 1972; Whitehead, 1987), and supersonic (Verdon and McCune, 1975; Adamczyk and Goldstein, 1978) regimes. In these models, the steady flow field is assumed to be uniform. The equations that describe the small disturbance unsteady flow field are linear constant coefficient equations, which can be solved analytically. These two-dimensional models are important since they are sometimes able to predict certain types of flutter qualitatively, notably unstalled supersonic torsional flutter in fans. However, because the models do not include the effects of steady blade loading, other forms of flutter, such as bending flutter, cannot be predicted.

Recently, three-dimensional semi-analytical methods have been developed to model unsteady flows in ducted fans (Namba, 1977; Chi, 1993). Like the classical two-dimensional flat-plate methods, these models assume the airfoils carry no steady load. Namba and Toshimitsu (1987) included limited loading effects in their three-dimensional double linearization method. These analyses demonstrated that three-dimensional effects can significantly alter the behavior of the unsteady flow field.

Despite the limited success of the classical two- and three-dimensional models, they still do not provide a fully satisfactory solution to the aeromechanics problem. When the classical models are used, they must be used in conjunction with correlations based on experience to compensate for effects not included in the basic theories. This approach often works for relatively modest changes in blade design, but cannot be used with confidence for significantly new designs. Furthermore, the use of the two-dimensional methods in three dimensions usually requires the questionable assumption that they may be used in strip theory fashion.

Contributed by the International Gas Turbine Institute and presented at the 37th International Gas Turbine and Aeroengine Congress and Exposition, Cologne, Germany, June 1-4, 1992. Manuscript received by the International Gas Turbine Institute February 11, 1992. Paper No. 92-GT-136. Associate Technical Editor: L. S. Langston.

Another approach that has been used to calculate unsteady periodic flows in cascades is to discretize the nonlinear fluid dynamic equations of motion on a computational grid that spans one or more blade passages. The discretized equations are then time-accurately time marched until all initial transients have decayed and a periodic state is reached. This approach has the advantage that many of the effects not included in the analytical models can be easily incorporated into the computational fluid dynamic (CFD) algorithm (e.g., arbitrary blade geometries, complicated shock structures, and various flow models). In recent years, a number of computational methods have been used to model unsteady flows in cascades. Several investigators have demonstrated the feasibility of time-accurately time marching the Euler equations (Fourmaux and Le Meur, 1987; Whitfield et al., 1987; Giles, 1988; Huff and Reddy, 1989) and Navier-Stokes equations (Huff, 1987; Rai, 1989a, 1989b) to analyze unsteady two- and three-dimensional flows in turbomachinery. However, due to the large number of grid points and the requirement than the analyses be both time-accurate and stable, these calculations are extremely expensive with supercomputer computational times measured in hours, days, or even weeks.

An alternative to the time-accurate time-marching methods, and the method used in this paper, is the linearized approach. In the linearized approach, the flow is assumed to be composed of a nonlinear mean or steady flow plus an unsteady perturbation flow. The linearized equations that describe the unsteady perturbation are linear variable coefficient equations for the unknown complex amplitude of the harmonic motion of the flow. A number of two-dimensional linearized harmonic potential (Whitehead and Grant, 1981; Verdon and Caspar, 1984; Hall and Verdon, 1991; Hall, 1993) and linearized harmonic Euler codes (Ni and Sisto, 1976; Hall and Crawley, 1989; Hall and Clark, 1993a, 1993b; Holmes and Chuang, 1993) have been developed to analyze the flutter and forced response of turbomachinery blade rows. Work on two-dimensional linearized harmonic Euler solvers has demonstrated the large computational time savings that can be achieved using linearized techniques while still modeling the dominant physics. For example, for a typical gust response problem, the linearized Euler technique is nearly two orders of magnitude faster than a time-marching Euler code and gives very similar predictions of the unsteady flow (Hall and Crawley, 1989).

While providing some qualitative and quantitative insight into the mechanisms of flutter and forced response, all of the linearized potential and Euler solvers developed to date have been two-dimensional. In this paper, we present a fully three-dimensional linearized Euler analysis capable of predicting unsteady flows in turbomachinery due to vibratory blade motion and incoming gusts (only the blade motion problem is considered here). The three-dimensional linearized Euler equations are derived for the general case of a rotating frame of reference. To solve the linearized Euler equations, we use the pseudo-time time-marching technique suggested by Ni and Sisto (1976). One advantage of this approach is that the equations become hyperbolic in pseudo-time so that existing time-marching algorithms can be employed to solve the linearized Euler equations efficiently. In this paper, the linearized equations are solved very efficiently using a Lax–Wendroff scheme with local time stepping and multiple-grid acceleration (Ni and Bogoian, 1989).

Another important feature of the present analysis is the use of a deforming computational grid. Although deforming computational grids have been used in nonlinear time-marching analyses (Huff, 1987; Huff and Reddy, 1989; Batina, 1990), until recently, most linearized analyses have used computational grids fixed in space. For fixed-grid analyses of flutter problems, an additional term must be added to the airfoil boundary conditions to extrapolate the flow variables from the boundary of the grid to the instantaneous location of the airfoil. This extrapolation term contains the gradient of the mean flow velocity, which is difficult to compute accurately, especially around the leading and trailing edges of the blade. One way to eliminate the extrapolation terms is to use a grid that continuously deforms with the airfoil. Whitehead and Grant (1981) used a transformed perturbation potential in their linearized harmonic potential analysis. The transformation can be viewed as equivalent to using a computational grid that

Nomenclature

AR = blade aspect ratio
$d\hat{\mathbf{A}}$ = elemental area vector
$d\mathbf{A}, d\mathbf{A}'$ = mean and perturbation elemental area vectors
$D, \partial D$ = control volume and control surface
$d\hat{\mathcal{V}}$ = elemental volume
$d\mathcal{V}, d\mathcal{V}'$ = mean and perturbation elemental volume
$\hat{e}$ = internal energy
f, g, h = grid motion perturbation functions
$\mathbf{f} = (f, g, h)^T$
$\hat{\mathbf{F}}, \hat{\mathbf{G}}, \hat{\mathbf{H}}$ = flux vectors
$\mathbf{F}, \mathbf{G}, \mathbf{H}$ = mean flow flux vectors
$\mathbf{F}', \mathbf{G}', \mathbf{H}'$ = perturbation flow flux vectors
G = linear blade-to-blade gap
$\hat{I}$ = rothalpy
M = Mach number
$\hat{\mathbf{n}}$ = unit normal
$\bar{\mathbf{n}}, \mathbf{n}'$ = mean and perturbation unit normals
$\hat{p}$ = static pressure
P, p = mean flow and perturbation flow static pressures
r_H, r_T = hub and tip radii
$\hat{\mathbf{R}}$ = surface displacement vector
$\hat{\mathbf{S}}$ = source term vector
$\mathbf{S}, \mathbf{S}'$ = mean flow and perturbation flow source terms
t = time
$\hat{u}, \hat{v}, \hat{w}$ = Cartesian components of velocity
U, V, W = mean flow velocity components
u, v, w = perturbation flow velocity components
$\hat{\mathbf{U}}$ = vector of conservation variables
$\mathbf{U}, \mathbf{u}$ = mean and perturbation conservation variables
$\hat{\mathbf{V}}$ = velocity vector
$\mathbf{V}, \mathbf{v}$ = mean and perturbation velocity vectors
w_c = aerodynamic work per cycle per unit span
W_c = total aerodynamic work per cycle
x, y, z = Cartesian coordinates
x, θ, r = cylindrical coordinates
$\hat{\mathbf{x}} = (x, y, z)^T$
β = inflow angle relative to axial direction
γ = ratio of specific heats
Θ = stagger angle
Θ_G = angular blade-to-blade gap
ξ, η, ζ = computational coordinates
$\hat{\rho}$ = static density
$\bar{\rho}, \rho$ = mean flow and perturbation flow static densities
σ = interblade phase angle
τ = time in computational coordinates
$\omega, \bar{\omega}$ = dimensional and reduced frequencies
Ω = rotation rate of machine

Subscripts

a = axial direction
T = total or stagnation quantity
x, y, z = Cartesian directions
$\mathbf{u}$ = due to perturbation in conservation variables
$\mathbf{x}$ = due to grid motion
$-\infty, \infty$ = far upstream and downstream regions

undergoes rigid body motion that conforms to the motion of plunging and pitching airfoils. Recently, Hall (1993) developed a potential solver based on a linearized variational principle that includes the effects of a deformable computational grid, which conforms to both rigid body and flexible blade motions. Hall and Clark (1993a, 1993b) and Holmes and Chuang (1993) have recently applied the deforming grid technique to the two-dimensional linearized Euler technique. In this paper, we extend the deforming grid technique to three dimensions.

Results are presented in this paper that demonstrate the accuracy and efficiency of the method, and demonstrate the effects of three dimensionality on unsteady flows in turbomachinery. Results are presented for both stationary and rotating cascades. Preliminary results indicate that three-dimensional effects are very important, and that strip theory may, in some cases, seriously overpredict the aerodynamic damping of vibrating blades.

Theoretical Approach

Flow Field Description. For many flows of interest in turbomachinery aeroelasticity, viscous effects are confined to thin boundary layers near the blade and casing surfaces. Under these circumstances, the Euler equations—which represent the conservation of mass, momentum, and energy for an inviscid, adiabatic flow—are a useful model of the flow field. Consider a Cartesian coordinate system with its x axis aligned with the axis of rotation of a blade row. The y and z axes rotate about the x axis with speed Ω, the rotational speed of the blade row. The nonlinear Euler equations in the rotating frame of reference are given by

$$\frac{\partial \hat{\mathbf{U}}}{\partial t}+\frac{\partial \hat{\mathbf{F}}}{\partial x}+\frac{\partial \hat{\mathbf{G}}}{\partial y}+\frac{\partial \hat{\mathbf{H}}}{\partial z}-\hat{\mathbf{S}}=0 \tag{1}$$

where $\hat{\mathbf{U}}$ is the vector of conservation variables, $\hat{\mathbf{F}}$, $\hat{\mathbf{G}}$, and $\hat{\mathbf{H}}$ are the so-called flux vectors, and $\hat{\mathbf{S}}$ is a vector of source terms. These vector quantities are given by

$$\hat{\mathbf{U}}=\begin{bmatrix}\hat{\rho}\\ \hat{\rho}\hat{u}\\ \hat{\rho}\hat{v}\\ \hat{\rho}\hat{w}\\ \hat{e}\end{bmatrix},\quad \hat{\mathbf{F}}=\begin{bmatrix}\hat{\rho}\hat{u}\\ \hat{\rho}\hat{u}^2+\hat{p}\\ \hat{\rho}\hat{u}\hat{v}\\ \hat{\rho}\hat{u}\hat{w}\\ \hat{\rho}\hat{u}\hat{I}\end{bmatrix},\quad \hat{\mathbf{G}}=\begin{bmatrix}\hat{\rho}\hat{v}\\ \hat{\rho}\hat{u}\hat{v}\\ \hat{\rho}\hat{v}^2+\hat{p}\\ \hat{\rho}\hat{v}\hat{w}\\ \hat{\rho}\hat{v}\hat{I}\end{bmatrix},$$

$$\hat{\mathbf{H}}=\begin{bmatrix}\hat{\rho}\hat{w}\\ \hat{\rho}\hat{u}\hat{w}\\ \hat{\rho}\hat{v}\hat{w}\\ \hat{\rho}\hat{w}^2+\hat{p}\\ \hat{\rho}\hat{w}\hat{I}\end{bmatrix},\quad \hat{\mathbf{S}}=\begin{bmatrix}0\\ 0\\ \hat{\rho}(\Omega^2 y+2\Omega\hat{w})\\ \hat{\rho}(\Omega^2 z-2\Omega\hat{v})\\ 0\end{bmatrix}$$

where $\hat{\rho}$ is the density, $\hat{p}$ is the pressure, $\hat{u}$, $\hat{v}$, and $\hat{w}$ are the x, y, and z components of velocity, $\hat{e}$ is the internal energy, and $\hat{I}$ is the rothalpy. The source terms that appear in the y and z momentum equations represent centrifugal and Coriolis forces. In this form, the effects of rotation appear explicitly in only the source terms. However, the pressure, $\hat{p}$, and the rothalpy, $\hat{I}$, are also functions of the rotation rate, i.e.,

$$\hat{p}=(\gamma-1)\left[\hat{e}-\frac{1}{2}\hat{\rho}(\hat{u}^2+\hat{v}^2+\hat{w}^2)+\frac{1}{2}\hat{\rho}\Omega^2 r^2\right] \tag{2}$$

and

$$\hat{I}=\frac{\hat{e}+\hat{p}}{\hat{\rho}}=\frac{\gamma}{\gamma-1}\frac{\hat{p}}{\hat{\rho}}+\frac{1}{2}(\hat{u}^2+\hat{v}^2+\hat{w}^2)-\frac{1}{2}\Omega^2 r^2 \tag{3}$$

Here r is the distance from the x axis ($r=\sqrt{y^2+z^2}$). Note that the flux vectors and source terms depend not only on the conservation variables and the rotation rate, but also on the *position* of the fluid particle, that is, $\hat{\mathbf{F}}=\hat{\mathbf{F}}(\hat{\mathbf{U}}, \hat{\mathbf{x}})$ where $\hat{\mathbf{x}}=(x, y, z)^T$.

For finite-volume calculations, the integral form of the Euler equations is more convenient. Integrating the nonlinear Euler equations [Eq. (1)] over a deforming control volume, D, bounded by the control surface, ∂D, gives after some manipulation

$$\frac{\partial}{\partial t}\iiint_D \hat{\mathbf{U}}\,d\hat{\mathcal{V}}+\iint_{\partial D}\left[\left(\hat{\mathbf{F}}-\hat{\mathbf{U}}\frac{\partial f}{\partial t}\right)d\hat{A}_x+\left(\hat{\mathbf{G}}-\hat{\mathbf{U}}\frac{\partial g}{\partial t}\right)d\hat{A}_y+\left(\hat{\mathbf{H}}-\hat{\mathbf{U}}\frac{\partial h}{\partial t}\right)d\hat{A}_z\right]-\iiint_D \hat{\mathbf{S}}\,d\hat{\mathcal{V}}=0 \tag{4}$$

Here f, g, and h are the x, y, and z displacements in the position of the control surface; and $d\hat{A}_x$, $d\hat{A}_y$, and $d\hat{A}_z$ are the scalar components of the elemental surface vector $d\hat{\mathbf{A}}$; and $d\hat{\mathcal{V}}$ is the elemental volume of the control volume.

The conventional method used to solve the unsteady nonlinear Euler equations for the case of a temporally periodic disturbance is to discretize the equations using finite-volume operators, and to time-accurately time march the discretized equations until any initial solution transients have disappeared leaving behind the desired periodic solution. Because of the requirement that the unsteady solution be both time-accurate and stable, however, the computational time required to solve the three-dimensional Euler equations using this approach is prohibitively large for design applications.

Fortunately, for many unsteady flows of interest in turbomachinery aeroelasticity applications, the unsteadiness in the flow is small compared to the mean flow and the source of the unsteadiness is harmonic or periodic. Hence, we will shortly make the assumption that the conservation variables may be represented as the sum of a mean flow plus a harmonic small perturbation unsteady flow.

In the present analysis, the computational grid conforms to the motion of the airfoils (for the flutter problem). Hence, the grid is assumed to undergo small harmonic deformation about its steady position, i.e.,

$$x(\xi, \eta, \zeta, \tau)=\xi+f(\xi, \eta, \zeta)e^{j\omega\tau} \tag{5}$$

$$y(\xi, \eta, \zeta, \tau)=\eta+g(\xi, \eta, \zeta)e^{j\omega\tau} \tag{6}$$

$$z(\xi, \eta, \zeta, \tau)=\zeta+h(\xi, \eta, \zeta)e^{j\omega\tau} \tag{7}$$

$$t(\xi, \eta, \zeta, \tau)=\tau \tag{8}$$

where f, g, and h are the first-order amplitudes of grid motion about the mean positions, ξ, η, and ζ.

Having defined the motion of the computational coordinate system, the unsteady flow field is now represented by the first-order perturbation series

$$\hat{\mathbf{U}}(\xi, \eta, \zeta, \tau)=\mathbf{U}(\xi, \eta, \zeta)+\mathbf{u}(\xi, \eta, \zeta)e^{j\omega\tau} \tag{9}$$

where $\mathbf{U}$ is the vector of mean or steady flow conservation variables, $\mathbf{u}$ is the vector of first-order perturbations in the conservation variables, and ω is the frequency of excitation. The mean flow and perturbation flow variables may be thought of as "attached" to the harmonically deforming computational grid. Therefore, an observer in the fixed coordinate system (x, y, z) sees unsteadiness in the flow due to both the unsteady perturbation in the conservation variables, $\mathbf{u}$, and the deformation of the mean flow field, $\mathbf{U}$.

Substitution of the perturbation assumptions [Eqs. (5)–(9)] into the expression for the flux vector $\hat{\mathbf{F}}$ results in the first-order perturbation series

$$\hat{\mathbf{F}}=\mathbf{F}+(\mathbf{F}_{\mathrm{u}}'+\mathbf{F}_{\mathrm{x}}')e^{j\omega\tau} \tag{10}$$

where $\mathbf{F}$ is the mean flow flux vector, $\mathbf{F}_{\mathrm{u}}'$ is the first-order perturbation in the flux vector due to the first-order perturbation in the conservation variables, $\mathbf{u}$, and $\mathbf{F}_{\mathrm{x}}'$ is the perturbation in the flux vector due to the grid motion, **f**. These perturbation fluxes are given by

$$\mathbf{F}_{\mathbf{u}}' = \frac{\partial \mathbf{F}}{\partial \mathbf{U}}\,\mathbf{u} \tag{11}$$

and

$$\mathbf{F}_{\mathbf{x}}' = \frac{\partial \mathbf{F}}{\partial \mathbf{x}}\,\mathbf{f} \tag{12}$$

where

$$\frac{\partial \mathbf{F}}{\partial \mathbf{U}} = \begin{bmatrix} 0 & 1 & 0 & 0 & 0 \\ -U^2 + \frac{\gamma-1}{2} V_T^2 & -(\gamma-3)U & (1-\gamma)V & (1-\gamma)W & \gamma-1 \\ -UV & V & U & 0 & 0 \\ -UW & W & 0 & U & 0 \\ -U\left(I - \frac{\gamma-1}{2} V_T^2\right) & I-(\gamma-1)U^2 & (1-\gamma)UV & (1-\gamma)UW & \gamma U \end{bmatrix}$$

and

$$\frac{\partial \mathbf{F}}{\partial \mathbf{x}} = \begin{bmatrix} 0 & 0 & 0 \\ 0 & (\gamma-1)\bar{\rho}\Omega^2\eta & (\gamma-1)\bar{\rho}\Omega^2\zeta \\ 0 & 0 & 0 \\ 0 & 0 & 0 \\ 0 & (\gamma-1)\bar{\rho}U\Omega^2\eta & (\gamma-1)\bar{\rho}U\Omega^2\zeta \end{bmatrix}$$

Here U, V, and W are the mean flow velocity components, V_T is the mean flow velocity magnitude, and I and $\bar{\rho}$ are the mean flow rothalpy and density, respectively. Note that the perturbation flux term $\mathbf{F}_{\mathbf{x}}'$ is zero for the case of a nonrotating frame of reference since the entries in the $\partial\mathbf{F}/\partial\mathbf{x}$ matrix are proportional to the rotation rate squared. Similar perturbation series exist for the remaining flux vectors, $\hat{\mathbf{G}}$ and $\hat{\mathbf{H}}$, and the vector of source terms, $\hat{\mathbf{S}}$.

Substitution of the perturbation series for the conservation variables, grid motion, flux vectors, and source terms into the integral form of the nonlinear Euler equations and collection of zeroth- and first-order terms gives the mean flow and linearized unsteady Euler equations, respectively. The mean flow Euler equations are given by

$$\iint_{\partial D} (\mathbf{F}, \mathbf{G}, \mathbf{H}) \cdot d\mathbf{A} - \iiint_D \mathbf{S}\, d\mathcal{V} = 0 \tag{13}$$

where $d\mathbf{A}$ and $d\mathcal{V}$ are the elemental area vector and elemental volume of the undeformed (mean) control volume. Similarly, the integral form of the linearized Euler equations is

$$\begin{aligned} j\omega \iiint_D \mathbf{u}\, d\mathcal{V} &+ \iint_{\partial D} \left(\frac{\partial \mathbf{F}}{\partial \mathbf{U}}\,\mathbf{u}, \frac{\partial \mathbf{G}}{\partial \mathbf{U}}\,\mathbf{u}, \frac{\partial \mathbf{H}}{\partial \mathbf{U}}\,\mathbf{u} \right) \cdot d\mathbf{A} \\ - \iiint_D \frac{\partial \mathbf{S}}{\partial \mathbf{U}}\,\mathbf{u}\, d\mathcal{V} &= -j\omega \iiint_D \mathbf{U}\, d\mathcal{V}' - \iint_{\partial D} (\mathbf{F}, \mathbf{G}, \mathbf{H}) \cdot d\mathbf{A}' \\ &- \iint_{\partial D} (\mathbf{F}_{\mathbf{x}}', \mathbf{G}_{\mathbf{x}}', \mathbf{H}_{\mathbf{x}}') \cdot d\mathbf{A} + j\omega \iint_{\partial D} \mathbf{U}\mathbf{f} \cdot d\mathbf{A} \\ &+ \iiint_D \mathbf{S}\, d\mathcal{V}' + \iiint_D \mathbf{S}_{\mathbf{x}}'\, d\mathcal{V} \end{aligned} \tag{14}$$

where $d\mathbf{A}'$ and $d\mathcal{V}'$ are the first-order perturbations in the elemental area vector and elemental volume of the deforming control volume. Here we have grouped homogeneous terms in the unknown perturbation **u** on the left-hand side and inhomogeneous terms on the right-hand side. The terms on the right-hand side of Eq. (14) arise from the motion of the grid and are identically zero for the case of a fixed grid. Note that the linearized harmonic Euler equations are time invariant; time does not appear explicitly since the equations have been cast in the frequency domain.

Near-Field Boundary Conditions. Having developed the governing equations of the unsteady perturbation flow, we next consider the near-field boundary conditions. Because the linearized Euler equations are linear, modes of blade motion or gusts may be superposed. Hence, without loss of generality, we assume the unsteady flow to have a fixed interblade phase angle, σ, from blade to blade. The flow field may then be solved in a single blade passage by applying complex periodicity conditions along the upstream and downstream periodic boundaries. For linear cascades that extend in the y direction, the complex periodicity condition takes the form

$$\mathbf{u}(x, y+G, z) = \mathbf{u}(x, y, z)e^{j\sigma} \tag{15}$$

where G is the blade-to-blade gap. For annular cascades, the periodicity condition is expressed as

$$\mathbf{u}(x, \theta+\Theta_G, r) = \mathbf{T}\mathbf{u}(x, \theta, r)e^{j\sigma} \tag{16}$$

where Θ_G is the angular distance between adjacent blades, and **T** is a matrix that rotates the velocity vector in the y, z plane through the angle Θ_G.

On the airfoil surfaces, we must ensure that no mass flows through the surface. The nonlinear solid wall boundary condition is given by

$$\hat{\mathbf{V}} \cdot \hat{\mathbf{n}} - \frac{\partial \hat{\mathbf{R}}}{\partial t} \cdot \hat{\mathbf{n}} = 0 \tag{17}$$

where $\hat{\mathbf{R}}$ is the position vector that describes the position of the airfoil surface, and $\hat{\mathbf{n}}$ is the surface unit normal. Expanding Eq. (17) in a perturbation series and collecting terms of first-order gives the linearized flow tangency condition

$$\mathbf{v} \cdot \bar{\mathbf{n}} = -\mathbf{V} \cdot \mathbf{n}' + j\omega \mathbf{r} \cdot \bar{\mathbf{n}} \tag{18}$$

where **V** and **v** are the mean flow and perturbation flow velocities, respectively, $\bar{\mathbf{n}}$ and $\mathbf{n}'$ are the mean and perturbation unit normals, and **r** is the perturbation in the position of the airfoil surface. Since the grid motion conforms to the motion of the airfoil, the perturbation in the blade position may be expressed as $\mathbf{r} = \mathbf{f}$. The first term on the right-hand side of Eq. (18) is the upwash due to blade rotation. The second term is the upwash due to the translational velocity of the blade. Note that because a deforming grid is used, the usual velocity extrapolation term found in fixed grid analyses does not appear. Also, Eq. (18) applies to all solid surfaces, not just airfoils. Hence, if the grid motion is such that the grid slides across curved surfaces, such as the hub or tip casing, then there will be an upwash required on these surfaces as well, even though the casing surfaces do not vibrate.

Numerical Solution Method

The general solution procedure is as follows. First, a three-dimensional H-grid is generated in a single blade passage of the cascade. The mean flow field is computed using a conventional steady Euler solver. Then, for each interblade phase angle, vibratory mode shape, and reduced frequency of interest, the grid motion is prescribed. The mean flow field and prescribed grid motion are then used to form the variable coefficients and the inhomogeneous part of the linearized Euler equations. Finally, the linearized Euler equations are discretized and solved on the steady computational grid.

Grid Generation. The computational grids used in this investigation are body-fitted *H*-grids. Although *C* and *O*-type grids are commonly used in steady flow calculations, these grids lack the resolution in the far-field to resolve acoustic, vortical, and entropic waves adequately. *H*-grids, on the other hand, provide good resolution throughout the computational domain.

The mean flow (steady) computational grid is generated using a combination of algebraic and elliptic grid generation techniques. The grid points on the airfoil surface are generated algebraically. The grid points on the upstream and downstream periodic boundaries and on the far-field boundaries are generated using transfinite interpolation. Finally, the grid points on the hub and tip casings and in the interior are generated using an elliptic grid generation technique based on the work of Thompson et al. (1974).

For unsteady flow problems involving blade motion, the grid motion $\mathbf{f}$ must also be specified, subject to a number of constraints. The motion of the grid must conform to the motion of the airfoils, and the motion of the grid at the periodic boundaries must satisfy complex periodicity. The grid may slide along the casing surfaces, but must have no component of motion normal to the casing. Finally, to simplify the application of the far-field boundary conditions, the motion of the grid in the far-field of the computational domain should go to zero. In the interior, the motion of the grid may be somewhat arbitrary, although for computational accuracy, a smooth distribution of grid motion is preferred. For this reason, Laplace's equation is used to describe the motion of the interior of the grid, i.e.,

$$\nabla^2 \mathbf{f} = 0 \tag{19}$$

A finite element scheme is used to discretize Laplace's equation on the steady computational grid, and the resulting system of linear equations is solved using successive line over-relaxation (SLOR). Note that since the grid motion is harmonic, the motion need only be calculated once prior to the solution of the linearized Euler equations.

Pseudo-Time Time Marching. Having defined the computational grid, solved for the mean flow field, and computed the unsteady grid motion, we next consider the integration of the linearized Euler equations. Note that because the linearized Euler equations [Eq. (14)] are solved in the frequency domain for a single frequency, ω, time derivatives are replaced by the operator $j\omega$. Furthermore, the unsteady perturbation $\mathbf{u}$ is time invariant. Hall and Crawley (1989) discretized the two-dimensional linearized Euler equations using a finite volume operator and solved the resulting large sparse linear system very efficiently using Gaussian elimination. In three dimensions, this approach would lead to a system of equations with an extremely large bandwidth, and hence, would be too expensive to solve using a direct method. Instead, we solve the three-dimensional linearized Euler equations using the pseudo-time technique originally proposed by Ni and Sisto (1976). Using this method, the perturbation conservation variables, $\mathbf{u}$, are assumed to be functions of both space and time so that Eq. (9) becomes

$$\hat{\mathbf{U}}(\xi, \eta, \zeta, \tau) = \mathbf{U}(\xi, \eta, \zeta) + \mathbf{u}(\xi, \eta, \zeta, \tau) e^{j\omega\tau} \tag{20}$$

Substitution of Eq. (20) into the nonlinear Euler equations and collection of first-order perturbation terms leads to the pseudo-time-dependent linearized Euler equations

$$\frac{\partial}{\partial \tau} \iiint_D \mathbf{u}\, d\mathcal{V} + j\omega \iiint_D \mathbf{u}\, d\mathcal{V} + \iint_{\partial D} \left(\frac{\partial \mathbf{F}}{\partial \mathbf{U}} \mathbf{u}, \frac{\partial \mathbf{G}}{\partial \mathbf{U}} \mathbf{u}, \frac{\partial \mathbf{H}}{\partial \mathbf{U}} \mathbf{u} \right) \cdot d\mathbf{A} - \iiint_D \frac{\partial \mathbf{S}}{\partial \mathbf{U}} \mathbf{u}\, d\mathcal{V} = \mathbf{b} \tag{21}$$

where $\mathbf{b}$ is the right-hand side of Eq. (14). Note that Eq. (21) is now hyperbolic in time. Furthermore, as time advances, $\mathbf{u}$ reaches a steady-state value so that the first term of Eq. (21) goes to zero and the solution to Eq. (14) is recovered. The advantage of this approach is that any of a number of well-developed time-marching algorithms can be used to solve the linearized Euler equations. Furthermore, since only the steady-state solution is desired, local time stepping and multiple-grid acceleration techniques can be used to speed convergence. The result is that the linearized Euler equations can be solved in a fraction of the time required to solve the unsteady flow problem by time-accurately time marching the nonlinear Euler equations.

We use a three-dimensional Lax–Wendroff scheme (Ni and Bogoian, 1989) to discretize and solve both the steady Euler and linearized unsteady Euler equations. The scheme is a second-order accurate, node-centered scheme that uses both local time stepping and multiple-grid acceleration. A combination of second and fourth difference smoothing is used to eliminate sawtooth modes and capture shocks. (For the subsonic cases reported in this paper, only fourth difference smoothing was used.)

Nonreflecting Far-Field Boundary Conditions. In the present unsteady linearized analysis, we assume that the blade row is isolated in an infinitely long annular duct. The computational domain is, by necessity, finite in extent. At the far-field computational boundaries, nonreflecting boundary conditions are required to prevent spurious reflections of outgoing pressure, entropy, and vorticity waves back into the computational domain. For two-dimensional problems, the behavior of the linearized equations can be described analytically (e.g., Verdon et al., 1975; Hall and Crawley, 1989; Giles, 1990) and then matched to the numerical solution at the far-field. For three-dimensional flow fields, however, the wave propagation behavior is known analytically for only a few special cases; no general analytical expression has been derived for the three-dimensional problem.

In this investigation, we follow the approach of Saxer and Giles (1990) and apply approximate nonreflecting boundary conditions at the far-field. We in effect unroll each radial station on the far-field computational boundary and treat is as if it were two dimensional. Furthermore, the source terms arising from rotation are neglected. We then apply the "exact" nonreflecting boundary conditions originally developed for two-dimensional linearized Euler solvers. After each iteration, the solution at each radial station is transformed into a sum of Fourier modes. (Fourier modes are the eigenmodes of two-dimensional wave propagation.) Each Fourier mode is further decomposed into characteristics representing two acoustic waves, two vorticity waves, and an entropy wave. At this point, those characteristics that correspond to waves entering from outside the computational domain are set to zero. The remaining modes are then inverse Fourier transformed to obtain the desired solution at the far-field boundary. In two dimensions, this process produces exact nonreflecting boundary conditions to within truncation error. In three dimensions, however, some reflections will occur, especially if there are significant radial variations in the solution.

Results

In this section, a number of test cases are presented to examine the accuracy of the linearized Euler analysis and to

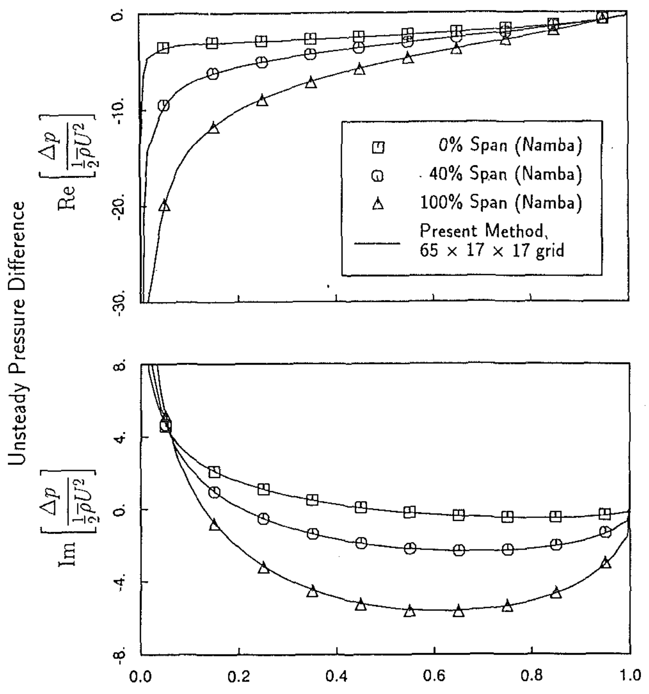

Fig. 1 Unsteady pressure distribution on surface of reference airfoil of linear flat-plate cascade with airfoils pitching about leading edge. Pitching distribution is linear from hub to tip. Θ = 45 deg, *AR* = 3.0, M = 0.7, $\bar{\omega}$ = 1.0, σ = 180 deg.

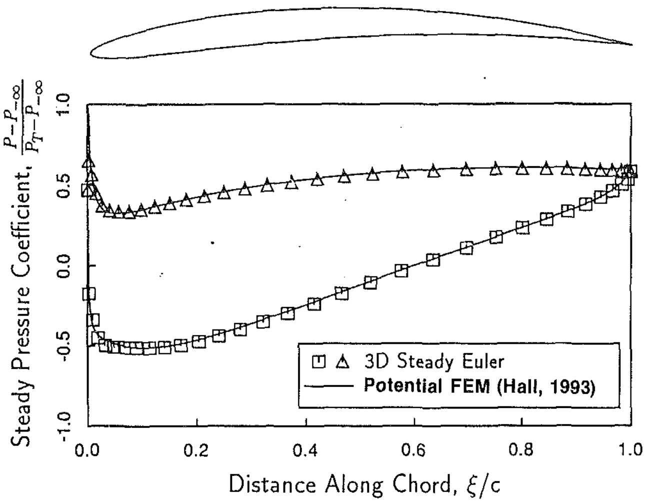

Fig. 2 Mean pressure distribution on surface of airfoils at Standard Configuration No. 10 cascade: *G* = 1.0, Θ = 45 deg, *AR* = 2.0, $\beta_{-\infty}$ = 55 deg, $M_{-\infty}$ = 0.7

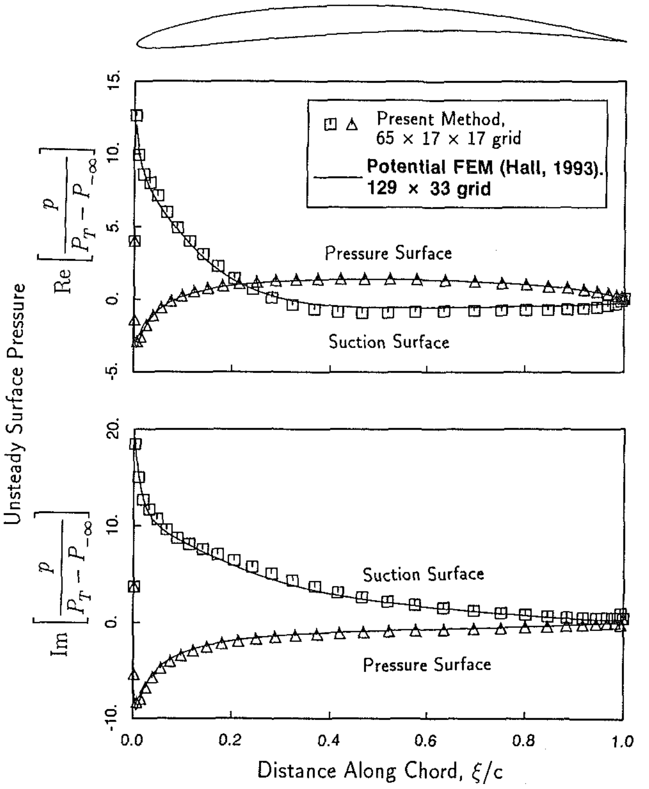

Fig. 3 Unsteady pressure distribution on reference airfoil of Standard Configuration No. 10 cascade with airfoils undergoing plunging motion. Plunging motion is uniform from hub to tip. $\bar{\omega}$ = 1.0, σ = 180 deg

demonstrate the effects of three dimensionality on unsteady flows. Unsteady flows due to blade motion (the aerodynamic damping problem) in both linear and annular cascade geometries are presented. The aerodynamic damping is important for both the flutter and forced response problems. Unless otherwise indicated, the results were computed on 65 × 17 × 17 node computational grids using three levels of multiple-grid acceleration.

Linear Flat-Plate Cascade. To test the accuracy of the present method, we first consider the case of a linear cascade of flat-plate airfoils vibrating in torsion. The stagger angle of the airfoils, Θ, is 45 deg, the aspect ratio, *AR*, is 3.0, and the gap-to-chord ratio, *G*, is 1.0. The airfoils are aligned with the mean flow. Hence, the mean flow through the cascade is uniform. For the case considered here, the mean flow Mach number, M, is 0.7. The airfoils vibrate in torsion about their leading edge with a reduced frequency, $\bar{\omega}$, of 1.0, based on chord and upstream velocity, and an interblade phase angle, σ, of 180 deg. The distribution of pitching amplitude is linear from hub to tip. Figure 1 shows the computed unsteady pressure difference across the airfoil surface. Also shown are the results of the semi-analytical three-dimensional method developed by Namba (1987). Note the extremely good agreement between the linearized Euler results and Namba's method, even near the leading edge where there is a square root singularity in the solution. These results demonstrate the ability of the linearized Euler analysis to model accurately unsteady flows due to three-dimensional vibratory mode shapes, at least for the case of lightly loaded cascades.

Subsonic Linear Compressor. To verify that the present three-dimensional linearized Euler analysis works properly in the limit of two-dimensional cascades with steady loading, we consider a linear cascade of compressor blades. The cascade considered here is the newly designated Standard Configuration No. 10, one in a series of standard turbomachinery aeroelastic test cases for validating unsteady aerodynamic theories (Bölcs and Fransson, 1986; Fransson, 1991). The airfoils of this cascade have a circular arc camber distribution with a maximum height of 5 percent of the chord. The thickness distribution is that of a NACA 0006 airfoil slightly modified so that the trailing edge is wedged. The gap-to-chord ratio, *G*, is 1.0, and the stagger, Θ, is 45 deg. For the present three-dimensional analysis, we selected an aspect ratio, *AR*, of 2.0. The steady inflow Mach number, $M_{-\infty}$, is 0.7, and the inflow angle, $\beta_{-\infty}$, measured from the axial direction is 55 deg. Figure 2 shows the computed steady pressure on the blade surface. Also shown for comparison is the pressure computed using a two-dimensional full potential method (Hall, 1993) on a 129 × 33 node computational grid. The two solutions are seen to agree very well. The maximum Mach number on the suction surface of the airfoil is about 0.92.

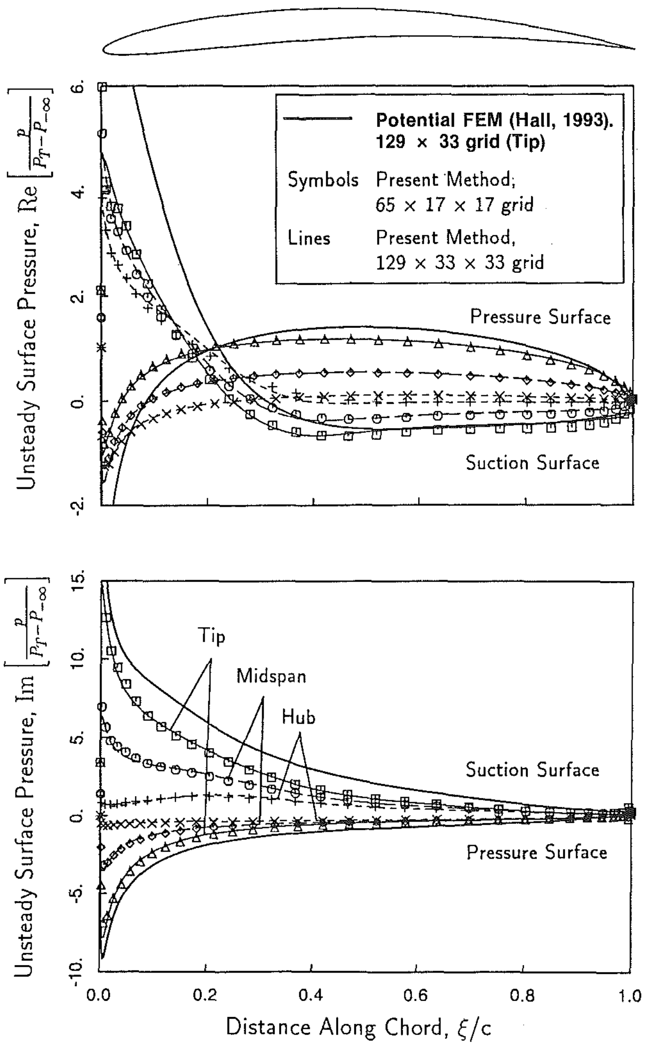

Fig. 4 Unsteady pressure distribution on surface of reference airfoil of Standard Configuration No. 10 cascade with airfoils vibrating in first bending mode: $\bar{\omega}$ = 1.0, σ = 180 deg

Having computed the mean flow solution, we now consider the case of the cascade of airfoils vibrating in plunge normal to the chord line with a reduced frequency, $\bar{\omega}$, of 1.0, and an interblade phase angle, σ, of 180 deg. For the first case considered, the motion is two dimensional, that is, the motion is uniform from hub to tip. Shown in Fig. 3 are the real and imaginary parts of the computed unsteady pressure distribution on the surface of the reference airfoil. Also shown is the unsteady pressure distribution computed using the two-dimensional linearized potential method due to Hall (1993). Note the good agreement between the two theories indicating that the present analysis produces the proper results, at least in the limit of two-dimensional flow. Also note that the solution is well behaved in the vicinity of the leading and trailing edges despite the use of a fairly coarse grid. This well-behaved solution results from using a deforming computational grid. Such high-quality solutions would be difficult to obtain on a coarse fixed grid.

Next, we consider the same linear compressor cascade, but now prescribe the blade motion to be three dimensional. The blades vibrate with the first-bending mode shape of a cantilevered beam. The mode shape is normalized such that the displacement at the tip is unity. Again, the reduced frequency, $\bar{\omega}$, is 1.0 and the interblade phase angle, σ, is 180 deg. Shown in Fig. 4 are the real and imaginary parts of the unsteady pressure distribution at three spanwise stations. These results were computed using two different computational grids of differing resolution to assess the accuracy of the solution. The solution computed on the 65 × 17 × 17 node grid is seen to be nearly identical to that computed on the 129 × 33 × 33 node grid. For low reduced frequencies, the accuracy of the solution is dominated by the accuracy of the solution around the leading and trailing edges. On a length scale comparable to the radius of the leading edge, the flow around the leading edge appears quasi-steady. Hence, if a deforming grid is used, the accuracy of the unsteady solution will be on a par with the accuracy of the steady flow solution, at least for low to moderate reduced frequencies. If a fixed grid were used, extrapolation terms in the airfoil boundary conditions would reduce the accuracy of the solution. At higher reduced frequencies, the resolution of the grid must be sufficient throughout the computational domain to resolve short wavelength disturbances.

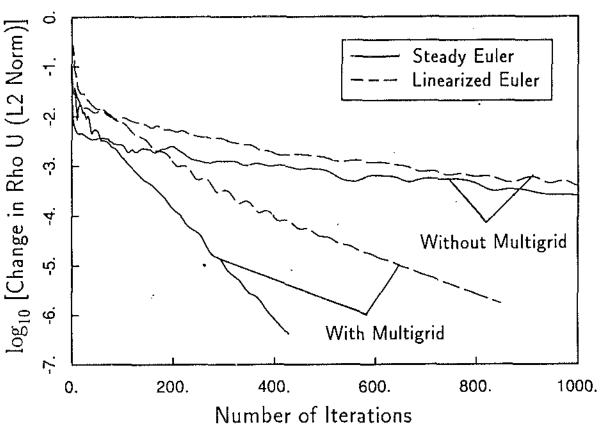

Fig. 5 Convergence histories for steady and unsteady solutions shown in Figs. 2 and 4

Also shown for comparison in Fig. 4 is the unsteady pressure distribution computed using Hall's two-dimensional linearized potential analysis at the tip section. Note that the response at the blade tip is larger than the response at the hub as would be expected from a strip theory analysis. However, the spanwise gradient in the pressure distribution is somewhat smaller than would be predicted by strip theory. Namba (1987) shows that this reduction in the spanwise gradient is due to the trailing streamwise vorticity. Also, comparing these results to Hall's, the shape of the imaginary part of the pressure distribution—that is, the part in phase with the upwash—is fairly well predicted by strip theory. The shape of the real part of the pressure distribution—the part out of phase with the upwash—is somewhat different than that predicted by strip theory.

Figure 5 shows convergence histories for the previous case computed on the 65 × 17 × 17 node computational grid. Without multiple-grid acceleration, but with local time stepping, the steady and unsteady solutions converge at approximately the same rate. With multiple-grid acceleration, both the steady and unsteady convergence rates are dramatically improved, although the unsteady solution converges at about half the rate of the steady solution. Although it is not yet clear why this difference occurs, the computational savings are still quite substantial. Using three levels of multiple-grid acceleration, the steady solution required about 44 minutes of CPU time to converge on a Stardent 3000 workstation while the unsteady solution required about 294 minutes. It should be pointed out that these codes are neither vectorized nor optimized. Nevertheless, these computer times are considerably shorter than would be required to time-accurately time march the nonlinear Euler equations. The large computational savings stem from the fact that only the steady-state solution to the linearized harmonic Euler equations is desired, and hence, both local time stepping and multiple-grid acceleration techniques may be used.

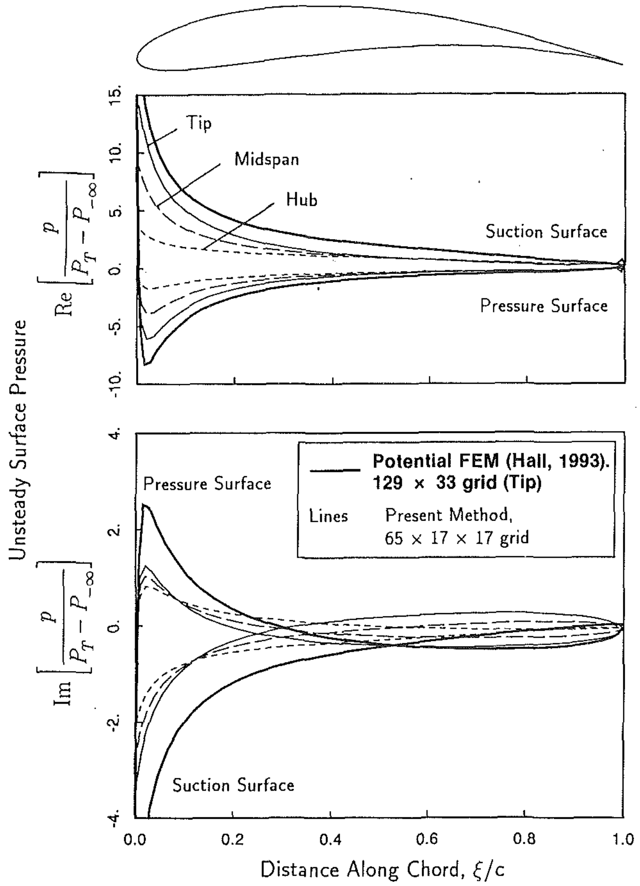

Fig. 6 Unsteady pressure distribution on surface of reference airfoil of Gostelow cascade with airfoils pitching about midchord. Pitching distribution is linear from hub to tip. $\bar{\omega}$ = 0.4, σ = 180 deg.

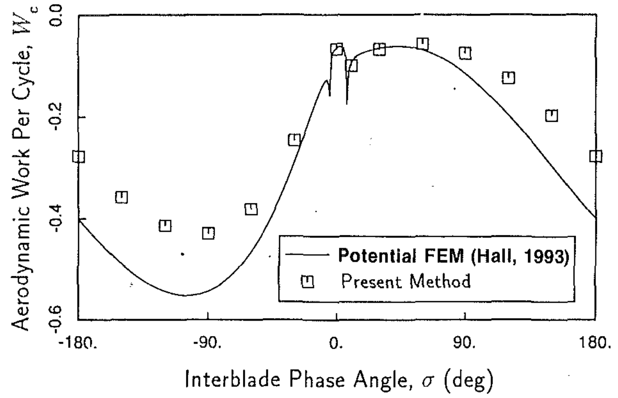

Fig. 7 Total aerodynamic work per cycle on reference airfoil of Gostelow cascade with airfoils pitching about midchord. Pitching distribution is linear from hub to tip. $\bar{\omega}$ = 0.4.

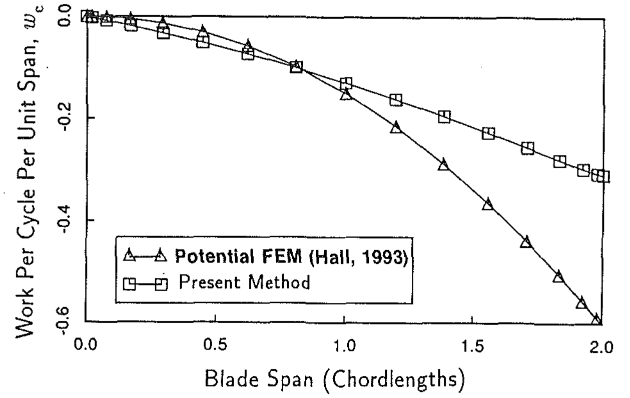

Fig. 8 Aerodynamic work per cycle per unit span on reference airfoil of Gostelow cascade with airfoils pitching about midchord. Pitching distribution is linear from hub to tip. $\bar{\omega}$ = 0.4, σ = 180 deg.

Low-Speed Linear Compressor. The next cascade considered is a linear cascade of Joukowski-like airfoils (Gostelow, 1984) operating in the low subsonic regime. The gap-to-chord ratio, G, is 0.990, the stagger angle, Θ, is 37.5 deg, and the aspect ratio, AR, is 2. For this example, the inflow angle, $\beta_{-\infty}$, is 53.5 deg, and the inflow Mach number, $M_{-\infty}$, is 0.25. The airfoils vibrate in pitch about their midchords with a linear distribution in amplitude from hub to tip. The reduced frequency, $\bar{\omega}$, is 0.4 and the interblade phase angle, σ, is 180 deg. Figure 6 shows the computed unsteady pressure distribution at three radial stations on the airfoil. Also shown for comparison is the unsteady pressure distribution computed using Hall's two-dimensional linearized potential analysis at the tip section. The shape of the real part of the unsteady pressure distribution agrees quite well with the strip theory results. The magnitude of the response increases from hub to tip as one would expect, although the pressure is nonzero at the hub and the magnitude at the tip is somewhat smaller than predicted by strip theory. The imaginary pressure distribution, on the other hand, is not well predicted by strip theory. The amplitudes of the response are approximately equal at the three radial stations. Furthermore, the shape of the distribution is somewhat different from the strip theory results.

Figure 7 shows the unsteady aerodynamic work done per cycle on the airfoil for a range of interblade phase angles (negative work per cycle corresponds to positive aerodynamic damping). The shape is nearly sinusoidal indicating that the airfoil is primarily influenced by its own motion and that of its two neighbors. Figure 7 also shows the work per cycle obtained using a linearized potential method applied in strip theory fashion. Note that the strip theory solution has a shape similar to the linearized Euler results, but the magnitude of the work is significantly overpredicted, especially for large negative interblade phase angles typical of those encountered in forced response problems.

Figure 8 shows the distribution of aerodynamic work along the span of the blade for the case where the airfoils vibrate in pitch with a reduced frequency, $\bar{\omega}$, of 0.4 and an interblade phase angle, σ, of -180 deg. Note that strip theory significantly overpredicts the work done near the tip of the airfoil. This is not surprising since the imaginary part of the pressure distribution at the tip of the airfoil is overpredicted by strip theory.

High-Speed Experimental Turbine. In this section, we compare our computational results to the experimental data for the Fourth Standard Configuration, a high-speed turbine studied by Bölcs and Fransson (1986). Although the geometry is that of a turbine, the annular blade row did not rotate in their experiment. Instead, inlet guide vanes induced swirl in the flow to produce the proper inflow angle. The stagger angle, Θ, is 56.6 deg, the hub to tip ratio, r_H/r_T, is 0.8, the number of blades, N, is 20, and the aspect ratio, AR, is 0.538. The blades have a uniform shape from hub to tip. Bölcs and Fransson measured both mean and unsteady surface pressures while the turbine blades vibrated in a plunging motion with a fixed interblade phase angle. For the case considered here (Fourth Standard Configuration, Case 2), the reported inflow angle, $\beta_{-\infty}$, at the midspan is 45 deg and the inflow Mach number, $M_{-\infty}$, is 0.26. The exit flow angle, β_{∞}, is 72 deg and the exit Mach number, M_{∞}, is 0.76. A number of investigators have found that the mean flow computational results match the experimental mean pressure distribution better if the inflow angle is taken to be 50 deg, and we will use this inflow angle as well.

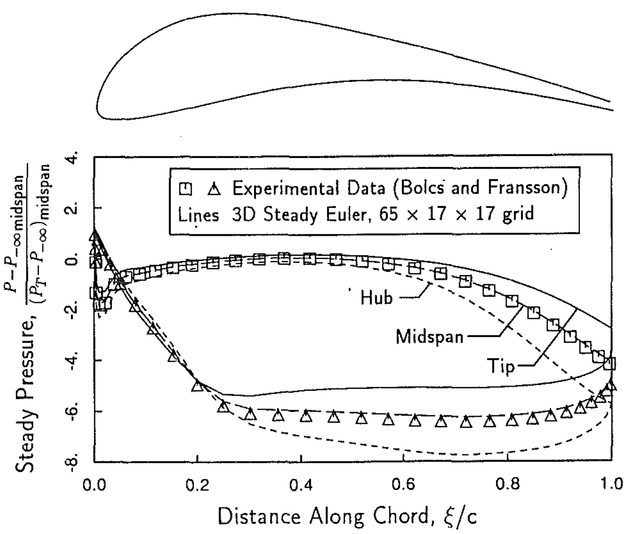

Fig. 9 **Mean pressure distribution on surface of airfoils of Fourth Standard Configuration turbine cascade. $N = 20$, $r_H/r_T = 0.8$, $\Theta = 56.6$ deg, $AR = 0.538$, $\beta_{-\infty} = 50$ deg, $M_{-\infty} = 0.26$, $\beta_\infty = 72$ deg, $M_\infty = 0.76$.**

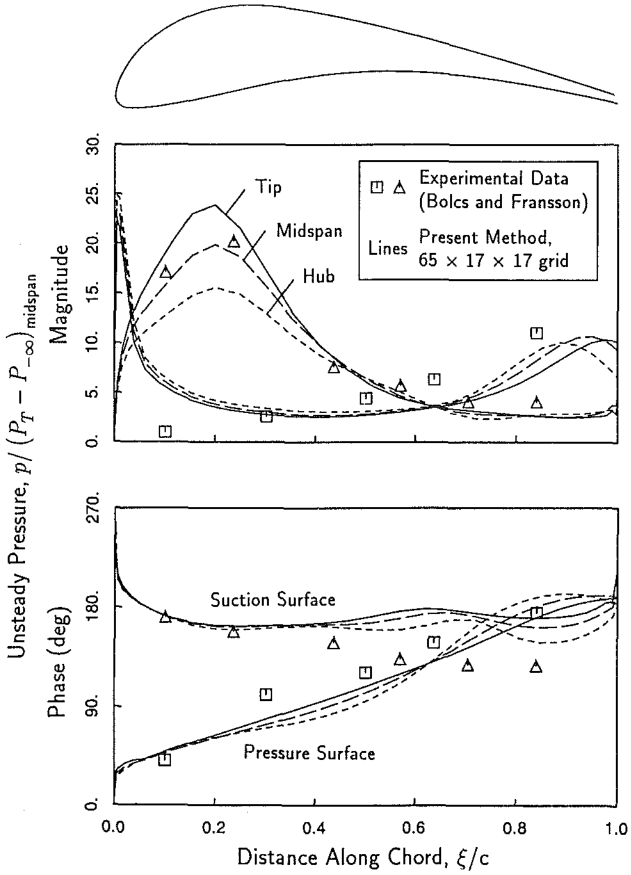

Fig. 10 **Unsteady pressure distribution on surface of airfoils of Fourth Standard Configuration turbine cascade undergoing plunging motion (Case 2): $\bar{\omega} = 0.13$, $\sigma = 90$ deg**

Figure 9 shows the computed mean flow solution at three radial stations along the blade. Also shown are the experimental data taken at the midspan station. The computational results of the present steady Euler solver are seen to be in good agreement with the experimental data. Also note the variation in loading from hub to tip. The swirl induced in the flow by the inlet guide vanes and subsequent turning of the inlet duct from the radial to axial direction produces a free vortex flow. Hence, the inflow angle is greater at the hub than at the tip.

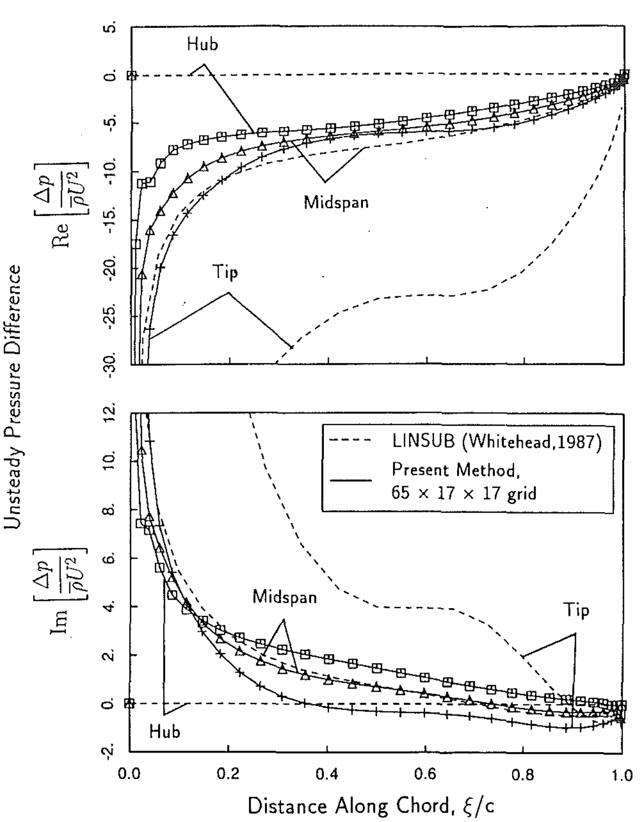

Fig. 11 **Unsteady pressure distribution on surface of reference airfoil of helical fan blade with airfoils vibrating in torsion about blade midchord. Pitching distribution is linear from hub to tip. $N = 18$, $AR_a = 2.0$, $c_a = 1.0$, $r_T = 4.0$, $r_H = 2.0$, $M_a = 0.5$, $\bar{\omega} = 0.4$, $\sigma = 180$ deg.**

Having calculated the steady flow, we computed the unsteady flow due to a plunging motion of the airfoils in a direction nearly perpendicular to the chord line with an interblade phase angle, σ, of 90 deg and a reduced frequency, $\bar{\omega}$, of 0.13 based on chord and nominal exit velocity. The blade in the experimental setup is hinged well below the hub. Hence, the motion at the hub is nonzero. We took the displacement to be unity at the midspan, 0.703 at the hub, and 1.307 at the tip. Shown in Fig. 10 are the magnitude and phase of the computed unsteady pressure distribution. The agreement between the present theory and the experimental results, while not exact, certainly shows the correct trends. Note that the three-dimensional effects for this case are fairly small. This should not be too surprising as the experiment was designed to produce essentially two-dimensional results.

Subsonic Helical Fan. In this section, we consider an idealized fan geometry. The airfoils are helical surfaces and the advance ratio is such that the airfoils have zero steady pressure loading. The case considered here is of an 18-bladed rotor with a hub-to-tip ratio of 0.5. The axial chord of the blade, c_a, is 1.0, and the tip radius, r_T is 4.0. The mean flow axial Mach number, M_a, is 0.5. The rotational speed of the fan is such that the relative inflow angle $\beta_{-\infty}$ at the midspan is 45 deg. For the unsteady case considered here, the blades pitch about their midchords with a reduced frequency, $\bar{\omega}$, of 0.4 based on axial chord and axial velocity, and the distribution of pitching amplitude is linear from hub to tip. Shown in Fig. 11 is the computed unsteady pressure difference across the airfoil surface. Also shown for comparison is the unsteady pressure difference predicted using Whitehead's LINSUB code (Whitehead, 1987) in a stripwise fashion. Note the generally poor agreement between the three-dimensional results and strip theory. Strip theory predicts that the response will be much larger at the tip than at the midspan or hub for two reasons. First, the dynamic pressure, which is proportional to the square of the relative velocity, is considerably larger at the tip. Second, the vibratory motion of the blade is largest at the tip. The unsteady pressure distributions found using the three-dimensional linearized Euler solver do not exhibit the strong spanwise variation in unsteady pressure predicted by strip theory. In fact, the imaginary part of the solution—the part that contributes to the aerodynamic damping—shows the opposite trend. These results have important implications on the prediction of flutter and forced response. For highly three-dimensional cascades, strip theory can be a poor predictor of aerodynamic damping.

Concluding Remarks

In this paper, we have presented a new three-dimensional linearized Euler solver that is capable of accurately and efficiently predicting unsteady small disturbance flows in turbomachinery blade rows. By using the pseudo-time time-marching approach, well developed finite-volume schemes can be adapted to solve the linearized Euler equations in a fraction of the time required to compute the unsteady flow field using conventional time-accurate time marching algorithms. An important feature of the present analysis is the use of a deforming computational grid. The deformable grid eliminates the need to include large extrapolation terms in the moving blade boundary conditions and improves the accuracy of the method, especially for thin airfoils typical of those found in modern compressors and fans. For engineering applications, good results can be obtained using fairly coarse grids. Furthermore, for low to moderate reduced frequencies, the accuracy of the unsteady solution is on a par with the accuracy of the steady flow solution.

Computational results were compared to experimental results and other unsteady aerodynamic analyses. Preliminary results of the present analysis indicate that three-dimensional effects are significant for both linear and annular cascades. For example, it was found that strip theory can be a poor predictor of aerodynamic damping. Furthermore, three-dimensional effects change the character of the component of the unsteady pressure distribution, which is out-of-phase with the upwash.

Acknowledgments

This work was supported by a research contract from General Electric Aircraft Engines with Dr. Andrew Chuang serving as technical monitor. The authors wish to acknowledge helpful discussions with Dr. Graham Holmes of the General Electric Corporate Research and Development Center.

References

Adamczyk, J. J., and Goldstein, M. E., 1978, "Unsteady Flow in a Supersonic Cascade With Subsonic Leading Edge Locus," *AIAA Journal*, Vol. 16, pp. 1248–1254.

Batina, J. T., 1990, "Three-Dimensional Flux-Split Euler Schemes Involving Unstructured Dynamic Meshes," AIAA Paper No. 90-1649.

Bölcs, A., and Fransson, T. H., 1986, "Aeroelasticity in Turbomachines: Comparison of Theoretical and Experimental Cascade Results," Air Force Office of Scientific Research, AFOSR-TR-87-0605.

Chi, R. M., 1993, "An Unsteady Lifting Surface Theory for Ducted Fan Blades," ASME JOURNAL OF TURBOMACHINERY, Vol. 115, pp. 175–188.

Fourmaux, A., and Le Meur, A., 1987, "Computation of Unsteady Phenomena in Transonic Turbines and Compressors," presented at the Fourth Symposium on Unsteady Aerodynamics and Aeroelasticity of Turbomachines and Propellers, Aachen University of Technology, Aachen, West Germany.

Fransson, T. H., 1991, private communication.

Giles, M. B., 1988, "Calculation of Unsteady Wake/Rotor Interaction," *AIAA Journal of Propulsion*, Vol. 4, No. 4, pp. 356–362.

Giles, M. B., 1990, "Nonreflecting Boundary Conditions for Euler Equation Calculations," *AIAA Journal*, Vol. 28, pp. 2050–2058.

Gostelow, J. P., 1984, *Cascade Aerodynamics*, Pergamon Press, New York, Chap. 5.

Hall, K. C., and Crawley, E. F., 1989, "Calculation of Unsteady Flows in Turbomachinery Using the Linearized Euler Equations," *AIAA Journal*, Vol. 27, No. 6, pp. 777–787.

Hall, K. C., and Clark, W. S., 1993a, "Linearized Euler Predictions of Unsteady Aerodynamic Loads in Cascades," *AIAA Journal*, Vol. 31, No. 3, pp. 540–550.

Hall, K. C., and Clark, W. S., 1993b, "Calculation of Unsteady Linearized Euler Flows in Cascades Using Harmonically Deforming Grids," *Unsteady Aerodynamics, Aeroacoustics, and Aeroelasticity of Turbomachines and Propellers*, H. M. Atassi, ed., Springer-Verlag, pp. 195–212.

Hall, K. C., and Verdon, J. M., 1991, "Gust Response Analysis for Cascades Operating in Non-uniform Mean Flows," *AIAA Journal*, Vol. 29, No. 9, pp. 1463–1471.

Hall, K. C., 1993, "Deforming Grid Variational Principle for Unsteady Small Disturbance Flows in Cascades," *AIAA Journal*, Vol. 31, No. 5, pp. 891–900.

Holmes, D. G., and Chuang, H. A., 1993, "2D Linearized Harmonic Euler Flow Analysis for Flutter and Forced Response," *Unsteady Aerodynamics, Aeroacoustics, and Aeroelasticity of Turbomachines and Propellers*, H. M. Atassi, ed., Springer-Verlag, pp. 213–230.

Huff, D. L., 1987, "Numerical Simulations of Unsteady, Viscous, Transonic Flow Over Isolated and Cascaded Airfoils Using a Deforming Grid," AIAA Paper No. 87-1316.

Huff, D. L., and Reddy, T. S. R., 1989, "Numerical Analysis of Supersonic Flow Through Oscillating Cascade Sections by Using a Deforming Grid," AIAA Paper No. 89-2805.

Namba, M., 1977, "Three-Dimensional Analysis of Blade Force and Sound Generation for an Annular Cascade in Distorted Flows," *Journal of Sound and Vibration*, Vol. 50, No. 4, pp. 479–508.

Namba, M., 1987, "Three-Dimensional Flows," *AGARD Manual on Aeroelasticity in Axial-Flow Turbomachines, Unsteady Turbomachinery Aerodynamics*, Vol. 1, Chap. 4, M. F. Platzer and F. O. Carta, eds., AGARD-AG-298.

Namba, M., and Toshimitsu, K., 1987, "Improved Double Linearization Method for Prediction of Mean Loading Effects on Subsonic and Supersonic Cascade Flutter," presented at the Fourth Symposium on Unsteady Aerodynamics and Aeroelasticity of Turbomachines and Propellers, Aachen University of Technology, Aachen, West Germany.

Ni, R. H., and Sisto, F., 1976, "Numerical Computation of Nonstationary Aerodynamics of Flat Plate Cascades in Compressible Flow," ASME *Journal of Engineering for Power*, Vol. 98, pp. 165–170.

Ni, R. H., and Bogoian, J. C., 1989, "Prediction of Three-Dimensional Multi-Stage Turbine Flow Field Using a Multiple-Grid Euler Solver," AIAA Paper No. 89-0203.

Rai, M. M., 1989a, "Three-Dimensional Navier-Stokes Simulations of Turbine Rotor-Stator Interaction: Part I—Methodology," *AIAA Journal of Propulsion and Power*, Vol. 5, No. 3, pp. 307–311.

Rai, M. M., 1989b, "Three-Dimensional Navier-Stokes Simulations of Turbine Rotor-Stator Interaction: Part II—Results," *AIAA Journal of Propulsion and Power*, Vol. 5, No. 3, pp. 312–319.

Saxer, A. P., and Giles, M. B., 1990, "Inlet Radial Temperature Redistribution in a Transonic Turbine Stage," AIAA Paper No. 90-1543.

Smith, S. N., 1972, "Discrete Frequency Sound Generation in Axial Flow Turbomachines," Aeronautical Research Council, London, Reports and Memoranda 3709.

Thompson, J. F., Thames, F. C., and Mastin, C. W., 1974, "Automatic Numerical Generation of Body-Fitted Curvilinear Coordinate System for Field Containing Any Number of Arbitrary Two-Dimensional Bodies," *Journal of Computational Physics*, Vol. 15, pp. 299–319.

Verdon, J. M., Adamczyk, J. J., and Caspar, J. R., 1975, "Subsonic Flow Past an Oscillating Cascade With Steady Blade Loading—Basic Formulation," *Unsteady Aerodynamics*, R. B. Kinney, ed., University of Arizona, Tucson, AZ, pp. 827–851.

Verdon, J. M., and McCune, J. E., 1975, "Unsteady Supersonic Cascades in Subsonic Axial Flow," *AIAA Journal*, Vol. 13, No. 2, pp. 193–201.

Verdon, J. M., and Caspar, J. R., 1984, "A Linearized Unsteady Aerodynamic Analysis for Transonic Cascades," *Journal of Fluid Mechanics*, Vol. 149, pp. 403–429.

Whitehead, D. S., 1960, "Force and Moment Coefficients for Vibrating Aerofoils in Cascade," Aeronautical Research Council, London, Reports and Memoranda 3254.

Whitehead, D. S., 1962, "Bending Flutter of Unstalled Cascade Blades at Finite Deflection," Aeronautical Research Council, London, Reports and Memoranda 3386.

Whitehead, D. S., and Grant, R. J., 1981, "Force and Moment Coefficients of High Deflection Cascades," *Proceedings of the 2nd International Symposium on Aeroelasticity in Turbomachines*, P. Suter, ed., Juris-Verlag, Zurich, pp. 85–127.

Whitehead, D. S., 1987, "Classical Two-Dimensional Methods," *AGARD Manual on Aeroelasticity in Axial-Flow Turbomachines, Unsteady Turbomachinery Aerodynamics*, Vol. 1, Chap. 2, M. F. Platzer and F. O. Carta, eds., AGARD-AG-298.

Whitfield, D. L., Swafford, T. W., and Mulac, R. A., 1987, "Three-Dimensional Unsteady Euler Solutions for Propfans and Counter-rotating Propfans in Transonic Flow," AIAA Paper No. 87-1197.

J. Fang
Research Associate.

H. M. Atassi
Professor.

Department of Aerospace
and Mechanical Engineering,
University of Notre Dame,
Notre Dame, IN 46556

Numerical Solutions for Unsteady Subsonic Vortical Flows Around Loaded Cascades

A frequency domain linearized unsteady aerodynamic analysis is presented for three-dimensional unsteady vortical flows around a cascade of loaded airfoils. The analysis fully accounts for the distortion of the impinging vortical disturbances by the mean flow. The entire unsteady flow field is calculated in response to upstream three-dimensional harmonic disturbances. Numerical results are presented for two standard cascade configurations representing turbine and compressor bladings for a reduced frequency range from 0.1 to 5. Results show that the upstream gust conditions and blade sweep strongly affect the unsteady blade response.

1 Introduction

The flow upstream of a turbomachine blade row is characterized by irregular inflow patterns, which arise from various flow phenomena such as inlet distortion and turbulence, viscous wakes, secondary flows, and rotor-stator interaction. When a blade row moves in a spatially nonuniform flow pattern, flow nonuniformities appear in the blade reference frame as three-dimensional vorticity waves impinging on the blades and known as *gusts* [1]. The interaction of these vortical waves with the blades produce fluctuating aerodynamic excitations, which result in unwanted vibration and noise. This phenomenon is a *forced response*, as opposed to self-excited instabilities such as blade flutter.

The most significant difference between flutter and forced response is that in the former the upstream inflow is potential, while in the latter the upstream inflow is essentially nonuniform and rotational. For loaded blades, the mean flow exhibits strong variation, which distorts the impinging vorticity waves as they interact with the blades and, as a result, *significantly* affect the unsteady aerodynamic forces [2, 3].

In turbomachine bladings, the blade passing frequency is the most important parameter affecting the physics of the unsteady flow. As a result, a frequency-domain formulation is commonly used for forced response analysis. For typical applications, the reduced frequency is in a range of 0.5 to 10.

The present paper is concerned with the effect of the gust upstream conditions on the forced response of typical loaded cascades. The authors have developed a numerical code for solving the unsteady Euler equations in a cascade geometry [4–6]. The mathematical formulation is based on Goldstein's [7] and Atassi and Grzedzinski's [8] splitting of the velocity field. This formulation leads to a single convective wave equation. The coefficients of this equation depend on the mean flow, which is calculated from a nonlinear steady cascade flow code. Atassi and Grzedzinski's splitting method has been used by Scott [9] and Scott and Atassi [10] for a single lifting airfoil, by Fang [4] for a slightly loaded cascade, and by Hall and Verdon [11] and Fang and Atassi [5] for a heavily loaded cascade.

The unsteady velocity associated with the far field acoustics may not vanish at infinity for flows around a cascade. A new far-field acoustic radiation condition was then derived by Fang [4] and Fang and Atassi [5] for three-dimensional vortical flows around a loaded cascade. This condition avoids the singularity associated with vortical flows downstream, and thus is suitable for numerical computations.

In the present paper, we present benchmark results for two standard cascade configurations [12]. This was recently recommended by a panel during the Sixth International Symposium on Unsteady Aerodynamics, Aeroacoustics and Aeroelasticity of Turbomachines and Propellers [13] in order to facilitate the comparison between theory and experiments. One of these configurations is the so-called first standard configuration corresponding to a low subsonic compressor cascade; the other is the third standard configuration representing a subsonic–transonic turbine cascade.

2 Mathematical Formulation

2.1 Linearized Euler's Equations. We assume an unsteady, inviscid, subsonic flow passing through a stationary, linear cascade of airfoils with velocity disturbances imposed on a uniform upstream velocity $U_{-\infty}\mathbf{i}_1$ (see Fig. 1). The governing equations are the continuity, momentum, and energy equations:

$$\frac{D\rho}{Dt}+\rho\nabla\cdot\mathbf{U}=0 \tag{1}$$

$$\rho\frac{D\mathbf{U}}{Dt}=-\nabla p \tag{2}$$

$$\frac{Ds}{Dt}=0 \tag{3}$$

where

Contributed by the International Gas Turbine Institute and presented at the 37th International Gas Turbine and Aeroengine Congress and Exposition, Cologne, Germany, June 1–4, 1992. Manuscript received by the International Gas Turbine Institute February 17, 1992. Paper No. 92-GT-173. Associate Technical Editor: L. S. Langston.

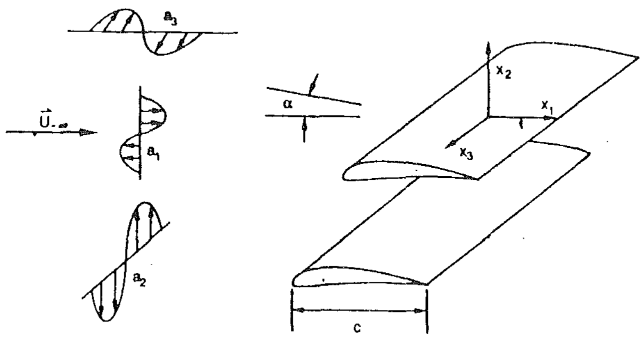

Fig. 1 Cascade of loaded airfoils in a three-dimensional gust

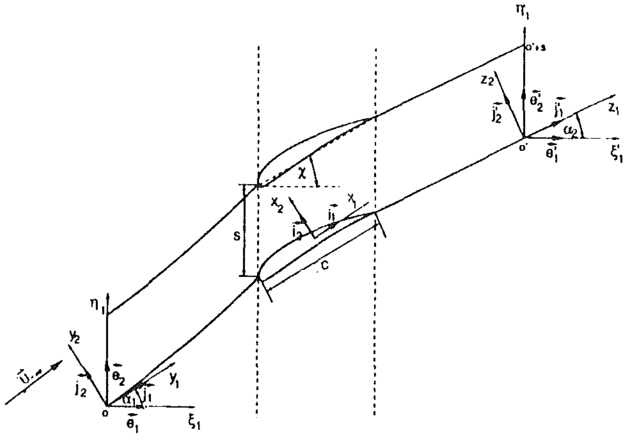

Fig. 2 Cascade computational coordinates

$$\frac{D}{Dt}=\frac{\partial}{\partial t}+\mathbf{U}\cdot\nabla$$

t denotes time, and ρ, $\mathbf{U}$, p, and s denote the fluid density, velocity, pressure, and entropy, respectively. We assume that the unsteady flow is a small perturbation and can be linearized about a mean flow, so that

$$\mathbf{U}(\mathbf{x},\,t)=\mathbf{U}_0(\mathbf{x})+\mathbf{u}(\mathbf{x},\,t) \tag{4}$$

$$p(\mathbf{x},\,t)=p_0(\mathbf{x})+p'(\mathbf{x},\,t) \tag{5}$$

$$\rho(\mathbf{x},\,t)=\rho_0(\mathbf{x})+\rho'(\mathbf{x},\,t) \tag{6}$$

$$s(\mathbf{x},\,t)=s_0(\mathbf{x})+s'(\mathbf{x},\,t) \tag{7}$$

where the subscript 0 denotes the steady mean flow quantities and $\mathbf{u}$, p', ρ', and s' are the unsteady velocity, pressure, density, and entropy disturbances, respectively. The coordinate system is shown in Fig. 2

Substituting Eqs. (4) to (7) into Eqs. (1) to (3) yields the zero-order and the first-order equations of continuity, momentum, and energy. We assume that the solutions to the zero-order equations, which are $\mathbf{U}_0$, p_0, ρ_0, and s_0 in Eqs. (4) to (7), are known and obtained by a mean flow solver. For a two-dimensional cascade geometry with a uniform upstream mean velocity and constant entropy, the mean flow velocity $\mathbf{U}_0$ is potential and therefore we can write $\mathbf{U}_0 = \nabla\Phi$. Neglecting the higher order terms yields the first order equations for $\mathbf{u}$, p', ρ', and s':

$$\frac{D_0\rho'}{Dt}+\rho'\,\nabla\cdot\mathbf{U}_0+\nabla\cdot(\rho_0\mathbf{u})=0 \tag{8}$$

$$\rho_0\left(\frac{D_0\mathbf{u}}{Dt}+\mathbf{u}\cdot\nabla\mathbf{U}_0\right)+\rho'\mathbf{U}_0\cdot\nabla\mathbf{U}_0=-\nabla p' \tag{9}$$

$$\frac{D_0 s'}{Dt}=0 \tag{10}$$

where

$$\frac{D_0}{Dt}=\frac{\partial}{\partial t}+\mathbf{U}_0\cdot\nabla$$

is the linearized material derivative associated with the mean flow. In the remainder of this paper we only consider vortical waves upstream and take $s' = 0$. For flows where $s' \neq 0$, an analysis similar to the present work can be developed. We further assume that there are no incident acoustic waves.

Since, for a cascade, outgoing acoustic waves may not vanish far upstream, the upstream total velocity must be of the form

$$\mathbf{U}(\mathbf{x},\,t)=U_{-\infty}\mathbf{i}_1+\mathbf{u}_g+\mathbf{u}_a \text{ as } x_1\rightarrow-\infty \tag{11}$$

where $\mathbf{u}_a = \mathbf{u}_a(\mathbf{x}, t)$ denotes the unsteady velocity associated with upstream acoustics, $\mathbf{u}_g = \mathbf{u}_g(\mathbf{x} - \mathbf{i}_1 U_{-\infty}t)$ is the upstream imposed vortical disturbance satisfying [1]

$$\nabla\cdot\mathbf{u}_g=0. \tag{12}$$

Because of the linear nature of the problem, without loss of generality, we take one Fourier component as the upstream vortical disturbance, so that

$$\mathbf{u}_g=\mathbf{a}e^{i[\mathbf{k}\cdot(\mathbf{x}-\mathbf{i}_1U_{-\infty}t)]}, \tag{13}$$

where the amplitude vector $\mathbf{a} = (a_1, a_2, a_3)$ satisfies $|\mathbf{a}| \ll U_{-\infty}$, $\mathbf{k} = (k_1, k_2, k_3)$ is the wave number vector, which gives the direction of propagation of the gust. Substituting Eq. (13) into Eq. (12) yields

$$\mathbf{a}\cdot\mathbf{k}=0. \tag{14}$$

The upstream condition for $\mathbf{u}$ is

$$\mathbf{u}\rightarrow\mathbf{u}_g+\mathbf{u}_a \text{ as } x_1\rightarrow-\infty \tag{15}$$

2.2 Decomposition of the Unsteady Velocity. Goldstein [7] proposed a unified approach to streaming motions with small unsteady vortical and entropy disturbances imposed on the upstream flow. For entropy-free disturbances, Goldstein splits the unsteady velocity into (*i*) a potential part, which entirely determines the unsteady pressure and satisfies a non-constant inhomogeneous convective wave equation, and (*ii*) a vortical part, which is a known function in terms of the imposed upstream disturbance and the mean flow Lagrangian coordinates. This substantially reduces the mathematical problem from a set of partial differential equation to a single wave equation.

For real flows around bodies, there will be a stagnation point at the body surface near the leading edge. The mean flow Lagrangian coordinates at this point and along the entire body surface and its wake become singular. Since the vortical velocity in Goldstein's splitting is proportional to the gradients of the mean flow Lagrangian coordinates, the vortical velocity becomes singular on the body surface and the wake. As a result, the boundary value problem has a singular body surface boundary condition and thus is not suitable for direct numerical calculations.

Atassi and Grzedzinski [8] noted that the total velocity cannot have such a strong singularity on the body surface. They further showed that it is possible to find a potential velocity field $\nabla\bar{\phi}$ that produces no pressure and that cancels the singular behavior of the vortical velocity along the body surface and its wake. The new splitting proposed by Atassi and Grzedzinski [8] decomposes the unsteady velocity field into the sum of (*i*) a vortical part $\mathbf{u}^{(R)}$ with no contribution to the unsteady pressure p' and which is a known function in terms of the upstream disturbances and the mean flow Lagrangian coordinates, and (*ii*) a potential part $\nabla\phi$

$$\mathbf{u}=\mathbf{u}^{(R)}+\nabla\phi. \tag{16}$$

$\mathbf{u}^{(R)}$ has the remarkable property that its normal ($\mathbf{n}$) and streamwise (τ) components vanish along the blade surface Σ and its wake W:

$$\mathbf{u}^{(R)} \cdot \mathbf{n} = 0 \text{ and } \mathbf{u}^{(R)} \cdot \boldsymbol{\tau} = 0 \text{ for } \mathbf{x} \in \Sigma + W. \tag{17}$$

The unsteady potential ϕ satisfies a single non-constant-coefficient, convective wave equation

$$\frac{D_0}{Dt}\left(\frac{1}{c_0^2}\frac{D_0\phi}{Dt}\right) - \frac{1}{\rho_0}\nabla \cdot (\rho_0 \nabla \phi) = \frac{1}{\rho_0}\nabla \cdot (\rho_0 \mathbf{u}^{(R)}), \tag{18}$$

where c_0 is the mean flow speed of sound. The vortical velocity $\mathbf{u}^{(R)} = (u_1^{(R)}, u_2^{(R)}, u_3^{(R)})$ is given by [8],

$$u_l^{(R)} = \mathbf{u}_g \cdot \frac{\partial \mathbf{X}}{\partial x_l} + \frac{\partial \tilde{\phi}}{\partial x_l} \quad . \, (l = 1, 2, 3), \tag{19}$$

where the components of $\mathbf{X} = (X_1, X_2, X_3)$ are defined as follows: $X_2 = X_2\,(x_1, x_2, x_3)$ and $X_3 = X_3(x_1, x_2, x_3)$ are independent integrals of the equations

$$\frac{dx_1}{U_{01}} = \frac{dx_2}{U_{02}} = \frac{dx_3}{U_{03}} \tag{20}$$

such that

$$X_2 \to x_2 \text{ and } X_3 \to x_3 \text{ as } x_1 \to -\infty, \tag{21}$$

where U_{0l} ($l = 1, 2, 3$) in Eq. (20) are the three components of the mean flow velocity $\mathbf{U}_0$. $X_1 = X_1(x_1, x_2, x_3)$ is defined as $X_1 = U_{-\infty}\Delta$, where Δ is Lighthill's "drift" function

$$\Delta(x_1, x_2, x_3) = \frac{x_1}{U_{-\infty}} + \int_{-\infty}^{x_1}\left[\frac{1}{U_{01}} - \frac{1}{U_{-\infty}}\right]dx_1', \tag{22}$$

The integral is carried out along a streamline. $\tilde{\phi}$ in Eq. (19) is a known function in terms of the gust conditions and the mean flow parameters. For a linear cascade, note that X_2 becomes the mean flow stream function Ψ_0 and X_3 becomes x_3. The expression for $\tilde{\phi}$ is given by [8] as

$$\tilde{\phi} = \frac{i}{k_1}\left\{a_1 + \frac{is^*(a_2k_1 - a_1k_2)}{2\pi(1 + ia_0U_{-\infty}k_1)} * \sin\left[\frac{2\pi}{s^*U_{-\infty}\rho_{-\infty}}(\Psi_0 - \Psi_0^{(0)})\right]\right\}e^{i\mathbf{k}\cdot(\mathbf{X} - \mathbf{i}_1 U_{-\infty}t)} \tag{23}$$

where $\rho_{-\infty}$ is the upstream mean flow density, $\Psi_0^{(0)}$ is the value of the mean flow stream function taken at the blade surface, s^* is the component of the cascade spacing perpendicular to the upstream mean flow, a_0 is

$$a_0 = -\left(\frac{\partial U_0}{\partial n_0}\right)_s^{-1} \tag{24}$$

where $U_0 = |\mathbf{U}_0|$, n_0 denotes the derivative in the outward direction normal to the blade surface, and the subscript s denotes the value taken at the leading edge stagnation point. The unsteady pressure is determined entirely by ϕ,

$$p' = -\rho_0 \frac{D_0\phi}{Dt}. \tag{25}$$

The boundary conditions for ϕ are as follows:

1 On the blade surface Σ, because of Eq. (17), ϕ satisfies

$$\mathbf{n} \cdot \nabla\phi = 0 \text{ for } \mathbf{x} \in \Sigma, \tag{26}$$

where $\mathbf{n}$ is the blade surface normal unit vector. Note that this boundary condition is well suitable for numerical computations.

2 The cascade quasi-periodicity condition:

$$\phi(\mathbf{x} + \mathbf{s}, t) = \phi(\mathbf{x}, t)e^{i\sigma}, \tag{27}$$

where $\mathbf{s}$ is the spacing vector and $\sigma = \mathbf{k} \cdot \mathbf{s}$ is the interblade phase angle.

3 The unsteady potential ϕ is not continuous across the wake but the unsteady pressure and the normal velocity are continuous. This can be expressed as follows:

$$\frac{D_0}{Dt}(\Delta\phi) = 0 \text{ and } \Delta(\nabla\phi \cdot \mathbf{n}) = 0 \text{ for } \mathbf{x} \in W, \tag{28}$$

where Δ denotes the jump in the value across the wake. In addition, we assume that the Kutta condition is satisfied at the trailing edge of the blades.

4 In the far field, the unsteady pressure must satisfy a nonreflective acoustic radiation condition. The condition used in the present work was developed by Fang [4] and Fang and Atassi [5]. Because of the importance of this condition, we give herein a brief derivation.

Upstream and downstream of the cascade, the mean flow will be uniform, thus the coefficients of the governing equation are constants. By taking the material derivative on both sides of the governing equation, Eq. (18), upstream and downstream, we have

$$\frac{1}{c_0^2}\frac{D_0^2 p'}{Dt^2} - \nabla^2 p' = 0, \tag{29}$$

where c_0 refers to the upstream or the downstream speed of sound. Note that p' is regular and continuous upstream and downstream. We expand p' in a Fourier series

$$p' = \sum_{n=-\infty}^{\infty} c_n p_n', \tag{30}$$

where the coefficients c_n are complex constants. p_n' has the general form

$$p_n' = e^{i[(a_n y_1 + b_n y_2 + k_3 y_3) - k_1 t]}. \tag{31}$$

By substituting Eq. (31) into Eqs. (29) and (27), the complex constants a_n and b_n are determined. Depending upon the values of a_n and b_n, Eq. (31) represents an unsteady pressure field with the following far field characteristics: (*i*) an exponentially decaying field, (*ii*) an exponential increasing field, (*iii*) waves propagating away from the row of the blades with constant amplitude, or (*iv*) waves propagating toward the cascade with constant amplitude. Those non-wave-type terms of Eq. (31) that exponentially increase in the far field are physically not acceptable. For a gust problem without far-field acoustic sources, those wave-type terms of Eq. (31) that represent waves propagating toward the row of blades do not exist physically. Consequently, p' on the boundary can be constructed as a sum of all decaying terms (*i*) and propagating modes (*iii*). The coefficients c_n in Eq. (30) can be calculated numerically.

This far field acoustic radiation condition is good for both upstream and downstream, though it is particularly suitable for the downstream. It avoids the singular behavior associated with the unsteady vortical velocity field, which becomes infinite and indeterminate in the wake. This singularity makes it impossible to construct a downstream condition directly for ϕ without approximation. Upstream, since the total flow is regular, it is then more convenient to use ϕ directly instead of p'. In this case, a derivation similar to what has been given by Eqs. (29), (30), and (31) can be obtained by replacing p' by ϕ^*, where ϕ^* is defined by

$$\phi^* = \phi - \tilde{\phi}. \tag{32}$$

3 Numerical Scheme

The boundary value problem given by Eqs. (18), (26), (27), (28), and the far-field boundary condition depends on the time t and the spanwise coordinate x_3. However, because of the form of the upstream gust condition (13) and the two-dimensional geometry of the cascade, it is possible to factor out these two variables. We introducing a dependent variable ψ such that

$$\phi = \psi(x_1, x_2)e^{i(k_3x_3 - k_1t)}. \tag{33}$$

Substituting Eq. (33) into Eqs. (18), (26), (27), (28), and the

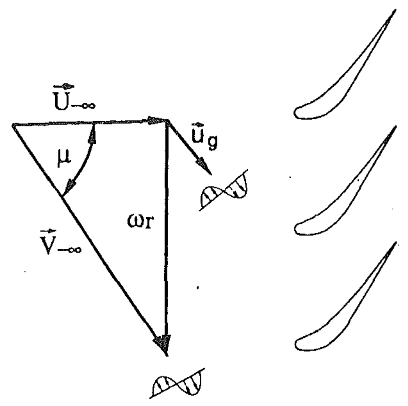

Fig. 3 Schematic of upstream disturbances in the blade reference frame for the third standard configuration. The angle from the machine axis to $U_{-\infty}$ is 1.2 deg.

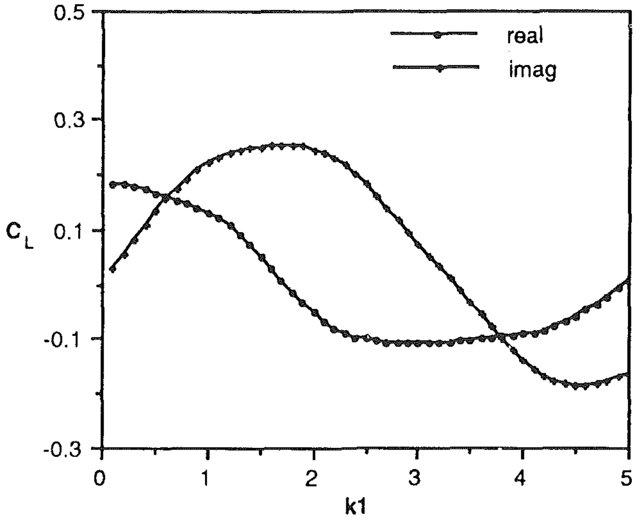

Fig. 4 Real and imaginary parts of the unsteady lift coefficient C_L versus reduced frequency k_1 for the third standard configuration in a one-dimensional gust (case 1). $M_{-\infty}$ = 0.25.

far-field boundary condition, we obtain an equation and boundary conditions for ψ.

The boundary value problem for ψ was solved using finite differencing approximations in a body-fitted coordinate system. One coordinate is the stream function Ψ_0 of the mean flow and the other is a family of straight lines parallel to the cascade stagger line. The computational domain is a single passage of the cascade.

The mean flow fields, which are entirely subsonic, were obtained by using McFarland's [14] subsonic steady cascade flow solver. The advantage of this solver is its efficiency. The mean flow properties were then calculated along streamlines using spatial marching technique.

The numerical scheme was validated [4, 5] by comparison with the results of a flat plate cascade [15]. The comparison showed very good agreement.

4 Results and Discussion

Based on the formulation presented in the previous sections, numerical solutions were obtained for the first and the third standard configurations [12]. The unsteady lift coefficient C_L and the normalized unsteady pressure P' will be plotted to examine the effects of the gust upstream conditions on the forced response and the unsteady pressure field of these two cascades. C_L is defined by:

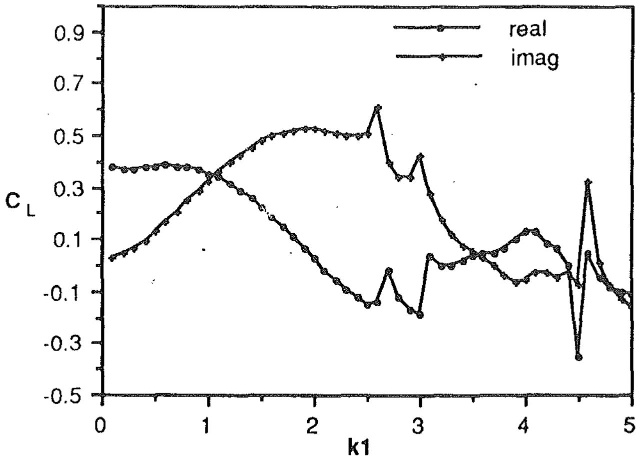

Fig. 5 Real and imaginary parts of the unsteady lift coefficient C_L versus reduced frequency k_1 for the third standard configuration in a two-dimensional gust (case 2). $M_{-\infty}$ = 0.25.

$$C_L = \frac{\overline{L}}{\pi \rho_{-\infty} c U_{-\infty} |\mathbf{a}| e^{ik_1 t}}$$

where L is the unsteady aerodynamic lift; P' is defined by

$$P' = \frac{\overline{p'}}{\rho_{-\infty} U_{-\infty} |\mathbf{a}| e^{ik_1 t}}$$

where p' is the unsteady aerodynamic pressure. The overbar indicates the complex conjugate.

4.1 Results for Third Standard Configuration.

For the third standard configuration, a high subsonic/transonic turbine profile, the numerical results were obtained for an upstream Mach number of 0.25, a range of reduced frequencies k_1 from 0.1 to 5, and an upstream flow angle of 1.2 deg. In order to determine the effect of the upstream gust conditions, we considered four cases corresponding to one-, two-, and three-dimensional gusts without and with sweep. These cases are defined as follows: (1) one-dimensional transverse gust, $\mathbf{a} = (0, 1, 0)$, and $\mathbf{k} = (k_1, 0, 0)$; (2) two-dimensional gust, $\mathbf{a} = (-0.707, 0.707, 0)$, and $\mathbf{k} = (k_1, k_2, 0)$, where $k_2 = k_1$; (3) three-dimensional gust without sweep, $\mathbf{a} = (-0.707, 0.707, 0)$, and $\mathbf{k} = (k_1, k_2, 1)$, where $k_2 = k_1$; (4) three-dimensional gust with a constant sweep of 19.1 deg, $\mathbf{a} = (-0.472, 0.818, -0.327)$, and $\mathbf{k} = (k_1, k_2, k_3)$, where $k_2 = k_1$, and k_3 is determined by the relationship (14). The interblade phase angle σ is determined by

$$\sigma = \mathbf{k} \bullet \mathbf{s}. \tag{34}$$

Figure 3 is a schematic of the upstream disturbances in the blade reference frame. $\mathbf{V}_{-\infty}$ represents the mean flow upstream absolute velocity, ωr is the circumferential velocity of blades, and $\mathbf{U}_{-\infty}$ is the relative velocity in the cascade reference frame. For a constant $\mathbf{U}_{-\infty}$, the variation of angle μ means the changes of $\mathbf{V}_{-\infty}$ and/or ωr. If the flow unsteadiness is caused by upstream flow velocity deficit, case 1 corresponds to an angle μ of 90 deg, cases 2 and case 3 to 45 deg, and μ is 60 deg for case 4.

Figure 4 shows the real and imaginary parts of the unsteady lift coefficient C_L versus reduced frequency k_1 for the third standard configuration in a one-dimensional gust (case 1) with $M_{-\infty}$ = 0.25. For this case, there is only one upstream and only one downstream acoustic mode and no additional modes cut on for the frequency range from 0.1 to 5. The variation of C_L is smooth in the absence of new acoustic modes cutting on. Figure 5 shows the real and imaginary parts of the unsteady lift coefficient C_L versus reduced frequency k_1 for the third standard configuration in a two-dimensional gust (case 2) with $M_{-\infty}$ = 0.25. For case 2, a downstream acoustic mode cuts

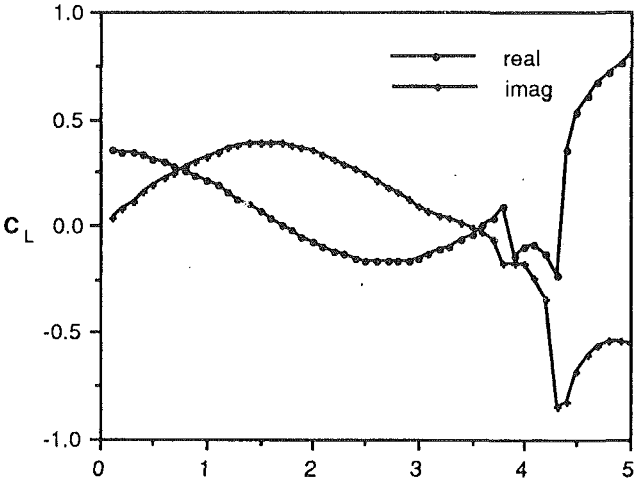

Fig. 6 Real and imaginary parts of the unsteady lift coefficient C_L versus reduced frequency k_1 for the third standard configuration in a three-dimensional gust without sweep (case 3). $M_{-\infty} = 0.25$.

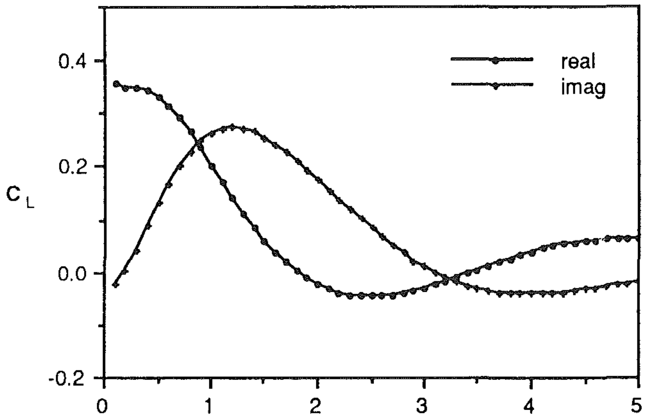

Fig. 7 Real and imaginary parts of the unsteady lift coefficient C_L versus reduced frequency k_1 for the third standard configuration in a three-dimensional gust with sweep (case 4). $M_{-\infty} = 0.25$.

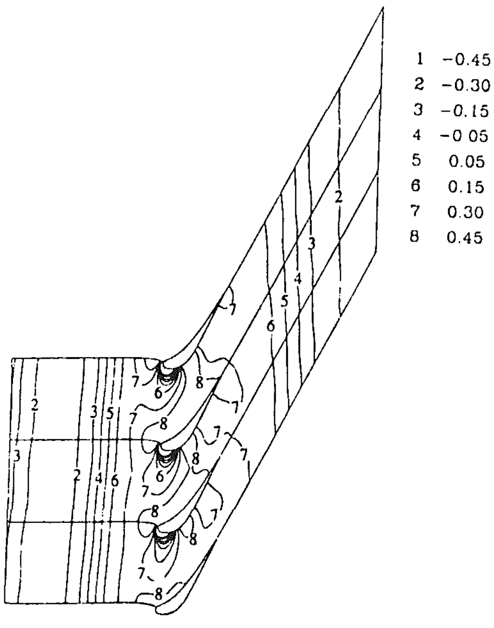

Fig. 8 Contours of the real part of the normalized unsteady pressure for the third standard configuration in a gust a = (0, 1, 0), k = (4, 0, 0). $M_{-\infty} = 0.25$.

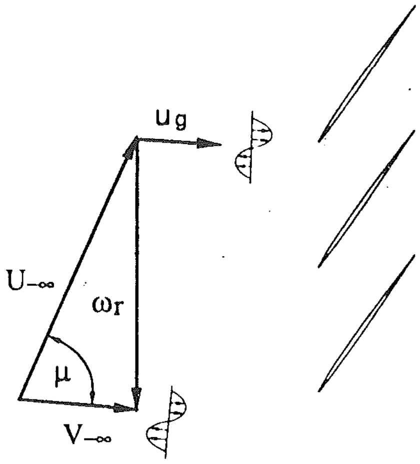

Fig. 9 Schematic of upstream unsteady disturbances in the blade reference frame for the first standard configuration. The angle from the machine axis to $U_{-\infty}$ is 62 deg.

on at $k_1 \approx 2.7$, this mode is cut off at $k_1 \approx 4.7$. At $k_1 \approx 3.1$, an upstream wave cuts on. Figure 6 shows the real and imaginary parts of the unsteady lift coefficient C_L versus reduced frequency k_1 for the third standard configuration in a three-dimensional gust without sweep (case 3) with $M_{-\infty} = 0.25$. For this case, there is no acoustic mode for $k_1 < 3.9$. An upstream mode cuts on at $k_1 = 3.9$ and cuts off at $k_1 = 4.3$. Figure 7 shows the real and imaginary parts of the unsteady lift coefficient C_L versus reduced frequency k_1 for the third standard configuration in a three-dimensional gust with sweep (case 4) with $M_{-\infty} = 0.25$. For this case, no acoustic mode exists for the entire frequency range and the plot of the unsteady lift coefficient versus the reduced frequency is smooth.

For this cascade flow conditions, the unsteady lift is larger for a two-dimensional gust than for a one-dimensional gust or a three-dimensional gust with sweep. Figure 7 shows that the effect of blade sweep is important; it significantly reduces the unsteady lift at moderate and high reduced frequencies. The results also show that the far field acoustic cut-on or cut-off has a strong influence in the near field unsteady pressure. Near these points, the unsteady lift exhibits large variations in both amplitude and phase angle with respect to the reduced frequency. It indicates that near these points, the system is very sensitive to the gust upstream conditions; therefore it should be studied for each specific case.

To illustrate the near field unsteady pressure variation as well as far field acoustic waves, the normalized unsteady pressure field for gust **a** = (0, 1, 0) **k** = (4, 0, 0) is shown in Fig. 8. Upstream analytical calculations show that one acoustic mode exists with a propagation direction of 176 deg from the machine axis. The numerical results given in this figure are consistent with this analytical result. Note that on the boundary, the wave propagates through it without spurious reflection. Downstream, the numerical results also confirms that an acoustic mode exists and propagates downstream in a direction of 6.2 deg from the machine axis, as predicted by analytical analysis.

4.2 Results for First Standard Configuration. For the first standard configuration, which is a low subsonic compressor cascade, the numerical results are presented for an upstream Mach number of 0.18, a range of k_1 from 0.1 to 5, and an upstream flow angle of 62 deg. The gust conditions presented are the same as those studied for the third standard configuration. Figure 9 shows the schematic of the upstream unsteady disturbances caused by upstream velocity deficit. Again, case 1 corresponds to an angle μ (see Fig. 9) of 90 deg, cases 2 and case 3 to 45 deg, and μ is 60 deg for case 4.

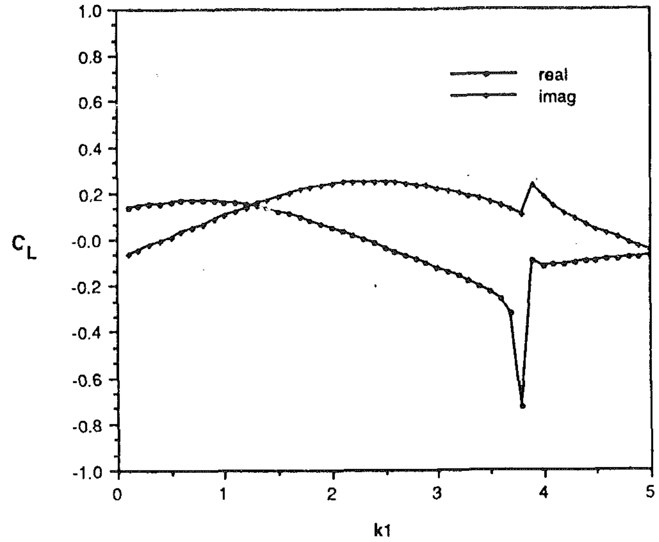

Fig. 10 Real and imaginary parts of the unsteady lift coefficient C_L versus reduced frequency k_1 for the first standard configuration in a one-dimensional gust (case 1). $M_{-\infty} = 0.18$.

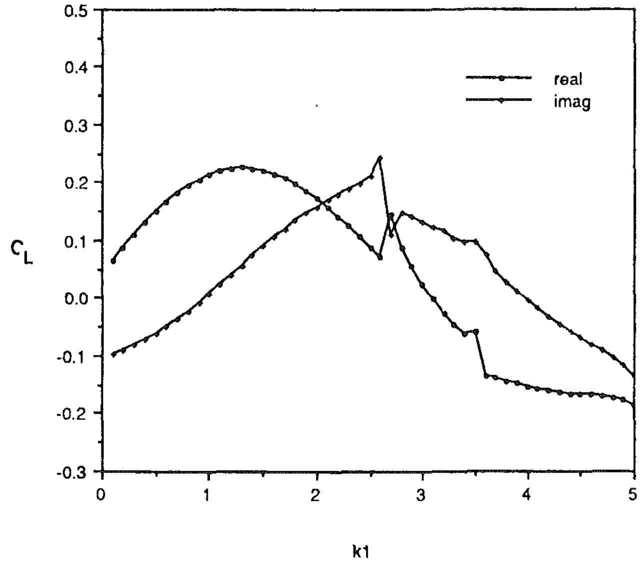

Fig. 11 Real and imaginary parts of the unsteady lift coefficient C_L versus reduced frequency k_1 for the first standard configuration in a two-dimensional gust (case 2). $M_{-\infty} = 0.18$.

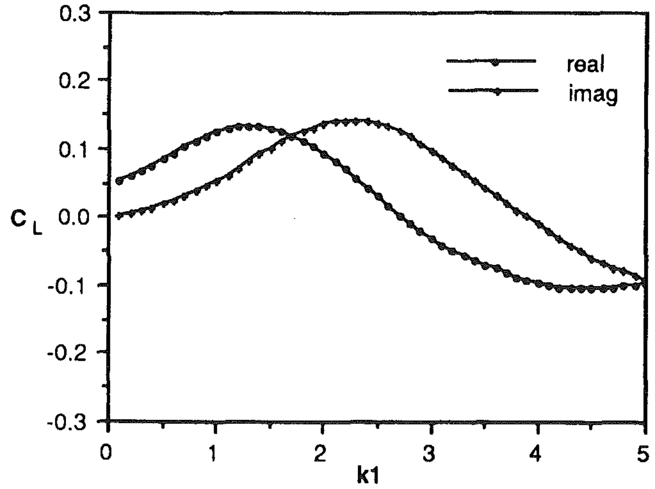

Fig. 12 Real and imaginary parts of the unsteady lift coefficient C_L versus reduced frequency k_1 for the first standard configuration in a three-dimensional gust without sweep (case 3). $M_{-\infty} = 0.18$.

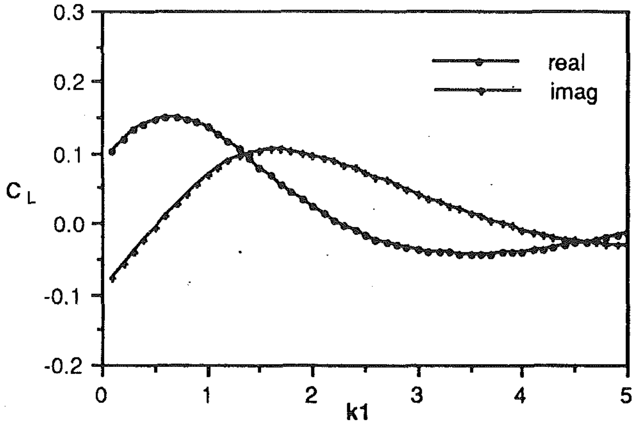

Fig. 13 Real and imaginary parts of the unsteady lift coefficient C_L versus reduced frequency k_1 for the first standard configuration in a three-dimensional gust with sweep (case 4). $M_{-\infty} = 0.18$.

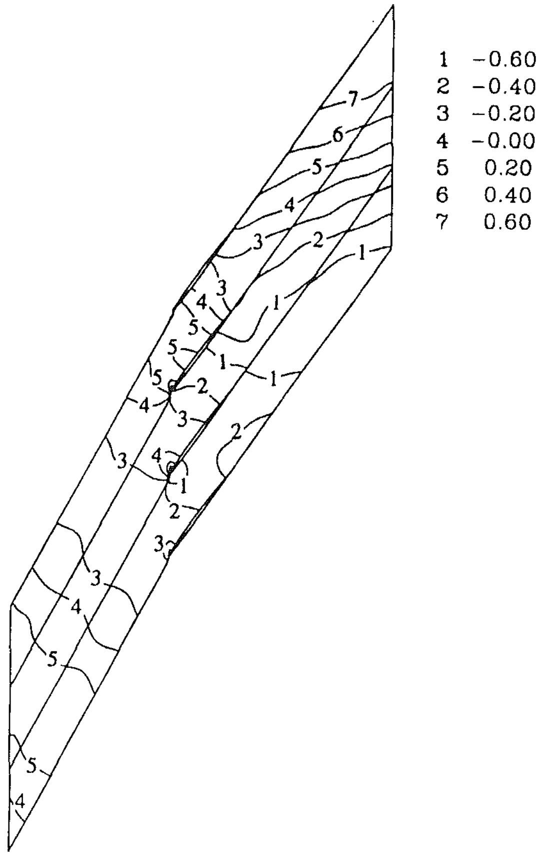

Fig. 14 Contours of the real part of the normalized unsteady pressure P' for the first standard configuration in a gust a = (0, 1, 0), k = (4, 0, 0). $M_{-\infty} = 0.18$.

Figures 10, 11, 12, and 13 show the real and imaginary parts of the unsteady lift coefficient for cases 1 to 4, respectively. For case 3 (Fig. 12) and case 4 (Fig. 13), there are no acoustic waves in the far field in the entire range of frequencies studied. The unsteady lift variations are smooth curves with respect to the reduced frequency. For case 1 (Fig. 10), one upstream mode and one downstream mode cut on at $k_1 \approx 3.9$. For case 2 (Fig. 11), one upstream mode and one downstream mode cut on at $k_1 \approx 2.7$ and cut off at $k_1 \approx 3.5$.

Comparing the results for this cascade configuration with those of the third configuration given in the last section, one can notice that a smaller mean flow turning cascade (the first standard configuration) induces a smaller unsteady lift. This difference becomes larger for two and three-dimensional gusts.

For three-dimensional gust with sweep, for both large and small turning mean flow, the unsteady lift decreases quickly as the reduced frequency increases. However, this difference is relatively small for one-dimensional gust but still exists. As an exception, when the system approaches the acoustic cut-on, the unsteady lift becomes large for a one-dimensional gust and then it drops quickly as the acoustic wave cuts on (see Fig. 10). This shows again the strong effects of the cut-on or cut-off of far field acoustics on the near field unsteady pressure.

The unsteady pressure field for gust $\mathbf{a} = (0, 1, 0)$ $\mathbf{k} = (4, 0, 0)$ is shown in Fig. 14. There is one upstream acoustic mode propagating in a direction of 228.8 deg from the machine axis. Also there is one downstream acoustic mode with a propagation direction of -59.2 deg from the machine axis. These results are in conformity with those predicted analytically.

5 Conclusion

Numerical solutions based on Atassi and Grzedzinski's [8] linearized analysis have been developed for subsonic compressible flows around a cascade of loaded airfoils subject to a three-dimensional gust. The numerical scheme developed can be used for a wide variety of unsteady vortical flow problems for a broad range of low and high reduced frequencies and Mach numbers.

This work presented the detailed aerodynamic results for two standard configurations for the unsteady response. The unsteady pressure fields were also given in contour form to demonstrate the near field unsteady pressure as well as the far field acoustics for two typical loaded cascades in a gust. These contours show that the present far field condition derived by Fang and Atassi [4, 5] satisfies the requirement of nonreflective acoustic radiation condition. It is hoped that the present results will be used as benchmarks for comparison with experiments and fully nonlinear codes.

This work demonstrated the effect of three-dimensional gust upstream condition on the unsteady responses for two typically loaded cascades. It was shown that the gust parameters strongly affect the cascade aerodynamic response. Especially, when the change of the gust parameters causes acoustic cut-ons or cut-offs, the cascade unsteady response is strongly affected.

The numerical scheme developed in the present work is highly efficient. Typical computation time per frequency is less than one minute on a scientific workstation RS/6000-530.

Acknowledgments

This work is supported by NASA Lewis Research Center under Grant NAG 732. The authors would like to thank John F. Groeneweg and Dennis Huff of NASA Lewis Research Center for their support and assistance.

References

1 Atassi, H. M., "Unsteady Vortical Disturbances About Bodies," in: *Proceedings of the Tenth U.S. National Congress of Applied Mechanics*, J. P. Lamb, ed., ASME, 1986.

2 Goldstein, M. E., and Atassi, H. M., "A Complete Second-Order Theory for the Unsteady Flow About an Airfoil Due to a Periodic Gust," *J. Fluid Mech.*, Vol. 74, 1976, pp. 741–765.

3 Atassi, H. M., "The Sears Problem for a Lifting Airfoil Revisited—New Results," *J. Fluid Mech.*, Vol. 141, 1984, pp. 109–122.

4 Fang, J., "Compressible Flows With Vortical Disturbances Around a Cascade of Airfoils," PhD thesis, University of Notre Dame, April 1991.

5 Fang, J., and Atassi, H. M., "Linearized Analysis of Cascade of Loaded Airfoils in a Gust," in: H. M. Atassi, ed., *Unsteady Aerodynamics, Aeroacoustics and Aeroelasticity of Turbomachines and Propellers*, Springer-Verlag, 1993, pp. 149–176.

6 Fang, J., and Atassi, H. M., "Aerodynamics of Loaded Cascade in Subsonic Flows Subject to Unsteady Three-dimensional Vortical Disturbances," AIAA Paper No. 92-0146, 1992.

7 Goldstein, M. E., "Unsteady Vortical and Entropic Distortions of Potential Flows Round Arbitrary Obstacles," *J. Fluid Mech.*, Vol. 89, 1978, pp. 433–468.

8 Atassi, H. M., and Grzedzinski, J., "Unsteady Disturbances of Streaming Motions Around Bodies," *J. Fluid Mech.*, Vol. 209, 1989, pp. 385–403.

9 Scott, J. S., "Compressible Flows With Periodic Vortical Disturbances Around Lift Airfoils," PhD thesis, University of Notre Dame, April 1990.

10 Scott, J. S., and Atassi, H. M., "Numerical Solutions of the Linearized Euler Equations for Unsteady Vortical Flows Around Lifting Airfoils," AIAA Paper No. 90-0694, 1990.

11 Hall, K. C., and Verdon, J. M., "Gust Response Analysis for Cascade Operating in Nonuniform Mean Flows," *AIAA Journal*, Vol. 29(9), Sept. 1991, pp. 1463–1471.

12 Bolcs ET, A., and Fransson, T. H., "Aeroelasticity in Turbomachines, Comparison of Theoretical and Experimental Cascade Results, Communication du Laboratoire de Thermique Appliquee et de Turbomachines," Technical Report, Lausanne, EPFL, 1986.

13 Atassi, H. M., ed., *Unsteady Aerodynamics, Aeroacoustics and Aeroelasticity of Turbomachines, and Propellers*, Springer-Verlag, 1993.

14 McFarland, E. R., "A Rapid Blade-to-Blade Solution for Use in Turbomachinery Design," ASME *Journal of Engineering for Gas Turbines and Power*, Vol. 106, 1984, pp. 376–382.

15 Ventres, C. S., "Nonsteady Compressible Aerodynamics Code for Linear Cascade," private communication.

E. H. Abed
Professor,
Department of Electrical Engineering and the
Institute for Systems Research,
University of Maryland,
College Park, MD 20742

P. K. Houpt
Manager, Systems and
Architectures Program,
Control Systems Laboratory,
Corporate Research and
Development Center,
General Electric Company,
Schenectady, NY 12301

W. M. Hosny
Staff Engineer,
Engine Operability Division,
Aircraft Engines Business Group,
General Electric Company,
Cincinnati, OH 45215

Bifurcation Analysis of Surge and Rotating Stall in Axial Flow Compressors

The surge and rotating stall post-instability behaviors of axial flow compressors are investigated from a bifurcation-theoretic perspective, using a model and system data presented by Greitzer (1976a). For this model, a sequence of local and global bifurcations of the nonliner system dynamics is uncovered. This includes a global bifurcation of a pair of large-amplitude periodic solutions. Resulting from this bifurcation are a stable oscillation ("surge") and an unstable oscillation ("anti-surge"). The latter oscillation is found to have a deciding significance regarding the particular post-instability behavior experienced by the compressor. These results are used to reconstruct Greitzer's (1976b) findings regarding the manner in which post-instability behavior depends on system parameters. Although the model does not directly reflect nonaxisymmetric dynamics, use of a steady-state compressor characteristic approximating the measured characteristic of Greitzer (1976a) is found to result in conclusions that compare well with observation. Thus, the paper gives a convenient and simple explanation of the boundary between surge and rotating stall behaviors, without the use of more intricate models and analyses including nonaxisymmetric flow dynamics.

1 Introduction

A factor that severely limits the operating envelope of modern gas turbine jet engines is the fact that the axial flow compressor can become unstable when operated near its maximum achievable pressure rise. At such an operating condition, a moderate disturbance can result in instability, or even loss, of the nominal operating point. In this circumstance, the compression system can assume one of basically two types of dynamic behavior. The first, known as *surge*, is a large-amplitude, periodic oscillation in which the compressor experiences a series of rapid flow reversals and recovery. The second, which is the more serious of the two, is known as *rotating stall* (or *nonrecoverable stall*). This behavior is characterized by very inefficient engine operation at constant mass flow and pressure rise. A complete shutdown of the engine and subsequent restart are usually required for recovery from this type of stall.

In this paper we investigate, from a bifurcation-theoretic perspective, the surge and rotating stall post-instability dynamic behavior of axial flow compressors. The model employed here is obtained directly from the theoretical compression system model presented by Greitzer (1976a), using also the data given by Greitzer (1976a, b) for an experimental compressor rig. For the model considered here, a sequence of local and global bifurcations of the nonlinear system dynamics is uncovered. This is used to reconstruct the findings of Greitzer (1976a) regarding the manner in which post-instability behavior depends on system parameters.

Greitzer (1976a) introduced a lumped parameter, nonlinear model of axial flow compressor dynamics, simulations of which agreed with experimental results (Greitzer, 1976b). Among the key contributions of (Greitzer, 1976a) was the introduction of a nondimensional parameter, B, the value of which was found to be a determinant of the nature of post-instability compressor behavior (surge versus rotating stall). Subsequently, others (Razavi, 1985; McCaughan, 1989a) have discussed surge and rotating stall behavior in the context of bifurcation theory. A particular bifurcation sometimes associated with surge, for instance, is the Hopf bifurcation, i.e., the emergence of a periodic solution from an equilibrium point as a parameter is quasistatically varied. The main assumption in the Hopf Bifurcation Theorem is that a pair of eigenvalues of the system linearization crosses the imaginary axis transversely at a critical value of the parameter (see, e.g., Hassard et al., 1981). Since, however, the Hopf bifurcation results in a small-amplitude periodic solution, and surge is known to be a large-amplitude motion, it is clear that some care is necessary in linking this bifurcation with the surge phenomenon. McCaughan (1989a), using a model including nonaxisymmetric dynamics (Moore and Greitzer, 1986), finds a global bifurcation of the periodic orbit resulting from a Hopf bifurcation. She links this global bifurcation with surge. In the present work, which was done independently of McCaughan (1989a, b), a similar global bifurcation is found for the simpler model addressed here.

The scope of the present paper is limited to an analysis of a theoretical compression system model (Greitzer, 1976a),

---

Contributed by the International Gas Turbine Institute and presented at the American Control Conference, San Diego, California, 1990. Manuscript received by the International Gas Turbine Institute October 22, 1992. Associate Technical Editor: L. S. Langston.

which has been refined significantly in later publications (Moore and Greitzer, 1986). Bifurcation analysis of these more intricate models, which account carefully for nonaxisymmetric dynamics, has been carried out independently by McCaughan (1989a, b) and by the authors and co-workers. However, the present paper is unique in two ways: (*i*) It results in a bifurcation-theoretic understanding of surge and rotating stall for the simple model of Greitzer (1976a) without the technical intricacies associated with more complex models; and (*ii*) the compressor characteristic used in this paper is based directly on the experimentally measured characteristic reported by Greitzer (1976a, b). By limiting the analysis for the most part to a second-order dynamic model, and by employing an analytical model based directly on Greitzer's (1976a, b) theoretical and experimental work, it is hoped that the present paper will be accessible to a wide audience and illustrate clearly the importance of bifurcations in the study of the surge and rotating stall phenomena.

We present evidence for a bifurcation sequence that predicts the observations of Greitzer (1976a) for both surge and rotating stall. Hopf bifurcation is accounted for in this work, but its role can be viewed as being of secondary significance. In this discussion, rotating stall and surge and their dependence on B are considered from a global bifurcation standpoint. Special care is taken in the choice of an analytical model for the steady-state compressor characteristic, which closely matches that reported by Greitzer (1976a). Using this characteristic, we detect a global (so-called "cyclic fold") bifurcation of a pair of large-amplitude periodic solutions. One of these is a stable limit cycle and corresponds to the surge type of stall, while the second is unstable and is therefore unobserved in experiments. We refer to this latter unstable oscillation as the *antisurge* oscillation, and to the former as the *surge* limit cycle. We find that the changing size and shape of the antisurge oscillation determines the critical value of B at which the post-instability behavior of the compression system switches from rotating stall to surge.

The presence of the global bifurcation of the surge and antisurge oscillations noted above depends strongly on the assumed compressor characteristic. For example, a cubic characteristic would not support such a bifurcation. We have chosen a more complicated algebraic model of the characteristic that faithfully represents *essential features* of the experimentally obtained characteristics studied by Greitzer (1976a, b). The critical values of B reported here do not coincide exactly with those found by Greitzer (1976a). There are many possible reasons for this, one of which is that the model used in our calculations is actually a reduced order version of the model of Greitzer (1976a), obtained by setting certain time constants to zero. Further simulations, in which these time constants are assigned appropriate positive values, have been done and do result in numerical agreement. These simulations are not of significant interest in themselves, and will not be presented here.

McCaughan (1989a) focused on an extension of Greitzer's model (Moore and Greitzer, 1986) that reflects nonaxisymmetric flow dynamics in addition to the axisymmetric flow dynamics assumed in the model of Greitzer, (1976a). In the present work, the *steady-state* compressor characteristic, being based on the experimental (*measured*) characteristic reported by Greitzer (1976a, b), does reflect the actual nonaxisymmetric flow of the real compressor. However, nonaxisymmetric flow *dynamics* are not modeled here, although the results of Moore and Greitzer (1986) can be used to extend the present work in that direction. In doing so, one would need to arrive at a new axisymmetric (*not measured*) characteristic, which, when used in the model of Moore and Greitzer (1986), results in the measured characteristic reported by Greitzer (1976a). This, in itself, is an interesting identification problem.

The paper is organized as follows. In Section II, we recall a nonlinear lumped parameter model from Greitzer (1976a) for the dynamics of an axial flow compressor, and summarize the observations of Greitzer (1976a) regarding dependence of the particular type of post-instability behavior on system parameters. In Section III, singular perturbation is used to reduce the order of the fourth-order model of Section II, resulting in a second-order nonlinear model. The model used in our simulations for the steady-state compressor characteristic is also discussed in Section III. In Section IV, we present the bifurcation sequence that occurs as an important nondimensional parameter B (Greitzer, 1976a) is quasi-statically varied. Analytical and simulation evidence for this bifurcation sequence, and implications for post-instability behavior, are also given in Section IV.

II Lumped Parameter Nonlinear Model

In this section, we recall the lumped parameter model of Greitzer (1976a) and summarize his observations regarding the circumstances of the appearance of the rotating stall and surge types of instabilities as a function of the nondimensional parameter B.

II.1 The Model. The fourth-order lumped parameter model introduced by Greitzer (1976a) is given, in nondimensional variables, by:

$$\frac{d\dot{m}_c}{dt}=B(C-\Delta P) \tag{1}$$

$$\frac{d\dot{m}_T}{dt}=\left(\frac{B}{G}\right)(\Delta P-F) \tag{2}$$

$$\frac{d\Delta P}{dt}=\left(\frac{1}{B}\right)(\dot{m}_c-\dot{m}_T) \tag{3}$$

$$\frac{dC}{dt}=\left(\frac{1}{\tau}\right)(C_{ss}-C) \tag{4}$$

Here, $\dot{m}_c$ (or $\dot{m}_T$) is the nondimensional compressor (or throttle) mass flow, ΔP is the nondimensional plenum pressure rise, and C is the nondimensional compressor pressure rise. The tilde notation used by Greitzer (1976a) for nondimensionalized quantities (e.g., $\tilde{\dot{m}}_c$, $\Delta\tilde{P}$) is not used here, due to the appearance here of only the nondimensional variables. Otherwise, the notation used above agrees with that of Greitzer. The steady-state compressor pressure rise characteristic is denoted by C_{ss} in Eq. (4), while F denotes the throttle pressure drop characteristic (both nondimensionalized). Three parameters appear in Eqs. (1)-(4): B, G, and τ. The first, B, is proportional to rotor speed. Expressions for the parameters B, G, and τ in terms of physical system parameters are given by Greitzer (1976a). Note that Eqs. (1)-(3) are based on physical considerations and a simplified system representation, while Eq. (4) is phenomenological and is meant to model the inherent relaxation of compressor pressure rise to the steady-state characteristic. Hence, the value of the time constant τ is to be obtained experimentally.

The compressor and throttle characteristics C_{ss} and F, respectively, are of fundamental importance in the analysis of system (1)-(4). This is because these characteristics are the source of the nonlinearity of Eqs. (1)-(4). The steady-state compressor characteristic C_{ss} (for an axial flow compressor) is often modeled as in Fig. 1, in which a hysteresis loop appears. Note that for such a plot, the nondimensional plenum pressure rise ΔP is not a single-valued function of the axial velocity parameter $\dot{m}_c$. Note also that the plot contains two (hysteresis) branches, which do not represent quasi-steady behavior, but rather indicate a "jump" (fast transient) between the lower and upper main branches of the characteristic. A quasi-steady characteristic may be obtained from that of Fig. 1 by replacing

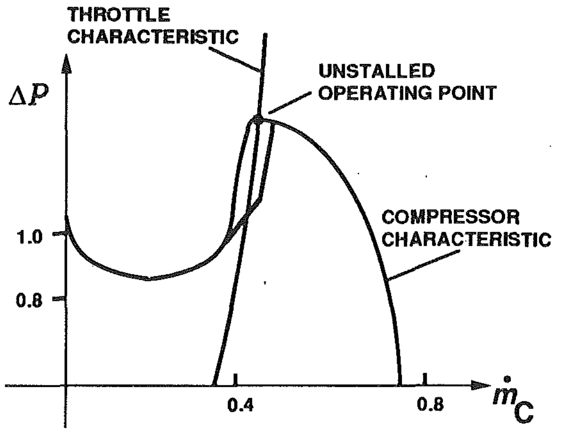

Fig. 1 Generic compressor and throttle characteristics

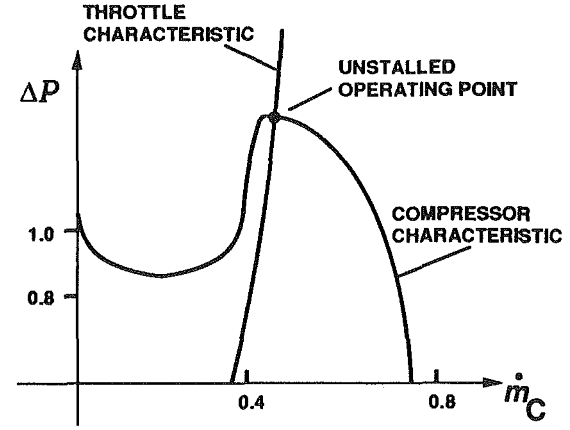

Fig. 2 Single-valued compressor and throttle characteristics

the two "jump branches" in the compressor characteristic with a single "transient branch" connecting the upper and lower branches of the characteristic, and smoothly connecting the remaining upper and lower branches of the characteristic. This is depicted in Fig. 2 for the case in which the transition branch is positively sloped. With a positively sloped transition branch, the compressor characteristic is single-valued. Were the transition branch negatively sloped, the overall compressor characteristic would, at least for a range of values of mass flow rate, be triple-valued. Even a single-valued compressor characteristic (such as that depicted in Fig. 2), however, can be consistent with the presence of a hysteresis loop. Loosely speaking, if the overall slope of the characteristic in the regime where hysteresis can occur is large compared to the throttle line slope, then hysteresis would occur as the throttle is slightly closed and then reopened. Thus, one is not removing the possibility of hysteresis by assuming a single-valued compressor characteristic.

To facilitate computer simulation of the model, we shall in the following adopt such a single-valued compressor characteristic. As for the throttle characteristic F, a typical plot also appears in Fig. 1. Note that this is a single-valued function giving the throttle pressure drop F in terms of the throttle mass flow $\dot{m}_T$. Moreover, the curve always has positive slope, and, for a variable area nozzle or valve type throttle, with ambient static pressure at the throttle discharge plane, we have the explicit representation

$$F=\left(\frac{A_c^2}{A_T^2}\right)\dot{m}_T^2 \tag{5}$$

in terms of the flow-through compressor and throttle areas A_c and A_T, respectively.

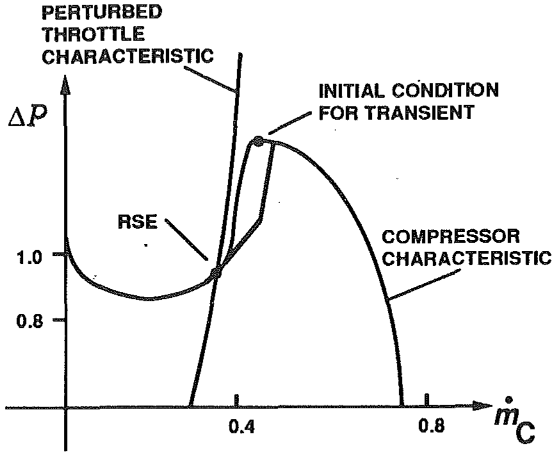

Fig. 3 Showing effect of perturbed throttle characteristic

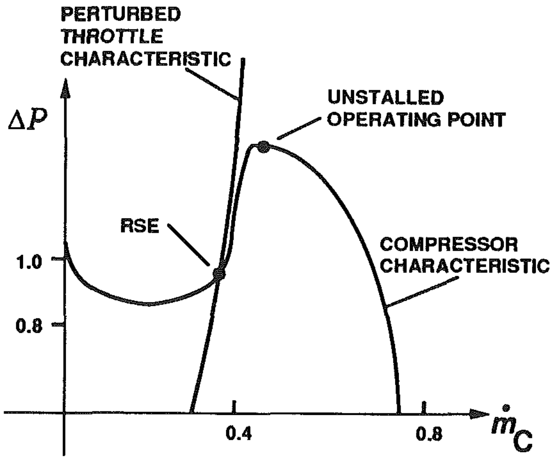

Fig. 4 Showing effect of perturbed throttle characteristic

II.2 Dynamic Behavior. Next we proceed to give a brief summary of the influence of the value of B on the dynamic behavior of Eqs. (1)-(4), as discussed by Greitzer (1976a, b). All physical data used by Greitzer originated from an experimental three-stage axial compressor. For each case of interest, the model (1)-(4) was simulated and the results were compared with those obtained experimentally.

To understand the manner in which initial conditions for the simulation were set up, we first investigate the conditions for equilibrium operation of Eqs. (1)-(4). At an equilibrium point, we have

$$C=C_{ss}=\Delta P=F \tag{6}$$

and

$$\dot{m}_c=\dot{m}_T \tag{7}$$

Therefore, an equilibrium point of Eqs. (1)-(4) occurs at the intersection of the compressor and throttle characteristics, graphed relative to the independent variable $\dot{m}_c$ (or, equivalently, $\dot{m}_T$). This is the same as saying that the steady-state operating point is determined by the requirements that (i) the mass flow through the compressor and the throttle are the same, and (ii) the pressure rise through the compressor equals the pressure drop through the throttle. Figure 1 depicts this situation for a stable operating point near the peak of the steady-state compressor characteristic.

Each simulation and corresponding experiment reported by Greitzer (1976a, b) begins from an initial condition obtained by perturbing the throttle line slightly to the left of its position in Fig. 1, with the operating point initially near the peak of the compressor characteristic. This is depicted in Fig. 3. (Figure 4 depicts the effect of such a pertubation assuming a single-

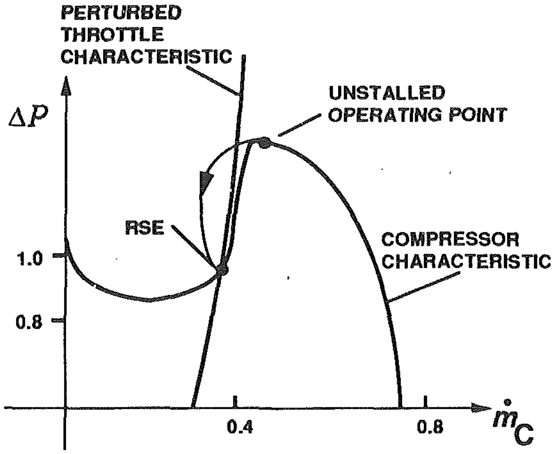

Fig. 5 Showing overdamped convergence to rotating stall

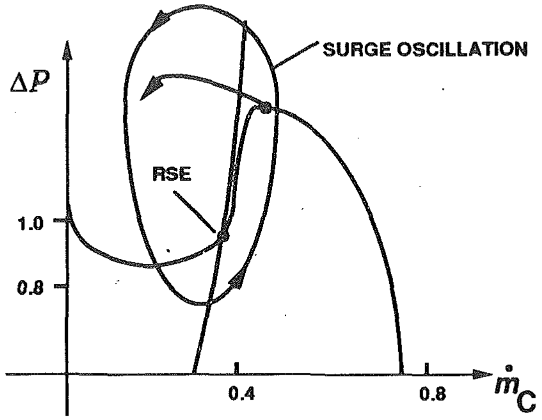

Fig. 6 Convergence to surge oscillation

valued steady-state compressor characteristic of the type shown in Fig. 2) Such a perturbation of the throttle line may result, for instance, from slightly closing the throttle (cf. Eq. (5)). Depending on the values of system parameters, especially B, the system was then observed either to converge to the equilibrium point on the lower branch of the compressor characteristic (rotating stall), or to converge to a large amplitude periodic motion (surge). In Figs. 3 and 4, the equilibrium on the lower branch of the compressor characteristic is denoted RSE, for *rotating stall equilibrium*.

The general dependence on B of the mode of stall encountered is now reviewed. For each of the following cases, we are concerned mainly with the trajectory starting from the initial condition identified above, namely that at the peak of the compressor characteristic, with the throttle line perturbed slightly to the left of the peak of the compressor characteristic (as in Figs. 3 and 4). The four cases are referred to as Regimes 1, 2, 3, and 4. Analytical and simulation evidence will be given in Section IV for these behaviors.

Regime 1: Small B. For small values of B, the trajectory settles on the rotating stall equilibrium. The motion is "overdamped," i.e., it doesn't exhibit an oscillatory component. (This is depicted in Fig. 5.)

Regime 2: Moderate B. At some point, although rotating stall is still the eventual limit of the trajectory, the transient is no longer overdamped, but is oscillatory.

Regime 3: Large B. For larger values of B, the trajectory no longer seeks the rotating stall equilibrium point, but rather converges to a large amplitude limit cycle motion. This is known as surge. (This is depicted in Fig. 6.)

Regime 4: Very Large B. As B is increased further, the system still converges to a large-amplitude, surge oscillation, but the nature and frequency of this limit cycle change drastically. Specifically, the limit cycle is now characterized by two time scales: a slow time scale while the trajectory remains near ("hugs") the compressor characteristic, and a fast time scale for motion between the main (left and right) compressor branches. (A figure illustrating this motion is given in Section IV.2.)

In the next section, the analytical model used in subsequent simulations is given. This involves order reduction of the model (1)-(4) as well as specification of the throttle and compressor characteristics.

III Second-Order Nonlinear Model

In this section, the surge and rotating stall instabilities and their dependence on B are obtained as byproducts of a general nonlinear dynamic study of Eqs. (1)-(4). The first step is to redraw the steady-state compressor characteristic in a way that facilitates the analysis.

III.1 Nonaxisymmetric Single-Valued Compressor Characteristic. As noted above, the hysteresis portion of the steady-state compressor characteristic as it is typically drawn (see Fig. 1) contains a deficiency. That is, it includes two branches that represent fast, *transient motions* as opposed to steady-state behavior. Instead, we choose to employ a single-valued function as in Fig. 2. The particular characteristic is presented in Section IV.2 below, which contains computer simulations illustrating the paper's main results.

III.2 Second-Order Reduced Model. The primary variables to the compressor user are mass flow ($\dot m_c$) and delivery pressure (ΔP) (Greitzer, 1976a). It is possible to approximate the fourth-order compressor model (1)-(4) by a second-order model in these variables alone. Although this approximation is not necessary for the results given below, it is useful in simplifying computations. Two basic assumptions are needed to perform the model order reduction: first, that the relaxation to the steady-state compressor characteristic implied by Eq.(4) occurs in a very short time (i.e., τ is small), and second, that the throttle inertial forces are negligible.

The first of these assumptions enables us to neglect Eq. (4) and replace C in Eq. (1) by C_{ss}. This is easily justified using Tikhonov's Theorem from singular perturbation theory, since τ may be viewed as a singular perturbation parameter. The second assumption implies

$$\Delta P = F(\dot m_T), \tag{8a}$$

and hence that $\dot m_T$ is given by

$$\dot m_T = F^{-1}(\Delta P) \tag{8b}$$

These facts imply that the primary variables $\dot m_c$, ΔP, are governed approximately by the system

$$\frac{d\dot m_c}{dt} = B(C_{ss}(\dot m_c) - \Delta P) \tag{9}$$

$$\frac{d\Delta P}{dt} = \left(\frac{1}{B}\right)\ (\dot m_c - F^{-1}(\Delta P)) \tag{10}$$

For the quadractic throttle characteristic (5), the system (9), (10) takes the form

$$\frac{d\dot m_c}{dt} = B(C_{ss}(\dot m_c) - \Delta P) \tag{11}$$

$$\frac{d\Delta P}{dt} = \left(\frac{1}{B}\right)\ \left(\dot m_c - \frac{A_T}{A_c}(\Delta P)^{1/2}\right) \tag{12}$$

Before investigating analytically the second-order model (9), (10) (or (11), (12)), we should discuss the equilibrium points of the system. Consider either a hysteretic characteristic as in Fig. 1, or a single-valued characteristic as in Fig. 2. Depictions of an "equivalent" throttle line relating ΔP and $\dot{m}_c$ appear in Figs. 1 and 2, along with the compressor characteristic. Equilibrium points are given by the points of intersection of the compressor characteristic and the throttle line. If the throttle line is moved to the left (closing the throttle), the rotating stall equilibrium point appears, as shown in Figs. 3 and 4, respectively.

IV Bifurcations and Stall Phenomena

IV.1 Local Analysis at Rotating Stall Equilibrium Point. Denoting by superscript 0 an equilibrium value of a state variable, and by a prime differentiation with respect to the argument of a function, the Jacobian matrix of the second-order reduced model (11), (12) is given by

$$B\begin{pmatrix} C_{ss}'(\dot{m}_c^0) & -1 \\ B^{-2} & -0.5A_TA_c^{-1}B^{-2}(\Delta P^0)^{-1/2} \end{pmatrix} \tag{13}$$

Singular perturabtion results imply that as $B\rightarrow 0$ the eigenvalues of the Jacobian matrix are asymptotically given by

$$B\left(C_{ss}'(\dot{m}_c^0)-2\frac{A_c}{A_T}(\Delta P^0)^{1/2}\right)+O(B^2), \tag{14a}$$

and

$$-\frac{A_T}{2A_cB(\Delta P^0)^{1/2}}+O(1). \tag{14b}$$

Each of the two quantities is both real and negative. (The former is negative because of the steepness of the throttle line, i.e., A_c/A_T is large, and, concurrently, $C_{ss}'(\dot{m}^0)$ is relatively small.) The negativity of the eigenvalues for small B is in agreement with the behavior discussed for Regime 1 in Section II.2 above, since it implies *overdamped* convergence of *nearby* trajectories to the equilibrium. Nothing can yet be said regarding the global behavior of trajectories.

As B increases, the asymptotic formulae (14*a*), (14*b*) suggest that the eigenvalues approach one another, meet, and break off in conjugate directions into the complex plane. This can be checked with the aid of the characteristic polynomial of the Jacobian matrix (13). It is more convenient to work with the following polynomial, which is the characteristic polynomial of $1/B$ times the matrix of Eq. (13):

$$\lambda^2+\left(\frac{A_T}{2A_CB^2(\Delta P^0)^{1/2}}-C_{ss}'(\dot{m}_c^0)\right)\lambda+\frac{1}{B^2}\left(1-\frac{A_TC_{ss}'(\dot{m}_c^0)}{2A_c(\Delta P^0)^{1/2}}\right) \tag{15}$$

The calculations are a bit involved.

The conditions for a Hopf bifurcation to occur for a given value of B at a known equilibrium point are, from C_{ss}', that

$$\frac{A_T}{2A_cB^2(\Delta P^0)^{1/2}}-C_{ss}'(\dot{m}_c^0)=0, \text{ and} \tag{16a}$$

$$1-\frac{A_TC_{ss}'(\dot{m}_c^0)}{2A_c(\Delta P^0)^{1/2}}>0 \tag{16b}$$

Note that, since $C_{ss}'(\dot{m}_c^0)$ is negative at the original stable operating point (at the peak of the compressor characteristic), condition (16*a*) cannot be satisfied there. So a Hopf bifurcation cannot occur at that equilibrium. However, conditions (16*a*), (16*b*) can be satisfied at the rotating stall equilibrium point. Indeed, condition (16*a*) implies that the corresponding value of B is

$$B_{\text{Hopf}}^c=\left(\frac{A_T}{2A_c(\Delta P^0)^{1/2}C_{ss}'(\dot{m}_c^0)}\right)^{1/2} \tag{17}$$

From Eqs. (5) and (6) it follows, however, that

$$F'(\dot{m}_T^0)=2\left(\frac{A_c}{A_T}\right)^2\dot{m}_T^0$$

$$=2\frac{A_c}{A_T}(\Delta P^0)^{1/2} \tag{18}$$

Together, Eqs. (17) and (18) imply

$$B_{\text{Hopf}}^c=\frac{1}{(F'(\dot{m}_c^0)C_{ss}'(\dot{m}_c^0))^{1/2}}. \tag{19}$$

IV.2 Bifurcation Sequence and Post-instability Behavior. In this section, the facts discussed above are pieced together to yield an overall picture of the global dynamics of the system (1)-(4) as a function of the nondimensional parameter B. The transition from overdamped to underdamped convergence to the rotating stall equilibrium as B is raised has already been explained. Also, we have seen that as B is increased further, the rotating stall equilibrium undergoes a Hopf bifurcation and simultaneously loses its stability. The conclusions we reach in this section are based on a combined use of analysis and simulation. In the simulations, the steady-state compressor characteristic is modeled using a complicated algebraic formula (half a page long). The details of this formula are not important, and so it will not be given here. Instead, we simply note that this formula achieves a characteristic curve that is a good approximation to that reported by Greitzer (1976a, b) for a specific three-stage compressor. Since this work was completed, the same characteristic has been coded using cubic splines. This provides a more flexible model, and was found also to simplify numerical calculations requiring differentiation.

We make some brief remarks on the simulations and the manner in which they are reported in the figures. The simulations were performed using the SIMNON software package (Elmqvist, 1975). The figures illustrating simulation results also include the SIMNON commands used to generate the simulations. In the SIMNON code, $\dot{m}_c$ and ΔP were denoted by *mcd* and *pd*, respectively. The notation *mcdr* and *pdr* occurs in the commands in figures generated by simultaneous simulations in both forward and reverse time. These are the variables $\dot{m}_c$ and ΔP, respectively, computed in reverse time.

Generally, for small values, of B, if the throttle line is perturbed so as to intersect the compressor characteristic only at the rotating stall equilibrium, then the latter equilibrium is the *global attractor* for the system. That is, every initial condition converges eventually to a rotating stall operating condition. Figure 7 depicts a simulation for the approximate model we

SIMNON COMMANDS:	>init mcd:0.48 >init pd:1.22 >plot pd(mcd) >par b:0.15 >simu 0 100 >

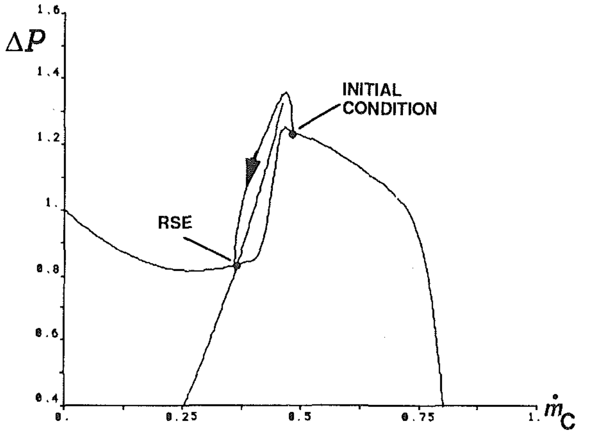

Fig. 7 Simulation showing convergence to rotating stall (B = 0.15)

SIMNON COMMANDS:

```
>init mcd:0.24872     >init pd:0.72609   >plot pd(mcd)
>par b:0.368      >init mcdr :0.43213  >init  pdr:0.9506
>simu  0  20     >plot  pdr(mcdr)    >simu   >
```

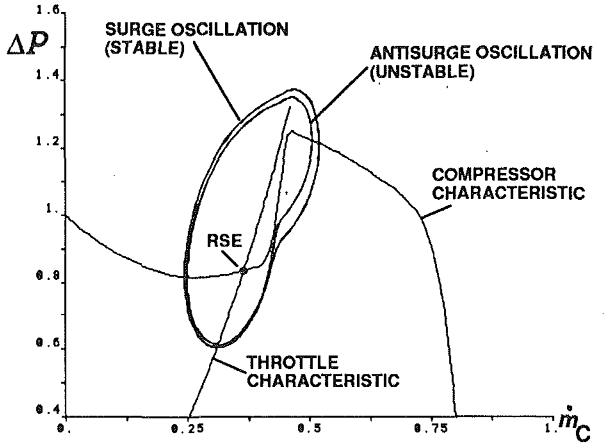

Fig. 8 Simulations showing birth of surge and antisurge oscillations (B = 0.368)

SIMNON COMMANDS:

```
>init mcd:0.23425      >init pd:0.58022   >plot pd(mcd)
>par b:0.45        >init mcdr :0.30193  >init  pdr:0.94693
>simu  0  20     >plot  pdr(mcdr)    >simu   >
```

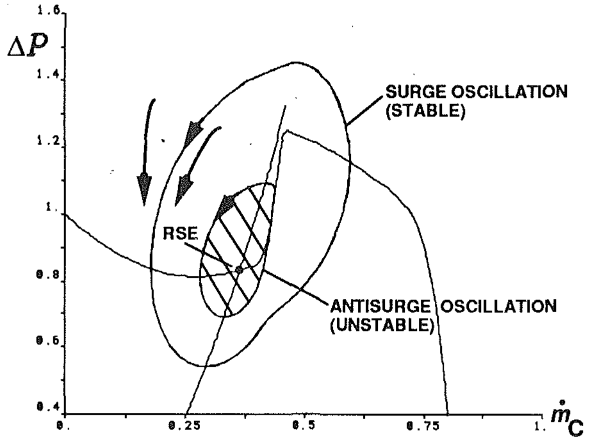

Fig. 9 Simulations showing stability domains and oscillations (B = 0.45)

SIMNON COMMANDS:

```
>init mcd:0.48       >init pd:1.22     >plot pd(mcd)
>par b:0.3757    >simu  0  20       >par b:0.3758
>simu 0 10     >
```

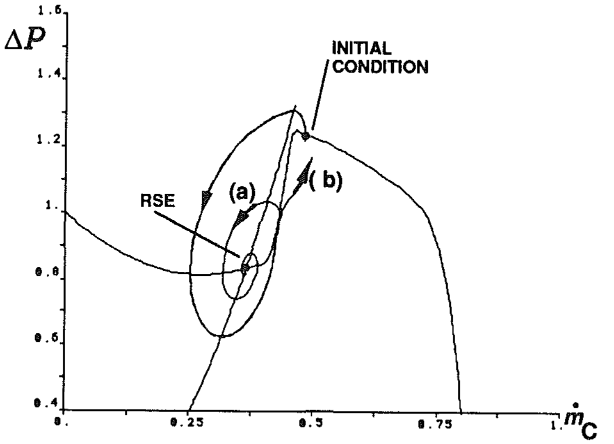

Fig. 10 Simulation (a) yields ratating stall (B = 0.3757); simulation (b) yields surge (B = 0.3758)

used for $B = 0.15$. This figure illustrates the behavior just noted for small values of B. (This can be seen to hold under general conditions by using a Liapunov function argument applied to a one-dimensional reduced-order system obtained by viewing B as a singular perturbation parameter. A simple quadratic Liapunov function in the (scalar) state variable of the reduced model can be seen to suffice.)

As B is raised past a value B_1, *two initially coincident periodic solutions are born, one stable and the other unstable*, and envelope the compressor characteristic. In the bifurcation literature, this is referred to alternatively as a cyclic fold bifurcation or a saddle-node bifurcation of periodic solutions (Thompson and Stewart, 1986). This is illustrated in Fig. 8, which depicts computer simulations of these periodic solutions for the hypothesized compressor characteristic. The unstable oscillation is found by simulation in *reverse time* with a judicious choice of initial conditions. Note that the unstable periodic solution lies within the stable one. We refer to that periodic solution as the *surge limit cycle* (or simply *surge*), and to the unstable periodic solution as the *antisurge oscillation* (or simply *antisurge*).

The antisurge oscillation forms the boundary of the domain of attraction of the rotating stall equilibrium point.[1] Note that, thus far, the peak of the compressor characteristic lies within the domain of attraction of the rotating stall equilibrium—agreeing with Greitzer's (1976a) simulation results (Regimes 1 and 2 of Section II.2 above). Thus, for these low values of B, rotating stall prevails as the steady-state post-instability behavior. In addition, the unstable periodic solution forms the finite part of the boundary of the domain of attraction of the companion stable periodic solution.

As B is increased further, the amplitude of the antisurge oscillation decreases steadily, until past a value B_2, the nominal equilibrium at the peak of the compressor characteristic no longer lies within this periodic solution. Instead, it now lies within the domain of attraction of the stable periodic solution, and so is attracted to it. *This is the initiation of surge* (Regime 3 of Section II.2 above). Figure 9 gives results of a simulation showing, in particular, the shrinking of the unstable periodic solution with increasing B. (In Fig. 9, $B = 0.45$). Figure 10 shows two simulations for the perturbed system, both starting at the same initial condition (the prestall equilibrium), but with slightly differing values of B. In one of the simulations, $B = 0.3757$, while in the other, $B = 0.3758$. For the smaller value of B, the rotating stall equilibrium is approached (trajectory (a) of Fig. 10). For the larger value of B, the surge oscillation is approached (trajectory (b) of Fig. 10). The simulation of Fig. 11 shows conclusively that this critical value of B, i.e., the value at which rotating stall gives way to surge, is precisely the value for which the antisurge oscillation passes through the initial condition.

As B is increased still further, the surge oscillation continues to envelope the compressor characteristic. In contrast, the unstable periodic solution shrinks, becoming vanishingly small, and finally collapses onto the rotating stall equilibrium point at some value B_3. Indeed,

$$B_3 = B^c_{\mathrm{Hopf}}$$

In Fig. 12, which corresponds to $B = 0.70$, the unstable periodic solution is shown by simulation to have reached a rather small amplitude. The Hopf bifurcation occurring in the model under consideration is simply this merging of the now small-

---

[1] This is true for the reduced second-order dynamic model. The implication for the full-order model is that the antisurge oscillation lies on the boundary of the domain of attraction.

SIMNON COMMANDS:	>init mcd:0.48 >init pd:1.22 >plot pd(mcd) >par b:0.3758 >simu 0 10 > init mcdr:0.48 >init pdr:1.22 >simu 0 20 >

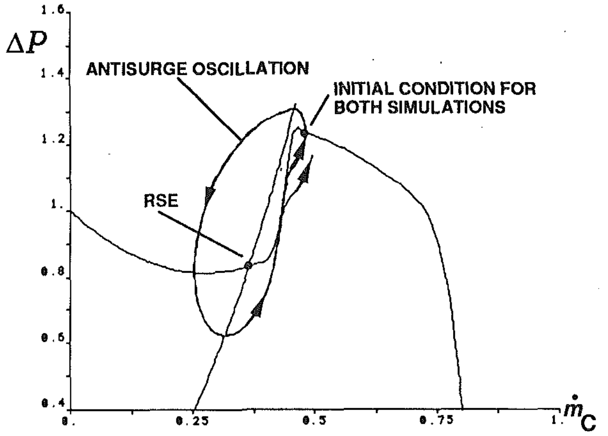

Fig. 11 Simulations showing coincidence of surge initiation and antisurge oscillation (B = 0.3758)

SIMNON COMMANDS:	>init mcd:0.31542 >init pd:0.53375 >plot pd(mcd) >par b:0.70 >init mcdr :0.41029 >init pdr:0.85673 >simu 0 20 >plot pdr(mcdr) >simu >

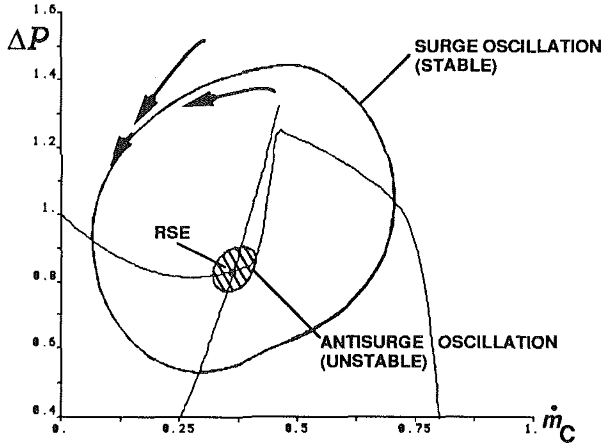

Fig. 12 Simulations showing shrinking antisurge oscillation (B = 0.70)

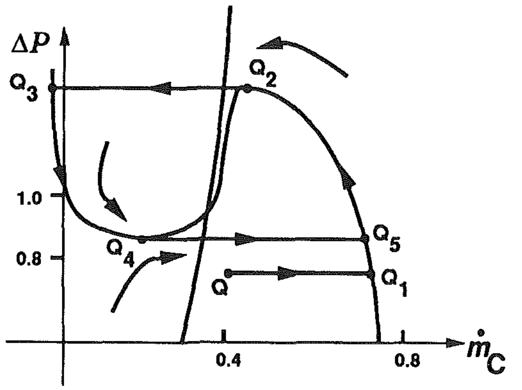

Fig. 13 Relaxation oscillation for very large B

amplitude antisurge oscillation with the rotating stall equilibrium point. For $B > B_3$, the rotating stall equilibrium point is no longer stable, and the unstable periodic solution no longer exists. The surge oscillation is now the global attractor of the system. Regime 3 of Section II.2 above is still in force.

We now proceed to prove the existence of this surge oscillation for very large B, and in doing so determine its location and character. For large B, the surge limit cycle is an instance of a *relaxation oscillation*, very much akin to the van der Pol oscillation. In this regime the oscillation is characterized by two widely separated time scales. This was observed by Greitzer (1976a), and was referred to as "Regime 4" in Section II.2 above. The situation is depicted in Fig. 13, which is purely illustrative. The proof below is closely related to a standard construction of the van der Pol oscillation (Nayfeh, 1973). See also Mischenko and Rozov (1980).

In the following, we admit any throttle characteristic F with positive slope. We divide Eq. (9) by Eq. (10) to get

$$\epsilon \frac{d\dot m_c}{d\Delta P} = \frac{C_{ss}(\dot m_c) - \Delta P}{\dot m_c - F^{-1}(\Delta P)} \tag{20}$$

where $\epsilon = B^{-2}$. If $\epsilon = 0$, then

$$\Delta P = C_{ss}(\dot m_c),$$

which states that solutions are relegated to the steady-state compressor characteristic. We shall assume that ϵ is very small, but nonzero. Referring to Fig. 13, consider a solution curve that starts at point Q. Since Q is off of the compressor characteristic, $d\dot m_c/d\Delta P$ is approximately $+\infty$ up to Q_1 where it hits the compressor characteristic. Since $d\dot m_c/d\Delta P$ is approximately $\pm\infty$ away from the compressor characteristic, the solution curve tends to stay on this characteristic. Also, from Eq. (10), and since point Q_1 lies to the right of the throttle line in Fig. 13, we will have that $d\Delta P/dt > 0$ while the solution remains near the right portion of the characteristic. This means that the trajectory will move away from Q_1 upward, until it reaches the vicinity of Q_2. There, the solution jumps horizontally to the left, since we will have $d\dot m_c/d\Delta P$ approximately $-\infty$. The solution then hits the compressor characteristic at Q_3 and again tends to remain on the characteristic. Since Q_3 lies to the left of the throttle line, Eq. (10) implies that $d\Delta P/dt < 0$ while the solution remains near the left portion of the characteristic. Hence the solution moves downward along this branch, until it arrives at the vicinity of point Q_4. There, it makes a horizontal rightward jump to Q_5. The solution exhibits a periodic counterclockwise motion thereafter, following the upper and lower branches of the compressor characteristic, with the exception of the horizontal jumps from Q_2 to Q_3 and from Q_4 to Q_5.

V Conclusion

A bifurcation sequence that is useful is explaining the dependence of observed stall behavior of axial flow compressors on the nondimensional parameter B has been presented. The model used is a simple nonlinear compression system model, which accounts for nonaxisymmetric flow only through the steady-state compressor characteristic, not dynamically. The presence of a global bifurcation of a periodic solution pair has been detected for this simple model and found to be of fundamental importance in predicting the nature of post-instability compression system behavior. Specifically, an unstable *antisurge* oscillation has been found to be present for a large range of values of the parameter, and the position of the initial condition relative to this oscillation was found to be a decisive factor in determining post-instability behavior. This gives a convenient and simple explanation of the boundary between surge and rotating stall behaviors, without the use of more advanced models including nonaxisymmetric flow dynamics. Analysis of the limiting cases of the bifurcation sequence as well as computer simulation have been employed in verifying its validity.

Acknowledgments

The authors are grateful to C. N. Nett for helpful discussions. They also thank R. Chen, L. P. Harris, D.-C. Liaw, R. Mani, A. Spang, and W. G. Steenken for many helpful comments. This work was supported in part by a contract to the University of Maryland from the General Electric Company, by NSF Grants ECS-86-57561 and CDR-88-03012, and by the AFOSR University Research Initiative Program under Grant AFOSR-90-0015.

References

Elmqvist, H., 1975, "SIMNON, An Interactive Simulation Program for Nonlinear Systems," Report TFRT-3091, Dept. of Automatic Control, Lund Institute of Technology, Lund, Sweden.

Greitzer, E. M., 1976a, "Surge and Rotating Stall in Axial Flow Compressors: Part I—Theoretical Compression System Model," ASME *Journal of Engineering for Power*, Vol. 98, pp. 190–198.

Greitzer, E. M., 1976b, "Surge and Rotating Stall in Axial Flow Compressors: Part II—Experimental Results and Comparison With Theory," ASME *Journal of Engineering for Power*, Vol. 98, pp. 199–217.

Hassard, B. D., Kazarinoff, N. D., and Wan, Y.-H., 1981, *Theory and Applications of Hopf Bifurcation*, Cambridge University Press, Cambridge, United Kingdom.

McCaughan, F. E., 1989a, "Application of Bifurcation Theory to Axial Flow Compressor Instability," ASME JOURNAL OF TURBOMACHINERY, Vol. 111, pp. 426–433.

McCaughan, F. E., 1989b, "Numerical Results for Axial Flow Compressor Instability," ASME JOURNAL OF TURBOMACHINERY, Vol. 111, pp. 434–441.

Mischchenko, E. F., and Rozov, N. Kh., 1989, *Differential Equations With Small Parameters and Relaxation Oscillations*, Plenum Press, New. York.

Moore, F. K., and Greitzer, E. M., 1986, "A Theory of Post-stall Transients in Axial Compression Systems: Part I—Development of Equations," ASME *Journal of Engineering for Gas Turbines and Power*, Vol. 108, pp. 68–76.

Nayfeh, A H., 1973, *Perturbation Methods*, Wiley, New York.

Razavi, H., 1985, "Nonlinear Global Stability Analysis of Compressor Stall Phenomena," Scientific Systems, Inc., Cambridge, MA; also, NASA CR-174908.

Thompson, J. M. T., and Stewart, H. B., 1986, *Nonlinear Dynamics and Chaos*, Wiley, Chichester, United Kingdom.